EDITORIAL BOARD

Academic Press is an imprint of Elsevier
The Boulevard, Langford Lane, Kidlington, Oxford, OX51GB, UK
32, Jamestown Road, London NW1 7BY, UK
Radarweg 29, PO Box 211, 1000 AE Amsterdam, The Netherlands
225 Wyman Street, Waltham, MA 02451, USA
525 B Street, Suite 1900, San Diego, CA 92101-4495, USA

First edition 2012

Library of Congress Cataloging-in-Publication Data
A catalog record for this book is available from the Library of Congress

British Library Cataloguing-in-Publication Data
A catalogue record for this book is available from the British Library

ISBN: 978-0-12-396534-9
ISSN: 1554-4516

Printed and bound in USA
12 13 14 15 11 10 9 8 7 6 5 4 3 2 1

CONTRIBUTORS

Revathi Appali
Institute of General Electrical Engineering, University of Rostock, Rostock, Germany, and Membrane Biophysics Group, The Niels Bohr Institute, University of Copenhagen, Copenhagen, Denmark

Vesna Arrigler
Institute of Biophysics, Faculty of Medicine, University of Ljubljana, Ljubljana, Slovenia

Alfred Blume
Institute of Chemistry—Physical Chemistry, Martin-Luther-University Halle-Wittenberg, Halle, Germany

Katarina Černe
Department of Pharmacology and Experimental Toxicology, Faculty of Medicine, University of Ljubljana, Ljubljana, Slovenia

Haim Diamant
Raymond and Beverly Sackler School of Chemistry, Tel Aviv University, Tel Aviv, Israel

Rumiana Dimova
Max Planck Institute of Colloids and Interfaces, Science Park Golm, Potsdam, Germany

Andreja Erman
Institute of Cell Biology, Faculty of Medicine, University of Ljubljana, Ljubljana, Slovenia

Emir Haleva
Raymond and Beverly Sackler School of Chemistry, Tel Aviv University, Tel Aviv, Israel

Thomas Heimburg
Membrane Biophysics Group, The Niels Bohr Institute, University of Copenhagen, Copenhagen, Denmark

Masayuki Imai
Department of Physics, Faculty of Science, Tohoku University, Sendai, Japan

Andrew D. Jackson
Membrane Biophysics Group, The Niels Bohr Institute, University of Copenhagen, Copenhagen, Denmark

Mojca Kerec-Kos
Faculty of Pharmacy, University of Ljubljana, Ljubljana, Slovenia

Borut Kobal
Department of Gynaecology, Division of Gynaecology and Obstetrics, University Medical Centre Ljubljana, Ljubljana, Slovenia

Ksenija Kogej
Department of Chemistry and Biochemistry, Faculty of Chemistry and Chemical Technology, University of Ljubljana, Ljubljana, Slovenia

Shigeyuki Komura
Department of Chemistry, Graduate School of Science and Engineering, Tokyo Metropolitan University, Tokyo, Japan

Annette Meister
Institute of Chemistry—Physical Chemistry, Martin-Luther-University Halle-Wittenberg, Halle, Germany

Lars D. Mosgaard
Membrane Biophysics Group, The Niels Bohr Institute, University of Copenhagen, Copenhagen, Denmark

Lucyna Mrówczyńska
Department of Cell Biology, Adam Mickiewicz University, Poznań, Poland

Primož Peterlin
Institute of Oncology, Ljubljana, Slovenia

Sanoop Ramachandran
Physique des Polymères, Université Libre de Bruxelles, Brussels, Belgium

Kazuhiko Seki
National Institute of Advanced Industrial Science and Technology (AIST), Tsukuba, Japan

Ursula van Rienen
Institute of General Electrical Engineering, University of Rostock, Rostock, Germany

Peter Veranič
Institute of Cell Biology, Faculty of Medicine, University of Ljubljana, Ljubljana, Slovenia

CHAPTER ONE

Giant Vesicles: A Biomimetic Tool for Membrane Characterization

Rumiana Dimova[1]
Max Planck Institute of Colloids and Interfaces, Science Park Golm, Potsdam, Germany
[1]Corresponding author: e-mail address: dimova@mpikg.mpg.de

Contents

1. Introduction 2
2. Membrane Material Properties 3
3. Effects of Embedded and Anchored Molecules 8
   3.1 Cholesterol 8
   3.2 Anchored molecules 12
   3.3 Transmembrane peptides 14
4. Vesicles in External Electric Fields 17
   4.1 Some basic relations about membranes in electric fields 17
   4.2 Vesicles in AC fields 19
   4.3 Vesicle response to DC pulses 24
5. Concluding Remarks 42
Acknowledgments 43
References 43

Abstract

Giant unilamellar vesicles (GUVs) have sizes in the range of 10–100 μm, which defines their unique property: they are visible under a light microscope. GUVs provide a handy biomimetic tool for displaying directly the response of the membrane on the cell-size scale. They represent model biomembrane systems for systematic measurements of mechanical and rheological properties of lipid bilayers as a function of membrane composition and phase state, surrounding media, and temperature. Here, we will give examples on how different embedded or anchored molecules can influence the bilayer characteristics. Membrane responses to external factors (e.g., ions, molecules, hydrodynamic flows, or electromagnetic fields) can be directly visualized under the microscope. We will give an extensive overview on the membrane response to electric fields. The vesicle behavior in these observations can be interpreted and understood considering the basic mechanical and dielectric properties of the membrane.

Advances in Planar Lipid Bilayers and Liposomes, Volume 16
ISSN 1554-4516
http://dx.doi.org/10.1016/B978-0-12-396534-9.00001-5

1. INTRODUCTION

The autonomy of the cell, the basic building unit of most living creatures, is ensured by a bounding membrane. The scaffold of this membrane is made of a double lipid layer, which is basically impermeable to all substances in the cellular environment except for water. The bilayer mechanical, dielectric, and rheological properties define the response of the membrane to external perturbations.

Studying the major properties of the plasma membrane and other intracellular membranes is the foundation of modern cellular biology. However, the field of membrane structure and characterization is attracting the attention of a growing number of scientists from various other disciplines such as biochemistry, soft matter, physics, colloid chemistry, bioengineering, etc. The basic research in this area builds upon studies performed on the simplest and minimal system mimicking cell membranes, namely model membranes. Examples of such model membranes are lipid monolayers at the air–water interface, solid-supported bilayers, black lipid membranes, vesicles, and bilayer stacks. Among them, vesicles or liposomes are membrane "bubbles" formed by bending and closing of a lipid bilayer. They are the most natural system because, shape- and structure-wise, they are closest to membranes of cells and cell organelles. Contrary to other model membrane systems, such as supported lipid bilayers or black lipid membranes, vesicles allow for control over the membrane tension (for vesicles with sizes in the micrometer range, this control can be directly exercised by micropipette aspiration, but osmotic inflation or deflation can also be used even though with lesser precision). In supported bilayers and black lipid membranes, important parameters such as the bending rigidity and the spontaneous curvature, as well as electroporation thresholds, may not be measured on tension-free membranes. Indeed, these systems have further disadvantages. Black lipid membranes usually retain some of the organic solvent used for their formation and are, thus, thicker. The use of supported bilayers as model membranes typically raises concerns about steric hindrance or effects arising from the support. None of these disadvantages applies to vesicles.

Vesicles are typically classified according to multilamellarity, that is, unilamellar and multilamellar, as well as according to size. Small unilamellar vesicles or SUVs are a few tens of nanometers in size, and large unilamellar vesicles or LUVs are in the 100-nm range [1]. The largest ones are called giant unilamellar vesicles or GUVs [2] and are an extraordinarily convenient

system for studying the membrane behavior [3,4]. Their diameter can vary in the range from 10 to 200 μm and therein lies their most unique property: they are visible under a light microscope. Compared to conventional vesicles with sizes in the range of 100 nm, these giants are a convenient tool for the observation of phenomena occurring at the cell-size scales. They are well visible under an optical microscope using various enhancing techniques like phase contrast, differential interference contrast, or confocal and standard fluorescence microscopy, the latter two being particularly useful in distinguishing domains on membranes (see Fig. 1.1). Thus, giant vesicles allow for direct manipulation and observation of membrane interactions and responses to external perturbations.

In this chapter, we give some examples about membrane-related processes and effects, the unraveling of which can be achieved via experiments on giant vesicles. The main topics to be covered here build upon our knowledge about the mechanical, dielectric, and rheological properties of membranes and their response to perturbations. In Section 2, some of the properties of pure lipid bilayers will be briefly described to set the grounds for interpretation of membrane interactions and the bilayer response to external perturbations. In Section 3, we will give some examples how some of these properties are altered by the presence of different species in the membrane, such as cholesterol, anchored macromolecules, and peptides. Detailed understanding of the response of membranes to electric fields is crucial for developing novel technologies for drug and gene delivery as well as electroporation-based protocols for cancer treatment. In Section 4, we will consider in details the morphological changes, membrane poration, and fusion that electric fields can induce on vesicles. This chapter concludes with a summary of the reviewed results and an outlook.

2. MEMBRANE MATERIAL PROPERTIES

The physical properties of the lipid bilayer are those that define its response to external perturbations. Knowing the mechanical, dielectric, and rheological characteristics of lipid membranes will prepare us to tackle problems related to stress induced in the bilayer by electric fields and the phenomena which it triggers, for example, dynamics of vesicle and cell deformation, bilayer instability and electroporation, and electrofusion. The bilayer tension, bending rigidity, and spontaneous curvature are those that govern the response of biomembranes and the morphological transitions they can undergo.

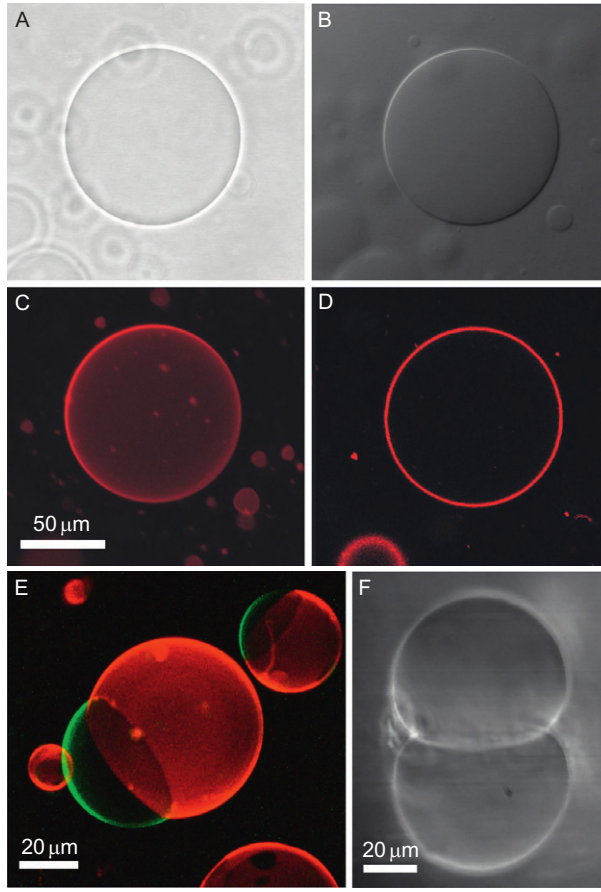

Figure 1.1 Snapshots of giant vesicles observed under different microscopy modes: (A) phase contrast; (B) differential interference contrast; (C, D) confocal microscopy where (C) is a projection averaged image and (D) is an equatorial section image. (A–D) Snapshots of the same vesicle. (E) Confocal 3D projection image of vesicles with immiscible fluid domains visualized with fluorescent dyes, which preferentially partition in one of the lipid phases. (F) Phase contracts side-view image of a vesicle sitting on a glass substrate (the mirror image of the vesicle reflected from the glass is also visible). The vesicle is deformed because of the density difference of the enclosed sucrose and external glucose solutions with osmolarity 200 mOsm/g. (A–D, F) *Reproduced from Ref. [3]* (http://dx.doi.org/10.1088/0953-8984/18/28/S04) by permission of IOP Publishing Ltd.

As a simple depiction of the lipid bilayer, one can consider it as a film or a slab, which may be bent, compressed or dilated, and sheared. At physiological temperatures, most natural lipid membranes are fluid. Thus, within this slab, the lipid molecules are free to move. Below the lipid phase transition temperature, single-component membranes crystallize. In this so-called gel phase, the relative motion of lipids and membrane inclusions is hindered. The fluidity of the membrane and the resistance to shear in the plane of the film is characterized by the shear surface viscosity, η_S (or by the diffusion coefficient of the lipids). For fluid membranes, typical values of η_S lie in the range $(1–5) \times 10^{-9}$ N s/m [5,6], but for gel-phase membranes, divergence is observed [6]. Polymer membranes are also highly viscous [7]. One may equivalently define a viscosity η_D related to the dilation and compression of the membrane. The value of η_D is on the order of 3.5×10^{-7} N s/m [8].

Phospholipid membranes in the fluid phase are very flexible: the energy required for their bending is comparable to the thermal energy. The bilayer bending rigidity, κ, which characterizes how easy it is to curve the lipid bilayer, is typically on the order of 0.9×10^{-19} J, which is equivalent to 20 $k_B T$ [9–11], where k_B is the Boltzmann constant and T is the absolute temperature. Because fluid membranes are so flexible, they fluctuate due to thermal noise. These fluctuations can be directly observed on tensionless giant vesicles under the microscope, which is the basis of the so-called fluctuation spectroscopy method used to measure the membrane bending rigidity [12–19]. When brought to the gel phase, the membrane bending rigidity increases significantly, the fluctuations get arrested, and at a few degrees below the main phase transition temperature, κ may attain values on the order of $15–20 \times 10^{-19}$ J ($\sim 350\ k_B T$) [6,20,21]. The bending rigidity of fluid membranes is extremely sensitive to the presence of membrane inclusions. In addition, depending on the type of the main lipid component building the bilayer, the effect of inclusions such as cholesterol may influence the bending rigidity in both directions, increase it or decrease it [19].

Measuring the bending rigidity κ for membranes in the fluid phase is already a handled task, and several different techniques have been developed for this purpose. One of them is based on measuring the projected area of a giant vesicle aspirated in a capillary (micropipette) as a function of the membrane tension [22]. The aspiration pressure defines the tension σ applied to the membrane. Measuring the relative area change in the regime

of low tension, also known as "entropic" tension [23,24], allows for extracting the value of κ:

$$\frac{A-A_0}{A_0} \approx \frac{k_B T}{8\pi\kappa} \ln\sigma/\sigma_{in} \tag{1.1}$$

Here A is the vesicle area at tension σ, and A_0 is the initial area for which $\sigma = \sigma_{in}$. In this limit, the aspiration pressure is very weak, and the membrane is practically not dilated but only its undulations are flattened out.

While weak tensions applied to a fluid membrane smooth out the bilayer undulations, high tensions can stretch the membrane leading to a change in the area per lipid molecule. The relative area change increases linearly with the membrane tension:

$$\frac{A-A_0}{A_0} \approx \frac{\sigma}{K_a} \tag{1.2}$$

In this regime, measuring the relative area change as a function of the membrane tension provides the stretching elasticity constant K_a. Thus, from one measurement of the relative area expansion at various tensions, one can extract both the bending rigidity and the stretching elasticity constants. The value of K_a is on the order of that characterizing the elasticity modulus of a rubber sheet with the same thickness ($\approx$4 nm). Typical values of K_a for fluid membranes lie in the range 200–300 mN/m [11] and for gel-phase membranes can reach higher values such as 850 mN/m [25].

Because membranes can be considered as being made of two parallel elastic sheets, the stretching elasticity modulus, K_a, can be approximately estimated using the following expression (see, e.g., Ref. [26]):

$$K_a = \frac{\alpha\kappa}{h^2} \tag{1.3}$$

where h is the membrane thickness, and α is a numerical constant characterizing the coupling between the membrane leaflets. A polymer brush model supported by experimental measurements yields $\alpha = 24$ [11], but note that h in this model is not exactly the membrane thickness as defined here. In contrast, molecular dynamics simulations lead to $\alpha \cong 48$, in agreement with a simple model based on the classical elasticity theory [27]. The coupling between the two elasticity moduli κ and K_a has been experimentally explored for pure lipid bilayers in Ref. [11].

Besides micropipette aspiration, another approach for measuring κ for lipid membranes consists of observing the shape fluctuations of a flaccid vesicle

under the action of thermal agitation only [13–19]. The analysis of the fluctuation modes allows estimating not only the bending rigidity but also the membrane spontaneous curvature [28,29]. The experimental approach consists of acquiring a time sequence of contours of a fluctuating vesicle. The contour is then presented in polar coordinates (R, φ) and expanded in Fourier series around the equivalent sphere radius, R_0, of the vesicle:

$$R(\varphi) = R_0 \left[1 + \sum_n a_n \cos(n\varphi) + \sum_n b_n \sin(n\varphi) \right] \tag{1.4}$$

where a_n and b_n are the amplitudes of mode n. The membrane spontaneous curvature, m, is proportional to the ratio of the mean square average values of the second and the third modes of the fluctuation spectra [28]:

$$m \propto \frac{\langle a_3^2 \rangle}{\langle a_2^2 \rangle} \equiv \bar{m} \tag{1.5}$$

The dimensionless curvature ratio, $\bar{m}$, can be determined directly from the statistics in the time sequence of the fluctuation modes.

Upon stretching, the lipid bilayer can sustain tensions up to about several milliNewtons per meter. At certain critical tension also known as the lysis tension, σ_{lys}, the membrane ruptures. For fluid membranes, σ_{lys} is on the order of 5–10 mN/m [30,31]. Note that the membrane tensile strength depends on the tension loading rate [32]. Membranes in the gel phase can sustain higher tensions and rupture at higher values of σ_{lys} [33]. Various types of membrane components (such as cholesterol or different lipids) can also influence the lysis tension [34].

After rupture or poration, the rearrangement of the lipids to close the bilayer sheet is energetically favorable because in this way the hydrophobic tails of the lipid molecules are shielded from exposure to water. The energy penalty of closing a hole in the membrane is described by the edge tension, γ, which is on the order of several picoNewtons [26]. The edge tension plays a strong role in processes depending on pore stability and resealing such as in electroporation, and electro-mediated gene and drug delivery.

In Table 1.1, we give some typical values of the constants discussed above for pure lipid membranes both in the fluid phase and in the gel phase.

Above, we mainly discussed the mechanical and rheological properties of membranes. However, electric properties of biomembranes play also a pivotal role in cellular functions. The membrane electric properties as well as membrane charging and polarization times are introduced in Section 4.1.1.

Table 1.1 Typical values for the characteristic properties of lipid membranes in fluid and gel phase

Membrane material property	Fluid-phase lipid membranes	Gel-phase lipid membranes
Bending rigidity, κ	0.9×10^{-19} J ($\sim 20\ k_B T$) (for data for various lipid bilayers, see Refs. [10,11,19])	14×10^{-19} J ($\sim 350\ k_B T$)[a] [6,20]
Stretching elasticity, K_a	240 mN/m (see, e.g., Ref. [11])	$\sim$850 mN/m [25]
Shear surface viscosity, η_S	$\sim 5 \times 10^{-9}$ N s/m [5,6]	Diverges [6]
Dilational surface viscosity, η_D	3.5×10^{-7} N s/m [8]	–
Lysis tension, σ_{lys}	3–10 mN/m [30,31,34]	$\geq$15 mN/m [33]

[a]This value corresponds to the bending rigidity of membranes at temperatures about 5 °C below the main phase transition temperature of the lipid.

3. EFFECTS OF EMBEDDED AND ANCHORED MOLECULES

In the previous section, we gave some typical values for the mechanical and rheological characteristics of pure phosphatidylcholine (or phosphocholine) membranes. However, the bilayer properties are influenced by compositional variation of the membrane as we will demonstrate in this section.

3.1. Cholesterol

It is a popular perception that cholesterol is unhealthy. However, it is a vital component of mammalian cell membranes. It constitutes up to about 50 mol% (or 30% of the mass) of the total lipid in the animal cell plasma membrane [35], which makes one wonder why the cell needs so much of it. Indeed, cholesterol is a key player in stabilizing membrane domains or rafts which are believed to be responsible for the correct functioning of membrane proteins [36]. It is also well known to modulate the physical properties of membranes.

A widely accepted view for decades has been that cholesterol increases the membrane bending rigidity in general. However, recently, it has become clear that its effect is not universal but rather depends on the specific architecture of

the lipid building the membrane. The conventional belief was that above the lipid phase transition temperature, cholesterol orders the acyl chains, inherently leading to an increase in the bending rigidity. This concept was supported by observations on lipids such as stearoyloleoylphosphatidylcholine (SOPC) [24,37], dimyristoylphosphatidylcholine (DMPC) [17,38], and palmitoyloleoylphosphatidylcholine (POPC) (not only in mixtures with cholesterol but with other sterols as well) [39]. However, as demonstrated in the last couple of years [19,40,41], the bending rigidity of membranes made of dioleoyphosphatidylcholine (DOPC) and cholesterol does not show any significant correlation with the cholesterol content.

This observation was first reported by the group of Nagle [42,43] based on measurements of the diffuse X-ray scattering from DOPC–cholesterol bilayer stacks. The properties of bilayer stacks, in general, differ from those of freely suspended single bilayers because in the stack; the membrane may not be fully hydrated; and its fluctuations are constrained by neighboring bilayers. Thus, the question arises whether single membranes, which are closer to cellular membranes, would behave in a similar manner. Recent measurements from our lab on single bilayers as in GUVs [19] provided the answer to this question. The tendency that cholesterol does not alter the bending rigidity of DOPC membranes was confirmed. Furthermore, cholesterol mixtures with other lipids, such as sphingomyelin (SM), for which data were not available, were also explored. The results demonstrated that increasing the amount of cholesterol in SM membranes leads to reduction in the bending rigidity. The results were obtained using two different experimental methods—fluctuation analysis and electrodeformation of vesicles [44,45], which were further developed to minimize the experimental effort [19]. Some data are given in Fig. 1.2. Comparison with available data in the literature is provided in Table 1.2.

A major difference between DOPC and the lipids on which earlier studies were performed (SOPC, POPC, DMPC) is that each of the acyl chains of DOPC contains a double bond. The affinity of cholesterol (Chol) to phosphocholine membranes was found to decrease markedly with the increase in the degree of unsaturation of the lipid chains [48]. SM is almost fully saturated. It has only one double bond in one of the acyl chains, which is located close to the headgroup region. The trend in the bending stiffness exhibited by SM:Chol mixtures follows neither the behavior of lipids with one mono-unsaturated chain such as SOPC, which are characterized by a bending rigidity that gradually increases with cholesterol content, nor the

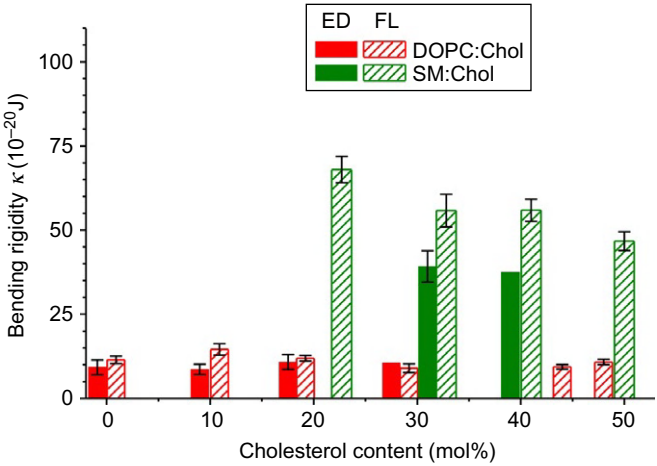

Figure 1.2 Bending rigidity of membranes made of different lipids as measured (i) by the electrodeformation method, indicated in the legend as ED (solid bars), and (ii) by fluctuation spectroscopy, indicated as FL (hatched bars). The error bars show the standard error from the mean value of a population of vesicles. The absence of an error bar indicates a single measurement. All measurements were performed at 23 °C. *Reproduced from Ref. [19]* (http://dx.doi.org/10.1039/B920629A) by permission of The Royal Society of Chemistry.

Table 1.2 Bending rigidity, κ, of membranes with various compositions (molar ratios) as obtained in Ref. [19] and reported in the literature

Membrane composition	**Values from Ref. [19] for the bending rigidity κ (10^{-20} J)**	**Other literature values for κ (10^{-20} J)**
DOPC		
	10.8 ± 1.0	8.5 ± 1 at 18 °C [11]; 7.6 ± 0.5 at 30 °C [42]; 8.5 ± 0.1 at 15 °C [42]; 1.6–1.7 ± 0.5[a] at 21 °C and 2.4–6.1 ± 1.2[a] at 23 °C [45]
DOPC:Chol		
90:10	11.6 ± 1.3	8.0 ± 0.8 at 30 °C [40]; 6.9 at 30 °C [43]
80:20	11.3 ± 1.2	7.3 ± 0.8 at 30 °C [40]; 7.2 at 30 °C [43]
70:30	9.2 ± 1.3	7.4 ± 0.8 at 30 °C [40]

Table 1.2 Bending rigidity, κ, of membranes with various compositions (molar ratios) as obtained in Ref. [19] and reported in the literature—cont'd

Membrane composition	Values from Ref. [19] for the bending rigidity κ (10^{-20} J)	Other literature values for κ (10^{-20} J)
56:44	9.4 ± 0.7	
50:50 *SM:Chol*	10.8 ± 0.8	12 ± 1.2 at 22 °C [46]
80:20	68.2 ± 4.2	
70:30	55.8 ± 4.9	
60:40	55.9 ± 3.3	
50:50 *DOPC:SM:Chol*	46.7 ± 2.8	31 ± 2[b] at 22 °C [46]
70:10:20	9.7 ± 0.5	
30:50:20		19 ± 5[b,c]; 80 ± 10[b,d] at 20 °C [47]
Red blood cell membranes		
LE (~50% Chol)	22.5 ± 0.8	26.8–47[e] at 25 °C [38]
LE with transmembrane peptides (~40% Chol)	22.5 ± 1.3	
Sterol-free LE		10 ± 1.5[e] at 25 °C [38]

[a]The values for κ reported in this reference were found to depend on the presence of silicone grease in the working chamber and on the applied method.
[b]The reported value for κ is for brain SM.
[c]The reported value is for the liquid-disordered phase.
[d]The reported value is for the liquid-ordered phase.
[e]The lipids in these measurements were from whole-cell extracts and not from plasma membranes extracts as used in Ref. [19]. The cholesterol content in these membranes was 40 mol%.
The measurements in Ref. [19] were performed at 23 °C. The error in κ represents the standard error from the mean value for a population of vesicles. Reproduced from Ref. [19] (http://dx.doi.org/10.1039/B920629A) by permission of The Royal Society of Chemistry.

one of lipids with two mono-unsaturated chains such as DOPC, which exhibit bending rigidities that are hardly affected by the cholesterol content. Instead, the addition of cholesterol from 20% to 50% to SM membranes leads to a gradual decrease in the membrane bending stiffness by about 30% (see Fig. 1.2).

To summarize, our data suggest that the effect of cholesterol is not universal, but rather specific to the type of lipid. The bending rigidity of saturated or mono-unsaturated lipids such as DMPC, SOPC, or POPC increases with cholesterol content, while that of double-unsaturated lipids such as DOPC is independent of the cholesterol fraction. In SM membranes, the bending rigidity is found to decrease with increasing cholesterol content. We cannot argue that these trends in the behavior of the different membrane types are universal for the specific degree of unsaturation. A more plausible view would be that the effect of cholesterol depends on the individual molecular architecture of the lipid combining the effect of unsaturation and acyl chain length, and probably the lipid interfacial region. Our results confirm not only that the widely accepted view about the rigidifying and stabilizing effect of cholesterol on membranes is ungrounded, but also that, as a rule, generalization about the effect of cholesterol on the material properties of membranes is not realistic.

3.2. Anchored molecules

The plasma membrane of living cells possesses a large number of asymmetrically distributed or anchored biomacromolecules. The intracellular leaflet of the membrane is connected to the polymer network of the cytoskeleton, which determines the membrane shape. The extracellular side is covered with anchored receptors and polysaccharides, which form the so-called glycocalix. In addition to their various biological functions, all anchored polymers tend to curve the membrane and, thus, to induce a spontaneous membrane curvature.

In general, the spontaneous curvature of pure lipid GUVs is close to zero because on a micron-size scale, the bilayer is symmetrical. However, in the presence of molecules which adsorb or incorporate in the external leaflet of the bilayer, the spontaneous curvature can change drastically when the membrane accommodates the foreign molecules. In order to illustrate the change in the spontaneous curvature of a vesicle, here we will discuss one example related to polymer anchoring in the bilayer.

Presumably, the simplest example of a polymer/membrane architecture consists of flexible polymers for which one end provides the membrane anchor, whereas all other polymer segments experience effectively repulsive interactions with the membrane. To realize such a system, we used vesicles containing biotinylated lipids. The vesicles were formed in the presence of the protein avidin. Because avidin has four sites for binding biotin groups, the produced vesicles were covered with "avidin anchor sites" which are able

to trap biotinylated molecules from the solution. We used λ-phage DNA with one biotinylated end (see Fig. 1.3A) as long polymers to study the curvature change induced by anchoring of the molecules to the membrane [49]. Curvature effects due to polymer grafting were theoretically addressed in previous studies [50–52]. One example of the effect of anchoring the DNA molecules onto the membrane is given in Fig. 1.3. The probability distributions of the

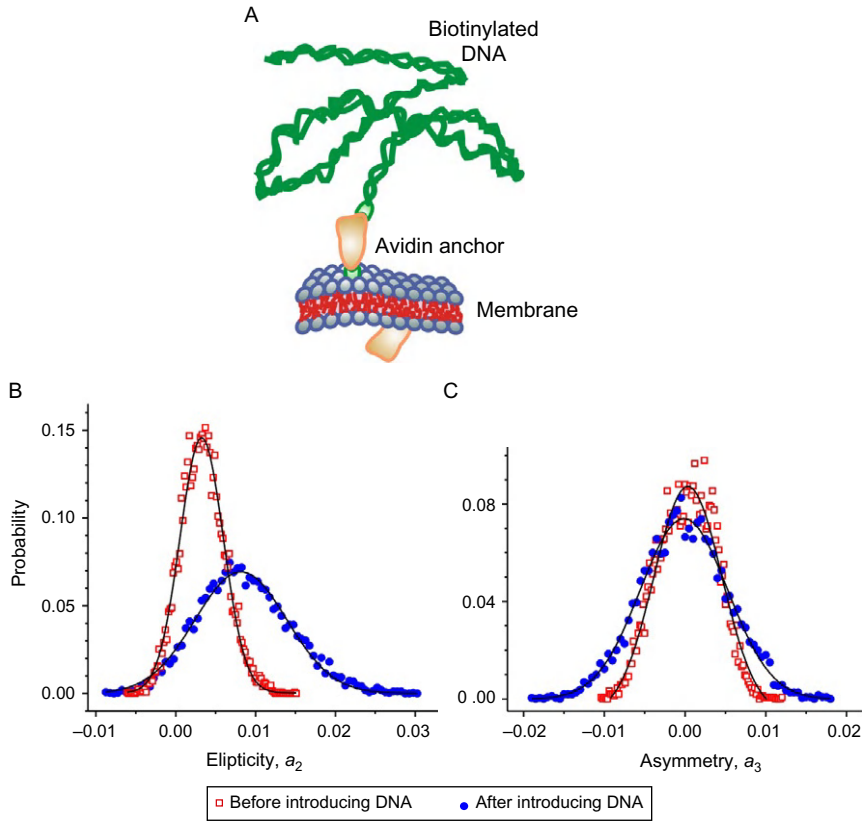

Figure 1.3 Effect of asymmetrically anchored DNA on the membrane spontaneous curvature. (A) Sketch of a DNA anchored to a bilayer via a biotin–avidin link. The size of the macromolecule and the bilayer thickness are not in scale. (B, C) Normalized histograms for the mode amplitudes a_2 (B) and a_3 (C) for a prolate vesicle in the absence and presence of biotinylated DNA in the vesicle exterior. The DNA in the solution anchors to the membrane leading to a change in the membrane fluctuation spectrum as illustrated by the changes in the mode distributions. The histogram statistics is done over about 7000 data points. The solid lines are Gaussian fits to the data. (B, C) *Reproduced from Ref. [49]* (http://dx.doi.org/10.1529/biophysj.106.100032) with permission from Elsevier.

second and third modes of the fluctuation spectra are given for a vesicle before and after exposing it to the DNA solution. The vesicle is initially a prolate whose ellipticity is characterized by the mean value of the mode a_2 (i.e., the position of the maximum in the histogram of a_2 in Fig. 1.3B). After introducing the DNA solution, the histograms for the different shape modes change as the DNA molecules are anchored to the membrane. The widths of the two distributions which correspond to the mean square average values $\langle {a_2}^2 \rangle$ and $\langle {a_3}^2 \rangle$ decrease, with a significantly more pronounced effect on $\langle {a_2}^2 \rangle$. This implies that the curvature ratio $\bar{m}$, see Eq. (1.5), and thus the membrane spontaneous curvature increase. As a consequence of such behavior, the vesicle may exhibit budding, whereby a smaller satellite vesicle is expelled from the body of the mother vesicle but remains connected to it via a narrow membrane tube.

By varying the amount of biotinylated lipids in the membrane, we could control the surface concentration of anchors. At low anchor concentrations, the spontaneous curvature of the membrane was found to increase linearly with the DNA concentration. The linear increase is consistent with theoretical predictions for polymer surface concentrations in the mushroom regime [50–52]. At higher anchor concentrations, which still belong to the mushroom regime, vesicle budding is observed.

3.3. Transmembrane peptides

More than half of all proteins within the cell interact with the membranes. Membrane proteins can be integral, that is, penetrating the lipid bilayer, peripheral, that is, external but bound with noncovalent bonds, and lipid-anchored, that is, external but bound with covalent bonds. In the previous section, we discussed the behavior of a system with an anchored biomacromolecule, mimicking to a certain extent the latter class of membrane proteins. We found out that an anchored molecule can dramatically change the membrane spontaneous curvature. Here, we will give one example on the effect of membrane inclusions, which typically represent parts of integral membrane proteins, namely transmembrane peptides.

The peptide we will consider is part of the fusion peptide (FP) of the human immunodeficiency virus (HIV). This peptide is part of the N-terminus of the viral envelope glycoprotein gp41 and is believed to play an important role in the viral entry process. During its life cycle, the HIV docks to the membrane of a target cell, inducing pore formation. The HIV FP FP23 is known to be responsible for secure anchoring in the target cell membrane.

To understand the immediate effect of this peptide on the cell membrane, we studied the influence of FP23 on the mechanical properties of model lipid bilayers [53]. For this purpose, GUVs were prepared from DOPC mixed with FP23 in various molar ratios. The bending stiffness of the vesicles was measured with fluctuation analysis and aspiration with micropipettes. The data obtained from both of these approaches show that the bending stiffness of the membrane decreases gradually with increasing concentration of FP23 in the bilayer. In Fig. 1.4A, we have plotted the value of the measured bending rigidities rescaled by the bending rigidity of the pure DOPC membrane. Low concentrations of only a few mol% FP23 are sufficient to decrease the bending stiffness of the lipid bilayer by about a factor of 2. These observations are consistent with measurements performed on bilayer stacks [54]. The decrease in the bending rigidity induced by the presence of the peptide is similar to that observed with cosurfactants [55] and theoretically expected for transmembrane inclusions (see, e.g., Ref. [56–58]).

Apart from measuring the changes in the bending rigidity, we also examined the effect of FP23 on the stretching elasticity modulus of the membrane, which was found to remain constant, $K_a \approx 124$ mN/m with standard error ± 18 mN/m, for different concentrations of FP23.

From the measured values of the bending rigidity and the stretching elasticity, we attempted to evaluate the coupling between the two membrane leaflets in the presence of the peptide. This coupling is characterized by the constant α introduced in Eq. (1.3). For completely bound leaflets, $\alpha = 12$ [59], whereas for freely sliding monolayers, $\alpha = 48$ [27]. A polymer brush model for the bilayer predicts the intermediate value $\alpha = 24$ [11].

Using our results for the elasticity constants κ and K_a (see Fig. 1.4B), we can estimate the value of the coupling constant α, provided that data for the membrane thickness h are available. For pure DOPC bilayers, $h = 2.7$ nm [60]. Thus, we obtain $\alpha \approx 18$, which is between values for the polymer brush model and for completely bound monolayers. Experiments based on X-ray scattering show only a slight thinning of DOPC bilayers containing FP23. For a peptide molar fraction of 6%, the bilayer thinning was estimated to be about 0.4 nm [61]. Thus, for the highest FP23 fraction measured here, the membrane thickness is minimum $d = 2.3$ nm. Taking this estimate, we obtain the monolayer coupling constant $\alpha \approx 38$. This finding suggests that the peptide significantly reduces the coupling between the two leaflets of the bilayer. The interleaflet interaction parameter α shifts toward values characteristic for freely sliding monolayers. On the molecular level, this result could be understood if one considers the peptide as an obstacle (or a

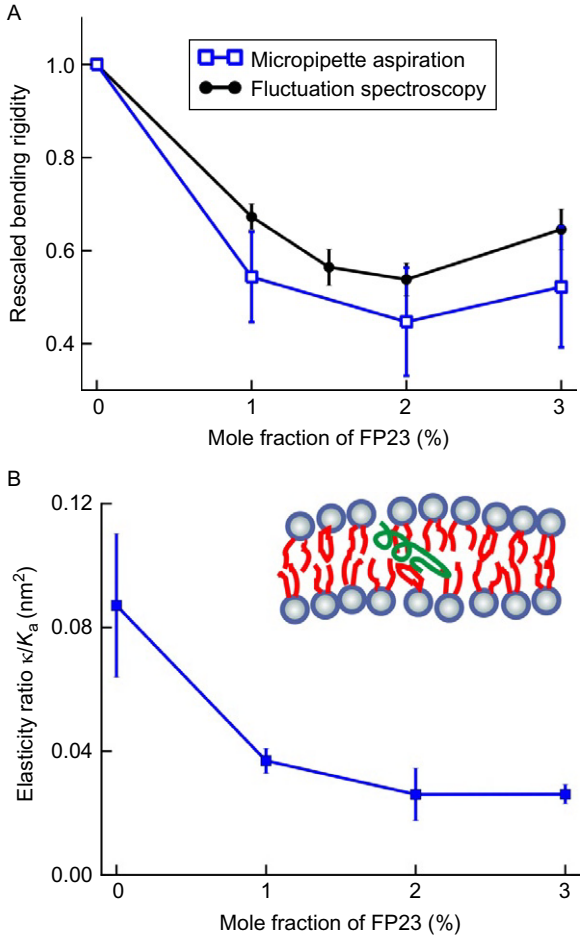

Figure 1.4 Effect of the transmembrane peptide FP23 on the elastic properties of DOPC membranes. (A) Relative changes in the bending rigidity as a function of the concentration of FP23 in DOPC bilayers. The data were rescaled by the bending rigidity of the pure DOPC bilayer. The two datasets correspond to the results obtained with fluctuation analysis (filled circles) and micropipette aspiration (open squares). (B) Dependence of the ratio between the bending rigidity and the stretching elasticity modulus, κ/K_a, for DOPC membranes with increasing mole fraction of FP23. The inserted peptide reduces the elasticity ratio of the bilayer. The error bars represent standard errors. The cartoon in the inset illustrates the decoupling effect the peptide has on the bilayer. *Data reproduced from Ref. [53]* (http://dx.doi.org/10.1088/1367-2630/13/2/025004) with the permission of IOP Publishing Ltd.

molecular spring) in the hydrophobic core of the bilayer, which effectively pushes the two monolayers apart (see cartoon inset in Fig. 1.4B). This novel result about the decreased interleaflet coupling and the exhibited strong reduction of the membrane bending rigidity may be important factors, defining the exact mechanism of action of the HIV FP upon viral fusion with the target membrane. The fusion of lipid bilayers involves intermediate states with high membrane curvature. The FP promotes such curved states, thus lowering the energy barrier for fusion.

4. VESICLES IN EXTERNAL ELECTRIC FIELDS

The exposure of biological membranes to electric fields can lead to a variety of responses. The interest toward understanding these responses is motivated by both applications and mechanistic aspects. External electric fields, whether weak alternating (AC) fields or strong direct current (DC) pulses, have emerged as a powerful method for cell manipulation in biomedical and biotechnological applications. For example, electric fields are employed in novel *in vivo* and *in situ* applications for tissue ablation, wound healing, and cancer treatment [62–67]. Strong electric fields can cause a significant increase in the electric conductivity and permeability of the cell plasma membrane. This phenomenon, also referred to as electroporation or electropermeabilization, is used for introducing various molecules in the cell, to which the membrane is otherwise impermeable [68,69]. In this section, we are going to discuss the effect of electric fields on lipid membranes.

4.1. Some basic relations about membranes in electric fields

4.1.1 Characteristic times in vesicle response

The response of membranes to electric fields involves dynamic physical processes occurring at different timescales. Free charges accumulate on boundaries separating media with different electric properties. A spherical vesicle polarizes on the Maxwell–Wagner timescale [70]:

$$t_{MW} = \frac{\varepsilon_{in} + \varepsilon_{ex}}{\lambda_{in} + 2\lambda_{ex}} \tag{1.6}$$

where ε_{in} and ε_{ex} are the dielectric constants, and λ_{in} and λ_{ex} are the conductivities of the solutions inside and outside the vesicle, respectively.

The lipid bilayer is impermeable to ions, and free charges accumulate at the surfaces on both sides of the membrane. Hence, the vesicle membrane acts as a capacitor, which charges on a timescale [71,72]:

$$t_c = RC_m\left(\frac{1}{\lambda_{in}}+\frac{1}{2\lambda_{ex}}\right) \tag{1.7}$$

where R is the vesicle radius and C_m is the membrane capacitance.

The capacitor charging time t_c is typically much longer than the Maxwell–Wagner time t_{MW}. For example, we can estimate $t_c \approx 10$ μs and $t_{MW} \approx 0.01$ μs for conditions corresponding to experiments on vesicles in 1 mM NaCl, namely $\varepsilon_{in} \approx \varepsilon_{ex} = 80\varepsilon_0$, where ε_0 is the vacuum permittivity, $\lambda_{in} \approx \lambda_{ex} \approx 10$ mS/m, $C_m \approx 0.01$ F/m^2, and $R \approx 10$ μm.

These timescales are a key to understanding the dynamic response of vesicles subjected to short electric pulses, as well as frequency dependence of vesicle deformation. Note that characteristic angular frequencies are defined as the inverse of the timescales in Eqs. (1.6) and (1.7), for example, $\omega_{MW} = 1/t_{MW}$. The experimental frequency, ν, is related to the angular one via $\nu = \omega/2\pi$.

4.1.2 Transmembrane potential and conditions for vesicle electroporation

As already mentioned, lipid membranes are essentially impermeable to ions. Thus, in the presence of an electric field, charges accumulate on both sides of the bilayer and give rise to a transmembrane potential [73]:

$$\Psi_m(t) = 1.5R|\cos\theta|E[1-\exp(-t/t_c)] \tag{1.8}$$

Here R is the radius of a spherical vesicle as above, θ is the tilt angle between the electric field and the surface normal, t is time, and t_c is the charging time as defined in Eq. (1.7). Equations (1.7) and (1.8) are valid only for a nonconductive membrane. Above some electroporation threshold, the transmembrane potential Ψ_m cannot be further increased and can even decrease due to transport of ions across the membrane [73,74].

The electroporation phenomenon can also be understood in terms of a critical stress in the bilayer created by the electric field. The transmembrane potential, Ψ_m, induces an effective electrical tension σ_{el}, as defined by the Maxwell stress tensor [30,75,76]. This tension is given by

$$\sigma_{el} = \varepsilon_m \frac{h}{h_e^2}\Psi_m^2 \tag{1.9}$$

where h is the total bilayer thickness, $h \approx 4$ nm, h_e is the dielectric thickness, $h_e \approx 2.8$ nm for lecithin bilayers [77,78], and ε_m is the membrane permittivity, $\varepsilon_m \approx 2\varepsilon_0$. For vesicles with some initial tension σ_0, the total tension reached during the pulse is

$$\sigma = \sigma_0 + \sigma_{el} \tag{1.10}$$

If the total membrane tension exceeds the lysis tension σ_{lys}, the vesicle ruptures. This corresponds to building up a certain critical transmembrane potential, $\Psi_m = \Psi_c$. According to Eqs. (1.9) and (1.10), this poration potential Ψ_c depends on the initial membrane tension σ_0 as previously reported [30,76,79]. The critical transmembrane potential for cell membranes is $\Psi_c \approx 1$ V (see, e.g., Refs. [80,81]). Similarly, for tension-free vesicles, the critical potential was measured to be similar [30]. Its value decreases when the initial membrane tension increases. In agreement with this expectation, nonfluctuating vesicles that exhibit an appreciable tension readily porate at $\Psi_c < 1$ V [82,83], that is, they porate at fields weaker than those needed to porate deflated vesicles with visibly undulating membranes.

4.2. Vesicles in AC fields

The question "how cells respond to AC fields?" has been addressed in a number of studies. In some of them, cells have been found to orient parallel or perpendicular to the field direction [84,85], and others report that cells deform in electric fields [85–87]. This difference is probably due to the membrane elasticity and coupling to the cytoskeleton as well as to the cell volume-to-area ratio. The orientation of the cells in the field was found to depend on the solution conductivity [84,85]. Similarly, the direction of cell elongation is influenced by the external conductivity [86,88]. In this section, we aim at drawing an overall picture of the spectrum of responses of model membranes to alternating electric fields at various field frequency and conductivity conditions. Vesicle deformations have been treated both experimentally and theoretically in the last couple of decades, but a comprehensive description reconciling observations and calculations has emerged only recently.

4.2.1 Vesicle deformation in AC fields

In AC fields, spherical giant vesicles adopt ellipsoidal shapes. Initiated by the seminal work of Winterhalter and Helfrich [89], this effect has been considered theoretically by several groups [90–93]. Experimental studies have shown that in AC fields of intermediate frequencies ($\sim$2 kHz), vesicles in pure water adopt prolate deformation with the longer axis oriented along the field direction [45]. At higher frequencies, a prolate-to-oblate transition was reported [91,94].

Thus, analogous to cells, the deformation of vesicles subjected to AC fields depends on the field frequency ν (or the angular frequency ω) and the

conductivity conditions. The latter can be described by the ratio between the internal and the external conductivities: $x = \lambda_{in}/\lambda_{ex}$. By systematically varying the field frequency and solution conductivities, we could construct a morphological diagram of the shape transitions observed in neutral phosphatidylcholine vesicles [95,96] (see Fig. 1.5A). At high frequencies, the vesicles are spherical independently of the conductivity ratio x. As the frequency decreases, vesicles with $x > 1$, that is, with the internal conductivity higher than the external one, become prolate ellipsoids corresponding to transition 1 in Fig. 1.5A, while vesicles with $x < 1$ adopt oblate shapes after undergoing transition 2. A further decrease in the frequency changes the vesicle shape at transition 4 from oblate to prolate for $x < 1$. For intermediate frequencies, an oblate vesicle can become prolate at transition 3 if the conductivity ratio is changed to $x > 1$. At the border conductivity range, $x \cong 1$, coexistence of the two shapes, prolate or oblate, can be observed [97].

The physical mechanism responsible for the vesicle electrodeformation is the interplay between the electric field partitioning in normal and tangential components, and the charging of the membrane interfaces. The lipid bilayer is an insulator and acts as a capacitor. At low frequencies, $\omega \ll 1/t_c$, see Eq. (1.7) for the definition of t_c, the large membrane impedance blocks current from flowing into the vesicle interior and the electric field lines are tangent to the membrane. The vesicle is squeezed at the equator and pulled at the poles by the radial Maxwell stress or pressure arising from the tangential electric field. As a result, the vesicle adopts a prolate shape.

At intermediate frequencies, $1/t_c < \omega < 1/t_{MW}$ (see Eq. 1.6 for definition of t_{MW}), the membrane is capacitively short circuited and displacement currents flow through it. The electric field lines penetrate the vesicle interior, and the electric field acquires a component normal to the membrane. When $x \neq 1$, that is, when there is an asymmetry between the internal and the external conductivities, the charge densities on the inner and outer membrane interfaces become imbalanced. These charges arise from the discontinuity of the permittivities across the interfaces and represent local accumulation of cations and anions at these interfaces. The sign of the net free charge density at the membrane is determined mainly by the conductivity ratio: schematic snapshots for $x > 1$ and $x < 1$ are sketched in panels (B) and (C) of Fig. 1.5. The interaction of the tangential and normal electric fields with the free charges produces lateral and normal forces, f_t and f_n, respectively. Depending on the polarity of the net free charge, f_t is directed toward either the poles or the equator, and f_n is directed inward or outward [98], leading to prolate or

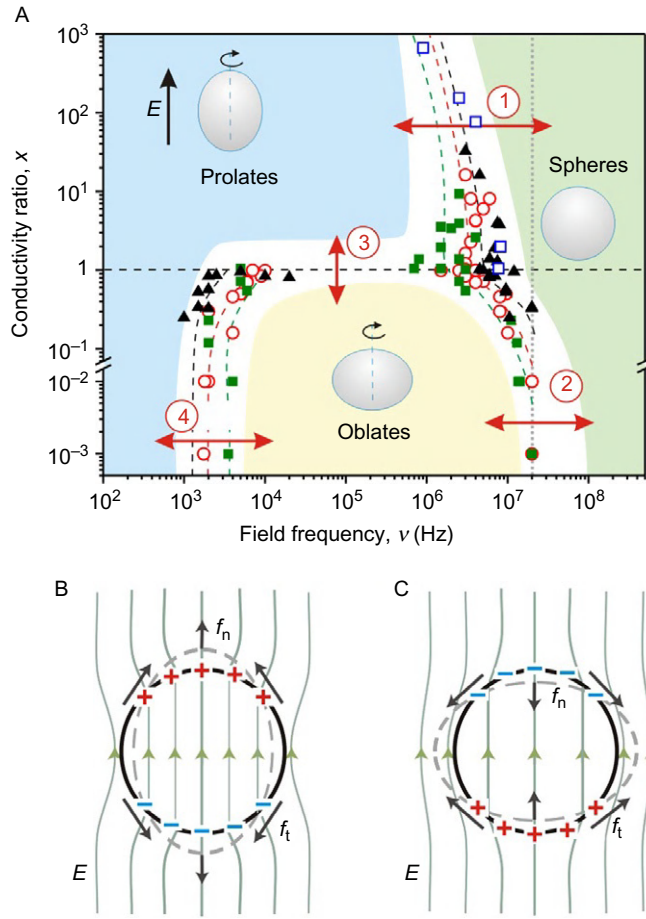

Figure 1.5 Vesicle deformation in AC fields. (A) Morphological diagram of the shapes of vesicles at different conductivity conditions ($x = \lambda_{in}/\lambda_{ex}$) and various field frequencies as determined experimentally. The symbols correspond to different internal conductivity, λ_{in}, in unit mS/m: 1.5 (solid squares), 6.5 (open circles), 13 (solid triangles), and 1000 (open squares). The dashed lines are guides to the eye, and the shaded areas indicate zones of specific morphology. The four types of morphological transitions are discussed in the text. The dotted vertical line shows the experimentally accessible frequency limit ($\nu = 2 \times 10^7$ Hz). Schematic views of the vesicle shapes are included as insets, and the electric field is indicated by an arrow. (B, C) Origin of the vesicle deformation in AC fields at intermediate frequency (see transition 3 in (A)): The black line shows the spherical vesicle geometry in the absence of field. The cartoons present snapshots of the net charge distribution at the vesicle interfaces at intermediate frequencies. Due to the difference in the conductivity conditions, the net charges across the membrane, illustrated with pluses and minuses, differ depending on the value of the conductivity ratio $x = \lambda_{in}/\lambda_{ex}$. The forces ($f_n$ and f_t) applied to the charges by the normal and the tangential electric fields deform the vesicles into prolates for higher internal conductivity, $x > 1$ (B), and oblates for higher external conductivity $x < 1$ (C). *Reproduced from Ref. [96]* (http://dx.doi.org/10.1039/B901963D) by permission of The Royal Society of Chemistry.

oblate vesicle shapes as indicated by transition 3 in Fig. 1.5A and sketched in Fig. 1.5B and C.

In the high-frequency regime, $\omega > 1/t_{MW}$, the electric charges cannot follow the oscillations of the electric fields. As a result, the net charge density decreases with the field frequency. This relaxes the shape of the vesicle from prolate ($x > 1$) or oblate ($x < 1$) to spherical (transitions 1 and 2 in Fig. 1.5A).

Earlier theoretical studies of vesicle deformation in AC fields have been limited to rather simple systems. For example, these studies omitted the asymmetry in the media conductivities [89,91,93], and their theoretical predictions are at odds with experiment (see, e.g., the supplementary material of Ref. [95]). Vesicle shapes in AC fields can be investigated within the framework of the energy minimization approach introduced by Winterhalter and Helfrich [89]. A recent detailed theoretical study accounting for the conductivity asymmetry across the membrane was able to correctly predict the morphological diagram shown in Fig. 1.5A [99]. Quantitatively, the theory provided reasonable values of the relative vesicle deformation for small vesicles with size of the order of 1 μm, but for giant vesicles with diameters in the range of 10–100 μm, the theory gives unreasonably large values. Another approach based on the balance of all forces exerted on the membrane was also reported [98]. This model, accounting for variable membrane tension and hydrodynamic forces, correctly described the vesicle deformation in AC fields.

4.2.2 Lipid flows triggered by inhomogeneous AC fields

As discussed in the previous section, electric fields induce forces at the vesicle interface. At intermediate frequencies, $1/t_c < \omega < 1/t_{MW}$, the lateral force f_t is involved in the vesicle deformation as shown in Fig. 1.5B and C. In addition, this force may also lead to fluid flows, analogous to flows induced in liquid droplets. However, there is a fundamental difference between droplets and vesicles, which arises from the properties of the lipid bilayer [100]. The membrane behaves as a two-dimensional nearly incompressible fluid. Under stress, it develops tension to keep its surface area constant. In uniform AC fields, membrane flow in the vesicle is not expected because the lateral electric stress is counterbalanced by the resulting axially symmetric membrane tension. In inhomogeneous fields however, this force balance is broken and a flow of lipids set off in order to restore it.

To visualize such flows along the membrane, one can employ giant vesicles with fluorescent domains as markers for the movement of the membrane [101]. Such fluid domains can be obtained if the membranes are made of a lipid

mixture, which, at room temperature, phase separates in two fluid phases (see, e.g., Refs. [102–104]). The two phases show as domains on the vesicles if a fluorescent dye is employed, which preferentially partitions in one of the phases. The membrane flow pattern can be resolved by following the motion of the domains with confocal microscopy [101]. To generate the inhomogeneous AC field, the vesicles can be prepared to be heavy, for example, by loading them with sucrose solution and placing them in glucose media. Due to the density difference of the two solutions, the vesicles sediment at the bottom of the observation chamber. The proximity of the bottom glass to the vesicle, as shown in Fig. 1.6A, leads to an asymmetric

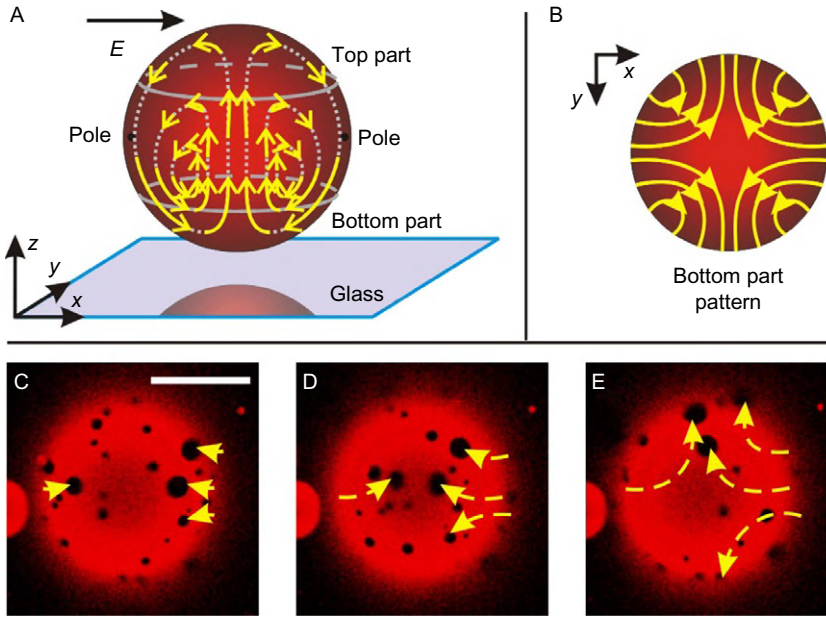

Figure 1.6 Membrane flow triggered on a giant vesicle exposed to an inhomogeneous AC field. The vesicle is located close to the bottom of the observation chamber as illustrated in (A), where the vesicle top and bottom parts, the poles and the field direction are indicated. The side and the bottom views of the flow lines on the vesicle surface are sketched in (A) and (B), respectively. The length of the arrows in (A) roughly corresponds to the amplitude of the flow velocity. The lipid flow induced by an AC field (36 kV/m, 80 kHz) on a giant vesicle with a diameter of about 150 μm, at external and internal conductivities of 25 mS/m and 0.3 mS/m, respectively, is shown in micrographs (C–E). The time between the consecutive snapshots is approximately 1.3 s. The dashed arrows indicate the trajectories of selected domains in the consecutive snapshots. *Reproduced from Ref. [101]* (http://dx.doi.org/10.1039/B811876K) by permission of The Royal Society of Chemistry.

field distribution at the membrane surface. The field strength is much higher at the lower vesicle part, facing the glass, than at the top part [101].

Such asymmetric field distribution leads to special membrane flow patterns, consisting of concentric closed trajectories organized in four symmetric quadrants, each extending from the bottom to the top of the vesicle (see Fig. 1.6). The flow is fastest at the periphery of the quadrant and at the bottom of the vesicle. The top and the bottom of the vesicle are stagnation points. The velocity of the domains (on the order of μm/s) can be altered by the field strength and frequency and by the conductivity of the external solution. Calculations of the lateral electric stress or surface force density on the membrane suggest that the vesicle experiences significant shear stress in the vicinity of the solid substrate [101]. As a result, a nonuniform and nonsymmetric membrane tension builds up. It triggers lipid flow toward the regions of highest tension, in analogy to Marangoni flows in monolayers [105–107].

These AC field-induced flows in giant vesicles have possible applications in microfluidic technologies. Giant vesicles in inhomogeneous AC fields or in hydrodynamic flows mimicking, for example, the situation of red blood cells in capillaries may be used as nanoreactors for fluid manipulation, that is, displacing, mixing, trapping, etc. Lipid mixing was already demonstrated in Ref. [101], while mixing of the solution encapsulated inside vesicles was shown in Ref. [96].

4.3. Vesicle response to DC pulses

The membrane "intolerance" toward letting solute molecules to easily cross it creates the main obstacle in biomedical applications where drugs or genes have to be introduced into the cell. One approach, which finds a broad use nowadays in overcoming the barrier functions of the membrane, relies on the temporary bilayer perforation when exposed to strong electric fields. This phenomenon, called electroporation, will be the main focus of this section.

4.3.1 Electrodeformation and electroporation of membranes in the fluid phase

In salt-free solutions, spherical vesicles subjected to electric pulses adopt ellipsoidal shapes, which relax back to the initial vesicle shapes after the end of the pulse. The degree of deformation of an ellipsoidal vesicle can be characterized by the aspect ratio of the two principal radii, a and b (see sketch in Fig. 1.7A). For $a/b = 1$, the vesicle is a sphere. The relaxation dynamics of

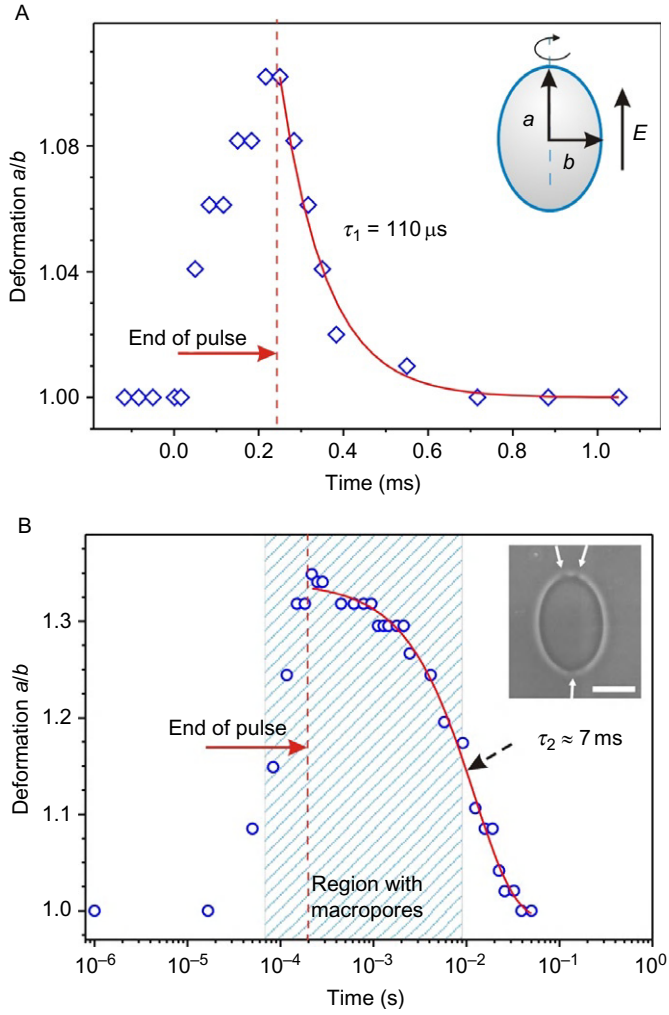

Figure 1.7 Deformation of vesicles exposed to square-wave DC pulses. (A) Response of a vesicle subjected to a pulse below the poration threshold: field strength $E = 100$ kV/m, pulse duration $t_p = 250$ μs; $\Psi_m(t = t_p) < \Psi_c$. The solid curve is an exponential fit with a decay time τ_1 as given in the figure. (B) Data from the response and relaxation of a vesicle, in which macropores were observed: $E = 200$ kV/m, $t_p = 200$ μs; $\Psi_m(t = t_p) > \Psi_c$. The relaxation is described by a single exponential fit (solid curve) with a decay time τ_2. The shaded area indicates the time interval when macropores were optically detected. The inset shows a vesicle with macropores at the two poles (see white arrows) recorded 1 ms after the beginning of the pulse. The scale bar corresponds to 10 μm. In both plots, time $t = 0$ was set as the beginning of the pulse. The dashed lines indicate the end of the pulse. *Reproduced from Ref. [97]* (http://dx.doi.org/10.1039/B703580B) by permission of The Royal Society of Chemistry.

this aspect ratio depends on whether the vesicle has been porated or not. In the absence of poration, the relaxation can be described by a single exponential with a characteristic decay time, τ_1. Figure 1.7A gives one example of the response of a giant vesicle, which is initially spherical. The pulse conditions in this case build up a transmembrane potential Ψ_m (see Eq. 1.8), which is below the poration limit characterized by the critical poration potential Ψ_c. The maximum deformation of this vesicle corresponds to about 10% change in the vesicle aspect ratio. The degree of vesicle deformation depends on the initial tension of the vesicle as well as on the excess area. The latter is defined as an excess compared to the area of a spherical vesicle of the same volume.

The typical decay time for the relaxation of nonporated vesicles, τ_1, is on the order of 100 μs. It is defined by the relaxation of the total membrane tension attained at the end of the pulse, which is the sum of the electrotension σ_{el} and the initial tension σ_0 (see Eq. 1.10). Thus, τ_1 relates mainly to the relaxation of membrane stretching: $\tau_1 \sim \eta_D/\sigma$, where η_D is the surface dilatational viscosity of the membrane (see Section 2). For membrane tensions of the order of 5 mN/m (which should be around the maximum tension before the membrane ruptures, $\sigma \cong \sigma_{lys}$) and for typical value of η_D (see Table 1.1), one obtains $\tau_1 \sim 100$ μs, which corresponds to the value experimentally measured (see Fig. 1.7A).

Porated vesicles exhibit more complex dynamics. The pores can reach various sizes depending on their location at the vesicle or cell surface (see, e.g., Refs. [81,108] and work cited therein). For the case of plane parallel electrodes, the poration occurs predominantly in the area at the poles of the vesicle facing the electrodes. This is because the transmembrane potential attains its maximal value at the two poles as expressed by the angular dependence in Eq. (1.8). With optical microscopy, only pores that are of diameter larger than about half a micron can be resolved. We refer to them as macropores since they are much larger than the average ones. The lifetime of macropores, τ_{pore}, observed in vesicles in the fluid state, varies with pore radius, r_{pore}, [109] and depends on the membrane edge tension, γ, and the membrane dilatational viscosity: $\tau_{pore} \sim 2r_{pore}\eta_D/\gamma$. For phosphatidylcholine vesicles with low tension, the lifetime τ_{pore} is typically shorter than 30 ms [76]. In Section 4.3.5, we will discuss the effect of membrane edge tension on pore resealing in detail.

Figure 1.7B shows the time dependence of the deformation of a vesicle in which macropores were observed. The maximum deformation is much higher than the one observed for nonporated vesicles (compare with the maximum aspect ratio a/b in Fig. 1.7A). The typical relaxation time

measured on different vesicles is $\tau_2 \cong 7 \pm 3$ ms. The relaxation process associated with τ_2 takes place during the time interval when pores are present (see shaded region and inset in Fig. 1.7B). Thus, τ_2 is determined by the closing of the pores: $\tau_2 \sim \eta_D r_{pore}/(2\gamma)$. The edge tension γ is on the order of 10^{-11} N [34,110]. For a typical pore radius of 1 μm, one obtains $\tau_2 \sim 10$ ms. When the vesicles have some excess area, the relaxation proceeds in two steps, fast relaxation characterized by τ_2 and a second, longer, relaxation with decay time τ_3: $0.5\ \text{s} < \tau_3 < 3\ \text{s}$ [76]. This latter relaxation time is related to the presence of some excess area available for shape changes and fluid displacement driven by the bent membrane.

4.3.2 Response of gel-phase membranes

As discussed in Section 2, the mechanical and rheological properties of membranes in the gel phase differ significantly from those of fluid membranes. These differences introduce new features in the response of gel-phase membranes to electric fields. We compared the response to DC pulses of a vesicle in the fluid phase, with that of a vesicle in the gel phase. The applied DC pulses were weak enough not to induce the formation of macropores in the membranes. Figure 1.8A shows the deformation of the two vesicle types in response to DC pulses with the duration of 300 μs. To achieve similar maximal degree of deformation in vesicles with comparable radii, stronger pulses had to be applied to the gel-phase vesicle as compared to the fluid one. Pulses with field strength of about 100 kV/m do not produce optically detectable deformations in gel-phase vesicles, while strong pulses of about 500 kV/m applied to the fluid-phase vesicles cause poration. The fluid vesicle gradually deforms and reaches maximal deformation (maximal aspect ratio a/b) at the end of the pulse as in Fig. 1.7A. The gel-phase vesicle responds significantly faster and exhibits a relaxation with a decay time of about 50 μs already during the pulse. This unusual intrapulse relaxation was found to be due to wrinkling of the membrane [111] as shown with the inset in Fig. 1.8A. Typical wavelengths of the wrinkles, Λ, lie in the range of 5–8 μm and were found to obey laws for wrinkling of elastic sheets [112–114]: $\Lambda = 2(\pi^2 l^2 \kappa/\sigma)^{1/4}$, where l is the characteristic length of the system, which in our case is the vesicle size, $l \cong 2R$. The bending stiffness, κ, of membranes in the gel phase is orders of magnitude higher than that of fluid membranes, see Table 1.1, which is one of the reasons why wrinkling on fluid vesicles is not observed. Furthermore, fluid membranes have zero shear modulus and deform smoothly rather than exhibiting wrinkles.

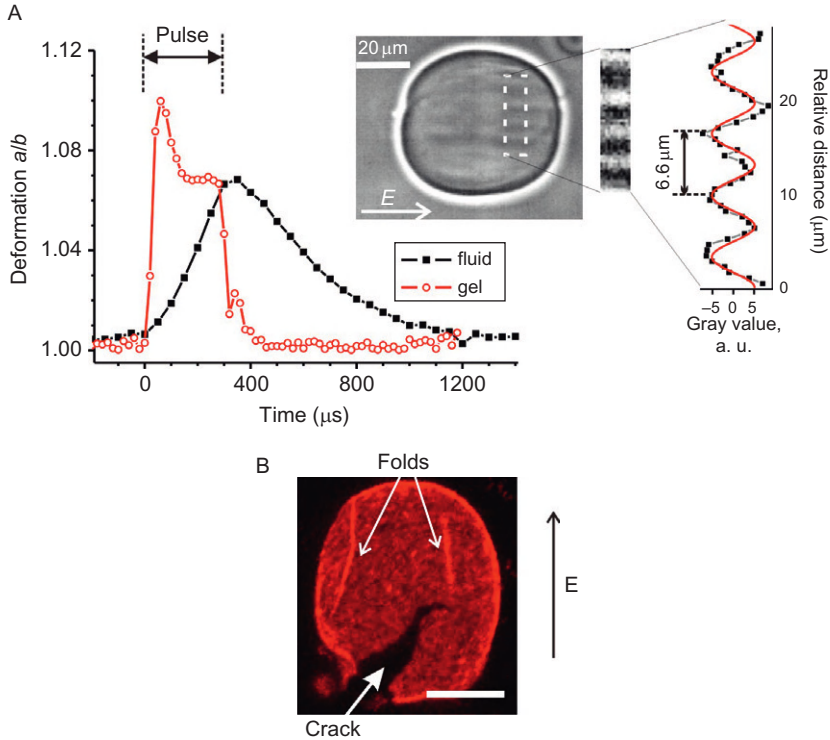

Figure 1.8 Deformation and poration of gel-phase vesicles. (A) Deformation response of a gel-phase vesicle with a radius of 22 μm, and a fluid-phase vesicle with a radius of 20 μm. The applied rectangular DC pulses were with duration of 300 μs as indicated in the graph. The field strength of the pulses was 500 and 80 kV/m for the gel and the fluid vesicle, respectively, which is below the corresponding poration thresholds for the two types of membranes. The gel-phase vesicle exhibits an intrapulse relaxation arising from wrinkling of the membrane. The vesicle wrinkling is visible in the inset snapshot recorded at time $t = 200$ μs. A magnified and enhanced section of the image indicated with a dashed rectangle is given to the right of the image, showing the membrane wrinkling parallel to the electric field direction. The gray value intensity from such a section is plotted and fitted with a sinusoidal function. The corresponding wavelength of the wrinkles is about 6.6 μm as indicated on the plot. (B) Electroporated gel-phase vesicle with radius 25 μm observed with confocal microscopy. Before the pulse, the vesicle was spherical. After applying a pulse with field strength of 600 kV/m and duration of 300 μs, the vesicle cracks open and folds as indicated by the arrows. The field direction is indicated with an arrow. The image was recorded a few seconds after the end of the pulse. A relatively big crack is visible in the vesicle as shown in the 3D projection of the vesicle top part. The scale bar represents 20 μm. *Reproduced from Ref. [111]* (http://dx.doi.org/10.1039/B925929E) by permission of The Royal Society of Chemistry.

The behavior of gel-phase vesicles exposed to stronger pulses above the poration threshold is also significantly different from that of porated fluid membranes. While pores in GUVs made of lipids in the fluid phase reseal within few tens of milliseconds, gel-phase giant vesicles exhibit long-living pores [96,111]. The pores may resemble cracks on solid shells, see Fig. 1.8B, which remain open for minutes. Similar arrest was reported for mechanically induced pores in membranes below the main phase transition temperature [25]. Having in mind that the pore lifetime is defined by the membrane viscosity ($\tau_{pore} \sim 2r_{pore}\eta_D/\gamma$, see the previous section), it is easy to understand the long lifetime of pores in gel-phase membranes. The membrane viscosity diverges when the membrane crosses the main phase transition [6]. Thus, the resealing process is strongly suppressed. The irregular shape of the pores in gel-phase vesicles may be further indicative of a relatively low edge tensions in such membranes.

One additional feature that differentiates the response of gel- from fluid-phase membranes is the critical poration threshold. As demonstrated in Fig. 1.8A, pulses that porate fluid vesicles lead only to deformation of gel-phase GUVs. The critical transmembrane potential for the latter was found to be in the range of 8–10 V [111]. This value is significantly higher than the critical potential of 1 V reported for fluid membranes [30,80,81]. Thus, membranes in the gel phase can stand higher tensile stresses (see Eq. 1.9). This is also confirmed by micropipette aspiration experiments, showing that fluid-phase dimyristoylphosphatidylcholine membranes undergo lysis at tensions around 2–3 mN/m, but when in the gel phase, the membranes rupture at tensions above 15 mN/m [33]. It is important to note that the rupture process depends on the loading rate [32,115,116]. At high loading rates, the membrane can sustain much higher tensions before it ruptures. Similar behavior was demonstrated by simulation studies, where fluid DPPC bilayers were shown to spontaneously rupture at tensions exceeding 90 mN/m [117].

4.3.3 Unusual behavior of charged membranes exposed to DC pulses

In the previous two sections, we discussed the electro-deformation and electroporation of vesicles made of single-component membranes in water. When negatively charged lipids, such as phosphatidylglycerol (PG) or phosphatidylserine, are present in the membrane, a very different response of the vesicles in the fluid phase can be observed, partially influenced by the medium conditions [118].

In buffered solutions containing EDTA, PC:PG vesicles with molar ratios 9:1, 4:1, and 1:1 behave in the same way as pure PC vesicles, that is, the pulses induce opening of macropores with a diameter up to about 10 μm, which reseal within tens of milliseconds. In nonbuffered solution, the membranes with low fractions of charged lipids (9:1 and 4:1) retain this behavior, but for membrane composition of 1:1 PC:PG, the vesicles collapse and disintegrate after electroporation [118] (see Fig. 1.9). Typically, one macropore forms and expands in the first 50–100 ms at a very high speed of approximately 1 mm/s. The entire vesicle content is released seen as darker fluid in Fig. 1.9A. The bursting is followed by restructuring of the membrane into what seem to be interconnected bilayer fragments in the first seconds and a tether-like structure in the first minute. Then the membrane stabilizes into interconnected micron-sized tubules and small vesicles (see Fig. 1.9B). Similar behavior is observed on vesicles prepared from lipid extracts from the plasma membrane of the red blood cells which also contain a fraction of

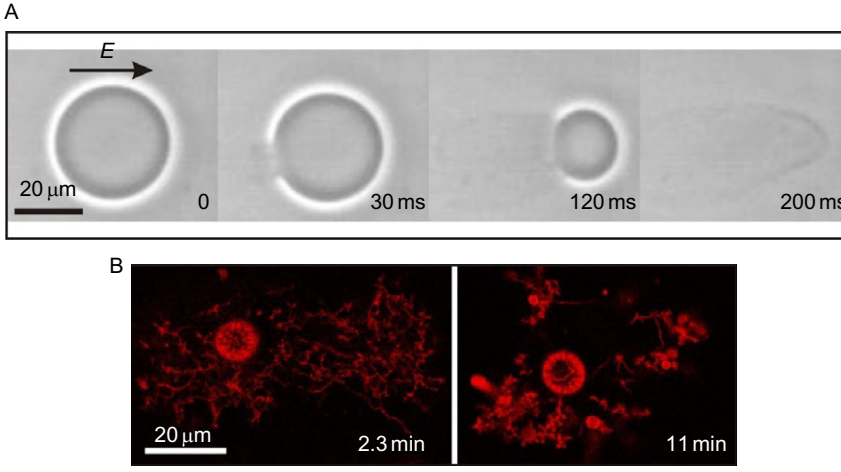

Figure 1.9 Bursting of charged (PC:PG 1:1) vesicles subjected to electric pulses. The time after the beginning of the pulse is marked on each image. The first four images are phase contrast microscopy snapshots from fast camera observation of a vesicle in salt solution subjected to a pulse with field strength 120 kV/m and duration 200 μs. The field direction is indicated in the first snapshot with an arrow. The vesicle bursts and disintegrates. The last two images show confocal cross-sections of a vesicle, which has been subjected to an electric pulse and has burst and rearranged into a network of tubes and smaller vesicles. *Reproduced from Ref. [96]* (http://dx.doi.org/10.1039/B901963D) by permission of The Royal Society of Chemistry.

charged lipids [118]. These observations suggest that the vesicle bursting and membrane instability are related to the amount of the charged lipid in the bilayer as theoretically predicted in earlier studies [119–121].

The amount of charged lipid in the bilayer is not the only factor triggering bursting of the synthetic membranes. In particular, as mentioned above, vesicles with high content of PG (50 mol%) do not burst in solutions containing EDTA. The latter molecule is a chelating agent generally added in solutions to bind multivalent ions possibly present as impurities in the solution, such as calcium [122]. The observation that EDTA suppresses bursting suggests that divalent ions present as impurities can act as a destabilizing agent in the process of vesicle bursting.

Plasma membranes should exhibit analogous bursting instability as that of the vesicles made of lipid extracts because their lipid composition is similar. However, cell membranes are subjected to internal mechanical constraints imposed by the cytoskeleton, which prevents their disintegration even if their membranes are prone to disruption when subjected to pulses. Instead, the pores in the cell membrane are stable for a long time [123] and can either lead to cell death by lysis or reseal depending on the media [69,124]. The latter is the key to efficient electroporation-based protocols for drug or gene transfer in cells. The results discussed in this section suggest that membrane charge as well as minute amounts of molecules such as EDTA might be important but not yet well understood regulating agents in these protocols.

4.3.4 Deformation dynamics of vesicles in salt solutions

In the previous three sections, we discussed the effect of the membrane composition and phase state on the response of vesicles to DC pulses. In this section, we consider the effect of presence of salt in the media. In the presence of salt in the vesicle exterior (e.g., NaCl solution with concentration above 0.1 mM), unusual shape changes are observed [125]. The vesicles adopt spherocylindrical shapes during the pulse. These deformations are short lived (their lifetime is about 1 ms) and occur only in the presence of salt outside the vesicles, irrespective of their inner content. When the solution conductivities inside and outside are the same, $\lambda_{in} \approx \lambda_{ex}$ ($x \approx 1$), vesicles with square-like cross-section are observed. For the case $\lambda_{in} < \lambda_{ex}$ ($x < 1$), the vesicles adopt disc-like shapes, while in the opposite case, $\lambda_{in} > \lambda_{ex}$ ($x > 1$), they deform into long cylinders with rounded caps; see Fig. 1.10C–E. The transition from tubes to discs is analogous to transition 3 (from prolates to oblates) in Fig. 1.5A observed in AC fields.

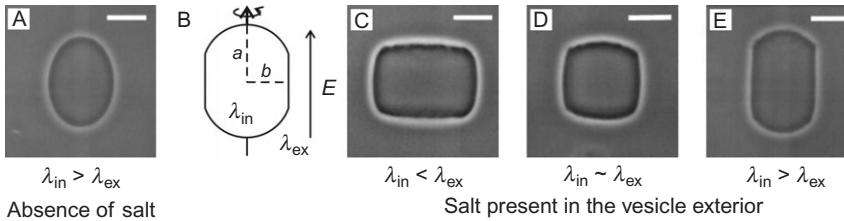

Figure 1.10 Deformation of vesicles in the absence and presence of salt at different conductivity conditions and subjected to DC pulses (200 kV/m, 200 μs). (A) In the absence of salt in the external solution, prolate deformation is observed. (B) Schematic illustration of a cross-section of a vesicle, which has adopted spherocylindrical deformation (a cylinder with spherical caps) when salt is present in the vesicle exterior as in (C)–(E). The field direction is indicated with an arrow. The presence of salt flattens the vesicle walls into disk-like (C), "square"-like (D), and tube-like (E) shapes. The scale bars correspond to 15 μm. *Reproduced from Ref. [125]* (http://dx.doi.org/10.1529/biophysj.106.081620) with permission from Elsevier.

The detected spherocylindrical deformations are nonequilibrium shapes and have a very short lifetime, which is why they have not been observed at standard video acquisition speed. The flattening of the vesicle walls starts during the applied pulse and is observed throughout a period of about 1 ms. The formation of these shapes is not well understood. They are observed also in the presence of small negatively charged nanoparticles in the vesicle exterior [96]. As discussed in Ref. [125], one possible explanation for the vesicle spherocylindrical deformation could be that ions or particles flatten the equatorial zone of the deformed vesicle. During the pulse, there is an inhomogeneity in the membrane tension due to the fact that the electric field is the strongest at the poles of the vesicle and almost zero close to the equator. The kinetic energy of the accelerated ions or particles hitting the equatorial (tensionless) region of the vesicle is higher than the energy needed to bend the membrane, thus leading to the observed deformation. In addition, particle-driven flows may be inducing membrane instability giving rise to higher order modes of the vesicle shape [126]. Yet another possible explanation may be related to a change in the spontaneous curvature of the bilayer due to particle or ion asymmetry across the membrane [127]. During the pulse, local and transient accumulation of particles or ions in the membrane vicinity can occur. The mechanism driving the cylindrical deformations might be a combination of nanoparticle electrophoresis and changes in the membrane spontaneous curvature. Furthermore, another influencing factor might be an electrohydrodynamic instability caused by electric fields interacting with flat membranes, which was predicted to

increase the membrane roughness [128]. Finally, the flexoelectric properties of the lipid membrane, first postulated by Petrov [129–131], might also be involved as recently proposed [132,133]. The interplay between interface ion concentration gradients combined with the overall ionic strength and the bilayer material properties and tension could be expected to produce the spherocylindrical deformation we observe. The mechanism behind the formation of these shapes remains poorly understood and requires further studies.

4.3.5 Electroporation as a method to measure membrane edge tensions

The edge tension drives the closing of pores in membranes. It plays a crucial role in membrane resealing mechanisms taking place after physical protocols for drug delivery, such as sonoporation [134] or electroporation [135]. Being able to experimentally measure the edge tension is thus of significant interest for understanding various biological events and physicochemical processes in membranes. However, only a few experimental methods have been developed to directly assess this physical quantity. Observations on open cylindrical giant vesicles exposed to AC fields [110] provided an estimate for the edge tension, but this technique did not allow for good control over the system. In another work, the vesicles were porated with an electric pulse, and the pores were kept open by externally adjusting the membrane tension with a micropipette [136]. Even though solid, this approach requires the use of sophisticated equipment such as a setup for vesicle micropipette aspiration. In Refs. [137,138], the pore closure dynamics in GUVs was visualized by means of using viscous glycerol solutions and fluorescent dyes in the membrane, both of which potentially influence the edge tension.

A much simpler approach is based on the electroporation of giant vesicles and observation of the pore closure dynamics with a fast digital imaging as reported in Ref. [34]. The analysis of the pore dynamics was based on the theoretical work of Brochard-Wyart *et al.* [8]. The process of pore closure was observed under phase contrast microscopy with a high-speed digital camera with acquisition speed above 1000 frames per second. In this way, the need of using viscous solutions to slow down the system dynamics was avoided, and the application of fluorescent dyes to visualize the vesicles as in Refs. [109,137,138] was not necessary. Vesicle electroporation in Ref. [34] was induced by applying electric pulses of 5-ms duration and field strength in the range of 20–80 kV/m. The pore dynamics typically consisted of four stages: growing, stabilization at some maximal pore radius, slow decrease in pore size, and fast closure (see, e.g., data in

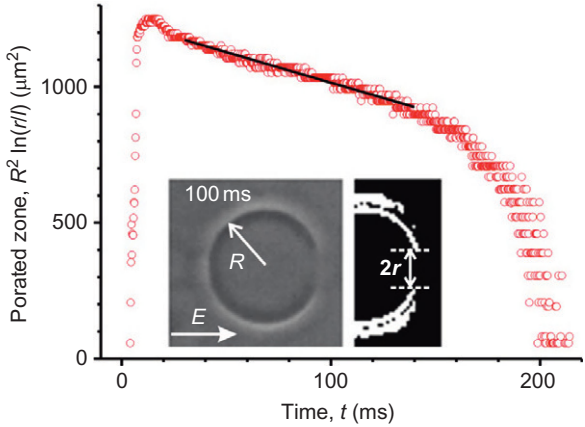

Figure 1.11 Evolution of the porated region in an egg PC vesicle as characterized by $R^2\ln(r/l)$ as a function of time t, Eq. (1.11) (note that to avoid plotting a dimensional value in the logarithmic term, we have introduced $l = 1$ μm). The open circles are experimental data, and the solid line is a linear fit, whose slope yields the edge tension γ. The inset shows a raw image (left) of a porated vesicle with a radius of 17 μm 100 ms after being exposed to an electric pulse with duration of 5 ms and amplitude of 50 kV/m. The field direction is indicated with an arrow. To the right is an enhanced and processed image of the vesicle half facing the cathode. The inner white contour corresponds to the location of the membrane. The pore radius is schematically indicated. *Reproduced from Ref. [34]* (http://dx.doi.org/10.1016/j.bpj.2010.09.032) with permission from Elsevier.

Fig. 1.11). The third stage of slow pore closure is the one, which can be used to determine the membrane edge tension applying the dependence derived in Ref. [8]:

$$R^2\ln(r) = -\frac{2\gamma}{3\pi\eta}t + C \tag{1.11}$$

where R and r are the vesicle and pore radii, respectively; γ denotes the edge tension; η is the viscosity of the aqueous medium; t is time; and C is a constant depending on the maximal pore radius reached. Then, one only has to consider the linear part of $R^2\ln(r)$ as a function of time corresponding to the slow closure stage. The slope of this dependence yields the value of the edge tension γ following Eq. (1.11). Figure 1.11 illustrates the analysis performed on one egg PC vesicle. Measurements on many vesicles yield for the average value of the edge tension of such membranes $\gamma = 14.3$ pN.

Using this approach, one can measure the edge tension in membranes of various compositions, thus characterizing the stability of pores in these membranes, and evaluate the effect of various inclusions. For example,

we found that the addition of cholesterol to DOPC membranes increases the edge tension confirming previously reported results [137]. The inverted-cone shape of cholesterol prevents it from locating at the rim of the pore. Thus, the presence of cholesterol requires more energy to rearrange the lipids along the pore walls increasing the edge tension. Surprisingly, doping DOPC membranes with another cone-shaped type of lipid such as dioleoylphosphatidyl-ethanolamine (DOPE) was found to decrease the edge tension, that is, DOPE is pore stabilizing [34]. Presumably, the molecular architecture of PE lipids leading to their tendency to form an inverted hexagonal phase, which facilitates fusion and vesicle leakage, see, for example, Ref. [139], is also responsible for stabilizing pores. A plausible explanation for this behavior is also provided by the propensity of PE to form interlipid hydrogen bonds [140,141]. Presumably, inter-PE hydrogen bonding in the pore region can effectively stabilize pores.

As demonstrated above, the edge tension is a sensitive parameter, which effectively characterizes the stability of pores in membranes. Collecting a database for the effect of various types of membrane inclusions will be useful for understanding the lifetime of pores in membranes with more complex compositions, which is important for achieving control over medical applications for drug and gene delivery in cells.

4.3.6 Vesicle electrofusion

Membrane electrofusion is vastly used in cell biology and biotechnology (see, e.g., Refs. [63,64,142] and the studies cited therein). One application aspect is based on the electrofusion of cells yielding multinucleated viable cells with new properties (this phenomenon is also known as hybridization; see, e.g., Ref. [64]). Other applications of electroporation and electrofusion are related to introducing molecules such as proteins, foreign genes (plasmids), antibodies, and drugs into cells.

When a DC pulse is applied to a couple of fluid-phase vesicles, which are in contact and oriented in the direction of the field, electrofusion can be observed. The necessary condition is that membrane poration is induced in the contact area between the two vesicles. The possible electrofusion steps are schematically illustrated in Fig. 1.12A.

4.3.6.1 Fusion dynamics

Membrane fusion is fast. The time needed for the formation of a fusion neck can be rather short as demonstrated by electrophysiological methods applied to the fusion of small vesicles with cell membranes [143–146]. The time

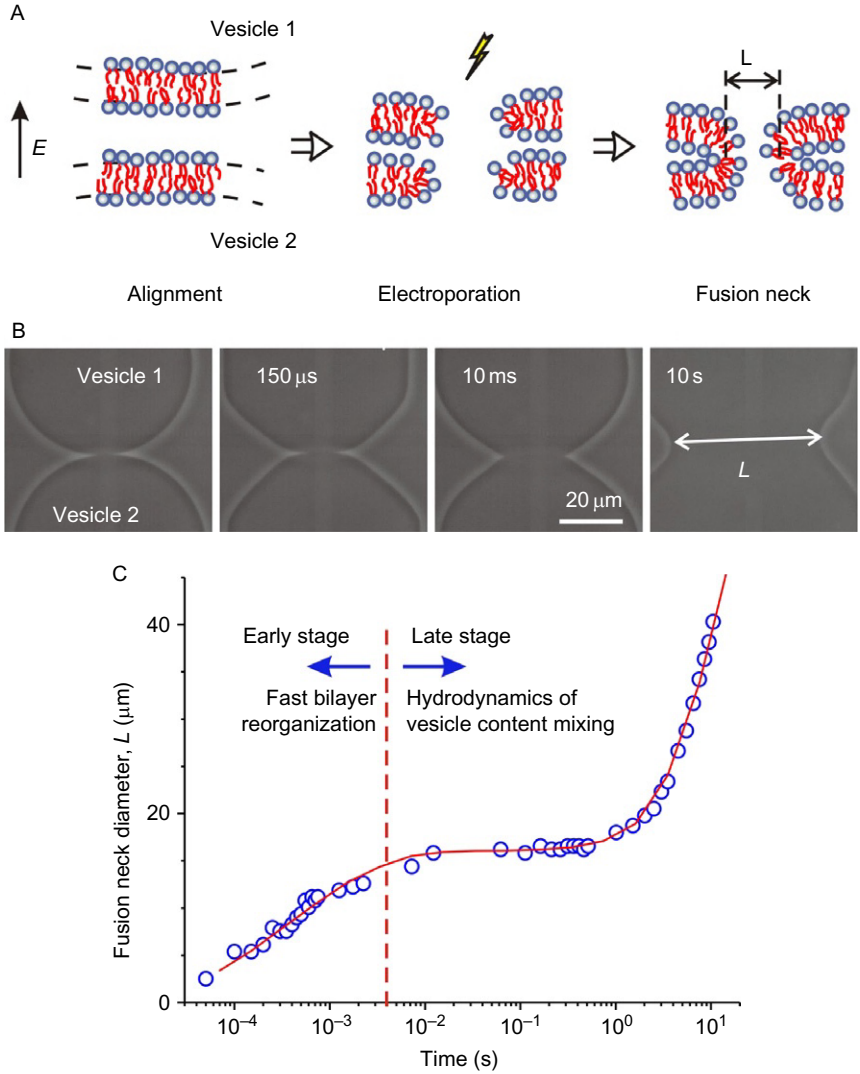

Figure 1.12 Vesicle electrofusion. (A) Schematic illustration of the possible steps of the electrofusion process: two lipid vesicles are brought into contact (only the membranes in the contact zone of the vesicles are sketched), followed by electroporation and formation of a fusion neck of diameter *L*. The pore sizes in the second cartoon are not in scale but almost an order of magnitude larger than the bilayer thickness. (B) Micrographs from the electrofusion of a vesicle couple. Only segments of the vesicles are visible. The external solution contains 1 mM NaCl, which causes flattening of the vesicle walls in the second snapshot (see Section 4.3.4). The amplitude of the DC pulse was 240 kV/m, and its duration was 120 μs. The time after the beginning of the pulse is indicated on the snapshots. (C) Time evolution of the fusion neck diameter, *L* formed between two vesicles with radii of about 15 μm. The solid curve is a guide to the eye. The vertical dashed line indicates the border between the two stages in the fusion dynamics. *Reproduced from Ref. [97]* (http://dx.doi.org/10.1039/B703580B) by permission of The Royal Society of Chemistry.

evolution of the observed membrane capacitance indicates that the formation of the fusion neck is presumably faster than 100 μs. Direct observation of the fusion of giant vesicles confirms this finding, suggesting that this time is even shorter [147,148]. An example of a few snapshots taken from the electrofusion of two GUVs with identical membrane composition and in the presence of salt is given in Fig. 1.12B. The overall deformation of each vesicle as seen in the second snapshot corresponds to the spherocylindrical shapes as observed with individual vesicles in the presence of salt. From such micrographs, one can measure the fusion neck diameter, denoted by L in Fig. 1.12A and B, and follow the dynamics of its expansion as shown in Fig. 1.12C.

From the data, two stages of the fusion process can be distinguished (note that the data are displayed in a semilogarithmic plot): an early one, which is very fast and with average expansion velocity of about 2×10^4 μm/s, followed by a later slower one with an expansion rate, which is orders of magnitude smaller (~ 2 μm/s). The early stage is governed by fast relaxation of the membrane tension built during the pulse, whereby the dissipation occurs in the bilayer. Essentially, the driving forces here are the same as those responsible for the relaxation dynamics of nonporated vesicles (as characterized by τ_1 in Section 4.3.2). In the later stage of fusion, the dynamics is mainly governed by the displacement of the volume of fluid around the fusion neck between the fused vesicles. The restoring force is related to the bending elasticity of the lipid bilayer [147,148].

The characteristic dynamics of the expansion of the fusion neck in electrofusing vesicles is similar to that observed with vesicles where the fusion is triggered in a different way, namely by using fusogenic molecules incorporated in the membrane (see Fig. 1.13). Giant vesicles functionalized with such molecules were brought in contact by means of micropipettes and observed to fuse after local injection of lanthanide ions, which complex the fusogenic molecules from the opposing bilayers [147]. Because the fusion of larger vesicles would lead to the expansion of the fusion neck to larger diameters, in Fig. 1.13, the neck diameter L is rescaled by $(R_1 + R_2)$, where R_1 and R_2 are the radii of the two vesicles before they were brought into contact. Inspection of Fig. 1.13 shows that the data from the two fusion protocols collapse between 50 μs and approximately 3 ms, that is, during the early stage of the fusion neck opening.

A more detailed comparison of the data reveals that the electrofusion data involve six orders of magnitude in time, whereas the ligand-mediated fusion data cover only three orders of magnitude in time. The different behavior of

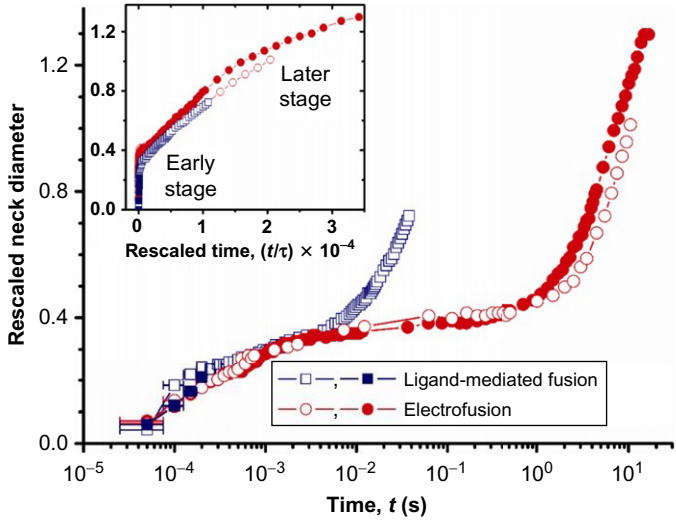

Figure 1.13 Rescaled fusion neck diameter $L/(R_1 + R_2)$ as a function of time t is plotted semilogarithmically for ligand-mediated fusion and electrofusion. The data sets collapse onto a single curve between 50 μs and 3 ms. The inset shows the rescaled fusion neck diameter as a function of the rescaled time t/τ (see text for definition of τ). The normalized data collapse onto a single curve for the later stages of the expansion of the fusion neck corresponding to $t/\tau > 10^3$. *Reproduced from Ref. [147]* (http://dx.doi.org/10.1073/pnas.0602766103), copyright 2006 National Academy of Sciences, USA.

the fusion neck diameter at later times is a result of the different tensions that the membranes experience during the later stage of the opening of the fusion neck. For ligand-mediated fusion, each of the two vesicles is aspirated by a micropipette, and the pressure is kept constant during the whole process, which implies that the membranes experience a large and essentially constant tension of the order of 5 mN/m. After the fusion neck has been formed, it opens rapidly because the rim of the neck is pulled by the large membrane tension. On the other hand, after electrofusion, the tension within the membranes relaxes as the rim of the neck opens up and is of the order of 0.05 mN/m.

It is instructive to use dimensional analysis to find an appropriate timescale, τ, for the later stage of the expansion of the fusion neck, that is, after a few milliseconds. The driving force for this expansion is provided by the membrane tension, σ, whereas the hydrodynamic or Stokes friction is governed by the viscosity, η, of the aqueous solution to be displaced. Our system is characterized by two well-separated length scales, the

membrane thickness, h, and a typical vesicle size, R. We choose $R = (R_1 + R_2)/2$. The only timescale, which one can obtain from a combination of the four variables σ, η, h, and R, is given by $\tau = (\eta R/\sigma) f(h/R)$ with the dimensionless function $f(h/R)$. Because $h \ll R$, we can replace $f(h/R)$ by $f(0)$ and, thus, ignore corrections of order (h/R). Then, for a typical effective vesicle size $R = 20$ μm, we obtain the timescales $\tau = 4.4$ μs for the aspirated vesicles and $\tau = 0.44$ ms for the electrofused vesicles.

One can calculate the corresponding value of τ for each vesicle couple and tension conditions. The parameter τ defines the rescaled time t/τ, see inset in Fig. 1.13 where we plot the rescaled fusion neck diameter, $L/(R_1 + R_2)$, as a function of t/τ. This rescaling leads to a collapse of data sets obtained from ligand-mediated fusion and electrofusion for the later stage of the expansion of the fusion neck with $t/\tau > 10^3$. Thus, we conclude that both fusion protocols lead to essentially the same dynamics.

4.3.6.2 Some applications of giant vesicle fusion

Having discussed the fusion dynamics of giant vesicles, we will now address two possible applications of this process based on the fusion of vesicles with different membrane compositions or different compositions of the enclosed solutions. First, we will illustrate the use of GUV electrofusion for creating composite membranes. Then, we will demonstrate how GUVs can be employed as microreactors suitable for the synthesis of nanoparticles.

Fusing two vesicles with different compositions of their membranes provides a promising tool for studying raft-like domains in membranes [103,104,149–152]. In particular, vesicle electrofusion is a very attractive experimental approach for producing multicomponent vesicles of well-defined composition [148]. One example for the fusion of two vesicles with different membrane composition is given in Fig. 1.14. To distinguish the vesicles according to their composition, two fluorescent markers have been used. In this particular example, one of the vesicles (vesicle 1) is composed of SM and cholesterol in 7:3 molar ratio and labeled in green. The other vesicle (vesicle 2) is composed of DOPC and cholesterol in 8:2 molar ratio and labeled in red (with fluorescence microscopy, the two vesicles can be distinguished by their color). Thus, the membrane of the fused vesicle is a three-component one. At room temperature, this lipid mixture separates into two phases, liquid ordered (rich in SM and cholesterol) and liquid disordered (rich in DOPC), which is why the final vesicle exhibits immiscible fluid domains. Then, starting with two (or more) domains produced by successive fusion, one can address the

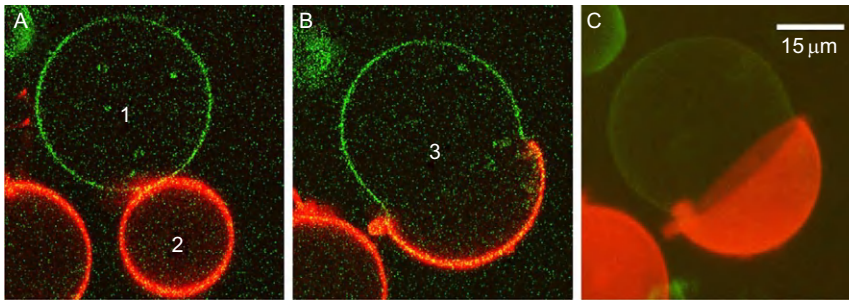

Figure 1.14 Creating a multidomain vesicle by electrofusion of two vesicles with different membrane compositions as observed with fluorescence microscopy. The images (A, B) are acquired with a confocal microscopy scans nearly at the equatorial plane of the fusing vesicles. (A) Vesicle 1 is made of SM and cholesterol (7:3) and labeled with one fluorescent dye (green). Vesicle 2 is composed of DOPC and cholesterol (8:2) and labeled with another fluorescent dye (red). (B) The two vesicles were subjected to an electric pulse (220 kV/m, duration 300 μs) and fused to form vesicle 3. Because the lipids with this final membrane composition form immiscible fluid phases, the resulting vesicle has two domains. (C) A three-dimensional image projection of vesicle 3 with the two domains formed from vesicles 1 and 2. *Reproduced from Ref. [97]* (http://dx.doi.org/10.1039/B703580B) by permission of The Royal Society of Chemistry.

question about the stability of such systems with respect to domain number and configuration.

Fusing two GUVs in order to initiate content-mixing reactions has been employed previously [153,154], but only recently, we have demonstrated that it can be applied for the synthesis of quantum-dot-like CdS nanoparticles in closed compartments [155,156]. The protocol consists of mixing two vesicle populations, one loaded with Na_2S and labeled with one fluorescent dye (red), the other loaded with $CdCl_2$ and labeled differently (green). The vesicle external media is Na_2S or $CdCl_2$ free. AC field is applied to align the vesicles in the direction of the field due to dielectric screening. In order to monitor the nanoparticle formation process, we locate a red-and-green vesicle couple and apply a DC pulse strong and long enough to porate each of the vesicles (typically, pulses of 50–200 kV/m field strength and 150–300 ms duration are sufficient). The steps of this protocol are schematically illustrated in Fig. 1.15A.

The product, in this case, quantum-dot-like CdS nanoparticles (with sizes between 4 and 8 nm as determined from transmission electron microscopy [155,156]), is visualized under laser excitation as a fluorescent bright spot in the fusion zone. Obviously, this protocol provides us with a visualizing

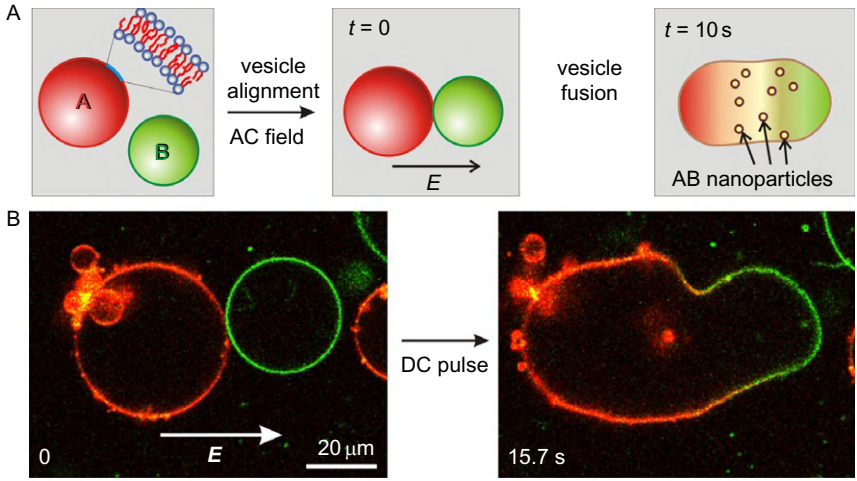

Figure 1.15 Electrofusion of giant vesicles as a method for nanoparticle synthesis. (A) Schematic illustration of the electrofusion protocol: Two populations of vesicles containing reactant A or B are mixed (in A- and B-free environment). The vesicles are subjected to an AC field to align them in the direction of the field and bring them close together. A DC pulse initiates the electrofusion of the two vesicles, and the reaction between A and B proceeds to the formation of nanoparticles encapsulated in the fused vesicle. (B) Confocal scans of vesicles loaded with 0.3 mM Na_2S (red) and 0.3 mM $CdCl_2$ (green) undergoing fusion. The direction of the field is indicated in the first snapshot. After fusion (second snapshot), fluorescence from the product is detected in the interior of the fused vesicle. The time after applying the pulse is indicated on the micrographs. *Reproduced from Ref. [155]* (http://dx.doi.org/10.1002/smll.200900560) with permission from John Wiley and Sons.

analytical tool to follow the reaction kinetics with high temporal sensitivity. This novel and facile method is especially suitable for the online monitoring of ultrafast physicochemical processes such as photosynthesis, enzyme catalysis, and photopolymerization, which usually require complex and abstracted spectroscopy technique at present. Another advantage of our approach for nanoparticle synthesis is that the process of particle nucleation and growth can be initiated at a chosen moment and location, and the formation process can be monitored directly. Furthermore, this system has the potential of implementing different manipulation tools (electric fields, micropipettes, optical tweezers, microfluidic devices, and microinjection systems) to influence the course of the synthesis.

The success of our new protocol has some implications for our current understanding of cell-based synthesis. The latter are believed to be

controlled by peptides or enzymes [157,158]. However, our results suggest that particle synthesis in cell-mimicking environment does not really require the presence of such biomolecules. Indeed, changes in the structure and topology of the membrane compartments are sufficient for cell-based nanoparticle synthesis. This outcome provides a new insight in the developing research on biomineralization mechanisms.

5. CONCLUDING REMARKS

While the top-down approach of cell biologists involves dealing with complex systems composed of an overwhelming number of molecular species whose role is not precisely and unequivocally defined, the approach of biophysicists is typically bottom-up. Applying basic physical principles to interpret the behavior of model systems made of just few components is the key giving us predictive power and understanding in tackling with more complex phenomena. Membrane biophysics builds upon studies performed predominantly on model membranes, including lipid monolayers at the air–water interface, solid-supported bilayers, black lipid membranes, vesicles, and bilayer stacks. Giant vesicles prove to be a particularly useful biomimetic tool displaying the response of the membrane directly under the microscope. While in the late 1970s till early 1990s the emphasis was given on characterizing basic mechanical and rheological properties of single- or two-component membranes as well as intermembrane interactions modulated by salts and polymers, the late 1990s and the beginning of this millennium mark the initiation of a trend in bringing gradual sophistication to the studied systems. This is helped by the progress, on the one hand, in the development and implementation of new experimental procedures and techniques breaking resolution limits [159]: fluorescence correlation spectroscopy, two-photon microscopy, optical trapping and single-molecule techniques, stimulated emission depletion microscopy, fluorescence lifetime image microscopy, ultrafast video imaging, some of which have been already applied to studies on GUVs (see, e.g., Refs. [5,147,160–163]). On the other hand, the advancement of computational power for computer simulations also sheds light on processes occurring on the atomic level. One of the pursued goals in the bottom-up approach is to progressively increase the complexity of model membrane systems and bring them closer to biological membranes so that cell membrane processes are more precisely reproduced and understood in detail. This requires increasing the complexity not only in terms of lipid composition but also in terms of

proteins and glycocalyx components. A helpful step in this direction is the reported recent progress in reconstitution of transmembrane proteins.

The issues addressed in this chapter demonstrate that cell-sized giant vesicles provide a very useful model for resolving various effects of inclusions, solutes, and external fields on lipid membranes because vesicle dynamics can be directly observed with optical microscopy. We have shown that the vesicle response to a palette of factors and conditions can be interpreted and understood considering the basic mechanical properties of the membrane. The reported observations demonstrate that giant vesicles as biomimetic membrane compartments can be of significant help to advance fundamental knowledge about the complex behavior of cells and membranes and can inspire novel practical applications.

ACKNOWLEDGMENTS

For the preparation of this chapter, I have profited from numerous experimental contributions and insightful discussions with skillful members of my group, and current and former collaborators. The work in our lab on vesicles in electric fields was initiated together with K. A. Riske. I would also like to thank S. Aranda, N. Bezlyepkina, M. D. Jordö, C. Haluska, R. L. Knorr, Y. Li, V. Nikolov, T. Portet, P. Shchelokovskyy, M. Staykova, and P. Yang. I also wish to acknowledge the valuable insights I got from the stimulating discussions with theoreticians such as R. Lipowsky, R. S. Gracià, P. M. Vlahovska, and T. Yamamoto.

REFERENCES

[1] D.D. Lasic, Liposomes: From Physics to Applications, Elsevier, Amsterdam, 1993.
[2] P.L. Luisi, P. Walde, Giant Vesicles, vol. 6, John Wiley & Sons, Ltd, Chichester, 2000.
[3] R. Dimova, S. Aranda, N. Bezlyepkina, V. Nikolov, K.A. Riske, R. Lipowsky, A practical guide to giant vesicles. Probing the membrane nanoregime via optical microscopy, J. Phys. Condens. Matter 18 (2006) S1151–S1176.
[4] P. Walde, K. Cosentino, H. Engel, P. Stano, Giant vesicles: preparations and applications, Chembiochem 11 (2010) 848–865.
[5] R. Dimova, C. Dietrich, A. Hadjiisky, K. Danov, B. Pouligny, Falling ball viscosimetry of giant vesicle membranes: finite-size effects, Eur. Phys. J. B 12 (1999) 589.
[6] R. Dimova, B. Pouligny, C. Dietrich, Pretransitional effects in dimyristoylphosphatidylcholine vesicle membranes: optical dynamometry study, Biophys. J. 79 (2000) 340–356.
[7] R. Dimova, U. Seifert, B. Pouligny, S. Förster, H.-G. Döbereiner, Hyperviscous diblock copolymer vesicles, Eur. Phys. J. B 7 (2002) 241–250.
[8] F. Brochard-Wyart, P.G. de Gennes, O. Sandre, Transient pores in stretched vesicles: role of leak-out, Phys. A 278 (2000) 32–51.
[9] D. Marsh, Elastic curvature constants of lipid monolayers and bilayers, Chem. Phys. Lipids 144 (2006) 146–159.
[10] U. Seifert, R. Lipowsky, Morphology of vesicles, in: R. Lipowsky, E. Sackmann (Eds.), Structure and Dynamics of Membranes (Handbook of Biological Physics), vol. 1a, Amsterdam, Elsevier, 1995, pp. 403–463.

[11] W. Rawicz, K.C. Olbrich, T. McIntosh, D. Needham, E. Evans, Effect of chain length and unsaturation on elasticity of lipid bilayers, Biophys. J. 79 (2000) 328–339.
[12] F. Brochard, J.F. Lennon, Frequency spectrum of flicker phenomenon in erythrocytes, J. Phys. 36 (1975) 1035–1047.
[13] M.B. Schneider, J.T. Jenkins, W.W. Webb, Thermal fluctuations of large quasi-spherical bimolecular phospholipid-vesicles, J. Phys. 45 (1984) 1457–1472.
[14] H. Engelhardt, H.P. Duwe, E. Sackmann, Bilayer bending elasticity measured by Fourier-analysis of thermally excited surface undulations of flaccid vesicles, J. Phys. Lett. 46 (1985) L395–L400.
[15] I. Bivas, P. Hanusse, P. Bothorel, J. Lalanne, O. Aguerrechariol, An application of the optical microscopy to the determination of the curvature elastic-modulus of biological and model membranes, J. Phys. 48 (1987) 855–867.
[16] J.F. Faucon, M.D. Mitov, P. Meleard, I. Bivas, P. Bothorel, Bending elasticity and thermal fluctuations of lipid-membranes—theoretical and experimental requirements, J. Phys. 50 (1989) 2389–2414.
[17] H.P. Duwe, J. Kaes, E. Sackmann, Bending elastic-moduli of lipid bilayers—modulation by solutes, J. Phys. 51 (1990) 945–962.
[18] J.R. Henriksen, J.H. Ipsen, Thermal undulations of quasi-spherical vesicles stabilized by gravity, Eur. Phys. J. E 9 (2002) 365–374.
[19] R.S. Gracia, N. Bezlyepkina, R.L. Knorr, R. Lipowsky, R. Dimova, Effect of cholesterol on the rigidity of saturated and unsaturated membranes: fluctuation and electrodeformation analysis of giant vesicles, Soft Matter 6 (2010) 1472–1482.
[20] K.R. Mecke, T. Charitat, F. Graner, Fluctuating lipid bilayer in an arbitrary potential: theory and experimental determination of bending rigidity, Langmuir 19 (2003) 2080–2087.
[21] C.H. Lee, W.C. Lin, J.P. Wang, All-optical measurements of the bending rigidity of lipid-vesicle membranes across structural phase transitions, Phys. Rev. E 6402 (2001) 020901.
[22] E. Evans, Entropy-driven tension in vesicle membranes and unbinding of adherent vesicles, Langmuir 7 (1991) 1900–1908.
[23] W. Helfrich, R.M. Servuss, Undulations, steric interaction and cohesion of fluid membranes, Nuovo Cimento D 3 (1984) 137–151.
[24] E. Evans, W. Rawicz, Entropy-driven tension and bending elasticity in condensed-fluid membranes, Phys. Rev. Lett. 64 (1990) 2094–2097.
[25] D. Needham, E. Evans, Structure and mechanical-properties of giant lipid (DMPC) vesicle bilayers from 20-degrees-c below to 10-degrees-c above the liquid-crystal crystalline phase-transition at 24-degrees-C, Biochemistry 27 (1988) 8261–8269.
[26] D. Boal, Mechanics of the Cell, Cambridge University Press, Cambridge, 2002.
[27] R. Goetz, G. Gompper, R. Lipowsky, Mobility and elasticity of self-assembled membranes, Phys. Rev. Lett. 82 (1999) 221–224.
[28] H.G. Dobereiner, E. Evans, M. Kraus, U. Seifert, M. Wortis, Mapping vesicle shapes into the phase diagram: a comparison of experiment and theory, Phys. Rev. E 55 (1997) 4458–4474.
[29] H.G. Dobereiner, G. Gompper, C.K. Haluska, D.M. Kroll, P.G. Petrov, K.A. Riske, Advanced flicker spectroscopy of fluid membranes, Phys. Rev. Lett. 91 (2003) 4.
[30] D. Needham, R.M. Hochmuth, Electro-mechanical permeabilization of lipid vesicles—role of membrane tension and compressibility, Biophys. J. 55 (1989) 1001–1009.
[31] K. Olbrich, W. Rawicz, D. Needham, E. Evans, Water permeability and mechanical strength of polyunsaturated lipid bilayers, Biophys. J. 79 (2000) 321–327.
[32] E. Evans, V. Heinrich, F. Ludwig, W. Rawicz, Dynamic tension spectroscopy and strength of biomembranes, Biophys. J. 85 (2003) 2342–2350.

[33] E. Evans, D. Needham, Physical-properties of surfactant bilayer-membranes—thermal transitions, elasticity, rigidity, cohesion, and colloidal interactions, J. Phys. Chem. 91 (1987) 4219–4228.
[34] T. Portet, R. Dimova, A new method for measuring edge tensions and stability of lipid bilayers: effect of membrane composition, Biophys. J. 99 (2010) 3264–3273.
[35] B.G. Gennis, Biomembranes: Molecular Structure and Function, Springer-Verlag, New York, 1989.
[36] K. Simons, E. Ikonen, Functional rafts in cell membranes, Nature 387 (1997) 569–572.
[37] J.B. Song, R.E. Waugh, Bending rigidity of SOPC membranes containing cholesterol, Biophys. J. 64 (1993) 1967–1970.
[38] P. Meleard, C. Gerbeaud, T. Pott, L. FernandezPuente, I. Bivas, M.D. Mitov, J. Dufourcq, P. Bothorel, Bending elasticities of model membranes: influences of temperature and sterol content, Biophys. J. 72 (1997) 2616–2629.
[39] J. Henriksen, A.C. Rowat, E. Brief, Y.W. Hsueh, J.L. Thewalt, M.J. Zuckermann, J.H. Ipsen, Universal behavior of membranes with sterols, Biophys. J. 90 (2006) 1639–1649.
[40] J.J. Pan, T.T. Mills, S. Tristram-Nagle, J.F. Nagle, Cholesterol perturbs lipid bilayers nonuniversally, Phys. Rev. Lett. 100 (2008) 198103.
[41] J.J. Pan, S. Tristram-Nagle, J.F. Nagle, Effect of cholesterol on structural and mechanical properties of membranes depends on lipid chain saturation, Phys. Rev. E 80 (2009) 021931.
[42] J. Pan, S. Tristram-Nagle, N. Kucerka, J.F. Nagle, Temperature dependence of structure, bending rigidity, and bilayer interactions of dioleoylphosphatidylcholine bilayers, Biophys. J. 94 (2008) 117–124.
[43] J.C. Mathai, S. Tristram-Nagle, J.F. Nagle, M.L. Zeidel, Structural determinants of water permeability through the lipid membrane, J. Gen. Physiol. 131 (2008) 69–76.
[44] M. Kummrow, W. Helfrich, Deformation of giant lipid vesicles by electric-fields, Phys. Rev. A 44 (1991) 8356–8360.
[45] G. Niggemann, M. Kummrow, W. Helfrich, The bending rigidity of phosphatidylcholine bilayers—dependences on experimental-method, sample cell sealing and temperature, J. Phys. II 5 (1995) 413–425.
[46] A. Roux, D. Cuvelier, P. Nassoy, J. Prost, P. Bassereau, B. Goud, Role of curvature and phase transition in lipid sorting and fission of membrane tubules, EMBO J. 24 (2005) 1537–1545.
[47] S. Semrau, T. Idema, L. Holtzer, T. Schmidt, C. Storm, Accurate determination of elastic parameters for multicomponent membranes, Phys. Rev. Lett. 100 (2008) 088101.
[48] T.P.W. McMullen, RNAH Lewis, R.N. McElhaney, Cholesterol-phospholipid interactions, the liquid-ordered phase and lipid rafts in model and biological membranes, Curr. Opin. Colloid Interface Sci. 8 (2004) 459–468.
[49] V. Nikolov, R. Lipowsky, R. Dimova, Behavior of giant vesicles with anchored DNA molecules, Biophys. J. 92 (2007) 4356–4368.
[50] R. Lipowsky, Bending of membranes by anchored polymers, Europhys. Lett. 30 (1995) 197–202.
[51] C. Hiergeist, R. Lipowsky, Elastic properties of polymer-decorated membranes, J. Phys. II 6 (1996) 1465–1481.
[52] M. Breidenich, R.R. Netz, R. Lipowsky, The shape of polymer-decorated membranes, Europhys. Lett. 49 (2000) 431–437.
[53] P. Shchelokovskyy, S. Tristram-Nagle, R. Dimova, Effect of the HIV-1 fusion peptide on the mechanical properties and leaflet coupling of lipid bilayers, New J. Phys. 13 (2011) 025004.
[54] S. Tristram-Nagle, J.F. Nagle, HIV-1 fusion peptide decreases bending energy and promotes curved fusion intermediates, Biophys. J. 93 (2007) 2048–2055.

[55] J. Israelachvili, Intermolecular and Surface Forces, Academic Press, London, 1992.
[56] S. Leibler, Curvature instability in membranes, J. Phys. 47 (1986) 507–516.
[57] J.B. Fournier, Nontopological saddle-splay and curvature instabilities from anisotropic membrane inclusions, Phys. Rev. Lett. 76 (1996) 4436–4439.
[58] I. Bivas, P. Meleard, Bending elasticity and bending fluctuations of lipid bilayer containing an additive, Phys. Rev. E 67 (2003) 012901.
[59] E.A. Evans, Bending resistance and chemically-induced moments in membrane bilayers, Biophys. J. 14 (1974) 923–931.
[60] N. Kucerka, J.F. Nagle, J.N. Sachs, S.E. Feller, J. Pencer, A. Jackson, J. Katsaras, Lipid bilayer structure determined by the simultaneous analysis of neutron and X-ray scattering data, Biophys. J. 95 (2008) 2356–2367.
[61] S. Tristram-Nagle, R. Chan, E. Kooijman, P. Uppamoochikkal, W. Qiang, D.P. Weliky, J.F. Nagle, HIV fusion peptide penetrates, disorders, and softens T-cell membrane mimics, J. Mol. Biol. 402 (2010) 139–153.
[62] E. Neumann, A.E. Sowers, C. Jordan, Electroporation and Electrofusion in Cell Biology, Plenum, New York, 1989.
[63] D.C. Chang, B.M. Chassy, J.A. Saunders, A.E. Sowers, Guide to Electroporation and Electrofusion, Academic Press, San Diego, 1992.
[64] U. Zimmermann, G.A. Neil, Electromanipulation of Cells, CRC Press, Boca Raton, 1996.
[65] J. Voldman, Electrical forces for microscale cell manipulation, Annu. Rev. Biomed. Eng. 8 (2006) 425–454.
[66] R.H.W. Funk, T.K. Monsees, Effects of electromagnetic fields on cells: physiological and therapeutical approaches and molecular mechanisms of interaction, Cells Tissues Organs 182 (2006) 59–78.
[67] M. Zhao, B. Song, J. Pu, T. Wada, B. Reid, G.P. Tai, F. Wang, A.H. Guo, P. Walczysko, Y. Gu, T. Sasaki, A. Suzuki, J.V. Forrester, H.R. Bourne, P.N. Devreotes, C.D. McCaig, J.M. Penninger, Electrical signals control wound healing through phosphatidylinositol-3-OH kinase-gamma and PTEN, Nature 442 (2006) 457–460.
[68] J. Teissie, M. Golzio, M.P. Rols, Mechanisms of cell membrane electropermeabilization: a minireview of our present (lack of ?) knowledge, Biochim. Biophys. Acta 1724 (2005) 270–280.
[69] E. Tekle, R.D. Astumian, P.B. Chock, Selective and asymmetric molecular-transport across electroporated cell-membranes, Proc. Natl. Acad. Sci. U.S.A. 91 (1994) 11512–11516.
[70] T.B. Jones, Electromechanics of Particles, Cambridge University Press, New York, 1995.
[71] H.P. Schwan, Dielectric properties of cells and tissues, in: A. Chiabrera, C. Nicolini, H.P. Schwan (Eds.), Interactions Between Electromagnetic Fields and Cells, Plenum Press, New York, 1985, pp. 75–97.
[72] C. Grosse, H.P. Schwan, Cellular membrane-potentials induced by alternating-fields, Biophys. J. 63 (1992) 1632–1642.
[73] K. Kinosita, I. Ashikawa, N. Saita, H. Yoshimura, H. Itoh, K. Nagayama, A. Ikegami, Electroporation of cell-membrane visualized under a pulsed-laser fluorescence microscope, Biophys. J. 53 (1988) 1015–1019.
[74] M. Hibino, M. Shigemori, H. Itoh, K. Nagayama, K. Kinosita, Membrane conductance of an electroporated cell analyzed by submicrosecond imaging of transmembrane potential, Biophys. J. 59 (1991) 209–220.
[75] I.G. Abidor, V.B. Arakelyan, L.V. Chernomordik, Y.A. Chizmadzhev, V.F. Pastushenko, M.R. Tarasevich, Electrical breakdown of bilayer lipid-membranes. 1. Main experimental facts and their qualitative discussion, Bioelectrochem. Bioenerg. 6 (1979) 37–52.

[76] K.A. Riske, R. Dimova, Electro-deformation and poration of giant vesicles viewed with high temporal resolution, Biophys. J. 88 (2005) 1143–1155.
[77] S.A. Simon, T.J. McIntosh, Depth of water penetration into lipid bilayers, Methods Enzymol. 127 (1986) 511–521.
[78] J.F. Nagle, S. Tristram-Nagle, Structure of lipid bilayers, Biochim. Biophys. Acta 1469 (2000) 159–195.
[79] J. Akinlaja, F. Sachs, The breakdown of cell membranes by electrical and mechanical stress, Biophys. J. 75 (1998) 247–254.
[80] T.Y. Tsong, Electroporation of cell-membranes, Biophys. J. 60 (1991) 297–306.
[81] J.C. Weaver, Y.A. Chizmadzhev, Theory of electroporation: a review, Bioelectrochem. Bioenerg. 41 (1996) 135–160.
[82] K.A. Riske, R. Dimova, Timescales involved in electro-deformation, poration and fusion of giant vesicles resolved with fast digital imaging, Biophys. J. 88 (2005) 241A.
[83] T. Portet, F.C.I. Febrer, J.M. Escoffre, C. Favard, M.P. Rols, D.S. Dean, Visualization of membrane loss during the shrinkage of giant vesicles under electropulsation, Biophys. J. 96 (2009) 4109–4121.
[84] J.L. Griffin, Orientation of human and avian erythrocytes in radio-frequency fields, Exp. Cell Res. 61 (1970) 113–120.
[85] F.J. Iglesias, M.C. Lopez, C. Santamaria, A. Dominguez, Orientation of Schizosaccharomyces pombe nonliving cells under alternating uniform and non-uniform electric-fields, Biophys. J. 48 (1985) 721–726.
[86] H. Engelhardt, H. Gaub, E. Sackmann, Viscoelastic properties of erythrocyte-membranes in high-frequency electric-fields, Nature 307 (1984) 378–380.
[87] H. Engelhardt, E. Sackmann, On the measurement of shear elastic-moduli and viscosities of erythrocyte plasma-membranes by transient deformation in high-frequency electric-fields, Biophys. J. 54 (1988) 495–508.
[88] U. Zimmermann, Electric field-mediated fusion and related electrical phenomena, Biochim. Biophys. Acta 694 (1982) 227–277.
[89] M. Winterhalter, W. Helfrich, Deformation of spherical vesicles by electric-fields, J. Colloid Interface Sci. 122 (1988) 583–586.
[90] H. Hyuga, K. Kinosita, N. Wakabayashi, Transient and steady-state deformations of a vesicle with an insulating membrane in response to step-function or alternating electric-fields, Jpn. J. Appl. Phys. Part 1 30 (1991) 2649–2656.
[91] M.D. Mitov, P. Meleard, M. Winterhalter, M.I. Angelova, P. Bothorel, Electric-field-dependent thermal fluctuations of giant vesicles, Phys. Rev. E 48 (1993) 628–631.
[92] H. Hyuga, K. Kinosita, N. Wakabayashi, Steady-state deformation of a vesicle in alternating electric-fields, Bioelectrochem. Bioenerg. 32 (1993) 15–25.
[93] P. Peterlin, S. Svetina, B. Zeks, The prolate-to-oblate shape transition of phospholipid vesicles in response to frequency variation of an AC electric field can be explained by the dielectric anisotropy of a phospholipid bilayer, J. Phys. Condens. Matter 19 (2007) 136220.
[94] P. Peterlin, S. Svetina, B. Zeks, The frequency dependence of phospholipid vesicle shapes in an external electric field, Pfluegers Arch./Eur. J. Physiol. 439 (2000) R139–R140.
[95] S. Aranda, K.A. Riske, R. Lipowsky, R. Dimova, Morphological transitions of vesicles induced by alternating electric fields, Biophys. J. 95 (2008) L19–L21.
[96] R. Dimova, N. Bezlyepkina, M.D. Jordo, R.L. Knorr, K.A. Riske, M. Staykova, P.M. Vlahovska, T. Yamamoto, P. Yang, R. Lipowsky, Vesicles in electric fields: some novel aspects of membrane behavior, Soft Matter 5 (2009) 3201–3212.
[97] R. Dimova, K.A. Riske, S. Aranda, N. Bezlyepkina, R.L. Knorr, R. Lipowsky, Giant vesicles in electric fields, Soft Matter 3 (2007) 817–827.

[98] P.M. Vlahovska, R.S. Gracia, S. Aranda-Espinoza, R. Dimova, Electrohydrodynamic model of vesicle deformation in alternating electric fields, Biophys. J. 96 (2009) 4789–4803.
[99] T. Yamamoto, S. Aranda-Espinoza, R. Dimova, R. Lipowsky, Stability of spherical vesicles in electric fields, Langmuir 26 (2010) 12390–12407.
[100] G. Taylor, Studies in electrohydrodynamics. I. The circulation produced in a drop by an electric field, Proc. R. Soc. Lond. Ser. A 291 (1966) 159–166.
[101] M. Staykova, R. Lipowsky, R. Dimova, Membrane flow patterns in multicomponent giant vesicles induced by alternating electric fields, Soft Matter 4 (2008) 2168–2171.
[102] S.L. Veatch, S.L. Keller, Organization in lipid membranes containing cholesterol, Phys. Rev. Lett. 89 (2002) 4.
[103] R. Lipowsky, R. Dimova, Domains in membranes and vesicles, J. Phys. Condens. Matter 15 (2003) S31–S45.
[104] C.C. Vequi-Suplicy, K.A. Riske, R.L. Knorr, R. Dimova, Vesicles with charged domains, Biochimica et Biophysica Acta 1798 (2010) 1338–1347.
[105] C. Marangoni, Ueber die Ausbreitung der Tropfen einer Flüssigkeit auf der Oberfläche einer anderen, Annu. Phys. Chem. 219 (1871) 337–354.
[106] D.A. Edwards, H. Brenner, D.T. Wasan, Interfacial Transport Processes and Rheology, Butterworth-Heinemann, Boston, MA, 1991.
[107] A.A. Darhuber, S.M. Troian, Principles of microfluidic actuation by modulation of surface stresses, Annu. Rev. Fluid Mech. 37 (2005) 425–455.
[108] W. Krassowska, P.D. Filev, Modeling electroporation in a single cell, Biophys. J. 92 (2007) 404–417.
[109] O. Sandre, L. Moreaux, F. Brochard-Wyart, Dynamics of transient pores in stretched vesicles, Proc. Natl. Acad. Sci. U.S.A. 96 (1999) 10591–10596.
[110] W. Harbich, W. Helfrich, Alignment and opening of giant lecithin vesicles by electric-fields, Z. Naturforsch. A Phys. Sci. 34 (1979) 1063–1065.
[111] R.L. Knorr, M. Staykova, R.S. Gracia, R. Dimova, Wrinkling and electroporation of giant vesicles in the gel phase, Soft Matter 6 (2010) 1990–1996.
[112] E. Cerda, L. Mahadevan, Geometry and physics of wrinkling, Phys. Rev. Lett. 90 (2003) 074302.
[113] E. Cerda, K. Ravi-Chandar, L. Mahadevan, Thin films—wrinkling of an elastic sheet under tension, Nature 419 (2002) 579–580.
[114] R. Finken, U. Seifert, Wrinkling of microcapsules in shear flow, J. Phys. Condens. Matter 18 (2006) L185–L191.
[115] E. Evans, V. Heinrich, Dynamic strength of fluid membranes, C. R. Phys. 4 (2003) 265–274.
[116] P.A. Boucher, B. Joos, M.J. Zuckermann, L. Fournier, Pore formation in a lipid bilayer under a tension ramp: modeling the distribution of rupture tensions, Biophys. J. 92 (2007) 4344–4355.
[117] H. Leontiadou, A.E. Mark, S.J. Marrink, Molecular dynamics simulations of hydrophilic pores in lipid bilayers, Biophys. J. 86 (2004) 2156–2164.
[118] K.A. Riske, R.L. Knorr, R. Dimova, Bursting of charged multicomponent vesicles subjected to electric pulses, Soft Matter 5 (2009) 1983–1986.
[119] H. Isambert, Understanding the electroporation of cells and artificial bilayer membranes, Phys. Rev. Lett. 80 (1998) 3404–3407.
[120] M.D. Betterton, M.P. Brenner, Electrostatic edge instability of lipid membranes, Phys. Rev. Lett. 82 (1999) 1598–1601.
[121] V. Kumaran, Instabilities due to charge-density-curvature coupling in charged membranes, Phys. Rev. Lett. 85 (2000) 4996–4999.
[122] K.A. Riske, H.G. Dobereiner, M.T. Lamy-Freund, Comment on "Gel-Fluid transition in dilute versus concentrated DMPG aqueous dispersions" J. Phys. Chem. B 107 (2003) 5391–5392.

[123] K. Schwister, B. Deuticke, Formation and properties of aqueous leaks induced in human-erythrocytes by electrical breakdown, Biochim. Biophys. Acta 816 (1985) 332–348.
[124] K. Kinosita, T.Y. Tsong, Formation and resealing of pores of controlled sizes in human erythrocyte-membrane, Nature 268 (1977) 438–441.
[125] K.A. Riske, R. Dimova, Electric pulses induce cylindrical deformations on giant vesicles in salt solutions, Biophys. J. 91 (2006) 1778–1786.
[126] V. Kantsler, E. Segre, V. Steinberg, Vesicle dynamics in time-dependent elongation flow: wrinkling instability, Phys. Rev. Lett. 99 (2007) 178102.
[127] R. Lipowsky, H.G. Dobereiner, Vesicles in contact with nanoparticles and colloids, Europhys. Lett. 43 (1998) 219–225.
[128] P. Sens, H. Isambert, Undulation instability of lipid membranes under an electric field, Phys. Rev. Lett. 88 (2002) 128102.
[129] A.G. Petrov, Flexoelectricity of lyotropics and biomembranes, Nuovo Cimento Soc. Ital. Fis. D 3 (1984) 174–192.
[130] A.G. Petrov, I. Bivas, Elastic and flexoelectric aspects of out-of-plane fluctuations in biological and model membranes, Prog. Surf. Sci. 16 (1984) 389–512.
[131] A.G. Petrov, Flexoelectricity of model and living membranes, Biochim. Biophys. Acta 1561 (2002) 1–25.
[132] L.T. Gao, X.Q. Feng, Y.J. Yin, H.J. Gao, An electromechanical liquid crystal model of vesicles, J. Mech. Phys. Solids 56 (2008) 2844–2862.
[133] L.T. Gao, X.Q. Feng, H.J. Gao, A phase field method for simulating morphological evolution of vesicles in electric fields, J. Comput. Phys. 228 (2009) 4162–4181.
[134] C.M.H. Newman, T. Bettinger, Gene therapy progress and prospects: ultrasound for gene transfer, Gene Ther. 14 (2007) 465–475.
[135] J.M. Escoffre, T. Portet, L. Wasungu, J. Teissie, D. Dean, M.P. Rols, What is (still not) known of the mechanism by which electroporation mediates gene transfer and expression in cells and tissues, Mol. Biotechnol. 41 (2009) 286–295.
[136] D.V. Zhelev, D. Needham, Tension-stabilized pores in giant vesicles—determination of pore-size and pore line tension, Biochim. Biophys. Acta 1147 (1993) 89–104.
[137] E. Karatekin, O. Sandre, H. Guitouni, N. Borghi, P.H. Puech, F. Brochard-Wyart, Cascades of transient pores in giant vesicles: line tension and transport, Biophys. J. 84 (2003) 1734–1749.
[138] P.H. Puech, N. Borghi, E. Karatekin, F. Brochard-Wyart, Line thermodynamics: adsorption at a membrane edge, Phys. Rev. Lett. 90 (2003) 128304.
[139] H. Ellens, J. Bentz, F.C. Szoka, Fusion of phosphatidylethanolamine-containing liposomes and mechanism of the L_{α}-H_{II} phase-transition, Biochemistry 25 (1986) 4141–4147.
[140] RNAH Lewis, R.N. McElhaney, Calorimetric and spectroscopic studies of the polymorphic phase-behavior of a homologous series of n-saturated 1,2-diacyl phosphatidylethanolamines, Biophys. J. 64 (1993) 1081–1096.
[141] D.A. Pink, S. McNeil, B. Quinn, M.J. Zuckermann, A model of hydrogen bond formation in phosphatidylethanolamine bilayers, Biochim. Biophys. Acta 1368 (1998) 289–305.
[142] K. Kinosita, T.Y. Tsong, Voltage-induced pore formation and hemolysis of human erythrocytes, Biochim. Biophys. Acta 471 (1977) 227–242.
[143] R. Llinas, I.Z. Steinberg, K. Walton, Relationship between presynaptic calcium current and postsynaptic potential in squid giant synapse, Biophys. J. 33 (1981) 323–351.
[144] M. Lindau, G.A. de Toledo, The fusion pore, Biochim. Biophys. Acta 1641 (2003) 167–173.
[145] I. Hafez, K. Kisler, K. Berberian, G. Dernick, V. Valero, M.G. Yong, H.G. Craighead, M. Lindau, Electrochemical imaging of fusion pore openings by electrochemical detector arrays, Proc. Natl. Acad. Sci. U.S.A. 102 (2005) 13879–13884.

[146] J.C. Shillcock, R. Lipowsky, Tension-induced fusion of bilayer membranes and vesicles, Nat. Mater. 4 (2005) 225–228.
[147] C.K. Haluska, K.A. Riske, V. Marchi-Artzner, J.M. Lehn, R. Lipowsky, R. Dimova, Time scales of membrane fusion revealed by direct imaging of vesicle fusion with high temporal resolution, Proc. Natl. Acad. Sci. U.S.A. 103 (2006) 15841–15846.
[148] K.A. Riske, N. Bezlyepkina, R. Lipowsky, R. Dimova, Electrofusion of model lipid membranes viewed with high temporal resolution, Biophys. Rev. Lett. 1 (2006) 387–400.
[149] C. Dietrich, L.A. Bagatolli, Z.N. Volovyk, N.L. Thompson, M. Levi, K. Jacobson, E. Gratton, Lipid rafts reconstituted in model membranes, Biophys. J. 80 (2001) 1417–1428.
[150] T. Baumgart, S.T. Hess, W.W. Webb, Imaging coexisting fluid domains in biomembrane models coupling curvature and line tension, Nature 425 (2003) 821–824.
[151] S.L. Veatch, S.L. Keller, Separation of liquid phases in giant vesicles of ternary mixtures of phospholipids and cholesterol, Biophys. J. 85 (2003) 3074–3083.
[152] N. Kahya, D. Scherfeld, K. Bacia, B. Poolman, P. Schwille, Probing lipid mobility of raft-exhibiting model membranes by fluorescence correlation spectroscopy, J. Biol. Chem. 278 (2003) 28109–28115.
[153] D.T. Chiu, C.F. Wilson, F. Ryttsen, A. Stromberg, C. Farre, A. Karlsson, S. Nordholm, A. Gaggar, B.P. Modi, A. Moscho, R.A. Garza-Lopez, O. Orwar, R.N. Zare, Chemical transformations in individual ultrasmall biomimetic containers, Science 283 (1999) 1892–1895.
[154] S. Kulin, R. Kishore, K. Helmerson, L. Locascio, Optical manipulation and fusion of liposomes as microreactors, Langmuir 19 (2003) 8206–8210.
[155] P. Yang, R. Lipowsky, R. Dimova, Nanoparticle formation in giant vesicles: synthesis in biomimetic compartments, Small 5 (2009) 2033–2037.
[156] P. Yang, R. Dimova, Nanoparticle synthesis in vesicle microreactors, in: A. George (Ed.), Biomimetic Based Applications, InTech, Rijeka, Croatia, 2011, pp. 523–552.
[157] R.R. Naik, S.J. Stringer, G. Agarwal, S.E. Jones, M.O. Stone, Biomimetic synthesis and patterning of silver nanoparticles, Nat. Mater. 1 (2002) 169–172.
[158] N. Kroger, M.B. Dickerson, G. Ahmad, Y. Cai, M.S. Haluska, K.H. Sandhage, N. Poulsen, V.C. Sheppard, Bioenabled synthesis of rutile (TiO(2)) at ambient temperature and neutral pH, Angew. Chem. Int. Ed. 45 (2006) 7239–7243.
[159] K. Simons, M.J. Gerl, Revitalizing membrane rafts: new tools and insights, Nat. Rev. Mol. Cell Biol. 11 (2010) 688–699.
[160] J. Korlach, P. Schwille, W.W. Webb, G.W. Feigenson, Characterization of lipid bilayer phases by confocal microscopy and fluorescence correlation spectroscopy, Proc. Natl. Acad. Sci. U.S.A. 96 (1999) 8461–8466.
[161] R.F.M. de Almeida, J. Borst, A. Fedorov, M. Prieto, AJWG Visser, Complexity of lipid domains and rafts in giant unilamellar vesicles revealed by combining imaging and microscopic and macroscopic time-resolved fluorescence, Biophys. J. 93 (2007) 539–553.
[162] R. Dimova, B. Pouligny, Optical dynamometry to study phase transitions in lipid membranes, in: A.M. Dopico (Ed.), Methods in Molecular Biology, vol. 400, Humana Press Inc., Totowa, NJ, 2007, pp. 227–236.
[163] J. Fitter, A. Katranidis, T. Rosenkranz, D. Atta, R. Schlesinger, G. Buldt, Single molecule fluorescence spectroscopy: a tool for protein studies approaching cellular environmental conditions, Soft Matter 7 (2011) 1254–1259.

CHAPTER TWO

Low-Frequency Sound Propagation in Lipid Membranes

Lars D. Mosgaard, Andrew D. Jackson, Thomas Heimburg[1]
Membrane Biophysics Group, The Niels Bohr Institute, University of Copenhagen, Copenhagen, Denmark
[1]Corresponding author: e-mail address: theimbu@nbi.dk

Contents

1. Introduction 52
2. The Propagating Soliton in Nerve Membranes 54
3. Brief Overview of Sound 56
4. System Response to Adiabatic Pressure Perturbations 58
   4.1 Relaxation function 61
   4.2 Response function 61
5. Adiabatic Compressibility 62
6. Results—The Speed of Sound 64
   6.1 Dispersion relation 66
7. Discussion 68
Appendix A. Derivation of the Dynamic Heat Capacity Using the Convolution Theorem 70
References 72

Abstract

In the recent years, we have shown that cylindrical biological membranes such as nerve axons under physiological conditions are able to support stable electromechanical pulses called solitons. These pulses share many similarities with the nervous impulse, for example, the propagation velocity as well as the measured reversible heat production and changes in thickness and length that cannot be explained with traditional nerve models. A necessary condition for solitary pulse propagation is the simultaneous existence of nonlinearity and dispersion, that is, the dependence of the speed of sound on density and frequency. A prerequisite for the nonlinearity is the presence of a chain-melting transition close to physiological temperatures. The transition causes a density dependence of the elastic constants which can easily be determined by an experiment. The frequency dependence is more difficult to determine. The typical timescale of a nerve pulse is 1 ms, corresponding to a characteristic frequency in the range up to 1 kHz. Dispersion in the sub-kilohertz regime is difficult to measure due to the very long wave lengths involved. In this contribution, we address theoretically the dispersion of the speed of sound in lipid membranes and relate it to experimentally accessible relaxation times by using linear response theory. This ultimately leads to an extension of the differential equation for soliton propagation.

Advances in Planar Lipid Bilayers and Liposomes, Volume 16
ISSN 1554-4516
http://dx.doi.org/10.1016/B978-0-12-396534-9.00002-7

ABBREVIATIONS

DPPC dipalmitoyl phosphatidylcholine
DSC differential scanning calorimetry

1. INTRODUCTION

Biological membranes are ubiquitous in the living world. Despite their diversity in composition, membranes of different cells or organelles are remarkably similar in structure and exhibit similar thermodynamic properties. They exist as thin, almost two-dimensional lipid bilayers whose primary function is to separate the interior of cells and organelles (subcellular compartment) from their external environments. This separation leads in turn to the creation of chemical and biological gradients which play a pivotal role in many cellular and subcellular processes, for example, adenosine triphosphate production. A particularly important feature of biomembranes is the propagation of voltage signals in the axons of neurons, which allows cells to communicate quickly over long distances, an ability that is vital for higher lifeforms such as animals [1,2].

Biological membranes exhibit a phase transition between an ordered and a disordered lipid phase near physiological conditions [3]. It has been shown that organisms alter their detailed lipid composition in order to maintain the temperature of this phase transition despite different growth conditions [4–6]. The biological implications of membrane phase transitions continue to be an area of active research. Near a phase transition, the behavior of the membrane changes quite drastically: The thermodynamic susceptibilities, such as heat capacity and compressibility, display a maximum, and the characteristic relaxation times of the membrane show a drastic slowing down [7–11].

The melting transition in lipid membrane is accompanied by a significant change of the lateral density by about -20%. Thus, the elastic constants are not only temperature dependent, but they are also sensitive functions of density. Together with the observed frequency dependence of the elastic constants (dispersion), this leads to the possibility of localized solitary pulse (or soliton) propagation in biomembrane cylinders such as nerve axons. With the emergence of the soliton theory for nerve pulse propagation, the investigation of sound propagation in lipid membranes close to the lipid melting transition has become an important issue [2]. The soliton model

describes nerve signals as the propagation of adiabatic localized density pulses in the nerve axon membrane. This view is based on macroscopic thermodynamics arguments in contrast to the well-known Hodgkin–Huxley model for the action potential that is based on the nonadiabatic electrical properties of single protein molecules (ion channels).[1] Using this alternative model, we have been able to make correct predictions regarding the propagation velocity of the nerve signal in myelinated nerves, along with a number of new predictions regarding the excitation of nerves and the role of general anesthetics [12]. In addition, the soliton model explains a number of observations about nerve signal propagation, which are not included in the Hodgkin and Huxley model, such as changes in the thickness of the membrane, changes in the length of the nerve, and the existence of phase-transition phenomena [13]. The solitary wave is a sound phenomenon which can take place in media displaying dispersion and nonlinearity in the density. Both of these criteria are met close to the main lipid transition. However, the magnitude of dispersion in the frequency regime of interest for nerve pulses (up to 1 kHz) is unknown [2]. Exploring sound propagation in lipid membranes is thus an important task for improving our understanding of mechanical pulse propagation in nerves. All previous attempts to explore sound propagation in lipid membranes have focused on the ultrasonic regime [9,14–16], and it has clearly been demonstrated that dispersion exists in this frequency regime. Furthermore, the low-frequency limit of the adiabatic compressibility of membranes (which determines the sound velocity) is equal to the isothermal compressibility, which is significantly larger than the compressibility in the megahertz regime. With the additional knowledge that relaxation times in biomembranes are of the order of milliseconds to seconds, it is quite plausible to expect significant dispersion effects in the frequent regime up to 1 kHz.

Theoretical efforts to describe sound propagation in lipid membranes near the lipid melting transition in the ultrasonic regime have been based on scaling theory, which assumes critical relaxation behavior during the transition [16,17]. However, a number low-frequency experiments, pressure jump experiments [10,18], and stationary perturbation techniques [11,19] all show noncritical relaxation dynamics. These findings have led us to propose a noncritical thermodynamical description of sound propagation in lipid membranes near the lipid melting transition for low frequencies based on linear response theory.

[1] For a comparison of the Hodgkin–Huxley model and the soliton theory, see Chapter 9.

In this chapter, we present a theoretical derivation of the magnitude of dispersion for membranes close to lipid melting transitions. The goal is to modify the wave equation for solitons in biomembranes. This will ultimately lead to a natural timescale for the pulse length, which we will explore in future work.

2. THE PROPAGATING SOLITON IN NERVE MEMBRANES

In the following, we present the hydrodynamic equations that govern the propagation of density waves in cylindrical membranes, in general, and in nerve membranes close to the chain-melting transition, in particular.

In it simplest formulation, the wave equation for compressible fluids assumes the form[2]:

$$\frac{\partial^2 \rho}{\partial t^2} = \nabla(c^2 \nabla \rho), \tag{2.1}$$

where

$$c = \sqrt{\left(\frac{\partial p}{\partial \rho}\right)_{S,0}} = \frac{1}{\sqrt{\kappa_S \rho}} \tag{2.2}$$

is the speed of sound for low-amplitude waves ($\Delta\rho \ll \rho_0$), κ_S is the adiabatic compressibility, and $\rho(x, t)$ is the density. If the speed of sound is roughly independent of density, this equation simplifies to

$$\frac{\partial^2 \rho}{\partial t^2} = c^2 \nabla^2 \rho. \tag{2.3}$$

The wave equation in one dimension is then given by

$$\frac{\partial^2 \rho}{\partial t^2} = \frac{\partial}{\partial x}\left(c^2 \frac{\partial}{\partial x}\rho\right). \tag{2.4}$$

For low-amplitude sound, we further assume that there is dispersion of the form

$$c^2 = c_0^2 + h_0 \omega^2 + \cdots, \tag{2.5}$$

[2] A derivation of the equation of sound, based on fluid dynamics, can be found in Ref. [20]. There are two basic assumptions in the derivation of the equation of sound: Perturbations are small, and sound propagation is an adiabatic process.

which corresponds to a Taylor expansion of the sound velocity with respect to frequency. The parameter h_0 indicates the magnitude of the dispersion. Due to symmetry arguments, only even power terms appear in this expansion. One way to generate this frequency dependence is to add a dispersion term to the wave equation

$$\frac{\partial^2 \rho}{\partial t^2} = \frac{\partial}{\partial x}\left(c^2 \frac{\partial}{\partial x}\rho\right) - h\frac{\partial^4}{\partial x^4}\rho. \tag{2.6}$$

The density of a small amplitude plane wave can be written as

$$\begin{aligned} \rho(x,t) &= \rho_0 + \Delta\rho \quad \text{with} \quad \Delta\rho = A\sin(kx - \omega t) \\ &\equiv A\sin(k(x - ct)). \end{aligned} \tag{2.7}$$

The amplitude of this plane wave is A, and its velocity is $c = \omega/k$. Inserting this into Eq. (2.4) yields the dispersion relation in Eq. (2.5) with $h_0 = h/c_0^2$. We have shown experimentally that the sound velocity close to melting transitions in lipid membranes is a sensitive nonlinear function of density. Thus, we expand

$$c^2 = c_0^2 + p\Delta\rho + q(\Delta\rho)^2 + \cdots. \tag{2.8}$$

The parameters p and q describe the nonlinear elastic properties of membranes. At temperatures slightly above the melting transition, lipid membranes have negative values for the parameter p and positive values for the parameter q. The final wave equation is given by

$$\frac{\partial^2 \rho}{\partial t^2} = \frac{\partial}{\partial x}\left((c_0^2 + p\Delta\rho + q(\Delta\rho)^2)\frac{\partial}{\partial x}\rho\right) - h\frac{\partial^4}{\partial x^4}\rho. \tag{2.9}$$

We have shown that this equation possesses analytical solitary solutions that in many aspects resemble the nerve pulse (see Fig. 2.1).

While the above equation makes use of the fact that the speed of sound is a known function of density, the dispersion constant h must be regarded as an adjustable parameter due to the absence of quantitative empirical data regarding dispersion in the low-frequency regime. The magnitude of h sets the width and the timescale of the mechanical pulse. In previous publications, it was adjusted to $h = 2\,\mathrm{m}^4/\mathrm{s}^2$ in order to match the observed width of the nerve pulse, which is about 10 cm. However, we will argue below that h is expected to be density dependent and that its functional form can be approximated using experimental knowledge about relaxation timescales and elastic constants. This will ultimately lead to a wave equation for

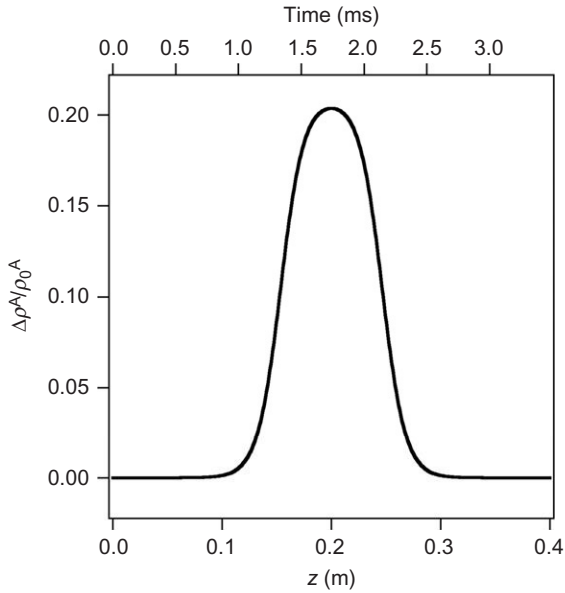

Figure 2.1 The propagating soliton using parameters appropriate for unilamellar DPPC vesicles and a dispersion constant $h = 2\text{m}^4/\text{s}^2$ (from Ref. [21]). The soliton has a width of about 10 cm and a duration of about 1 ms, which is very similar to action potentials in myelinated nerves.

the mechanical pulse in nerve axons that is free of adjustable parameters and has a timescale that is fixed by the thermodynamics of the system.

3. BRIEF OVERVIEW OF SOUND

Sound is a propagating low-amplitude density wave in compressible medium which, due to its adiabatic nature, is accompanied by a corresponding temperature wave. The equation governing sound propagation is universal. This generality implies that sound propagation is determined solely by the macroscopic thermodynamical properties of the system.

As mentioned above, the equation of sound for low-amplitude waves has the following form:

$$\frac{\partial^2 p}{\partial t^2} = c^2 \nabla^2 \rho.$$

The general solution has the following form:

$$\rho = A \exp(i\omega(t - x/\hat{c})), \tag{2.10}$$

which is merely Eq. (2.7) in complex notation. Due to dispersion and the absorption of sound in a real medium, the effective speed of sound, $\hat{c}$, is a complex quantity. The real part of the speed of sound will cause a phase shift (as a result of dispersion), and the imaginary part will lead to a decrease in the amplitude or intensity of the sound as it propagates (attenuation). This can be seen by inserting the complex speed of sound into Eq. (2.10).

$$\rho = A\exp(i\omega(t - x\mathrm{Re}(\hat{c})/|\hat{c}|^2))\exp(-x\omega\mathrm{Im}(\hat{c})/|\hat{c}|^2), \tag{2.11}$$

where

$$u = \left(\frac{\mathrm{Re}(\hat{c})}{|\hat{c}|^2}\right)^{-1} \tag{2.12}$$

is the effective speed of sound which would be measured in an experiment.

In 1928, Herzfeld and Rice extended the theory of sound by arguing that internal vibrational modes of polyatomic molecules require time to approach thermal equilibrium with translational degrees of freedom [22]. If the timescale of the density (or pressure) perturbation is similar to or less than the timescale of these internal relaxation times, the temperature response of the system will lag behind that of the perturbation. This will prevent the internal degrees of freedom from taking up all the heat and will result in a decrease in the effective heat capacity.[3] This decrease in the effective heat capacity results in hysteresis and in dissipation of heat.

In 1962, Fixman applied the basic ideas of Herzfeld and Rice to describe the viscosity of critical mixtures [23]. He was motivated by the intimate relation between viscosity and attenuation. Critical mixtures of fluids display a second-order transition which is indicated by a critical slowdown of the relaxation rates of the order parameters. In contrast to Herzfeld and Rice, Fixman did not limit his attention to the rates of translational and internal degrees of freedom but rather considered a continuum of long-wavelength fluctuations in the order parameter. With this change of perspective, he made the connection between the transfer rates and relaxation rates of order parameters in viscous systems. The slowdown during a transition means large changes in the dynamic heat capacity of the system and thereby in the speed of sound.

Following the argument of Fixman, the slowing down of the characteristic relaxation rate during the lipid melting transition will cause hysteresis

[3] Note that the effective heat capacity will be referred to as the dynamic heat capacity.

and dissipation of heat. Even in the absence of critical phenomena, internal friction and heat conduction as introduced by Stokes [24] and Kirchhoff [25], respectively, can cause hysteresis and dissipation. However, within cooperative transitions, these are secondary effects and we will disregard them for low frequencies.

4. SYSTEM RESPONSE TO ADIABATIC PRESSURE PERTURBATIONS

Sound is the propagation of a pressure wave that is followed by a temperature wave as a consequence of its adiabatic nature. Thermodynamically, changes in pressure (dP) and temperature (dT) couple to a change in the entropy (dS) of the system:

$$dS = \left(\frac{\partial S}{\partial T}\right)_p dT + \left(\frac{\partial S}{\partial p}\right)_T dp, \tag{2.13}$$

where $c_p = T(\partial S/\partial T)_p$ is the heat capacity at constant pressure. Using a well-known Maxwell relation, $(\partial S/\partial p)_T$ can be rewritten as $(\partial S/\partial p)_T = -(\partial V/\partial T)_p$,

$$\begin{aligned}\left(\frac{\partial S}{\partial p}\right)_T &= -\left(\frac{\partial V}{\partial T}\right)_p \\ &= -\left(\frac{\partial S}{\partial T}\right)_p \left(\frac{\partial V}{\partial S}\right)_p \\ &= -\frac{c_p}{T}\left(\frac{\partial V}{\partial S}\right)_p.\end{aligned} \tag{2.14}$$

Another Maxwell relation, $(\partial V/\partial S)_p = (\partial T/\partial p)_S$, allows us to write Eq. (2.14) as

$$\left(\frac{\partial S}{\partial p}\right)_T = -\frac{c_p}{T}\left(\frac{\partial T}{\partial p}\right)_S. \tag{2.15}$$

Constant entropy implies that no heat is dissipated into the environment but only moved between different degrees of freedom within a closed system. At transitions, the Clausius–Clapeyron relation[4] can be used:

[4] The use of the Clausius–Clapeyron relation can be justified by the weak first-order nature of the lipid melting transition [26].

$$\left(\frac{\partial p}{\partial T}\right)_S = \frac{\Delta H}{T\Delta V}, \tag{2.16}$$

where ΔH and ΔV are the enthalpy (or excess heat) and volume changes (excess volume) associated with the transition [11]. Note that these are constant system properties for a given transition that can be determined experimentally.

The change in entropy (Eq. 2.13) can now be written as

$$\mathrm{d}S = c_p(T,p)\left(\frac{\mathrm{d}T}{T} - \left(\frac{\Delta V}{\Delta H}\right)\mathrm{d}p\right). \tag{2.17}$$

It is clear from Eq. (2.17) that the heat capacity acts as a transfer function that couples adiabatic changes in pressure to changes in entropy.

Equation (2.17) governs the equilibrium properties of the thermodynamical system. However, here we consider the propagation of sound, which is a nonequilibrium process. The theory of sound considers the limit of small changes in pressure and temperature for which close-to-equilibrium dynamics can be assumed. This implies linear relations between perturbations and system responses. For this reason, it is also called linear response theory.

In any real system, transfer rates are finite and changes happen in finite time. Thus, the changes in pressure and temperature can be represented as rates, and Eq. (2.17) can be rewritten as

$$\Delta S = \int \mathrm{d}S = \int c_p(t)\left[\frac{\dot{T}(t)}{T_0} - \left(\frac{\Delta V}{\Delta H}\right)\dot{p}(t)\right]\mathrm{d}t, \tag{2.18}$$

where $\dot{T} = \partial T/\partial t$ and $\dot{p} = \partial p/\partial t$ are rates. Note that $T_0 = T_{\text{equilibrium}}$, which holds if absolute changes in temperature upon pressure changes are very small.

If changes in pressure or temperature happen faster than the transfer rate (or relaxation rate), the energy transferred during this change will be only a part of the amount otherwise transferred. Considering Eq. (2.17), the finite transfer rate will lower the effective transfer function, in this case the heat capacity. This means that also the heat capacity must contain a relaxation term, $(1-\Psi_{c_p})$, with $0 \le \Psi_{c_p} \le 1$. This function describes the equilibration of the system. As the system approaches equilibrium, $(1-\Psi_{c_p})$ approaches unity. Below, we will assume that the function Ψ_{c_p} is an exponentially decaying function of time. Equation (2.18) must then be written as a convolution:

$$\Delta S(t) = \int_{-\infty}^{t} \left[c_p(\infty) + \Delta c_p(1 - \Psi_{c_p}(t - t'))\right] \left(\frac{\dot{T}(t')}{T_0} - \frac{\Delta V}{\Delta H}\dot{p}(t')\right) \mathrm{d}t', \tag{2.19}$$

where $\Delta S(t)$ is the time-dependent change in entropy, $c_p(\infty)$ is the part of the heat capacity that relaxes more rapidly than the changes in the pressure and temperature considered. In the lipid bilayer system, $c_p(\infty)$ is the heat capacity contribution from lipid chains, which we consider as a background contribution. Δc_p is the part of the heat capacity which relaxes on timescales of a similar order or longer than the perturbation timescale. In the lipid membrane system this is the excess heat capacity. In Eq. (2.19), it has been assumed that the mechanisms of relaxation are the same for pressure and temperature. This assumption has been justified experimentally and numerically in the literature [10,14,27,28].

After partial integration of Eq. (2.19), subsequent Fourier transformation and the use of the convolution theorem, Eq. (2.19) can be transformed into (see Appendix)

$$\Delta S(\omega) = c_p(\omega)\left(\frac{T(\omega)}{T_0} - \frac{\Delta V}{\Delta H}p(\omega)\right). \tag{2.20}$$

$T(\omega)$ and $p(\omega)$ can be regarded as periodic variations of temperature and pressure, respectively. We have also now introduced the frequency-dependent heat capacity,

$$c_p(\omega) = c_p(\infty) - \Delta c_p \int_0^{\infty} \mathrm{e}^{-i\omega t}\dot{\Psi}_{c_p}(t)\mathrm{d}t. \tag{2.21}$$

From Eq. (2.21), the frequency-dependent transfer function (dynamic heat capacity)[5] can be found, giving a full description of how a lipid bilayer responds to adiabatic pressure perturbations. Both $c_p(\infty)$ and Δc_p are experimentally available using differential scanning calorimetry (DSC). The only unknown is the relaxation function, Ψ_{c_p}.

[5] It is important note to the difference between the dynamic heat capacity (frequency dependent) and the normally known equilibrium heat capacity. The equilibrium heat capacity is a constant system property, whereas the dynamic heat capacity is an effective heat capacity that can be less than or equal to the equilibrium heat capacity as a consequence of the finite transfer rates in real systems.

4.1. Relaxation function

The relaxation function of the heat capacity is related to the rate of energy transfer from the membrane to the environment. The fluctuation–dissipation theorem ensures that the rate of energy transfer is equivalent to the relaxation behavior of energy fluctuations. Since the heat capacity is a measure of enthalpy fluctuations, the relaxation function of the heat capacity must be the relaxation function of the enthalpy fluctuations [11].

The relaxation behavior of the fluctuations of enthalpy in pure lipid vesicles has been considered theoretically, numerically, and experimentally, showing that the relaxation of enthalpy is well described by a single exponential function [10,18]:

$$(H-\langle H\rangle)(t)=(H-\langle H\rangle)(0)\exp\left(-\frac{t}{\tau}\right), \tag{2.22}$$

where $(H-\langle H\rangle)(0)$ serves only as a proportionality constant and τ is the relaxation time. For various pure lipid membranes close to melting transitions, it was further found that relaxation times are proportional to the excess heat capacity,

$$\tau=\frac{T^2}{L}\Delta c_p, \tag{2.23}$$

where L is a phenomenological coefficient. For large unilamellar vesicles (LUV) of dipalmitoyl phosphatidylcholine (DPPC), $L=13.9\times10^8$ JK/(s mol) [10].

4.2. Response function

Using the relaxation function of the enthalpy fluctuation as the relaxation function of the dynamic heat capacity,

$$\Psi_{c_p}=\exp\left(-\frac{t}{\tau}\right). \tag{2.24}$$

Equation (2.21) can be solved and the dynamic heat capacity can be determined as

$$\begin{aligned} c_p(\omega)&=c_p(\infty)-\Delta c_p\int_0^\infty \mathrm{e}^{-i\omega t}\left(-\frac{1}{\tau}\right)\mathrm{e}^{-t/\tau}\mathrm{d}t \\ &=c_p(\infty)+\Delta c_p\left(\frac{1-i\omega\tau}{1+(\omega\tau)^2}\right). \end{aligned} \tag{2.25}$$

Note that the above derivations can be carried out with lateral pressure instead of pressure; the choice of using pressure is entirely for notational convenience.

5. ADIABATIC COMPRESSIBILITY

In estimating the speed of sound in the plane of a lipid membrane during the melting transition, the response of the membrane to sound (the dynamic heat capacity) must be related to the lateral adiabatic compressibility. The adiabatic lateral compressibility is defined as

$$\kappa_S^A = -\frac{1}{A}\left(\frac{\partial A}{\partial \Pi}\right)_S, \tag{2.26}$$

where Π is the lateral pressure. The adiabatic lateral compressibility can be rewritten in the following form [29]:

$$\kappa_S^A = \kappa_T^A - \frac{T}{A c_p^{\text{system}}}\left(\frac{\partial A}{\partial T}\right)_\Pi^2, \tag{2.27}$$

where

$$\kappa_T^A = -\frac{1}{A}\left(\frac{\partial A}{\partial \Pi}\right)_T = \kappa_T^A(\infty) + \frac{\gamma_A^2 T}{A}\Delta c_p \tag{2.28}$$

is the isothermal lateral compressibility, $\kappa_T{}^A(\infty)$ is the part of the isothermal lateral compressibility that relaxes faster than changes in the pressure and temperature considered, and $c_p{}^{\text{system}}$ is the heat capacity of the total thermodynamical system, that is, the lipid membrane plus the accessible surrounding aqueous medium that serves as a buffer for heat transfer. In the last equality, the empirical proportionality $\Delta A = \gamma_A \Delta H$ has been used [2,27], with $\gamma_A = 0.893\,\text{m}^2/\text{J}$ for a lipid bilayer of DPPC.

In the literature on attenuation and dissipation of sound in critical media, a different form of Eq. (2.27) is often used to relate the dynamic heat capacity and the adiabatic compressibility, using the dynamic heat capacity as the heat capacity of the total system [17,30]. This can be done in a straight forward manner by employing the Pippard–Buckingham–Fairbank relations [31,32]. The main difference between this approach and the one adopted here is that their compressible medium is three dimensional, and the system heat capacity is that of this medium. In contrast, the lipid membrane system is

a pseudo-two dimensional (the bilayer) embedded in a three-dimensional aqueous medium that serves as a heat reservoir (see Fig. 2.2). Therefore, the aqueous medium contributes significantly to the features of the membrane in a frequency-dependent manner.

Imagine a standing temperature wave in the bilayer. The transfer of heat from the wave to the surrounding water will be time dependent, see Fig. 2.2 for visualization. In the limit of $\omega \to 0$, the amount of water (heat reservoir) participating will effectively go to infinity. In the other extreme, $(\omega \to \infty)$, no heat will be transferred to the surrounding heat reservoir. Evidently, the heat capacity of the total system is frequency dependent:

$$c_p^{\text{system}}(\omega) = c_p^{\text{lipid}} + c_p^{\text{reservoir}}(\omega) \tag{2.29}$$

where $c_p{}^{\text{lipid}} = \Delta c_p + c_p(\infty)$ is the complete heat capacity (in equilibrium) of the lipid membrane and $c_p{}^{\text{reservoir}}(\omega)$ is the heat capacity of the participating heat reservoir. In this approach, it is the size of the contributing heat reservoir that is frequency dependent.

Using the proportionality relation $\Delta A = \gamma_A \Delta H$ in Eq. (2.27) and assuming that $(\partial A/\partial T)_\Pi$ in the chain-melting transition region is completely dominated by the transition-associated change in area, the following approximation can be made [14]:

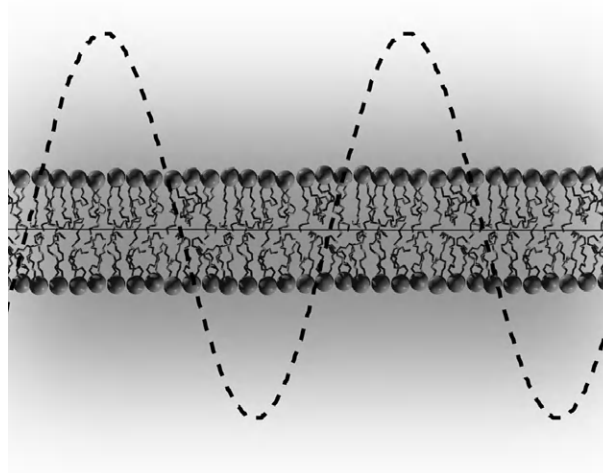

Figure 2.2 Visualization of temperature wave in the plane of a lipid bilayer. The coloring indicates heat penetrating into the surrounding water.

$$\begin{aligned}\kappa_S^A &\approx \kappa_T^A(\infty) + \frac{\gamma_A^2 T}{A}\Delta c_p - \frac{\gamma_A^2 T}{A}\frac{(\Delta c_p)^2}{c_p^{\text{system}}} \\ &= \kappa_T^A(\infty) + \frac{\gamma_A^2 T}{A}\left(\Delta c_p - \frac{(\Delta c_p)^2}{c_p^{\text{system}}}\right).\end{aligned} \tag{2.30}$$

The parenthesis has the units of a heat capacity and is frequency dependent through the frequency dependence of the size of the associated heat reservoir. We pose as an ansatz here that this parenthesis is the effective heat capacity of the lipid membrane in a finite adiabatically isolated heat reservoir, which is equivalent to the dynamic heat capacity of the lipid membrane following the above argument:

$$\Delta c_p(\omega) = \Delta c_p - \frac{(\Delta c_p)^2}{c_p^{\text{system}}}. \tag{2.31}$$

Numerical justification of this ansatz will be published at a later point.

Using this ansatz, the dynamic heat capacity can be related directly to the adiabatic lateral compressibility through Eq. (2.30):

$$\kappa_S^A = \kappa_T^A(\infty) + \frac{\gamma_A^2 T}{A}\Delta c_p(\omega), \tag{2.32}$$

where the $\Delta c_p(\omega)$ is the dynamic heat capacity without background. In this equation, we use the area of the lipid bilayer.

6. RESULTS—THE SPEED OF SOUND

The goal is to estimate the speed of sound and its frequency dependence in the plane of a lipid membrane. From the estimated dynamic heat capacity equation (2.25), the adiabatic lateral compressibility can found using the proposed relation (Eq. 2.32). The lateral speed of sound can then be estimated using Eq. (2.2) as

$$c^A = \frac{1}{\sqrt{\kappa_S^A \rho^A}},$$

where ${\kappa_S}^A$ is a function of the frequency, ω. The effective speed of sound is given by Eq. (2.12)

$$u = \left(\frac{\mathrm{Re}(c^A)}{|c^A|^2} \right)^{-1}.$$

Using the previous two equations, one can show that

$$u^2(\omega) = (\rho^A)^{-1} \frac{2}{\mathrm{Re}(\kappa_S^A) + |\kappa_S^A|}. \tag{2.33}$$

Inserting the estimated adiabatic lateral compressibility from Eqs. (2.32) and (2.25) into Eq. (2.33), the effective speed of sound squared takes the analytic form:

$$u^2(\omega) = \frac{2}{\frac{1}{c_1^2} + \frac{1}{c_2^2}\frac{1}{(1+(\omega\tau)^2)} + \sqrt{\left(\frac{1}{c_1^2} + \frac{1}{c_2^2}\frac{1}{(1+(\omega\tau)^2)}\right)^2 + \left(\frac{1}{c_2^2}\frac{\omega\tau}{(1+(\omega\tau)^2)}\right)^2}}, \tag{2.34}$$

with the notation

$$c_1^2 \equiv \left(\rho^A \kappa_T^A(\infty)\right)^{-1} \tag{2.35}$$

and

$$c_2^2(\omega) \equiv \left(\rho^A \frac{\gamma_A^2 T}{A} \Delta c_p(\omega) \right)^{-1}. \tag{2.36}$$

Here, c_1 is the lateral speed of sound of the membrane outside the transition, and c_2 is the component of the lateral speed of sound related to the lipid melting transition.

All variables in Eq. (2.34) can be found from the excess heat capacity of the lipid melting transition and the fluid fraction,[6] which can be obtained using DSC. The area, the lateral density, and the background isothermal compressibility are all directly related to the fluid fraction [28]. The relaxation time can be estimated from its phenomenological proportionality relation to the excess heat capacity, Eq. (2.23). The proposed analytic expression for the effective speed of sound (Eq. 2.34) is shown in Fig. 2.3, where the excess heat capacity and the fluid fraction are taken from Monte Carlo simulations of the lipid melting transition in LUV of DPPC. The simulation has been carried out in a manner similar to that described in Ref. [33].

[6] The fluid fraction is the fraction of a considered lipid system that is in the fluid phase.

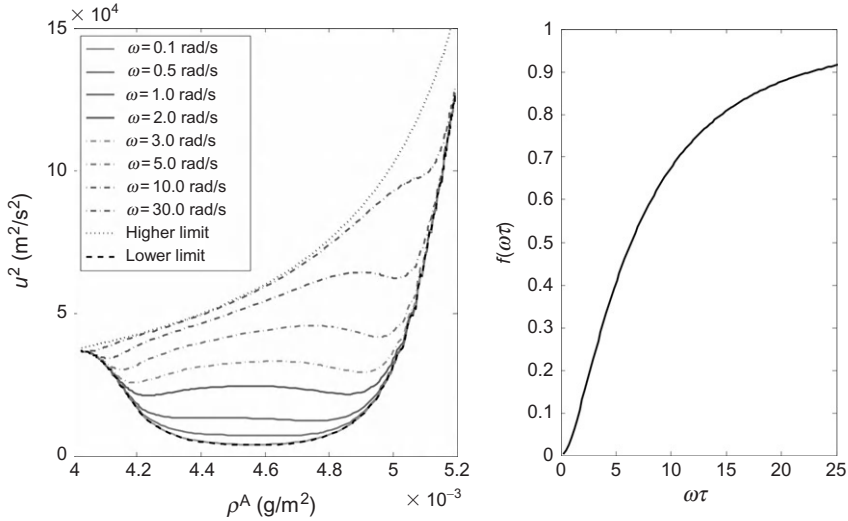

Figure 2.3 *Left*: The effective lateral speed of sound squared as a function of density at different angular frequencies along with the limiting cases: $\omega \to 0$ and $\omega \to \infty$. *Right*: The generic function, $f(\omega\tau)$, that takes the effective lateral speed of sound squared, at a given lateral density, from the low-frequency limit ($f(\omega\tau \to 0) = 0$) to the high-frequency limit ($f(\omega\tau \to \infty) = 1$).

The frequency dependence of the speed of sound is described by the function, $f(\omega\tau)$ with $0 \leq f(\omega\tau) \leq 1$, defined by

$$u^2(\omega\tau) = u_0^2 + (u_\infty^2 - u_0^2) f(\omega\tau) \tag{2.37}$$

where $u_0 \equiv u(\omega\tau \to 0)$ and $u_\infty \equiv u(\omega\tau \to \infty)$. From Eq. (2.34) we see that

$$\begin{aligned} u_0^2 &= \left(\frac{1}{c_1^2} + \frac{1}{c_2^2} \right)^{-1} \\ u_\infty^2 &= c_1^2. \end{aligned} \tag{2.38}$$

See Fig. 2.3 (right). The generic function f was chosen to be a function of the dimensionless quantity $\omega\tau$ rather than ω in order to render it independent of the lateral density.

6.1. Dispersion relation

In the soliton model described by Eq. (2.4), dispersion was assumed to be small and independent of the lateral density due to the lack of detailed information of the frequency dependence of the speed of sound as a function

of density. Using the considerations of the previous sections, we can now estimate the dispersion in lipid membranes. In the soliton model, the extent of dispersion is described by the parameter, h. Assuming that dispersion is small, h can be related to the lateral speed of sound as

$$u^2 \approx u_0^2 + \frac{h\omega^2}{u_0^2} + \cdots. \tag{2.39}$$

Equation (2.39) corresponds to a Taylor expansion of the lateral speed of sound squared to second order.[7] Expanding Eq. (2.34) to second order,

$$u^2 \approx u_0^2 + u_0^4 \frac{3c_1^2 + 4c_2^2}{4c_2^2(c_1^2 + c_2^2)}\omega^2\tau^2, \tag{2.40}$$

we see that the dispersion parameter has the following form:

$$h = u_0^6 \frac{3c_1^2 + 4c_2^2}{4c_2^2(c_1^2 + c_2^2)}\tau^2. \tag{2.41}$$

Using the excess heat capacity and the fluid fraction for large unilamellar vesicles of DPPC as used in Fig. 2.3, we can estimate the density dependence of the dispersion parameter $h(\rho_A)$ as shown in Fig. 2.4.

Here, the density of the fluid phase is approximately 4×10^{-3} g/m^2, the maximum of the dispersion parameter corresponds to the chain-melting

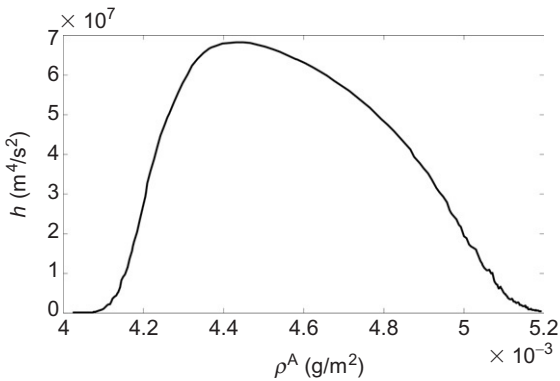

Figure 2.4 The dispersion parameter, h, as a function of lateral density for LUV of DPPC, based on the proposed expression for the lateral speed of sound.

[7] The first-order term is zero since the speed of sound squared is symmetric around $\omega = 0$.

transition maximum, and the density of the gel phase is 5×10^{-3} g/m^2. It is clear that the dispersion parameter is strongly dependent on the lateral density of the membrane.

The density-dependent dispersion parameter, $h(\rho^A)$, will finally enter the differential equation (Eq. 2.4) for the propagating nerve pulse. In the original treatment, h was considered an adjustable constant that determined the timescale of a solitary pulse in nerve axons. In the present extension, $h(\rho^A)$ is fully determined by the cooperative nature of the membrane system and does not contain adjustable parameters. Preliminary calculations indicate that this dispersion parameter will yield a natural timescale for the propagating soliton in nerve axons.

7. DISCUSSION

The response of lipid membranes to adiabatic periodic pressure perturbations (sound) is closely related to the relaxation behavior of the system [22,23]. Using thermodynamics and linear response theory, we have described the response of the lipid membrane to a perturbation with the assumption that the relaxation function has a simple exponential dependence on time. We obtain a form for the dynamic heat capacity which can be understood as the effective heat capacity when the lipid membrane is subject to periodic adiabatic pressure perturbations. The dynamic heat capacity was then related to the adiabatic lateral compressibility using the idea that the size of the associated water reservoir is frequency dependent [14]. The adiabatic lateral compressibility was then used to obtain an expression for the effective speed of sound as a function of frequency.

The major assumption in our approach concerns the nature of the relaxation function. We have previously studied the relaxation behavior of the lipid membrane in the vicinity of the melting transition at low frequencies.[8] This means that the lipid melting transition is assumed to be *non*critical. The single exponential relaxation behavior should, however, only be considered as a low-frequency approximation. In a number of ultrasonic experiments, it has been shown that a single exponential is insufficient to describe the dynamics of the cooperative processes involved in lipid melting in the ultrasonic regime [9,14–16]. In these ultrasonic experiments, some phase-transition phenomena are even apparent in the megahertz regime. Single

[8] The time resolution of experiments from our group is 0.3 s corresponding to 3.3 Hz. Relaxation profiles on longer time scales are well approximated by a single exponential decay [10,18].

exponential relaxation behavior, and thereby the validity of the estimated speed of sound, is thus limited to frequencies comparable to the relaxation rate or lower.

van Osdol *et al.* [19] have made adiabatic pressure perturbation experiments on unilaminar and multilaminar vesicles of DPPC. They studied relaxation behavior of the lipid membrane by measuring the frequency dependence of the effective heat capacity and the compressibility as a function of frequency. Although the data available for unilamellar vesicles are very limited and have large errors, it can still serve to illustrate qualitative tendencies of the effective heat capacity, see Fig. 2.5, that are similar to the theoretical results reported here. The effective frequency dependence of the speed of sound shown in Fig. 2.3 is dominated by the cooperative properties of the lipid melting transition of DPPC. In this model system, the relaxation time during the transition is as slow as seconds. In biological membranes such as membranes of nerves, realistic characteristic relaxation times can be assumed to be of the order of 1–100 ms. This change in

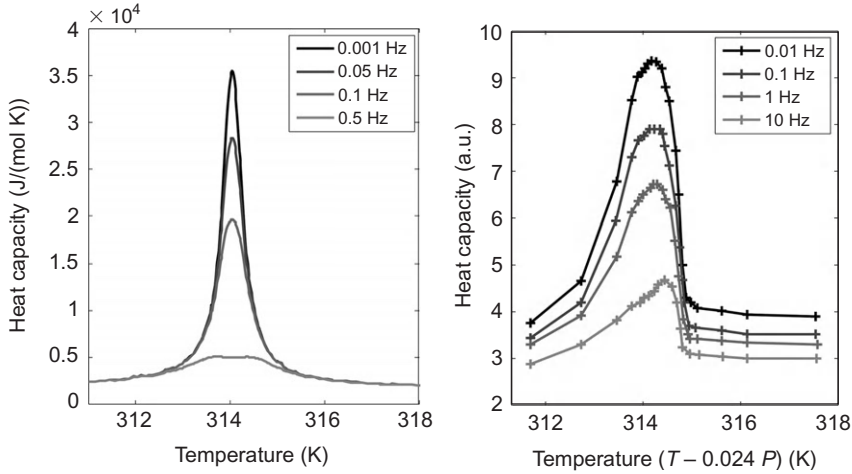

Figure 2.5 *Left*: The calculated dynamic heat capacity for LUV of DPPC at different frequencies. *Right*: The effective heat capacity profiles for LUV of DPPC at different frequencies, measured by van Osdol *et al.* [19]. The measured effective heat capacities have not been corrected for contributions from the experimental setup, and a direct comparison is therefore not possible. The theoretical dynamic heat capacity shows the same qualitative features as the measurements—a dramatic decrease in the height of the excess heat capacity with increasing frequency and a relatively constant width. The difference in frequency scales seen in the two panels is due to an estimated difference of more than a factor of 10 in the characteristic relaxation time. Frequencies are given in units of Hz = $(1/2\pi)$ rad/s.

relaxation times between the model system and biological membrane expands the upper limit of the frequency range for which our approach is likely to be valid from the hertz to kilohertz regime, assuming that the general behavior of pure lipid and biological membranes is otherwise similar. Since the duration of a nerve pulse is roughly 1 ms, the relevant frequency components contained in a nerve pulse can be estimated to be 1 kHz or less. The relevant frequency range for nerve pulses is thus covered by our proposed expression for the effective speed of sound. The present results may thus provide useful insights regarding sound propagation in an otherwise inaccessible regime and can extend our understanding of the nature of nerve signals.

In future studies, the linear response theory described in this chapter will help to define an intrinsic length scale of the electromechanical soliton proposed by us as an alternative description for the nervous impulse.

APPENDIX A. DERIVATION OF THE DYNAMIC HEAT CAPACITY USING THE CONVOLUTION THEOREM

The purpose of this appendix is to provide additional details in the derivation of the frequency-dependent heat capacity given in Eq. (2.25) starting from Eq. (2.19). The change in entropy is a convolution of the applied perturbation and the relaxation of the transfer function—the effective heat capacity. The perturbation is well defined at all times and can safely be assumed to be zero for $t \to -\infty$. The relaxation function is only defined from $[0, \infty]$, where $t = 0$ is the time at which the system starts to equilibrate. The relaxation function, Ψ, is chosen such that $\Psi(t \to 0) = 1$ and $\Psi(t \to \infty) = 0$. To accommodate the chosen form of the relaxation function, the convolution can be written as follows:

$$\Delta S(t) = \int_{-\infty}^{t} (c_p(\infty) + \Delta c_p(1 - \Psi(t - t'))) \left(\frac{\dot{T}(t')}{T_0} - \frac{\Delta V}{\Delta H} \dot{p}(t') \right) \mathrm{d}t', \quad \text{(A.1)}$$

$$\Delta S(t) = \int_{-\infty}^{t} g(t - t') \dot{f}(t') \mathrm{d}t', \quad \text{(A.2)}$$

where $g(t - t')$ is the transfer function and $\dot{f}(t')$ is the perturbation. Note that $\dot{f}(t) = \mathrm{d}f(t)/\mathrm{d}t$, $c_p(\infty)$ is the component of the heat capacity not associated with the melting transition, and T_0 is the equilibrium temperature.

Integration by parts allows us to rewrite Eq. (A.2) to the following form:

$$\Delta S(t) = \left[g(t') \int \dot{f}(t') \mathrm{d}t' \right]_{-\infty}^{t} - \int_{-\infty}^{t} \left(\int \dot{f}(t'') \mathrm{d}t'' \right) \dot{g}(t - t') \mathrm{d}t'. \tag{A.3}$$

The first term in Eq. (A.3) takes the form:

$$\begin{aligned} \left[g(t') \int \dot{f}(t') \mathrm{d}t' \right]_{-\infty}^{t} &= [g(t') f(t')]_{-\infty}^{t} \\ &= g(t) f(t) - g(-\infty) f(-\infty), \end{aligned} \tag{A.4}$$

where

$$f(t') = \frac{(T(t') - T_0)}{T_0} - \frac{\Delta V}{\Delta H} (p(t') - p_0).$$

Assuming that the system is in equilibrium as $t' \to -\infty$ and $f(t' \to -\infty) = 0$, simplifies Eq. (A.4):

$$g(t) f(t) - g(-\infty) f(-\infty) = c_p(\infty) f(t). \tag{A.5}$$

The second term in Eq. (A.3) can be rewritten by changing the variable to $t'' = t - t'$

$$\int_{-\infty}^{t} \left(\int \dot{f}(t') \mathrm{d}t' \right) \dot{g}(t - t') \mathrm{d}t' = - \int_{0}^{\infty} f(t - t'') \dot{g}(t'') \mathrm{d}t'', \tag{A.6}$$

where the integration limits have been changed accordingly.

Since we are interested in sinusoidal perturbations, we consider the Fourier transform of Eq. (A.1) and find:

$$\Delta \hat{S}(\omega) = \int_{-\infty}^{\infty} \Delta S(t) \mathrm{e}^{-i\omega t} \mathrm{d}t, \tag{A.7}$$

$$\Delta \hat{S}(\omega) = \int_{-\infty}^{\infty} \left(c_p(\infty) f(t) + \int_{0}^{\infty} f(t - t'') \dot{g}(t'') \mathrm{d}t'' \right) \mathrm{e}^{-i\omega t} \mathrm{d}t. \tag{A.8}$$

The Fourier transform of the first term in Eq. (A.8) can be carried out without complications:

$$c_p(\infty) \int_{-\infty}^{\infty} f(t) \mathrm{e}^{-i\omega t} \mathrm{d}t = c_p(\infty) \hat{f}(\omega). \tag{A.9}$$

The second term of Eq. (A.8) can be rewritten as follows:

$$\int_{-\infty}^{\infty} \int_{0}^{\infty} f(t - t'') \dot{g}(t'') \mathrm{e}^{-i\omega t} \mathrm{d}t'' \mathrm{d}t = \int_{0}^{\infty} \dot{g}(t'') \int_{-\infty}^{\infty} f(t - t'') \mathrm{e}^{-i\omega t} \mathrm{d}t \mathrm{d}t''. \tag{A.10}$$

Changing variables again, $t' = t - t''$, the Fourier transform of the second term in Eq. (A.8) can be split into two terms:

$$\begin{aligned}\int_0^\infty \dot{g}(t'')\int_{-\infty}^\infty f(t-t'')\mathrm{e}^{-i\omega t}\mathrm{d}t''\mathrm{d}t &= \int_0^\infty \dot{g}(t'')\int_{-\infty}^\infty f(t')\mathrm{e}^{-i\omega(t'+t'')}\mathrm{d}t'\mathrm{d}t'' \\ &= \int_0^\infty \dot{g}(t'')\mathrm{e}^{-i\omega t''}\mathrm{d}t''\int_{-\infty}^\infty f(t')\mathrm{e}^{-i\omega t'}\mathrm{d}t' \\ &= \hat{f}(\omega)\int_0^\infty \mathrm{e}^{-i\omega t}\dot{g}(t)\mathrm{d}t. \end{aligned} \tag{A.11}$$

This is known as the convolution theorem. From Eqs. (A.11) and (A.9), Eq. (A.7) can be written as

$$\Delta\hat{S}(\omega) = \left(c_p(\infty) + \int_0^\infty \mathrm{e}^{-i\omega t}\dot{g}(t)\mathrm{d}t\right)\hat{f}(\omega), \tag{A.12}$$

where

$$\hat{f}(\omega) = \frac{\hat{T}(\omega)}{T_0} - \frac{\Delta V}{\Delta H}\hat{p}(\omega) \text{ and } \dot{g}(t) = -\Delta c_p \dot{\Psi}(t).$$

The Fourier transform of Eq. (A.2) takes the final form:

$$\Delta\hat{S}(\omega) = \left(c_p(\infty) - \Delta c_p\int_0^\infty \mathrm{e}^{-i\omega t}\dot{\Psi}(t)\mathrm{d}t\right)\left(\frac{\hat{T}(\omega)}{T_0} - \frac{\Delta V}{\Delta H}\hat{p}(\omega)\right) \tag{A.13}$$

$$\Delta\hat{S}(\omega) = c_p(\omega)\left(\frac{\hat{T}(\omega)}{T_0} - \frac{\Delta V}{\Delta H}\hat{p}(\omega)\right). \tag{A.14}$$

Using $\Psi(t) = \exp(-t/\tau)$, the dynamic heat capacity, $c_p(\omega)$, is found to be

$$c_p(\omega) = c_p(\infty) + \frac{\Delta c_p}{\tau}\int_0^\infty \mathrm{e}^{-i\omega t}\mathrm{e}^{-t/\tau}\mathrm{d}t \tag{A.15}$$

$$c_p(\omega) = c_p(\infty) + \Delta c_p\left(\frac{1 - i\omega\tau}{1 + (\omega\tau)^2}\right), \tag{A.16}$$

which has the form of a Debye relaxation term.

REFERENCES

[1] A.L. Hodgkin, A.F. Huxley, A quantitative description of membrane current and its application to conduction and excitation in nerve, J. Physiol. 117 (1952) 500–544.
[2] T. Heimburg, A.D. Jackson, On soliton propagation in biomembranes and nerves, Proc. Natl. Acad. Sci. U.S.A. 102 (2005) 9790–9795.
[3] D.L. Melchior, H.J. Morowitz, J.M. Sturtevant, T.Y. Tsong, Characterization of the plasma membrane of Mycoplasma laidlawii. VII. Phase transitions of membrane liquids, Biochim. Biophys. Acta 219 (1970) 114–122.

[4] J.R. Hazel, Influence of thermal acclimation on membrane lipid composition of rainbow trout liver, Am. J. Physiol. Regul. Integr. Comp. Physiol. 287 (1979) R633–R641.
[5] E.F. DeLong, A.A. Yayanos, Adaptation of the membrane lipids of a deep-sea bacterium to changes in hydrostatic pressure, Science 228 (1985) 1101–1103.
[6] T. Heimburg, Thermal Biophysics of Membranes, Wiley VCH, Berlin, Germany, 2007.
[7] T.Y. Tsong, T.-T. Tsong, E. Kingsley, R. Siliciano, Relaxation phenomena in human erythrocyte suspensions, Biophys. J. 16 (1976) 1091–1104.
[8] T.Y. Tsong, M.I. Kanehisa, Relaxation phenomena in aqueous dispersions of synthetic lecithins, Biochemistry 16 (1977) 2674–2680.
[9] S. Mitaku, T. Date, Anomalies of nanosecond ultrasonic relaxation in the lipid bilayer transition, Biochim. Biophys. Acta 688 (1982) 411–421.
[10] P. Grabitz, V.P. Ivanova, T. Heimburg, Relaxation kinetics of lipid membranes and its relation to the heat capacity, Biophys. J. 82 (2002) 299–309.
[11] W.W. van Osdol, R.L. Biltonen, M.L. Johnson, Measuring the kinetics of membrane phase transition, J. Bioener. Biophys. Methods 20 (1989) 1–46.
[12] T. Heimburg, A.D. Jackson, On the action potential as a propagating density pulse and the role of anesthetics, Biophys. Rev. Lett. 2 (2007) 57–78.
[13] S.S.L. Andersen, A.D. Jackson, T. Heimburg, Towards a thermodynamic theory of nerve pulse propagation, Prog. Neurobiol. 88 (2009) 104–113.
[14] S. Halstenberg, T. Heimburg, T. Hianik, U. Kaatze, R. Krivanek, Cholesterol-induced variations in the volume and enthalpy fluctuations of lipid bilayers, Biophys. J. 75 (1998) 264–271.
[15] W. Schrader, H. Ebel, P. Grabitz, E. Hanke, T. Heimburg, M. Hoeckel, M. Kahle, F. Wente, U. Kaatze, Compressibility of lipid mixtures studied by calorimetry and ultrasonic velocity measurements, J. Phys. Chem. B 106 (2002) 6581–6586.
[16] S. Halstenberg, W. Schrader, P. Das, J.K. Bhattacharjee, U. Kaatze, Critical fluctuations in the domain structure of lipid membranes, J. Chem. Phys. 118 (2003) 5683–5691.
[17] J.K. Bhattacharjee, F.A. Ferrell, Scaling theory of critical ultrasonics near the isotropic-to-nematic transition, Phys. Rev. E 56 (1997) 5549–5552.
[18] H.M. Seeger, M.L. Gudmundsson, T. Heimburg, How anesthetics, neurotransmitters, and antibiotics influence the relaxation processes in lipid membranes, J. Phys. Chem. B 111 (2007) 13858–13866.
[19] W.W. van Osdol, M.L. Johnson, Q. Ye, R.L. Biltonen, Relaxation dynamics of the gel to liquid crystalline transition of phosphatidylcholine bilayers. Effects of chainlength and vesicle size, Biophys. J. 59 (1991) 775–785.
[20] L.D. Landau, E.M. Lifshitz, Fluid Mechanics, Course of Theoretical Physics, vol. 6, second ed., Pergamon Press, Oxford, 1987.
[21] T. Heimburg, A.D. Jackson, Thermodynamics of the nervous impulse, in: K. Nag (Ed.), Structure and Dynamics of Membranous Interfaces, Wiley, Hoboken, NJ, 2008, pp. 317–339.
[22] K.F. Herzfeld, F.O. Rice, Dispersion and absorption of high frequency sound waves, Phys. Rev. 31 (1928) 691–695.
[23] M. Fixman, Viscosity of critical mixtures: dependence on viscosity gradient, J. Chem. Phys. 36 (1962) 310–318.
[24] C.G. Stokes, On the theories of the internal friction of fluids in motion, and of the equilibrium and motion, Trans. Cambridge Phil. Soc. 8 (1845) 287–305.
[25] G. Kirchhoff, Über den Einfluss der Wärmeleitung in einem Gase auf die Schallbewegung, Ann. Phys. 210 (1868) 177–193.
[26] J.F. Nagle, Theory of the main lipid bilayer phase transition, Annu. Rev. Phys. Chem. 31 (1980) 157–196.

[27] H. Ebel, P. Grabitz, T. Heimburg, Enthalpy and volume changes in lipid membranes. I. The proportionality of heat and volume changes in the lipid melting transition and its implication for the elastic constants, J. Phys. Chem. B 105 (2001) 7353–7360.
[28] T. Heimburg, Mechanical aspects of membrane thermodynamics. Estimation of the mechanical properties of lipid membranes close to the chain melting transition from calorimetry, Biochim. Biophys. Acta 1415 (1998) 147–162.
[29] A.H. Wilson, Thermodynamics and Statistical Mechanics, Cambridge University Press, Cambridge, 1957.
[30] M. Barmatz, I. Rudnick, Velocity and attenuation of first sound near the lambda point of helium, Phys. Rev. 170 (1968) 224–238.
[31] A.B. Pippard, Thermodynamic relations applicable near lambda-transition, Philos. Mag. 1 (1956) 473–476.
[32] M.J. Buckingham, W.M. Fairbank, Progress in Low Temperature Physics, North-Holland Publishing Co., Amsterdam, 1961.
[33] T. Heimburg, R.L. Biltonen, A Monte Carlo simulation study of protein-induced heat capacity changes, Biophys. J. 70 (1996) 84–96.

CHAPTER THREE

Interactions of Biopolymer Chitosan with Plasma Membrane in Biomedical Applications

Peter Veranič*[1], Andreja Erman*, Mojca Kerec-Kos[†]
*Institute of Cell Biology, Faculty of Medicine, University of Ljubljana, Ljubljana, Slovenia
[†]Faculty of Pharmacy, University of Ljubljana, Ljubljana, Slovenia
[1]Corresponding author: e-mail address: peter.veranic@mf.uni-lj.si

Contents

1. Introduction 76
2. Chitosan as an Absorption Enhancer 77
   2.1 Urinary bladder 77
   2.2 Caco-2 cells 81
   2.3 Mechanism of permeability enhancement 82
3. Use of the Cytolytic Effect of Chitosan 82
   3.1 Lytic effect of chitosan on urinary bladder epithelial cells 83
   3.2 Use of the lytic effects of chitosan in basic research of the urothelium 85
4. Use of Chitosan in Tissue Engineering 86
5. Conclusion 88
References 88

Abstract

Chitosan is a cationic polysaccharide mainly used as an absorption enhancer for various pharmaceutics. The high density of positive charge on a chitosan molecule enables it to attach to the plasma membrane of most epithelial cells. Intravesical application of chitosan to urinary bladder recently revealed a destructive effect of this polysaccharide on superficial terminally differentiated epithelial cells, possibly due to the very specific structure of the apical membrane in these cells. This discovery broadens the application of chitosan to studies of urinary bladder regeneration mechanisms and indicates new possibilities for treating chronic bacterial cystitis and the removal of superficial urothelial tumors. Due to the chemical similarity of chitosan to aminoglycan molecules of proteoglycans in extracellular matrix, this molecule is widely used as a scaffolding material in tissue engineering for the needs of reconstructive medicine. No toxic effects were found after the application of chitosan in tissue engineering indicating for different effects on cell membranes after apical and basolateral application. This chapter presents current understanding of the effects of chitosan on plasma membrane in the most common described applications of this biopolymer.

Advances in Planar Lipid Bilayers and Liposomes, Volume 16
ISSN 1554-4516
http://dx.doi.org/10.1016/B978-0-12-396534-9.00003-9

ABBREVIATIONS

ATP adenosine-5′-triphosphate
DAPI 4′,6-diamidino-2-phenylindole
EDTA ethylenediaminetetraacetic acid
FITC fluorescein-isothiocyanate
LPS lipopolysaccharide
MOX moxifloxacin

1. INTRODUCTION

Chitosan is a cationic polysaccharide composed of glucosamine and *N*-acetyl glucosamine. It is obtained by partial N-deacetylation of chitin, one of the most abundant natural polysaccharides. In general, chitosan is regarded as a biocompatible, biodegradable, and nontoxic polymer [1,2]. Chitosan has been widely used in cosmetics [1], biotechnology [3], and reconstructive medicine. However, the mechanisms responsible for chitosan activity, including interactions with membrane lipids, are not known in detail, even though they are essential for understanding the effects and proper use of this biopolymer. The interaction of chitosan with cell membranes is by no means simple, since its positive charge causes chitosan to interact strongly with negatively charged [4] and neutral [5–8] phospholipids in membranes. A possible mechanism for the action of chitosan is a combination of electrostatic and hydrophobic interactions between chitosan and phospholipids [9]. When chitosan is able to penetrate the lipid bilayer, the molecules can interact by hydrophobic interactions with membrane lipid chains. In densely packed membrane lipids, the binding is mainly due to electrostatic interactions between NH_3^+ groups of chitosan and negatively charged phosphoryl groups of phospholipids [10]. It is interesting that binding and extraction of cholesterol have long been proposed as a major mechanism of the action of chitosan, often offered as a food additive to remove cholesterol from food and decrease lipoprotein content in blood. However, studies of the interaction between chitosan and membrane models proved that chitosan binds to cholesterol monolayers but does not remove cholesterol from the monolayer [10].

Interactions between chitosan and membrane lipids were mainly studied because of the discovery of a bactericidal activity of chitosan [7]. It has been shown that chitosan increases the permeability of the inner and outer membrane of Gram-negative bacteria *Escherichia coli* and *Staphylococcus aureus*.

Additionally, this agent disrupts the bacterial cell membrane, with the release of the cellular content. The damage to the bacterial membrane is caused by an electrostatic interaction between positively charged amino groups of chitosan and negatively charged phosphoryl groups of bacterial phospholipids.

In spite of the cytotoxic effect of chitosan toward prokaryotic cells, this biopolymer is regarded as nontoxic if used with eukaryotic cells. Multiple studies have proven that the effect of chitosan on eukaryotic cells greatly depends on the concentration, length of treatment, cell type, and application protocol, always involving interaction with the plasma membrane. The focus of this chapter is to present the effects of various applications of chitosan in biomedicine (a) influencing tissue permeability as an absorption enhancer, (b) for destruction of certain cell types, if applied from the apical side of cells, and (c) as a promising natural scaffold material in tissue engineering for the needs of regenerative medicine. The biomedical application of chitosan is discussed in the light of the interactions of this biopolymer with plasma membrane.

2. CHITOSAN AS AN ABSORPTION ENHANCER

Chitosan increases tissue permeability and is widely studied as an absorption enhancer of various drugs. Many *in vitro* experiments, as well as some *in vivo* studies, have shown that chitosan increases the transport of substances across Caco-2 cells [11–15], as well as urinary bladder [16,17], intestinal [18], ocular [19], nasal [20,21], buccal [22,23], and vaginal [23] mucosae. Its influence on tissue permeability depends on the molecular weight, degree of deacetylation, as well as the positive charge of the polymer [2,24,25]. Its influence on tissue permeability and good bioadhesive properties makes chitosan a promising polymer for use in drug delivery systems.

2.1. Urinary bladder

It has been well documented recently that chitosan affects the permeability of the urinary bladder wall [16,17,26]. Dispersion of this polysaccharide influences the permeation of the model drug moxifloxacin into pig urinary bladder wall, in a time- and concentration-dependent manner (Fig. 3.1). After 1 h of application, even at a concentration of 0.0005% (w/v), chitosan dispersion significantly enhances the permeability of the urinary bladder wall for the model drug, and the maximum effect on

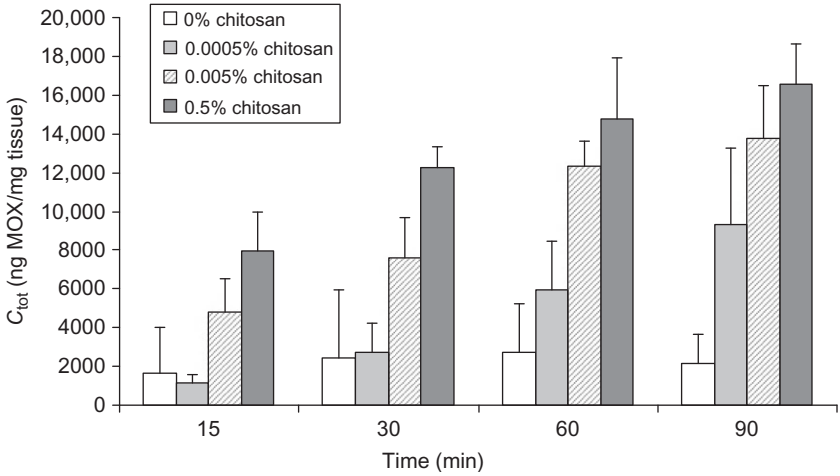

Figure 3.1 Cumulative amounts of moxifloxacin (MOX) that permeated into urinary bladder wall exposed to a solution of moxifloxacin or to 0.0005, 0.005, or 0.5% (w/v) dispersion of chitosan with moxifloxacin (mean ± SD, $n = 6$) for 15, 30, 60, and 90 min.

tissue permeability is achieved at a 0.005% (w/v) concentration. Within 90 min, the effect of chitosan on the tissue amounts of the model drug moxifloxacin gradually increases and approaches a plateau. At lower concentrations of chitosan, a longer period of time is needed to approach the maximum effect of chitosan on tissue permeability [17].

It was reported in our previous study [17] that increased permeability of pig urinary bladder wall for the model drug moxifloxacin is accompanied by morphological changes to the urothelium. After 15 min of exposure to 0.0005% (w/v) chitosan, the tight junctions between superficial cells become partly opened, but no desquamation of the urothelium occurs and the superficial cells do not show any signs of necrosis. However, incubation of the tissue for 15 min in a 0.005% (w/v) dispersion of chitosan results in necrosis of the cells, and the tight junctions between necrotic cells are mainly destroyed.

The permeability barrier of the urothelium, which prevents the diffusion of substances from urine into the bladder wall, is composed of tight junctions between superficial cells, as well as membrane plaques and a layer of glycosaminoglycans on the apical surface of superficial cells [27–29]. At lower concentrations and shorter exposure times, chitosan does not significantly increase the permeation of the model drug moxifloxacin into pig urinary bladder wall, although the structure of tight junctions is affected (Figs. 3.2 and 3.3). The remaining permeability barriers obviously still prevent

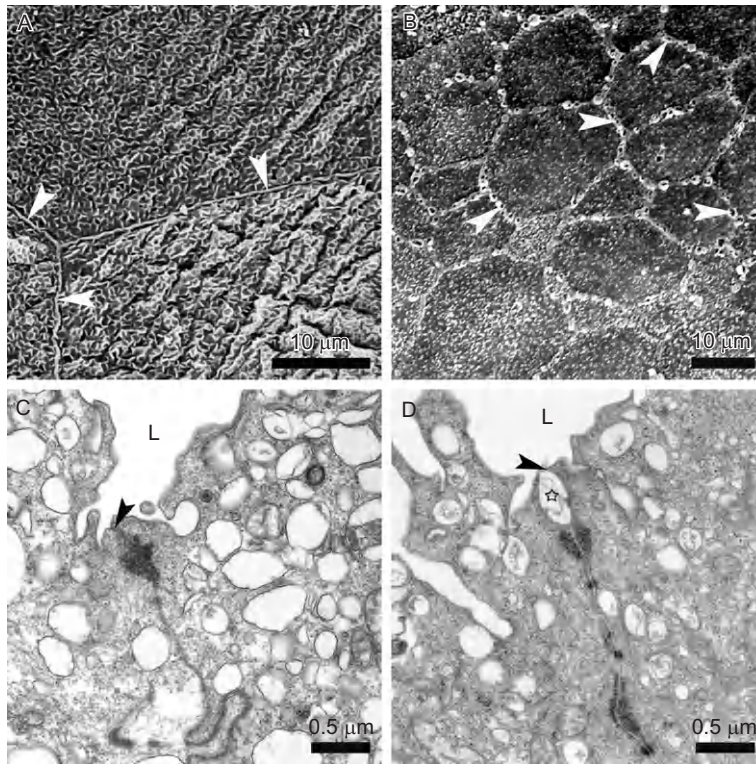

Figure 3.2 Effect of chitosan on tight junctions between superficial urothelial cells. Structurally and functionally normal tight junctions (arrowheads) between superficial cells in normal urothelium of adult mice (control) observed with scanning electron microscope (A) and with transmission electron microscope (C). Partially opened tight junctions (arrowheads) after 15-min exposure to 0.0005% (w/v) chitosan observed with scanning electron microscope (B) and morphologically changed tight junctions (arrowheads) after 15-min exposure to 0.0005% (w/v) chitosan observed with transmission electron microscope (D). The enlarged intercellular space is marked with an asterisk. L, lumen of the urinary bladder.

increased diffusion of moxifloxacin into the bladder wall. The removal of the superficial layer is thus crucial for significantly enhanced permeation of substances into the bladder wall. The intermediate and basal cells do not express tight junctions and obviously do not offer a significant permeability barrier [17].

Calcium ions, when applied to the luminal surface of the urinary bladder simultaneously with chitosan, decrease the effect of chitosan on urothelial permeability in a concentration-dependent way. A 0.015-M concentration

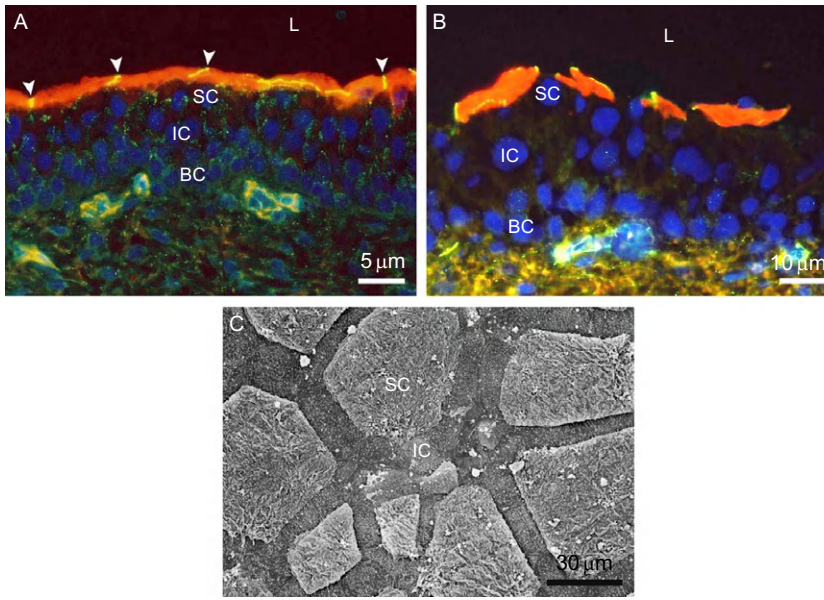

Figure 3.3 Terminally differentiated superficial cells marked by immunofluorescence against differentiation marker cytokeratin 20 (red fluorescence) and tight junctions (arrowheads pointing to yellow lines) marked by immunofluorescence against tight junction protein ZO-1 in normal urothelium of adult mice (control) (A) and disrupted tight junctions between superficial cells after 15-min exposure to 0.005% (w/v) chitosan. (B). Contracted superficial urothelial cells due to disconnected intercellular junctions. Underlying intermediate cells are thus partially exposed to the luminal surface (C). SC, superficial cells; IC, intermediate cells; BC, basal cells; L, lumen of the urinary bladder. In (A) and (B), nuclei are stained with DAPI (blue fluorescence). Panels (A) and (B) were made with a fluorescent microscope, panel (C) with a scanning electron microscope.

of calcium does not significantly hinder the effect of 0.5% (w/v) chitosan on the permeability of the urinary bladder wall. On the other hand, a 0.1-M concentration of calcium completely negates the effect of 0.5% (w/v) chitosan. The effect of calcium on permeation of the model drug is much greater than would be expected from the morphological changes because the addition of calcium only slightly reduced the desquamation of urothelium caused by chitosan. Calcium may prevent chitosan from forming stronger interactions with the negatively charged surface of the urothelium, which is an important step in absorption enhancement [16]. Moreover, calcium ions are essential for cells to maintain intercellular junctions that can enhance the formation of the diffusion barrier [30].

A similar effect as with calcium can be observed after using chitosan in combination with heparin. Heparin is a sulfated glycosaminoglycan commonly used in the treatment of interstitial cystitis as a mucosal surface protection [31,32]. It does not influence the permeability of the intact urothelium. However, if it is applied to urothelium preliminarily treated with 0.005% or 0.001% (w/v) chitosan, heparin significantly decreases the permeability of the bladder wall. In the presence of heparin, the permeation of the model drug pipemidic acid is not significantly different than with intact tissue [33]. This is in accordance with the results of other studies, in which heparin was reported to restore both the impermeability and the antiadherence properties of urothelium preliminarily injured by an acid, a detergent, or protamine sulfate [34,35]. Heparin is thought to form a layer on the surface of the damaged urothelium, which compensates for the urothelial permeability barriers that normally prevent the transport of substances from urine into the bladder wall. The impermeability of the urinary bladder wall is restored, but to a degree dependent on the urothelial damage.

2.2. Caco-2 cells

The influence of chitosan on tissue permeability has been extensively studied on Caco-2 cells, which serve as a model of intestinal epithelium [13,15,36,37]. It has also been shown for Caco-2 cells that chitosan increases the permeability of the cells in a dose- and time-dependent way [13–15]. A proposed mechanism by which chitosan increases the permeability of Caco-2 cells is a combination of mucoadhesion and the effect of the polymer on the proteins of tight junctions (ZO-1, occludin, claudin-4) and F-actin [12,13,15,38]. After 30 min of exposure of the apical side of Caco-2 cells to 0.1% (w/v) chitosan, half of the cells remained intact, while large intracellular vacuoles and swollen endoplasmic reticulum cisternae appeared in the remaining cells. However, tight junctions, organelles, and microvilli remained intact, as in the control cells [13]. After 1 h of treatment of Caco-2 cells with 0.1% (w/v) chitosan, redistribution of ZO-1 and occludin occurred [12–15]. Translocation of ZO-1 and occludin from the membrane to cytoskeleton of Caco-2 cells depends on the concentration of applied chitosan. Chitosan has been proven not to cause any significant changes in adenosine-5′-triphosphate (ATP) levels of Caco-2 cells. Chitosan does not, therefore, affect the tight junctions of Caco-2 cells via a depletion of intracellular ATP [15].

2.3. Mechanism of permeability enhancement

Protonated amino groups of chitosan enable the polymer to interact with a negatively charged epithelial surface or mucus via electrostatic interactions [36]. A higher charge density is obtained at acidic pH values, since the pK_a value of the D-glucosamine residue of chitosan is about 6.2–7.0 [39]. Artursson *et al.* [36] proposed that chitosan, as a cationic macromolecule, could displace cations from electronegative sites on plasma membrane, which require cations for their dimensional stability. The charge density of chitosan is therefore considered to be an important factor in the drug absorption enhancement caused by this polymer. It can thus be concluded that in both urothelium and Caco-2 cells, the opening of tight junctions is dependent on the density of positive charge on the chitosan molecules. However, in the urothelium, chitosan triggers another mechanism, involving cell destruction, which has a much more intensive effect on the increased permeability of bladder tissue.

3. USE OF THE CYTOLYTIC EFFECT OF CHITOSAN

In spite of the generally accepted low toxicity of chitosan, a specific lytic effect has been detected in urothelial cells after the use of higher concentrations of chitosan. It appears that chitosan directly affects only terminally differentiated urothelial cells that cover the surface of bladder urothelium. After being in contact with these cells at appropriately high concentrations, chitosan causes a disruption of the apical membrane, which results in necrosis and desquamation of these cells [40] (Fig. 3.4).

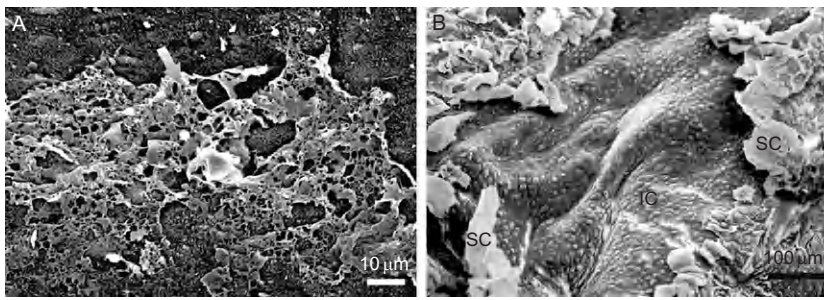

Figure 3.4 Chitosan layer (arrow) covering the luminal surface of the urothelium (A). (B) Exposed layer of intermediate urothelial cells (IC) due to massive desquamation of terminally differentiated superficial urothelial cells (SC) after 60-min exposure to 0.005% (w/v) chitosan. Both figures were made with a scanning electron microscope.

3.1. Lytic effect of chitosan on urinary bladder epithelial cells

The urothelium is a three-layered epithelium composed of highly differentiated superficial cells, which line the lumen of the bladder, underlying intermediate cells and basal cells at the basal lamina. Superficial cells, which are in close contact with urine, form a blood–urine permeability barrier with well-developed tight junctions, a specialized apical plasma membrane and a layer of glycosaminoglycans on the apical surface [27,29]. Despite its mechanical stability, the urothelium quickly responds to various stress factors with massive desquamation of urothelial cells. Urothelial desquamation can be induced by a specific signal, to which urothelial cells respond by interruption of cell–cell contacts, leading to detachment of viable cells. This type of desquamation is found during normal postnatal remodeling of urothelial tissue, after the treatment of experimental animals by stress hormones and after the exposure of experimental animals to prolonged illumination [41,42]. On the other hand, desquamation can also appear as a consequence of the action of mechanical or chemical stress factors causing severe damage, which results in cell detachment of mostly necrotic cells. This type of desquamation was reported after intravesical instillation of bacterial lipopolysaccharide (LPS) [43] and EDTA [44].

Subsequently, the results of *ex vivo* experiments showed that chitosan at a 0.5% (w/v) concentration enhances the permeability of isolated pig urinary bladder wall by massive desquamation of urothelial cells [17]. This finding was not in accordance with the results obtained with Caco-2 cells, in which chitosan increased the permeability of the cell monolayer by opening the tight junctions between cells [13,15]. Experiments with chitosan were also performed with live experimental animals and the results confirmed the action of chitosan as an inducer of urothelial desquamation [40]. However, the precise mechanism of induction of urothelial cell desquamation is still poorly understood, and further investigations must therefore be performed to illuminate the mode of action of chitosan on urothelial cells. It is suspected that chitosan adheres to the apical membrane of superficial cells and, at higher concentrations and longer exposure times, it causes necrosis and subsequent desquamation of necrotic superficial cells (Fig. 3.5). Due to membrane injuries of superficial cells, the release of their cellular content and lysosomal enzymes triggers a chain reaction of cell death of neighboring cells, causing a gradual progress of urothelial destruction into deeper cell layers. These results are in accordance with the results of permeability studies. Namely, it has already been reported that chitosan

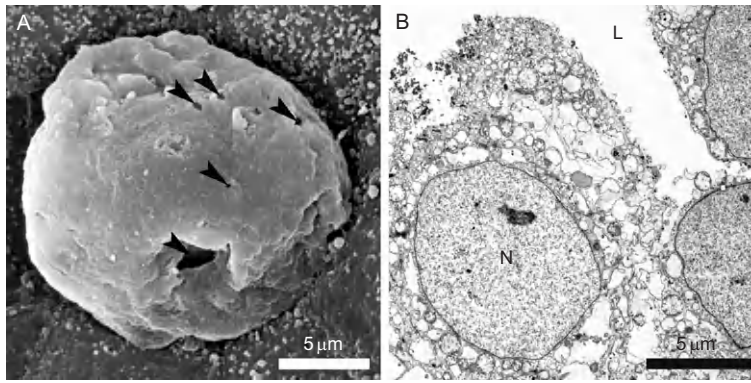

Figure 3.5 Necrosis of superficial cells after 60-min exposure to 0.5% (w/v) chitosan. Necrotic superficial urothelial cell with injuries to the apical plasma membrane seen as holes (arrowheads) (A) and necrotic superficial cell with typical morphological features of late necrosis, such as disrupted apical plasma membrane, disintegrated chromatin (N) and vacuolized cytoplasm (B). (A) Scanning electron microscope and (B) transmission electron microscope. L, lumen of the urinary bladder.

destroys the architecture of the urothelium and thus affects the permeability barrier, depending on the exposure time and concentration of chitosan [17].

The apical plasma membrane of terminally differentiated superficial cells is a specifically structured membrane, composed predominantly of rigid "urothelial plaques" of thickened membrane, interspersed by normal membrane areas called hinge regions [45,46]. The main constituents of urothelial plaques are specific transmembrane proteins, uroplakins, which are highly glycosylated proteins contributing to the urothelial glycocalyx [47]. Due to the cationic nature of chitosan, this polymer can adhere to negatively charged groups of glycosaminoglycans in plaque regions, as well as in hinge regions of the apical membrane of superficial cells. It is therefore possible that breaks in the apical membrane appear because of the discrete domains in the apical membrane, with two different viscoelastic properties, to which the rigid chitosan layer is attached. The breaks in the membrane can appear through many interactions of the chitosan layer with the apical membrane during repeated stretching and contraction of the urothelium. Membrane breaks induce severe membrane injuries, which are visible as holes in the apical plasma membrane (Fig. 3.5).

This speculation is confirmed by intravesical application of chitosan with covalently attached fluorescein-isothiocyanate (FITC, a fluorescent dye). After prolonged exposure, fluorescently labeled chitosan was found in the

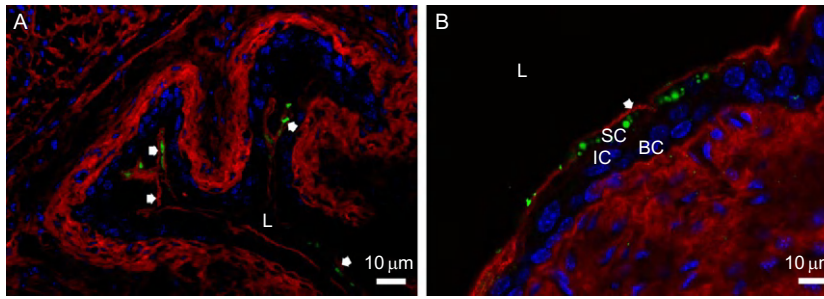

Figure 3.6 Green fluorescence of 0.005% (w/v) chitosan with covalently attached fluorescein-isothiocyanate (FITC) in the lumen of mouse urinary bladder after 5-min exposure to chitosan (A). Green fluorescence of 0.005% (w/v) chitosan with FITC in the cytoplasm of superficial urothelial cells after 20-min exposure to chitosan (B). Arrows show the subapical network of cytokeratin 20 in superficial urothelial cells. Nuclei are stained with DAPI (blue fluorescence). SC, superficial cells; IC, intermediate cells; BC, basal cells; L, lumen of the urinary bladder.

cytoplasm of terminally differentiated superficial cells, proving entry of chitosan through the injured apical plasma membrane (Fig. 3.6).

3.2. Use of the lytic effects of chitosan in basic research of the urothelium

It is worth mentioning that the aforementioned toxic effect of chitosan on the urothelium could even be turned to advantage in biomedical research, since removal of urothelial cells can be induced by chitosan in a way that is highly controllable through the period of exposure and the concentration of chitosan. The regeneration of urothelial tissue can thereafter be observed *in vivo*. Intravesical instillation of chitosan at an appropriate concentration and for a suitable time period could therefore be a very useful model for the efficient removal of urothelial cells, providing the possibility of studying urothelial regeneration. It has already been reported that the application of a 0.005% (w/v) dispersion of chitosan for 20 min resulted in the almost complete removal of the superficial cell layer, which was followed by the restoration of the differentiated superficial layer of cells within an hour [40].

It has also been found that an intravesical instillation of 0.5% (w/v) dispersion of chitosan for 1 h removes superficial and intermediate cells so that only one urothelial cell layer remains. Longer periods of treatment (1.5–2 h) with the same concentration of chitosan cause complete eradication of the urothelium, down to the basal lamina (Fig. 3.7). Chitosan, therefore, is a useful tool for fast and simple removal of urothelial cells, controlled by

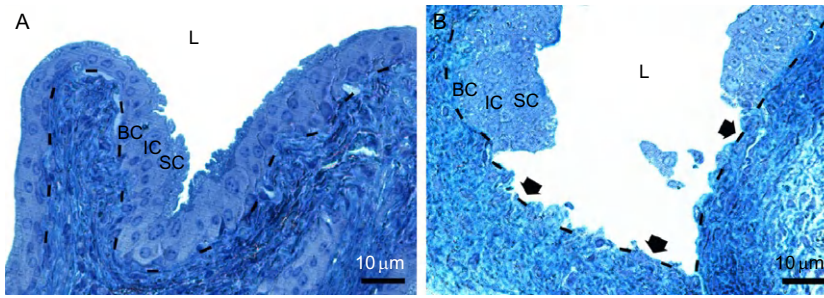

Figure 3.7 Semithin sections of normal urothelium of adult mouse (A) and after 120-min exposure to 0.5% (w/v) chitosan (B). Regions of the urothelium in which the basal lamina is exposed due to the complete removal of all three urothelial cell layers are marked with arrows. The basal lamina is marked with a broken line. Epon semithin sections are stained with Toluidine blue. SC, superficial cells; IC, intermediate cells; BC, basal cells; L, lumen of the urinary bladder.

the concentration of chitosan and the time of its action. Intravesical application of chitosan also has some other advantages in comparison to the use of previously known inducers of urothelial cell desquamation. The first is that complete regeneration after chitosan treatment is faster than after cell removal induced by other agents, such as cyclophosphamide or protamine sulfate. An additional advantage is that urothelial regeneration after chitosan application approaches normal physiological regeneration more accurately and with a minor inflammatory response in comparison to regeneration after cyclophosphamide [48–50].

Removal of urothelial cells by chitosan treatment is therefore one of many areas of broad chitosan application. Promising results of chitosan use for basic investigations of urothelial tissue also give this polymer the possibility of application in clinical practice, such as auxiliary intravesical treatment of bacterial cystitis or superficial bladder cancer.

4. USE OF CHITOSAN IN TISSUE ENGINEERING

In tissue engineering, as a crucial technology used in regenerative medicine, the damaged tissue of an organ is replaced with *in vitro* grown tissue. Such pieces of tissue require a scaffold upon which cells can attach, grow, and differentiate. It is also important that the scaffold material enables diffusion of nutrients and growth factors during *in vitro* growth and after integration into organs. The scaffold also serves for handling during integration of the newly designed tissue in the damaged organ. Various materials can be

used for scaffolding, both synthetic and naturally occurring [51]. Even though synthetic materials have the advantage of being repeatedly produced with a great precision, they usually elicit a chronic inflammatory response in a host organ, which prevents normal regeneration of the tissue and limits its functioning. The advantage of naturally occurring biomaterials is that they normally appear in tissues and can be well integrated into the original extracellular matrix of the neighboring tissue. The biomaterials most often used for scaffolding are collagens, chitosan, and their combinations.

Chitosan, as a linear polysaccharide consisting of D-glucosamine residues, shares similarities with naturally appearing glycosaminoglycans, which support the majority of tissues, especially connective tissues. Because of its physical and chemical properties, it is often used as a support material for the growth of cells *in vitro* or even as a scaffold for inserting *ex vivo* grown tissue into various organs, such as joints, bone, or skin.

A combination of chitosan and collagen has been proven to be even more successful than pure chitosan scaffolds [52]. The connection between chitosan and collagen enables stable scaffold architecture. Several molecules can be applied to bind these two extracellular matrix components. The most successful results have been obtained with glutaraldehyde and genipin. These binding agents enable, in addition to stable architecture of the scaffold, also partial degradation and remodeling. The benefit of such a dynamic and biodegradable scaffold is that it guarantees growth and proper adaptation after insertion into the tissue of organisms. Such a scaffold provides support for developing cells, which can proliferate and differentiate into normal tissue [53,54].

Glutaraldehyde has been used most frequently in the formation of extracellular matrix through freezing and freeze drying. By this process, pores are formed inside the scaffold that enable a better supply of growth factors and food and diffusion of metabolites, all of which enhance cell growth and development [55]. The disadvantage of glutaraldehyde is its considerable cytotoxicity. New binding agents have therefore been employed, such as genipin. Genipin is derived from the plant *Gardennia jasminoides* and is a suitable nontoxic binding molecule for linking chitosan and collagen into the designed extracellular matrix. A scaffold created by genipin also forms pores, which favors tissue growth and differentiation [56,57].

It is interesting that chitosan, used as a scaffold material, has never been reported to have a toxic effect on cells, in spite of long-term contact with cells. No toxic effects have been observed, even if urothelial cells were grown on a pure chitosan matrix [58]. A possible explanation for the difference in properties that chitosan expresses as a scaffold material in comparison

to application from the apical side of epithelial cells might lie in the different contacts that cells form with molecules on the apical side and basolateral side of the cell. The contact with chitosan at the basolateral membrane is thought to be by junctional proteins arranged into junctional complexes [59].

5. CONCLUSION

Chitosan has versatile application in biomedicine, due to the various effects that this polysaccharide expresses on the plasma membrane of cells, depending on the concentration, duration of treatment, and type of tissue to which it is applied. In addition to use in basic research of urothelium, chitosan could also have a great potential for clinical application as an auxiliary antimicrobial drug in the treatment of uroinfections. Another promising area of chitosan use is in the treatment of superficial bladder tumors by the application of chitosan as a nanoparticulate carrier system for cytostatic Mitomycin C, enabling a high concentration of the drug attached close to the tumor, controlled release of the drug, and the prevention of systemic side effects of the cytostatic [60]. The role of chitosan as a scaffolding material in combination with collagen is also very promising, simulating the natural environment for cell end tissue growth in tissue culturing, serving for reconstructive medicine and in studies of epithelial mesenchymal interactions. Further investigations of the interaction of chitosan with cell membranes should be encouraged, as a counterbalance to chemical drugs and synthetic materials and their widespread use in the world.

REFERENCES

[1] L.P. Sun, Y.M. Du, J.H. Yang, X.W. Shi, J. Li, X.H. Wang, J.F. Kennedy, Conversion of crystal structure of the chitin to facilitate preparation of a 6-carboxychitin with moisture absorption-retention abilities, Carbohydr. Polym. 66 (2006) 168–175.
[2] A.K. Singla, M. Chawla, Chitosan: some pharmaceutical and biological aspects—an update, J. Pharm. Pharmacol. 53 (2001) 1047–1067.
[3] I. Agerkvist, Mechanisms of flocculation with chitosan in *Escherichia coli* disintegrates: effects of urea and chitosan characteristics, Colloids Surf. 69 (1992) 173–187.
[4] V.G. Babak, G.A. Vikhoreva, I.G. Lukina, Interaction between carboxymethylchitin and tetradecyltrimethylammonium bromide: phase separation, surface tension and stability of microscopic foam films and foams, Colloids Surf. A 128 (1997) 75–89.
[5] J. Guo, Q. Ping, G. Jiang, L. Huang, Y. Tong, Chitosan-coated liposomes: Characterization and interaction with leuprolide, Int. J. Pharm. 260 (2003) 167–173.
[6] P. Perugini, I. Genta, F. Pavanetto, B. Conti, S. Scalia, A. Baruffini, Study on glycolic acid delivery by liposomes and microspheres, Int. J. Pharm. 196 (2000) 51–61.
[7] H. Liu, Y.M. Du, X.H. Wang, L.P. Sun, Chitosan kills bacteria through cell membrane damage, Int. J. Food Microbiol. 95 (2004) 147–155.

[8] N. Fang, V. Chan, Interaction of liposome with immobilized chitosan during main phase transition, Biomacromolecules 4 (2003) 581–588.
[9] F.J. Pavinatto, A. Pavinatto, L. Caseli, D.S. Santos Jr., T.M. Nobre, M.E. Zaniquelli, O.N. Oliveira Jr., Interaction of chitosan with cell membrane models at the air-water interface, Biomacromolecules 8 (2007) 1633–1640.
[10] F.J. Pavinatto, C.P. Pacholatti, E.A. Montanha, L. Caseli, H.S. Silva, P.B. Miranda, T. Viitala, O.N. Oliveira, Cholesterol mediates chitosan activity on phospholipid monolayers and LB films, Langmuir 25 (17) (2009) 10051–10061.
[11] O. Felt, P. Buri, R. Gurny, Chitosan: a unique polysaccharide for drug delivery, Drug Dev. Ind. Pharm. 24 (11) (1998) 979–993.
[12] N.G.M. Schipper, S. Olsson, J.A. Hoogstraate, A.G. de Boer, K.M. Vårum, P. Artursson, Chitosans as absorption enhancers for poorly absorbable drugs 2: mechanism of absorption enhancement, Pharm. Res. 14 (7) (1997) 923–929.
[13] V. Dodane, M.A. Khan, J.R. Merwin, Effect of chitosan on epithelial permeability and structure, Int. J. Pharm. 182 (1999) 21–32.
[14] G. Ranaldi, I. Marigliano, I. Vespignani, G. Perozzi, Y. Sambuy, The effect of chitosan and other polycations on tight junction permeability in the human intestinal Caco-2 cell line, J. Nutr. Biochem. 13 (2002) 157–167.
[15] J. Smith, E. Wood, M. Dornish, Effect of chitosan on epithelial cell tight junctions, Pharm. Res. 21 (1) (2004) 43–49.
[16] M. Kerec, M. Bogataj, P. Veranič, A. Mrhar, Permeability of pig urinary bladder wall: the effect of chitosan and the role of calcium, Eur. J. Pharm. Sci. 25 (1) (2005) 113–121.
[17] M.K. Kos, M. Bogataj, P. Veranič, A. Mrhar, Permeability of pig urinary bladder wall: time and concentration dependent effect of chitosan, Biol. Pharm. Bull. 29 (8) (2006) 1685–1691.
[18] H.L. Lueßen, B.J. de Leeuw, M.W.E. Langemeÿer, A.B.G. de Boer, J.C. Verhoef, H.E. Junginger, Mucoadhesive polymers in peroral peptide drug delivery. VI. Carbomer and chitosan improve the intestinal absorption of the peptide rug buserelin in vivo, Pharm. Res. 13 (11) (1996) 1668–1672.
[19] M.J. Alonso, A. Sánchez, The potential of chitosan in ocular drug delivery, J. Pharm. Pharmacol. 55 (2003) 1451–1463.
[20] P. Sinswat, P. Tengamnuay, Enhancing effect of chitosan on nasal absorption of salmon calcitonin in rats: comparison with hydroxypropyl- and dimethyl-β-cyclodextrins, Int. J. Pharm. 257 (1–2) (2003) 15–22.
[21] S. Yu, Y. Zhao, F. Wu, X. Zhang, W. Lu, H. Zhang, Q. Zhang, Nasal insulin delivery in the chitosan solution: in vitro and in vivo studies, Int. J. Pharm. 281 (1–2) (2004) 11–23.
[22] S. Şenel, A.A. Hincal, Drug permeation enhancement via buccal route: possibilities and limitations, J. Control. Release 72 (2001) 133–144.
[23] G. Sandri, S. Rossi, F. Ferrari, M.C. Bonferoni, C. Muzzarelli, C. Caramella, Assessment of chitosan derivatives as buccal and vaginal penetration enhancers, Eur. J. Pharm. Sci. 21 (2004) 351–359.
[24] N.G.M. Schipper, K.M. Vårum, P. Artursson, Chitosans as absorption enhancers for poorly absorbable drugs. 1: influence of molecular weight and degree of acetylation on drug transport across human intestinal epithelial (Caco-2) cells, Pharm. Res. 13 (11) (1996) 1686–1692.
[25] M. Huang, E. Khor, L.Y. Lim, Uptake and cytotoxicity of chitosan molecules and nanoparticles: effects of molecular weight and degree of deacetylation, Pharm. Res. 21 (2) (2004) 344–353.
[26] I. Grabnar, M. Bogataj, A. Mrhar, Influence of chitosan and polycarbophil on permeation of a model hydrophilic drug into the urinary bladder wall, Int. J. Pharm. 256 (1–2) (2003) 167–173.

[27] S.A. Lewis, Everything you wanted to know about the bladder epithelium but were afraid to ask, Am. J. Physiol. Renal Physiol. 278 (2000) 867–874.
[28] C.L. Parsons, D. Boychuk, S. Jones, R. Hurst, H. Callahan, Bladder surface glycosaminoglycans: an epithelial permeability barrier, J. Urol. 143 (1990) 139–142.
[29] G. Apodaca, The uroepithelium: not just a passive barrier, Traffic 5 (2004) 117–128.
[30] F. Lacaz-Vieira, Calcium site specificity: Early Ca2+-related tight junction events, J. Gen. Physiol. 110 (1997) 727–740.
[31] M.B. Chancellor, N. Yoshimura, Treatment of interstitial cystitis, Urology 63 (3 Suppl. 1) (2004) 85–92.
[32] C.L. Parsons, Epithelial coating techniques in the treatment of interstitial cystitis, Urology 45 (1997) 100–104.
[33] M.K. Kos, M. Bogataj, A. Mrhar, Heparin decreases permeability of pig urinary bladder wall preliminarily enhanced by chitosan, Drug Dev. Ind. Pharm. 34 (2) (2008) 215–220.
[34] W.B. Gill, K.W. Jones, K.J. Ruggiero, Protective effects of heparin and other sulfated glycosaminoglycans on crystal adhesion to injured urothelium, J. Urol. 127 (1982) 152–154.
[35] J.C. Nickel, J. Downey, A. Morales, L. Emerson, J. Clark, Relative efficacy of various exogenous glycosaminoglycans in providing a bladder surface permeability barrier, J. Urol. 160 (2) (1998) 612–614.
[36] P. Artursson, T. Lindmark, S.S. Davis, L. Illum, Effect of chitosan on the permeability of monolayers of intestinal epithelial cells (Caco-2), Pharm. Res. 11 (9) (1994) 1358–1361.
[37] G. Borchard, H.L. Lueßen, A.G. de Boer, J.C. Verhoef, C.M. Lehr, H.E. Junginger, The potential of mucoadhesive polymers in enhancing intestinal peptide drug absorption. III. Effects of chitosan-glutamate and carbomer on epithelial tight junctions in vitro, J. Control. Release 39 (1996) 131–138.
[38] T.H. Yeh, L.W. Hsu, M.T. Tseng, P.L. Lee, K. Sonjae, Y.C. Ho, H.W. Sung, Mechanism and consequence of chitosan-mediated reversible epithelial tight junction opening, Biomaterials 32 (26) (2011) 6164–6173.
[39] R. Hejazi, M. Amiji, Chitosan-based gastrointestinal delivery systems, J. Control. Release 89 (2003) 151–165.
[40] P. Veranič, A. Erman, M. Kerec Kos, M. Bogataj, A. Mrhar, K. Jezernik, Rapid differentiation of superficial urothelial cells after chitosan-induced desquamation, Histochem. Cell Biol. 131 (2009) 129–139.
[41] P. Veranič, K. Jezernik, Succession of events in desquamation of superficial cells as a response to stress induced by prolonged constant illumination, Tissue Cell 33 (2001) 280–285.
[42] A. Erman, D. Zupančič, K. Jezernik, Apoptosis and desquamation of urothelial cells in tissue remodeling during rat postnatal development, J. Histochem. Cytochem. 57 (2009) 521–530.
[43] P. Veranič, K. Jezernik, The response of junctional complexes to induced desquamation in mouse urinary bladder epithelium, Biol. Cell 92 (2000) 105–113.
[44] O. Nativ, E. Dalal, G. Hidas, M. Aronson, EDTA-induced urothelial cell shedding for the treatment of superficial bladder cancer in the mouse, Int. J. Urol. 13 (2006) 1344–1346.
[45] J.M. Caruthers, M.A. Bonnevile, The asymmetric unit membrane (AUM) structure in the luminal plasma membrane of urothelium: the effect of trypsin on the integrity of the plaques, J. Ultrastruct. Res. 71 (1980) 288–302.
[46] G. Min, H. Wang, T.T. Sun, X.P. Kong, Structural basis for tetraspanin functions as revealed by the cyro-EM structure of uroplakin complexes at the 6-Å resolution, J. Cell Biol. 173 (2006) 975–983.
[47] C.C. Hu, F.X. Liang, G. Zhou, L. Tu, C.H. Tang, J. Zhou, G. Kreibich, T.T. Sun, Assembly of urothelial plaques: tetraspanin function in membrane protein trafficking, Mol. Biol. Cell 16 (2005) 3937–3950.

[48] J. Lavelle, S. Meyers, R. Ramage, D. Doty, S. Bastacky, G. Apodaca, M. Zeidel, Protamine-sulphate-induced cystitis: a model of selective cytodestruction of the urothelium, Urology 57 (2001) 113.
[49] G.W. Locher, E.H. Cooper, Repair of rat urinary bladder epithelium following injury by cyclophosphamide, Invest. Urol. 8 (1970) 116–123.
[50] R. Romih, D. Koprivec, D. Štiblar-Martinčič, K. Jezernik, Restoration of the rat urothelium after cyclophosphamide treatment, Cell Biol. Int. 25 (2001) 531–537.
[51] S.F. Badylak, Naturally occurring scaffold materials, in: A. Atala, R. Lanza, R. Thompson, R. Nerem (Eds.), Principles of Regenerative Medicine, Academic Press, Burlington, MA, 2008.
[52] N.M. Breyner, R.C. Hell, L.R. Carvalho, C.B. Machado, I.N. Peixoto Filho, P. Valerio, M.M. Pereira, A.M. Goes, Effect of three dimensional chitosan porous scaffold on the differentiation of mesenchymal stem cells into chondrocytes, Cells Tissues Organs 191 (2010) 119–128.
[53] L. Bacáková, E. Filová, F. Rypácek, V. Svorcík, V. Starý, Cell adhesion on artificial materials for tissue engineering, Physiol. Res. 53 (2004) 35–45.
[54] V. Mironov, R.P. Visconti, V. Kasyanov, G. Forgacs, C.J. Drake, R.R. Markwald, Organ printing: tissue spheroids as building blocks, Biomaterials 30 (2009) 2164–2174.
[55] B. Hoffmann, D. Seitz, A. Mencke, A. Kokott, G. Ziegler, Glutaraldehyde and oxidized dextran as crosslinker reagents for chitosan-based scaffold for cartilage tissue engineering, J. Mater. Sci. Mater. Med. 20 (7) (2009) 1495–1503.
[56] A. Al-Ammar, J.L. Drummond, A.K.B. Bedran-Russo, The use of collagen cross-linking agents to enhance dentin bond strength, J. Biomed. Mater. Res. B Appl. Biomater. 91 (1) (2009) 419–424.
[57] J.P. Beier, D. Klumpp, M. Rudisile, R. Dersh, J.H. Wendorff, O. Bleiziffer, A. Arkudas, E. Polykandriotis, R.E. Horch, U. Kneser, Collagen matrices from sponge to nano: new perspective for tissue engineering of skeletal muscle, BMC Biotechnol. 9 (34) (2009) 1–14.
[58] T. Drewa, J. Adamowicz, A. Krawczyk, J. Polasik, J. Pielichowski, J. Lysik, Chitosan scaffold enhances angiogenesis within an in vitro reconstructed bladder wall, an Animal Study, Curr. Urol. 1 (2007) 72–76.
[59] A. Senköü, A. Simsek, F.I. Sahin, S. Menevse, C. Özogul, E. Baki Denkbas, E. Piskin, Interaction of cultured chondrocytes with chitosan scaffold, J. Bioact. Compat. Polym. 16 (2001) 135–144.
[60] E. Bilensoy, C. Sarisozen, G. Esendagli, A.L. Dogan, Y. Aktas, M. Sen, N.A. Mungan, Intravesicalcationic nanoparticles of chitosan and polycaprolactone for the delivery of Mitomycin C to bladder tumors, Int. J. Pharm. 371 (2009) 170–176.

CHAPTER FOUR

Single-Chain Bolaphospholipids: Temperature-Dependent Self-assembly and Mixing Behavior with Phospholipids

Annette Meister[1,2], **Alfred Blume**

Institute of Chemistry—Physical Chemistry, Martin-Luther-University Halle-Wittenberg, Halle, Germany
[1]Corresponding author: e-mail address: annette.meister@chemie.uni-halle.de
[2]Current address: ZIK HALOmem—membrane structure and dynamics, Martin-Luther-University Halle-Wittenberg, Halle, Germany.

Contents

1. Introduction 94
2. Temperature-Dependent Self-assembly of Single-Chain Bolalipids 96
   2.1 Formation of helical nanofibers and micellar aggregates 97
   2.2 Chain length-dependent self-assembly 101
   2.3 Chain structure-dependent self-assembly 104
   2.4 Headgroup structure-dependent self-assembly 107
   2.5 Self-assembly of bolalipid mixtures 116
3. Mixing Behavior of Single-Chain Bolalipids with Phospholipids 120
4. Conclusions 123
Acknowledgments 124
References 124

Abstract

Bipolar lipids (bolalipids) are composed of one or two long hydrophobic spacers and two polar headgroups attached to their ends. In water, they form various types of aggregate structures such as micelles, discs, fibers, tapes, tubes, or vesicles. The shape of the formed aggregates strongly depends on the head-to-spacer diameter ratio of the bolalipid as well as on electrostatic interactions and the possibility of forming hydrogen bonds between neighboring headgroups. This review focuses on symmetrical single-chain bolalipids, where two identical polar phosphocholine or phosphodimethylethanolamine headgroups are connected by one long hydrophobic alkyl chain spacer. These bolalipids proved to be capable of gelling water very efficiently by forming a dense network of fibers. The fibers exhibit a helical superstructure with hydrophobic pockets, where double-chain phospholipids can easily be inserted. The temperature-dependent self-assembly of the bolalipids in water and their mixing behavior with conventional phospholipids was

Advances in Planar Lipid Bilayers and Liposomes, Volume 16
ISSN 1554-4516
http://dx.doi.org/10.1016/B978-0-12-396534-9.00004-0

investigated by differential scanning calorimetry, transmission electron microscopy, small-angle neutron scattering, Fourier transform infrared spectroscopy, and rheological measurements.

1. INTRODUCTION

Amphiphiles such as classical surfactants and phospholipids are composed of an uncharged, zwitterionic, or charged hydrophilic headgroup and one or two hydrophobic acyl chains. In water, they spontaneously form aggregates above the critical micellar concentration due to the hydrophobic effect. The shape of the formed aggregates (spherical, cylindrical and inverted micelles, vesicles, and planar bilayers) strongly depends on geometrical packing factors as well as on the headgroup charge. Israelachvili [1] introduced the critical packing parameter, the magnitude of which controls the preferred aggregate shape.

In the past 30 years, a new class of amphiphilic molecules has been attracting increasing attention. These are bipolar lipids (bolalipids) that are composed of one or two long hydrophobic spacers and two polar headgroups attached to their ends. Bolalipids are naturally occurring substances that are found in membranes of archaebacteria. Archaeal liposomes (archaeosomes) are made from natural bipolar tetraether lipids found in Archaea or from synthetically derivated compounds. Their high degree of physical rigidity and chemical stability favors an application as nonviral gene delivery system for *in vivo* transfection [2–6]. Bipolar tetraether lipids are thought to span the membrane when mixed with classical lipids, thus acting as rivets keeping both membrane leaflets together and allowing the archaebacteria to maintain membrane integrity [7–10]. These membrane-spanning properties make bolalipids attractive candidates for drug delivery systems [11–16] or supported membrane biosensor devices [17,18]. However, atomic force microscopy investigations as well as predictions from mean field theory indicate that in the case of an hydrophobic mismatch between the monopolar lipid hydrocarbon chains and the membrane-spanning bolalipid chains, the lipid mixture may phase separate [19,20].

Since bolalipids are difficult to isolate from natural membranes, considerable effort has been devoted to the synthesis of novel bolalipids featuring specific structural peculiarities of archaebacterial membrane lipids [21–25]. Some of these synthetic bolalipids could be successfully applied for the reconstitution of integral membrane proteins [26,27]. Several simplified model compounds,

such as single-chain bipolar amphiphiles (bolaamphiphiles), have been synthesized to understand the complex relationship between chain composition, spacer properties, headgroup structure, and aggregate shape [28–30]. Sugar, peptide, and nucleic acid moieties were applied as hydrophilic headgroups that are well known to form diverse and multiple hydrogen-bond networks [31–33].

A few years ago, unsymmetrical single-chain bolaamphiphiles with headgroups of different sizes and chemical structures became the origin for a new class of supramolecular structures, the self-assembled organic nanotubes. They are expected to play a leading role in mesoscale host–guest science since they intrinsically possess two open ends, flexibility of the membrane wall, and tunable surface functionalities. Fluorescently labeling of nanotube or guest protein allows to detect the encapsulation and release phenomena of guest proteins [34–36]. Recently, functionalized organic nanotubes were successfully applied as tubular nonviral gene transfer vectors [37] that are coassembled of bipolar nucleic acid-, glycol-, and PEG-lipids complexed with DNA (bolaplexes) [38].

Symmetrical single-chain bolalipids are especially interesting and challenging since they are known to form a large variety of aggregate structures such as micelles, nanofibers, tubes, and vesicles. Bolalipids with headgroups containing aspartic [39], ascorbic [40], orotic [41], or glutamic [42] acid; phenylalanine [43,44]; urea [45]; or vernonia oil [46] were synthesized recently, and their pH and temperature-dependent self-assembly was studied extensively. But also synthetic modifications of the hydrophobic alkyl spacer region by introducing bis(alkoxy)phenylene [47] and chromophores [48] were described recently. L- or D-glutamic acid-based bolalipids were found to form chiral helical nanotubes [49,50], and self-sorting based on chiral recognition in a *trans*-1,2-bisureido cyclohexane moiety was demonstrated [51].

In the past years, the use of bolalipid/additive mixtures has become the most promising approach to tune morphologies. Since it is still not possible to predict the aggregate shape for new, chemically modified single-chain bolalipids, it is sometimes easier to fine-tune the self-assembly process by adding classical lipids or surfactants to the bolalipid suspension [52–54]. By adjusting the content of additive, various morphologies could be stabilized [55], and the insertion and stabilization of solubilized integral membrane proteins [56], amyloid Aβ (1–42) peptides [57], or hemoglobin [58] were realized.

We have been able to synthesize symmetrical single-chain bolalipids, where two identical polar phosphocholine or phosphodimethylethanolamine headgroups are connected by one long hydrophobic alkyl chain spacer. The

temperature- and pH-dependent self-assembly of these bolalipids in water and their mixing behavior with conventional phospholipids was investigated by differential scanning calorimetry (DSC), transmission electron microscopy (TEM), small-angle neutron scattering (SANS), Fourier transform infrared (FT-IR) spectroscopy, and rheological measurements and will be discussed in more detail in this chapter.

2. TEMPERATURE-DEPENDENT SELF-ASSEMBLY OF SINGLE-CHAIN BOLALIPIDS

Recently, single-chain polymethylene-1,ω-bis-phosphocholines (PC-C*n*-PC), -phosphodimethylethanolamines (Me_2PE-C*n*-Me_2PE), and -phosphomonomethylethanolamines (MePE-C*n*-MePE) with even-numbered chain lengths between 22 and 34 carbon atoms (Fig. 4.1) became accessible by different synthetic strategies [59–62].

PC-C*n*-PC, *n* = 22–34

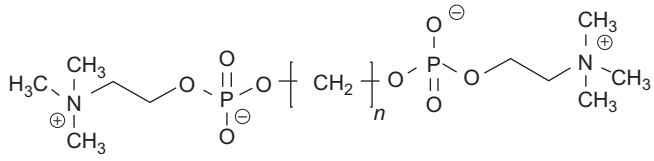

Me_2PE-C*n*-Me_2PE, *n* = 22–34

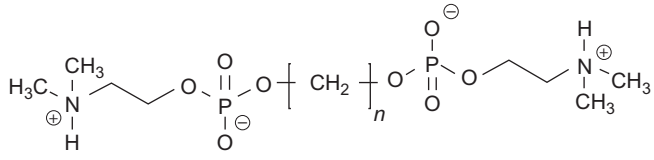

MePE-C*n*-MePE, *n* = 32

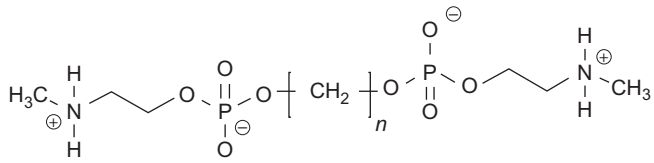

Figure 4.1 Chemical structure of the symmetric single-chain bolalipids PC-C*n*-PC, Me_2PE-C*n*-Me_2PE, and MePE-C*n*-MePE consisting of an alkyl spacer of different chain lengths and two phosphocholine, phosphodimethylethanolamine, or phosphomonomethylethanolamine headgroups, respectively.

Additional headgroup variations were performed by introducing hydroxyl, amino, sulfur, allyl, and propynyl containing groups as well as carboxylic acids, such as lipoic acid, sorbic acid, and lysine [63,64]. The hydrophobic chain region was modified by the introduction of sulfur and oxygen atoms or a diacetylene group in the middle of the alkyl chain [65].

The physicochemical characterization of this variety of bolalipids and its self-assembled aggregates enabled us to get a better understanding of the complex relationship between the bolalipid headgroup structure, chain composition, and aggregate shape.

2.1. Formation of helical nanofibers and micellar aggregates

The self-assembly of PC-C*n*-PC bolalipids in water is exclusively driven by hydrophobic interactions of the long alkyl chains [59,66]. This leads to the formation of a dense network of nanofibers that gels water very efficiently (Fig. 4.2A inset). In the case of PC-C34-PC, the nanofibers have a thickness of 5–7 nm as judged by cryo-TEM (Fig. 4.2A), corresponding approximately to the molecular length of the bolalipid. AFM tapping-mode investigations of PC-C34-PC elucidated a helical superstructure of the

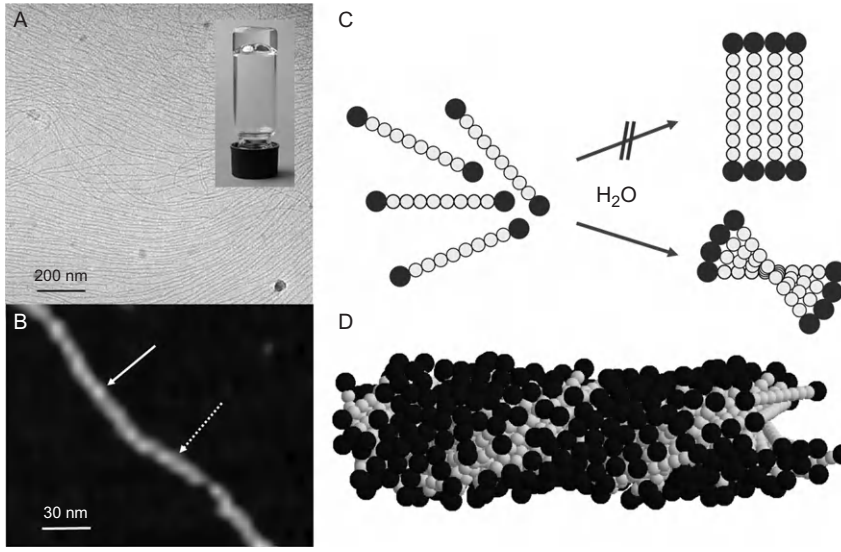

Figure 4.2 Self-assembly of PC-C*n*-PC. (A) Cryo-electron micrograph with hydrogel (inset) and (B) AFM tapping-mode image of the fiber structure of PC-C34-PC. The solid arrow indicates a right-handed and dotted arrow a left-handed helical fiber segment. (C) Schematic view of self-assembled, single-chain bolalipids in water forming helical fibers. (D) Helical fiber segment from Monte Carlo simulation. *Reprinted with permission from Ref. [67]. Copyright (2008) ACS.*

nanofibers with both chiral forms built up by achiral bolalipid molecules. The arrows in Fig. 4.2B point to fiber segments with right- (solid arrow) and left-handed (dotted arrow) helical structure within one fiber segment. The line scan displays a helical pitch of 8 nm (not shown) [67].

Because of the larger space requirements of the bolalipid headgroups compared to the small cross-sectional area of the alkyl chain, packing restrictions play an important role during the aggregation process. As a result, bilayer or monolayer membrane structures with parallel-oriented molecules are not sufficiently stabilized by the hydrophobic effect because the chains cannot get into close enough contact. Instead, the molecules are arranged slightly twisted relative to each other so that the hydrophobic chains can get in close enough contact. This twisted arrangement leads to a helical cylindrical structure with a diameter that corresponds to the molecular length (Fig. 4.2C). Our proposed model was confirmed by Monte Carlo simulations of a coarse-grained model, where the alkyl chain is represented by several small beads and the headgroup by one bead, which has a slightly larger diameter [67,68].

The helical nanofibers have lengths of up to several micrometers as evident from electron microscopic images. In the solution, they entangle and form a network cross-linked by physical contacts between the fibers. This cross-linking occurs because the surface of the fibers has grooves where hydrophobic groups are exposed to water. A contact between different fibers is therefore advantageous and decreases the hydrophobic surface area exposed to water. The cross-linking leads to the formation of a hydrogel as mentioned above and shown in Fig. 4.2A [67]. This hydrogel is almost clear and is stable even at concentrations of the bolalipid of only 0.3 mg/ml. Investigations of this hydrogel show that it has viscoelastic behavior previously not observed for other types of hydrogels. Below a strain of ca. 40–50% viscoelastic behavior is observed, where the storage and loss moduli G' and G'', respectively, are almost constant and not dependent on the deformation amplitude (Fig. 4.3). In this region, the storage modulus G' is always higher than the loss modulus G''. The increase in G' and G'' in the amplitude sweep experiment is due to strain stiffening at high amplitudes before a crossover of G' and G'' is observed, indicating the loss of the gel character.

When the hydrogel formed by the bolalipid is heated, a drastic change in behavior is immediately obvious just by visual inspection. Above ca. 50 °C, the hydrogel character disappears and a clear solution is obtained. Upon cooling, a gradual reformation of the hydrogel is observed. When the sample

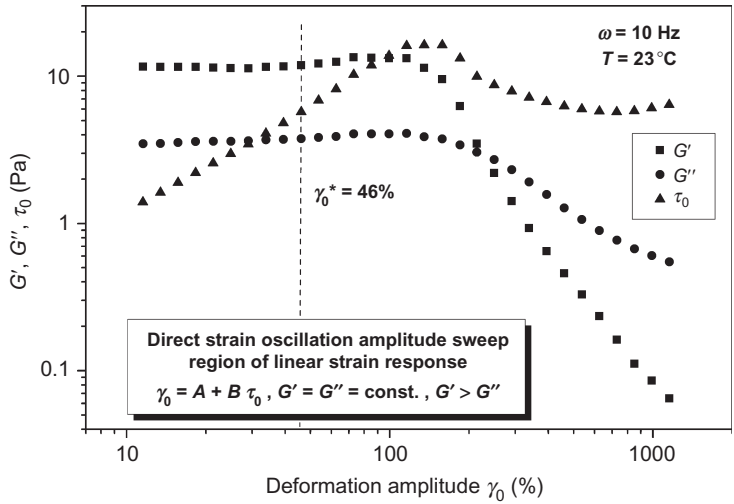

Figure 4.3 Rheological behavior of a PC-C32-PC (10 mM, ca. 0.8 wt.%) hydrogel in a controlled strain experiment a yield strain of ca. 40–50% was determined.

is investigated by DSC, three endothermic peaks are seen where the lowest temperature peak is very small followed by a larger peak at a temperature where the hydrogel character is lost and an additional high-temperature peak with larger width (Fig. 4.4A) [66]. The two lower temperature peaks seem to show a dependence on equilibration time at low temperature. By FT-IR spectroscopic investigations of the wave number of the symmetric CH_2-vibrational band as a function of temperature, it is possible to determine the amount of *gauche*-conformers in a long alkyl chain. For an all-*trans* alkyl chain, the wave number of this band is usually located below 2849 cm^{-1}. The frequency increases when *gauche*-conformers are formed due to an increase in disorder. The analysis showed that the fluidity of the alkyl chains indeed increases in a cooperative fashion at the temperature where the largest transition peak is observed (Fig. 4.4B) [66]. At high temperature, a further increase in fluidity is observed. Cooling the sample shows a hysteresis phenomenon, that is, the reformation of the all-*trans* conformation of the chains and the fiber aggregation takes time and is dependent on the concentration. These observations could be supported by rheological measurements as a function of temperature (not shown).

The loss of the hydrogel character is due to the formation of small micellar aggregates above the main transition. This could be verified by dynamic light scattering (DLS) experiments as well as by electron microscopy. Figure 4.5

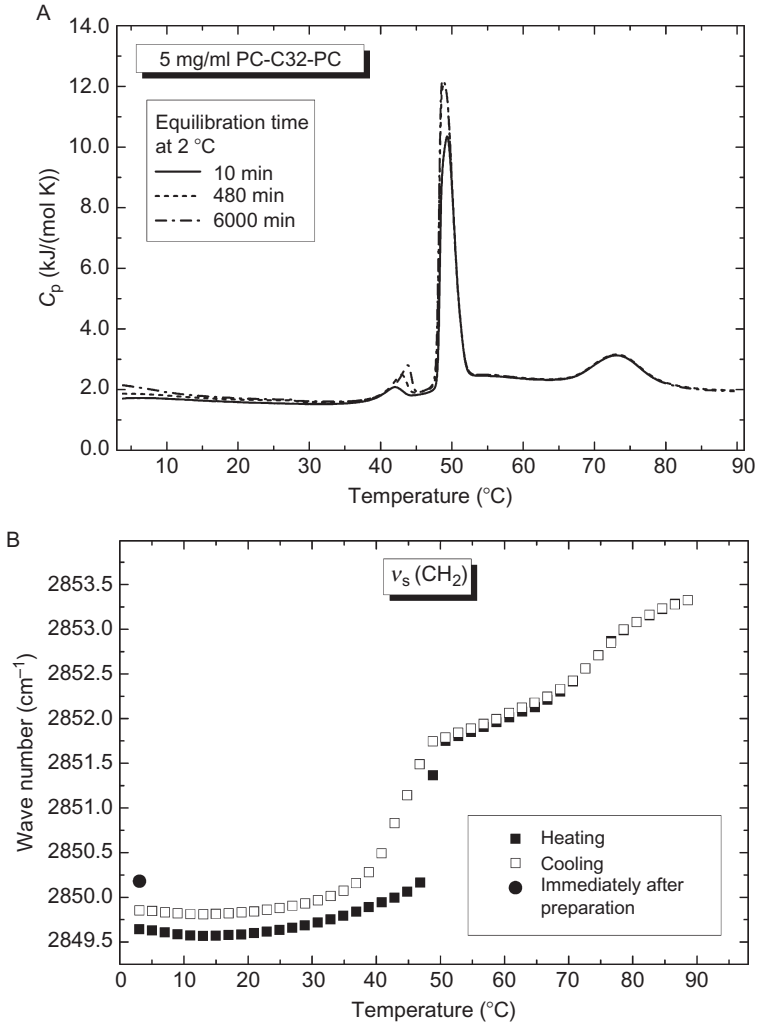

Figure 4.4 (A) DSC curves of a sample of PC-C32-PC with different equilibration times at low temperature. (B) Wave number of the symmetric CH_2-stretching vibrational band of PC-C32-PC as a function of temperature. *Reprinted with permission from Ref. [66]. Copyright (2004) ACS.*

shows two cryo-TEM images of samples prepared at a temperature of 20 °C where fibers are present (A) and at 60 °C, where the cryo-TEM image shows only faint spherical particles (B).

In addition to DLS, we also characterized the samples by SANS at different temperatures. Figure 4.6 shows the scattering curves at 25 °C, where the slope indicates the presence of long fibers of a diameter of ca. 5 nm, and

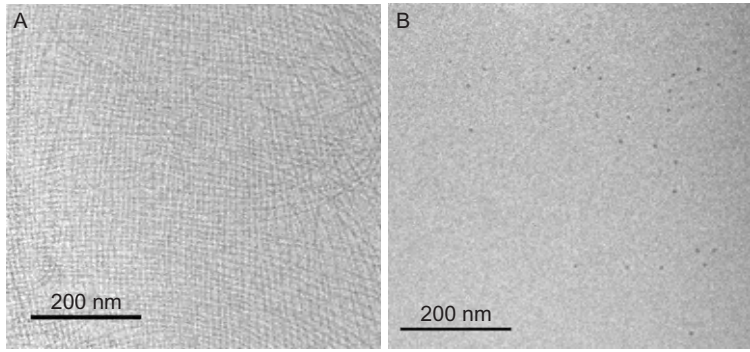

Figure 4.5 Cryo-TEM images of a sample of PC-C32-PC in water at 20 °C (A) and 60 °C (B) (A. Meister, A. Blume, unpublished results).

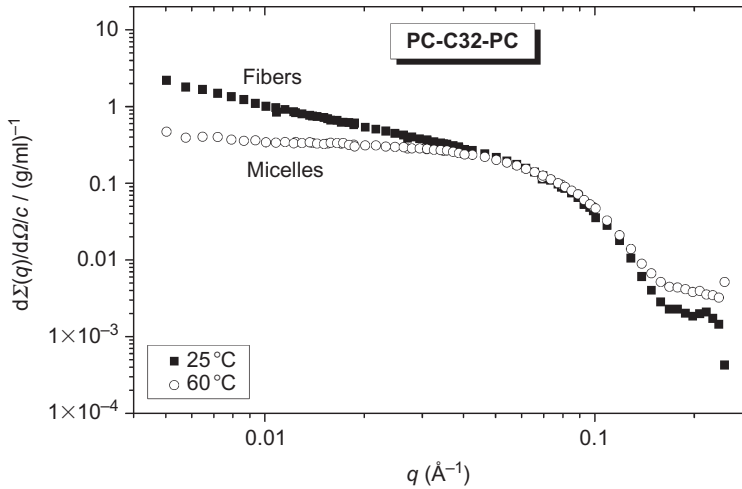

Figure 4.6 Small angle neutron scattering data for a sample of 1 mg/ml PC-C32-PC in D_2O at temperature as indicated. *Adapted with permission from Ref. [69]. Copyright (2007) ACS.*

at 60 °C, where small micellar aggregates with a diameter of ca. 6–7 nm seem to exist [69].

2.2. Chain length-dependent self-assembly

The thermotropic behavior and the rheological properties of the hydrogels resulting from the formation of the nanofiber network can be tuned by changing the length of the long alkyl chain. *A priori* one would expect a reduced stability of the nanofibers with decreasing chain length. This is indeed observed as is shown in Fig. 4.7 for a series of PC-C*n*-PC bolalipids

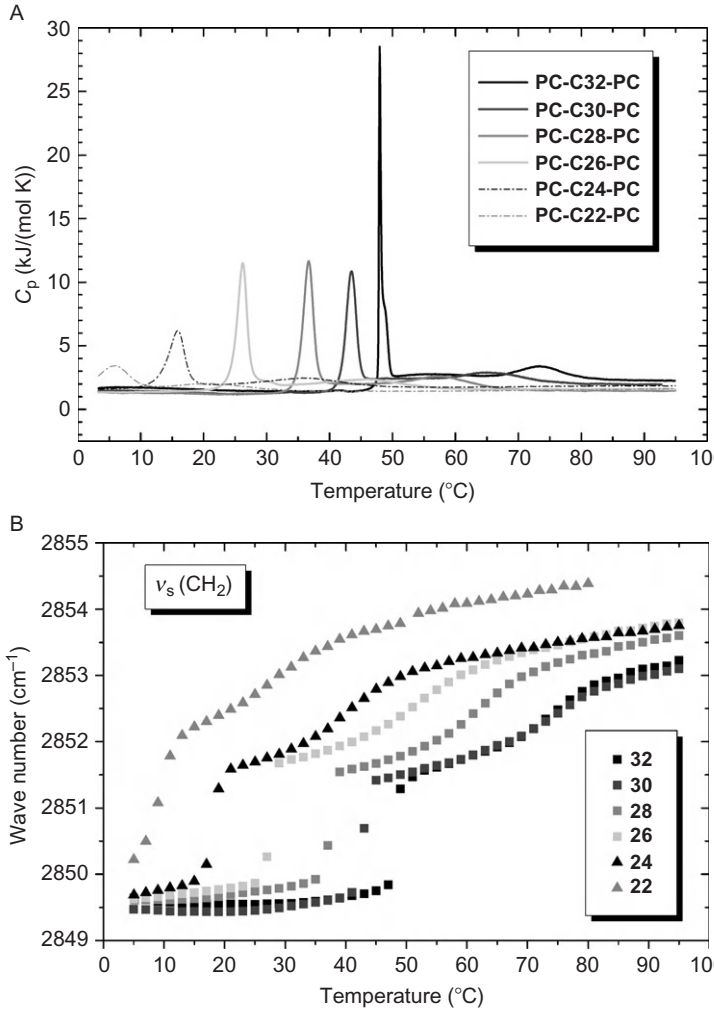

Figure 4.7 (A) DSC curves of PC-C*n*-PCs with different chain lengths as indicated. (B) Wave number of the symmetric CH_2-vibrational band as a function of temperature for PC-C*n*-PCs with different chain lengths. *Adapted by permission of John Wiley and Sons [61].*

with chains varying from 22 to 32 carbon atoms [61]. Figure 4.7A shows the DSC curves of the samples. Clearly, the main transition peak indicating the breakup of the fibers into micellar aggregates is shifted to lower temperature with decreasing chain length. Simultaneously, the width of the transition increases, that is, the transition becomes less cooperative. Also, the broader high-temperature peak characteristic for the transition between two different types of micelles is shifted to lower temperature. Figure 4.7B shows the frequency of the symmetric stretching vibration of the CH_2 groups as a

function of temperature as determined from temperature-dependent FT-IR experiments of aqueous samples. At low temperature, where exclusively fibers are present, the wave number of the symmetric CH_2-stretching band is again below 2850 cm^{-1}, a characteristic value for almost all-*trans* alkyl chains. The increase in wave number is caused by an increase in disorder of the chain, that is, the average number of *gauche*-conformers increases abruptly at the first transition, where the fibers transform into micellar aggregates. Also, the transition between the two types of micelles is connected with a further increase in disorder of the chains.

A further observation is that the wave number at low temperature is almost the same for all compounds, indicating that the chains are in an almost all-*trans* conformation, regardless of the chain length. However, at high temperature, the shorter analogues show higher wave numbers. This means that the disorder in both types of micelles increases with decreasing chain length.

TEM and cryo-TEM images proved that the aggregation state remained the same, only that the transitions between the different types of aggregates were shifted to lower temperature with decreasing chain length [61].

When the transition temperatures between the different aggregate types are plotted as a function of chain length, a continuous increase in the transition temperatures is observed; only the difference in temperature between the fiber–micelle and the micelle I–micelle II transition seems to increase slightly (Fig. 4.8) [62]. At present, we have no information about the

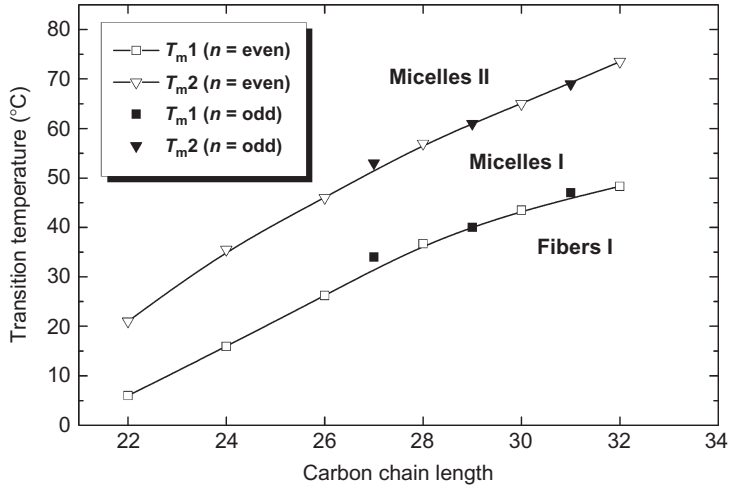

Figure 4.8 Transition temperatures of bolaphospholipids of the type PC-C*n*-PC as a function of chain length. No even–odd effect is observed as all temperature fall onto a continuous curve. *Adapted with permission from Ref. [62]. Copyright (2008) ACS.*

different types of micelles only that the high-temperature aggregate has more disorder in the chains, as indicated by the FT-IR data already discussed.

2.3. Chain structure-dependent self-assembly

Another possibility to tune the aggregation behavior of long-chain bolalipids is the introduction of heteroatoms and/or double or triple bonds into the long alkyl chain. Figure 4.9 shows a C32 chain with two oxygen atoms (middle) or two sulfur atoms (bottom) in the long chain. The deviation from the straight all-*trans* conformation of the pure alkyl chain (top) is immediately evident. In addition, the chains become more polar by the introduction of heteroatoms [64].

As expected, the packing of the molecules in the fibers is now perturbed leading also to a decrease of the transition temperature from fibrous to micellar aggregates. Figure 4.10 shows the DSC curves of the three different bolalipids with the normal alkyl chain, the chain with two oxygen atoms, and the sulfur-substituted chain. The fiber–micelle transition for the analogues with heteroatoms is shifted to lower temperature by ca. 40 K. Whereas the sulfur-containing bolalipid still shows a pronounced cooperative transition, the one for the oxygen-containing lipid is drastically decreased and broadened. However, in both cases, fibers are still present below this transition as can be seen in Fig. 4.11 for the sulfur-containing compound [64].

Another possibility to change the chemical structure of the chains is the introduction of triple bonds, for instance. Figure 4.12 shows the drastic change occurring in the C32 all-*trans* alkyl chain when two conjugated triple bonds are introduced into the chain. A strong perturbation of the chain packing in the nanofibers can be expected, which is indeed observed [70]. Due to the

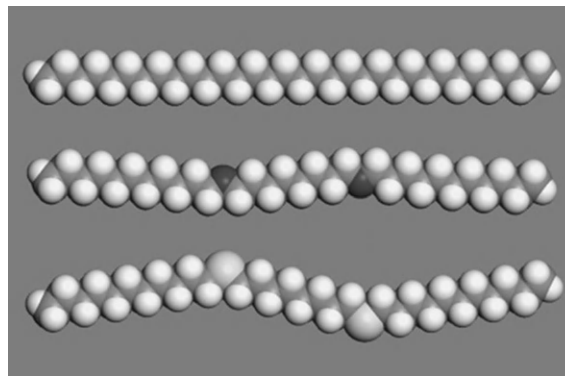

Figure 4.9 CPK models of a C32 alkyl chain in all-*trans* conformation (top) the chain is interrupted by two oxygen atoms (middle) or by two sulfur atoms (bottom) leading to kinks in the chain. *Adapted by permission of John Wiley and Sons [64].*

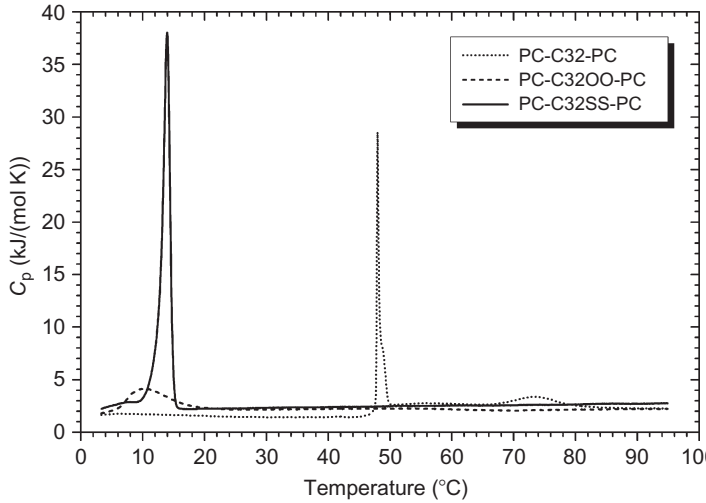

Figure 4.10 DSC curves of bolalipids with PC headgroups and modified chains. *Adapted by permission of John Wiley and Sons [64].*

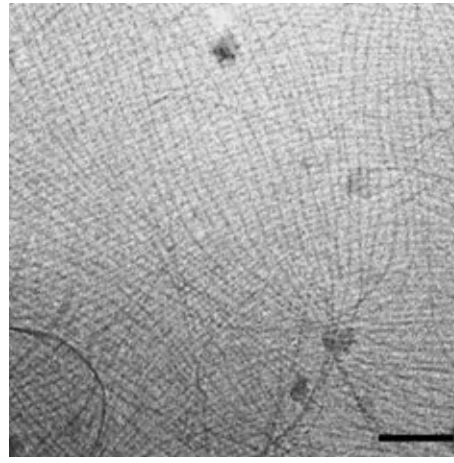

Figure 4.11 Cryo-TEM image of a sample of PC-C32SS-PC in water prepared at 7 °C [70]. The bar corresponds to 100 nm.

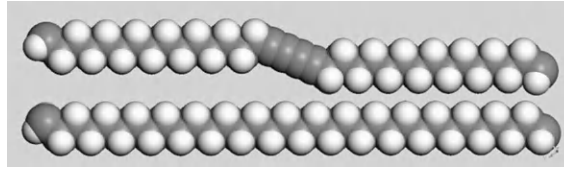

Figure 4.12 CPK models of a C34 alkyl chain (bottom) and a C34 alkyl chain with two conjugated triple bonds in the middle of the chain (top) [70].

kink in the chain induced by the two triple bonds, the fibers are very unstable and convert into micellar aggregates already at low temperature just above the freezing point of water. However, when the chain length is increased and thus the stretches with *trans*-conformational segments are getting longer, then the stability of the fibers is again higher, and the fiber–micelle transition shifts to ca. 18 °C as seen in the DSC curves shown in Fig. 4.13A.

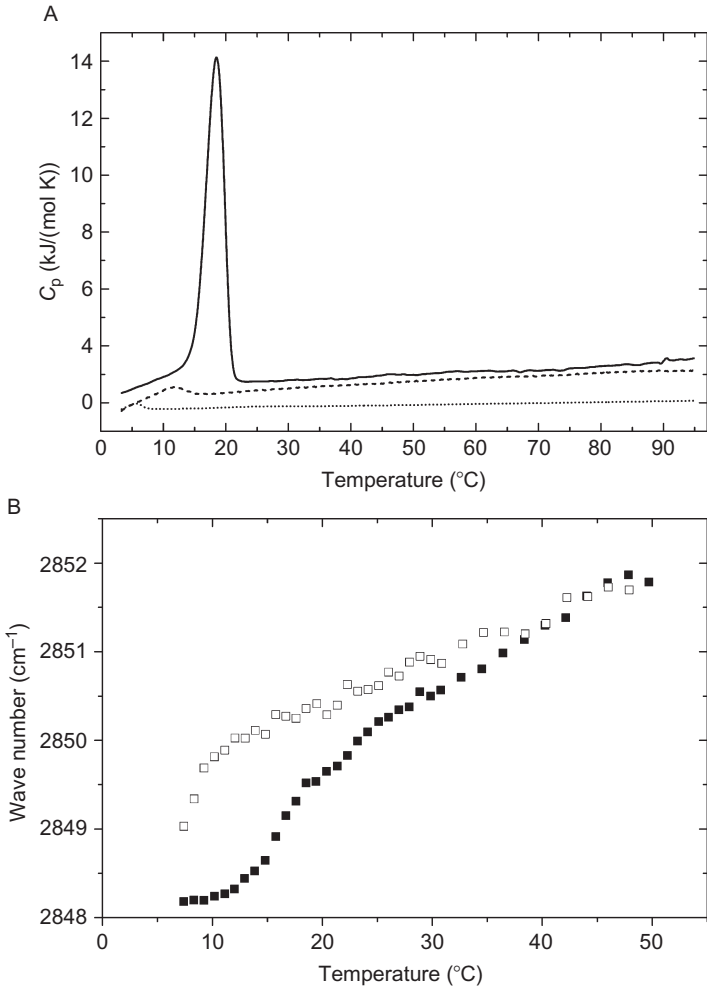

Figure 4.13 (A) DSC heating scans of suspensions of PC-C32diAc-PC (dotted curve, $c = 10$ mg/ml), PC-C34diAc-PC (dashed curve, $c = 1$ mg/ml), and PC-C36diAc-PC (solid curve, $c = 1$ mg/ml) in water. The heating rate was 20 K/h. (B) IR spectroscopic data of an aqueous suspension of PC-C34diAc-PC ($c = 50$ mg/ml). Wave number of the symmetric methylene stretching vibration as a function of temperature. Heating, filled squares; cooling, open squares [70].

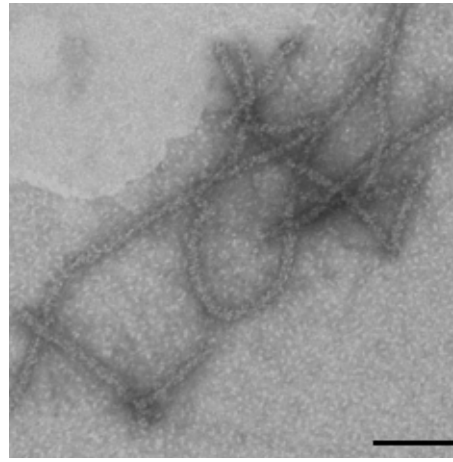

Figure 4.14 TEM image of a suspension of PC-C34diAc-PC at 5 °C. The sample was stained with uranyl acetate [70]. The bar corresponds to 100 nm.

However, as the TEM image in Fig. 4.14 shows, the fibers are relatively short, leading to a less pronounced gelation of the system [70].

Also, the self-assembly of the fibers after cooling from temperatures above the fiber–micelle transition shows a strong hysteresis and is occurring only slowly. This is particularly evident from the analysis of the frequency of the CH_2-vibrational bands determined upon heating and subsequent cooling as shown in Fig. 4.13B. Upon cooling, the shift of the maximum of the CH_2 band occurs at much lower temperature, and the original value is only restored after a considerable waiting period.

2.4. Headgroup structure-dependent self-assembly

The formation of nanofibers by these bolalipids is obviously caused by the mismatch of the cross-sectional area of the single alkyl chain and the headgroup. The question now arose how a variation in headgroup size, charge, and chemical structure would change the aggregation behavior. The first variation in headgroup structure was already described in the introduction and shown in Fig. 4.1. The replacement of methyl groups by H-atoms reduces the size of the headgroup. However, an additional effect occurring due to this substitution is the possibility that now intermolecular hydrogen bonds can be formed between the dimethyl ammonium group and the neighboring phosphate group, where the proton acts as the donor

and the oxygens of the phosphate are the acceptor atoms for the hydrogen bonds. We first performed a systematic investigation of the compound Me_2PE-C*n*-Me_2PE with a C32 alkyl chain to compare the behavior of this bolalipid to the PC-C*n*-PC [60].

Me_2PE-C32-Me_2PE also forms a fiber network at room temperature as was immediately evident from the formation of a hydrogel at room temperature and at low concentration of the bolalipid. The hydrogel had the same clear appearance as the one shown in Fig. 4.2 for the related analogue PC-C32-PC. Rheological measurements at low temperature showed, however, that this hydrogel is more stable and has stronger viscoelastic properties than hydrogels of PC-C32-PC. Figure 4.15 shows amplitude and frequency sweep experiments performed with a hydrogel at low temperature. The amplitude sweep shows that up to approximately 30% G' and G'' are independent of the deformation (Fig. 4.15A). This is the linear viscoelastic regime. The increase in G' and G'' observed at higher deformations before the crossover is due to strain stiffening. The following decrease indicates the transition from gel to the sol state. In the frequency sweep, G' shows a plateau up to 10 rad/s (Fig. 4.15B), and G'' increases with increasing angular frequency until a crossover at 20 rad/s occurs [72]. The behavior at high angular frequency is probably due to wall slip at the interfaces between the cone and the plate, respectively, with the sample. The data show that this hydrogel has a wide range for linear viscoelastic behavior. When the sample concentration is increased to 8 mg/ml, the values for G' and G'' increase strongly, and G' is larger than G'' by a factor of more than 10. Frequency sweep experiments show that no crossover is now observed up to frequencies of 200–300 rad/s. This behavior is quite remarkable as it shows the bolalipid gels are different from gels of worm-like micelles, where the "fibers" are very flexible and continuous breaking and reformation of the worm-like micelles occur. Due to the high degree of order (all-*trans* alkyl chains) inside the bolalipid fibers, the reactions leading to breaking and reformation are much slower so that the gels show much stronger elastic behavior than gels of worm-like micelles. The bolalipid gels are therefore more similar to gels of biological materials, built up from collagen or actin and fibrin fiber networks.

PC-C32-PC shows a strong temperature-dependent behavior of the aggregation properties (see above). This can also be observed for the compound Me_2PE-C32-Me_2PE. The DSC curves (Fig. 4.16) show an even more complicated behavior [69]. For Me_2PE-C32-Me_2PE at pH 5, three

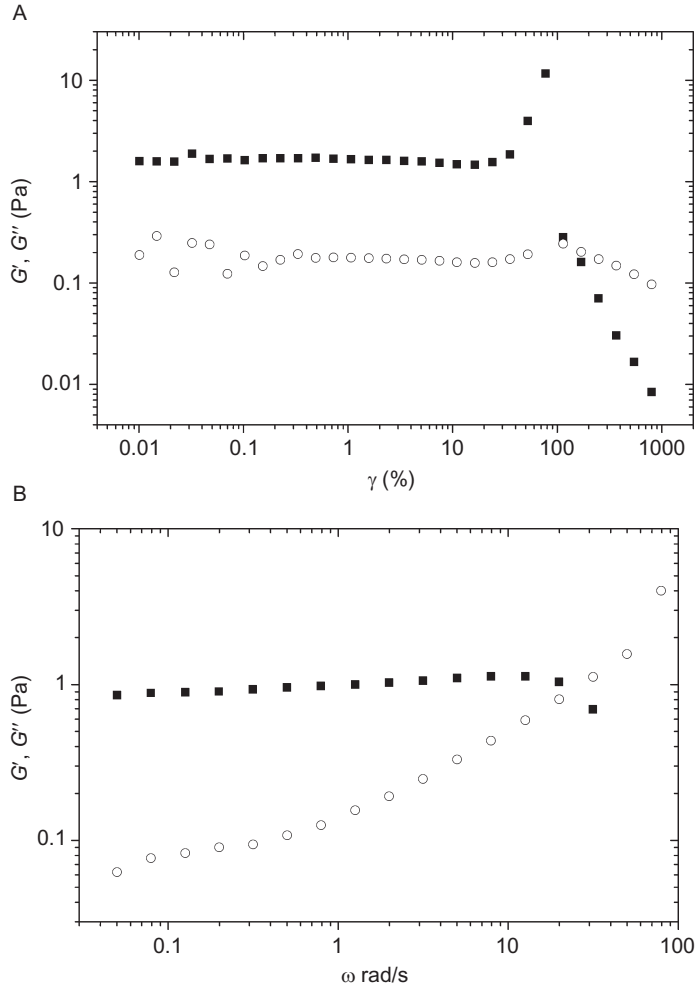

Figure 4.15 (A) Amplitude sweep (with $\omega = 1$ rad/s) and (B) frequency sweep (with $\gamma = 1\%$) of a suspension of Me_2PE-C32-Me_2PE ($c = 1$ mg/ml) in buffer at pH 5 at 2 °C. G', filled squares; G'', open circles. *Reprinted with permission from Ref. [71]. Copyright (2011) ACS.*

thermotropic transitions are evident where the first two transition peaks are of almost equal height and the high-temperature transition is much smaller. The first transition is connected with an increase in *gauche*-conformers in the chain, the fibers are still intact, and only their length is slightly decreased. At the second transition, the fibers break apart into micellar aggregates

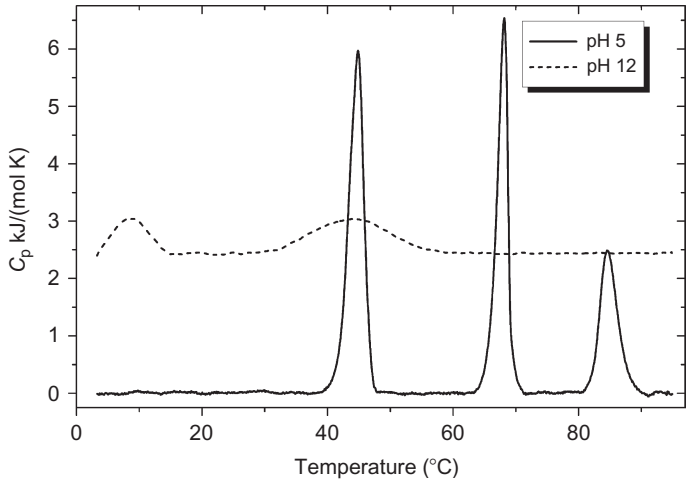

Figure 4.16 DSC heating curves of aqueous suspensions ($c = 1$ mg/ml) of Me_2PE-C32-Me_2PE in buffer at pH 5 and 12 (adjusted with NaOH solution). The heating rate was 20 K/h. The DSC curves are vertically shifted for clarity. *Adapted with permission from Ref. [71]. Copyright (2011) ACS.*

with increased chain fluidity. The third transition, finally, is again due to a transition between two different types of micellar aggregates, as was also observed for PC-C32-PC (see above). The fluidity of the chain increases further as can be seen from FT-IR spectroscopic measurements. When the pH of the sample is titrated to 12, the proton of the dimethyl ammonium headgroup dissociates and the headgroup becomes negatively charged. No hydrogen bonding is possible any more. The thermotropic behavior changes completely, and only two transitions can be seen in the DSC curve. TEM images of these samples show that only short fiber pieces are still present, and the cross-linking of the fibers leading to gelation is no longer possible [69,71].

Rheological measurements (Fig. 4.17) as a function of temperature showed that the viscoelastic behavior is more or less lost at the first transition due to a breakdown of the entanglement of the fibers and a slight reduction in fiber length. At the second transition, the fibers completely break apart into micellar-like aggregates, and the viscoelastic behavior is completely lost. The viscosity is now very similar to that of pure water. The third transition seen in the DSC scans is due to a transition between two different types of micelles. This temperature region is not accessible in rheological experiments due to loss of water by evaporation [71].

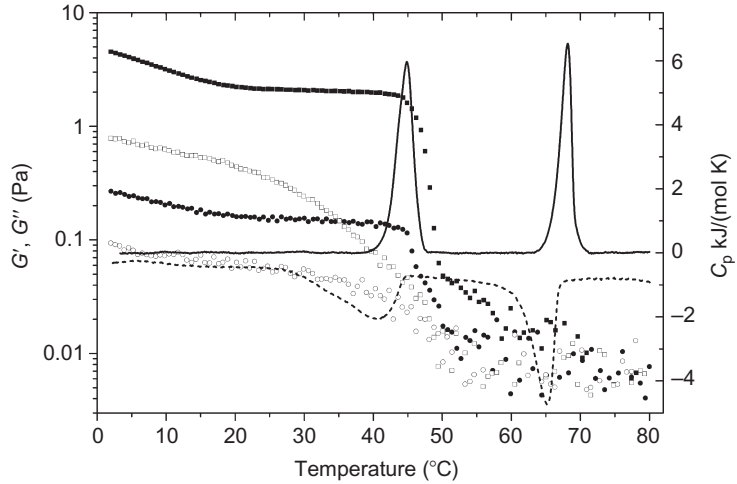

Figure 4.17 DSC curves (solid line, heating; dashed line, cooling) and rheological data (G', filled and open squares; G'': filled and open circles) of an aqueous suspension of Me_2PE-C32-Me_2PE in buffer at pH 5 ($c = 1$ mg/ml). Heating, filled symbols; cooling, open symbols. The heating and cooling rate was 20 K/h. Deformation ($\gamma = 1\%$) and angular frequency ($\omega = 1$ rad/s) were chosen inside the linear viscoelastic region. *Adapted with permission from Ref. [71]. Copyright (2011) ACS.*

When the sample of Me_2PE-C32-Me_2PE is titrated to pH 12, only two transitions are visible, and TEM images show that below the first transition short fiber segments are present, whereas above this transition elongated micellar-like aggregates can be seen [71]. As discussed above, this change in behavior is due to the fact that the headgroup is now negatively charged and that hydrogen bonding can no longer occur as the proton has dissociated. Addition of salt to the sample can partially revert the electrostatic effect as the negative charges at the surface of the fibers can be shielded by counterion condensation. The DSC curves in Fig. 4.18A show that addition of 250 mM NaCl leads to a thermotropic behavior with three transitions which is almost identical to the one observed for the sample at pH 5 without salt with the difference that the upper two transitions occur at slightly lower temperature (Fig. 4.18B). The rheological behavior of the sample, that is, the temperature dependence of G' and G'' shown in Fig. 4.18B, clearly indicates that indeed, the formation of a hydrogel is induced by the addition of salt. The viscoelastic behavior breaks down at the first transition where the

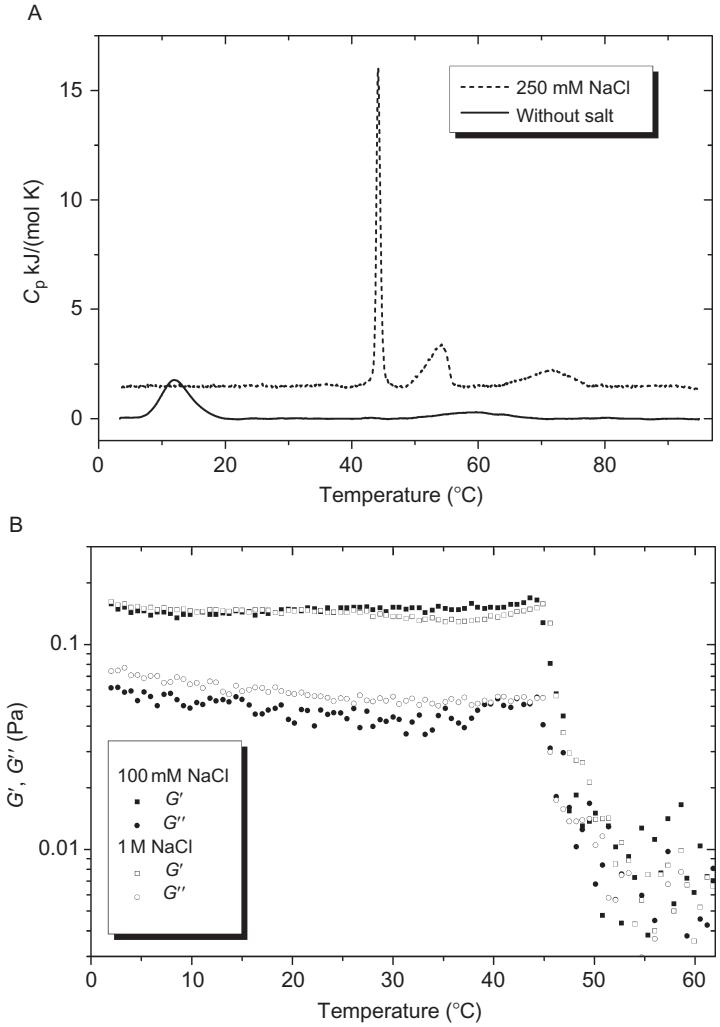

Figure 4.18 (A) DSC curves of Me_2PE-C32-Me_2PE at pH 11 with and without additional salt. (B) Temperature dependence of the rheological parameters G' and G'' for Me_2PE-C32-Me_2PE at pH 11 with two different NaCl concentrations. *Adapted with permission from Ref. [71]. Copyright (2011) ACS.*

entanglements of the fibers are lost. The difference between G' and G'' stays almost constant over the whole temperature range below the transition. An increase in salt concentration to 1 M NaCl has no significant further effect, indicating that the charges are already shielded at a concentration of 100 mM NaCl.

The bolalipids Me_2PE-C*n*-Me_2PE show a similar chain length-dependent behavior as the PC-C*n*-PC analogues. With increasing chain length, the transitions are shifted to higher temperature as expected. However, one significant difference exists in that Me_2PE-C*n*-Me_2PE bolalipids with shorter chains show only two transitions, namely the fiber I–micelle I and the micelle I–micelle II transition. Figure 4.19 shows DSC scans of

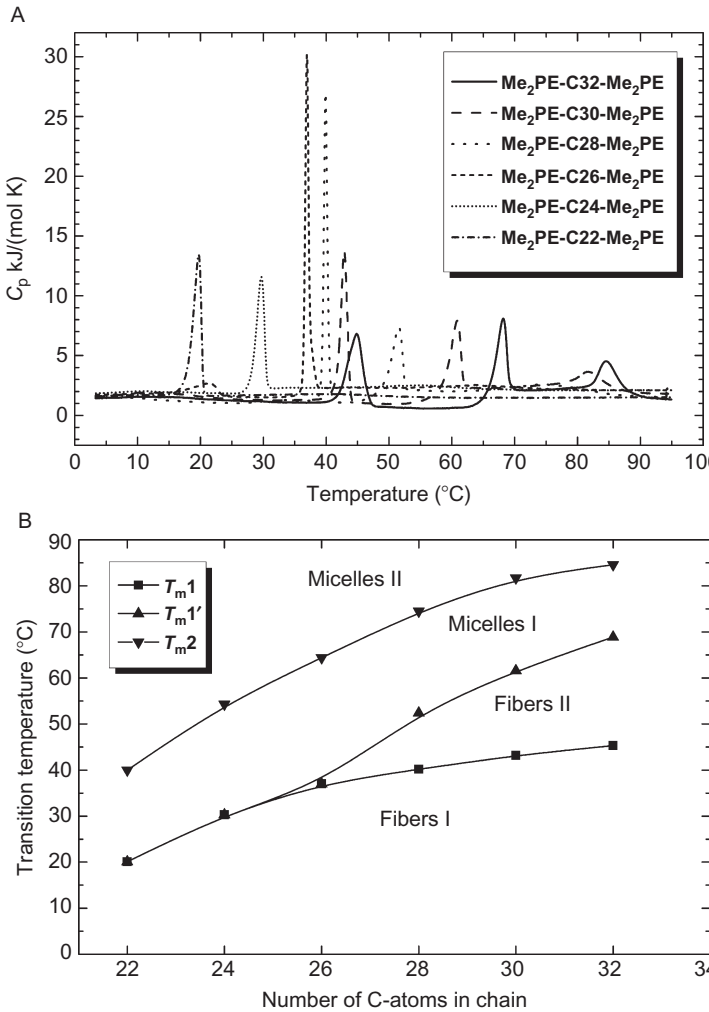

Figure 4.19 (A) DSC curves of aqueous samples of Me_2PE-C*n*-Me_2PE bolalipids with different alkyl chain lengths. (B) Transition temperatures as a function of chain length. *Adapted from Ref. [62].*

these compounds with different chain lengths (A) and the resulting "phase diagram" (B) [62].

For the data of the samples shown in the figures above, the bolalipids had a maximum chain length of 32 C-atoms. A change in aggregation behavior is seen when the length of the alkyl chain is further increased. This can be expected because the influence of the mismatch in steric requirements decreases when the alkyl chain becomes very long. A prime example where at room temperature still fibers are formed, but are metastable, is the compound Me_2PE-C*n*-Me_2PE with 34 or 36 C-atoms [72].

After the preparation of the samples and the formation of nanofibers at room temperature, they transform into square lamellae upon standing at room temperature. The square lamellae grow up to an edge length of about 100 nm, and the original nanofibers are still linked to one corner or to two always opposite corners of the squares. Figure 4.20 shows a TEM image with negative staining (A) and a cryo-TEM image of the sample (B). In the right image, the square lamellae can also be seen oriented edge-on leading to higher contrast.

Upon further incubation at room temperature for a week or more, a gel cake is formed and water is expelled when the gel cake becomes very compact (Fig. 4.21) [72].

Apparently, the gel cake is composed of clusters of stacked lamellae. Excess water between the clusters of lamellae is slowly released during syneresis; however, the hydration of the headgroups remains unchanged, and the amount of water trapped between adjacent single lamellae is only slightly

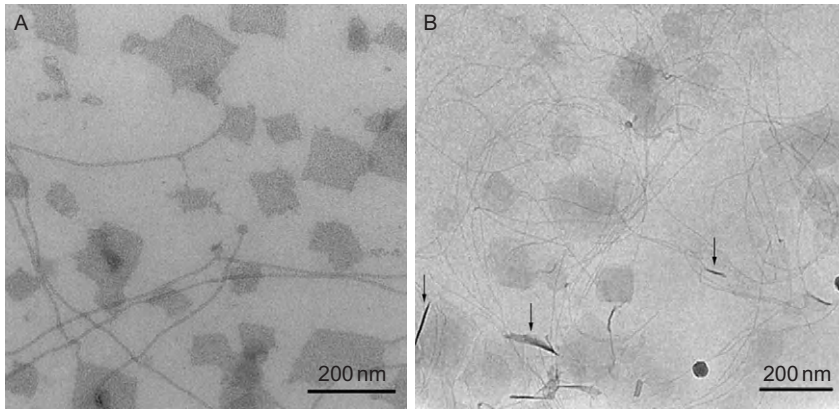

Figure 4.20 (A) TEM image with negative staining using uranyl acetate of Me_2PE-C36-Me_2PE. (B) Cryo-TEM image of Me_2PE-C34-Me_2PE. Arrows point to squares viewed edge-on [72]. *Reproduced by permission of The Royal Society of Chemistry.*

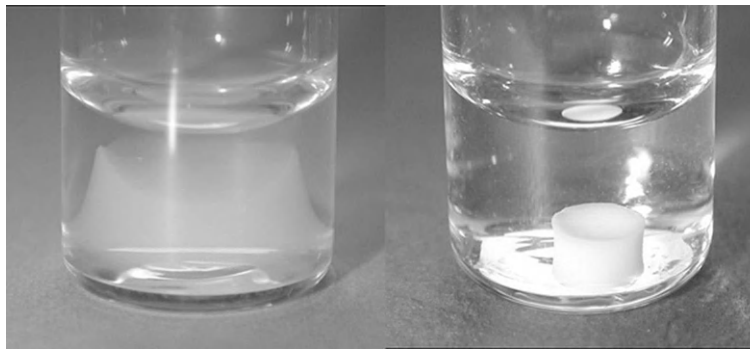

Figure 4.21 Gel cake formation of Me_2PE-C34-Me_2PE (1 mg/ml) by syneresis after 3 days (left) and 1 week (right) [72]. *Reproduced by permission of The Royal Society of Chemistry.*

reduced. This could be confirmed by X-ray diffraction experiments of the wet gel cake after taking it out of the surrounding water. The gel cake was placed on microscopic coverslip so that the X-ray beam could be oriented in different directions with respect to the expected stacking direction of the lamellae. The analysis of the 2D diffraction patterns leads to the conclusion that the spacing between the partially oriented lamellae is 3.44–3.5 nm. As the length of the bolalipid is ca. 6 nm, this spacing can only occur if the molecules are tilted with respect to the normal to the lamellar surface. The analysis of the wide angle reflections leads to the model shown in Fig. 4.22, where the chains are tilted by 55° in a complicated crisscross fashion minimizing the mismatch between the space required by the headgroups and the chains, respectively, and optimizing the van-der-Waals contacts.

When the headgroup size of the bolalipid is further reduced by replacing the second methyl group with an H-atom (Fig. 4.1), the aggregation behavior changes completely. The bolalipid MePE-C32-MePE does not form fiber aggregates any more but lamellar sheets, as shown in the cryo-TEM image in Fig. 4.23 [62]. The alkyl chains in these sheets are ordered so that the lamellar sheets are very inflexible as seen in the electron micrograph. When the temperature is increased, an order–disorder transition is seen by DSC at a temperature of ca. 80 °C. Whether the lamellar arrangement still persists above this temperature or whether micellar-like aggregates are formed is still unclear because of experimental difficulties in obtaining scattering data at this high temperature.

The chemical structure of the headgroup of the bolalipid can be varied in many different ways. As long as the steric requirement of the headgroup is

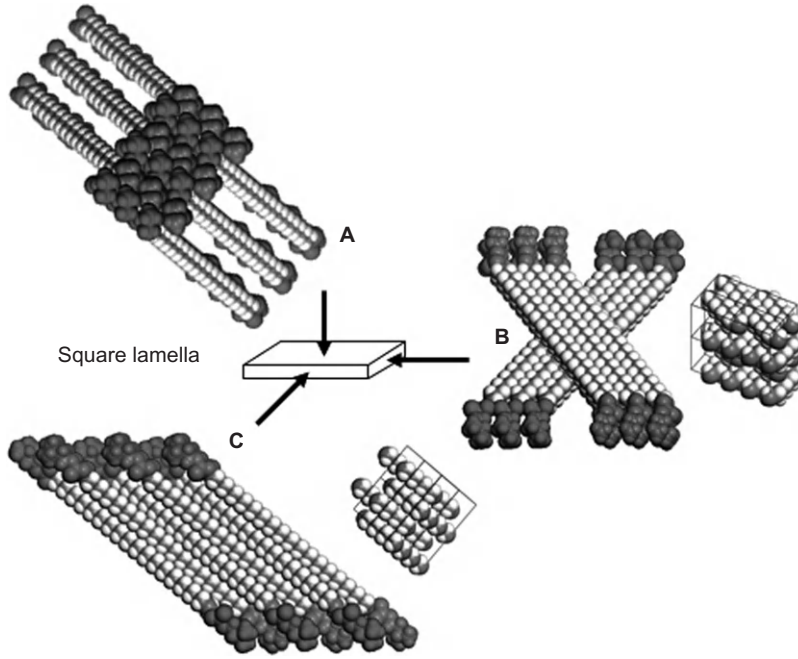

Figure 4.22 Molecular arrangement of Me_2PE-C34-Me_2PE within the square lamellae, seen from the top (A), the side (B), and the front (C). Headgroups of identical gray indicate the same tilting direction of the bolalipids. In (A), 18 bolalipids with neighboring headgroups are presented to show the densely packed headgroup arrangement [72]. *Reproduced by permission of the Royal Society of Chemistry.*

much higher than the cross-sectional area of the chain, normally fiber structures are formed. The fiber–micelle transition is, however, dependent on the structure of the headgroup, whether it is zwitterionic, charged, and/or able to form intermolecular hydrogen bonds. The physicochemical aggregation behavior of these compounds has been intensively investigated [64].

2.5. Self-assembly of bolalipid mixtures

The mixing behavior of phospholipids in lamellar lyotropic phases has been studied in great detail, and it has been found that ideal or nonideal mixing is the rule and that the tendency for immiscibility in lamellar phases is increased if the difference between the acyl chain lengths becomes larger than four CH_2 groups. The mixing behavior is modulated by differences in the headgroup size. It was also found that immiscibility in the low-temperature-ordered lamellar gel phases is more pronounced than that in the liquid-crystalline lamellar phases [73]. The nanofibers formed by the bolalipids described here

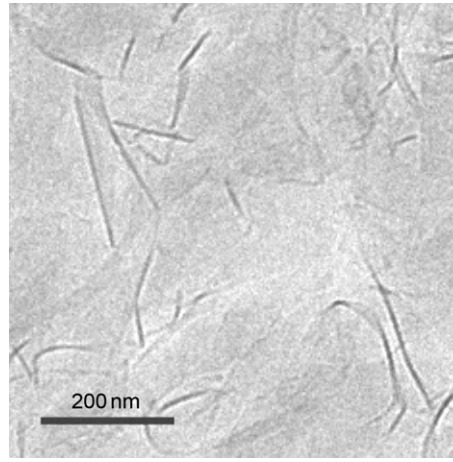

Figure 4.23 Cryo-TEM image of an aqueous suspension of MePE-C32-MePE in buffer solution at pH 5 quenched from 20 °C. *Reprinted with permission from Ref. [62]. Copyright (2008) ACS.*

show characteristic fiber–micelle transitions where the temperature of this transition depends on the chain length of the bolalipid. The question arose whether this transition can be tuned to a desired temperature by just mixing two bolalipids of different chain lengths and/or headgroup structures. As the bolalipid molecules within the fibers are ordered with an almost all-*trans* conformation of the chains, it seemed likely that the mixing could be nonideal or that even immiscibility could occur once the chain length difference became too large. We therefore performed mixing experiments of bolalipids with the same headgroup and different chain lengths as well as experiments, where also the headgroups had a different chemical structure [62].

Figure 4.24A shows DSC scans of an equimolar mixture of PC-C*n*-PCs with a chain length difference of four CH_2 groups. The transition peaks for the equimolar mixture is located at almost exactly the intermediate temperature of the transitions of the pure compounds. This indicates that these two bolalipids mix almost ideally in the fibers. Cryo-TEM images proved that indeed, fibers are present at room temperature. The DSC scans in Fig. 4.24B are from an equimolar mixture of Me_2PE-C28/32-ME_2PE. Again, the two bolalipids differ in chain length by four CH_2 groups. In this case, the equimolar mixture behaves as if the two compounds are not ideally miscible any more. Particularly, the transition from fiber II to micelle I is shifted much more to lower temperature than expected for ideal mixing. As the stability of the fibers is also due to intermolecular interactions between the

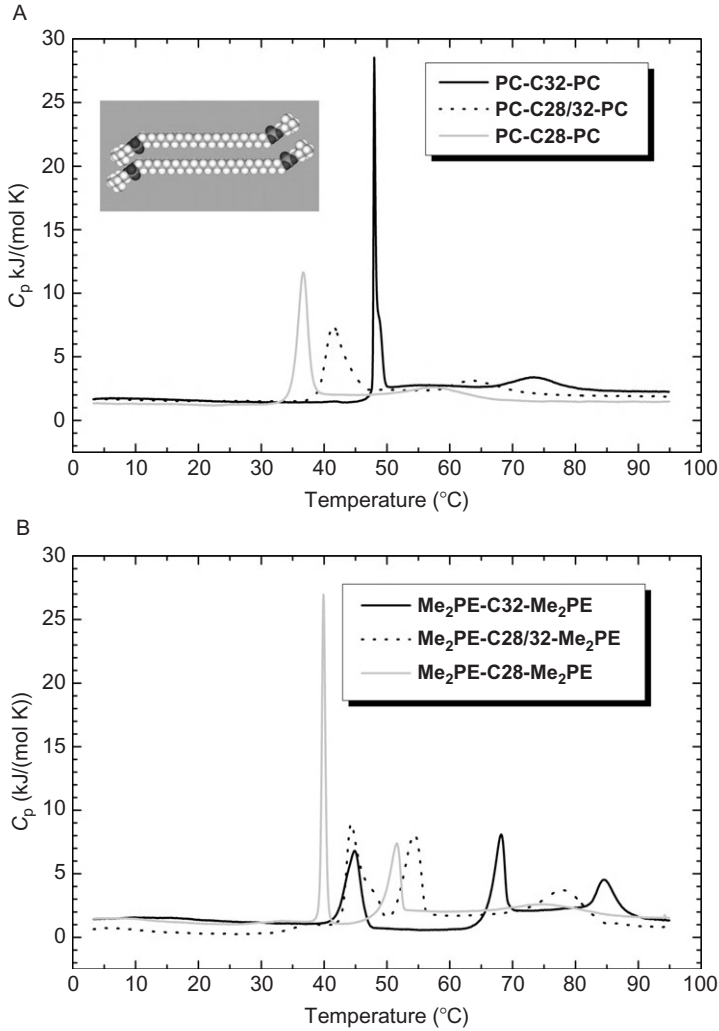

Figure 4.24 (A) DSC heating curves of an equimolar mixture (1 mg/ml) of PC-C28/32-PC. Data for the pure bolalipids are presented for comparison. (B) DSC heating curves of an equimolar mixture (1 mg/ml) of Me_2PE-C28/32-ME_2PE. Data for the pure bolalipids are presented for comparison. *Reprinted with permission from Ref. [62]. Copyright (2008) ACS.*

headgroups by hydrogen bonding, the mismatch in molecular length apparently prevents this additional stabilization to be very effective. Therefore, the transition temperature for the fiber–micelle transition in the mixture is located at more or less the same temperature as observed for the bolalipid with the shorter chain.

In the systems described above, the bolalipids had different chain lengths, but the same chemical structure of the headgroup. As the thermotropic behavior is also dependent on the headgroup, we also studied mixtures where the chain length of the two bolalipids was the same but had different headgroups structures. Figure 4.25 shows a DSC curve for a 1:1 mixture of PC-C32-PC/Me_2PE-C32-Me_2PE in comparison to the curves of the two pure compounds. In the case of PC-C32-PC, two transitions are evident, and for Me_2PE-C32-Me_2PE, the already more complicated behavior with three transitions can be seen. In the 1:1 mixture, the DSC curve shows also three transitions where the second transition connected with the fiber–micelle transformation is located at a temperature in between the transitions for the two pure compounds. It appears as if in the mixture, the behavior is dominated by the bolalipid Me_2PE-C32-Me_2PE. The presence of fibers below and above the first transition was verified by cryo-TEM and SANS measurements [62].

The results of the mixing experiments with bolalipids with different chain lengths show that the possibility exists to tune the transition behavior in the hydrogel-forming systems in any desired way. The lowest transition temperature, where the cross-linking of the fibers is disrupted, can be adjusted by mixing two different bolalipids of the type Me_2PE-C*n*-Me_2PE. Also, the temperature of the complete breakdown of the fibers into

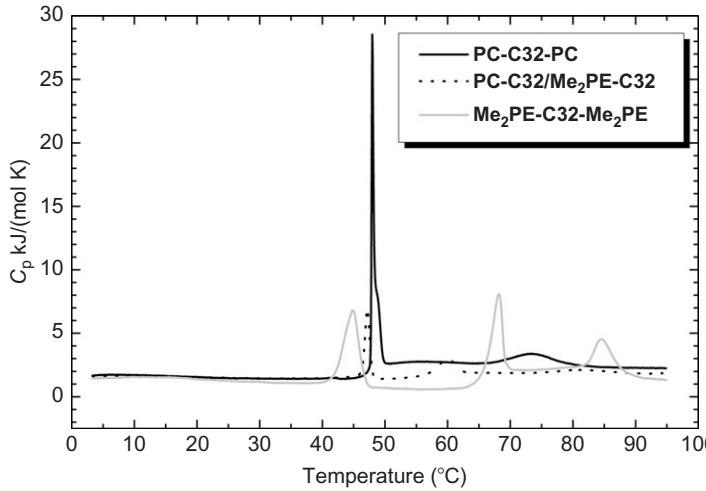

Figure 4.25 DSC heating curve of an equimolar mixture (1 mg/ml) of PC-C32-PC/Me_2PE-C32-Me_2PE. Data for the pure bolalipids are presented for comparison. *Reprinted with permission from Ref. [62]. Copyright (2008) ACS.*

micellar-like aggregates can be adjusted by either mixing two bolalipids with identical headgroups but different chain lengths, or mixing of bolalipids with different headgroups and/or chain lengths, for instance, mixing Me_2PE-C*n*-Me_2PE bolalipids with PC-C*n*-PC analogues [62].

3. MIXING BEHAVIOR OF SINGLE-CHAIN BOLALIPIDS WITH PHOSPHOLIPIDS

As we already mentioned in Section 1, the addition of classical lipids or surfactants is up to now the only way to stabilize vesicles that are built up by symmetrical single-chain bolalipids. In general, it is not easy to decide, whether the single-chain bolalipids adapt an U-shaped or a transmembrane conformation within the vesicle bilayer [74,75].

We tested the ability of the long-chain bolalipid PC-C32-PC to insert into phospholipid vesicles of DPPC, DMPC, and POPC [76]. From a point of molecular length, PC-C32-PC should fit in its all-trans conformation into the bilayers of these classical phospholipids (Fig. 4.26A–C).

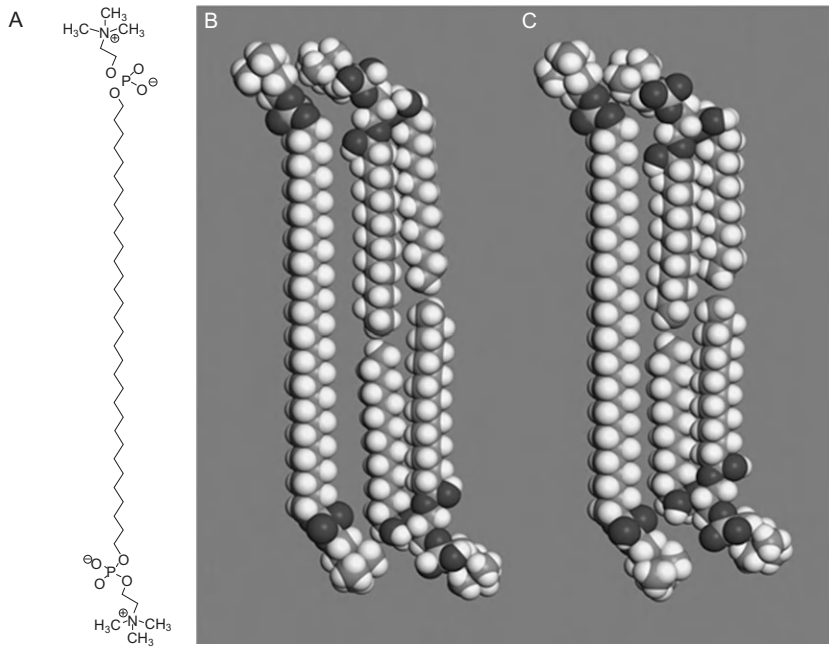

Figure 4.26 Chemical structure of PC-C32-PC (A). Comparison of the length of PC-C32-PC with DPPC (B) and DMPC (C) in schematic bilayer orientation. *Reproduced by permission of The Royal Society of Chemistry [76].*

The phospholipid DPPC has a chain length of 16 carbon atoms representing half the length of the bolalipid chain. Due to the missing glycerol backbone in PC-C32-PC, the molecule seems to be slightly shorter than the thickness of an ordered bilayer of DPPC with perpendicular chains. In comparison with DMPC, the bolalipid seems to be slightly longer.

The thermotropic behavior of aqueous suspensions of PC-C32-PC/DPPC mixtures at different molar ratios was investigated by DSC (Fig. 4.27A). The thermograms indicate, for all mixing ratios, a constant main transition temperature at 41.7 °C, and with increasing amount of PC-C32-PC, an additional shoulder appears at higher temperatures (~45 °C). However, the almost unaltered main transition temperature of the DPPC clearly indicates that PC-C32-PC can only be inserted into the DPPC vesicles to a minor extent. Since DPPC forms faceted vesicles at room temperature, it is conceivable that the bolalipid is incorporated into the vesicle at defects of the faceted bilayer structure. Cryo-TEM proves the presence of faceted vesicles and fibers even at a low molar ratio of 1:16 (Fig. 4.28A).

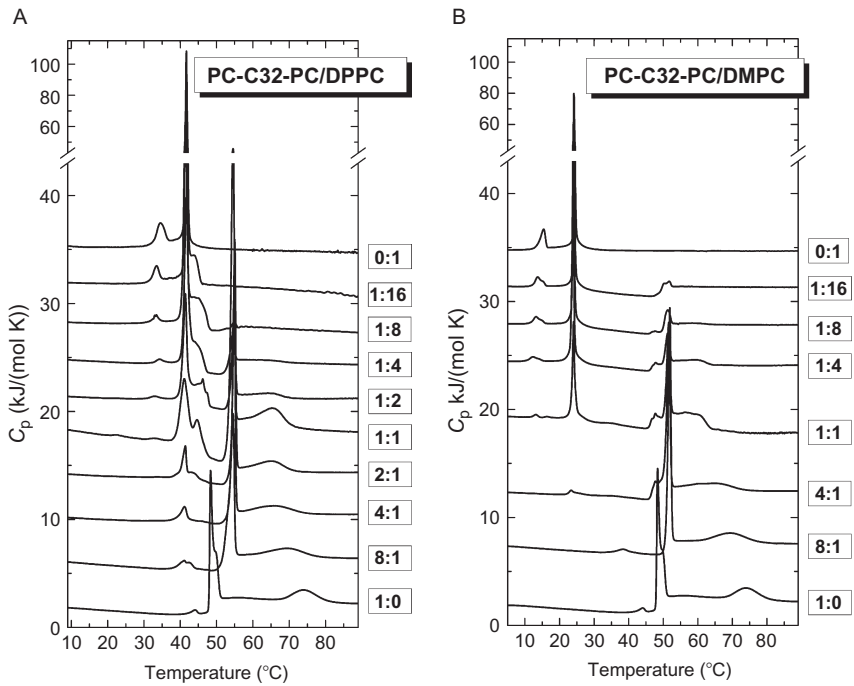

Figure 4.27 DSC curves of aqueous suspensions of PC-C32-PC/DPPC (A) and PC-C32-PC/DMPC (B) with different molar ratios. *Reproduced by permission of The Royal Society of Chemistry [76].*

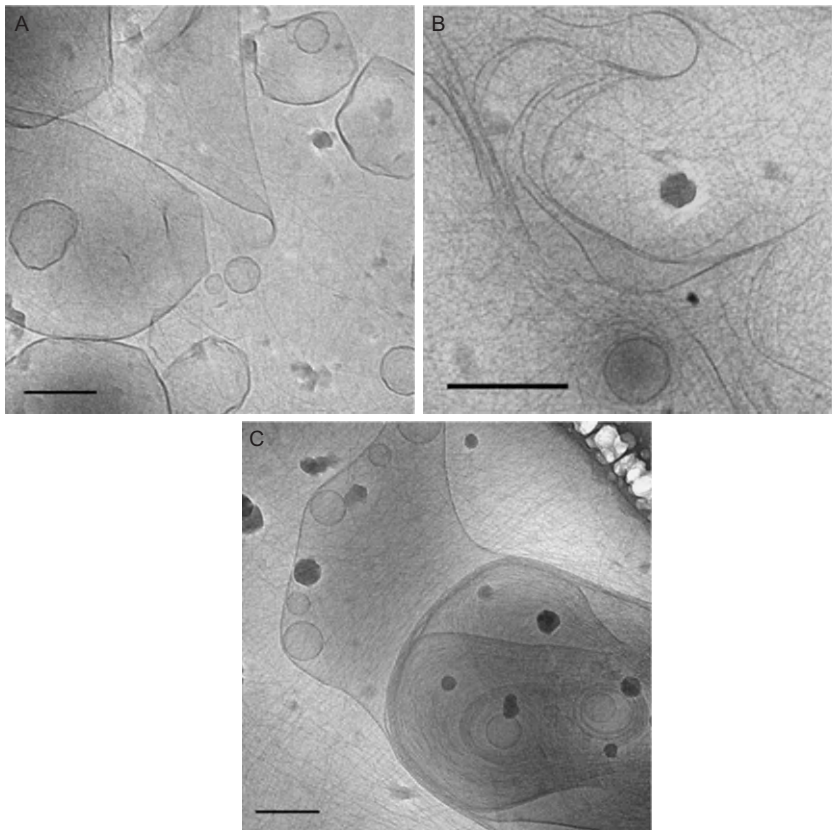

Figure 4.28 Cryo-TEM images of 3 mM aqueous suspensions of PC-C32-PC/DPPC mixture with different molar ratios (A, B) and PC-C32-PC/POPC (C). The samples are quenched from room temperature. The bar corresponds to 200 nm. (A) 1:16, (B) 4:1, (C) 1:8. *Reproduced by permission of The Royal Society of Chemistry [76].*

The thermograms of the PC-C32-PC/DPPC mixtures with high bolalipid content show a shift of the main transition for the fibers (48.4 °C) by 6 K to higher temperature (Fig. 4.27A). This is caused by the insertion of DPPC into the hydrophobic pockets of the PC-C32-PC fibers that are still exposed to water. Obviously, this process stabilizes the fiber structure.

The calorimetric measurements of PC-C32-PC/DMPC mixtures at different molar ratios show that the main transition temperature of the slightly shorter DMPC at 24.2 °C is not affected by an increasing amount of the bolalipid (Fig. 4.27B). From this, we conclude that DMPC vesicles are

not able to incorporate PC-C32-PC at all. On the other hand, the transition temperature for the main transition of PC-C32-PC is shifted to higher temperatures by 3 K, which indicates a stabilizing effect of the inserted DMPC. A similar stabilizing effect of the fiber structure was observed for a 1:1 PC-C32-PC/POPC mixture indicating a shift of the PC-C32-PC main transition by 4 K (not shown). The cryo-TEM image in Fig. 4.28C shows a dense network of fibers with some fibers being enclosed in large vesicular structures since they follow the curvature of the bilayer [76].

Our results indicate that the single-chain bolalipid PC-C32-PC has no tendency to be inserted into lipid bilayers of DPPC, DMPC, and POPC in a membrane-spanning conformation. Instead, the lipid bilayer forming phospholipids are incorporated into the hydrophobic pockets of the bolalipid fiber structure to a measurable extent. This behavior can be explained by packing problems, which are caused by a larger space requirement of the PC headgroups of the bolalipid compared to the small cross-sectional area of the alkyl chain. A transmembrane conformation would create a void volume within the membrane that could not be filled by chains of the bilayer forming lipid. Instead, the fiber arrangement of the bolalipids seems to be a state of lower energy, which is therefore preferred [76].

4. CONCLUSIONS

The results described in this review clearly show that the shape of self-assembled bolalipid aggregates strongly depends on the head-to-spacer diameter ratio of the bolalipid as well as on electrostatic interactions and the possibility of forming hydrogen bonds between neighboring headgroups. The results of the mixing experiments with bolalipids of different chain lengths show that it is possible to tune the transition behavior in these hydrogel-forming systems in any desired way. In addition, the temperature of the complete breakdown of the fibers into micellar-like aggregates can be adjusted by either mixing two bolalipids with identical headgroups but different chain lengths or mixing of bolalipids with different headgroups and/or chain lengths. Finally, our results indicate that the single-chain bolalipid PC-C32-PC has no tendency to be inserted into lipid bilayers of DPPC, DMPC, and POPC in a membrane-spanning conformation. Instead, the lipid bilayer forming phospholipids are incorporated into the hydrophobic pockets of the bolalipid fiber structure due to packing problems, which are caused by a larger space requirement of the PC headgroups of the bolalipid compared to the small cross-sectional area of the alkyl chain.

ACKNOWLEDGMENTS

We are very grateful to all, who have contributed to this work, namely M. Bastrop, B. Dobner, S. Drescher, G. Förster, G. Graf, G. Hause, A. Hauser, G. Hempel, K. Köhler, K. Mäder, and F. Ziethe from the Martin-Luther-University Halle-Wittenberg and our collaboration partners from other universities. This work was financially supported by the Deutsche Forschungsgemeinschaft (Projects Bl 182/19-1-3), the Cluster of Excellence "Nanostructured Materials" of the state of Saxony-Anhalt, and the Fonds der Chemischen Industrie.

REFERENCES

[1] J.N. Israelachvili, Intermolecular and Surface Forces, Academic Press, London, 1991.
[2] G.D. Sprott, D.L. Tolson, G.B. Patel, Archaeosomes as novel antigen delivery systems, FEMS Microbiol. Lett. 154 (1997) 17–22.
[3] G. Réthoré, T. Montier, T. Le Gall, P. Delépine, S. Cammas-Marion, L. Lemiègre, P. Lehn, T. Benvegnu, Archaeosomes based on synthetic tetraether-like lipids as novel versatile gene delivery systems, Chem. Commun. (2007) 2054–2056.
[4] C. Lainé, E. Mornet, L. Lemiègre, T. Montier, S. Cammas-Marion, C. Neveu, N. Carmoy, P. Lehn, T. Benvegnu, Folate-equipped pegylated archaeal lipid derivatives: synthesis and transfection properties, Chem. Eur. J. 14 (2008) 8330–8340.
[5] M. Brunelle, A. Polidori, S. Denoyelle, A.-S. Fabiano, P.Y. Vuillaume, S. Laurent-Lewandowski, B. Pucci, A structure-activity investigation of hemifluorinated bifunctional bolaamphiphiles designed for gene delivery, C. R. Chim. 12 (2009) 188–208.
[6] A. Jacquemet, J. Barbeau, L. Lemiègre, T. Benvegnu, Archaeal tetraether bipolar lipids: structures, functions and applications, Biochimie 91 (2009) 711–717.
[7] J.L. Gabriel, P.L.G. Chong, Molecular modeling of archaebacterial bipolar tetraether lipid membranes, Chem. Phys. Lipids 105 (2000) 193–200.
[8] S. Li, F. Zheng, X. Zhang, W. Wang, Stability and rupture of archaebacterial cell membrane: a model study, J. Phys. Chem. B 113 (2009) 1143–1152.
[9] P.L.-G. Chong, M. Sulc, R. Winter, Compressibilities and volume fluctuations of archaeal tetraether liposomes, Biophys. J. 99 (2010) 3319–3326.
[10] J. Barbeau, S. Cammas-Marion, P. Auvray, T. Benvegnu, Preparation and characterization of stealth archaeosomes based on a synthetic PEGylated archaeal tetraether lipid, J. Drug Deliv. 2011 (2011) 396068.
[11] G.B. Patel, G.D. Sprott, Archaeobacterial ether lipid liposomes (archaeosomes) as novel vaccine and drug delivery systems, Crit. Rev. Biotechnol. 19 (1999) 317–357.
[12] M. Brard, C. Lainé, G. Réthoré, I. Laurent, C. Neveu, L. Lemiègre, T. Benvegnu, Synthesis of archaeal bipolar lipid analogues: a way to versatile drug/gene delivery systems, J. Org. Chem. 72 (2007) 8267–8279.
[13] T. Benvegnu, L. Lemiègre, S. Cammas-Marion, New generation of liposomes called archaeosomes based on natural or synthetic lipids as innovative formulations for drug delivery, Recent Pat. Drug Deliv. Formul. 3 (2009) 206–220.
[14] T. Benvegnu, L. Lemiègre, S. Cammas-Marion, Archaeal lipids: innovative material for biotechnological applications, Eur. J. Org. Chem. 2008 (2008) 4725–4744.
[15] P.L.G. Chong, Archaebacterial bipolar tetraether lipids: physico-chemical and membrane properties, Chem. Phys. Lipids 163 (2010) 253–265.
[16] S. Grinberg, N. Kipnis, C. Linder, V. Kolot, E. Heldman, Asymmetric bolaamphiphiles from vernonia oil designed for drug delivery, Eur. J. Lipid Sci. Technol. 112 (2010) 137–151.
[17] B.A. Cornell, V.L.B. Braach-Maksvytis, L.G. King, P.D.J. Osman, B. Raguse, L. Wieczorek, et al., A biosensor that uses ion-channel switches, Nature 387 (1997) 580–583.

[18] J.H. Furhop, T. Wang, Bolaamphiphiles, Chem. Rev. 104 (2004) 2901–2938.
[19] G.S. Longo, D.H. Thompson, I. Szleifer, Stability and phase separation in mixed monopolar lipid/bolalipid layers, Biophys. J. 93 (2007) 2609–2621.
[20] K. Mulligan, D. Brownholland, A. Carnini, D.H. Thompson, L.J. Johnston, AFM investigations of phase separation in supported membranes of binary mixtures of POPC and an eicosanyl-based bisphosphocholine bolalipid, Langmuir 26 (2010) 8525–8533.
[21] T. Markowski, S. Drescher, A. Meister, G. Hause, A. Blume, B. Dobner, Synthesis of optically pure diglycerol tetraether model lipids with non-natural branching pattern, Eur. J. Org. Chem. 2011 (2011) 5894–5904.
[22] T. Benvegnu, M. Brard, D. Plusquellec, Archaeabacteria bipolar lipid analogues: structure, synthesis and lyotropic properties, Curr. Opin. Colloid Interf. Sci. 8 (2004) 469–479.
[23] M. Nakamura, R. Goto, T. Tadokoro, M. Shibakami, Construction of higher-ordered monolayer membranes derived from archaeal membrane lipid-inspired cyclic lipids with longer alkyl chains, J. Colloid Interface Sci. 310 (2007) 630–642.
[24] M. Berchel, L. Lemiègre, S. Trépout, O. Lambert, J. Jeftic, T. Benvegnu, Synthesis of unsymmetrical saturated or diacetylenic cationic bolaamphiphiles, Tetrahedron Lett. 49 (2008) 7419–7422.
[25] A. Jacquemet, L. Lemiègre, O. Lambert, T. Benvegnu, How the stereochemistry of a central cyclopentyl ring influences the self-assembling properties of archaeal lipid analogues: synthesis and cryoTEM observations, J. Org. Chem. 76 (2011) 9738–9747.
[26] W. Febo-Ayala, S.L. Morera-Félix, C.A. Hrycyna, D.H. Thompson, Functional reconstitution of the integral membrane enzyme, isoprenylcysteine carboxyl methyltransferase, in synthetic bolalipid membrane vesicles, Biochemistry 45 (2006) 14683–14694.
[27] S.-H. Hyun, H.-k. Kim, J.-M. Kim, D.H. Thompson, Oriented insertion of phi29 N-hexahistidine-tagged gp10 connector protein assemblies into C20BAS bolalipid membrane vesicles, J. Am. Chem. Soc. 132 (2010) 17053–17055.
[28] A. Meister, A. Blume, Self-assembly of bipolar amphiphiles, Curr. Opin. Colloid Interf. Sci. 12 (2007) 138–147.
[29] T. Shimizu, Molecular self-assembly into one-dimensional nanotube architectures and exploitation of their functions, Bull. Chem. Soc. Jpn. 81 (2008) 1554–1566.
[30] Y. Zhao, J. Zhao, Y. Yan, Z. Li, J. Huang, Unprecedented parallel packing of unsymmetrical bolaamphiphiles driven by π-π stacking of cinnamoyl groups, Soft Matter 6 (2010) 3282–3288.
[31] N. Kameta, M. Masuda, H. Minamikawa, T. Shimizu, Self-assembly and thermal phase transition behavior of unsymmetrical bolaamphiphiles having glucose- and amino-hydrophilic headgroups, Langmuir 23 (2007) 4634–4641.
[32] J.H. Jung, J.A. Rim, E.J. Cho, S.J. Lee, I.Y. Jeong, N. Kameta, M. Masuda, T. Shimizu, Stabilization of an asymmetric bolaamphiphilic sugar-based crown ether hydrogel by hydrogen bonding interaction and its sol-gel transcription, Tetrahedron 63 (2007) 7449–7456.
[33] N. Kameta, G. Mizuno, M. Masuda, H. Minamikawa, M. Kogiso, T. Shimizu, Molecular monolayer nanotubes having 7-9 nm inner diameters covered with different inner and outer surfaces, Chem. Lett. 36 (2007) 896–897.
[34] N. Kameta, M. Masuda, G. Mizuno, N. Morii, T. Shimizu, Supramolecular nanotube endo sensing for a guest protein, Small 4 (2008) 561–565.
[35] N. Kameta, K. Yoshida, M. Masuda, T. Shimizu, Supramolecular nanotube hydrogels: remarkable resistance effect of confined proteins to denaturants, Chem. Mater. 21 (2009) 5892–5898.
[36] N. Kameta, M. Masuda, H. Minamikawa, Y. Mishima, I. Yamashita, T. Shimizu, Functionalizable organic nanochannels based on lipid nanotubes: Encapsulation and nanofluidic behavior of biomacromolecules, Chem. Mater. 19 (2007) 3553–3560.

[37] W. Ding, M. Wada, N. Kameta, H. Minamikawa, T. Shimizu, M. Masuda, Functionalized organic nanotubes as tubular nonviral gene transfer vector, J. Control. Release 156 (2011) 70–75.
[38] N. Jain, Y. Arntz, V. Goldschmidt, G. Duportail, Y. Mély, A.S. Klymchenko, New unsymmetrical bolaamphiphiles: synthesis, assembly with DNA, and application for gene delivery, Bioconjug. Chem. 21 (2010) 2110–2118.
[39] S. Chen, B. Song, Z. Wang, X. Zhang, Self-organization of bolaamphiphiles bearing biphenyl mesogen and aspartic-acid headgroups, J. Phys. Chem. C 112 (2008) 3308–3313.
[40] C. Dolle, P. Magrone, S. Riva, M. Ambrosi, E. Fratini, N. Peruzzi, P. Lo Nostro, Symmetric and asymmetric bolaamphiphiles from ascorbic acid, J. Phys. Chem. B 115 (2011) 11638–11649.
[41] Z.-X. Chen, X.-X. Su, S.-P. Deng, Molecular recognition of melamine by vesicles spontaneously formed from orotic acid derived bolaamphiphiles, J. Phys. Chem. B 115 (2011) 1798–1806.
[42] T. Wang, J. Jiang, Y. Liu, Z. Li, M. Liu, Hierarchical self-assembly of bolaamphiphiles with a hybrid spacer and L-glutamic acid headgroup: pH- and surface-triggered hydrogels, vesicles, nanofibers, and nanotubes, Langmuir 26 (2010) 18694–18700.
[43] M.Z. Menzenski, I.A. Banerjee, Self-assembly of supramolecular nanostructures from phenylalanine derived bolaamphiphiles, New J. Chem. 31 (2007) 1674–1680.
[44] S. Ray, A.K. Das, A. Banerjee, PH-responsive, bolaamphiphiles-based smart metallohydrogels as potential dye-adsorbing agents, water purifier, and vitamin B12 carrier, Chem. Mater. 19 (2007) 1633–1639.
[45] A. Pal, S. Karthikeyan, R.P. Sijbesma, Coexisting hydrophobic compartments through self-sorting in rod-like micelles of bisurea bolaamphiphiles, J. Am. Chem. Soc. 132 (2010) 7842–7843.
[46] S. Grinberg, V. Kolot, C. Linder, E. Shaubi, V. Kas'yanov, R.J. Deckelbaum, E. Heldman, Synthesis of novel cationic bolaamphiphiles from vernonia oil and their aggregated structures, Chem. Phys. Lipids 153 (2008) 85–97.
[47] Y. Yan, W. Xiong, X. Li, T. Lu, J. Huang, Z. Li, H. Fu, Molecular packing parameter in bolaamphiphiles solutions: adjustment of aggregate morphology by modifying the solution conditions, J. Phys. Chem. B 111 (2007) 2225–2230.
[48] H. Shao, J. Seifert, N.C. Romano, M. Gao, J.J. Helmus, C.P. Jaroniec, D.A. Modarelli, J.R. Parquette, Amphiphilic self-assembly of an n-type nanotube, Angew. Chem. Int. Ed. 49 (2010) 7688–7691.
[49] J. Jiang, T. Wang, M. Liu, Creating chirality in the inner walls of silica nanotubes through a hydrogel template: chiral transcription and chiroptical switch, Chem. Commun. 46 (2010) 7178–7180.
[50] H. Cao, J. Jiang, X. Zhu, P. Duan, M. Liu, Hierarchical co-assembly of chiral lipid nanotubes with an azobenzene derivative: optical and chiroptical switching, Soft Matter 7 (2011) 4654–4660.
[51] A. Pal, P. Besenius, R.P. Sijbesma, Self-sorting in rodlike micelles of chiral bisurea bolaamphiphiles, J. Am. Chem. Soc. 133 (2011) 12987–12989.
[52] Y. Yan, T. Lu, J. Huang, Recent advances in the mixed systems of bolaamphiphiles and oppositely charged conventional surfactants, J. Colloid Interface Sci. 337 (2009) 1–10.
[53] H.E.-S. Ali, Synthesis, surface properties and antimicrobial activity of bolaamphiphiles/oppositely charged conventional surfactant mixed systems, J. Surfact. Deterg. 10 (2007) 117–124.
[54] F. Goursaud, M. Berchel, J. Guilbot, N. Legros, L. Lemiègre, J. Marcilloux, D. Plusquellec, T. Benvegnu, Glycine betaine as a renewable raw material to "greener" new cationic surfactants, Green Chem. 10 (2008) 310–320.

[55] Y. Chen, Y. Liu, R. Guo, Aggregation behavior of an amino acid-derived bolaamphiphiles and a conventional surfactant mixed system, J. Colloid Interface Sci. 336 (2009) 766–772.
[56] Q. Li, R. Mittal, L. Huang, B. Travis, C.R. Sanders, Bolaamphiphile-class surfactants can stabilize and support the function of solubilized integral membrane proteins, Biochemistry 48 (2009) 11606–11608.
[57] E.M. Smoak, M.P. Dabakis, M.M. Henricus, R. Tamayev, I.A. Banerjee, Interactions of amyloid Aβ (1–42) peptide with self-assembled peptide nanospheres, J. Pept. Sci. 17 (2011) 14–23.
[58] Y. Chen, Y. Liu, R. Guo, S. Xian, Interaction of hemoglobin with vesicles and tubes formed from mixtures of histidine-derived bolaamphiphiles and conventional surfactants, J. Solution Chem. 40 (2011) 48–60.
[59] K. Köhler, G. Förster, A. Hauser, B. Dobner, U.F. Heiser, F. Ziethe, W. Richter, F. Steininger, M. Drechsler, H. Stettin, A. Blume, Self-assembly in a bipolar phosphocholine-water system: the formation of nanofibers and hydrogels, Angew. Chem. Int. Ed. 43 (2004) 245–247.
[60] K. Köhler, A. Meister, G. Förster, B. Dobner, S. Drescher, F. Ziethe, W. Richter, F. Steininger, M. Drechsler, G. Hause, A. Blume, Conformational and thermal behavior of a pH-sensitive bolaform hydrogelator, Soft Matter 2 (2006) 77–86.
[61] S. Drescher, A. Meister, A. Blume, G. Karlsson, M. Almgren, B. Dobner, General synthesis and aggregation behavior of a series of single-chain 1, ω-bis(phosphocholines), Chem. Eur. J. 13 (2007) 5300–5307.
[62] A. Meister, S. Drescher, V.M. Garamus, G. Karlsson, G. Graf, B. Dobner, A. Blume, Temperature-dependent self-assembly and mixing behavior of symmetrical single-chain bolaamphiphiles, Langmuir 24 (2008) 6238–6246.
[63] S. Drescher, G. Graf, G. Hause, B. Dobner, A. Meister, Amino-functionalized single-chain bolalipids: synthesis and aggregation behavior of new basic building blocks, Biophys. Chem. 150 (2010) 136–143.
[64] S. Drescher, A. Meister, G. Graf, G. Hause, A. Blume, B. Dobner, General synthesis and aggregation behavior of new single-chain bolaphospholipids: variations in chain and headgroup structures, Chem. Eur. J. 14 (2008) 6796–6804.
[65] S. Drescher, K. Helmis, A. Langner, B. Dobner, Synthesis of novel symmetrical, single-chain, diacetylene-modified bolaamphiphiles with different alkyl chain lengths, Monatsh. Chem. 141 (2010) 339–349.
[66] K. Köhler, G. Förster, A. Hauser, B. Dobner, U.F. Heiser, F. Ziethe, W. Richter, F. Steininger, M. Drechsler, H. Stettin, A. Blume, Temperature-dependent behavior of a symmetric long-chain bolaamphiphile with phosphocholine headgroups in water: from hydrogel to nanoparticles, J. Am. Chem. Soc. 126 (2004) 16804–16813.
[67] A. Meister, S. Drescher, I. Mey, M. Wahab, G. Graf, V.M. Garamus, G. Hause, H.-J. Mögel, A. Janshoff, B. Dobner, A. Blume, Helical nanofibers of self-assembled bipolar phospholipids as template for gold nanoparticles, J. Phys. Chem. B 112 (2008) 4506–4511.
[68] M. Wahab, P. Schiller, R. Schmidt, H.-J. Mögel, Monte Carlo study of the self-assembly of achiral bolaform amphiphiles into helical nanofibers, Langmuir 26 (2010) 2979–2982.
[69] A. Meister, M. Bastrop, S. Koschoreck, V.M. Garamus, T. Sinemus, G. Hempel, S. Drescher, B. Dobner, W. Richtering, K. Huber, A. Blume, Structure-property relationship in stimulus-responsive bolaamphiphile hydrogels, Langmuir 23 (2007) 7715–7723.
[70] G. Graf, Ph.D. Thesis, Martin-Luther-Universität Halle-Wittenberg, 2011.
[71] G. Graf, S. Drescher, A. Meister, B. Dobner, A. Blume, Self-assembled bolaamphiphile fibers have intermediate properties between crystalline nanofibers and wormlike

micelles: formation of viscoelastic hydrogels switchable by changes in pH and salinity, J. Phys. Chem. B 115 (2011) 10478–10487.
[72] A. Meister, S. Drescher, G. Karlsson, G. Hause, U. Baumeister, G. Hempel, V.M. Garamus, B. Dobner, A. Blume, Formation of square lamellae by self-assembly of long-chain bolaphospholipids in water, Soft Matter 6 (2010) 1317–1324.
[73] A. Blume, P. Garidel, Lipid model membranes and biomembranes, in: R.B. Kemp (Ed.), Handbook of Thermal Analysis and Calorimetry. Vol. 4: From Macromolecules to Man, Elsevier Press, Amsterdam, 1999, pp. 109–173.
[74] D.P. Holland, A.V. Struts, M.F. Brown, D.H. Thompson, Bolalipid membrane structure revealed by solid-state ^{2}H NMR spectroscopy, J. Am. Chem. Soc. 130 (2008) 4584–4585.
[75] D.P. Brownholland, G.S. Longo, A.V. Struts, M.J. Justice, I. Szleifer, H.I. Petrache, M.F. Brown, D.H. Thompson, Phase separation in binary mixtures of bipolar and monopolar lipid dispersions revealed by ^{2}H NMR spectroscopy, small angle X-ray scattering, and molecular theory, Biophys. J. 97 (2009) 2700–2709.
[76] A. Meister, K. Köhler, S. Drescher, B. Dobner, G. Karlsson, K. Edwards, G. Hause, A. Blume, Mixing behavior of a symmetrical single-chain bolaamphiphiles with phospholipids, Soft Matter 3 (2007) 1025–1031.

CHAPTER FIVE

Dynamics of Heterogeneity in Fluid Membranes

Shigeyuki Komura*[1], Sanoop Ramachandran[†], Kazuhiko Seki[‡], Masayuki Imai[§]

*Department of Chemistry, Graduate School of Science and Engineering, Tokyo Metropolitan University, Tokyo, Japan
[†]Physique des Polymères, Université Libre de Bruxelles, Brussels, Belgium
[‡]National Institute of Advanced Industrial Science and Technology (AIST), Tsukuba, Japan
[§]Department of Physics, Faculty of Science, Tohoku University, Sendai, Japan
[1]Corresponding author: e-mail address: komura@tmu.ac.jp

Contents

1. Introduction 130
2. Membrane Hydrodynamics 133
3. Dynamics of Concentration Fluctuations 136
   3.1 Time-dependent Ginzburg–Landau model 136
   3.2 Effective diffusion coefficient 138
   3.3 Membrane as a 2D microemulsion 143
   3.4 Related works 145
4. Phase Separation Dynamics 146
   4.1 Domain coarsening 146
   4.2 Model and simulation technique 147
   4.3 Domain growth dynamics 148
   4.4 Correlated diffusion 151
   4.5 Related works 154
5. Conclusion and Outlook 159
Acknowledgments 161
References 161

Abstract

In this chapter, we investigate the dynamics of heterogeneity observed in multicomponent fluid membranes, particularly focusing on hydrodynamic effects due to the membrane and solvent. Two situations are discussed separately: above and below the miscibility transition temperature. In the former case, we calculate the wave number dependence of the effective diffusion coefficient by changing the temperature and/or the thickness of the bulk fluid. We also obtain the effective diffusion coefficient when multicomponent membranes are regarded as two-dimensional microemulsions. For the case below the transition temperature, we study the domain growth exponent in a binary membrane using a particle-based simulation method. With the addition

Advances in Planar Lipid Bilayers and Liposomes, Volume 16
ISSN 1554-4516
http://dx.doi.org/10.1016/B978-0-12-396534-9.00005-2

of bulk solvent, a change in the growth exponent from two- to three-dimensional nature is observed. Along with the measurement of correlated diffusion, we conclude that the phase separation takes place through the Brownian coagulation process in our simulation. We shall review some other works which are related to the present subject.

1. INTRODUCTION

Biological membranes typically contain various components such as lipid mixtures, sterols, and proteins that are indispensable to cell functions [1,2]. Rather than being uniformly distributed in the membrane, there is growing evidence that some cellular components are incorporated in domains arising from lateral lipid segregation in membranes. In 1997, Simons and Ikonen proposed a hypothesis which suggested that some lipids organize themselves into submicron-sized domains termed "lipid rafts" [3]. It was postulated that lipid rafts serve as platforms for proteins which attribute certain functionality to each domain.

In 2006, the definition of lipid rafts was proposed as follows [4]: "Membrane rafts are small (10–200 nm), heterogeneous, highly dynamic, sterol- and sphingolipid-enriched domains that compartmentalize cellular processes. Small rafts can sometimes be stabilized to form larger platforms through protein-protein and protein-lipid interactions." In spite of such a definition, the existence of lipid rafts is still debatable [5]. This is because lipid rafts have not yet been directly observed *in vivo*. One of the key issues that has been repeatedly asked is concerned with the lateral size and lifetime of lipid domains or clusters. The reported value ranges from 20 to 200 nm for the size, and from 10^{-2} to 10^{3} s for the lifetime [6]. Recently, a high-resolution observation of the lipid dynamics in living cells is achieved using stimulated emission depletion fluorescent microscopy [7]. They reported that sphingomyeline and membrane proteins are transiently (10–20 ms) trapped in about 20 nm diameter areas.

Stimulated by the lipid raft hypothesis, studies on artificial model membranes have been developed intensively in the last decade. Especially, the phase behavior of ternary giant vesicles composed of saturated lipids with high chain-melting temperature, unsaturated lipids with low chain-melting temperature, and cholesterol has been investigated for various mixtures [8,9]. It is known that such a ternary membrane is homogeneously mixed in the high-temperature region. By decreasing the temperature, the membrane undergoes a phase separation between the coexisting liquid-ordered (L_o) and liquid-disordered (L_d) phases. As a typical example, we show in Fig. 5.1 the phase diagram of a ternary vesicle consisting of DOPC (dioleoylphosphatidylcholine), PSM

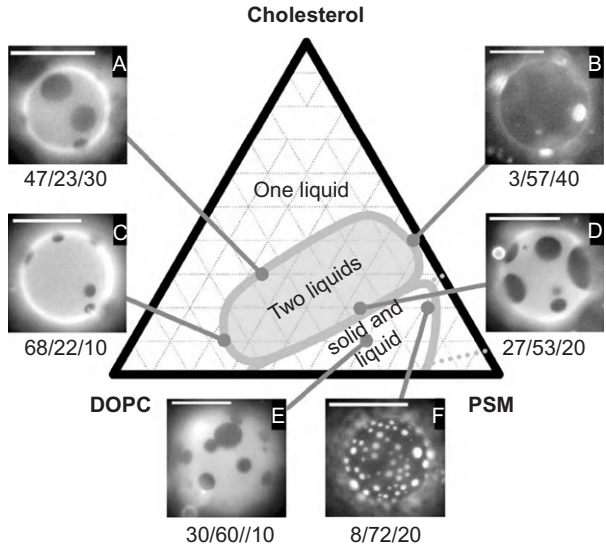

Figure 5.1 Phases observed by fluorescence microscopy of giant unilamellar vesicles containing mixture of DOPC, PSM, and cholesterol at 298 K. The dark liquid phase is rich in PSM and cholesterol, while the bright liquid phase is rich in DOPC. *Adapted from Ref. [10].*

(*N*-palmitoyl-D-sphingomyelin) and cholesterol together with several fluorescence micrographs [10]. In these pictures, dark liquid domains are rich in PSM and cholesterol, while bright liquid ones are rich in DOPC. The minority liquid phase forms circular domains which undergo lateral Brownian motion on the vesicle. In order to determine the ternary phase diagrams and to identify the domain morphologies, a large amount of research has been conducted using various experimental techniques [11].

On the other hand, behaviors of multicomponent membranes above the transition temperature have also gained much attention. Performing deuterium NMR experiments, Veatch *et al.* made a notable attempt to investigate critical fluctuations in lipid mixtures consisting of DOPC, DPPC (dipalmitoylphosphatidylcholine), and cholesterol [12]. A broadening of NMR resonances in the vicinity of the critical point was attributed to the compositional fluctuations on the scale less than 50 nm in the membrane. A more quantitative analysis of critical fluctuations using fluorescence microscopy was addressed by Honerkamp-Smith *et al.* for ternary mixtures of DPPC, diPhyPC (diphytanoylphosphatidylcholine), and cholesterol [13]. Typical microscope pictures of concentration fluctuations are shown in Fig. 5.2 for higher temperatures. From the measurement of the critical exponents, the authors concluded that the critical behavior in ternary membranes belongs to the universality class

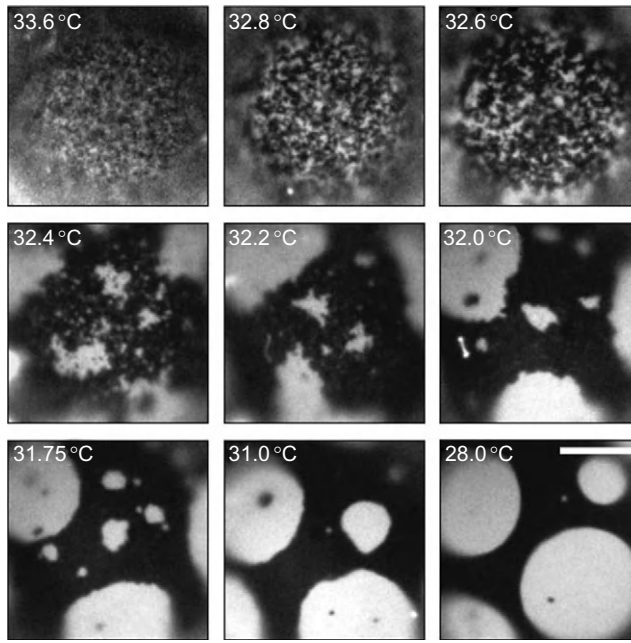

Figure 5.2 Giant vesicle consisting of DPPC, diPhyPC, and cholesterol passing through a critical temperature at $T_c \approx 32.5\,^{\circ}\mathrm{C}$. For temperatures above T_c, the vesicle exhibits concentration fluctuations. For temperatures below T_c, the vesicle undergoes a macroscopic phase separation. The scale bar corresponds to 20 μm. *Adapted from Ref. [13].*

of the two-dimensional (2D) Ising model [14]. Furthermore, by analyzing the correlation length and the line tension, it was shown that giant plasma membrane vesicles extracted from that of living rat basophil leukemia cells also exhibit a critical behavior [15]. These results allow us to speculate that lateral heterogeneity present in real cell membranes at physiological conditions could correspond to critical fluctuations.

As mentioned in the first paragraph, it is important to note that lipid rafts are highly dynamical objects. Being stimulated by various experiments, we shall discuss in this chapter the dynamics of heterogeneity in multicomponent membranes. It will be stressed that the hydrodynamic interaction mediated not only by the fluid membrane itself but also by the bulk solvent plays an essential role in the dynamics of multicomponent membranes at large scales. We discuss the cases of above and below the miscibility transition temperature separately.

In Section 2, we first provide a general framework of the membrane hydrodynamics. In Section 3, we investigate the dynamics of critical concentration fluctuations above the transition temperature. Based on the Ginzburg–Landau approach with full hydrodynamics, we calculate the wave

number dependence of the effective diffusion coefficient. We shall also consider the situation when the multicomponent membranes form microemulsions [16]. In Section 4, we study the domain growth dynamics below the transition temperature using dissipative particle dynamics (DPD) simulations. We show that the presence of a bulk fluid will alter the domain growth exponent from that of 2D to 3D, indicating a significant role played by the membrane–solvent coupling. In order to elucidate the underlying physical mechanism of this effect, we look into the diffusion properties in the membrane by measuring two-particle correlated diffusion. We show that quasi-2D phase separation proceeds by the Brownian coagulation (BC) mechanism which reflects the 3D nature of the bulk solvent. We will also compare our results with the related works in the literatures.

2. MEMBRANE HYDRODYNAMICS

In this section, we first establish the governing equations for the fluid membrane and its surrounding environment. Our aim is to derive the membrane mobility tensors which will be used in the later sections. More details of the calculation are given in Refs. [17,18].

As shown in Fig. 5.3, we assume that the membrane is an infinite planar sheet of liquid, and its out-of-plane fluctuations are totally neglected, which is justified for typical bending rigidities of bilayers. The liquid membrane is embedded in a bulk fluid such as water or solvent that is bounded by hard walls. Such a situation is worth considering because biological membranes interact strongly with other cells, substrates, or even the underlying cytoskeleton which can affect the structural and transport properties of the

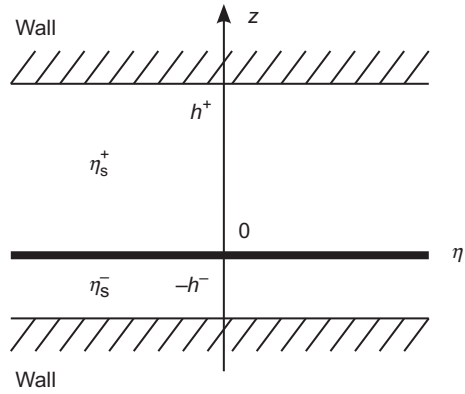

Figure 5.3 Schematic picture showing a planar liquid membrane having 2D viscosity η located at $z=0$. It is sandwiched by a solvent of 3D viscosity $\eta_s^{\pm}$. Two impenetrable walls are located at $z=\pm h^{\pm}$ bounding the solvent.

membrane. Let $\mathbf{v}(\mathbf{r})$ be the 2D velocity of the membrane fluid and the 2D vector $\mathbf{r}=(x,y)$ represents a point in the plane of the membrane. We first assume the membrane to be incompressible

$$\nabla\cdot\mathbf{v}=0, \tag{5.1}$$

where ∇ is a 2D differential operator. We work in the low-Reynolds number regime of the membrane hydrodynamics so that the inertial effects can be neglected. This allows us to use the 2D Stokes equation given by [19]

$$\eta\nabla^2\mathbf{v}-\nabla p+\mathbf{f}_{\mathrm{s}}+\mathbf{F}=0, \tag{5.2}$$

where η is the 2D membrane viscosity, $p(\mathbf{r})$ the 2D in-plane pressure, $\mathbf{f}_{\mathrm{s}}(\mathbf{r})$ the force exerted on the membrane by the surrounding fluid ("s" stands for the solvent), and $\mathbf{F}(\mathbf{r})$ is any other force acting on the membrane which we shall discuss in later sections.

As presented in Fig. 5.3, the membrane is fixed in the xy-plane at $z=0$. The upper ($z>0$) and the lower ($z<0$) fluid regions are denoted by "+" and "−," respectively. The velocities and pressures in these regions are written as $\mathbf{v}^{\pm}(\mathbf{r},z)$ and $p^{\pm}(\mathbf{r},z)$, respectively. Since the 3D viscosity of the upper and the lower solvent can be different, we denote them as $\eta_{\mathrm{s}}^{\pm}$, respectively. Consider the situation in which impenetrable walls are located at $z=\pm h^{\pm}$, where h^{+} and h^{-} can be different in general. Similar to the liquid membrane, the solvent in both regions are taken to be incompressible

$$\tilde{\nabla}\cdot\mathbf{v}^{\pm}=0, \tag{5.3}$$

where $\tilde{\nabla}$ represents a 3D differential operator. We also neglect the solvent inertia, and hence, it obeys the 3D Stokes equations

$$\eta_{\mathrm{s}}^{\pm}\tilde{\nabla}^2\mathbf{v}^{\pm}-\tilde{\nabla}p^{\pm}=0. \tag{5.4}$$

The presence of the surrounding solvent is important because it exerts force on the fluid membrane. This force, indicated as $\mathbf{f}_{\mathrm{s}}$ in Eq. (5.2), is given by the projection of $(\boldsymbol{\sigma}^{+}-\boldsymbol{\sigma}^{-})_{z=0}\cdot\hat{\mathbf{e}}_z$ on the xy-plane. Here $\hat{\mathbf{e}}_z$ is the unit vector along the z-axis, and $\boldsymbol{\sigma}^{\pm}$ are the stress tensors due to the solvent

$$\boldsymbol{\sigma}^{\pm}=-p^{\pm}\mathbf{I}+\eta_{\mathrm{s}}^{\pm}\left[\tilde{\nabla}\mathbf{v}^{\pm}+\left(\tilde{\nabla}\mathbf{v}^{\pm}\right)^{\mathrm{T}}\right]. \tag{5.5}$$

In the above, $\mathbf{I}$ is the identity tensor and the superscript "T" indicates the transpose.

Using the stick boundary conditions at $z=0$ and $z=\pm h^{\pm}$, we solve the hydrodynamic equations (5.3) and (5.4) to obtain $\mathbf{f}_{\mathrm{s}}$. Then we calculate the membrane velocity from Eq. (5.2) as

$$\mathbf{v}[\mathbf{k}] = \mathbf{G}[\mathbf{k}]\cdot\mathbf{F}[\mathbf{k}], \tag{5.6}$$

where $\mathbf{v}[\mathbf{k}]$ and others are the Fourier components defined such as by

$$\mathbf{v}(\mathbf{r}) = \int \frac{d\mathbf{k}}{(2\pi)^2}\mathbf{v}[\mathbf{k}]\exp(i\mathbf{k}\cdot\mathbf{r}), \tag{5.7}$$

with $\mathbf{k} = (k_x, k_y)$. After some calculations, one can show that the mobility tensor $\mathbf{G}[\mathbf{k}]$ in Fourier space is given by [17,18]

$$G_{\alpha\beta}[\mathbf{k}] = \frac{1}{\eta k^2 + k\left[\eta_s^+ \coth(kh^+) + \eta_s^- \coth(kh^-)\right]}\left(\delta_{\alpha\beta} - \frac{k_\alpha k_\beta}{k^2}\right), \tag{5.8}$$

with $\alpha, \beta = x, y$ and $k = |\mathbf{k}|$. For simplicity, we consider the case when the two walls are located at equal distances from the membrane, that is, $h^+ = h^- = h$. Then the above mobility tensor becomes

$$G_{\alpha\beta}[\mathbf{k}] = \frac{1}{\eta[k^2 + \nu k\coth(kh)]}\left(\delta_{\alpha\beta} - \frac{k_\alpha k_\beta}{k^2}\right), \tag{5.9}$$

where $\nu^{-1} = \eta/2\eta_s$ with $\eta_s = (\eta_s^+ + \eta_s^-)/2$. An almost equivalent expression to Eq. (5.9) has been derived for Langmuir monolayers in which there is only one wall or a substrate [20,21]. In the following, we will employ Eq. (5.9) as the general membrane mobility tensor.

We now discuss the two limiting situations of Eq. (5.9). Saffman and Delbrück (SD) investigated the case when the two walls are located infinitely away from the membrane, which is called as the free membrane case [22–24]. Taking the limit of $kh \gg 1$ in Eq. (5.9), the mobility tensor becomes [25,26]

$$G_{\alpha\beta}^{\text{free}}[\mathbf{k}] = \frac{1}{\eta(k^2 + \nu k)}\left(\delta_{\alpha\beta} - \frac{k_\alpha k_\beta}{k^2}\right). \tag{5.10}$$

The quantity ν^{-1} is called as the SD hydrodynamic screening length. The real space expression of this mobility tensor is obtained by the Fourier transform of Eq. (5.10) [21,25,26]

$$\begin{aligned} G_{\alpha\beta}^{\text{free}}(\mathbf{r}) = {} & \frac{1}{4\eta}\left[\mathbf{H}_0(\nu r) - Y_0(\nu r) + \frac{2}{\pi\nu^2 r^2} - \frac{\mathbf{H}_1(\nu r)}{\nu r} + \frac{Y_1(\nu r)}{\nu r}\right]\delta_{\alpha\beta} \\ & + \frac{1}{4\eta}\left[-\frac{4}{\pi\nu^2 r^2} + \frac{2\mathbf{H}_1(\nu r)}{\nu r} - \frac{2Y_1(\nu r)}{\nu r} - \mathbf{H}_0(\nu r) + Y_0(\nu r)\right]\frac{r_\alpha r_\beta}{r^2}, \end{aligned} \tag{5.11}$$

where $r = |\mathbf{r}|$. In the above, $\mathbf{H}_n(z)$ are Struve functions and $Y_n(z)$ are Bessel functions of the second kind.

Evans and Sackmann (ES) considered the opposite $kh \ll 1$ limit, for which the membrane is confined between the two walls although the solvent is still left [27]. In this case, Eq. (5.9) takes the following form:

$$G^{\mathrm{con}}_{\alpha\beta}[\mathbf{k}] = \frac{1}{\eta(k^2+\kappa^2)}\left(\delta_{\alpha\beta} - \frac{k_\alpha k_\beta}{k^2}\right). \tag{5.12}$$

In the above, $\kappa^{-1} = \sqrt{\nu^{-1}h}$ is called as the ES hydrodynamic screening length, and it is the geometric mean of ν^{-1} and h [28]. The above mobility tensor was used in a phenomenological membrane hydrodynamic model with momentum decay [26,29–31]. The real space representation of the above mobility tensor becomes

$$\begin{aligned} G^{\mathrm{con}}_{\alpha\beta}(\mathbf{r}) = {} & \frac{1}{2\pi\eta}\left[K_0(\kappa r) + \frac{K_1(\kappa r)}{\kappa r} - \frac{1}{\kappa^2 r^2}\right]\delta_{\alpha\beta} \\ & + \frac{1}{2\pi\eta}\left[-K_0(\kappa r) - \frac{2K_1(\kappa r)}{\kappa r} + \frac{2}{\kappa^2 r^2}\right]\frac{r_\alpha r_\beta}{r^2}, \end{aligned} \tag{5.13}$$

where $K_n(z)$ are the modified Bessel functions of the second kind. In Section 3, we shall mainly use the general mobility tensor Eq. (5.9), whereas either Eq. (5.10) or (5.12) is used in Section 4.

3. DYNAMICS OF CONCENTRATION FLUCTUATIONS

3.1. Time-dependent Ginzburg–Landau model

In this section, we use the idea of critical dynamics to calculate the effective diffusion coefficient in multicomponent lipid membranes. Based on Ginzburg–Landau approach with full hydrodynamics, we calculate the decay rate of the concentration fluctuations occurring in membranes [32,33]. We deal with the general case where the membrane is surrounded by a bulk solvent and two walls as depicted in Fig. 5.3. We also study the situation when the multicomponent membranes form 2D microemulsions [16]. This interesting viewpoint is motivated by a recent work which predicts the reduction of the line tension in membranes containing saturated, unsaturated, and hybrid lipids (one tail saturated and the other unsaturated) [34–37]. We shall explore the concentration fluctuations in 2D microemulsion with full hydrodynamics.

Consider a two-component fluid membrane composed of lipid A and lipid B whose local area fractions are denoted by $\phi_{\mathrm{A}}(\mathbf{r})$ and $\phi_{\mathrm{B}}(\mathbf{r})$, respectively. Since the relation $\phi_{\mathrm{A}}(\mathbf{r}) + \phi_{\mathrm{B}}(\mathbf{r}) = 1$ holds, we introduce a new

variable defined by $\psi(\mathbf{r}) = \phi_A(\mathbf{r}) - \phi_B(\mathbf{r})$. Then the simplest form of the free-energy functional $\mathcal{F}\{\psi\}$ describing the fluctuation around the homogeneous state is

$$\mathcal{F}\{\psi\} = \int d\mathbf{r}\left[\frac{a}{2}\psi^2 + \frac{c}{2}(\nabla\psi)^2\right], \tag{5.14}$$

where $a > 0$ is proportional to the temperature difference from the critical temperature T_c and $c > 0$ is related to the line tension.

The time evolution of concentration in the presence of hydrodynamic flow is given by the time-dependent Ginzburg–Landau equation for a conserved order parameter [38]

$$\frac{\partial\psi}{\partial t} + \nabla\cdot(\mathbf{v}\psi) = \Lambda\nabla^2\frac{\delta F}{\delta\psi}, \tag{5.15}$$

where Λ is the kinetic coefficient. In the membrane hydrodynamic equation (5.2), we need to incorporate the thermodynamic force due to the concentration fluctuations. Hence we have

$$\mathbf{F} = -\psi\nabla\frac{\delta\mathcal{F}}{\delta\psi}. \tag{5.16}$$

We implicitly assume that the relaxation of the velocity $\mathbf{v}$ is much faster than that of concentration ψ. The membrane velocity can be formally solved as follows using the appropriate 2D mobility tensor $G_{\alpha\beta}(\mathbf{r}, \mathbf{r}')$ derived in the previous section

$$v_\alpha(\mathbf{r}, t) = \int d\mathbf{r}' G_{\alpha\beta}(\mathbf{r}, \mathbf{r}')\left(\nabla'_\beta\psi\right)\frac{\delta\mathcal{F}}{\delta\psi(\mathbf{r}')}. \tag{5.17}$$

Since our interest is in the concentration fluctuations around the homogeneous state, we define $\delta\psi(\mathbf{r}, t) = \psi(\mathbf{r}, t) - \bar{\psi}$, where the bar indicates the spatial average. The free-energy functional expanded in powers of $\delta\psi$ becomes

$$\mathcal{F}\{\delta\psi\} = \int d\mathbf{r}\left[\frac{a}{2}(\delta\psi)^2 + \frac{c}{2}(\nabla\delta\psi)^2\right]. \tag{5.18}$$

Substituting Eq. (5.17) into Eq. (5.15), we get

$$\frac{\partial\delta\psi(\mathbf{r}, t)}{\partial t} = \Lambda\nabla^2\frac{\delta\mathcal{F}}{\delta(\delta\psi)} - \int d\mathbf{r}'(\nabla_\alpha\delta\psi(\mathbf{r}))G_{\alpha\beta}(\mathbf{r}, \mathbf{r}')\left(\nabla'_\beta\delta\psi(\mathbf{r}')\right)\frac{\delta\mathcal{F}}{\delta(\delta\psi(\mathbf{r}'))}. \tag{5.19}$$

We now consider the dynamics of the time-correlation function defined by

$$S(\mathbf{r},t)=\langle\delta\psi(\mathbf{r}_1,t)\delta\psi(\mathbf{r}_2,0)\rangle, \tag{5.20}$$

where $\mathbf{r}=\mathbf{r}_2-\mathbf{r}_1$. Within the factorization approximation [39], the spatial Fourier transform of $S(\mathbf{r},t)$ defined by

$$S[\mathbf{k},t]=\int d\mathbf{r}S(\mathbf{r},t)\exp(-i\mathbf{k}\cdot\mathbf{r}) \tag{5.21}$$

satisfies the following equation

$$\frac{\partial S[\mathbf{k},t]}{\partial t}=-\left(\Gamma^{(1)}[\mathbf{k}]+\Gamma^{(2)}[\mathbf{k}]\right)S[\mathbf{k},t]. \tag{5.22}$$

The first term, $\Gamma^{(1)}[\mathbf{k}]$, denotes the van Hove part of the relaxation rate given by

$$\Gamma^{(1)}[\mathbf{k}]=\Lambda k_{\mathrm{B}}Tk^2\chi^{-1}[\mathbf{k}]. \tag{5.23}$$

Here, the static correlation function is defined by

$$\chi[\mathbf{k}]=\langle\delta\psi[\mathbf{k}]\delta\psi[-\mathbf{k}]\rangle=\frac{k_{\mathrm{B}}T}{c\left(k^2+\xi^{-2}\right)}, \tag{5.24}$$

where $\xi=(c/a)^{1/2}$ is the correlation length, k_{B} the Boltzmann constant, and T the temperature.

As for the second term in Eq. (5.22), $\Gamma^{(2)}[\mathbf{k}]$ denotes the hydrodynamic part of the decay rate given by

$$\Gamma^{(2)}[\mathbf{k}]=\frac{1}{\chi[\mathbf{k}]}\int\frac{d\mathbf{q}}{(2\pi)^2}k_\alpha G_{\alpha\beta}[\mathbf{q}]k_\beta\chi[\mathbf{k}+\mathbf{q}]. \tag{5.25}$$

When we use Eq. (5.9) for the mobility tensor $G_{\alpha\beta}$, the hydrodynamic part of the decay rate is expressed with an integral as

$$\Gamma^{(2)}[\mathbf{k}]=\frac{k_{\mathrm{B}}T}{\eta\chi[\mathbf{k}]}\int\frac{d\mathbf{q}}{(2\pi)^2}\frac{\chi[\mathbf{q}]}{|\mathbf{k}-\mathbf{q}|^2+\nu|\mathbf{k}-\mathbf{q}|\coth(|\mathbf{k}-\mathbf{q}|h)}\frac{k^2q^2-(\mathbf{k}\cdot\mathbf{q})^2}{|\mathbf{k}-\mathbf{q}|^2}. \tag{5.26}$$

3.2. Effective diffusion coefficient

We now introduce an effective diffusion coefficient (due only to the hydrodynamic part) $D[\mathbf{k}]$ defined by

$$\Gamma^{(2)}[\mathbf{k}] = k^2 D[\mathbf{k}]. \tag{5.27}$$

In order to deal with dimensionless quantities, we rescale all the lengths by the SD hydrodynamic screening length $\nu^{-1} = \eta/2\eta_s$ such that $K = k/\nu$, $Q = q/\nu$, $X = \xi\nu$, and $H = h\nu$. Then $D[\mathbf{k}]$ can be rewritten as

$$D[K;X,H] = \frac{k_B T}{4\pi^2\eta}\left(1+K^2X^2\right)\int_0^\infty \mathrm{d}Q \int_0^{2\pi} \mathrm{d}\theta \frac{Q^3 \sin^2\theta}{\left(1+Q^2X^2\right)\left[G^2 + G^{3/2}\coth\left(\sqrt{G}H\right)\right]}, \tag{5.28}$$

with $G = K^2 + Q^2 - 2KQ\cos\theta$. Since this integral cannot be performed analytically, we evaluate it via a numerical method. We explore the dependencies of D on the variable K, and the parameters X and H. Notice that the dimensionless correlation length X also measures the proximity of the temperature with respect to the critical temperature T_c.

In Fig. 5.4, we plot the diffusion coefficient D (scaled by $k_B T/4\pi\eta$) as a function of dimensionless wave number K for a different solvent thickness H while the correlation length is fixed to $X = 1$ (i.e., fixed temperature). In the limit of $K \ll 1$, D is almost a constant. The calculated D starts to increase

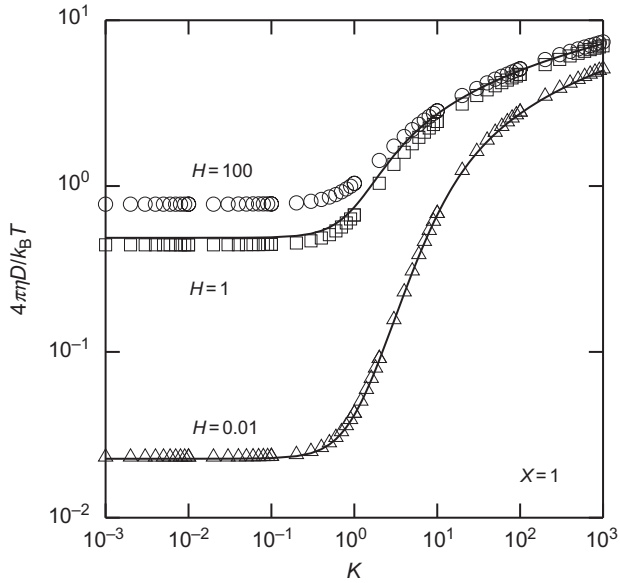

Figure 5.4 Scaled effective diffusion coefficient D as a function of K for $H = 0.01$, 1, and 100 when $X = 1$. The solid lines are from the analytical expression given in Eq. (5.29) obtained in the limit of small H.

around $K \approx 1$, and a logarithmic behavior (extracted via numerical fitting) is seen for $K \gg 1$. In this plot, we see that D becomes smaller for smaller values of H. Figure 5.5 shows the diffusion coefficient D as a function of wave number K for different X (i.e., different temperatures) while the solvent height is fixed to $H = 1$. Here D is nearly constant for $K \ll 1/X$ and follows an S-shaped curve with increasing K. Finally, a logarithmic dependence is observed for large K. We note that this logarithmic behavior for $K \gg 1/X$ is in contrast to that of 3D critical fluids given by the Kawasaki function which increases linearly with the wave number [40].

In Fig. 5.6, we explore the effect of the correlation length X on D for different values of H when $K = 10^{-3}$. The quantity X is a measure of an effective size of the correlated region formed transiently in the membrane due to thermal fluctuations. When $X \ll 1$, the diffusion coefficient D decreases only logarithmically, which is typical for a pure 2D system [22–24]. The proximity to the walls results in a loss of momentum from the membrane [29]. This leads to a rapid suppression of the velocity field within the membrane. Consequently, the values of D are smaller for smaller H. The flattening of the curves for $X \gg 1$ is due to the dominance of the X^2 terms in the numerator and denominator in Eq. (5.28). In Fig. 5.7,

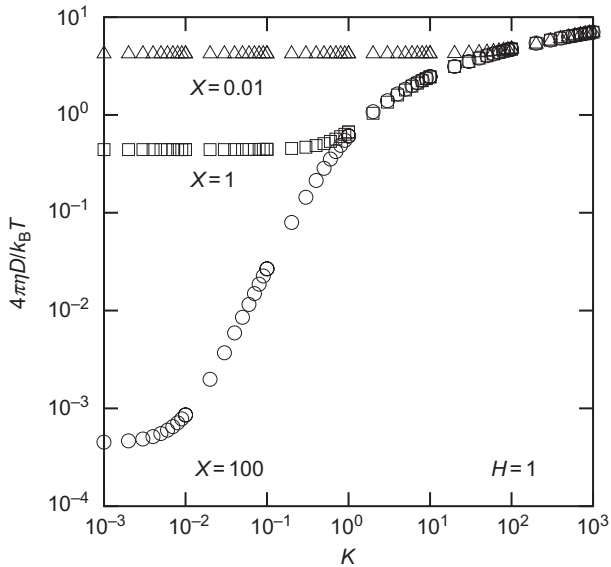

Figure 5.5 Scaled effective diffusion coefficient D as a function of K for $X = 0.01$, 1, and 100 when $H = 1$.

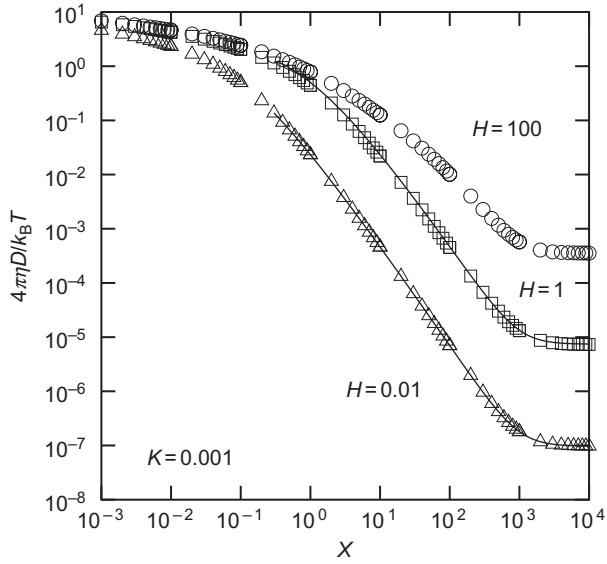

Figure 5.6 Scaled effective diffusion coefficient D as a function of X for $H=0.01$, 1, and 100 when $K=10^{-3}$. The solid lines are from the analytical expression given in Eq. (5.29) obtained in the limit of small H.

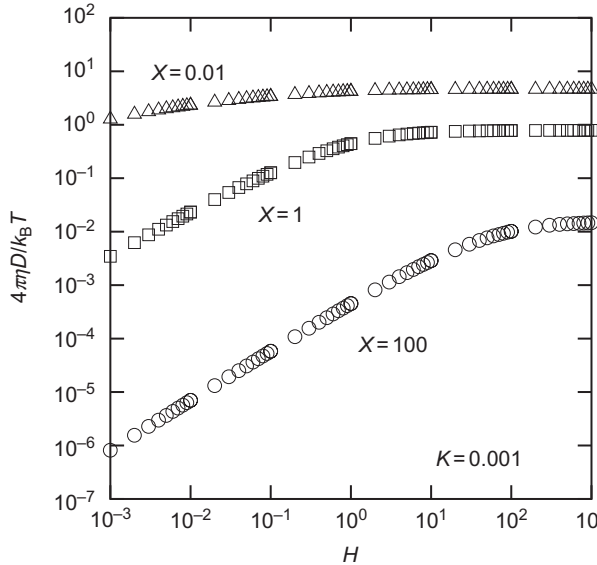

Figure 5.7 Scaled effective diffusion coefficient D as a function of H for $X=0.01$, 1, and 100 when $K=10^{-3}$.

we plot D as a function of H for different values of X when $K=10^{-3}$. Here the values of D are smaller for larger X, as it should be. In general, there is a monotonic increase of D followed by a saturation to a constant value for larger H. It is interesting to note that the crossover occurs when $H\approx X$ holds.

For confined membranes (small h), we showed in Section 2 that the general mobility tensor Eq. (5.9) reduces to $G^{\rm con}_{\alpha\beta}$ given by Eq. (5.12). In this case, one can obtain an analytical expression for the effective diffusion coefficient [32]. In terms of the dimensionless quantities K, X, and H, it is written as

$$\begin{aligned} D[K;X,H]=\frac{k_{\rm B}T}{4\pi\eta}\frac{1+K^2X^2}{2K^2X^2}\Bigg[&-\ln\left(\frac{X}{\sqrt{H}}\right)\\ &+\frac{H}{X^2}\left(1+K^2X^2\right)\ln\left(\frac{X}{\sqrt{H}(1+K^2X^2)}\right)\\ &+\frac{H\Omega}{2X^2}\ln\left(\frac{K_+^4+K_-^2+K_+^2\Omega}{\Omega-K_-^2-1}\right), \end{aligned} \tag{5.29}$$

where

$$\Omega=\sqrt{\left(K^2X^2+X^2/H-1\right)^2+4K^2X^2}, \tag{5.30}$$

and

$$K_\pm=\sqrt{K^2X^2\pm X^2/H}. \tag{5.31}$$

Equation (5.29) is plotted using solid lines in Fig. 5.4 for $H=0.01$ and 1 with $X=1$. For $H=0.01$, the analytical and numerical data coincide, giving credence to accuracy of the numerical solutions. It is seen that even for $H=1$, the agreement is still acceptable. For $H=100$, however, a significant deviation is observed (not shown), which is expected as this limit is beyond the valid range of Eq. (5.29).

The solid lines in Fig. 5.6 also represent the analytical result of Eq. (5.29). It is seen that the analytical and the numerical data points almost coincide for $H=0.01$ and 1. The agreement between the numerical result and the analytical expression is beyond the expected range of $H\ll 1$ and reaches up to $H\approx 1$, as pointed out by Stone and Ajdari [28]. Hence Eq. (5.29) is useful in analyzing the experimental data in many situations.

When the critical temperature T_c is approached from above, the correlation length diverges according to $\xi\approx|T-T_c|^{-\bar{\nu}}$, where $\bar{\nu}$ is the critical

exponent. When T_c is approached from below, on the other hand, the order parameter given by the difference in lipid compositions vanishes as $\delta\psi \approx (T_c - T)^{\bar{\beta}}$. From the experiments on model multicomponent vesicles, these critical exponents were found to have values close to $\bar{\beta} = 1/8$ and $\bar{\nu} = 1$, respectively [13]. Furthermore, the experiment on giant plasma membrane vesicles measured the critical exponent $\bar{\gamma} = 7/4$ which characterizes the critical behavior of the osmotic compressibility [15]. These static exponents seem to coincide with the exact results of the 2D Ising model [14]. The description presented in this section uses a mean-field approach, and therefore, the corresponding exponents are $\bar{\beta} = 1/2$, $\bar{\nu} = 1/2$, and $\bar{\gamma} = 1$, respectively. The discrepancies between these values are still under discussion.

3.3. Membrane as a 2D microemulsion

The role of surfactant molecules in 3D microemulsions is to reduce the surface tension at the interface between oil and water. In an analogy to 3D microemulsions, hybrid lipids (one chain unsaturated and the other saturated) act as lineactant molecules which stabilize finite-sized domains in 2D. In other words, hybrid lipids play a similar role to surfactant molecules at the interface between L_o and L_d domains. It should be also noticed that hybrid lipids form a major percentage of all naturally existing lipids [41]. Based on a simple model of hybrid lipids, Brewster *et al.* showed that finite-sized domains can be formed in equilibrium [34,35]. A subsequent model predicted that domains are even more stabilized in a system of saturated/hybrid/cholesterol lipid membranes [36,37]. Being motivated by this idea, we calculate the decay rate of concentration fluctuations when the free energy of the multicomponent membrane has the form of a 2D microemulsion.

The free-energy functional for a microemulsion includes a higher order derivative term and is expressed in terms of $\delta\psi$ as [16]

$$\mathcal{F}_{\mathrm{ME}}\{\delta\psi\} = \int \mathrm{d}\mathbf{r}\left[\frac{a}{2}(\delta\psi)^2 + \frac{c}{2}(\nabla\delta\psi)^2 + \frac{g}{2}\left(\nabla^2\delta\psi\right)^2\right], \tag{5.32}$$

with $a, g > 0$ and $c < 0$. The negative value of c creates 2D interfaces, while the term with positive g is a stabilizing term. This form of the free energy has been used previously to study coupled modulated bilayers [42,43]. As in the previous section, the decay rate of the correlation function can be split into two parts. First, the van Hove part now becomes

$$\Gamma^{(1)}_{\mathrm{ME}}[\mathbf{k}] = \Lambda k_{\mathrm{B}} T k^2 \chi^{-1}_{\mathrm{ME}}[\mathbf{k}], \tag{5.33}$$

where the static correlation function $\chi_{\mathrm{ME}}[\mathbf{k}]$ is [44]

$$\chi_{\mathrm{ME}}[\mathbf{k}] = \frac{k_{\mathrm{B}}T}{gk^4 + ck^2 + a}. \tag{5.34}$$

By defining

$$k_0^2 = -\frac{c}{2g}, \tag{5.35}$$

$$\sigma^4 = \frac{a}{g} - \left(\frac{c}{2g}\right)^2, \tag{5.36}$$

we can write the static correlation function as

$$\chi_{\mathrm{ME}}[\mathbf{k}] = \frac{k_{\mathrm{B}}T}{g\left[\left(k^2 - k_0^2\right)^2 + \sigma^4\right]}. \tag{5.37}$$

On plotting χ_{ME} as a function of k, a peak appears at $k = k_0$ followed by a $1/k^4$ decay. The width of the peak is given by σ. A lamellar phase appears when $\sigma = 0$. Notice that $c = 0$ is called the Lifshitz point at which the peak occurs for $k = 0$. Using the form of Eq. (5.37), we can write Eq. (5.33) as

$$\Gamma_{\mathrm{ME}}^{(1)}[\mathbf{k}] = \Lambda g k^2 \left[\left(k^2 - k_0^2\right)^2 + \sigma^4\right]. \tag{5.38}$$

Similar to the previous section, we next write the hydrodynamic part of the decay rate in terms of the effective diffusion coefficient $D_{\mathrm{ME}}[\mathbf{k}]$ as

$$\Gamma_{\mathrm{ME}}^{(2)}[\mathbf{k}] = k^2 D_{\mathrm{ME}}[\mathbf{k}]. \tag{5.39}$$

Using the mobility tensor given by Eq. (5.9), we can write D_{ME} as

$$D_{\mathrm{ME}}[K; K_0, \Sigma, H] = \frac{k_{\mathrm{B}}T}{4\pi^2\eta}\left[\left(K^2 - K_0^2\right)^2 + \Sigma^4\right] \times \int_0^\infty \mathrm{d}Q \int_0^{2\pi} \mathrm{d}\theta \frac{Q^3 \sin^2\theta}{\left[\left(Q^2 - K_0^2\right)^2 + \Sigma^4\right]\left[G^2 + G^{3/2}\coth\left(\sqrt{G}H\right)\right]}, \tag{5.40}$$

where $K = q/v, K_0 = q_0/v, Q = q/v, \Sigma = \sigma/v, H = hv$, and $G = K^2 + Q^2 - 2KQ\cos\theta$.

In Fig. 5.8, we plot D_{ME} as a function of K for different values of H when $K_0 = \Sigma = 1$ are fixed. When $K \ll 1$, D shows a constant value. We also observe the 2D characteristic of logarithmic behavior of D for $K \gg 1$.

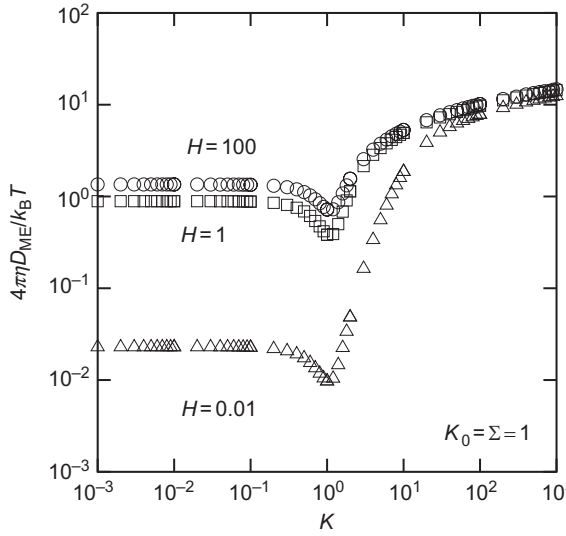

Figure 5.8 Scaled effective diffusion coefficient D_{ME} as a function of K for $H=0.01$, 1, and 100 when $K_0=\Sigma=1$.

For $K\ll 1$, the effect of the outer environment is felt with the suppression of the diffusion coefficient with smaller H. The curves almost overlap when $K\gg 1$, indicating the negligible effect of the outer environment at large wave numbers. An interesting feature of D_{ME} is the dip occurring at $K\approx K_0$ which does not exist for binary critical fluids. This can be attributed to the peak at $k=k_0$ in $\chi_{ME}[\mathbf{k}]$ [39,44]. We also note that, for 3D microemulsions, the effective diffusion coefficient varies linearly with the wave number when it is large enough [39], which is in contrast to the present 2D microemulsions.

3.4. Related works

In addition to the present theory, there are some other theoretical works on concentration fluctuations in multicomponent membranes. Using renormalization group techniques, Tserkovnyak and Nelson calculated protein diffusion in a multicomponent membrane close to a rigid substrate [45]. They pointed out that, in the vicinity of the critical point, the effective protein diffusion coefficient acquires a power-law behavior. Inaura and Fujitani first discussed concentration fluctuations in free membranes surrounded by a 3D solvent [46]. They used the mobility tensor $G^{free}_{\alpha\beta}$ in Eq. (5.10) and calculated numerically the effective diffusion coefficient.

Hence their calculation corresponds to the special case of the present theory. Haataja also discussed critical dynamics in multicomponent lipid membranes and showed that the effective diffusion coefficient exhibits a crossover from a logarithmic behavior to an algebraic dependence (inversely proportional to the correlation length) for larger length scales [47]. However, since an approximate empirical relation for the diffusion coefficient of a moving object was employed [48], his theory should be distinguished from ours. Concentration fluctuations in membranes in the absence of hydrodynamic effect was recently discussed by McConnell [49].

4. PHASE SEPARATION DYNAMICS

4.1. Domain coarsening

Although biomembranes can be regarded as 2D viscous fluids, they are not isolated pure 2D systems since lipids are coupled to the adjacent solvent. Hence it is of great interest to investigate the phase separation dynamics in such a quasi-2D liquid membrane in the presence of hydrodynamic interaction. (We use the word "quasi-2D" whenever the membrane is coupled to the bulk fluid.) To address this problem, we consider a 2D binary viscous membrane in contact with a bulk solvent. We employ a simple model in which the membrane is confined to a plane with the bulk fluid particles added above and below. In our model using DPD simulation technique, the exchange of momentum between the membrane and the bulk solvent is naturally taken into account. We particularly focus on the effect of bulk solvent on the quasi-2D phase separation.

Before explaining our simulation, let us briefly review here the general knowledge about phase separation of binary fluids following a quench [50]. The dynamic scaling hypothesis assumes that there exists a scaling regime characterized by the average domain size R that grows with time t as $R \sim t^{\alpha}$ with an universal exponent α. For 3D off-critical binary fluids, there is an initial growth by the BC process [51], followed by the Lifshitz–Slyozov (LS) evaporation–condensation process [52]; both mechanisms show a growth exponent $\alpha = 1/3$. For critical mixtures, there is an intermediate $\alpha = 1$ regime owing to hydrodynamic flow effect [53]. This is followed by a late time inertial regime of $\alpha = 2/3$ [54]. The scenario is slightly different for pure 2D systems [55]. For an off-critical mixture, it was predicted that after the initial formation of domains, they grow by the BC mechanism with a different exponent $\alpha = 1/2$ (as will be explained later), followed by a crossover to the LS mechanism which gives $\alpha = 1/3$ even in 2D. For critical mixtures, on the other hand, the initial quench produces an interconnected

structure which coarsens and then breaks up due to the interface diffusion with an exponent $\alpha = 1/2$. After the breakup processes, coarsening takes place through BC that is again characterized by the $\alpha = 1/2$ scaling [51]. These predictions were confirmed by molecular dynamics simulations in 2D [56]. The exponent $\alpha = 1/2$ was also observed in 2D lattice-Boltzmann simulations in the presence of thermal noise for a critical mixture [57].

4.2. Model and simulation technique

We use a structureless model of the 2D fluid membrane within the DPD framework [58,59]. As shown in Fig. 5.9, the 2D membrane is represented by a single layer of particles confined to a plane. In order to study phase separation, we introduce two species of particles, A and B. The bulk fluid which we call as "solvent" (S) is also represented by single particles of same size as that of the membrane particles. All particles have the same mass m.

In DPD, the interaction between any two particles, within a range r_0, is linearly repulsive. The pairwise interaction leads to full momentum conservation, which in turn brings out the correct fluid hydrodynamics. The force on a particle i is given by

$$m\frac{d\mathbf{v}_i}{dt} = \sum_{j\neq i}\left[\mathbf{F}_{ij}^{C}(\mathbf{r}_{ij}) + \mathbf{F}_{ij}^{D}(\mathbf{r}_{ij},\mathbf{v}_{ij}) + \mathbf{F}_{ij}^{R}(\mathbf{r}_{ij})\right], \tag{5.41}$$

where $\mathbf{r}_{ij} = \mathbf{r}_i - \mathbf{r}_j$ and $\mathbf{v}_{ij} = \mathbf{v}_i - \mathbf{v}_j$. Of the three types of forces acting on the particles, the conservative force on particle i due to j is $\mathbf{F}_{ij}^{C} = a_{ij}\omega(r_{ij})\hat{\mathbf{r}}_{ij}$,

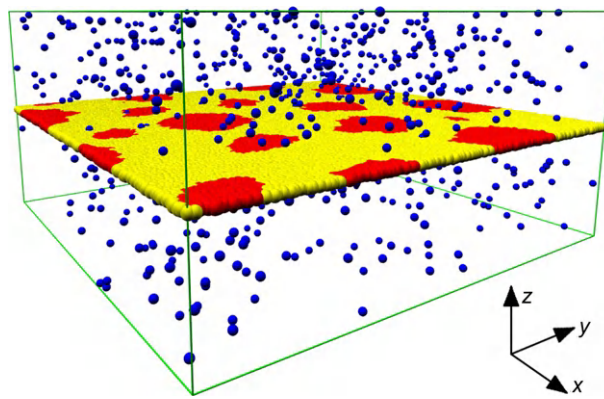

Figure 5.9 Image of the fluid membrane with the bulk fluid called solvent. The yellow (A) and red (B) particles represent the two components constituting the membrane, while blue ones (S) represent the solvent. For clarity, only a fraction of the solvent particles are shown.

where a_{ij} is an interaction strength and $\hat{\mathbf{r}}_{ij} = \mathbf{r}_{ij}/r_{ij}$ with $r_{ij} = |\mathbf{r}_{ij}|$. The second type of force is the dissipative force $\mathbf{F}_{ij}^{\mathrm{D}} = -\Gamma_{ij}\omega^2(r_{ij})(\hat{\mathbf{r}}_{ij}\cdot\mathbf{v}_{ij})\hat{\mathbf{r}}_{ij}$, where Γ_{ij} is the dissipative strength for the pair (i, j). The last is the random force $\mathbf{F}_{ij}^{\mathrm{R}} = \sigma_{ij}(\Delta t)^{-1/2}\omega(r_{ij})\zeta_{ij}\hat{\mathbf{r}}_{ij}$, where σ_{ij} is the amplitude of the random noise for the pair (i, j), and ζ_{ij} is a random variable with zero mean and unit variance which is uncorrelated for different pairs of particles and different time steps. The dissipative and random forces act as a thermostat, provided the fluctuation–dissipation theorem $\sigma_{ij}^2 = 2\Gamma_{ij}k_{\mathrm{B}}T$ is satisfied. The weight factor is chosen as $\omega(r_{ij}) = 1 - r_{ij}/r_0$ up to the cutoff radius r_0 and zero thereafter. The particle trajectories are obtained by solving Eq. (5.41) using the velocity-Verlet integrator. In the simulation, r_0 and m set the scales for length and mass, respectively, while $k_{\mathrm{B}}T$ sets the energy scale. The time is measured in units of $\tau = (mr_0^2/k_{\mathrm{B}}T)^{1/2}$. The numerical value of the amplitude of the random force is assumed to be the same for all pairs such that $\sigma_{ij} = 3.0$ $[(k_{\mathrm{B}}T)^3 m/r_0^2]^{1/4}$, and the fluid density is set as $\rho = 3.0$. We set $k_{\mathrm{B}}T = 1$ and the integration time step is chosen to be $\Delta t = 0.01\tau$.

The membrane is constructed by placing particles in the xy-plane in the middle of the simulation box (see Fig. 5.9). Owing to the structureless representation of the constituent particles, we apply an external potential so as to maintain the membrane integrity. This is done by fixing the z-coordinates of all the membrane particles. The work involves the systematic variation of the height of the simulation box starting from the pure 2D case. In the absence of solvent, we work with a 2D-box of dimensions $L_x \times L_y = 80 \times 80$ with 19,200 particles constituting the membrane. For the quasi-2D studies, we add solvent particles S above and below the membrane and increase the height of the box as $L_z = 5, 20$ and 40. For all the cases, there are 19,200 membrane particles. The largest box size ($L_z = 40$) has 748,800 solvent particles. The box with height $L_z = 40$ is found to be sufficiently large enough to prevent the finite-size effect which affects the membrane–solvent interaction. The system is then subject to periodic boundary conditions in all the three directions. For phase separation simulations, we introduce two species of membrane particles A and B. The interaction parameter between various particles are given by $a_{\mathrm{AA}} = a_{\mathrm{BB}} = a_{\mathrm{SS}} = a_{\mathrm{AS}} = a_{\mathrm{BS}} = 25$ and $a_{\mathrm{AB}} = 50$. In order to do a quench, the membrane is first equilibrated with a single component, following which a fraction of the particles are instantaneously changed to the B type.

4.3. Domain growth dynamics

First, we describe the results of the phase separation dynamics. The snapshots for A:B composition set to 70:30 (off-critical mixture) are shown in Fig. 5.10 for both pure 2D case (A) and quasi-2D case with $L_z = 40$ (B). Qualitatively,

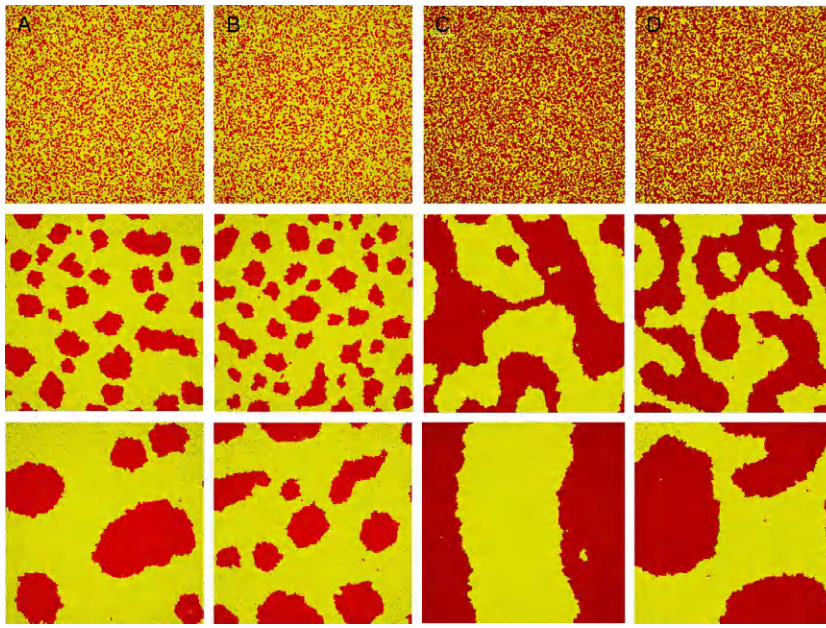

Figure 5.10 The snapshots of a 70:30 (off-critical) mixture undergoing phase separation at $t = 0$, 150, and 1000 (top to bottom) for a pure 2D (A) and quasi-2D system with $L_z = 40$ (B). The same sequences of a 50:50 (critical) mixture for a pure 2D (C) and quasi-2D system (D).

it is seen that the domains for the quasi-2D case are smaller in size when compared at the same time step. We also monitor the average domain size $R(t)$ which can be obtained from the total interface length $L(t)$ between the two components. This is because $R(t)$ and $L(t)$ are related by $L(t) = 2\pi N(t)$ $R(t)$, where $N(t)$ is the number of domains. The area occupied by the B-component is given by $\mathcal{A} = \pi N(t) R^2(t)$ which is a conserved quantity. Then we have

$$R(t) = 2\mathcal{A}/L(t). \tag{5.42}$$

When the domain size grows as $R \sim t^{\alpha}$, one has $L \sim t^{-\alpha}$ and $N \sim t^{-2\alpha}$. The domain size $R(t)$ for 70:30 mixture is shown in Fig. 5.11. In this plot, an average over 10 independent trials has been taken. It can be seen that the pure 2D case has a growth exponent $\alpha = 1/2$. Upon the addition of solvent, we observe that the exponent shifts to a lower value of $\alpha = 1/3$. This exponent is reminiscent of the phase separation dynamics of an off-critical mixture in 3D. By systematically increasing the amount of solvent in the system by changing the height L_z, we can see a clear deviation from the pure 2D

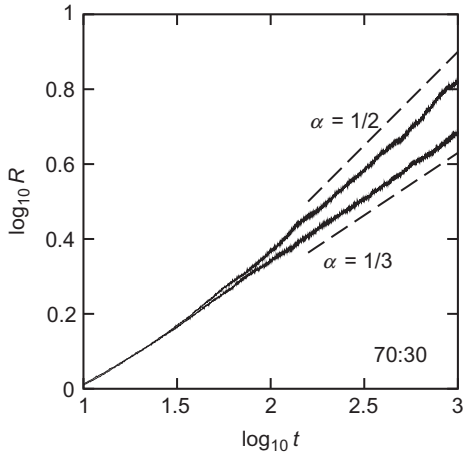

Figure 5.11 The average domain size R as a function of time t for a 70:30 off-critical mixture. The upper curve is the pure 2D case showing an $\alpha = 1/2$ scaling, and the lower curve is the quasi-2D case when $L_z = 40$ showing a distinct $\alpha = 1/3$ scaling.

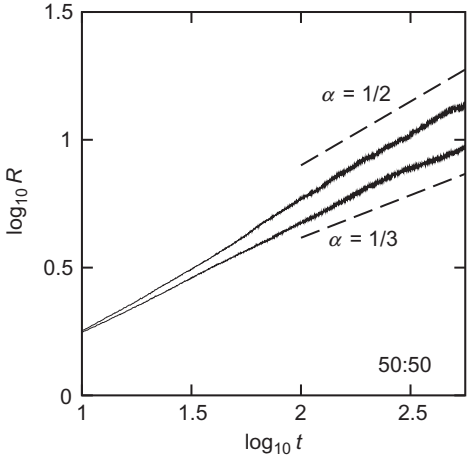

Figure 5.12 The average domain size R as a function of time t for a 50:50 critical mixture. The upper curve is the pure 2D case showing an $\alpha = 1/2$ scaling, and the lower curve is the quasi-2D case when $L_z = 40$ showing a distinct $\alpha = 1/3$ scaling.

behavior (not shown). There is no further change if L_z is increased beyond 40. A larger system size $L_x \times L_y = 200 \times 200$ also produced the same scaling for the pure 2D case, which demonstrates that finite-size effects are small.

In Fig. 5.12, we show the result for a component ratio of 50:50 (critical mixture), whereas the corresponding patterns are given in Fig. 5.10C and D for 2D and quasi-2D cases, respectively. In this case, the growth exponent

for the pure 2D case is less obvious owing to rapid coarsening of the domains. However, by simulating a bigger system 200×200 with the same areal density, an $\alpha = 1/2$ exponent is indeed obtained. Similar to the off-critical case, the growth of the domains is slowed down by the addition of solvent and the exponent is reduced to $\alpha = 1/3$. These results indicate that solvent is responsible for slowing down the growth dynamics.

The observed exponent $\alpha = 1/2$ in pure 2D systems can be explained in terms of the BC mechanism [55]. From dimensional analysis, the 2D diffusion coefficient of the domain is given by $D_2 \sim k_B T/\eta$, where η is the membrane 2D viscosity. Using the relation

$$R^2 \sim D_2 t \sim \left(\frac{k_B T}{\eta}\right) t, \tag{5.43}$$

we find $R \sim t^{1/2}$. For 3D systems, on the other hand, the diffusion coefficient of the droplet is inversely proportional to its size, $D_3 \sim 1/R$, a well-known Stokes–Einstein relation. Hence the BC mechanism in 3D gives rise to an exponent $\alpha = 1/3$. (In general, the exponent is $\alpha = 1/d$, where d is the space dimension.) The change in the exponent from $\alpha = 1/2$ to $1/3$ due to the addition of solvent implies the crossover from 2D to 3D behaviors of the phase separation dynamics even though the lateral coarsening takes place only within the 2D geometry. Notice that the LS mechanism shows an exponent of $\alpha = 1/3$ in both 2D and 3D. We thus conclude that our simulations are still in the early time of the coarsening dynamics.

4.4. Correlated diffusion

In order to justify our argument, it is necessary to examine the size dependence of the domain diffusion coefficient in quasi-2D systems. This can be calculated by tracking the mean-squared displacement of domains of various radii. The equivalent information can be more efficiently obtained by calculating the two-particle longitudinal coupling diffusion coefficient in a single component membrane rather than in a binary system.

Consider a pair of particles separated by a 2D vector $\mathbf{r}$, undergoing diffusion in the fluid membrane. The two-particle mean-squared displacement is given by [25,26]

$$\left\langle \Delta r_\alpha^k \Delta r_\beta^l \right\rangle = 2 D_{\alpha\beta}^{kl}(\mathbf{r}) t, \tag{5.44}$$

where Δr_α^k is the displacement of the particle $k(=1,2)$ along the axis $\alpha(=x, y)$, and $D_{\alpha\beta}^{kl}$ is the diffusion tensor giving self-diffusion when $k = l$ and the

coupling between them when $k \neq l$. The x-axis is defined along the line connecting a pair of particles 1 and 2, that is, $\mathbf{r} = r\hat{x}$. Hence, we have $D^{12}_{xy} = 0$ by symmetry. The longitudinal coupling diffusion coefficient, $D_{\mathrm{L}}(r) = D^{12}_{xx}(r\hat{x})$, gives the coupled diffusion along the line of centers of the particles.

We first describe the analytical expression of $D_{\mathrm{L}}(r)$ for the free membrane case, which can be essentially obtained from Eq. (5.11) (see Ref. [17] for details). Using the Einstein relation for over-damped dynamics, we obtain

$$D_{\mathrm{L}}^{\mathrm{free}}(r) = \frac{k_{\mathrm{B}}T}{4\pi\eta}\left[-\frac{2}{\nu^2 r^2} + \frac{\pi \mathbf{H}_1(\nu r)}{\nu r} - \frac{\pi Y_1(\nu r)}{\nu r}\right]. \tag{5.45}$$

At short distances $r \ll \nu^{-1}$, the asymptotic form of the above expression becomes

$$D_{\mathrm{L}}^{\mathrm{free}}(r) \approx \frac{k_{\mathrm{B}}T}{4\pi\eta}\left[\ln\left(\frac{2}{\nu r}\right) - \gamma + \frac{1}{2}\right], \tag{5.46}$$

where $\gamma = 0.5772\ldots$ is Euler's constant. At large inter-particle separations $r \gg \nu^{-1}$, on the other hand, Eq. (5.45) reduces to

$$D_{\mathrm{L}}^{\mathrm{free}}(r) \approx \frac{k_{\mathrm{B}}T}{2\pi\eta\nu r} = \frac{k_{\mathrm{B}}T}{4\pi\eta_{\mathrm{s}} r}, \tag{5.47}$$

showing the asymptotic $1/r$ decay which reflects the 3D nature of this limit. Notice that Eq. (5.47) depends only on the solvent viscosity η_{s} but not on the membrane viscosity η any more.

In Fig. 5.13, we plot the measured longitudinal coupling diffusion coefficient D_{L} as a function of 2D distance r. In these simulations, we have worked with only single component membranes with the same system sizes and number of particles as those used for the phase separation simulations. We have also taken average over 20 independent trials. In the pure 2D case without any solvent, D_{L} shows a logarithmic dependence on r. This is consistent with Eq. (5.46) obtained when the coupling between the membrane and solvent is very weak so that the membrane can be regarded almost as a pure 2D system. Using Eq. (5.46) as an approximate expression, we get from the fitting as $k_{\mathrm{B}}T/4\pi\eta \approx 0.89 \times 10^{-2}$ and $\nu^{-1} \approx 20$. In an ideal case, the SD screening length should diverge due to the absence of solvent. The obtained finite value for ν^{-1} is roughly set by the half of the system size in the simulation.

When we add solvent ($L_z = 40$), the D_{L} is decreased and no longer behaves logarithmically. In this case, we use the full expression Eq. (5.45) for the fitting and obtained $k_{\mathrm{B}}T/4\pi\eta \approx 1.35 \times 10^{-2}$ and $\nu^{-1} \approx 1$. In the above

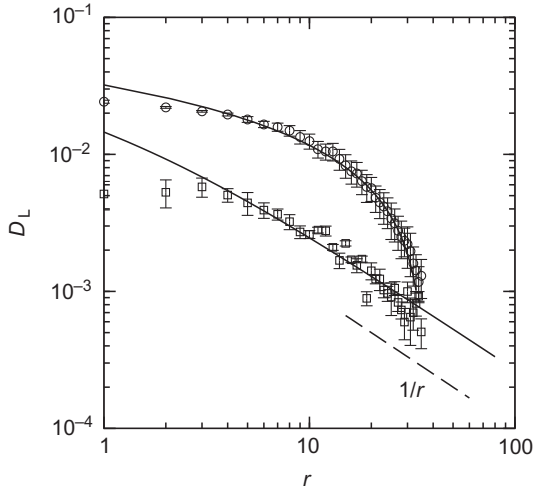

Figure 5.13 Longitudinal coupling diffusion D_L as a function of particle separation r. The upper circles are data for the pure 2D case. The lower squares correspond to the case with solvent when $L_z = 40$. The upper solid line is the fit by Eq. (5.46), and the lower solid line is the fit by Eq. (5.45). The dashed line shows the $1/r$ dependence.

two fits, we have neglected the first two points as they lie outside the range of validity, $r \gg 1$, of Eq. (5.45). Since $\nu^{-1} \approx 1$ when the solvent is present, the data shown in Fig. 5.13 are in the crossover region, $r \gtrsim \nu^{-1}$, showing an approach toward the asymptotic $1/r$ dependence as in Eq. (5.47). Hence we conclude that the solvent brings in the 3D hydrodynamic property to the diffusion in membranes. This is the reason for the exponent $\alpha = 1/3$ in the phase separation dynamics and justifies that it is mainly driven by BC mechanism.

In our simulations, the membrane and the solvent have very similar viscosities. This sets the SD length scale to be of the order of unity (in units of particle size), which is consistent with the value $\nu^{-1} \approx 1$ obtained from the fitting. As explained above, the fit also provides the 2D membrane viscosity as $\eta \approx 6$, and hence we obtain as $\eta_s \approx 3$. In real biomembranes sandwiched by water, the value of the SD length is much larger than the lipid size and is in the order of submicron scale [23]. Hence the 3D nature of hydrodynamics should be observed for large enough domains [60].

For confined membranes, on the other hand, the appropriate mobility tensor is $G^{\rm con}_{\alpha\beta}$ given by Eq. (5.12). In this case, the longitudinal coupling diffusion coefficient can be obtained as [17]

$$D_{\rm L}^{\rm con}(r) = \frac{k_{\rm B}T}{2\pi\eta}\left[\frac{1}{\kappa^2 r^2} - \frac{K_1(\kappa r)}{\kappa r}\right], \tag{5.48}$$

where $K_1(z)$ is modified Bessel function of the second kind (see also Eq. 13). At short distances $r \ll \kappa^{-1}$, we have

$$D_{\mathrm{L}}^{\mathrm{con}}(r) \approx \frac{k_{\mathrm{B}}T}{4\pi\eta}\left[\ln\left(\frac{2}{\kappa r}\right) - \gamma + \frac{1}{2}\right], \tag{5.49}$$

which is almost identical to Eq. (5.46) except ν is replaced now by κ. At long distances $r \gg \kappa^{-1}$, on the other hand, we get

$$D_{\mathrm{L}}^{\mathrm{con}}(r) \approx \frac{k_{\mathrm{B}}T}{2\pi\eta\kappa^2 r^2} = \frac{k_{\mathrm{B}}Th}{4\pi\eta_{\mathrm{s}} r^2}, \tag{5.50}$$

which exhibits a $1/r^2$ dependence. This is in contrast to Eq. (5.47). Repeating the similar scaling argument, we predict that, in the presence of walls, the domain growth exponent should be $\alpha = 1/4$ within the BC mechanism. A similar simulation with two confining hard walls is required as a next step. In biological systems, the above situation with solid walls can be relevant because the cell membranes are strongly anchored to the underlying cytoskeleton or are tightly adhered to other cells.

4.5. Related works

We mention here several related works on the phase separation dynamics below the transition temperature. Veatch and Keller observed the kinetics of domain growth on ternary vesicles as presented in Fig. 5.14 [9]. For a

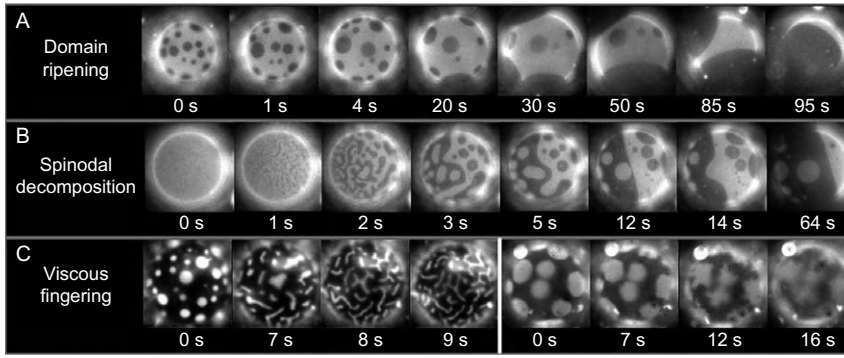

Figure 5.14 Phase separation dynamics on ternary giant vesicles. (A) Brownian coagulation observed for 1:1 DOPC/DPPC + 25% Chol., (B) spinodal decomposition observed for 1:1 DOPC/DPPC + 35% Chol., (C) viscous fingering observed for 1:9 DOPC/DPPC + 25% Chol. (left series) and 1:1 DOPC/DMPC + 25% Chol. (right series). *Adapted from Ref. [9].*

vesicle with an off-critical composition, dark circular domains grow by colliding and coalescing with each other rather than through the LS evaporation–condensation process (Fig. 5.14A). When the composition is nearly critical, spinodal decomposition takes place when the temperature is decreased through transition point (Fig. 5.14B). For a highly asymmetric composition as in Fig. 5.14C, striped domains are observed when the temperature is raised; possibly viscous fingering.

The domain growth exponent α was first measured by Saeki *et al.* for ternary vesicles composed of DOPC, DPPC, and cholesterol [61]. They indeed observed a power-law behavior and reported a rather small value $\alpha = 0.15$. The reason for this slow dynamics was partially attributed to the curvature of the domain portion. Subsequently, Yanagisawa and some of the present authors found that the domain coarsening processes are classified into two types, that is, normal coarsening and trapped coarsening [62]. In the former case, the domains having flat circular shape grow through BC process, although the growth exponent was found to be $\alpha = 2/3$. For the trapped coarsening, on the other hand, the domain growth is suppressed at a certain domain size because the repulsive inter-domain interactions obstruct the coalescence of domains. A two-color imaging technique of the trapped domains revealed that this repulsive interactions are induced by the budding of domains. By observing the motion of domains, they also found that each domain is attracted toward the largest one following the flow around it. This is a strong indication of the hydrodynamic interactions acting between the domains.

As for computer simulations, Laradji and Kumar performed a DPD study on phase separation dynamics in both two-component vesicles and open membranes using a coarse-grained model for the membrane lipids [63–65]. In their model, the self-assembly of a bilayer in the presence of solvent is naturally taken into account. For off-critical case, they obtained an exponent $\alpha \approx 0.3$ which is in good agreement with our simulation result, $\alpha \approx 1/3$. Similar to our observation, they also reported that the BC process takes place rather than the LS evaporation–condensation process. However, when the excess area of a vesicle is large enough, domains are no more flat and reshape into caps. In such a case, Eq. (5.42) is not valid and it is more convenient to measure the interface length $L(t)$. According to their simulation, it scales as $L(t) \sim t^{-0.4}$, indicating that the interfacial length decreases faster as compared to the case of small excess area. For membranes with critical composition, the growth exponent was found to be $\alpha \approx 0.5$ for both vesicles and open membranes. This value is in contrast to our result $\alpha \approx 1/3$ as shown in Fig. 5.12. In Fig. 5.15, we

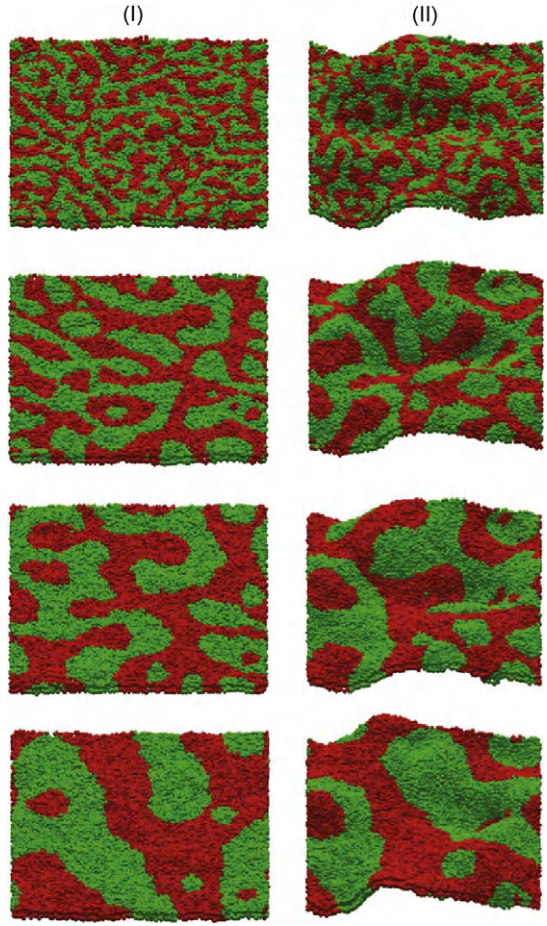

Figure 5.15 The snapshots for a 50:50 critical mixture undergoing phase separation for open membranes with different projected areas (I and II). Adapted from Ref. [64].

present a sequence of spinodal decomposition for open membranes obtained from their simulation. One of the differences between their simulation and ours is that the membrane is not allowed to exhibit out-of-plane fluctuations in our case. In their subsequent work, the effect of asymmetry in the bilayer lipid composition was studied [66]. Notice that flip-flop events are extremely rare in their simulation. This asymmetry sets a spontaneous curvature for domains which are capped. Interestingly, they found that the coupling between the spontaneous curvature and composition effectively leads to micro-phase separation. The observed scaling behavior was $L(t) \sim t^{-0.13}$, indicative of a

logarithmic growth. Obviously, such a bilayer nature of fluid membranes is not taken into account in our simulation.

Camley *et al.* [67,68] and Fan *et al.* [69] performed numerical simulations of 2D version of model H using the mobility tensor of Eq. (5.10) for free membranes. The basic formulation of this model is given by that described in Section 3.1 except that the free-energy functional in Eq. (5.14) is replaced with

$$\mathcal{F}\{\psi\} = \int d\mathbf{r}\left[\frac{a}{2}\psi^2 + \frac{1}{4}\psi^4 + \frac{c}{2}(\nabla\psi)^2\right], \tag{5.51}$$

where $a<0$ is now negative in order to study the domain growth below the transition temperature. In the dynamical equations, Camley *et al.* included Gaussian white thermal noise terms which are distributed with variances set by the fluctuation–dissipation theorem [67,68]. By using reasonable parameter values, they were almost successful in reproducing the experimentally observed pattern evolution given in Fig. 5.14B. For the domain growth law, it was pointed out that the scaling behavior $R\sim t^{\alpha}$ would hold only when $R\ll v^{-1}$ or $R\gg v^{-1}$ because it requires the fact that R is the only relevant length scale.

For off-critical mixtures, there are at least two coarsening mechanism in this model: BC process and LS evaporation–condensation process, as mentioned before. The LS mechanism is essentially driven by the line tension λ between coexisting phases, and the corresponding growth law is given by [50]

$$R\sim(\Lambda\lambda t)^{1/3}, \tag{5.52}$$

where Λ is the kinetic coefficient given in Eq. (5.15). Notice that this exponent $\alpha=1/3$ does not depend on the dimensionality of the system. (In 3D, for example, the line tension λ is replaced with a surface tension.) On the other hand, the BC mechanism leads to $\alpha=1/2$ for $R\ll v^{-1}$ and $\alpha=1/3$ for $R\gg v^{-1}$, as we have discussed in detail. All these different scaling regimes have been confirmed by their numerical simulation [68], in agreement with our DPD simulation.

For critical mixtures, however, the results are rather complex. Figure 5.16 shows the time evolution of the phase-separated patterns for a mixture of critical composition [69]. Comparing Fig. 5.16E and F, for example, we notice that the morphologies and sizes of the elongated domains have changed considerably, whereas more isotropic ones remain almost the same. As a result, isolated circular domains coarsen slower than elongated

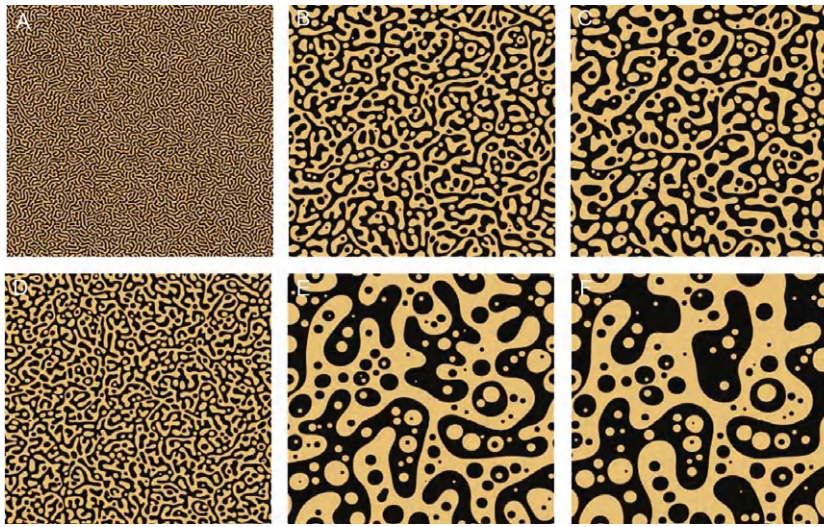

Figure 5.16 Time sequences of concentration maps during spinodal decomposition for different combinations of membrane and solvent viscosities (A–C and D–F). Time increases from left to right. Adapted from Ref. [69].

ones. From this observation together with quantitative analysis, they concluded that dynamical scaling breaks down since a single length scale cannot represent the domain distribution for different times [68,69]. Such a violation of the scaling behavior was reported before for pure 2D binary fluids [70,71]. Nevertheless, Camley *et al.* also found a region of apparent scaling where $\alpha = 1/2$ holds [68]. Although this may not be a universal feature, the power-law behavior seems to appear due to the competition between thermal and hydrodynamic effects. Furthermore, even a value close to $\alpha = 1/3$ was observed when the kinetic coefficient Λ is large [68]. This is what they call the "Cahn-Hilliard" regime in which bulk diffusion described by Λ is dominant. As a whole, the domain coarsening in critical mixtures seems to be far from universal and may dependent on the membrane viscosity.

In some other models, membranes undergoing simultaneously a phase separation and permanent exchange of lipids with the surrounding medium were considered [72,73]. For example, Foret proposed the following dynamical equation in the absence of flow [74]

$$\frac{\partial \psi}{\partial t} = \Lambda \nabla^2 \frac{\delta \mathcal{F}}{\delta \psi} - \gamma \left(\psi - \bar{\psi} \right), \tag{5.53}$$

where γ is the typical exchange rate, $\bar{\psi}$ is the average value of ψ, and $\mathcal{F}$ is given by Eq. (5.51). This equation should be contrasted with Eq. (5.15). It is interesting to note that the above equation also describes the dynamics of block copolymer systems which undergo micro-phase separation [75]. It is well known for block copolymers that the domain growth will eventually stop, and the domain size reaches a stationary value. Hence Eq. (5.53) gives rise to finite-sized raft domains in equilibrium. We point out here that 2D microemulsion discussed in Section 3.3 also exhibits a micro-phase separation below the transition temperature. Gómez *et al.* proposed a similar model in which only cholesterol is recycled [76,77]. As a generalization of these models, Fan *et al.* discussed the influence of nonequilibrium lipid transport, membrane compartmentalization, and membrane proteins on the phase separation dynamics [78–80]. Recently, micro-phase separation in nonequilibrium membrane was discussed in Ref. [81]. It should be noted, however, that the hydrodynamic effect is not taken into account in these models.

5. CONCLUSION AND OUTLOOK

In this chapter, we have discussed the dynamics of heterogeneity in multicomponent fluid membranes particularly focusing on hydrodynamic effects. For membranes above the transition temperature, we have investigated the kinetics of critical concentration fluctuations in two-component mixtures. Based on the time-dependent Ginzburg–Landau approach with full hydrodynamics, the wave number dependence of the effective diffusion coefficient was calculated as a function of the temperature and/or the thickness of the bulk fluid. For membranes below the transition temperature, we have discussed the effects of an embedding bulk solvent on the phase separation dynamics using DPD simulations. We have shown that the presence of a bulk fluid alters the domain growth exponent from that of 2D to 3D, indicating the significant role played by the membrane–solvent coupling. We further demonstrated that quasi-2D phase separation proceeds by the BC mechanism which reflects the 3D nature of the bulk solvent.

Even though the models presented in this chapter capture the essential physics, they are simplistic in several respects. The bending stiffness of typical membranes is of the order of $10k_BT$ which may be not always large enough to neglect the out-of-plane displacements of the membrane. The dynamics

of out-of-plane fluctuations of a homogeneous membrane was previously studied by Levine and MacKintosh [82]. It is worthwhile to comment that the presence of a substrate or the second membrane would suppress out-of-plane membrane fluctuations [83,84]. In our treatment, we have also neglected the effects of membrane curvature which can be significant when the radius of curvature becomes close to the hydrodynamic screening length. Henle *et al.* considered the diffusion of a point object on a spherically closed membrane [85,86]. The extension of this work to finite-sized objects is an interesting but difficult proposition.

In some theories, viscoelasticity of an infinitely large flat membrane has been considered [87,88]. Although it turned out that membranes are purely viscous in the latest report [89], their experimental technique using particle tracking microrheology provides us with a new clue to investigate the dynamical responses of lipid bilayers coupled to the surrounding environments. Recently, viscoelasticity of phospholipid Langmuir monolayers in a liquid-condensed phase was measured using active microrheology technique [90]. From our point of view, however, the viscoelasticity of the surrounding media is more important for large-scale dynamics in membranes. This is indeed the case according to the recent work by Granek who calculated the frequency-dependent transverse fluctuations of a membrane surrounded by viscoelastic media [91]. Currently, we are investigating the lateral dynamics in a purely viscous lipid membrane surrounded by viscoelastic media whose viscosity is a frequency-dependent one $\eta_s[\omega]$ [92]. For example, the frequency-dependent membrane mobility tensor is obtained as

$$G_{\alpha\beta}[\mathbf{k},\omega] = \frac{1}{\eta k^2 + 2\eta_s[\omega]k' \coth(k'h) + i\omega\rho}\left(\delta_{\alpha\beta} - \frac{k_\alpha k_\beta}{k^2}\right), \tag{5.54}$$

where

$$k' = k\left(1 + \frac{i\omega\rho_s}{\eta_s[\omega]k^2}\right)^{1/2}. \tag{5.55}$$

In the above, ρ and ρ_s are the densities of the membrane and solvent, respectively. In the limit of $\omega \to 0$, these expressions reduce to Eq. (5.9). Using Eq. (5.54), we can show that the mean square displacement of a disk embedded in the membrane exhibits an anomalous diffusion [92]. An useful relation which connects the mean square displacement and the solvent modulus is obtained.

ACKNOWLEDGMENTS

We thank D. Andelman, H. Diamant, Y. Fujitani, G. Gompper, T. Hamada, Y. Hirose, T. Kato, P. B. S. Kumar, S. L. Keller, C.-Y. D. Lu, N. Oppenheimer, and Y. Sakuma for useful discussions. This work was supported by KAKENHI (Grant-in-Aid for Scientific Research) on Priority Area "Soft matter physics" and Grant No. 21540420 from the MEXT of Japan. This work was also supported by the JSPS Core-to-Core Program "International research network for nonequilibrium dynamics of soft matter."

REFERENCES

[1] B. Alberts, A. Johnson, P. Walter, J. Lewis, M. Raff, Molecular Biology of the Cell, Garland Science, New York, 2008.
[2] R. Lipowsky, E. Sackmann, Structure and Dynamics of Membranes, Elsevier, Amsterdam, 1995.
[3] K. Simons, E. Ikonen, Functional rafts in cell membranes, Nature 387 (1997) 569–572.
[4] L.J. Pike, Rafts defined: a report on the Keystone symposium on lipid rafts and cell function, J. Lipid Res. 47 (2006) 1597–1598.
[5] M. Leslie, Do lipid rafts exist? Science 334 (2011) 1046–1047.
[6] J. Fan, M. Sammalkorpi, M. Haataja, Formation and regulation of lipid microdomains in cell membranes: theory, modeling and speculation, FEBS Lett. 584 (2010) 1678–1684.
[7] C. Eggeling, C. Ringemann, R. Medda, G. Schwarzmann, K. Sandhoff, S. Polyakova, V.N. Belov, B. Hein, C. von Middendorff, A. Schönle, S.W. Hell, Direct observation of the nanoscale dynamics of membrane lipids in a living cell, Nature 457 (2009) 1159–1162.
[8] S.L. Veatch, S.L. Keller, Organization in lipid membranes containing cholesterol, Phys. Rev. Lett. 89 (2002) 268101.
[9] S.L. Veatch, S.L. Keller, Separation of liquid phases in giant vesicles of ternary mixtures of phospholipids and cholesterol, Biophys. J. 85 (2003) 3074–3083.
[10] S.L. Veatch, S.L. Keller, Miscibility phase diagrams of giant vesicles containing sphingomyelin, Phys. Rev. Lett. 94 (2005) 148101.
[11] S.L. Veatch, S.L. Keller, Seeing spots: complex phase behavior in simple membranes, Biochim. Biophys. Acta 1746 (2005) 172–185.
[12] S.L. Veatch, O. Soubias, S.L. Keller, K. Gawrisch, Critical fluctuations in domain forming lipid mixtures, Proc. Natl. Acad. Sci. U.S.A. 104 (2007) 17650–17655.
[13] A.R. Honerkamp-Smith, P. Cicuta, M. Collins, S.L. Veatch, M. Schick, M. den Nijs, S.L. Keller, Line tensions, correlation lengths and critical exponents in lipid membranes near critical points, Biophys. J. 95 (2008) 236–246.
[14] L. Onsager, Crystal statistics: a two-dimensional model with an order-disorder transition, Phys. Rev. 65 (1944) 117–149.
[15] S.L. Veatch, P. Cicuta, P. Sengupta, A. Honerkamp-Smith, D. Holowka, B. Baird, Critical fluctuations in plasma membrane vesicles, ACS Chem. Biol. 3 (2008) 287–293.
[16] G. Gompper, M. Schick, Self-assembling Amphiphilic Systems, Academic, New York, 1994.
[17] S. Ramachandran, S. Komura, K. Seki, G. Gompper, Dynamics of a polymer chain confined in a membrane, Eur. Phys. J. E 34 (2011) 46.
[18] K. Seki, S. Ramachandran, S. Komura, Diffusion coefficient of an inclusion in a liquid membrane supported by a solvent of arbitrary thickness, Phys. Rev. E 84 (2011) 021905.
[19] L.D. Landau, E.M. Lifshitz, Fluid Mechanics, Pergamon Press, Oxford, 1987.
[20] D.K. Lubensky, R.E. Goldstein, Hydrodynamics of monolayer domains at the air-water interface, Phys. Fluids 8 (1996) 843–854.

[21] Th.M. Fischer, The drag on needles moving in a Langmuir monolayer, J. Fluid Mech. 498 (2004) 123–137.
[22] P.G. Saffman, M. Delbrück, Brownian motion in biological membranes, Proc. Natl. Acad. Sci. U.S.A. 72 (1975) 3111–3113.
[23] P.G. Saffman, Brownian motion of thin sheets of viscous fluid, J. Fluid Mech. 73 (1976) 593–602.
[24] B.D. Hughes, B.A. Pailthorpe, L.R. White, The translational and rotational drag on a cylinder moving in a membrane, J. Fluid Mech. 110 (1981) 349–372.
[25] N. Oppenheimer, H. Diamant, Correlated diffusion of membrane proteins and their effect on membrane viscosity, Biophys. J. 96 (2009) 3041–3049.
[26] N. Oppenheimer, H. Diamant, Correlated dynamics of inclusions in a supported membrane, Phys. Rev. E 82 (2010) 041912.
[27] E. Evans, E. Sackmann, Translational and rotational drag coefficients for a disk moving in a liquid membrane associated with a rigid substrate, J. Fluid Mech. 194 (1988) 553–561.
[28] H. Stone, A. Ajdari, Hydrodynamics of particles embedded in a flat surfactant layer overlying a subphase of finite depth, J. Fluid Mech. 369 (1998) 151–173.
[29] K. Seki, S. Komura, Brownian dynamics in a thin sheet with momentum decay, Phys. Rev. E 47 (1993) 2377–2383.
[30] S. Komura, K. Seki, Diffusion constant of a polymer chain in biomembranes, J. Phys. II 5 (1995) 5–9.
[31] S. Ramachandran, S. Komura, M. Imai, K. Seki, Drag coefficient of a liquid domain in a two-dimensional membrane, Eur. Phys. J. E 31 (2010) 303–310.
[32] K. Seki, S. Komura, M. Imai, Concentration fluctuations in binary fluid membranes, J. Phys. Condens. Matter 19 (2007) 072101.
[33] S. Ramachandran, S. Komura, K. Seki, M. Imai, Hydrodynamic effects on concentration fluctuations in multicomponent membranes, Soft Matter 7 (2011) 1524–1531.
[34] R. Brewster, P.A. Pincus, S.A. Safran, Hybrid lipids as a biological surface-active component, Biophys. J. 97 (2009) 1087–1094.
[35] R. Brewster, S.A. Safran, Line active hybrid lipids determine domain size in phase separation of saturated and unsaturated lipids, Biophys. J. 98 (2010) L21–L23.
[36] T. Yamamoto, R. Brewster, S.A. Safran, Chain ordering of hybrid lipids can stabilize domains in saturated/hybrid/cholesterol lipid membranes, Europhys. Lett. 91 (2010) 28002.
[37] T. Yamamoto, S.A. Safran, Line tension between domains in multicomponent membranes is sensitive to degree of unsaturation of hybrid lipids, Soft Matter 7 (2011) 7021–7033.
[38] P.M. Chaikin, T.C. Lubensky, Principles of Condensed Matter Physics, Cambridge University Press, Cambridge, 1995.
[39] M. Nonomura, T. Ohta, Decay rate of concentration fluctuations in microemulsions, J. Chem. Phys. 110 (1999) 7516–7523.
[40] K. Kawasaki, Kinetic equations and time correlation functions of critical fluctuations, Ann. Phys. 61 (1970) 1–56.
[41] G. van Meer, D. Voelker, G. Feigenson, Membrane lipids: where they are and how they behave, Nat. Rev. Mol. Cell Biol. 9 (2008) 112–124.
[42] Y. Hirose, S. Komura, D. Andelman, Coupled modulated bilayers: a phenomenological model, Chemphyschem 10 (2009) 2839–2846.
[43] Y. Hirose, S. Komura, D. Andelman, Concentration fluctuations and phase transitions in coupled modulated bilayers, submitted.
[44] M. Teubner, R. Strey, Origin of the scattering peak in microemulsions, J. Chem. Phys. 87 (1987) 3195–3200.

[45] Y. Tserkovnyak, D.R. Nelson, Conditions for extreme sensitivity of protein diffusion in membranes to cell environments, Proc. Natl. Acad. Sci. U.S.A. 103 (2006) 15002–15007.
[46] K. Inaura, Y. Fujitani, Concentration fluctuation in a two-component fluid membrane surrounded with three-dimensional fluids, J. Phys. Soc. Jpn. 77 (2008) 114603.
[47] M. Haataja, Critical dynamics in multicomponent lipid membranes, Phys. Rev. E 80 (2009) 020902.
[48] E.P. Petrov, P. Schwille, Translational diffusion in lipid membranes beyond the Saffman-Delbrück approximation, Biophys. J. 94 (2008) L41–L43.
[49] H. McConnell, Composition fluctuations, correlated response, and protein solvation in membranes, J. Chem. Phys. 132 (2010) 205102.
[50] A.J. Bray, Theory of phase-ordering kinetics, Adv. Phys. 51 (2002) 481–587.
[51] K. Binder, D. Stauffer, Theory for the slowing down of the relaxation and spinodal decomposition of binary mixtures, Phys. Rev. Lett. 33 (1974) 1006–1009.
[52] E.M. Lifshitz, L.P. Pitaevskii, Physical Kinetics, Pergamon Press, Oxford, 1981.
[53] E.D. Siggia, Late stages of spinodal decomposition in binary mixtures, Phys. Rev. A 20 (1979) 595–605.
[54] H. Furukawa, Effect of inertia on droplet growth in a fluid, Phys. Rev. A 31 (1995) 1103–1108.
[55] M.S. Miguel, M. Grant, J.D. Gunton, Phase separation in two-dimensional binary fluids, Phys. Rev. A 31 (1985) 1001–1005.
[56] P. Ossadnik, M.F. Gyure, H.E. Stanley, S.C. Glotzer, Molecular dynamics simulation of spinodal decomposition in a two-dimensional binary fluid mixture, Phys. Rev. Lett. 72 (1994) 2498.
[57] G. Gonnella, E. Orlandini, J.M. Yeomans, Phase separation in two-dimensional fluids: the role of noise, Phys. Rev. E 59 (1999) R4741–R4744.
[58] R.D. Groot, P.B. Warren, Dissipative particle dynamics: bridging the gap between atomistic and mesoscopic simulation, J. Chem. Phys. 107 (1997) 4423–4435.
[59] P. Espanol, P. Warren, Statistical mechanics of dissipative particle dynamics, Europhys. Lett. 30 (1995) 191–196.
[60] P. Cicuta, S.L. Keller, S.L. Veatch, Diffusion of liquid domains in lipid bilayer membranes, J. Phys. Chem. B 111 (2007) 3328–3331.
[61] D. Saeki, T. Hamada, K. Yoshikawa, Domain-growth kinetics in a cell-sized liposome, J. Phys. Soc. Jpn. 75 (2006) 013602.
[62] M. Yanagisawa, M. Imai, T. Masui, S. Komura, T. Ohta, Growth dynamics of domains in ternary fluid vesicles, Biophys. J. 92 (2007) 115–125.
[63] M. Laradji, P.B.S. Kumar, Dynamics of domain growth in self-assembled fluid vesicles, Phys. Rev. Lett. 93 (2001) 198105.
[64] M. Laradji, P.B.S. Kumar, Domain growth, budding and fission in phase-separating self-assembled fluid bilayers, J. Chem. Phys. 123 (2005) 224902.
[65] S. Ramachandran, M. Laradji, P.B.S. Kumar, Lateral organization of lipids in multi-component liposomes, J. Phys. Soc. Jpn. 78 (2009) 041006.
[66] M. Laradji, P.B.S. Kumar, Anomalously slow domain growth in fluid membranes with asymmetric transbilayer lipid distribution, Phys. Rev. E 73 (2006) 040901(R).
[67] B.A. Camley, F.L.H. Brown, Dynamic simulations of multicomponent lipid membranes over long length and time scales, Phys. Rev. Lett. 105 (2010) 148102.
[68] B.A. Camley, F.L.H. Brown, Dynamic scaling in phase separation kinetics for quasi-two-dimensional membranes, J. Chem. Phys. 135 (2011) 225106.
[69] J. Fan, T. Han, M. Haataja, Hydrodynamic effects on spinodal decomposition kinetics in planar lipid bilayer membranes, J. Chem. Phys. 133 (2010) 235101.
[70] A.J. Wagner, J.M. Yeomans, Breakdown of scale invariance in the coarsening of phase-separating binary fluids, Phys. Rev. Lett. 80 (1998) 1429.

[71] A.J. Wagner, M.E. Cates, Phase ordering of two-dimensional symmetric binary fluids: a droplet scaling state, Europhys. Lett. 56 (2001) 556.
[72] M.S. Turner, P. Sens, N.D. Socci, Nonequilibrium raftlike membrane domains under continuous recycling, Phys. Rev. Lett. 95 (2005) 168301.
[73] L. Foret, Aggregation on a membrane of particles undergoing active exchange with a reservoir, Eur. Phys. J. E 35 (2012) 12.
[74] L. Foret, A simple mechanism of raft formation in two-component fluid membranes, Europhys. Lett. 71 (2005) 508.
[75] I.W. Hamley, The Physics of Block Copolymers, Oxford University Press, Oxford, 1998.
[76] J. Gómez, F. Sagués, R. Reigada, Actively maintained lipid nanodomains in biomembranes, Phys. Rev. E 77 (2008) 021907.
[77] J. Gómez, F. Sagués, R. Reigada, Nonequilibrium patterns in phase-separating ternary membranes, Phys. Rev. E 80 (2009) 011920.
[78] J. Fan, M. Sammalkorpi, M. Haataja, Domain formation in the plasma membrane: roles of nonequilibrium lipid transport and membrane proteins, Phys. Rev. Lett. 100 (2008) 178102.
[79] J. Fan, M. Sammalkorpi, M. Haataja, Lipid microdomains: structural correlations, fluctuations, and formation mechanisms, Phys. Rev. Lett. 104 (2010) 118101.
[80] J. Fan, M. Sammalkorpi, M. Haataja, Influence of nonequilibrium lipid transport, membrane compartmentalization, and membrane proteins on the lateral organization of the plasma membrane, Phys. Rev. E 81 (2010) 011908.
[81] P. Sens, M.S. Turner, Microphase separation in nonequilibrium biomembranes, Phys. Rev. Lett. 106 (2011) 238101.
[82] A.J. Levine, F.C. MacKintosh, Dynamics of viscoelastic membranes, Phys. Rev. E 66 (2002) 061606.
[83] S. Sankararaman, G.I. Menon, P.B.S. Kumar, Two-component fluid membranes near repulsive walls: linearized hydrodynamics of equilibrium and nonequilibrium states, Phys. Rev. E 66 (2002) 031914.
[84] N. Gov, A.G. Zilman, S. Safran, Hydrodynamics of confined geometries, Phys. Rev. E 70 (2004) 011104.
[85] M.L. Henle, R. McGotry, A.B. Schofield, A.D. Dinsmore, A.J. Levine, The effect of curvature and topology on membrane hydrodynamics, Europhys. Lett. 84 (2008) 48001.
[86] M.L. Henle, A.J. Levine, Hydrodynamics in curved membranes: the effect of geometry on particulate mobility, Phys. Rev. E 81 (2010) 011905.
[87] B.A. Camley, F.L.H. Brwon, Beyond the creeping viscous flow limit for lipid bilayer membranes: theory of single-particle microrheology, domain flicker spectroscopy, and long-time tails, Phys. Rev. E 84 (2011) 021904.
[88] T. Han, M. Haataja, Comprehensive analysis of compositional interface fluctuations in planar lipid bilayer membranes, Phys. Rev. E 84 (2011) 051903.
[89] C.W. Harland, M.J. Bradley, R. Parthasarathy, Phospholipid bilayers are viscoelastic, Proc. Natl. Acad. Sci. U.S.A. 107 (2010) 19146 108 (2011) 14705.
[90] S.Q. Choi, S. Steltenkamp, J.A. Zasadzinski, T.M. Squires, Active microrheology and simultaneous visualization of sheared phospholipid monolayers, Nat. Commun. 2 (2011) 312.
[91] R. Granek, Membrane surrounded by viscoelastic continuous media: anomalous diffusion and linear response to force, Soft Matter 7 (2011) 5281.
[92] S. Komura, S. Ramachandran, K. Seki, EPL 97 (2012) 68007.

CHAPTER SIX

Lipid Microdomains—Structure, Function, and Controversies

Lucyna Mrówczyńska[1]
Department of Cell Biology, Adam Mickiewicz University, Poznań, Poland
[1]Corresponding author: e-mail address: lumro@amu.edu.pl

Contents

1. Introduction 166
2. Lipid Bilayer—From "the Ocean of Lipids" to "the Mosaic of Lipid Microdomains" 168
   2.1 Insights into the lateral lipid microdomains organization 168
   2.2 Outer and inner membrane leaflets lipid microdomains 171
   2.3 Proteins in lipid microdomains 172
3. Membrane Microdomains Are Defined—The Lipid Rafts Definition 174
4. Detergent Insolubility of Membrane Microdomains—Artifacts or Facts 174
   4.1 Lipid microdomains versus DRMs 174
   4.2 The curvature factor and the DRMs' structure 176
5. The Search for the Universal Lipid Raft Marker 178
6. Visualization of Microdomains in Intact Cells and in Model Membrane Systems—State of the Art 180
7. Biological Importance of Lipid Microdomains Health and Diseases 184
   7.1 Lipid microdomains as signaling and sorting platforms 184
   7.2 Lipid microdomains in disease pathogenesis 187
8. Conclusions 188
Acknowledgment 189
References 189

Abstract

Lipid microdomains, referred to as membrane microdomains, membrane rafts, or lipid rafts, are the highly dynamic nanoscale liquid-ordered, sphingolipid-, and sterol-rich domains in the plasma membrane. Lipid microdomains recruit specific proteins and form sophisticated lipid–protein assemblies as the result of lipid–lipid, lipid–protein, and protein–protein interactions that are involved in many cellular processes, including signaling pathways, endocytosis, and protein sorting. Moreover, lipid microdomains play a role in pathogenesis of various diseases. Resistance of cold nonionic detergent Triton X-100 to solubilization is used as a common tool to study lipid rafts structure; however, detergent-based artifacts were observed. Despite a vast amount of experimental work in which the noninvasive, detergent-free methods were used, the facts concerning the structure and functions of lipids microdomains in living cells are still

Advances in Planar Lipid Bilayers and Liposomes, Volume 16
ISSN 1554-4516
http://dx.doi.org/10.1016/B978-0-12-396534-9.00006-4

disputable. This chapter consists of selected topics on current knowledge on membrane microdomains enriched with controversial data, and it presents variety of factors responsible for the impressive dynamic of plasma membrane planar organization.

ABBREVIATIONS

AFM atomic force microscopy
CTB cholera toxin subunit B
DRMs detergent-resistant membranes
GA glutaraldehyde
GM1 monosialoganglioside M1
GPI glycosylphosphatidylinositol
GPLs glycerophospholipids
GUVs giant unilamellar vesicles
K562 erythroleukemia cell line K562
l_d liquid disordered
l_o liquid ordered
MβCD methyl-β-cyclodextrin
PFA paraformaldehyde
PM plasma membrane
REH non-T, non-B acute lymphoblastic leukemia cell line REH
RT room temperature (~24 °C)
TX-100 Triton X-100

1. INTRODUCTION

The detailed studies concerning the plasma membrane (PM) structure and lipid–protein relationships extended during twentieth century. In the PM fluid mosaic model by Singer and Nicolson [1], lipids form the homogeneous "fluid" bilayer for the floating "mosaic" of membrane proteins. A liquid crystalline phase formed by homogeneous lipids was concerned as the only possible one to maintain the membrane proteins functions, and both lipids and proteins molecules were randomly distributed. No influence of lipids on the proteins distribution or on function was postulated. The influence of cytoskeleton on the distribution of membrane proteins was not taken into account.

In the late 1970s, the lipids' chemical structure and behavioral heterogeneity were explored providing the strong indication that the bilayer contains many more lipid types that are necessary to create a simple protein scaffold. Lipid molecules form the bilayer by weak forces, for example, Van der Walls's or electrostatic interactions, can therefore partition laterally, and

form distinct complexes or domains. In the beginning of the 1980s, the co-existence of different separated lipid domains, gel- and fluid-like, formed by different lipid types in bilayer, was experimentally evidenced [2,3].

In 1988, Simons and van Meer [4] proposed the working hypothesis, explaining differences between the lipid and protein composition in apical and basolateral membranes of epithelial cells. According to this hypothesis, the glycosphingolipids and glycosylphosphatidylinositol (GPI)-anchored proteins occur exclusively in the PM outer leaflet; they are linked in the *trans*-Golgi network (TGN) and are incorporated as an assembly into the apical membrane. This finding was the starting point for the "lipid raft concept" that indicated a heterogenic structure of the PM, described as the "sea" of unsaturated phospholipids with floating small, liquid-ordered sphingolipid-, and cholesterol-rich domains anchoring specific proteins [5]. The term "lipid raft" corresponds to something rigid; therefore, it seems to be controversial to describe precisely the dynamic character of lipid microdomains [6–8]. Despite this controversial meaning, the name "lipid rafts" is alternatively used with "lipid microdomains," "membrane microdomains," or "membrane rafts," or just "rafts" in the literature in the field, and in the chapter.

Lipid microdomains recruit "raftophilic" proteins involved in the membrane-associated events characterizing posttranslational lipid modifications, for example, double acylation with saturated fatty acids [9–11], in contrast to "raftophobic," non-raft-associated proteins [12]. Different lipid and protein contents make lipid rafts varied platforms involved in different cellular processes, such as cell signaling, membrane vesiculation and budding, endocytosis, cell adhesion, formation of immunological synapse, or cytoskeleton organization [6–8,13,14]. The role of lipid rafts in various diseases pathogenesis [15–18] is well established. The significant modification in the lipid rafts' structure, and thereby functions, induced by dietary lipids, was confirmed [19,20].

Lipid microdomains have been detected in the eukaryotic cells of the PM including mammalian [15,16,21], plant [22,23], and yeast one [24,25]. Although rafts were initially thought to be exclusively located in the PM, the increasing evidence suggests their presence in subcellular compartments, such as the TGN [26,27] or lysosomal membrane [28]. Because of lipid and protein composition varieties that significantly differ from the PM (e.g., low content of sphingolipids), the data concerning presence of rafts in organelle are controversial, at least in the case of mitochondria [29–32].

Over the past decade, lipid rafts' structure and functions have not only been the subject of many studies but also various controversies due to the insufficient

or conflicted results concerning their structure, size, lifetime, and cellular diversity that have been estimated with distinct scientific approaches [7,33–35]. A commonly used method to isolate rafts from the PM is based on their resistance to nonionic detergent Triton X-100 (TX-100) at 4 °C [9,36]. It was assumed that detergent-insoluble sphingolipid-, cholesterol-rich domains, also called detergent-resistant membranes (DRMs), correspond to lipid rafts in the PM of living cells [5,37]. However, different detergents and modifications of isolation conditions create conflicting results concerning the DRMs' composition [38–43]. Therefore, state-of-the-art methods are involved in the rafts structure–activity studies. Numerous data support the existence of a dynamic nanometer-scale "membrane-organizing principle" in the PM of living cells and show their great diversity [14].

The main idea of the chapter is to present facts and controversies concerning the heterogeneity of lipid microdomains.

2. LIPID BILAYER—FROM "THE OCEAN OF LIPIDS" TO "THE MOSAIC OF LIPID MICRODOMAINS"

The diversity of lipids provides strong indication that the lipid bilayer, composed of two opposing leaflets, cannot be a simple protein scaffold. Cellular lipidomic analysis presents more than 7700 molecular species of glycerophospholipids (GPLs); more than 3900 sphingolipids; and thousands of mono-, di-, and tri-glycerides [44]. In eukaryotic cells, over 1000 different lipid types are involved in the PM bilayer formation. Membrane lipids are divided into the three main classes: GPLs, sphingolipids, and sterols. Mammalian cell membrane contains only one type of sterol, cholesterol, but there is a huge variety of GPLs and sphingolipids. Phytosterols and ergosterol are, respectively, important components of the plant and yeast PM. The role of sterols in the eukaryotic PM organization is well established [45]. In mammalian cells, around 90% of cellular cholesterol is located in the PM [46]. The impressive lipid polymorphism of the PM and the diversity of the bilayer structure could be explained by the mechanism of cells accommodation to changeable environmental conditions during evolution.

2.1. Insights into the lateral lipid microdomains organization

Each lipid molecule has its individual molecular structure, called the theoretical molecular shape [47,48]. Depending on the length and degree of acyl chains unsaturation, three basic molecular shapes of lipids molecules are distinguished: conical, inverted cone, and cylindrical. According to

biophysical and biochemical predictions, the lipid lateral organization in the bilayer depends on the molecular shape of the lipid molecules [15,47,48]. Cone-shaped lipids, for example, phosphatidylethanolamine, or inverted cone-shaped sphingolipids, for example, sphingomyelin and glycosphingolipids, contain saturated acyl chains that allow them to pack tightly together. Sphingolipids can self-associate by hydrogen bounds between the hydroxyl group of the sphingosine and the α-hydroxyl group of fatty acids; therefore, they are essential in the lateral bilayer organization. Cylindrical shaped GPLs, for example, phosphatidylcholine, the most abundant membrane lipids, are rich in kinked unsaturated acyl chains with one or two double bonds, which are loosely packed at physiological temperature. The differences in the chemical structure and in the intrinsic molecular shape of a lipid molecule determine a distinct behavior of saturated (sphingolipids) and unsaturated (GPLs) lipids, and they lead to their diverse distribution in a bilayer and in consequence induce lateral phase separation [15,49,50]. Two main phases are distinguished: the solid-like (gel) phase, formed by lipids with tightly packed lipid acyl chains (e.g., sphingolipids), and liquid-disordered (l_d) phase, enriched in lipids with mobile unsaturated acyl chains (e.g., GPLs).

The intermediate phase between the solid-like and liquid-disordered phases is the liquid-ordered (l_o) phase in which long acyl chains of lipids are tightly packed but still posses high lateral mobility. The existence of sphingolipid-, cholesterol-enriched l_o domains segregated from bulk unsaturated GPLs creates the lateral asymmetry in the outer leaflet of bilayer at physiological temperature [5,6,36]. A schematic model of lipid domain organization in the PM is proposed in Fig. 6.1. Due to sphingosine moiety and the long-chain saturated fatty acid in sphingomyelin molecule, sphingolipids-, and cholesterol-rich (l_o) domains are thicker than the surrounding unsaturated phospholipids matrix (l_d) [51]. The influence of line tension (i.e., the interfacial energy at the domain edge) on the lateral PM organization (e.g., size and shape of lipid microdomains) was experimentally confirmed [53].

In the outer leaflet of bilayer, cholesterol molecules partition preferentially with saturated acyl chains of sphingolipids rather than with kinked acyl chains of phospholipids in l_d domains [54]. Hydrogen bonding between the 3-OH group of cholesterol and the amide group of sphingolipids is basic in the formation of cholesterol–sphingolipids l_o domains. In the absence of cholesterol, the hydrocarbon chains of sphingolipids are tightly packed

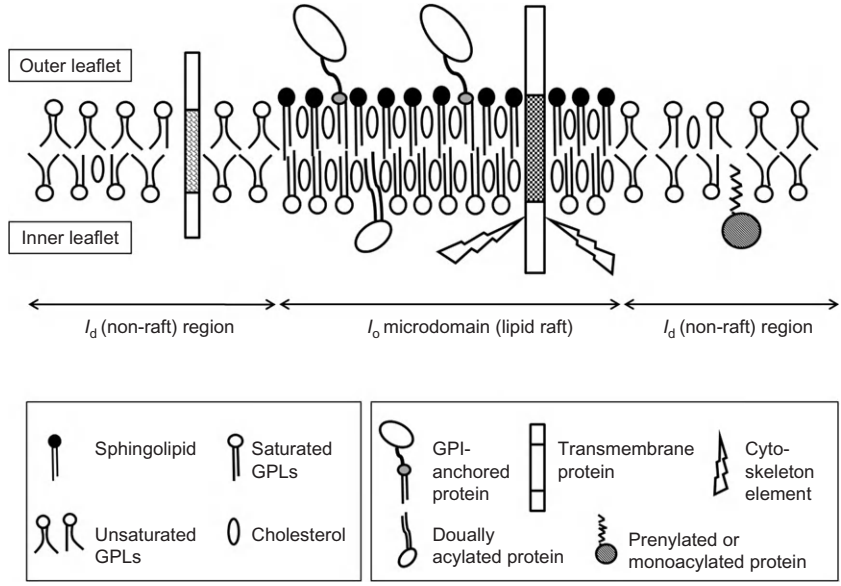

Figure 6.1 Schematic representation of l_o microdomain (lipid raft) and l_d (non-raft) regions in the plasma membrane. Sphingolipids, cholesterol, and saturated glycerophospholipids (GPLs) form tightly packed l_o microdomains within unsaturated GPLs l_d environment. l_o microdomains are thicker than the rest of the bilayer [51]. Sphingolipids are restricted to the outer leaflet of the bilayer, whereas cholesterol is present in both leaflets. GPI-anchored and transmembrane proteins with specific lipid modification are associated with l_o microdomains. Monoacylated and prenylated proteins are excluded from l_o microdomains [10]. Lipid rafts are anchored to elements of the cytoskeleton via electrostatic interactions [52].

and form a solid-like phase. Cholesterol is predominantly located in the inner leaflet of the PM, for example, the inner leaflet of the PM contains approximately 75% and 85% of total membrane cholesterol in erythrocyte [55] and in the synaptic PM [56], respectively. Cholesterol content and its asymmetric distribution in the PM undergo modification in physiological condition by dietary lipids [20], in aging [56], in obesity [57], during hypercholesterolemia [58,59], but also in the progress of many diseases, for example, multiple sclerosis [60] or cancer [61].

Ganglioside, such as cholesterol, interacts preferentially with sphingolipids; therefore, they are concentrated in l_o domains in the outer layer of the PM [62]. Many types of gangliosides are distinguished due to various combinations of sugar residue (glucose, galactose, *N*-acetylgalactosamine, *N*-acetylglucosamine, and fructose) attached to the strongly hydrophobic ceramide backbones [63].

All ganglioside molecules, except from ganglioside GM3, are cone shaped that explains their interaction with inverted cone-shaped sphingolipids molecules and l_o domains formation. Therefore, gangliosides are an important component of lipid microdomains. Gangliosides constitute generally around 1% of the total PM lipid content, with exception of PM neurons that constitute up to 10% of the lipid content [63], and they are probably involved in the formation of tissue-specific ganglioside-rich microdomains. Exogenous gangliosides can incorporate into the PM and modify lipid rafts structure and function [64].

In conclusion, the current picture of the PM is mosaic in regard to distinct lipid microdomains, lipid rafts "floating" in unsaturated GPLs, "l_d—sea" [5,6]. Recently, it has been proposed that certain GPLs with unsaturated acyl chains form their own microdomains by excluding cholesterol [65]. Therefore, homogeneous "GPLs sea" can be also mosaic in structure.

2.2. Outer and inner membrane leaflets lipid microdomains

Lipids and proteins are asymmetrically distributed between the outer and the inner leaflet of PM. Sphingomyelin, phosphatidylcholine, and glycosphingolipids are almost exclusively distributed in the outer leaflet, while phosphatididylserine, phosphatidylethanolamine, and phosphatidylinositol are present in the inner leaflet of the PM in abundance [66]. Therefore, l_o domains, enriched in sphingolipids and glycosphingolipids, are confining to the outer leaflet of the PM [67].

Cholesterol occurs in both leaflets of the PM and forms complexes not exclusively with sphingolipids but also with GPLs with saturated fatty acids in the inner leaflet [68] (Fig. 6.1). Moreover, l_o domains combine with cholesterol and SLPE (1-stearoyl-2-linoleoyl-*sn*-glycero-3-phosphatidylethanolamine) or with mono- or di-unsaturated phosphatidylethanolamine species-rich, and they have been found in the inner leaflet of model membranes [69]. Cholesterol-rich microdomains have been observed in the inner leaflet of the PM of Swiss mouse embryonic fibroblasts by expressing the C-terminal domain 4 (D4) of cholesterol-binding θ-toxin (perfringolysin) [70].

Although the coupling between the PM leaflets was confirmed in theoretical considerations [71], the communication between the outer and the inner leaflet domains is not known in details. As for coupling between the outer and the inner leaflets of the PM, it has been shown that the clustering of the outer leaflet-associated receptors triggers the inner leaflet signaling by aggregating lipid rafts in T cells [72]. Similar to observation

in biological membranes, l_o domains in the outer layer in giant unilamellar vesicles (GUVs) have the potential to aggregate lipids in the inner layer [50]. To explain the connection between both monolayers, it has been proposed that GPLs chains from the inner leaflet (e.g., phosphatidylethanolamine and phosphatidylserine) can interact with long acyl chains of sphingolipids from the outer leaflet [6,66]. Such a chain–chain interaction between both PM layers is additionally stabilized by cholesterol which is present in both leaflets of the bilayer [73].

Apart from the lipid–lipid interaction in the PM coupling, transmembrane proteins are suggested to be involved in the maintenance of the outer–inner leaflet domain connection [68,74]. Moreover, the cytoskeleton role in the outer–inner leaflet domains coupling via electrostatic interactions was confirmed [52,75,76].

2.3. Proteins in lipid microdomains

About one-third of the genome encodes membrane proteins and many other proteins that are partly membrane associated [14]. Lipid rafts are estimated to contain from 0.3% to 2% of total membrane protein content [77]. In mature human erythrocytes, the PM consists of at least 340 proteins [78], on the basis of Bradford's assays [79]—3–4% of them—or based on colloidal Coomassie staining [80]—less than 1%, are rafts associated. Lipid microdomains can include or exclude proteins to variable time, also as short as <0.1 ms, that makes their protein content variable [81]. Rafts' association modifies proteins' function; on the other hand, the protein acts as the raft organizer, that is they modulate raft size and curvature by altering (reducing) the line tension at the raft boundary [53].

L_o domain environment is not accessible for membrane proteins, especially in regard to protein movement in and out of rafts. Therefore, the lateral segregation of membrane proteins depends on their particular affinity for l_o domains [10,82]. Moreover, the X-ray diffraction data show higher thickness of raft, in comparison to a non-raft region of bilayer [51]. It has been postulated that lipid rafts recruit proteins with long transbilayer domains according to highly specific "hydrophobic matching" between amino acid sequence of protein and the thick hydrocarbon region of the bilayer [82]. The details about the interaction between the transmembrane segments of rafts proteins and "lipid shells," in particular, what type of amino acid sequence of protein transmembrane segment is more preferred by the thicker bilayer, are still unknown.

The protein set of lipid rafts has been established by biochemical analysis of DRMs isolated from the PM in the presence of cold nonionic detergent TX-100 [9,36]. All DRM proteins characterize the cotranslational or posttranslational hydrophobic modifications that increase their affinity to l_o domains [9–11]. The first example, the GPI anchor, structurally heterogeneous within the lipid moiety, is a well-established hallmark of raft-associated proteins (e.g., CD59 or Thy-1 proteins), anchored to the outer leaflet of the PM (Fig. 6.1). The next example of DRM proteins is dually acylated proteins, that is, myristoylated and/or palmitoylated (but not monoacylated), associated with the inner leaflet of the PM (e.g., the Src-family tyrosine kinases such as Fyn, Lck, Lyn; α subunit of heterotrimeric G protein; integral erythrocyte membrane proteins: flotillin-1, flotillin-2, and stomatin; or neuronal protein GAP-43) [13,75,80,83]. Other types of rafts-associated proteins are cholesterol-binding protein (e.g., caveolins) [84], or phospholipid-binding protein (e.g., anexin family proteins such as synexin or sorcin), which bind lipid microdomains in a calcium-dependent manner [75].

In contrast to multiple myristoylated and/or palmitoylated, prenylated proteins are not found in DRMs [10]. The reason of raftophobicity of prenylated proteins is probably the structure, not only hydrophobicity index of the prenyl group, that is, a farnesyl or geranylgeranyl moiety, which is as hydrophobic as palmitoyl or myristoyl, but it posses spatial (branched) conformation. Therefore, prenylated proteins are excluded from rafts (Fig. 6.1).

Although band3 and glycophorin, the integral proteins of the human erythrocyte PM, are detected in DRMs [42,80], many transmembrane proteins with hydrophobic α-helices are classified as raftophobic. The reason for excluding the protein from rafts is probably a "hydrophobic mismatch" between lipids and amino acid sequence of the protein transmembrane domain. Moreover, apart from the amino acid sequence of protein transmembrane domain, both extracellular and intracellular domain structures determine protein association with l_o domains [7].

An enrichment of cytoskeletal proteins, including actin, fodrin (non-erythroid spectrin), and spectrin, has been found in DRMs isolated from many cells types, including neutrophils [85] and erythrocytes [52,75], yet in the case of erythrocytes, results are dependent on DRMs' isolation conditions [80]. *In situ* imaging of DRMs by atomic force microscopy (AFM) confirmed the cytoskeleton–raft association [86].

In conclusion, both the structural affinity to l_o domains and the hydrophobicity of lipid modification determine proteins targeting to l_o domains [10].

3. MEMBRANE MICRODOMAINS ARE DEFINED—THE LIPID RAFTS DEFINITION

Lipid rafts are heterogenic in structure; therefore, it is controversial to define them in detail. Due to the distinct chemical structure, raft size is controversial, as it varies from 20 to 30 lipid molecules and 1 to 3 proteins, up to 1200 nm in diameter wide signaling platform [86]. Raft lifetime varies from milliseconds to minutes, and the factors involved in the rafts platform formation and maintenance are still unknown.

Despite the heterogenic raft nature, two main types of lipid rafts are distinguished: heterogeneous "planar rafts" and "invaginated rafts" also called caveolae that are formed with the participation of caveolin proteins [84]. Flask-shaped caveolae are the only one morphologically identifiable type of lipid microdomains in mammalian cells, the most numerous in endothelial cells, adipocytes, and in smooth muscle cells [87].

The commonly acceptable general definition of lipid rafts was introduced at the 2006 Keystone Symposium of Lipid Rafts and Cell Function (Steamboat Springs, CO, March 23–28, 2006) by biophysicists, biochemists, and cell biologists: "Lipid rafts are small (10–200 nm), heterogeneous, highly dynamic, sterol- and sphingolipid-enriched domains that compartmentalize cellular processes. Small rafts can sometimes be stabilized to form larger platforms through protein-protein and protein-lipid interactions" [88].

4. DETERGENT INSOLUBILITY OF MEMBRANE MICRODOMAINS—ARTIFACTS OR FACTS

4.1. Lipid microdomains versus DRMs

The first method to isolate sphingolipid-, cholesterol-rich rafts from the PM is based on their insolubility during the PM solubilization by nonionic TX-100 at +4 °C [9,36]. DRMs were spontaneously identified with lipid rafts in the PM of living cells [4,5,37]. However, cholesterol resists TX-100 solubilization at +4 °C only when it is associated with sphingomyelin [89]; therefore, the detergent-based procedure at +4 °C to isolate rafts is criticized. Namely, many membrane lipids that exist in fluid detergent-soluble phase at physiological temperature 37 °C turn into gel-, detergent-resistant phase, at +4 °C. Therefore, a membrane fraction isolated at +4 °C differs from the one existing at physiological temperature. On the one hand, certain data suggest that temperature is not a crucial factor in the lateral segregation of

membrane component [90]; on the other hand, the incubation condition, that is, the buffer composition, temperature, and different solubilization time, influences DRMs' composition [91–93]. The TX-100-based DRMs' isolation technique could namely induce the formation of the new artificial domains in the PM or lead to the production of mixed rafts within a native membrane or even with different cellular compartments [34,38,43,94–96]. Moreover, DRMs have been isolated from the PM as a mixture of membrane sheets and vesicles of various sizes that were estimated by electron microscopy [77,92]. In AFM the size of DRMs frequently exceeds 15–20 μm^2, namely, one order of magnitude higher than the raft size detected in the PM of living cells [86]. Therefore, the use of TX-100 as a suitable tool for raft isolation is doubtful, and DRMs are considered as detergent artifacts [34,97]. In contrary, fission and budding of the raft-like l_o domains from heterogeneous GUVs, but not the new domain formation or their coalescence, in the TX-100, Brij 98, and LysoPC presence was observed [98]. However, the differences between the model and biological membrane structure in data analysis should be taken into consideration.

Many mild detergents have been used to prepare DRMs (Lubrol, Brij 96, Brij 98, Zwitterionic, CHAPS, TX-114, Tween 20, C_8E_{12}, Lubrol WX, CHAPS), and unsurprisingly, differences in DRMs' structure were obtained. Namely, Heffer-Lauc *et al.* [40] studied nine different detergents to isolate rafts from the brain tissue sections. They observed the significant gangliosides (GM1 and GD1) and GPI-anchored protein (Thy-1) redistribution, both within and between the tissue sections, depending on the detergent type, incubation time, and temperature. Delaunay *et al.* [41] showed that the inner leaflet of rafts, including rafts proteins, was solubilized by TX-100 more effectively, in comparison with Lubrol WX. Furthermore, detergent solubilization depended not only on the detergent type but also on both the bilayer saturability by its molecules and the dynamics of the detergent-lipid mixed micelle formation [99,100]. It should be noted that DRMs are a cocktail of various raft types, with additional protein contaminations from the subcellular compartment, particularly from mitochondria [29]. Comparative analysis of rafts with detergent-free and detergent-based methods showed significant differences in the lipids' composition and content, especially in the cholesterol content [101]. Similarly, microscopic analysis of raft composition at physiological temperature and neutral pH, using membrane tension to generate large domains, showed rafts as sphingolipid- and GPI-anchored protein rich but cholesterol poor [102]. Moreover, cholesterol distribution was equal between the raft and the non-raft PM regions, contrary to the standard view.

One of the driving forces in DRMs' production is the mechanism of membrane solubilization, which is unique to each individual detergent, and depends on the solubilization conditions and detergent/lipid ratio. The strength of lipid and protein interaction within rafts is the next one. Therefore, DRMs lack certain proteins when the associations of these proteins with lipids are too weak and not resistant to solubilization [96,97]. Raft-associated proteins are resistant to detergent solubilization depending on their structure. Hence, the presence and even mostly absence of proteins in DRMs cannot reflect the raft protein set in the PM. For example, depending on the detergent type and the isolation conditions multidrug resistance protein 1 (MRP1) was detected [103,104] or not [105] in DRMs isolated from the human tumor cell lines which overexpress this protein. However, due to the detergent-free method, MRP1 was exclusively found in the lipid rafts, and its transport activity was significantly cholesterol dependent [106]. In contrary, we did not found a cholesterol-dependent MRP1 transport activity in the erythrocyte PM that suggests its location outside the rafts [107]. However, cell specificity, in regard to MRP1 raft association, cannot be excluded.

4.2. The curvature factor and the DRMs' structure

During the first step, when detergent molecules partition into bilayer, they modify the surface ratio of its two leaflets generating changes in bilayer spontaneous curvature and membrane lipid redistribution according to their intrinsic molecular shape (e.g., cone or inverted cone), to the energetically favorable regions. Amphiphile molecules incorporated into the erythrocyte PM affect bilayer bending in specific ways, resulting in either stomatocytic (invaginated) or spiculated echinocytic (exvaginated) cell shapes [108]. In our previous studies, we found a negative correlation between the membrane curvature induced by TX-100 in erythrocytes and that preferred by DRM-associated membrane components [108–110]. Namely, raft markers as ganglioside GM1 and proteins CD59, stomatin, synexin, and sorcin were found in the outward curved membrane upon echinocytic erythrocyte transformation induced by the increases of intracellular calcium. However, the proteins poorly colocalized with GM1 rafts in the same spiculae indicate their not mutual segregation and argue their association with different rafts. In the line with our idea, that echinophilicity promotes DRMs' partition, echinophobic, transmembrane glycoprotein CD47, was found not to associate with the erythrocyte DRMs [80].

Based on our data and the literature in the field, we have proposed a hypothesis explaining a membrane curvature-dependent segregation of the PM

components during solubilization by TX-100, which is related to the stomatocytogenic (inward membrane bending) effect of TX-100 [111]. Stomatocytogenic TX-100 cannot effectively solubilize membrane components with preference for outward membrane curvature (Fig. 6.2). Namely, preferential incorporation of TX-100 into the inner leaflet of the PM results in a relative expansion of this leaflet in comparison with the outer leaflet, and in accordance with the bilayer-couple model, it induces stomatocytic shape transformation of erythrocytes [114]. In line with our model, the TX-100 ability to preferably solubilize inner leaflet lipids has been proposed

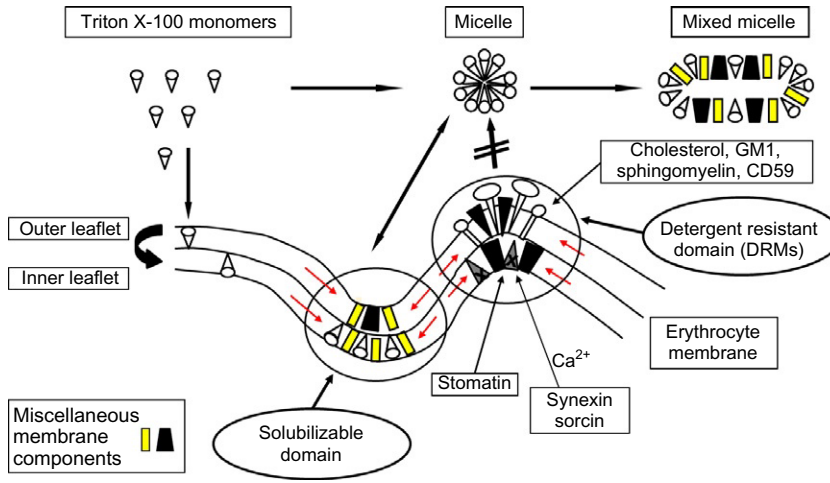

Figure 6.2 Membrane components curvature-dependent lateral segregation which can occur during Triton X-100 (TX-100) solubilization. TX-100 monomers intercalate into erythrocyte membrane, accumulate in the inner membrane leaflet, and induce membrane invaginations, thereby indirectly prompt outward bent membrane areas at the borders of invaginations. Outward curved membrane regions, where outward membrane curvature preferring membrane components are segregated and accumulated, remain unsolubilized (DRMs) due to the weak ability of TX-100 monomers (because of its preferential inner leaflet distribution and conical shape) to accumulate in these regions. Accumulation of TX-100 in invaginations (i.e., solubilizable domains) contributes, due to unfavorable interaction of TX-100 with cholesterol [112,113], to segregation of cholesterol and sphingomyelin into detergent-resistant domains. Low temperature (+4 °C) used during solubilization work to slow down membrane intercalation of TX-100 monomers, resulting in a more effective lateral segregation of membrane components. The model is highly schematic; therefore, the relation between proteins and lipids size is not maintained. Adapted from Ref. [111] with permission.

[41,92]. Preferably accumulating in the inner leaflet, TX-100 thereby indirectly creates the outward bending membrane areas at the borders of these invaginations where the membrane components that prefer the outward bilayer curvature, that is, echinophilic components [109,110], are accumulated and protected from TX-100 solubilization (Fig. 6.2). Similarly, other membrane components are accumulated in the flat membrane regions, where the TX-100 monomer concentration is low. Moreover, a low temperature (+4 °C) during solubilization works to slow down membrane intercalation of monomeric TX-100, resulting in a more complete lateral segregation of membrane components before the PM final solubilization. TX-100 accumulation in invaginations (i.e., solubilizable domains) contributes, due to unfavorable interaction of TX-100 with cholesterol [112,113], to the segregation of cholesterol and sphingomyelin into DRMs (Fig. 6.2).

Although other cell types may react to detergent incorporation with distinct membrane bending patterns other than flexible human erythrocytes, it should be taken into account that detergent molecules may induce the microcurvature and they can stimulate the lateral movement of a membrane component during the PM solubilization and thereby can create artifact-rich DRMs.

5. THE SEARCH FOR THE UNIVERSAL LIPID RAFT MARKER

According to the rafts' definition from 2006 [88], lipid rafts are sphingolipid- and cholesterol-rich assemblies. There are hundreds of sphingolipid species involved in the outer layer of the PM formation in different raft types; therefore, unique sphingolipid could not be the universal raft markers.

Cholesterol is the only sterol type that is present in the mammalian PM, and it is crucial for lipid rafts planar organization [5,6]. Experiments with methyl-β-cyclodextrin (MβCD), the most popular cholesterol chelating-drug, confirm the cholesterol role in the raft maintenance [29,109]. Other cholesterol-depleting agents, such as drugs nystatin and filipin, or plant-derived saponin, are much less efficient at cholesterol sequestration in the PM [29]. Although, on the one hand, MβCD is the most popular specific cholesterol-depleting agent, it is partly controversial because it preferentially excludes cholesterol from the l_d-non-raft domains, rather than from the l_o-raft domains [115]. It has been shown that for many raft-associated proteins, interaction with cholesterol is crucial. Namely, cholesterol depletion results in the epidermal growth factor (EGF) receptor exclusion

from lipid rafts, inducing its functional alternation [116]. Therefore, MβCD plays a double role as a cholesterol and rafts-associated depleting agent.

The other way to modulate raft structure is by using sphingolipid-depleting agents [76] or sphingomyelinase (SMase) [117]. Interestingly, SMase hydrolysis of sphingomyelin to ceramide results in the generation of the large ceramide-enriched membrane domains that cluster different receptors and alter cell activity effectively [118,119].

Lidocaine hydrochloride, an amphipathic local aesthetic, reversibly disrupts raft structure in the erythrocyte membrane depleting raft-associated proteins flotillin-1 and aquaporin-1 from rafts, unchanging the cholesterol or sphingolipids content. Additionally, lidocaine alters the raft-associated Gα function, involved in the cellular signaling [120].

Proteins are involved in the raft structure maintenance, but rafts recruit many of them for a millisecond only to accentuate the rafts dynamics [48]. Additionally, different proteins are associated with distinct raft types [104,121]; therefore, they cannot be universal raft markers. Interestingly, a flotillin homologue, AtFlot1, the integral protein present in the PM of the animal cells, was found in rafts isolated from *Arabidopsis* [122], indicating the specific conserved raft-related functions. Using fluorescence correlation spectroscopy (FCS) method, Lenne *et al.* [76] showed diminishment of the lipid microdomains lateral organization after disruption of action-based cytoskeleton.

Monosialoganglioside M1 (GM1), serving as a cholera toxin receptor in the PM, is a known lipid raft marker [72]. However, gangliosides GM1 and GM3 have been recently found in the distinct domains of the PM related to the curvature factor and intrinsic molecular shape [63,123,124]. Moreover, the little or no colocalization of GM1 and GPI-anchored proteins, Thy-1, and the palmitoylated transmembrane adaptor LAT in the mast cell PM was found [125].

Non-sphingolipid, glycerol-type glycolipid, phosphatidylglucoside (PtdGlc) has been proposed to be another raft marker found in the outer leaflet of the PM [126]. However, some types of rafts do not contain glycolipids; therefore, the role of PtdGlc as a marker is limited to glycolipid-contained rafts only.

The lipid microdomain structure is much more complex than predicted from the DRM analysis. The universal structural raft marker(s) do not exist, neither for the various cell types nor for the given ones, apart from cholesterol depletion. Function, not the structure, should be taken into account in this context when lipid microdomains are classified.

6. VISUALIZATION OF MICRODOMAINS IN INTACT CELLS AND IN MODEL MEMBRANE SYSTEMS—STATE OF THE ART

There is no credible proof for the idea that DRMs are identical with *in vivo* lipid rafts, and therefore, connection between DRMs and lipid rafts remains controversial. The DRM fraction analysis is an indirect method, and the more direct evidence of rafts in the native PM has been demanded. Moreover, DRM assay cannot be used to estimate lipid domain size in the native PM. For this reason, the modern noninvasive, detergent-free approaches are necessary to be used for the further investigation. Rafts cannot be directly visualized by the conventional microscopic techniques because of small dimensions, for example, diameter from 6 to 14 nm [81].

Data obtained by the state-of-the-art methods support the existence of differences in the lipid and protein composition nanometer-scale microdomains in the living cells, which confines constituents for up to a few to hundred milliseconds and permanently undergoes structural changes [76].

Stimulated emission depletion far-field fluorescence nanoscopy allows the detection of a single diffusing (lipid) molecule in the nanoscale domains and analysis of the dynamics of the living cells membrane components. This optical recording of the molecular time traces and fluctuation data in tunable nanoscale areas is an excellent method to direct the dynamics study of biomolecules in the PM [127]. Another powerful approach to visualize and examine membrane microdomains on the surface of living cells, including estimation of their size, as well as lipid–protein and lipid–lipid interactions, is fluorescence resonance energy transfer (FRET) [128]. Fluorescence recovery after photobleaching (FRAP) allows to study how lipid rafts as assemblies impact protein and lipid diffusion in the PM [129]. The FCS methods are useful to study the diffusion behavior of various membrane components [76]. Single-particle tracking allows analysis of the dynamic behavior of the individual proteins and lipids in the living cell membrane [130].

Lipid rafts can be visualized by AFM that additionally offers an excellent approach to visualize directly the effect of the detergent action and solubilization with time [53,86,100]. Immunoelectron microscopy analysis (immunogold-labeling EM analysis) reveals more complex topographical organization of membrane microdomains, especially proteins detected by antibodies conjugated with different size nanoparticles [125,131,132].

Flow cytometry has been proposed as a useful tool for the comparative analysis of the lipid microdomain composition in blood cells and various tumor cells, for example, erythroleukemic cells [133,134].

Larger raft platforms are detectable in a fluorescence microscope, upon cross-linking of single raft markers, for example, ganglioside GM1 binding by fluorophore-conjugated subunit B cholera toxin (CTB) and further cross-linking of CTB–GM1 mobile complexes by anti-CTB antibodies [72,109,110,131,135], or by antibody-mediated cross-linking of raft-associated proteins, for example, GPI-anchored proteins [72,131]. The visualization of lipid rafts only by fluorophore-conjugated CTB without further antibody cross-linking was less successful in our previous studies with the human erythrocytes [108].

With the usage of fluorescence microscopy, we have studied cross-linking of ganglioside GM1 by the fluorophore (Alexa 555)-labeled CTB in the human erythrocyte PM, and how raft-associated proteins (e.g., CD59, stomatin, sorcin, synexin) distribute in CTB–anti-CTB–GM1 platforms in control discoid and calcium-induced echinocytic human erythrocytes [109,110]. Cross-linking of ganglioside GM1 by CTB plus anti-CTB resulted in the formation of usually 40–60 patches distributed evenly over the membrane in discoid erythrocytes and no capping of patches occurred [109]. Patching of GM1 did not affect the discoid shape of erythrocytes (Fig. 6.3A). Cells' pretreatment with MβCD abolished ganglioside GM1 patching [109]. We found no accumulation of neither DRM-associated proteins CD59, stomatin (Fig. 6.3C), sorcin, and synexin, into GM1 patches (Fig. 6.3B), nor no-DRM-associated integral protein CD47. Our study indicates that GM1 rafts in the human erythrocyte membrane are poor in DRM-associated proteins.

To indicate the morphology of echinocytic erythrocytes induced by calcium ionophore A23187, scanning electron micrograph is shown in Fig. 6.4A. In calcium-induced echinocytic erythrocytes, CTB–anti-CTB–GM1 complexes accumulated at the top of spiculae (Fig. 6.4B). DRM-associated proteins CD59, sorcin, synexin, and stomatin (Fig. 6.4C), but not no-DRM-associated protein CD47, also showed similar curvature-dependent lateral distribution as GM1 complexes. However, the DRM-associated proteins only partially colocalized with CTB–anti-CTB–GM1 complexes at the top of spiculae (to compare Fig. 6.4B and C). Therefore, echinophilicity of membrane components is proposed to contribute to the DRM association of membrane components [109,110]. Our study describes a new method to examine both properties of lipid raft components and raft composition in intact cells.

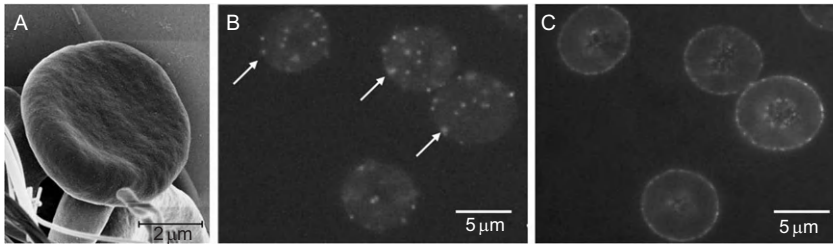

Figure 6.3 Distribution of CTB plus anti-CTB cross-linked ganglioside GM1 in discoid human erythrocytes. Scanning electron micrograph showing discoid human erythrocyte pretreated with CTB plus anti-CTB (A). Fluorescence micrographs (mid-plane cross-section) showing discoid human erythrocytes treated with Alexa 555 conjugated CTB (4 μg/ml, 60 min at RT) and anti-CTB (60 min, RT), fixed with 5% paraformaldehyde (PFA) plus 0.01% glutaraldehyde (GA) (60 min, RT) (B) and stained for stomatin (C). Treatment with CTB plus anti-CTB induced the formation of distinct GM1 patches (arrows) (B). Stomatin remained evenly distributed around the membrane (C). No accumulation of stomatin to GM1 patches was detected—signals from the same corresponding fields are indicated in (B) and (C). Adapted from Ref. [110] with permission.

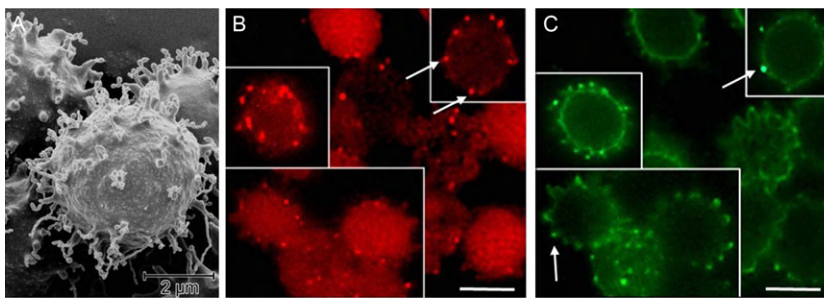

Figure 6.4 Distribution of CTB plus anti-CTB cross-linked ganglioside GM1 in echinocytic human erythrocytes. Scanning electron micrograph showing echinocytic human erythrocytes treated with calcium ionophore A23187 (2 μm, 15 min, 37 °C) (A). Fluorescence micrographs (mid-plane cross-section) showing human erythrocytes pretreated with Alexa 555-conjugated CTB (4 μg/ml, 60 min at RT) and anti-CTB (60 min, RT), treated with calcium ionophore A23187 (2 μm, 15 min, 37 °C), fixed with 5% PFA plus 0.01% GA (60 min, RT) (B) and stained for stomatin (C). CTB–anti-CTB–GM1 complexes accumulated at the tips of the echinocytic spiculae (arrows) (B), while stomatin accumulated in whole spiculae and at the tips of echinocytic spiculae (arrows) (C). Stomatin shown only partial colocalization with GM1 patches—signals from the same corresponding fields are indicated in (B) and (C). Scale bar = 5 μm. Adapted from Ref. [110] with permission.

Visualization of CTB–GM1 and CTB–anti-CTB–GM1 raft platform in the PM of erythroleukemia cell line K562 (Fig. 6.5A and B) and non-T, non-B acute lymphoblastic leukemia cell line, REH (Fig. 6.5C and D) indicates a few smaller patches and one big cap [135]. In comparison with erythrocytes, differences in GM1 staining may explain the distinct cytoskeleton organization in the nucleated K562 and REH cells. Moreover, CTB binding to GM1 results in endocytosis of CTB–GM1 complexes in nucleated cells [136], that is, K562 and REH cells, yet erythrocytes lack the ability to endocytosis.

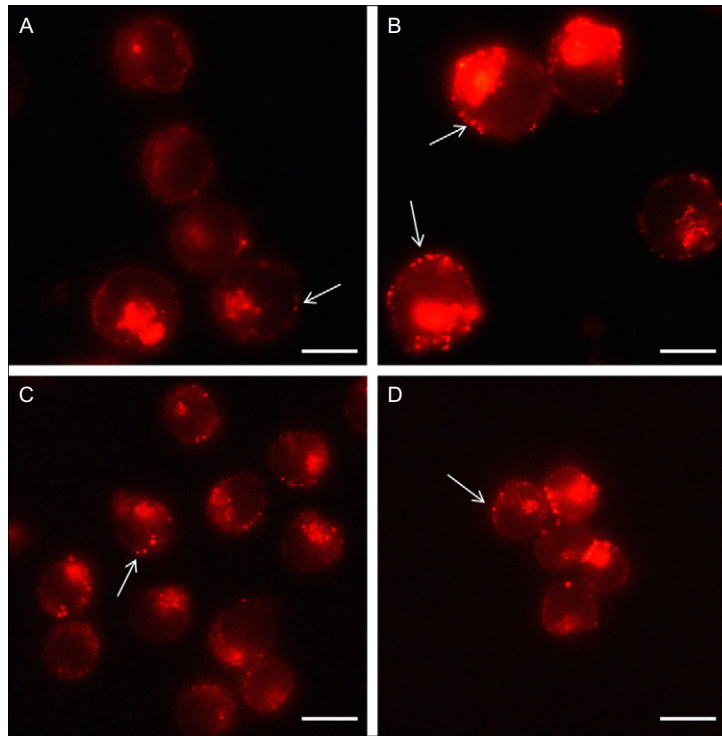

Figure 6.5 Distribution of cross-linked ganglioside GM1 in K562 and REH cells. Fluorescence micrographs (mid-plane cross-section) of Alexa 555-conjugated CTB only (4 μg/ml, 60 min at RT) or CTB plus anti-CTB treated and fixed with 5% PFA plus 0.01% GA (60 min, RT) K562 (A, B) and REH cells (C, D), respectively. Both cell types showing one large cap and a few smaller GM1 patches (arrows). Additional cross-linking using anti-CTB further accentuated capping (B, D). Scale bar = 10 μm. Adapted from Ref. [135] with permission.

To study the lipid microdomain properties, several different model systems have been applied [137–140]. The coexistence of laterally segregated cholesterol- and sphingolipids-rich (l_o) and cholesterol-poor (l_d) domains have been visualized by partitioning different fluorescent probes into both planar [141] and vesicular model systems [50,142]. Due to the suitable size (similar to or bigger than animal cell), GUVs are the most useful to visualize and study raft-like domains by optical microscopy [50,98,102,137], in contrast to small and large unilamellar vesicles with diameters of several nanometers or from 100 to 200 nm, respectively. It has been shown that cholesterol and sphingolipid domains can be much larger ($\sim$10 μm in diameter) in GUVs than in PM [50,143]. Moreover, properties of raft domains (e.g., size, shape, and lifetime) in GUVs are significantly dependent on the experimental conditions. According to the lipid rafts' definition [88], rafts are stabilized not only by lipid–lipid but also by lipid–protein mutually interactions in PM; therefore, the differences between GUVs raft-like domains and PM rafts can be explained by the presence of specific raft-associated proteins and the interaction of cytoskeleton with raft components in biological membranes [144]. Furthermore, different PM-associated events, that is, membrane budding and fission, lipid turnover within bilayer in response to the different stimuli, etc., make PM rafts much more dynamic and less predictable structures compared with raft-like domains in the model membrane systems.

7. BIOLOGICAL IMPORTANCE OF LIPID MICRODOMAINS HEALTH AND DISEASES

7.1. Lipid microdomains as signaling and sorting platforms

Lipid rafts may constitute up to 30–40% of the PM area [87,145]. The picture of rafts coming from stochastic Monte Carlo models of protein molecule dynamics in the PM shows lipid microdomains as an excellent nanochamber reaction that facilitates and maximizes protein–protein interactions [81]. The highly dynamic protein partition into lipid microdomains and the interprotein collisions explain the rafts' role in different signal transduction pathways.

Many receptors activation is regulated not only by ligand binding but also, mostly, by their association with lipid rafts. For the raft-associated receptors and many signaling molecules "location is everything" [146]. Apart

from different types of receptors, selective association of ion channels with lipid rafts is proposed as an important factor in channel activity regulation by a variety of raft-dependent mechanisms [147].

Receptors exclusion from lipid rafts or rafts structure disruption leads to the ligand-independent receptor activation, as it was shown for Fas (CD95) receptor in keratinocytes [148], or inactivation, in case of DCC (deleted in colorectal cancer) receptor, a putative tumor suppressor [117], and epidermal growth factor receptor in MDA-MB-231and MCF-7 breast cancer cell lines [61,149], or prostate cancer cell line PC-3 and LNCaP [61]. Dietary long-chain (*n*-3) PUFA, for example, eicosapentanoic acid and docosahexaenoic acid incorporates into lipid rafts and modulates their lipid structure, inducing redistribution of membrane receptor that diminishes their function dramatically [20,149].

In T cells, the most studied cell type in the field, small rafts with different receptors coalesce into the bigger platforms called immunological synapses to enable the fast recognition and elimination of target cells [72]. In resting cells, single rafts contain only a few proteins and are dispersed around the membrane. Recently, we have shown that coalescence of GM1 rafts by CTB increases the sensitivity of K562 erythroleukemic cells to natural killer cells more than 10% in comparison with the untreated cells [135]. Interestingly, a similar treatment of non-T, non-B acute lymphoblastic REH leukemia cells, insensitive to NK cell-mediated cytotoxicity, had no effect on their sensitivity to be killed, despite the almost identical GM1 rafts patching pattern (compare Fig. 6.5A, B and C, D). GM1 accumulates in an immunological synapse formed between the target and effector cells during their "molecular" recognition [133]. Therefore, we postulate that certain proteins, involved in the target cells recognition, accumulate within GM1–CTB and even more within larger GM1–CTB–anti-CTB platforms. Blocking experiments with various combinations of antibodies against receptors involved in the immunological synapse formation, namely MICA/B, ULBP-2, and/or CD59, could not inhibit the increased sensitivity mediated by CTB, indicating more complex target-effector cells' pattern recognition.

The picture of rafts as signaling and sorting platforms and their role in cancerogenesis, as a result of structural protein set changes, has been emphatically documented (see Ref. [18] for the review). Moreover, cancer cells contain a higher level of lipid rafts in opposite to their control counterparts; therefore, the result of the raft-disruptive agents in a cancer therapy would be beneficial [61].

According to the structural and functional analysis, three different types of rafts have been involved in the formation of a highly restrictive blood–brain barrier structure [150]. Scaffolding rafts are the first type associated with the interendothelial junctions and adhesion of brain endothelial cells to basal lamina. Adhesion rafts are the second type, playing a role in the immune cell adhesion and migration across brain endothelium, and transporter rafts are the third type, involved in transendothelial transport of ions and nutrients. Lipid rafts' redistribution and clustering are essential for the cell shape changes during migration across different endothelium and during cell movement, including leukocytes or carcinoma cells [151,152].

A particularly important subclass of immobile lipid microdomains are caveolae ("little caves"), the only morphologically identifiable type of lipid rafts in the majority of mammalian cell types. Caveolae are the flask-shaped invaginations of the PM, 50–100 nm in diameter, that occupy from 4% to 35% of the PM area [87] and that are distinguished from bulk/planar lipid rafts by the presence of the small transmembrane, oligomeric, cholesterol-binding protein: caveolin-1 [153]. Caveolins (caveolin-1, -2, -3) form homo-oligomers that consist approximately of 14 monomers. Each caveolin monomer binds to one cholesterol monomer, and it is linked covalently to three palmitate chains. This linkage prevents the lateral mobility of palmitate chains in the bilayer and facilitates the recruitment of the order-preferring lipids into caveolae to form stable-ordered domains. The expressions of caveolin in lymphocytes, cells which lack caveolae, promote caveolae formation [154]. Caveolae are specialized in the macromolecular vesicular transport, that is, non-clatrin-mediated endocytosis and transcytosis, and cholesterol transport, and they play an important role in the cellular signaling, that is, serving as sites for phosphatidylinositol bisphosphate hydrolysis. Certain types of enveloped and nonenveloped viruses, for example, SV40, enter cells by caveolae-mediated endocytosis [155].

Erythrocyte, during their lifespan ($\sim$ 120 days), traverses around 200 km (120 miles), completing 1.7×10^5 circulatory cycles, and looses around 20% of their surface in the egzovesiculation process. Rafts are proposed as an egzovesicle organizer in both erythroid [108,121] and nonerythroid cells [156]. At the blood bank, erythrocytes' rafts undergo structural remodeling, and depending on the storage time and egzovesiculation, it can be intensified [157].

An important signal transduction disregulation increases with age due to the cholesterol content increase in the outer leaflet of synaptic PMs [158]. The best documented lipid raft-related processes observed in aging are the T-cell receptor signaling disregulation and the cellular senescence-related signaling.

7.2. Lipid microdomains in disease pathogenesis

The role of lipid rafts in both the proper brain function and neurodegeneration, for example, Alzheimer's disease (for review, see Ref. [17]) is well established. Alteration of the asymmetric distribution of cholesterol and its high content in the exofacial leaflet of the PM [56] contributes to the formation of senile plaques consisting of the neurotoxic form the amyloid-beta protein (Aβ), one of the pathological manifestation of Alzheimer's disease. On the other hand, Aβ oligomerization was not totally prevented after the PM cholesterol depletion with MβCD [159] but was strongly ganglioside dependent [160,161]. Moreover, amyloid fibrils induced abnormal stabilization of GM1-rafts [160].

Lipid rafts from human frontal cortex are dramatically affected at an early stage of Parkinson's disease (PD) and incidental Parkinson's disease (iPD) [162]. In both PD and iPD cortices, lipid rafts exhibited significant decrease of *n*-3 and *n*-6 long-chain polyunsaturated fatty acids and significant increase in saturated acids in comparison with the control brains. Moreover, phosphatidylserine and phosphatidylinositol were increased, when the cerebrosides, sulfatides, and plasmalogen levels were significantly decreased. A dramatic alternation in the lipid profile of microdomains, which significantly increases their order, is proposed as a reason of the incorrect lipid raft signaling in both PD and iPD.

Prion diseases are infectious neurological disorders characterized by the structural conversion of the normal cellular prion protein, PrP^{c}, to its pathological isoform "scrapie" PrP^{Sc} [15,16]. PrP^{c}, like other GPI-anchored proteins, is associated with lipid rafts. In addition to GPI anchor, the N-terminal domain of PrP^{c} contains an additional raft-targeting sequence. Raft environment, that is, cholesterol, is crucial for the PrP^{c} surface localization and promotes its conversion into a pathological form [163].

Numerous studies have demonstrated that lipid microdomains in a host cell membrane can be targeted by different pathogens, including viruses, bacterial toxins, or parasites. Pathogens use protein and/or lipid component of rafts, for example, GPI-anchored protein and/or ganglioside, sphingomyelin, or cholesterol, to bind and to enter the host cell.

Lipid rafts are important participants during the binding and adhesion process of bacteria, and in their cellular entry. Moreover, lipid rafts are involved in the bacterial-mediated signaling activation [164]. CTB, a protein secreted by a Gram-negative bacterium *Vibrio cholerae*, is an example of toxin which binds in a pentavalent manner with high affinity to GM1, a known lipid raft marker [131]. The oligosaccharide portion of GM1 is responsible for the cholera toxin-specific binding.

The rafts' role in the infectious cycles of enveloped viruses is well characterized [15,16,165,166]. Viruses, similar to bacteria, can use both protein and lipid rafts' content. The well-characterized examples are viruses of influenza and HIV-1 (human immunodeficiency virus). HIV-1 uses raft-associated proteins CD4 and CXCR4 as a receptor and a co-receptor (see Ref. [167] for review). Moreover, lipid rafts are crucial for HIV-1 assembly and budding process. HIV-1 lipid bilayer has long been known to be enriched, relative to the host cell PM, in cholesterol and sphingolipids. Additionally, GPI-anchored proteins were found incorporated into HIV-1 particles; on the other hand, Gag and envelope proteins were detected in host cell rafts. Lipid rafts' disruption by MβCD markedly (70–80%) decreases virus infection and impairs HIV-1 particles production and its release efficiency.

The simian SV40 virus (SV40), a nonenveloped virus, targets lipid rafts during infection. SV40 initiates its internalization process by inducing membrane curvature through multivalent binding of its VP1 pentamers to GM1 [155]. The association of SV40 with GM1 is only sufficient to induce the dramatic membrane curvature that leads to the invagination formation in the PM and model membranes. Moreover, other polyomaviruses and certain bacterial toxins, produced by *Shiga* and *V. cholerae*, use glycosphingolipids as a cellular gate and initiate their internalization process by the creation of membrane curvature, leading to the coat-independent endocytosis [136].

Protozoan *Plasmodium falciparum* causes the most virulent form of human malaria, a disease that afflicts 200–300 million people worldwide, and kills over a million children each year, primarily in developing countries [78]. The infection of human erythrocytes by malaria parasite *P. falciparum* is a lipid raft-associated protein-dependent process [79,80,168]. The PM cholesterol depletion dramatically diminishes plasmodium cycle [169].

8. CONCLUSIONS

Over the past decade, the structure and function of lipid microdomains has been the subject of controversies, mainly because of the insufficient or conflicted results concerning their structure. In this regard, the precise physiological function of lipid microdomains seems to be elusive. Nevertheless, the increasing evidence obtained with the modern scientific approaches strongly confirms the PM compartmentalization in the living cells and its role in many cellular processes' regulation and in various diseases' pathogenesis. The great heterogeneity of lipid microdomains and their dynamic nature are facts that should be taken into account in further studies.

ACKNOWLEDGMENT

I am immensely grateful to Prof. Józef Bielawski and Prof. Henry Hägerstrand for introducing me into the fascinating research of PM.

REFERENCES

[1] S.J. Singer, G.L. Nicolson, The fluid mosaic model of the structure of cell membranes, Science 175 (1972) 720–731.
[2] R.D. Klausner, A.M. Kleinfeld, R.L. Hoover, M.J. Karnovsky, Lipid domains in membranes. Evidence derived from structural perturbations induced by free fatty acids and lifetime heterogeneity analysis, J. Biol. Chem. 255 (1980) 1286–1295.
[3] M.J. Karnovsky, A.M. Kleinfeld, R.L. Hoover, R.D. Klausner, The concept of lipid domains in membranes, J. Cell Biol. 94 (1982) 1–6.
[4] K. Simons, G. van Meer, Lipid sorting in the epithelial cells, Biochemistry 27 (1988) 6197–6202.
[5] K. Simons, E. Ikonen, Functional rafts in cell membranes, Nature 387 (1997) 569–572.
[6] D.A. Brown, E. London, Structure and function of sphingolipid- and cholesterol-rich membrane rafts, J. Biol. Chem. 275 (23) (2000) 17221–17224.
[7] L.J. Pike, Lipid rafts: heterogeneity on the high seas, Biochem. J. 378 (2004) 281–292.
[8] D. Lingwood, K. Simons, Lipid rafts as a membrane organizing principle, Science 327 (2010) 46–50.
[9] D.A. Brown, J.K. Rose, Sorting of GPI-anchored proteins to glycolipid-enriched membrane subdomains during transport to the apical cell surface, Cell 68 (1992) 533–544.
[10] K.A. Melkonian, A.G. Ostermeyer, J.Z. Chen, M.G. Roth, D.A. Brown, Role of lipid modifications in targeting proteins to detergent-resistant membrane rafts. Many raft proteins are acylated, while few are prenylated, J. Biol. Chem. 274 (1999) 3910–3917.
[11] I. Levental, M. Grzybek, K. Simons, Greasing their way: lipid modifications determine protein association with membrane rafts, Biochemistry 49 (2010) 6305–6316.
[12] A. Kusumi, K. Suzuki, Toward understanding the dynamics of membrane-raft-based molecular interactions, Biochim. Biophys. Acta 1746 (2005) 234–251.
[13] K. Simons, D. Toomre, Lipid rafts and signal transduction, Nat. Rev. Mol. Cell Biol. 1 (2000) 31–39.
[14] K. Simons, J.L. Sampaio, Membrane organization and lipid rafts, Cold Spring Harb. Perspect. Biol. 3 (10) (2011) a004697.
[15] J. Fantini, N. Garmy, R. Mahfoud, N. Yah, Lipid rafts: structure, function and role in HIV, Alzheimer's and Prion diseases, Expert Rev. Mol. Med. 4 (2002) 1–22.
[16] K. Simons, R. Ehehalt, Cholesterol, lipid rafts, and disease, J. Clin. Invest. 110 (2002) 597–603.
[17] K.S. Vetrivel, G. Thinakaran, Membrane rafts in Alzheimer's disease beta-amyloid production, Biochim. Biophys. Acta 1801 (2010) 860–867.
[18] S. Staubach, F.G. Hanisch, Lipid rafts: signalling and sorting platforms of cells and their roles in cancer, Expert Rev. Proteomics 8 (2011) 263–277.
[19] E.J. Park, M. Suh, B. Thomson, A.B. Thomson, K.S. Ramanujam, M.T. Clandinin, Dietary ganglioside decreases cholesterol content, caveolin expression and inflammatory mediators in rat intestinal microdomains, Glycobiology 15 (2005) 935–942.
[20] P. Yaqoob, S.R. Shaikh, The nutritional and clinical significance of lipid rafts, Curr. Opin. Clin. Nutr. Metab. Care 13 (2010) 156–166.
[21] A. Pralle, P. Keller, E.L. Florin, K. Simons, J.K. Horber, Sphingolipid-cholesterol rafts diffuse as small entities in the plasma membrane of mammalian cells, J. Cell Biol. 148 (2000) 997–1008.

[22] S. Mongrand, J. Morel, J. Laroche, S. Claverol, J.P. Carde, M.A. Hartmann, M. Bonneu, F. Simon-Plas, R. Lessire, J.J. Bessoule, Lipid rafts in higher plant cells: purification and characterization of Triton X-100-insoluble microdomains from tobacco, J. Biol. Chem. 279 (2004) 36277–36286.
[23] S. Mongrand, T. Stanislas, E.M. Bayer, J. Lherminier, F. Simon-Plas, Membrane rafts in plant cells, Trends Plant Sci. 15 (2010) 656–663.
[24] K. Malínská, J. Malínský, M. Opekarová, W. Tanner, Visualization of protein compartmentation within the plasma membrane of living yeast cells, Mol. Biol. Cell 14 (2003) 4427–4436.
[25] E. Lauwers, B. André, Association of yeast transporters with detergent-resistant membranes correlates with their cell-surface location, Traffic 7 (2006) 1045–1059.
[26] I. Gkantiragas, B. Brügger, E. Stüven, D. Kaloyanova, X.Y. Li, K. Löhr, F. Lottspeich, F.T. Wieland, J.B. Helms, Sphingomyelin-enriched microdomains at the Golgi complex, Mol. Biol. Cell 12 (2001) 1819–1833.
[27] R.W. Klemm, C.S. Ejsing, M.A. Surma, H.J. Kaiser, M.J. Gerl, J.L. Sampaio, Q. de Robillard, C. Ferguson, T.J. Proszynski, A. Shevchenko, K. Simons, Segregation of sphingolipids and sterols during formation of secretory vesicles at the trans-Golgi network, J. Cell Biol. 185 (2009) 601–612.
[28] A. Taute, K. Wätzig, B. Simons, C. Lohaus, H. Meyer, A. Hasilik, Presence of detergent-resistant microdomains in lysosomal membranes, Biochem. Biophys. Res. Commun. 298 (2002) 5–9.
[29] L.J. Foster, C.L. de Hoog, M. Mann, Unbiased quantitative proteomics of lipid rafts reveals high specificity for signalling factors, Proc. Natl. Acad. Sci. U.S.A. 100 (2003) 5813–5818.
[30] L. Bini, S. Pacini, S. Liberatori, S. Valensin, M. Pellegrini, R. Raggiaschi, V. Pallini, C.T. Baldari, Extensive temporally regulated reorganization of the lipid raft proteome following T-cell antigen receptor triggering, Biochem. J. 369 (2003) 301–309.
[31] Y.Z. Zheng, K.B. Berg, L.J. Foster, Mitochondria do not contain lipid rafts, and lipid rafts do not contain mitochondrial proteins, J. Lipid Res. 50 (2009) 988–998.
[32] C.N. Poston, E. Duong, Y. Cao, C.R. Bazemore-Walker, Proteomic analysis of lipid raft-enriched membranes isolated from internal organelles, Biochem. Biophys. Res. Commun. 415 (2011) 355–360.
[33] M. Cebecauer, D.M. Owen, A. Markiewicz, A.I. Magee, Lipid order and molecular assemblies in the plasma membrane of eukaryotic cells, Biochem. Soc. Trans. 37 (2009) 1056–1060.
[34] S. Munro, Lipid rafts: elusive or illusive? Cell 115 (2003) 377–388.
[35] J.F. Hancock, Lipid rafts: contentious only from simplistic standpoints, Nat. Rev. Mol. Cell Biol. 7 (2006) 456–462.
[36] D.A. Brown, E. London, Structure and origin of ordered lipid domains in biological membranes, J. Membr. Biol. 164 (1998) 103–114.
[37] D.A. Brown, E. London, Function of lipid rafts in biological membranes, Annu. Rev. Cell Dev. Biol. 14 (1998) 111–136.
[38] D. Lichtenberg, F.M. Goni, H. Heerklotz, Detergent-resistant membranes should not be identified with membrane rafts, Trends Biochem. Sci. 30 (2005) 430–436.
[39] D.A. Brown, Lipid rafts, detergent-resistant membranes, and raft targeting signals, Physiology 21 (2006) 430–439.
[40] M. Heffer-Lauc, B. Viljetić, K. Vajn, R.L. Schnaar, G. Lauc, Effects of detergents on the redistribution of gangliosides and GPI-anchored proteins in brain tissue sections, J. Histochem. Cytochem. 55 (8) (2007) 805–812.
[41] J.L. Delaunay, M. Breton, G. Trugnan, M. Maurice, Differential solubilization of inner plasma membrane leaflet components by Lubrol WX and Triton X-100, Biochim. Biophys. Acta 1778 (2008) 105–112.

[42] C.C. Domingues, A. Ciana, A. Buttafava, C. Balduini, E. de Paula, G. Minetti, Resistance of human erythrocyte membranes to Triton X-100 and C12E8, J. Membr. Biol. 227 (2009) 39–48.
[43] M. Ingelmo-Torres, K. Gaus, A. Herms, E. Gonzales-Moreno, A. Kassan, M. Bosch, T. Grewal, F. Tebar, C. Enrich, A. Pol, Triton X-100 promotes a cholesterol dependent condensation of the plasma membrane, Biochem. J. 420 (2009) 373–381.
[44] M. Sud, E. Fahy, D. Cotter, A. Brown, E.A. Dennis, C.K. Glass, A.H. Merrill Jr. R.C. Murphy, C.R. Raetz, D.W. Russell, S. Subramaniam, LMSD: LIPID MAPS structure database, Nucleic Acids Res. 35 (2007) D527–D532.
[45] P.L. Yeagle, Lipid regulation of cell membrane structure and function, FASEB J. 3 (1988) 1833–1842.
[46] Y. Lange, M.H. Swaisgood, B.V. Ramos, T.L. Steck, Plasma membranes contain half the phospholipid and 90% of the cholesterol and sphingomyelin in cultured human fibroblasts, J. Biol. Chem. 264 (1989) 3786–3793.
[47] J.N. Israelachvili, S. Marcelja, R.G. Horn, Physical principles of membrane organization, Q. Rev. Biophys. 13 (1980) 121–200.
[48] A. Rietveld, K. Simons, The differential miscibility of lipids as the basis for the formation of functional membrane rafts, Biochim. Biophys. Acta 1376 (1998) 467–479.
[49] R.C. Mateo, A.U. Acuña, J.C. Brochon, Liquid-crystalline phases of cholesterol/lipid bilayers as revealed by the fluorescence of trans-parinaric acid, Biophys. J. 68 (1995) 978–987.
[50] C. Dietrich, L.A. Bagatolli, Z.N. Volovyk, N.L. Thompson, M. Levi, K. Jacobson, E. Gratton, Lipid rafts reconstituted in model membranes, Biophys. J. 80 (2001) 1417–1428.
[51] M. Gandhavadi, D. Allende, A. Vidal, S.A. Simon, T.J. McIntosh, Structure, composition, and peptide binding properties of detergent soluble bilayers and detergent resistant rafts, Biophys. J. 82 (2002) 1469–1482.
[52] A. Ciana, C. Balduni, G. Minetti, Detergent-resistant membranes in human erythrocytes and their connection to the membrane-skeleton, J. Biosci. 30 (2005) 317–328.
[53] A.J. García-Sáez, S. Chiantia, P. Schwille, Effect of line tension on the lateral organization of lipid membranes, J. Biol. Chem. 282 (2007) 33537–33544.
[54] B. Ramsted, J.P. Slotte, Membrane properties of sphingomyelins, FEBS Lett. 531 (2002) 33–37.
[55] F. Schroeder, G. Nemecz, W.G. Wood, C. Joiner, G. Morrot, M. Ayraut-Jarrier, P.F. Devaux, Transmembrane distribution of sterol in the human erythrocyte, Biochim. Biophys. Acta 1066 (1991) 183–192.
[56] W.G. Wood, U. Igbavboa, W.E. Müller, G.P. Eckert, Cholesterol asymmetry in synaptic plasma membranes, J. Neurochem. 116 (2011) 684–689.
[57] R. Cazzola, M. Rondanelli, S. Russo-Volpe, E. Ferrari, B. Cestaro, Decreased membrane fluidity and altered susceptibility to peroxidation and lipid composition in overweight and obese female erythrocytes, J. Lipid Res. 45 (2004) 1846–1851.
[58] M. Martínez, A. Vayá, L. Gil, R. Martí, J. Dalmau, J. Aznar, The cholesterol/phospholipid ratio of the erythrocyte membrane in children with familial hypercholesterolemia. Its relationship with plasma lipids and red blood cell aggregability, Clin. Hemorheol. Microcirc. 18 (1998) 259–263.
[59] G. Ozdemirler, S. Küçük, Y. Orhan, G. Aykaç-Toker, M. Uysal, Lipid and protein oxidation in erythrocyte membranes of hypercholesterolemic subjects, Clin. Biochem. 34 (2001) 335–339.
[60] G.M. Hon, M.S. Hassan, S.J. van Rensburg, S. Abel, P. van Jaarsveld, R.T. Erasmus, T. Matsha, Red blood cell membrane fluidity in the etiology of multiple sclerosis, J. Membr. Biol. 232 (2009) 25–34.

[61] Y.C. Li, M.J. Park, S.K. Ye, C.W. Kim, Y.N. Kim, Elevated levels of cholesterol-rich lipid rafts in cancer cells are correlated with apoptosis sensitivity induced by cholesterol-depleting agents, Am. J. Pathol. 168 (2006) 1107–1118.
[62] L. Cantu, M. Corti, P. Brocca, E. Del Favero, Structural aspects of ganglioside-containing membranes, Biochim. Biophys. Acta 1788 (2009) 202–208.
[63] I. Mocchetti, Exogenous gangliosides, neuronal plasticity and repair, and the neurotrophins, Cell. Mol. Life Sci. 62 (2005) 2283–2294.
[64] M. Simons, T. Friedrichson, J.B. Schulz, M. Pitto, M. Masserini, T.V. Kurzchalia, Exogenous administration of gangliosides displaces GPI-anchored proteins from lipid microdomains in living cells, Mol. Biol. Cell 10 (1999) 3187–3196.
[65] S.R. Shaikh, M.A. Edidin, Membranes are not just rafts, Chem. Phys. Lipids 144 (2006) 1–3.
[66] E.E. Williams, Membrane lipids: what membrane physical properties are conserved during physiochemically-induced membrane restructuring? Am. Zool. 38 (1999) 280–290.
[67] L.J. Pike, Lipid rafts: bringing order to chaos, J. Lipid Res. 44 (2003) 55–67.
[68] P.F. Devaux, R. Morris, Transmembrane asymmetry and lateral domains in biological membranes, Traffic 5 (2004) 241–246.
[69] M. Grzybek, J. Kubiak, A. Łach, M. Przybyło, A.F. Sikorski, A Raft-associated species of phosphatidylethanolamine interacts with cholesterol comparably to sphingomyelin. A Langmuir-Blodgett monolayer study, PLoS One 4 (2009) e5053.
[70] M. Hayashi, Y. Shimada, M. Inomata, Y. Ohno-Iwashita, Detection of cholesterol-rich microdomains in the inner leaflet of the plasma membrane, Biochem. Biophys. Res. Commun. 335 (2006) 713–718.
[71] J.N. Israelachvili, Theoretical considerations on the asymmetric distribution of charged phospholipid molecules on the inner and outer layers of curved bilayer membranes, Biochim. Biophys. Acta 323 (1973) 659–663.
[72] P.W. Janes, S.C. Ley, A.L. Magee, Aggregation of lipid rafts accompanies signalling via the T cell antigen receptor, Cell Biol. 147 (1999) 447–461.
[73] M.D. Collins, S.L. Keller, Tuning lipid mixtures to induce or suppress domain formation across leaflets of unsupported asymmetric bilayers, Proc. Natl. Acad. Sci. U.S.A. 105 (2008) 124–128.
[74] L.J. Pike, The challenge of lipid rafts, J. Lipid Res. 50 (2009) S323–S328.
[75] U. Salzer, R. Prohaska, Stomatin, flotillin-1, and flotillin-2 are the major integral proteins of erythrocyte lipid rafts, Blood 97 (2001) 1141–1143.
[76] P.F. Lenne, L. Wawrezinieck, F. Conchonaud, O. Wurtz, A. Boned, X.J. Guo, H. Rigneault, H.T. He, D. Marguet, Dynamic molecular confinement in the plasma membrane by microdomains and the cytoskeleton meshwork, EMBO J. 25 (2006) 3245–3256.
[77] A.I. Magee, I. Parmryd, Detergent-resistant membranes and the protein composition of lipid rafts, Genome Biol. 4 (2003) a234.
[78] E.M. Pasini, M. Kirkegaard, P. Mortensen, H.U. Lutz, A.W. Thomas, M. Mann, In-depth analysis of the membrane and cytosolic proteome of red blood cells, Blood 108 (2006) 791–801.
[79] S. Lauer, J. VanWye, T. Harrison, H. McManus, B.U. Samuel, N.L. Hiller, N. Mohandas, K. Haldar, Vacuolar uptake of host components, and a role for cholesterol and sphingomyelin in malarial infection, EMBO J. 19 (2000) 3556–3564.
[80] S.C. Murphy, B.U. Samuel, T. Harrison, K.D. Speicher, D.W. Speicher, M.E. Reid, R. Prohaska, P.S. Low, M.J. Tanner, N. Mohandas, K. Haldar, Erythrocyte detergent-resistant membrane proteins: their characterization and selective uptake during malarial infection, Blood 103 (2004) 1920–1928.

[81] D.V. Nicolau, K. Burrage, R.G. Parton, J.F. Hancock, Identifying optimal lipid raft characteristics required to promote nanoscale protein-protein interactions on the plasma membrane, Mol. Cell. Biol. 26 (2006) 313–323.
[82] T.J. McIntosh, A. Vidal, S.A. Simon, Sorting of lipids and transmembrane peptides between detergent-soluble bilayers and detergent-resistant rafts, Biophys. J. 85 (2003) 1656–1666.
[83] A. Arni, S.A. Keilbaugh, A.G. Ostermeyer, D.A. Brown, Association of GAP-43 with detergent-resistant membranes requires two palmitoylated cysteine residues, J. Biol. Chem. 273 (43) (1998) 28478–28485.
[84] Y.Z. Zheng, C. Boscher, K.L. Inder, M. Fairbank, D. Loo, M.M. Hill, I.R. Nabi, L.J. Foster, Differential impact of caveolae and caveolin-1 scaffolds on the membrane raft proteome, Mol. Cell. Proteomics 10 (2011) M110.007146.
[85] T. Nebl, K.N. Pestonjamasp, J.D. Leszyk, J.L. Crowley, S.W. Oh, E.J. Luna, Proteomic analysis of a detergent-resistant membrane skeleton from neutrophil plasma membranes, J. Biol. Chem. 277 (2002) 43399–43409.
[86] M.C. Giocondi, V. Vié, E. Lesniewska, J.P. Goudonnet, C. Le Grimellec, In situ imaging of detergent-resistant membranes by atomic force microscopy, J. Struct. Biol. 131 (2000) 38–43.
[87] R.G. Parton, Caveolae—from ultrastructure to molecular mechanisms, Nat. Rev. Mol. Cell Biol. 4 (2003) 162–167.
[88] L.J. Pike, Rafts defined: a report on the keystone symposium on lipid rafts and cell function, J. Lipid Res. 47 (2006) 1597–1598.
[89] K.S. Koumanov, C. Tessier, A.B. Momchilova, D. Rainteau, C. Wolf, P.J. Quinn, Comparative lipid analysis and structure of detergent-resistant membrane raft fractions isolated from human and ruminant erythrocytes, Arch. Biochem. Biophys. 434 (2005) 150–158.
[90] E.B. Babiychuk, A. Draeger, Biochemical characterization of detergent-resistant membranes: a systematic approach, Biochem. J. 397 (2006) 407–416.
[91] X. Chen, R.J. Morris, M.J. Lawrence, P.J. Quinn, The isolation and structure of membrane lipid rafts from rat brain, Biochimie 89 (2007) 192–196.
[92] X. Chen, A. Jen, A. Warley, M.J. Lawrence, P.J. Quinn, R.J. Moris, Isolation at physiological temperature of detergent-resistant membranes with properties expected of lipid rafts: the influence of buffer composition, Biochem. J. 417 (2009) 525–533.
[93] C.C. Domingues, A. Ciana, A. Buttafava, B.R. Casadei, C. Balduini, E. de Paula, G. Minetti, Effect of cholesterol depletion and temperature on the isolation of detergent-resistant membranes from human erythrocytes, J. Membr. Biol. 234 (2010) 195–205.
[94] H. Heerklotz, Triton promotes domain formation in lipid raft mixtures, Biophys. J. 83 (2002) 2693–2701.
[95] H. Heerklotz, H. Szadkowska, T. Anderson, J. Seelig, The sensitivity of lipid domains to small perturbations demonstrated by the effect of Triton, J. Mol. Biol. 329 (2003) 793–799.
[96] S. Schuck, M. Honsho, K. Ekroos, A. Shevchenko, K. Simons, Resistance of cell membranes to different detergents, Proc. Natl. Acad. Sci. U.S.A. 100 (2003) 5795–5800.
[97] L.H. Chamberlain, Detergents as tools for the purification and classification of lipid rafts, FEBS Lett. 559 (2004) 1–5.
[98] G. Staneva, M. Seigneuret, K. Koumanov, G. Trugnan, M.I. Angelova, Detergents induce raft-like domains budding and fission from giant unilamellar heterogeneous vesicles: a direct microscopy observation, Chem. Phys. Lipids 136 (1) (2005) 55–66.

[99] C. Arnulphi, J. Sot, M. García-Pacios, J.L. Arrondo, A. Alonso, F.M. Goñi, Triton X-100 partitioning into sphingomyelin bilayers at subsolubilizing detergent concentrations: effect of lipid phase and a comparison with dipalmitoylphosphatidylcholine, Biophys. J. 93 (2007) 3504–3514.
[100] A.E. Garner, D.A. Smith, N.M. Hooper, Visualisation of detergent solubilisation of membranes: implications for the isolation of rafts, Biophys. J. 94 (2008) 1326–1340.
[101] L.J. Pike, X. Han, K.N. Chung, R.W. Gross, Lipid rafts are enriched in arachidonic acid and plasmenylethanolamine and their composition is independent of caveolin-1 expression: a quantitative electrospray ionization/mass spectrometric analysis, Biochemistry 41 (2002) 2075–2088.
[102] A.G. Ayuyan, F.S. Cohen, Raft composition at physiological temperature and pH in the absence of detergents, Biophys. J. 94 (2008) 2654–2666.
[103] K. Klappe, J.W. Hinrichs, B.J. Kroesen, H. Sietsma, J.W. Kok, MRP1 and glucosylceramide are coordinately over expressed and enriched in rafts during multidrug resistance acquisition in colon cancer cells, Int. J. Cancer 110 (2004) 511–522.
[104] J.W. Hinrichs, K. Klappe, M. van Riezen, J.W. Kok, Drug resistance-associated changes in sphingolipids and ABC transporters occur in different regions of membrane domains, J. Lipid Res. 46 (2005) 2367–2376.
[105] E. Cerf, R. Gasper, J.D. Belani, S. Rychnovsky, X.B. Chang, F. Buyse, J.M. Ruysschaert, Multidrug resistance protein 1 is not associated to detergent-resistant membranes, Biochem. Biophys. Res. Commun. 355 (2007) 1025–1030.
[106] C. Marbeuf-Gueye, V. Stierle, P. Sudwan, M. Salerno, A. Garnier-Suillerot, Perturbation of membrane microdomains in GLC4 multidrug-resistant lung cancer cells—modification of ABCC1 (MRP1) localization and functionality, FEBS J. 274 (2007) 1470–1480.
[107] M. Bobrowska-Hägerstrand, A. Wróbel, L. Mrówczyńska, T. Söderström, H. Hägerstrand, Modulation of MRP1-like efflux activity in human erythrocytes caused by membrane perturbing agents, Mol. Membr. Biol. 20 (2003) 255–259.
[108] H. Hägerstrand, L. Mrówczyńska, U. Salzer, R. Prohaska, K.A. Michelsen, V. Kralj-Iglič, A. Iglič, Curvature-dependent lateral distribution of raft markers in the human erythrocyte membrane, Mol. Membr. Biol. 23 (2006) 277–288.
[109] L. Mrówczyńska, H. Hägerstrand, Patching of ganglioside M1 in human erythrocytes—distribution of CD47 and CD59 in patched and curved membrane, Mol. Membr. Biol. 25 (2008) 258–265.
[110] L. Mrówczyńska, U. Salzer, S. Perutková, A. Iglič, H. Hägerstrand, Echinophilic proteins stomatin, sorcin, and synexin locate outside ganglioside M1 (GM1) patches in the erythrocyte membrane, Biochem. Biophys. Res. Commun. 401 (2010) 396–400.
[111] L. Mrówczyńska, U. Salzer, A. Iglič, H. Hägerstrand, Curvature factor and membrane solubilisation, with particular reference to membrane rafts, Cell Biol. Int. 269 (10) (2011) 991–995.
[112] A. Tsamaloukas, H. Szadkowska, H. Heerklotz, Thermodynamic comparison of the interactions of cholesterol with unsaturated phospholipid and sphingomyelins, Biophys. J. 90 (2006) 4479–4487.
[113] A. Tsamaloukas, H. Szadkowska, H. Heerklotz, Nonideal mixing in multicomponent lipid/detergent systems, J. Phys. Condens. Matter 18 (2006) 1125–1138.
[114] M.P. Sheetz, S.J. Singer, Biological membranes as bilayer couples. A molecular mechanism of drug-erythrocyte interactions, Proc. Natl. Acad. Sci. U.S.A. 71 (1974) 4457–4461.
[115] S. Ilangumaran, D.C. Hoessli, Effects of cholesterol depletion by cyclodextrin on the sphingolipid microdomains of the plasma membrane, Biochem. J. 335 (1998) 433–440.

[116] L.J. Pike, L. Casey, Cholesterol levels modulate EGF receptor-mediated signalling by altering receptor function and trafficking, Biochemistry 41 (2002) 10315–10322.
[117] C. Furne, V. Corset, Z. Hérincs, N. Cahuzac, A.O. Hueber, P. Mehlen, The dependence receptor DCC requires lipid raft localization for cell death signaling, Proc. Natl. Acad. Sci. U.S.A. 103 (2006) 4128–4133.
[118] Y. Zhang, X. Li, K.A. Becker, E. Gulbins, Ceramide-enriched membrane domains—structure and function, Biochim. Biophys. Acta 1788 (2009) 178–183.
[119] B. Stancevic, R. Kolesnick, Ceramide-rich platforms in transmembrane signaling, FEBS Lett. 584 (2010) 1728–1740.
[120] K. Kamata, S. Manno, M. Ozaki, Y. Takakuwa, Functional evidence for presence of lipid rafts in erythrocyte membranes: Gsalpha in rafts is essential for signal transduction, Am. J. Hematol. 83 (2008) 371–375.
[121] U. Salzer, P. Hinterdorfer, U. Hunger, C. Borken, R. Prohaska, $Ca^{(++)}$-dependent vesicle release from erythrocytes involves stomatin-specific lipid rafts, synexin (annexin VII), and sorcin, Blood 99 (2002) 2569–2577.
[122] G.H. Borner, D.J. Sherrier, T. Weimar, L.V. Michaelson, N.D. Hawkins, A. Macaskill, J.A. Napier, M.H. Beale, K.S. Lilley, P. Dupree, Analysis of detergent-resistant membranes in Arabidopsis. Evidence for plasma membrane lipid rafts, Plant Physiol. 137 (2005) 104–116.
[123] P. Janich, D. Corbeil, GM1 and GM3 gangliosides highlight distinct lipid microdomains within the apical domain of epithelial cells, FEBS Lett. 581 (2007) 1783–1787.
[124] A. Fujita, J. Cheng, M. Hirakawa, K. Furukawa, S. Kusunoki, T. Fujimoto, Gangliosides GM1 and GM3 in the living cell membrane form clusters susceptible to cholesterol depletion and chilling, Mol. Biol. Cell 18 (2007) 2112–2122.
[125] B.S. Wilson, S.L. Steinberg, K. Liederman, J.R. Pfeiffer, Z. Surviladze, J. Zhang, L.E. Samelson, L.H. Yang, P.G. Kotula, J.M. Oliver, Markers for detergent-resistant lipid rafts occupy distinct and dynamic domains in native membranes, Mol. Biol. Cell 15 (2004) 2580–2592.
[126] Y. Nagatsuka, M. Hara-Yokoyama, T. Kasama, M. Takekoshi, F. Maeda, S. Ihara, S. Fujiwara, E. Ohshima, K. Ishii, T. Kobayashi, K. Shimizu, Y. Hirabayashi, Carbohydrate-dependent signalling from the phosphatidylglucoside-based microdomain induces granulocytic differentiation of HL60 cells, Proc. Natl. Acad. Sci. U.S.A. 100 (2003) 7454–7459.
[127] C. Eggeling, C. Ringemann, R. Medda, G. Schwarzmann, K. Sandhoff, S. Polyakova, V.N. Belov, B. Hein, C. von Middendorff, A. Schönle, S.W. Hell, Direct observation of the nanoscale dynamics of membrane lipids in living cells, Nature 457 (2009) 1159–1162.
[128] L.M. Loura, M. Prieto, FRET in membrane biophysics: an overview, Front. Physiol. 2 (2011) a82.
[129] A.K. Kenworthy, Fluorescence recovery after photobleaching studies of lipid rafts, Methods Mol. Biol. 398 (2007) 179–192.
[130] A. Kusumi, I. Koyama-Honda, K. Suzuki, Molecular dynamics and interactions for creation of stimulation-induced stabilized rafts from small unstable steady-state rafts, Traffic 5 (2004) 213–230.
[131] T. Harder, P. Scheiffele, P. Verkade, K. Simons, Lipid domain structure of the plasma membrane revealed by patching of membrane components, J. Cell Biol. 141 (1998) 929–942.
[132] E.L. Brown, D.S. Lyles, A novel method for analysis of membrane microdomains: vesicular stomatitis virus glycoprotein microdomains change in size during infection, and those outside of budding sites resemble sites of virus budding, Virology 310 (2003) 343–358.

[133] S. Thomas, A. Preda-Pais, S. Casares, T.D. Brumeanu, Analysis of lipid rafts in T cells, Mol. Immunol. 41 (2004) 399–409.
[134] E. Kiss, P. Nagy, A. Balogh, J. Szöllosi, J. Matkó, Cytometry of raft and caveola membrane microdomains: from flow and imaging techniques to high throughput screening assays, Cytometry A 73 (2008) 599–614.
[135] L. Mrówczyńska, M. Bobrowska-Hägerstrand, H. Hägerstrand, C. Lindqvist, Increased sensitivity of cholera toxin B treated K562 cells to natural killer cells, Cell. Immunol. 269 (2011) 1–4.
[136] D.J. Chinnapen, H. Chinnapen, D. Saslowsky, W.I. Lencer, Rafting with cholera toxin: endocytosis and trafficking from plasma membrane to ER, FEMS Microbiol. Lett. 266 (2007) 129–137.
[137] A.T. Hammond, F.A. Heberle, T. Baumgart, D. Holowka, B. Baird, G.W. Feigenson, Crosslinking a lipid raft component triggers liquid ordered-liquid disordered phase separation in model plasma membranes, Proc. Natl. Acad. Sci. U.S.A. 102 (2005) 6320–6325.
[138] Y.H. Chan, S.G. Boxer, Model membrane systems and their applications, Curr. Opin. Chem. Biol. 11 (2007) 581–587.
[139] J.R. Silvius, I.R. Nabi, Fluorescence-quenching and resonance energy transfer studies of lipid microdomains in model and biological membranes, Mol. Membr. Biol. 23 (2006) 5–16.
[140] M.T. Stöckl, A. Herrmann, Detection of lipid domains in model and cell membranes by fluorescence lifetime imaging microscopy, Biochim. Biophys. Acta 1798 (2010) 1444–1456.
[141] S.L. Veatch, S.L. Keller, Organization in lipid membranes containing cholesterol, Phys. Rev. Lett. 89 (2002) 268101.
[142] S.L. Veatch, S.L. Keller, Separation of liquid phases in giant vesicles of ternary mixtures of phospholipids and cholesterol, Biophys. J. 85 (2003) 3074–3083.
[143] J. Fan, M. Sammalkorpi, M. Haataja, Formation and regulation of lipid microdomains in cell membranes: theory, modeling, and speculation, FEBS Lett. 584 (2010) 1678–1684.
[144] H.J. Kaiser, D. Lingwood, I. Levental, J.L. Sampaio, L. Kalvodova, L. Rajendran, K. Simons, Order of lipid phases in model and plasma membranes, Proc. Natl. Acad. Sci. U.S.A. 106 (2009) 16645–16650.
[145] A. Landry, R. Xavier, Isolation and analysis of lipid rafts in cell-cell interactions, Methods Mol. Biol. 341 (2006) 251–282.
[146] M. Dykstra, A. Cherukuri, H.W. Sohn, S.J. Tzeng, S.K. Pierce, Location is everything: lipid rafts and immune cell signaling, Annu. Rev. Immunol. 21 (2003) 457–481.
[147] C. Dart, Lipid microdomains and the regulation of ion channel function, J. Physiol. 588 (2010) 3169–3178.
[148] R. Gniadecki, Depletion of membrane cholesterol causes ligand-independent activation of Fas and apoptosis, Biochem. Biophys. Res. Commun. 320 (2004) 165–169.
[149] P.D. Schley, D.N. Brindley, C.J. Field, (n-3) PUFA alter raft lipid composition and decrease epidermal growth factor receptor levels in lipid rafts of human breast cancer cells, J. Nutr. 137 (2007) 548–553.
[150] A. Dodelet-Devillers, R. Cayrol, J. van Horssen, A.S. Haqqani, H.E. de Vries, B. Engelhardt, J. Greenwood, A. Prat, Functions of lipid raft membrane microdomains at the blood-brain barrier, J. Mol. Med. 87 (2009) 765–774.
[151] R.M. Larive, L. Baisamy, S. Urbach, P. Coopman, N. Bettache, Cell membrane extensions, generated by mechanical constraint, are associated with a sustained lipid raft patching and an increased cell signaling, Biochim. Biophys. Acta 1798 (2010) 389–400.
[152] S. Mañes, R. Ana Lacalle, C. Gómez-Moutón, C. Martínez-A, From rafts to crafts: membrane asymmetry in moving cells, Trends Immunol. 24 (2003) 320–326.

[153] A.W. Cohen, R. Hnasko, W. Schubert, M.P. Lisanti, Role of caveolae and caveolins in health and disease, Physiol. Rev. 84 (2004) 1341–1379.
[154] A.M. Fra, E. Williamson, K. Simons, R.G. Parton, De novo formation of caveolae in lymphocytes by expression of VIP21-caveolin, Proc. Natl. Acad. Sci. U.S.A. 92 (1995) 10339–10343.
[155] H. Ewers, W. Römer, A.E. Smith, K. Bacia, S. Dmitrieff, W. Chai, R. Mancini, J. Kartenbeck, V. Chambon, L. Berland, A. Oppenheim, G. Schwarzmann, T. Feizi, P. Schwille, P. Sens, A. Helenius, L. Johannes, GM1 structure determines SV40-induced membrane invagination and infection, Nat. Cell Biol. 12 (2010) 11–18.
[156] A.M. Marzesco, M. Wilsch-Bräuninger, V. Dubreuil, P. Janich, K. Langenfeld, C. Thiele, W.B. Huttner, D. Corbeil, Release of extracellular membrane vesicles from microvilli of epithelial cells is enhanced by depleting membrane cholesterol, FEBS Lett. 583 (2009) 897–902.
[157] A.G. Kriebardis, M.H. Antonelou, K.E. Stamoulis, E. Economou-Petersen, L.H. Margaritis, I.S. Papassideri, Storage-dependent remodeling of the red blood cell membrane is associated with increased immunoglobulin G binding, lipid raft rearrangement, and caspase activation, Transfusion 47 (2007) 1212–1220.
[158] Y. Ohno-Iwashita, Y. Shimada, M. Hayashi, M. Inomata, Plasma membrane microdomains in aging and disease, Geriatr. Gerontol. Int. 10 (2010) S41–S52.
[159] S. Wada, M. Morishima-Kawashima, Y. Qi, H. Misono, Y. Shimada, Y. Ohno-Iwashita, Y. Ihara, Gamma-secretase activity is present in rafts but is not cholesterol-dependent, Biochemistry 42 (2003) 13977–13986.
[160] S.I. Kim, J.S. Yi, Y.G. Ko, Amyloid β oligomerization is induced by brain lipid rafts, J. Cell. Biochem. 99 (2006) 878–889.
[161] M. Bucciantini, D. Nosi, M. Forzan, E. Russo, M. Calamai, L. Pieri, L. Formigli, F. Quercioli, S. Soria, F. Pavone, J. Savistchenko, R. Melki, M. Stefani, Toxic effects of amyloid fibrils on cell membranes: the importance of ganglioside GM1, FASEB J. 26 (2012) 818–831.
[162] N. Fabelo, V. Martín, G. Santpere, R. Marín, L. Torrent, I. Ferrer, M. Díaz, Severe alterations in lipid composition of frontal cortex lipid rafts from Parkinson's disease and incidental Parkinson's disease, Mol. Med. 17 (2011) 1107–1118.
[163] S. Gilch, C. Kehler, H.M. Schätzl, The prion protein requires cholesterol for cell surface localization, Mol. Cell. Neurosci. 31 (2006) 346–353.
[164] F. Lafont, F.G. van der Goot, Bacterial invasion via lipid rafts, Cell. Microbiol. 7 (2005) 613–620.
[165] A. Ono, E.O. Freed, Plasma membrane rafts play a critical role in HIV-1 assembly and release, Proc. Natl. Acad. Sci. U.S.A. 98 (2001) 13925–13930.
[166] A. Ono, Relationships between plasma membrane microdomains and HIV-1 assembly, Biol. Cell 102 (2010) 335–350.
[167] A.A. Waheed, E.O. Freed, Lipids and membrane microdomains in HIV-1 replication, Virus Res. 143 (2009) 162–176.
[168] S.C. Murphy, N.L. Hiller, T. Harrison, J.W. Lomasney, N. Mohandas, K. Haldar, Lipid rafts and malaria parasite infection of erythrocytes, Mol. Membr. Biol. 23 (2006) 81–88.
[169] E. Nagao, K.B. Seydel, J.A. Dvorak, Detergent-resistant erythrocyte membrane rafts are modified by a *Plasmodium falciparum* infection, Exp. Parasitol. 102 (2002) 57–59.

CHAPTER SEVEN

Polyelectrolytes and Surfactants in Aqueous Solutions: From Dilute to Concentrated Systems

Ksenija Kogej[1]
Department of Chemistry and Biochemistry, Faculty of Chemistry and Chemical Technology, University of Ljubljana, Ljubljana, Slovenia
[1]Corresponding author: e-mail address: ksenija.kogej@fkkt.uni-lj.si

Contents

1. Introduction 200
2. Polyelectrolytes 202
3. Surfactants 205
4. Mixed PEL–Surfactant Solutions 207
   4.1 General concepts 207
   4.2 Binding isotherms and critical association concentration 209
   4.3 Solubility of PSCs 213
   4.4 Size of PEL–surfactant complexes 219
   4.5 Structure of PEL–Surfactant Complexes 223
   4.6 Effect of bound surfactant on PEL properties 229
5. Relation with Hydrophobically Associating Polymers 232
6. Concluding Remarks 233
References 234

Abstract

Polyelectrolyte–surfactant mixtures have attracted considerable research interest in the past decades due to their widespread appearance in nature and technology. Many different systems have been studied with the purpose to identify the key features that effect their behavior and performance. In this chapter, we review our studies on polyelectrolyte–surfactant interactions in a particular system involving a strong polyelectrolyte, poly(styrenesulfonate), PSS, and oppositely charged surfactants. The interest in PSS is due to its concealed hydrophobic character related to benzene rings in its functional groups. Owing to this feature, PSS interacts strongly with oppositely charged surfactants through electrostatic and additional hydrophobic interactions, which involve solubilization of hydrophobic groups of PSS in surfactant micelles. We demonstrate that this characteristic has an important effect on binding isotherms, critical association concentration values, and free energy changes associated with the binding process, so as on the solubility and structure of the ensuing polyelectrolyte–surfactant complexes (PSCs). Good solution stability of PSCs involving PSS enabled the determination of several solution properties of soluble PSCs.

Advances in Planar Lipid Bilayers and Liposomes, Volume 16
ISSN 1554-4516
http://dx.doi.org/10.1016/B978-0-12-396534-9.00007-6

1. INTRODUCTION

Polyelectrolytes (PELs), surfactants, and their mixtures are ubiquitous in nature and technology. Many naturally occurring macromolecules are PELs, for example, nucleic acids, polysaccharides, polypeptides, and proteins. Due to their ionizing ability and polarity, they are obviously water soluble, although their backbone may be hydrophobic, for example, a hydrocarbon chain. Water solubility is crucial in biological systems because life on a molecular level is based on processes taking place in aqueous environment. The role of PELs in living organisms ranges from simple actions (e.g., imparting high viscosity, inducing swelling) to more advanced functions (e.g., storing and transmitting biological information). Similarly, the second group of compounds, that is, surfactants (an abbreviated name for surface active agents), is abundant in all living organisms. Besides surface activity, a characteristic property of surfactants is self-association with micelles and other aggregates. Surfactants of natural origin are usually termed polar lipids. Their function in biological environment is to provide water solubility to hydrophobic substances (a phenomenon referred to as solubilization), to act as emulsifiers, dispersants, to modify surfaces, and they are constituent parts of various natural membranes and much more than that.

In addition to these unique properties and functions of PELs and surfactants, both species are often encountered jointly in living organisms and in various fields of application. When present together in aqueous solutions, they can reveal rather unique interaction effects. In particular, if they are oppositely charged, their mutual attraction is very strong, leading to association and formation of PEL–surfactant complexes (PSCs). PSCs are composed of aggregates in which surfactant is self-associated into micelle-like forms that are interconnected by the polyion chain. Surfactant molecules are thus bound by the polyion collectively, not individually as is the case with simple ions, and form a very strong complex with the PEL. In the biological context, the existence of lipoprotein complexes is known from the middle of the previous century [1], and since then, PEL (or more generally polymer)–surfactant complexes have been extensively investigated [2,3]. A recent review on DNA interactions with polymers and surfactants highlights the biological significance of the field [4]. It is thus undoubtedly important to understand interactions between PELs and surfactants and to be able to predict the effect of various parameters on them.

Naturally occurring PELs have complex structures. In addition to hydrophilic ionizable groups, they may also contain hydrophobic groups that are

needed for their specific biological function but on the other hand limit their solubility in water and lead to characteristic chain conformations (e.g., helical) or processes in solution (e.g., coil-to-globule transitions). Lipids too may be structurally and functionally very diverse. Therefore, one usually aims at studying simpler model systems in order to make the interpretation of results easier and to be able to relate them in a straightforward manner to structural properties of the components and to external conditions (e.g., solution ionic strength or pH, temperature, concentration).

In this chapter, we outline basic principles that govern interactions and formation of (self-)associated, and possibly highly ordered, structures in PEL–surfactant systems by using as an example a synthetic PEL with hydrophobic functional groups to mimic similar features of biological polymers. The selected PEL is poly(styrenesulfonate), PSS, a strong anionic PEL with aromatic benzene rings carrying the charged sulfonate groups, which assign the poly(styrenesulfonate anion), PSS^-, a concealed hydrophobic character. Pure PSS solutions with no added amphiphilic molecules demonstrate behavior typical for highly charged PELs, for example, high solution viscosity and strong binding of oppositely charged ions [5–8]. The hydrophobicity of aromatic side groups is not revealed in solution behavior of NaPSS. For example, viscosity of a sodium salt solution of PSS, NaPSS, does not indicate any characteristic chain conformations (helical, compact coil) or self-associated states that would arise from this structural feature [8–10]. NaPSS solution behavior differs considerably from that of so-called hydrophobically associating polymers, HAPs, which contain nonpolar hydrocarbon chains as side groups. It is well known that HAPs exhibit unusual rheological properties as a consequence of the formation of amphiphilic aggregates in polar media [11]. However, the concealed hydrophobic character of NaPSS comes into effect when "external" hydrophobic domains are present in the system, as is the case in mixed solutions with surfactants when surfactant molecules form self-associated structures having a hydrophobic core. It was recognized early by Kwak *et al.* [12] that styrene sulfonate, SS^-, groups of the PSS chain are incorporated into the hydrophobic interior of such surfactant aggregates. Later, it was also shown that this specific interaction strongly reduces surfactant aggregation numbers relative to those of free micelles [13–15], which may consequently affect the microstructure of the aggregates [16–18]. It will be demonstrated in this chapter that the highlighted hydrophobic involvement of the polyion in PSC formation strongly marks interactions of cationic surfactants with the PSS^- anion [19,20] and properties of the ensuing complex [16,20,21].

As surfactants, our focus are single chain and oppositely charged (cationic) surfactants of two types: alkylpyridinium salts, abbreviated as C_nPX, and alkyltrimethylammonium salts, abbreviated as C_nTAX, where n denotes the number of carbon (C) atoms in the surfactant's alkyl chain and X the halide counterion (X = C and B for Cl^- and Br^- ions, respectively). The usual abbreviations for the corresponding surfactants with dodecyl and hexadecyl (or cetyl) chains with either chloride or bromide as counterion are DPC (DPB) and CPC (CPB) or DTAC (DTAB) and CTAC (CTAB), respectively. These surfactants are widely used in studies of various PEL–surfactant mixtures, which offers good basis for mutual comparison. Besides, their self-association properties, in particular, their critical micelle concentration values, are comparable when the same chain length and counterion are in question [20].

We will start with the description of some basic features of pure PEL and surfactant solutions that are important to understand the behavior in mixed systems. The main aim of this chapter is to present characteristic phenomena in dilute PEL–surfactant mixtures and also in more concentrated dense phases that are interesting from the application viewpoint.

2. POLYELECTROLYTES

PELs are macromolecules composed of *monomer* groups with substituents that adopt charges when dissolved in an appropriate solvent [5–8]. Herein, we restrict our treatment to linear PELs, excluding branched or cross-linked ones, in polar solvents. In water (the most abundant polar solvent), linear PELs dissociate into long polyions (or macroions) and low molecular weight and small counterions (of opposite charge to the polyion) in sufficient number to secure the condition of electroneutrality. A schematic illustration of an anionic PEL in solution is given in Fig. 7.1A. With no additional electrolyte present, that is, in pure water, polyions and their accompanying counterions are the only charged species in solution. However, in practice, there are nearly always other solutes present as well, most often low molecular weight salts that contribute additional counterions and also coions, that is ions of the same sign as the polyion.

Polyions contain covalently linked anionic or cationic groups and acquire a huge charge upon ionization, whereas counterions are usually mono- or divalent and greatly outnumber the polyions. The resulting asymmetry in charge and size is the most important feature of PELs that defines their solution properties. The decisive parameter in controlling solution behavior of

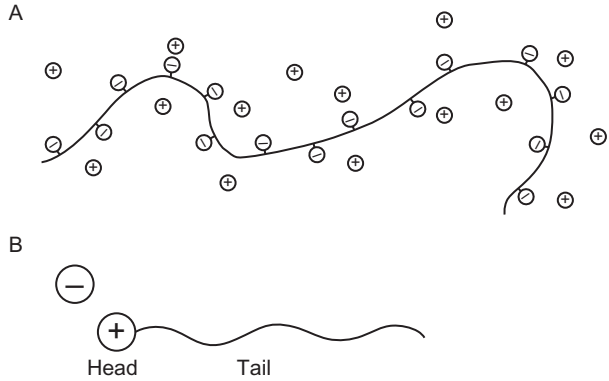

Figure 7.1 Schematic presentation of (A) a linear anionic polyelectrolyte together with its counterions and of (B) a single hydrocarbon chain cationic surfactant (with its counterion) in aqueous solution. Note that drawings are not in proportion one with the other.

PELs is the polyion's charge density, which is determined by the average distance between charged groups on the polymer chain and by their valency. Similar to simple electrolytes, PELs can be classified as either strong, having all functional groups ionized, or weak, having only a certain fraction of groups ionized, which is most commonly achieved by changing the solution's pH. Strong PELs typically contain sulfonate (e.g., NaPSS, carrageenans) or phosphate groups (e.g., RNA, DNA, polyphosphates), whereas weak PELs often contain carboxyl groups (e.g., alginate, pectate, hyaluronate, sodium poly(acrylate), NaPA).

Repulsion between like charges along the polyion chain leads to highly extended chain conformations and results in high viscosity of salt-free PEL solutions. Viscosity depends strongly on the ionic strength of the medium. Addition of electrolytes screens the repulsion between polyion charges and thus contributes to chain contraction, which in turn leads to a decrease in viscosity. The effect on viscosity of adding small amounts of NaCl to an aqueous NaPSS solution at 25 °C is demonstrated in Fig. 7.2 [22]. The polyion concentration, c_P, is $c_P = 5 \times 10^{-4}$ mol of monomer groups per volume (usually abbreviated as monomol/L), which is frequently used in studies of PEL–surfactant interactions.

High electrostatic field around the polyion attracts counterions and repels coions. Thus, an ion atmosphere is created around the polyion. This situation is known as the electric double layer, which is composed of a fixed charge on the polyion surface and an equal but opposite charge of ions distributed in the surrounding solution in accordance with the action of electrostatic forces and Brownian motion of particles. A common way to calculate

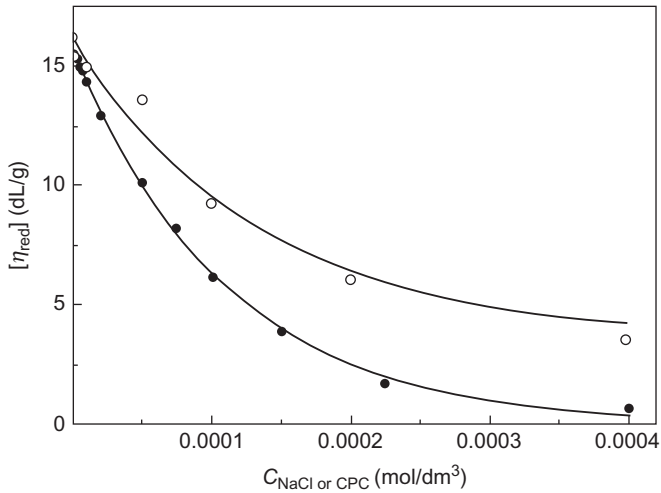

Figure 7.2 The effect of NaCl (open circles) and CPC (filled circles) on the reduced viscosity, $[\eta_{red}]$, of an aqueous NaPSS solution at 25 °C: $c_p = 5 \times 10^{-4}$ monomol/L.

the distribution of ions in PEL solution is to use the Poisson–Boltzmann equation for the cylindrical symmetry, which is the most suitable approximation for chain geometry in salt-free linear PEL solutions. A schematic presentation of a cylindrical electric double layer can be found in Ref. [23]. In the scope of this chapter, we avoid reporting equations and approaches how to solve them, as these topics are extensively treated in various text books covering the field of PEL research and also in this journal [5–8,23]. An example of counterion distribution around a cylindrical polyion is given in Fig. 7.3. It shows the variation of the local concentration, c, of monovalent counterions with the radial distance r from the polyion axis in a salt-free PEL solution (c_{av} is the average concentration of monovalent counterions in solution). Parameters used in the calculation procedure correspond to aqueous NaPSS solutions with $c_p = 5 \times 10^{-4}$ monomol/L [19,20].

The results demonstrate a well-known phenomenon termed ion binding, that is, a pronounced accumulation of counterions in the vicinity of the polyion, which is a consequence of strong electrostatic attraction between highly charged polyion and oppositely charged counterions. The concentration of counterions close to the polyion may exceed their average concentration in solution by a factor of 1000 and more, depending on the polyion's charge density and counterion valency and size. For the purpose of this calculation, the size of monovalent counterions, given as their radius r ($= 0.3$ nm), was estimated from the size of the charged head group of

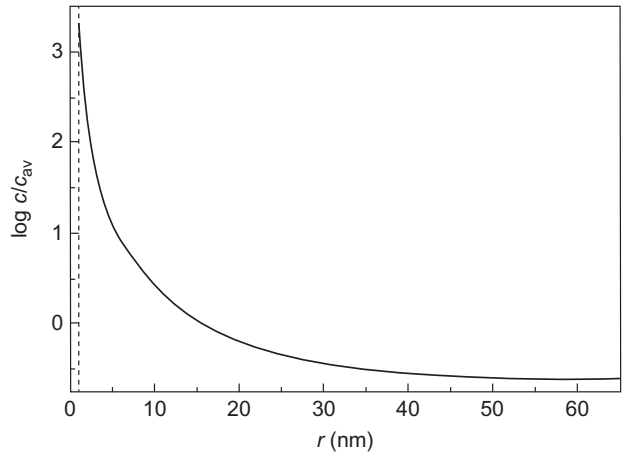

Figure 7.3 The variation of the concentration ratio, c/c_{av}, of monovalent counterions (with a radius 0.3 nm) with the radial distance r from the polyion axis (c is the local and c_{av} is the average concentration of counterions in solution). The dashed line indicates the distance of closest approach of the counterion to the polyion axis. Parameters used in the calculation correspond to aqueous solutions of poly(styrenesulfonate) anion without added salt at 25 °C. Polyelectrolyte concentration is $c_p = 5 \times 10^{-4}$ monomol/L.

alkylpyridinium surfactants [24]. Clearly, the surfactant counterion would approach the polyion with its charged group and not with its hydrocarbon tail. The hydrophobic character of the surfactant counterion was not taken into consideration in this calculation.

3. SURFACTANTS

Surfactants (S) are amphiphilic molecules composed of two well-separated parts of different polarities (or water affinity) in the same molecule (Fig. 7.1B): a hydrophobic part with low solubility in water (usually a long nonpolar hydrocarbon chain, also called tail) and a hydrophilic part which is highly water soluble (a polar group, also called head, that may ionize in water or not). Due to their dual nature, surfactants adsorb at various surfaces/interfaces, which leads to surface/interfacial tension lowering (hence also their name), and form aggregates in solutions. It is worthwhile to mention that adsorption of surfactants on hydrophobic particles can lead to solubilization of hydrophobic compounds in aqueous solutions, a phenomenon profitably exploited in nature and technology.

Single surfactant molecules are called *unimers*, to draw a distinction between *monomers*, an expression that refers to covalently linked repeat units in

a polymer chain. Aggregation (also self-association or micellization) has characteristics of a highly cooperative process: a larger number of surfactant unimers take part in the process simultaneously. Both phenomena, adsorption and self-association, are driven by the tendency of the hydrophobic groups to minimize their contact with water. This is the origin of the so-called hydrophobic effect [25].

Micelles start to form above a well-defined concentration in solution called *critical micelle concentration*, CMC. CMC is clearly demonstrated in concentration dependencies of various physicochemical properties of surfactant solutions by a distinctive and abrupt change in slope at a well-defined concentration value [26], which is also the basis for comparison of micellization with a phase separation process. According to this idea, micelles present a new (pseudo) phase that separates out of a solution saturated with surfactant unimers. In contrast to unimers, micelles are highly water soluble and not surface active. CMC values in water at 25 °C for surfactants with cetyl (dodecyl) chains discussed in this chapter are 6.3×10^{-4} (1.52×10^{-2}) M for CPC (DPC) and 9.1×10^{-4} ($1.44–1.52 \times 10^{-2}$) M for CTAB (DTAB) [19,20,27]. As one can see, CMC decreases with increasing chain length but is not much affected by the nature of surfactant head group.

Shapes of micellar aggregates depend on the polarity of the solvent and on structural properties of individual surfactant molecules, more specifically on their geometry, which involves the head group size and the length, the number and eventual branching (or other structural modification) of hydrocarbon chains attached to it. In water, the polar head groups are facing the solvent, and the nonpolar tails are hidden in the aggregate interior, whereas in organic solvents, the situation is the other way round. The simplest geometry of surfactant aggregate is a sphere for which the expression micelle is normally used, although "micelle" may also be a general term for all surfactant aggregates irrespective of their shape. Other frequent aggregate shapes in polar solvents (water) are elongated micelles, cylinders, and curved (as in vesicles) or flat double layers.

Which shape will arise depends on the balance between hydrophilic and hydrophobic (or lipophilic) part of the molecule, which may be conveniently expressed in terms of the critical packing parameter, CPP [28]. CPP relates the head group area, a, the extended length, l, and the volume, v, of the hydrocarbon part of surfactant unimer into a dimensionless parameter through expression $\mathrm{CPP} = v/(l\,a)$. Its values define aggregate shape. Typical boundary values of CPP are (i) $\mathrm{CPP} \leq 0.33$ for spherical micelles, (ii) $0.33 \leq \mathrm{CPP} \leq 0.5$ for cylindrical micelles, (iii) $0.5 \leq \mathrm{CPP} < 1$ for curved

bilayers (e.g., in vesicles), and (iv) CPP = 1 for planar bilayers. Obviously, l and v are primarily determined by the number of carbon atoms, n_C, in the chain and can be calculated from expressions $l/\text{nm} = (0.15 + 0.1265\ n_C')$ and $v/\text{nm}^3 = (0.0274 + 0.0269\ n_C')$, in which n_C' is the number of carbon atoms in the chain that are embedded in the micelle core. Tanford [25] showed that the numerical value of n_C' is lower than n_C, the total number of carbon atoms per chain. A rough estimate, based on statistical mechanics of hydrocarbon chain dimensions, is that $n_C' = n_C - 1$. Adding the second hydrocarbon chain (as in phospholipids) increases v and CPP, which favors aggregates with lower curvature (vesicles and bilayers). On the other hand, a is difficult to estimate precisely because it is strongly influenced by interactions of the head groups with themselves and with the solvent. Electrostatic repulsion and hydration increase the head group area and thus decrease CPP, whereas addition of salt (in particular in the case of surfactants with ionic head groups) reduces a through screening of electrostatic repulsions between them and leads to an increase in CPP; consequently, the aggregate interface becomes less curved, and spherical micelles can transform into cylindrical ones. Similar effects may be achieved by changing the temperature. Variation of ionic strength and temperature thus offers a convenient way to alter surfactant aggregate shape. In addition to these relatively simple shapes, liquid-crystalline mesophases are formed at higher surfactant concentrations, ranging from cubic to hexagonal and lamellar.

4. MIXED PEL–SURFACTANT SOLUTIONS

4.1. General concepts

The presence of a polyion has a large effect on self-association properties of surfactants, in particular, in the case of ionic surfactants with an opposite charge to the polyion. Figure 7.3 demonstrates that cations, surfactant or any other, are strongly attracted by the polyanion. Their concentration at the polyion surface can be more than three orders of magnitude higher than their average concentration in solution. It may be concluded that due to pure electrostatic attraction between PSS^- anion and surfactant cations, there is also an extensive accumulation of nonpolar parts of surfactant ions in layers close to the polyion. Locally, CMC can be reached or even exceeded at total surfactant concentrations far below the CMC, and surfactant unimers can start forming micelle-like aggregates in the vicinity of the polyion. These aggregates are sometimes called polyion-induced micelles [16,19,20]. The threshold concentration at which they start to form has

characteristics of a CMC and is called *critical association concentration*, CAC. It signifies the onset of cooperative self-association of surfactant unimers induced by the electrostatic field of the polyion. The ensuing aggregates have a considerably higher charge compared to unimeric surfactant (or to other eventually present simple counterions) and thus bind to the polyion much more strongly. Actually, they become "trapped" in regions of high electrostatic potential of the polyion as multivalent counterions.

Such binding is a highly cooperative process, as emphasized above. Evidently, the hydrophobic effect, driving self-association of surfactant unimers, makes an important distinction between cooperative surfactant binding and the binding of simple inorganic counterions, which is anticooperative. Anti-cooperative binding leads to a uniform distribution of simple counterions along the polyion chain, as schematically depicted in Fig. 7.1A, whereas cooperative binding of surfactant counterions is distinctively localized in the form of self-assembled aggregates. The notion of the localized surfactant binding can be appreciated from the second drawing in Fig. 7.5, which will be discussed below. Another view of the driving force for the described cooperative binding is in terms of a large entropy increase associated with the binding process and is very important in the case of charged components. Both the polyion and the charged surfactant micelles alone bind a substantial amount of their own counterions, which are released into the solution when surfactant aggregates bind to the polyion, and this leads to a favorable change in entropy. Although the association process itself reduces the number of particles in solution, their increase due to counterion release greatly surmounts this reduction.

The interaction of surfactants with PELs can be discussed from two perspectives, as suggested by Linse *et al.* [29]: from a "PEL-centered" and from a "surfactant-centered" perspective. According to the first accession, the focus is the effect of surfactant binding on typical PEL properties (e.g., viscosity), whereas the fact that surfactant is self-associated in conjunction with the polyion is more or less ignored. In PSS mixtures with cationic surfactants, this idea was pursued when studying the effect of bound surfactant on various physicochemical properties of the PSS^- anion (see Section 4.6) [16,21,30]. The second viewpoint, on the other hand, ensues from a presumption that surfactant binding by the PEL is essentially micellization induced (or perturbed) by the polyion. In this frame, the interest is in the effect of the polyion on surfactant self-association tendency (e.g., on the lowering of the CAC in comparison with the CMC; Section 4.2 [16,27]) and on morphological features of surfactant aggregates in conjunction with the polyion (Section 4.5) [16–18]. In our further discussion, we will use both approaches as appropriate.

4.2. Binding isotherms and critical association concentration

The standard evidence of cooperativity is offered by the shape of surfactant binding isotherms, that is, plots of the degree of binding, β, as a function of free surfactant concentration, c_S^f. The most convenient and precise method to determine binding isotherms of cationic surfactants by anionic PELs is by using potentiometric measurements based on surfactant ion-selective membrane electrodes. The approach was first introduced by Satake and Yang [31] for studying interactions between sodium decyl sulfate and poly(L-lysine) or poly(L-ornithine) in aqueous solutions and later applied by Kwak *et al.* to various cationic surfactant–anionic PEL systems [32–35].

Examples of binding isotherms for DPC and CPC binding by NaPSS in water and in aqueous NaCl solutions at 25 °C are presented in Fig. 7.4 [19]. The curves show that when the surfactant is gradually added to the PEL solution, first there is no significant interaction (below a certain rather low c_S^f, β is close to 0), whereas above a well-defined c_S^f β shows an abrupt and steep increase (at approximately constant c_S^f), which is characteristic for cooperative binding. The value of c_S^f at this point defines the CAC, whereas the steepness of the isotherm presents a measure of the degree of cooperativity.

The screening effect of added neutral salt (NaCl in the present case) is reflected in the shift of the isotherms to higher c_S^f, that is, to higher CAC

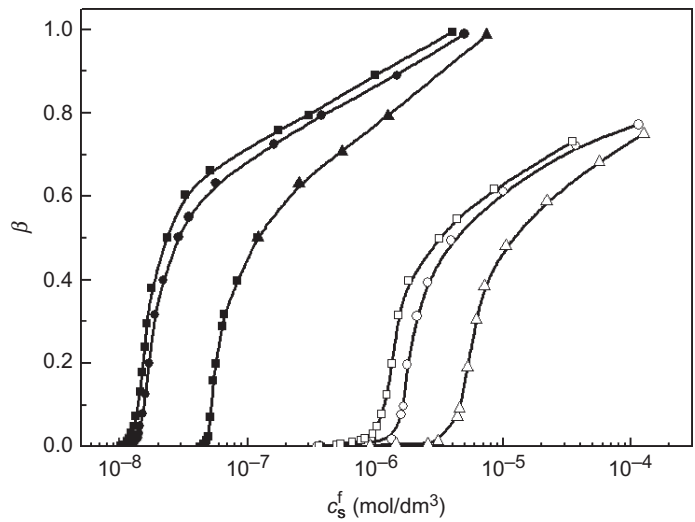

Figure 7.4 Binding isotherms for DPC (open symbols) and CPC (filled symbols) binding by NaPSS in water (squares) and in aqueous 0.01 (circles) and 0.1 M NaCl (triangles) solutions at 25 °C *(adapted with permission from Ref. [19]. Copyright 1988 American Chemical Society).*

values. The increase of c_S^f at β values above the cooperative binding region (c.f., the leveling off of the isotherms for $\beta > 0.6$) indicates saturation of the polyion with surfactant ions. In the case of CPC binding by NaPSS, β reaches a value close to 1 in the saturation region, indicating that each charged group on the polyion is occupied by a surfactant cation. The formation of a 1:1 charge complex is confirmed also by the elemental analysis of the precipitated PSC [36]. Clearly, shorter chain surfactant (DPC) binds less strongly as indicated by higher CAC values and by β values below 1 in the saturation region.

CAC values for DPC and CPC binding by NaPSS in water and in aqueous NaCl solutions at 25 °C are reported in Table 7.1, together with the corresponding CMC values for pure DPC and CPC [19,20]. While CMC decreases with increasing salt concentration, CAC shows an opposite trend. Both effects of salt are due to electrostatic screening. In the formation of free micelles of ionic surfactants, the added salt screens electrostatic repulsion between head groups on the micellar surface and thus promotes micelle formation, which results in a lower CMC. On the other hand, salt also screens attractive electrostatic interactions between the polyion and surfactant counterions, which results in a weaker binding and in an increase in CAC.

The surfactant-centered perspective is very convenient in explaining the concept of CAC. CAC may be considered as surfactant's CMC in the presence of the PEL. Higher CAC is related to higher CMC because more surfactant has to be added to the PEL solution so that its concentration close to the polyion exceeds the CMC, and the aggregates can start to form. The lowering of CAC relative to the CMC is a convenient measure of the

Table 7.1 Critical micelle concentration, CMC, values in pure DPC and CPC solutions, and critical association concentration, CAC, values and free energy changes, ΔG^{o}_{mb} (see text), for DPC and CPC binding by NaPSS in aqueous solutions without and with added NaCl at 25 °C

Surfactant	c_{NaCl} (mol/L)	CMC (mol/L)	CAC (mol/L)	$-\Delta G^{o}_{mb}$ (kJ/mol)
DPC	0	1.52×10^{-2}	9×10^{-7}	24.1
	0.01	1.24×10^{-2}	13×10^{-7}	22.7
	0.1	0.45×10^{-2}	30×10^{-7}	18.1
CPC	0	6.3×10^{-4}	1×10^{-8}	27.4
	0.01	1.6×10^{-4}	1.3×10^{-8}	23.3
	0.1	0.38×10^{-4}	3×10^{-8}	17.7

The polyelectrolyte concentration is $c_p = 5 \times 10^{-4}$ monomol/L.

strength of interaction between the polyion and the surfactant cations. Stronger interactions result in lower CAC values.

According to a frequently used phase separation model for micelle formation, the molar free energy change of micellization, ΔG_m^o, is related to the CMC by [2,37]

$$\Delta G_m^o = RT \ln \mathrm{CMC} \tag{7.1}$$

An analogous expression can be written for the free energy change of surfactant binding to the PEL, ΔG_b^o

$$\Delta G_b^o = RT \ln \mathrm{CAC} \tag{7.2}$$

The free energy change for the process free micelles $\leftrightarrow$ polyion-bound micelles is then related to the ratio between CAC and CMC through

$$\Delta G_{mb}^o = RT \ln \left(\frac{\mathrm{CAC}}{\mathrm{CMC}} \right) \tag{7.3}$$

where ΔG_{mb}^o is a measure of the stability enhancement of the polyion-induced micelles relative to the free ones. Large negative ΔG_{mb}^o values indicate that micelles formed in the polyion domain are more stable than the free ones. The lower is the CAC relative to the CMC, the more negative is ΔG_{mb}^o, and the more favorable is the interaction between surfactant ions and the polyion. ΔG_{mb}^o values for DPC and CPC interaction with NaPSS, reported in Table 7.1, show that the presence of the polyion strongly stabilizes surfactant micelles. One of the main reasons for this is the previously mentioned counterion release.

Additional ΔG_{mb}^o values for the binding of C_nTAB surfactants by NaPSS in water and in aqueous NaBr solutions are plotted in Fig. 7.5 in dependence on n_C, together with the data from Table 7.1 and with those for DTAB binding by NaPA in aqueous NaBr solutions. The latter values were calculated from the CMC data for DTAB [27] and from the CAC data for DTAB binding by NaPA, which are reported in the NaBr concentration range up to 0.01 M [38]. The PA^- and the PSS^- are both vinyl-based polyions and have the same structural value of the linear charge density parameter, which is the main property that governs electrostatic binding. The nature of the charged functional group, however, is different: the completely ionized carboxyl groups are hydrophilic, whereas benzene rings carrying the charged SS^- are hydrophobic. Any difference in binding parameters can thus be attributed to specific interactions between the polyion and surfactant micelles on the account of benzene rings in the PSS chain.

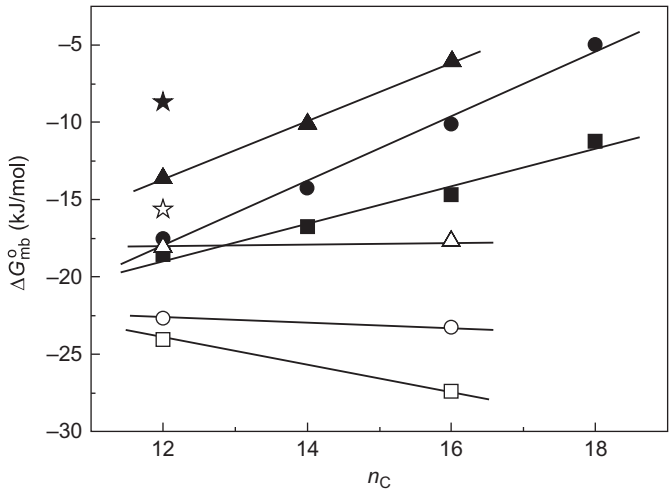

Figure 7.5 The dependence of ΔG^{o}_{mb} on the number of C atoms, n_C, in the hydrocarbon chain for C_nTAB (filled symbols) and C_nPC (open symbols) binding by NaPSS in water (squares) and in aqueous NaBr (or NaCl) solutions: c_{NaBr} (c_{NaCl}) = 0.01 (circles) and 0.1 M (triangles). The corresponding ΔG^{o}_{mb} values for DTAB binding by NaPA in water (open star) and in 0.01 M NaBr (filled star) are included for comparison (see text).

For C_nTAB surfactants, ΔG^{o}_{mb} becomes less negative with increasing chain length, suggesting that the gain in stability is larger for shorter chain surfactants. Stability enhancement is more pronounced in solutions with no added electrolyte, which could be attributed to stronger attractive interactions between the polyion and surfactant micelles in this case. The difference in surfactant binding by NaPSS and NaPA (comparison is possible only in the DTAB case) is reflected in lower CAC and thus more negative ΔG^{o}_{mb} values in the NaPSS case. Evidently, the hydrophobic character of NaPSS contributes to additional stabilization of the polyion-induced micelles, which is achieved through solubilization of benzene rings in micelle interior. The phenomenon of solubilization was revealed by NMR studies in dilute PSS–surfactant solutions [12]. These studies showed that hydrophobic benzene rings of the PSS chain are incorporated in the hydrophobic interior of a micelle somewhere close to the micelle surface and are not situated in the surrounding aqueous medium, as is the case with hydrophilic carboxyl groups on the PA chain. Such solubilization may also be regarded as mixed micelle formation and contributes to stronger interactions of surfactant with the PSS.

In the case of C_nPC surfactants, the effect of surfactant chain length on ΔG^{o}_{mb} is surprisingly small. ΔG^{o}_{mb} is almost independent of n_C in 0.01 and

0.1 M NaCl but shows a clear decreasing trend in water. At the same time, ΔG^{o}_{mb} is lower in comparison with C_nTAB surfactants. These differences between both types of surfactants may be attributed to the presence of hydrophobic pyridinium rings in the head group of C_nPC surfactants, which leads to favorable π–π stacking interactions between aromatic rings of the polyion and those of the surfactant cations. It is reasonable to expect that these interactions become more pronounced with increasing solvent polarity (i.e., in solutions with added salt) because of the decreased solubility of the nonpolar aromatic groups in more polar environment and the related higher tendency to avoid aqueous medium. This can be achieved through PSC formation. On the other hand, the attraction between oppositely charged ions decreases with increasing salt concentration. The final result of these two opposing effects is the observed insensitivity (or even the reversed trend, if the first effect is more pronounced) of ΔG^{o}_{mb} with respect to surfactant's chain length. These results show that structural features of all interacting species are important in apprizing the final effects.

4.3. Solubility of PSCs

An important consequence of surfactant binding to the polyion is the reduction of the effective polyion charge by the bound surfactant micelles, which ultimately leads to precipitation of the PSC from solution if charge compensation is sufficient. Deposition of an insoluble PSC as a protective layer on various surfaces is one of the very frequent ways of application of PEL–surfactant mixtures. It is often desirable that PSCs are very stable, that is, that they do not redissolve and are being washed away from the surface even at high surfactant (or PEL) excess or in solutions with high salt concentration. Or it may be convenient that the PSC is soluble in the concentrated phase, but precipitates upon dilution, which is utilized in the application of hair conditioners to the surface of the hair. Precipitation (or phase separation) is also a way to concentrate PEL–surfactant mixtures. The type of phase separation relevant to PEL–surfactant mixtures treated in this chapter is referred to as *associative phase separation* [39] because it is based on strong mutual attraction/association between oppositely charged micelles and polyions. It leads to enrichment of both components in one (dense) phase, in the form of a polyion–surfactant ion complex salt, which is in equilibrium with a dilute phase. The complex salt with the stoichiometric ratio between surfactant and polyion charges (the 1:1 charge complex) is

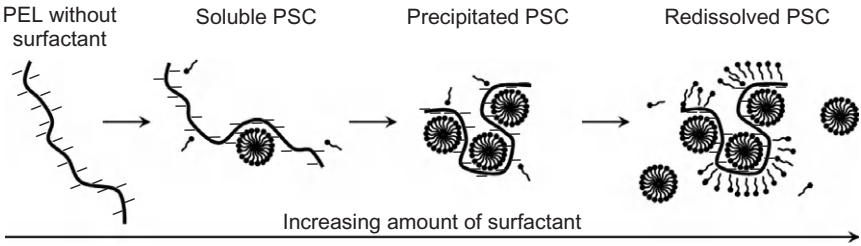

Figure 7.6 Typical sequence of associated structures appearing upon surfactant addition to an oppositely charged polyelectrolyte (counterions of the surfactant and the polyelectrolyte are not shown).

free of simple ions; these are released into the equilibrium (dilute) water solution upon PSC formation.

Figure 7.6 gives a schematic presentation of a typical sequence of associated structures and of the one- and two- (or possibly multi[1])-phase regions, involving the precipitated PSC in equilibrium with a dilute aqueous solution of excess simple ions, that appear upon surfactant addition to the PEL. Usually, some critical degree of complexation between the free polyion chain and the surfactant aggregates has to be reached to induce precipitation, which depends on the effectiveness of mutual charge compensation/screening. Redissolution (also solubilization) of the precipitated PSC is achieved by additional *hydrophobic binding* of surfactant unimers to the precipitated PSC, which results, in case of cationic surfactants treated in this chapter, in water-soluble positively charged colloidal particles. This additional hydrophobic association is limited to solutions with excess of the surfactant and depends on the tendency of surfactant molecules for further binding to the PSC, with their hydrocarbon chains oriented toward the predominately hydrophobic complex. It entirely differs in nature from the specific hydrophobic interaction between PSS^- and surfactant micelles in the polyion-rich regime. Clearly, the competing process to this hydrophobic binding is the formation of free surfactant micelles. If this is the preferred way for the surfactant tails to avoid unwanted contact with water, binding to the PSC will not be favorable, and it will be difficult to redissolve the precipitate. Consequently, the two-phase region will be broad.

[1] Phase equilibria in PEL–surfactant mixtures may involve also coexistence of three phases (see Refs. [36,40,41]). Often, the dense-precipitated phase includes two structures, for example, cubic and hexagonal. In the schematic presentation in Fig. 7.6, possible higher order structures and multiphase regions are ignored. We refer to this region simply as the precipitation region, irrespective of the number of phases in the dense phase.

It can be expected that the width of the two-phase region depends on the concentration of components, on their structural features, on salt content in the system, and on other factors. In a certain polyion–surfactant ion pair, it is important to identify the range of surfactant ion-to-polyion charge ratios, designated herein as S^+/P^- (where S^+ denotes the surfactant cation and P^- the charged group on the polyanion), where the precipitate is formed, or alternatively to identify conditions in which the PSC is soluble, either in the polyion or in the surfactant ion-rich regime, and to relate the structure of the complex phase with its performance. Structure–performance relationship is one of the most important aspects that should be taken into account in the design of pharmaceutical (and other) formulations.

Figure 7.7 shows the extension of one- and two-phase regions in aqueous NaPSS solutions, in the absence and in the presence of NaCl (at a concentration 0.1 M), upon CPC addition [42]. CPPSS denotes the complex salt formed between CP^+ cations and the PSS^- anion. Note that CP^+ cations form a 1:1 charge complex with the PSS^- anion, as ascertained previously by binding isotherms (Fig. 7.4). Thus, $S^+/P^- = 1$ corresponds to a stoichiometric CPPSS complex with a zero net charge, $S^+/P^- < 1$ to the polyion-rich regime (excess of negative charge) and $S^+/P^- > 1$ to the surfactant ion-rich regime (excess of positive charge). Note that in order to assure electroneutrality in nonstoichiometric PSCs (S^+/P^- below or above 1), additional positive (Na^+) or negative ions (Cl^-) have to be present in the system. Data for three different polyion chain lengths are included in Fig. 7.7: two medium-long PSS chains, PSS-M1 and PSS-M2, with an average number

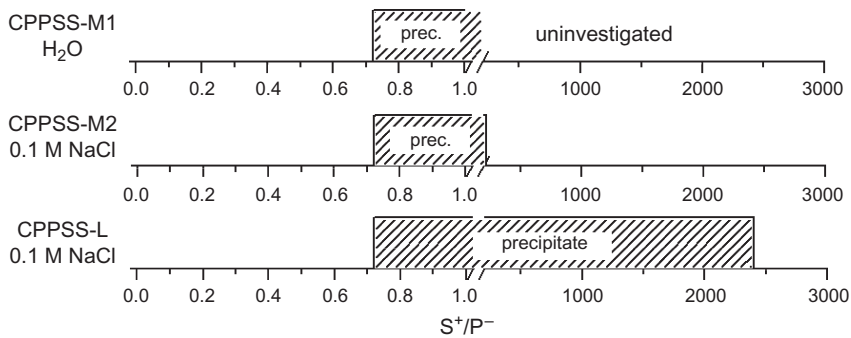

Figure 7.7 One- (unshaded) and two-phase regions (shaded) observed in CPPSS-M1 (M2) and CPPSS-L complex solutions in 0.1 M NaCl in dependence on the S^+/P^- charge ratio. Total solute concentrations are in the range of 7–16 wt% (CPPSS-M1) and 2–23 wt % (CPPSS-L), depending on the S^+/P^- value *(adapted with permission from Ref. [42]. Copyright 2011 American Chemical Society).*

of 340 and 740 monomer units in a chain, respectively, and considerably longer PSS chains, PSS-L, with an average number of almost 11,000 monomer units in a chain [21,42].

The isotropic one-phase region in the PEL-rich regime extends up to $S^+/P^- = 0.71$, irrespective of the polyion chain length or salt concentration, whereas the ensuing two-phase region in the surfactant-rich regime broadens up to very high S^+/P^- values and obviously depends on the polyion length: at the redissolution limit in 0.1 M NaCl, S^+/P^- is around 240 for PSS-M2 and around 2400 for PSS-L. The width of the two-phase region for CPPSS-M1 (the shortest polyion chain) in water without added NaCl was not determined. However, on the basis of other results, it may be deduced that shorter polyion chains contribute to narrowing of the two-phase region, whereas stronger electrostatic attraction in salt-free solutions to its broadening; one might thus expect a comparable width of the two-phase region as for the CPPSS-M2 case in 0.1 M NaCl.

A very similar result on complex solubility was obtained also for PSS^- complexes with CTA^+ cations, involving the lowest molecular weight PSS^- anion (PSS-M1). Systematic studies of phase behavior were performed in mixtures of the corresponding CTAPSS complex salt and NaPSS or CTAC in water [36] (in contrast to the CPPSS case, simple salt was not present in CTAPSS complex solutions). A broad range of solute concentrations and S^+/P^- values was investigated. Partial results of these investigations are presented in Fig. 7.8 for solute concentrations up to 40 wt%. The limit between the homogeneous one-phase solution and the two-phase region involving a precipitate and a dilute solution in the PEL-rich regime is at $S^+/P^- = 0.71$ in systems with total mass concentrations below 30 wt% (in perfect agreement with results obtained for the CPPSS case; compare with Fig. 7.7) and widens even up to $S^+/P^- = 0.89$ in systems with total mass concentrations around 40 wt%. These figures denote that only 0.4 mol (or merely 0.12 mol at higher mass concentrations) of NaPSS is sufficient to dissolve 1 mol of CTAPSS. In the PSS^- case, the PSC is thus very easily dissolved by adding excess of the PEL, upon which a nonstoichiometric PSC is formed. The redissolution seems to be largely independent of the nature of the charged surfactant head group. Note, however, that at total weight concentrations above 40%, the two-phase region in CTAPSS complex solutions broadens considerably toward lower S^+/P^- values. The complete phase diagram is discussed in Ref. [36].

In contrast to the PEL-rich regime, a large excess of CTAC (the surfactant-rich regime) is needed to dissolve CTAPSS. However, in this

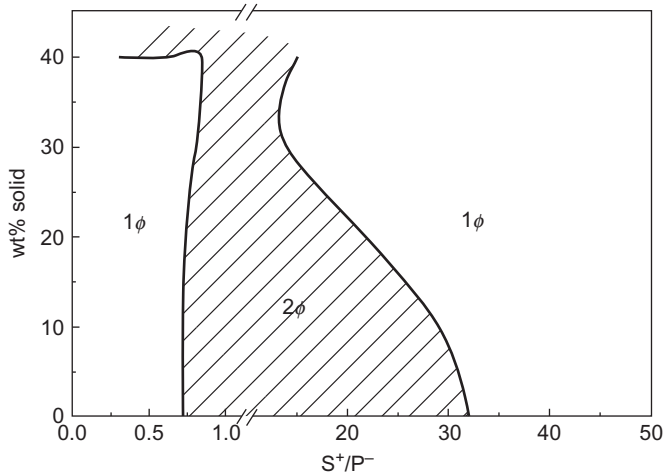

Figure 7.8 One- (unshaded) and two-phase regions (shaded) observed in CTAPSS-M1 complexes in water in dependence on the S^+/P^- charge ratio and total weight % of solid in solution.

case, the CTAC excess is considerably lower in comparison with the CPC excess in the previous case. Between 30 (at total mass concentration of 10 wt%) and 13 mol (at total mass concentration of 30 wt%) of CTAC is needed per 1 mol of CTAPSS for its dissolution in water with no simple salt added. By comparing results for CTAPSS–CTAC mixtures with those for CPPSS–CPC mixtures, we again recognize that the nature of surfactant's head group plays an important role, which would deserve a separate study. The required excess of CPC for CPPSS complex dissolution was considerably larger. It is to be noted that almost no attention was devoted to the role of surfactant head group in the association process with oppositely charged PELs until now.

It can be concluded that surfactant binding by the oppositely charged polyion is highly favorable, whereas its binding to the predominately hydrophobic complex is in fact unfavorable. We will see later on that surfactant prefers to form free micelles and only passively binds to the complex. In contrast to cooperative binding in the PEL-rich regime, the binding in the surfactant-rich regime is noncooperative (or perhaps even anticooperative [36]). This leads to a difficult redissolution of the complex. The longer the polyion chain, the broader the two-phase region, which may be explained by taking into account two effects: (i) longer chains give rise to stronger polyion-mediated attraction between micelles, thus making it difficult for the precipitated complex to redissolve, and (ii) the entropy of mixing is considerably lower for the system with longer chains.

The solubility issue of PSCs in the PEL-rich regime is very different in the case of other PELs, for example, with a completely ionized PA^- anion [43] or with a natural anionic polysaccharide hyaluronate, Hy^- [44,45]. In these two cases, homogeneous one-phase solutions in the PEL-rich regime are stable only for S^+/P^- ratios considerably lower than 1. Looking from the direction of surfactant addition to a pure PA^- (or Hy^-) solution, already a small addition induces precipitation of the PSC [45]. The motivation to compare PSS^- with PA^- (or Hy^-) is clear. Both PA^- and Hy^- are intrinsically hydrophilic polyions, meaning that no hydrophobic participation of the polyion chain in micelle formation is expected and binding occurs only through electrostatic interaction. The surfactant micelles may be assumed to be separated from the oppositely charged polyion by a layer of water molecules. Due to the absence of an intimate contact between the polymer chain and the interior of surfactant aggregates, the chain is free to wrap around the micelle, and as a result, it provides a really effective compensation of its charge. This ultimately leads to an early precipitation of the PSC when surfactant is added to the PA^- anion. An important consequence of such purely electrostatic binding is that micelles formed in the presence of PA^- keep the same aggregation numbers as free micelles [13,14,46] because the polyion merely replaces simple counterions on the micelle surface and thus provides an equivalent electrostatic shielding between the charged surfactant head groups.

In the PSS^- case, on the other hand, surfactant binding by the polyion involves additional participation of the hydrophobic styrene groups in micelle formation [12]. Inclusion of these groups into micelle surface is responsible for an increase in the distance between surfactant head groups, which is equivalent to an increase in the head group area a (see above) and leads to a considerable reduction in aggregation numbers of PSS-induced micelles relative to those in pure surfactant solutions [13–15]. It can also be imagined that the screening of the micellar charge by polyion charges (or vice versa) becomes less efficient due to this specific way of PSS interaction with surfactant aggregates, which ultimately makes PSCs with PSS soluble up to higher degrees of complexation (higher S^+/P^- values) in comparison with PA.

Another way to redissolve the precipitated PSCs is by adding a high excess of simple salt to the stoichiometric complex. The complex disintegrates because of the reduced electrostatic attraction between the polyion and surfactant micelles at sufficiently high salt concentrations. The driving force for micelle formation at the polyion weakens to the point where free

micelles become more favorable than the polyion-induced ones. Free surfactant micelles and free polyion chains coexist in such solutions. For example, in DTAB complexes with slightly cross-linked PA gels, this happens at NaBr concentrations higher than 0.25 M [47]. Similarly, the presence of NaBr at 0.25 M totally suppresses phase separation in NaHy solution with added C_{14}TAB [45]. Again, a much higher electrolyte (NaCl) concentration is required to disintegrate the CPPSS complex, that is, more than 0.8 and 1.1 M to disintegrate complexes involving medium-long (PSS-M2) and long (PSS-L) chains, respectively, which corresponds to a molar excess of NaCl over the CPPSS complex salt 150 and 300, respectively [42]. This is another proof of additional stabilization of CP^+ complexes with PSS^- through hydrophobic and π–π stacking interactions.

A general conclusion derived from these results is that strong electrostatic binding of PSS to micelles, reinforced by the highlighted hydrophobic interaction, promotes dissolution of the precipitated PSC when the polyion salt is added and stabilizes the dense (PSC) phase when the surfactant salt is added. The width of the two-phase region involving the precipitate is broad, and high salt concentrations are needed to redissolve the stoichiometric PSC. All this is a consequence of the distinctive tendency of PSS^- to bind to CP^+ micelles through hydrophobic interactions.

4.4. Size of PEL–surfactant complexes

Important information on molecular characteristics of PSCs in solution is obtained from light scattering, LS, measurements. We have employed dynamic light scattering, DLS, to determine the hydrodynamic radii, R_h, of particles that are present in CP^+–PSS^- mixtures, in homogeneous one-phase solutions in the PEL- and in the surfactant-rich regime [42]. The emphasized broad one-phase region in the PEL-rich regime enabled LS measurements up to $S^+/P^- = 0.71$, whereas in the surfactant-rich regime, studies could be performed only at very high surfactant excess, which corresponded to $S^+/P^- = 240$ or 2400 in the CPPSS-M2 and CPPSS-L case, respectively (c.f., Fig. 7.7).

Figure 7.9A shows size distributions for CPPSS solutions with $S^+/P^- = 0.5$ in 0.1 M NaCl. Data for pure PELs in 0.1 M NaCl are included for comparison and show that at this NaCl concentration, the polyion chains are already rather coiled with average R_h values of 10.4 and 69.5 nm in the case of PSS-M2 and PSS-L, respectively (compare this with fully extended chain lengths, which are 186 nm in the PSS-M2 and almost 28 μm in the PSS-L case, as calculated from the length, 0.252 nm, of the monomer unit

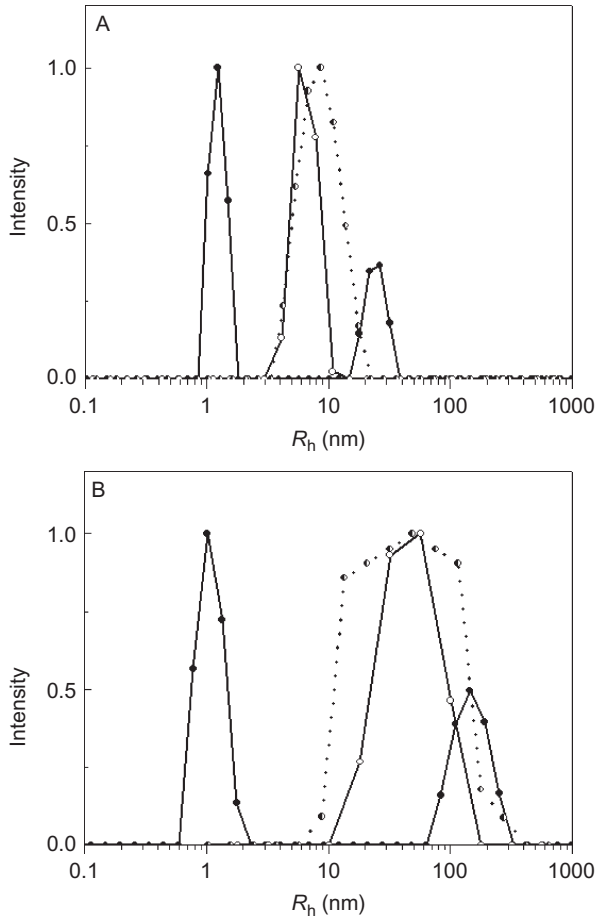

Figure 7.9 Normalized size distributions of hydrodynamic radii, R_h, in NaPSS solutions without (half filled circles and dotted lines) and with added CPC at $S^+/P^- = 0.5$ (open circles) and 240 (PSS-M2) or 2400 (PSS-L; filled circles) in 0.1 M NaCl: (A) medium-long chains (PSS-M2) and (B) long chains (PSS-L).

and the average degree of polymerization of the corresponding polyions). Size distributions of pure PELs in 0.1 M NaCl are rather broad, although samples with low polydispersity index, PI, were used for these measurements (in both cases, PI was below 1.2 [42]). Such result is expected because the measured R_h values are an average over all possible chain conformations in solution under the relevant conditions.

Adding the surfactant by keeping NaCl concentration unchanged leads to a further decrease in size to $R_h = 7.7$ (CPPSS-M2) and 59.1 nm

(CPPSS-L). According to the schemes in Fig. 7.6, the reduction in R_h is expected (as a consequence of polyion wrapping around surfactant micelles), but in fact, it is not very pronounced. The reason for this is that surfactant binding to the polyion simultaneously increases the molar mass of particles. Size distributions in Fig. 7.9 show that the average size of complexes is about the same as the size of free polyion chains. An important difference, however, is that the width of size distributions in PSC solutions is considerably reduced in comparison with pure PEL solutions.

Narrowing of size distributions in conditions of moderate ionic strength is frequently observed also in the case of various interpolyelectrolyte complexes, PECs, for example, in PECs formed between DNA chains and synthetic polycations in aqueous solutions with NaCl concentrations up to 0.3 M [48]. On the basis of LS measurements, the authors have concluded that this is due to the decreased thermodynamic quality of the solvent for complexes with increasing hydrophobicity (decreasing charge). The situation is very similar in the case of PSCs treated in this chapter. It may be proposed that parts of the polyion chain to which surfactant micelles are bound become hydrophobic and as such tend to hide from water (they become "thermodynamically inactive"; see Section 4.6). This can be achieved by forming more compact aggregates with these parts hidden in the "core" of the particle and the less hydrophobic parts (the uncomplexed/free portions of the polyion chain) constituting the regions exposed to water. In agreement with this, LS measurements showed [42] that CPPSS complexes with $S^+/P^- = 0.5$ have a roughly spherical shape and a considerably higher packing density than the free polyion chains. In the CPPSS-L case, the packing density actually reached a maximum at $S^+/P^- = 0.5$. Such compaction inside the (still soluble) PSC leads to smaller fluctuations in particle sizes, as demonstrated by the results in Fig. 7.9. It may also be expected that the exposed parts retain the same effective charge density as the free polyion chains, which is confirmed by zeta (ζ)-potential measurements and by determining various thermodynamic and transport properties that depend on effective polyion charge (these properties are discussed in Section 4.6.). The ζ-potential of CPPSS particles with $S^+/P^- = 0.5$ and that of free polyion chains (values in brackets) is $\zeta = -23.5$ (-26) and -38 (-38) mV for CPPSS-M2 and CPPSS-L complexes, respectively [42]. Clearly, the bound surfactant has practically no effect on ζ-potential in the range of S^+/P^- values up to 0.5.

The reduction in R_h and the described compaction is reflected in a strong viscosity decrease of a PEL solution upon surfactant addition. Figure 7.2

shows comparative effect of CPC and NaCl addition on $[\eta_{red}]$ of an aqueous NaPSS solution. CPC causes stronger reduction of $[\eta_{red}]$ than the same concentration of NaCl. Clearly, NaCl provides only simple electrostatic screening between the polyion charges and consecutive decrease in chain extension, whereas binding of surfactant micelles leads to an additional decrease. Taking into account the increase of the molar mass of the polymer chain upon surfactant binding, viscosity reduction induced by CPC is actually rather large, in accordance with the above compaction picture.

The compaction phenomena have received considerable attention in recent years in biomedical studies involving DNA. DNA is a highly charged anionic PEL with an even higher linear charge density than NaPSS and interacts strongly with oppositely charged multivalent ions and of course also with surfactant micelles [4]. Addition of cation surfactants to DNA solutions has been used to purify DNA by condensation and precipitation [49] or to achieve renaturation and ligation of DNA [50]. There are also applications of DNA–surfactant complexes in controlled delivery of genetic material into cells. Naked DNA, due to its size and high charge density, is unlikely to enter the cells by itself. In this connection, liposomes have been used as vehicles for gene delivery [51].

According to size distributions in Fig. 7.9, no free CP^+ micelles were detected in CPPSS solutions in the PEL-rich regime.[2] The non-stoichiometric CPPSS complexes coexist with free surfactant unimers, the concentration of which is equal to the CAC. For CPC binding by NaPSS in 0.1 M NaCl, the value of CAC ($=3\times10^{-8}$ M; c.f., Table 7.1) suggests that the number of individual surfactant ions is very small. Because of their small size (individual CP^+ ions in water are probably smaller than 2.35 nm, which is the sum of l_{C16} and r_{CP+}, because the hydrocarbon chain in a highly polar aqueous medium takes up a rather compact conformation), their contribution to total scattering of solution is small and it is difficult to ascertain their presence in solution.

DLS analysis was performed also for the redissolved CPPSS complexes in the surfactant-rich regime [42]. Redissolution was achieved by a gradual addition of CPC to a suspension of the stoichiometric complex ($S^+/P^-=1$) in 0.1 M NaCl. CPC concentration at the redissolution limit was very high, that is, 0.43 and 0.64 M for CPPSS-M2 and CPPSS-L complexes,

[2] The expected R_h of free CPC micelles is at least 3 nm. This value is estimated from the length of an extended hexadecyl chain, that is, $l_{C16}=2.05$ nm, from the size of the pyridinium head group, that is, $r_{CP+}=0.3$ nm, and by taking into account some hydration layer of water molecules around the micelle.

respectively. It is important to stress that these concentrations are far above the CMC of CPC in 0.1 M NaCl (CMC $= 3.8 \times 10^{-5}$ M at 25 °C [19]); consequently, free micelles are present in solution. Size distributions for CPPSS-M2 and CPPSS-L complexes (Fig. 7.9, filled circles) reveal the presence of two populations of particles with a considerably different size. A rough estimate of the apparent R_h values for these species is: $R_{h,1} = 1.24$ and 1.1 nm and $R_{h,2} = 20$ and 150 nm in CPPSS-M2 and CPPSS-L solutions, respectively. There is no doubt that the larger R_h value corresponds to solubilized complexes. The size of the redissolved complexes is by at least a factor of 2 larger than the size of soluble complexes in the PEL-rich regime due to additional layer of hydrophobically bound surfactant cations. Such particles have a positive charge.

The smaller hydrodynamic radius is attributed to free CPC micelles, although it is considerably smaller than the value proposed above for the radius of a spherical CPC micelle at concentrations not far above the CMC. By taking into account high CPC concentrations in suspensions of solubilized complexes, it is of course reasonable to expect free surfactant aggregates in these solutions. However, their size is only apparent, since the estimation of R_h by DLS measurements is based on the viscosity of pure water, which may differ significantly from the environment viscosity in such highly concentrated mixtures. This could be the reason for an underestimation of micelle size. Number distributions (derived from size distributions in Fig. 7.8A and B; not shown) demonstrate that micelles greatly outnumber the complexes. As anticipated above, the tendency of surfactant to form free micelles is considerably larger than its affinity to bind to the PSC. The added CPC only passively binds to the PSC, and thus a large excess is needed to achieve sufficient binding and redissolution of the complex.

4.5. Structure of PEL–Surfactant Complexes

Precipitation/phase separation is the way not only to concentrate PEL–surfactant mixtures but also to induce structural ordering in the system. Structure formation always involves self-association of surfactant unimers into aggregates (micelles) of different geometries. In pure surfactant solutions, these aggregates first form a disordered micellar solution and at high enough concentrations organize into structures that display crystalline-like order. For example, in aqueous CTAB solutions at 25 °C (no PEL present, therefore, $S^+/P^- \to \infty$), the disordered micellar phase extends to concentrations somewhat above 40 wt% and is then followed by the ordered

hexagonal phase [52]. In the presence of a PEL, however, structures with long-range liquid-crystalline order are observed at considerably lower total weight concentrations of solutes [16–18]. Obviously, the role of the polyion is to bring surfactant ions together. The precipitated complex often contains very low amount of water (50 wt% or less) even though its overall content in the system is large, and these dense phases display crystalline-like structures similar to those found in concentrated surfactant systems, for example, cubic [16–18,40,53,54], hexagonal [16–18,40,41], and lamellar [18,55]. The focus on structural studies is the way how surfactant unimers self-assemble in conjunction with the PEL. More or less, the surfactant-centered viewpoint is pursued here, although structures of PSCs are influenced by both, the polyion and the surfactant-ion properties. Among the polyion characteristics, its charge density, chain length, and flexibility are important, whereas with surfactant-ion properties, the decisive factor is the hydrocarbon chain length. On top of this, structures are controlled by the amount of simple salt in the system.

There are different methods to prepare PSCs. One is by the *conventional way* of mixing the components (PEL salt, M^+P^-, and surfactant salt, S^+X^-), which produces various amounts of simple salt (M^+X^-) in the surrounding medium, depending on the mixing ratio, and the PSC (combination S^+P^-, the complex salt). If the mixing ratio varies, also the amount of salt released upon PSC formation varies, leading to different contributions to screening. Since electrostatic interactions (c.f., Fig. 7.3) and the degree of binding (c.f., Fig. 7.4) depend strongly on the degree of screening, this may also lead to structural changes.

The other way of mixing the components is the so-called alternative way, introduced recently by Piculell and coworkers in extensive studies of phase behavior in NaPA–surfactant mixtures [40,41,54]. In order to avoid the uncontrollable/unwanted and variable presence of simple salt, the complex salt (S^+P^-) was used therein as the starting point for the preparation of PEL–surfactant mixtures. It was mixed with water and either the surfactant (S^+X^-) or the PEL salt (M^+P^-), thus delivering only the neutralizing amount of one type of simple ions (M^+ or X^-) into the solution. The attraction between charged species is completely unscreened in this case for all possible mixing ratios, which makes interpretation easier.

We have used the conventional way of complex preparation for structural investigations in the case of NaPSS mixtures with DPC and CPC by mixing aqueous solutions of pure NaPSS and DPC (CPC) salts [16–18]. Structures of complexes were determined by synchrotron small-angle X-ray scattering, SAXS, in solutions with total weight concentration of solutes (DPC or

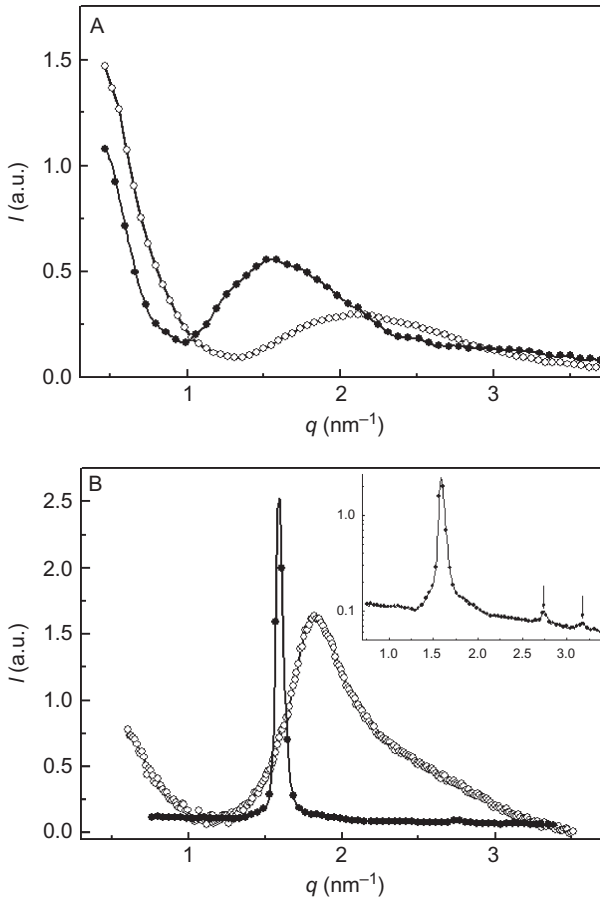

Figure 7.10 (A) SAXS patterns of a one-phase micellar DPPSS (open circles) and CPPSS solution (filled circles) with $S^+/P^- = 0.70$; (B) SAXS patterns of DPPSS and CPPSS precipitated complexes with $S^+/P^- = 1$. In the inset, higher order peaks are indicated for the CPPSS complex.

CPC + NaPSS) around 1 wt% or lower. Examples of scattering patterns for $S^+/P^- = 0.7$ (one-phase samples; c.f., Fig. 7.7) are shown in Fig. 7.10A and for the stoichiometric ratio $S^+/P^- = 1.0$ (two-phase samples) in Fig. 7.10B. $S^+/P^- \geq 0.72$ produced a precipitated (dense phase) in equilibrium with a dilute aqueous phase (c.f., Fig. 7.7). Scattering patterns in Fig. 7.10B are for the precipitates, whereas those of the corresponding equilibrium aqueous phases were smooth curves without any peak (not shown), demonstrating that they contain no or very low amount of dissolved PSC and excess of surfactant or PEL. As we can see, all scattering

patterns display either one broad peak (Fig. 7.10A) or a sharp Bragg-like peak (Fig. 7.10B) that is accompanied by higher order peaks (in the inset of Fig. 7.10B higher order peaks are indicated by arrows for the CPPSS complex with $S^+/P^- = 1$). Scattering pattern for pure NaPSS solution displayed no correlation peak (curve not shown), whereas for pure CPC solutions (no PEL added; curves not shown), a clear correlation peak due to micelles was observed only for CPC concentrations around 10 wt% or more (well above the CMC of this surfactant), which is considerably higher than solute concentrations in PSC solutions.

One broad peak suggests that surfactant aggregates (the polyion-induced micelles) are packed at short separations (side by side) along the polyion chain, but no long-range liquid-crystalline order is indicated due to the absence of a characteristic sharp first-order peak (and additional higher order peaks). This is typical for disordered micellar solutions and all one-phase samples in the homogeneous PEL-rich regime ($S^+/P^- < 0.72$) conformed to this picture. As long as the PSC stays in solution, it does not form any structure with long-range periodicity. The position of the scattering peak is a measure of the center-to-center separation between the polyion-bound micelles, expressed as a distance d, which is calculated from $d = 2\pi/q$ (where $q = (4\pi/\lambda)\sin\theta$ is the value of the scattering vector at the peak maximum, λ the wavelength of X-rays, and 2θ the scattering angle).

The size of scattering domains, L, and the degree of disorder, Δ/d, in soluble complexes can be estimated from the width of the peak at the half-maximum intensity, denoted as β_S, by applying the following expressions [56,57]:

$$L = \frac{\lambda}{\beta_S \cos\theta} \tag{7.4}$$

$$\frac{\Delta}{d} = \frac{1}{\pi}\sqrt{\frac{\beta_S d}{\lambda}} \tag{7.5}$$

In Eq. (7.4), Δ is the width of fluctuations in distances d between neighboring scattering units. For sharp peaks, β_S and Δ are small, meaning that the degree of order is high (or the degree of disorder, Δ/d, is low). The value $\Delta/d \approx 0.22$ signifies the boundary between "liquid-type" scattering, which already shows effects related to interference between particles, and "gas-type" scattering (higher Δ/d values), where interference effects are absent. For example, for $\Delta/d \approx 0.2$, scattering patterns already show a strong correlation peak due to interparticle correlations, as is the case for curves plotted in Fig. 7.10A. Structural parameters evaluated from SAXS patterns are reported in Table 7.2. The

Table 7.2 Structural parameters for DPPSS and CPPSS complexes in water obtained from peak positions in SAXS curves

Complex	S^+/P^-	*d* (nm)	*L* (nm)	Δ/d
DPPSS	0.3	2.58	5.2	0.22
	0.5	2.73	6.4	0.21
	0.7	2.84	6.7	0.21
	1.0 (1. peak)	3.26	10.7	0.18
	1.5 (1. peak)	3.31	11.8	0.16
CPPSS	0.3	3.52	9.0	0.20
	0.5	3.63	8.8	0.20
	0.7	3.80	9.2	0.20
	1.0 (1. peak)	4.01		<0.1
	1.3 (1. peak)	3.95		<0.1

For hexagonal samples, *d* is reported only for the first-order peak.

intermicellar distances increase from 2.58 (3.52) at $S^+/P^- = 0.3$ to 2.84 (3.80) nm at $S^+/P^- = 0.7$ in the DPC (CPC) case, which is considerably larger than the corresponding values obtained for pure DPC and CPC solutions. In a 10 wt % surfactant solution *d* is 5.86 and 7.75 nm for DPC and CPC, respectively.

The *d* values in PSC solutions agree with the diameter of a spherical surfactant micelle, which is mainly determined by the length of two surfactant's hydrocarbon chains ($2l_{C12} = 3.08$ nm and $2l_{C16} = 4.1$ nm; c.f., also Footnote 2). The results therefore conform to the model presented previously, according to which surfactant micelles are bound adjacently to the polyion (in groups of several micelles, as depicted in Fig. 7.4) and are not distributed randomly along the chain. Polyion induces micellization at concentrations far below the CMC and at the same time brings the micelles together. By comparing *d* values in complexes with micellar diameter deduced from surfactant's hydrocarbon chains, it is obvious that such polyion-induced micelles in DPPSS (CPPSS) aggregates are considerably compressed. This is due to inclusion of the PSS chain in the aggregate surface (the specific hydrophobic interaction, highlighted above). Besides, aggregate size increases with increasing S^+/P^-.

Important additional information on PSC features is contained in structural parameters *L* and Δ/d. The degree of disorder, Δ/d, is constant, whereas

L (and d) increases with increasing S^+/P^-, suggesting that the number of micelles bound per one chain is constant, whereas the size of ordered regions, and along with this the size of micelles, increases. Increasing micellar size is in agreement with literature data on aggregation numbers in CTAB–NaPSS solutions, which were also shown to increase with increasing S^+/P^- [13,15,46]. In addition, data in Table 7.2 demonstrate that complexes with a longer chain surfactant (CPC) are more ordered than those with a shorter chain surfactant (DPC), which may be attributed to stronger micellization tendency of the more hydrophobic surfactant, its higher aggregation numbers, and therefore stronger interactions with the polyion.

SAXS patterns of dense CPPSS phases (Fig. 7.10B) all display a sharp first-order peak and additional higher order peaks that fit the ratio $1:\sqrt{3}:\sqrt{4}$, which is characteristic for a hexagonal closed-packed arrangement of cylindrical surfactant aggregates. In this case, d is the Bragg distance between the lattice planes, which is obtained from the position of the first scattering peak (in Table 7.2, only the d value for the first peak is given), and also agrees with the length of two cetyl (or dodecyl) chains. In the DPPSS case, however, higher order peaks were not explicitly seen. The hexagonal ordering was proposed on the basis of the height and sharpness of the first-order peak in comparison with the micellar peak (compare Fig. 7.10A and B). Parameters L and Δ/d are usually not reported for liquid crystalline-like structures [57]. The calculated Δ/d values for such samples are below 0.1, while according to the theory, only high values (>0.1) of this parameter are characteristic for real objects like assemblies of molecules in a liquid medium [57]. Such was the case with CPPSS complexes. As a whole, data derived from SAXS curves show that dense precipitates with PSS^- anion are highly ordered. Structural ordering obviously increases with increasing S^+/P^- ratio (decreasing net charge of the complex) and with increasing surfactant chain length.

The alternative way of complex preparation was used in studies of phase behavior in PSS mixtures with CTA^+ cations [36]. In agreement with results for CPPSS case, only the disordered micellar phase and the ordered hexagonal phase were identified also in systems with the CTAPSS complex salt. Scattering patterns were very similar to the ones shown in Fig. 7.10 and are therefore note reported. The derived d values for one-phase CTAPSS samples from the PEL-rich regime ($S^+/P^- < 0.9$) are plotted in Fig. 7.11, together with those for CPPSS case. They increase with increasing S^+/P^- (more surfactant available for binding to the polyion) and are evidently lower in CPPSS solution in comparison with the CTAPSS ones. All this is due to the reasons discussed previously.

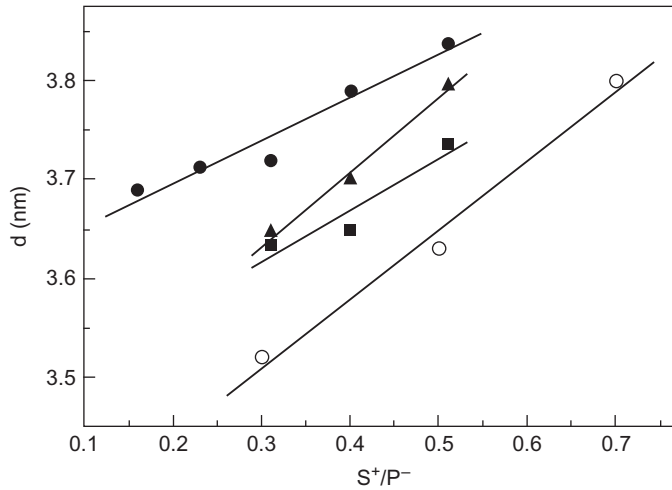

Figure 7.11 Values of characteristic distances *d* in CTAPSS (filled symbols) and CPPSS (open symbols) complex solutions from the one-phase region (in the polyelectrolyte-rich regime) in dependence on S^+/P^-. Total weight concentrations of solutes in CTAPSS solutions are 10 (filled circles), 20 (filled triangles), and 30 wt% (filled squares). Data for CTAPSS solutions apply to zero simple salt concentration. In the CPPSS case (open circles), total weight and salt (NaCl) concentrations change in dependence on the S^+/P^- ratio (see text).

As a conclusion, it is interesting to note that no cubic phase was found in surfactant complexes with the PSS anion. Cubic structure of the type P*m*3*n* is often observed in surfactant mixtures with polyacrylate anion [40,41,54,58,59]. Several reasons may be responsible for this difference, among them also the specific hydrophobic interaction when PSS anion is involved.

4.6. Effect of bound surfactant on PEL properties

Properties of PEL solutions depend on the polyion charge density. With weak PELs, tuning the polyion charge is achieved by varying the degree of ionization, α, of functional, for example, carboxyl, groups, which is easily realized by adjusting the solution pH. One of very important properties of PEL solutions is the osmotic coefficient, ϕ, which is a measure of the fraction of free[3] counterions in PEL solutions and directly depends on the polyion charge density [5–7]. For example, osmotic coefficient of aqueous solutions of poly (acrylic acid), HPA, with ionizable carboxyl groups increases smoothly

[3] In this context, the expression "free" refers to those counterions that are not condensed (or electrostatically bound) by the polyion.

with decreasing α (c.f., Fig. 7.12: the dashed line), which is a consequence of increasing fraction of free ions as the polyion charge is reduced.

Contrary to weak PELs, functional groups of strong PELs, like sulfonate groups in poly(styrenesulfonic acid), HPSS, are completely ionized irrespective of pH. However, strong binding of cationic surfactants to charged

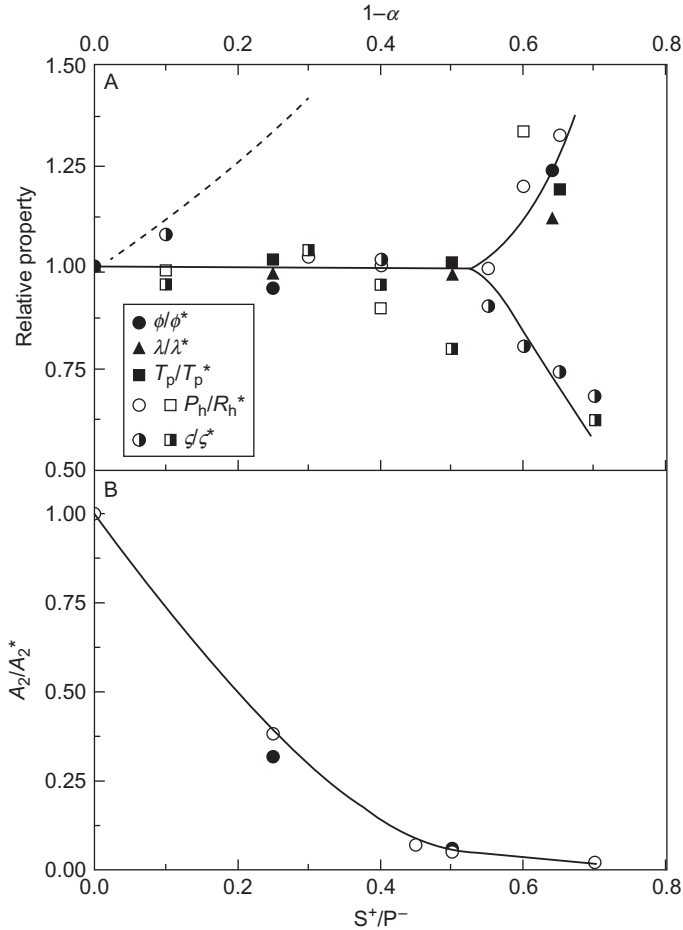

Figure 7.12 (A) Relative values of osmotic coefficient, ϕ/ϕ^*, polyion transport number, T_p/T_p^*, molar conductivity, λ/λ^*, ζ-potential, ζ/ζ^*, and hydrodynamic radius, R_h/R_h^* in CPPSS solutions in dependence on S^+/P^-. Data for ζ/ζ^* and R_h/R_h^* are given for PSS-L (circles) and PSS-M2 chains (squares), whereas data for other properties apply to PSS-M1 chains. The dashed line indicates the trend in ϕ/ϕ^* values in HPA solutions in dependence on $(1-\alpha)$ (c.f., upper axis). (B) Relative values of the second virial coefficient, A_2/A_2^*, in CPPSS solutions. Open and filled circles are for PSS-L and PSS-M2 chains, respectively.

groups may offer a way to tune polyion charge by a different/alternative approach. This idea was pursued in measurements of various thermodynamic and transport properties of the PSS^- anion in which different portions of the polyion charge were "neutralized" by CP^+ cations by employing the alternative way of complex preparation, that is, excluding simple salt as in the CTAPSS case [16,19–21,30]. These measurements constitute the PEL-centered approach to studying PEL–surfactant interactions and provide an indirect proof of localized surfactant binding by the polyion.

Figure 7.12 shows various properties of aqueous CPPSS complex solutions plotted as relative values (i.e., ratios between their values in CPPSS solutions and the corresponding value for pure HPSS, which is designated by an asterisk) versus S^+/P^-. All properties are roughly constant up to 50% coverage ($S^+/P^- = 0.5$) of the polyion with surfactant aggregates. The dashed line indicates the trend in $\phi/\phi^\star$ values for HPA solutions, which are plotted against $(1-\alpha)$ (see the upper axis in Fig. 7.12A; note that only $\phi/\phi^\star$ values below 1.5 are shown). In the HPA case, α has the same numerical value as $(1-S^+/P^-)$, yet their meaning is different. While α gives the fraction of *ionized* carboxyl groups on the PA^- anion, $(1-S^+/P^-)$ gives the fraction of *free* sulfonate groups on the PSS^- anion.[4] The distribution of these charged groups is rather different: it is regular (i.e., random) in the PA case and irregular in the PSS case (c.f., Fig. 7.6). Irregular (localized) surfactant binding results in long uninterrupted charged portions on the polyion and in portions that are blocked by surfactant micelles, whereas ionization leads to evenly distributed COO^- groups. Surfactant aggregates can be viewed as "site bound." The idea of "site binding" is especially convenient in the case of PSS^- anion owing to the anchoring of SS^- groups in the micellar interior. The migration of surfactant aggregates parallel to the chain is thus highly unlikely.

Results in Fig. 7.12A clearly confirm that surfactant binding by the polyion is localized. The uncomplexed (free) part of the polyion chain behaves as a fully charged rod, and consequently, all properties are roughly constant in the S^+/P^- range where this is valid. In the PSS case, this is up to 50% coverage ($S^+/P^- = 0.5$) of the polyion charge with surfactant aggregates. In view of the experimental results, the occupied/blocked parts of the polyion may be considered as thermodynamically inactive.[5]

[4] Or alternatively,$(1-\alpha)$ is the fraction of unionized/protonated carboxyl groups on the PA anion and S^+/P^- the fraction of sulfonate groups on the PSS anion that are blocked by CP^+.

[5] This statement is based on a presumption that thermodynamic properties of PEL solutions are influenced only (or primarily) by polyion charge, which is reasonable with strong PELs like NaPSS. The uncharged/blocked portions of the chain do not contribute to their values.

The dependency changes for $S^+/P^- > 0.5$. For example, osmotic coefficients, ϕ, molar conductivity, λ, and transport numbers, T_p, start to increase, whereas ζ-potential starts to decrease, suggesting that the approximation of the constant polyion charge density is no longer valid. At higher coverage, the shielding of the polyion charge by surfactant aggregates becomes more extensive due to conformational changes and steric effects, which leads to a decrease in the effective polyion charge density similar to the one in solutions of weak PELs induced by reduction of α. Consequently, solution properties start to change in a way similar to weak PELs.

This picture is confirmed also by taking into account the joint trend in R_h and ζ. While the relative R_h values start to increase for $S^+/P^- > 0.5$ (aggregates become larger on the account of surfactant binding and intermolecular association [42]), the relative ζ values start to decrease, announcing the beginning of precipitation (i.e., the proximity of the two-phase region). In accordance with this, relative values of the second virial coefficient, A_2 (Fig. 7.12B), drop to very low values (close to zero) as the two-phase region is approached.

5. RELATION WITH HYDROPHOBICALLY ASSOCIATING POLYMERS

It is of interest to briefly relate features of PSS–surfactant mixtures with those involving HAPs. Another common name for HAPs is hydrophobically modified polymers. HAPs are copolymers of a water-soluble monomer, which is in a large excess, and a very hydrophobic comonomer, present in small fractions, typically below 5 mol%) [11]. Hydrophobic groups are usually alkyl chains of various lengths, ranging from short (methyl, ethyl, butyl, etc.) to long ones (dodecyl, hexadecyl, and octadecyl). Such structure can be achieved by chemically attaching alkyl chains to functional groups on the polymer, thus hydrophobically modified polymers. HAPs with sufficiently long side chains tend to (self-)associate in aqueous solutions into intra- and intermolecular aggregates, presumably of a micellar type.

In contrast to HAPs, PSS^- anion lacks the ability to self-associate, although it contains hydrophobic groups on each monomer unit. This may be attributed to two factors: first, SS^- groups are "too short," and second, each hydrophobic moiety contains a charged group resisting association. Intermolecular association of HAPs leads to increased viscosities of HAP

solutions in comparison with the corresponding unmodified polymer, which may even be enhanced by increasing salt concentration [60]. This is in sharp contrast with salt dependency of viscosity in PSS solutions, which decreases smoothly upon increasing salt content (see Fig. 7.2).

It was demonstrated that HAPs associate with surfactants into aggregates with finite hydrophobic domains [61,62]. In these studies, surfactant binding by HAPs was looked at as co-micellization or mixed micelle formation. Depending on the HAP and surfactant concentration, mixed micelles may contain alkyl groups belonging to one or more polymer chains. In the latter case, cross-linking of the polymer chains occurs, leading to pronounced viscosity enhancement in dilute (typically around 1 wt%) HAP solution. This is not observed in mixtures with unmodified polymers and also not in those with PSS (c.f., Fig. 7.2). Finally, it is to be noted that HAPs can associate even with surfactants of the same charge [62], which is not the case with PSS. Thus, in the PSS case, surfactant association is a prerequisite for mixed micelle formation, whereas with HAPs, the hydrophobic domains are present from the very beginning of the association process and have the capacity to gradually solubilize individual surfactant molecules. Often, no CAC is observed with HAPs [29].

6. CONCLUDING REMARKS

In this chapter, on PEL–surfactant interactions, we have reviewed principal properties of particular mixtures involving poly(styrenesulfonate) anion, PSS^-, and cationic surfactants. We have demonstrated the importance of the "concealed" hydrophobic character of PSS for its interactions with surfactants. Although it contains hydrophobic moieties, PSS itself does not form self-associate structures, which draws a distinction between PSS and hydrophobically modified PELs. Hydrophobic nature of styrenesulfonate groups, SS^-, of PSS becomes effective only when hydrophobic domains are available in the system, which are offered by the micellized surfactant.

It is demonstrated in this chapter that strong electrostatic interactions, reinforced by the specific hydrophobic interaction of SS^- groups with micelle interior, lead to very strong binding of cationic surfactants by PSS with several distinctive differences in comparison with other systems, which are thoroughly discussed from different viewpoints. On first thought, strong interactions should contribute to more efficient precipitation of the PSC from solution, when surfactant is gradually added to a PEL solution. However, PSCs involving PSS exhibit very good solution stability as long as the

polyion is in some charge excess but redissolve with difficulty when adding excess of the surfactant. All this can be explained by invoking the specific interaction. Although rather broad knowledge was acquired on PEL–surfactant systems throughout the years, very little attention was devoted to the nature of surfactant's charged group. Our results demonstrate that this also plays an important role in PEL–surfactant interactions and would deserve a more detailed study.

REFERENCES

[1] D.G. Dervichian, Lipo-proteins, Discuss. Faraday Soc. 6 (1949).
[2] E.D. Goddard, K.P. Ananthapadmanabhan (Eds.), Interactions of Surfactants with Polymers and Proteins, CRC Press, Boca Raton, 1993.
[3] J.C.T. Kwak (Ed.), Polymer-Surfactant Systems, In: Surfactant Science Series, vol. 77, Marcel Dekker, New York, 1998.
[4] (a)in: R.S. Dias, B. Lindman (Eds.), DNA interactions with polymers and surfactants, John Wiley & Sons, Inc, Hoboken, New Jersey, 2008(b)R.S. Dias, K. Dawson, M.G. Miguel, Interactions of DNA with surfactants in solution, in: R.S. Dias, B. Lindman (Eds.), DNA interactions with polymers and surfactants, John Wiley & Sons, Inc, Hoboken, NJ, 2008, pp. 89–117 (Chapter 4).
[5] R.W. Armstrong, U.P. Strauss, Polyelectrolytes, in: H.F. Mark, N.G. Gaylord, N.M. Bikales (Eds.), Encyclopedia of Polymer Science and Technology, vol. 10, Interscience, New York, 1968.
[6] A. Katchalsky, Z. Alexandrowitz, O. Kedem, Polyelectrolyte solutions, in: B.E. Conway, R.G. Barradas (Eds.), Chemical Physics of Ionic Solutions, Wiley, New York, 1966, pp. 295–346.
[7] F. Oosawa, Polyelectrolytes, New York, Marcel Dekker, 1971.
[8] H. Dautzenberg, W. Jaeger, J. Kötz, B. Philipp, Ch. Seidel, D. Stscherbina, Polyelectrolytes: Formation, Characterization, and Application, Carl Hanser Verlag, Munich, 1994.
[9] J. Cohen, Z. Priel, Y. Rabin, Viscosity of dilute polyelectrolyte solutions, J. Chem. Phys. 88 (1988) 7111–7116.
[10] J. Cohen, Z. Priel, Y. Rabin, Molecular-weight dependence of viscosity in dilute polyelectrolyte solutions—the low salt limit, Polym. Commun. 29 (1988) 235–236.
[11] Hydrophobically associating polymers, P. Dubin, J. Bock, R.M. Davies, D.N. Schulz, C. Thies (Eds.), Macromolecular Complexes in Chemistry and Biology, Springer-Verlag, Berlin Heidelberg, 1994, pp. 3–116.
[12] Z. Gao, R.E. Wasylishen, J.C.T. Kwak, An NMR study of the binding between polyelectrolytes and surfactants in aqueous solutions, J. Colloid Interface Sci. 126 (1988) 371–376.
[13] M. Almgren, P. Hansson, E. Mukhtar, J. van Stam, Aggregation of alkyltrimethylammonium surfactants in aqueous poly(styrenesulfonate) solutions, Langmuir 8 (1992) 2405–2412.
[14] P. Hansson, M. Almgren, Interaction of alkyltrimethylammonium surfactants with polyacrylate and poly(styrenesulfonate) in aqueous solution. Phase behavior and surfactant aggregation numbers, Langmuir 10 (1994) 2115–2124.
[15] M. Andersson, P.J. Råsmark, C. Elvingson, P. Hansson, Single microgel particle studies demonstrate the influence of hydrophobic interactions between charged micelles and oppositely charged polyions, Langmuir 21 (2005) 3773–3781.
[16] K. Kogej, Association and structure formation in oppositely charged polyelectrolyte-surfactant mixtures, Adv. Colloid Interface Sci. 158 (2010) 68–83.

[17] K. Kogej, G. Evmenenko, E. Theunissen, H. Berghmans, H. Reynaers, Investigation of structures in polyelectrolyte/surfactant complexes by X-ray scattering, Langmuir 17 (2001) 3175–3184.
[18] K. Kogej, G. Evmenenko, E. Theunissen, J. Škerjanc, H. Berghmans, H. Reynaers, W. Bras, Formation of ordered microstructures in polyelectrolyte/surfactant systems: linear anionic polyelectrolytes and cetylpyridinium chloride, Macromol. Rapid Commun. 21 (2000) 1226–1233.
[19] J. Škerjanc, K. Kogej, V. Vesnaver, Polyelectrolyte-surfactant interactions. Enthalpy of binding of dodecyl- and cetylpyridinium cations to poly(styrenesulfonate) anion, J. Phys. Chem. 92 (1988) 6382–6385.
[20] K. Kogej, J. Škerjanc, Surfactant binding to polyelectrolytes, in: Ts. Radeva (Ed.), Physical Chemistry of Polyelectrolytes, Surfactant Science Series, vol. 99, Marcel Dekker, New York, 2001, pp. 793–827 (Chapter 27).
[21] J. Škerjanc, K. Kogej, Thermodynamic and transport properties of polyelectrolyte-surfactant complex solutions at various degrees of complexation, J. Phys. Chem. 93 (1989) 7913–7915.
[22] K. Kogej, J. Škerjanc, Hydrodynamic investigations of polyelectrolyte-surfactant complexes in aqueous solutions, Acta. Chim. Slov. 46 (1999) 481–492.
[23] K. Bohinc, T. Slivnik, A. Iglič, V. Kralj-Iglič, Membrane electrostatics. A statistical mechanical approach to the functional density theory of electric double layer, Adv. Planar Lipid Bilayers Liposomes 8 (2008) 107–154.
[24] O. Enea, P.P. Singh, L.G. Hepler, Apparent molal heat capacities and volumes of pyridine and methyl-substituted pyridines in aqueous solution at 25 °C, J. Sol. Chem. 6 (1977) 719–725.
[25] C. Tanford, The Hydrophobic Effect: Formation of Micelles and Biological Membranes, Wiley, New York, 1980.
[26] D.F. Evans, H. Wennerström, The Colloidal Domain: Where Physics, Chemistry, Biology, and Technology Meet, Wiley, New York, 1999.
[27] K. Kogej, J. Škerjanc, Fluorescence and conductivity studies of polyelectrolyte induced aggregation of alkyltrimethylammonium bromides, Langmuir 15 (1999) 4251–4258.
[28] J.N. Israelachvili, D.J. Mitchell, B.W. Ninham, Theory of self-assembly of hydrocarbon amphiphiles into micelles and bilayers, J. Chem. Soc. Faraday Trans. 2 (72) (1976) 1525–1568.
[29] P. Linse, L. Picullel, P. Hansson, Models of polymer-surfactant complexation, in: J.C.T. Kwak (Ed.), Polymer-Surfactant Systems, Surfactant Science Series, vol. 77, Marcel Dekker, New York, 1998, pp. 193–238 (Chapter 5).
[30] J. Škerjanc, K. Kogej, Electrical transport in polyelectrolyte-surfactant complex solutions at various degrees of complexation, in: K.S. Schmitz (Ed.), Macro-Ion Characterization: From Dilute Solutions to Complex Fluids, ACS Symposium Series 548. American Chemical Society, Washington, DC, 1994, pp. 268–275 (Chapter 20).
[31] I. Satake, Y.T. Yang, Interaction of sodium decyl sulfate with poly(L-ornithine) and poly(L-lysine) in aqueous solutions, Biopolymers 15 (1976) 2263–2275.
[32] K. Hayakawa, J.C.T. Kwak, Surfactant-polyelectrolyte interactions. 1. Binding of dodecyltrimethylammonium ions by sodium dextran sulfate and sodium poly (styrenesulfonate) in aqueous solution in the presence of sodium chloride, J. Phys. Chem. 86 (1982) 3866–3870.
[33] K. Hayakawa, J.P. Santerre, J.C.T. Kwak, Study of surfactant-polyelectrolyte interactions. Binding of dodecyl- and tetradecylammonium bromide by some carboxylic polyelectrolytes, Macromolecules 16 (1983) 1642–1645.
[34] A. Malovikova, K. Hayakawa, J.C.T. Kwak, Binding of alkylpyridinium cations by anionic polysaccharides, ACS Symp. Ser. 253 (1984) 225–239.
[35] K. Hayakawa, J.C.T. Kwak, Study of surfactant-polyelectrolyte interactions. 2. Effect of multivalent counterions on the binding of dodecyltrimethylammonium ions by sodium

dextran sulfate and sodium poly(styrenesulfonate) in aqueous solution, J. Phys. Chem. 87 (1983) 506–509.
[36] S. Sitar, B. Goderis, P. Hansson, K. Kogej, Phase diagram and structures in mixtures of poly(styrenesulfonate anion) and alkyltrimethylammonium cations in water: significance of specific hydrophobic interaction, J. Phys. Chem. B 116 (2012) 4634–4645.
[37] B. Lindman, H. Wennerström, Micelles. Amphiphile aggregation in aqueous solution, Top. Curr. Chem. 87 (1980) 1–83.
[38] P. Hansson, M. Almgren, Polyelectrolyte-induced micelle formation of ionic surfactants and binary surfactant mixtures studied by time-resolved fluorescence quenching, J. Phys. Chem. 99 (1995) 16684–16693.
[39] L. Piculell, B. Lindman, Association and segregation in aqueous polymer/polymer, polymer/surfactant, and surfactant/surfactant mixtures: similarities and differences, Adv. Colloid Interface Sci. 41 (1992) 149–178.
[40] A. Svensson, L. Piculell, B. Cabane, P. Ilekti, A new approach to the phase behavior of oppositely charged polymers and surfactants, J. Phys. Chem. B 106 (2002) 1013–1018.
[41] A. Svensson, J. Norrman, L. Piculell, Phase behavior of polyion-surfactant ion complex salts: effects of polyion length and surfactant chain length, J. Phys. Chem. B 110 (2006) 10332–10340.
[42] S. Prelesnik, S. Larin, V. Aseyev, H. Tenhu, K. Kogej, Water soluble non-stoichiometric complexes between sodium poly(styrenesulfonate) and cetylpyridinium chloride in aqueous NaCl solutions. A static and dynamic light scattering study, J. Phys. Chem. B 115 (2011) 3793–3803.
[43] K. Thalberg, B. Lindman, K. Bergfeldt, Phase behavior of polyacrylate and cationic surfactants, Langmuir 7 (1991) 2893–2898.
[44] K. Thalberg, B. Lindman, Interaction between hyaluronan and cationic surfactants, J. Phys. Chem. 93 (1989) 1478–1483.
[45] K. Thalberg, B. Lindman, G. Karlstrom, Phase behavior of a system of cationic surfactant and anionic polyelectrolyte: the effect of salt, J. Phys. Chem. 95 (1991) 6004–6011.
[46] P. Hansson, M. Almgren, Interaction of alkyltrimethylammonium surfactants with polyacrylate and poly(styrenesulfonate) in aqueous solution: phase behavior and surfactant aggregation numbers, Langmuir 19 (1994) 2115–2124.
[47] P. Nilsson, J. Unga, P. Hansson, Effect of salt and surfactant concentration on the structure of polyacrylate gel/surfactant complexes, J. Phys. Chem. B 111 (2007) 10959–10964.
[48] T. Andersson, V. Aseyev, H. Tenhu, Complexation of DNA with poly(methacryl oxyethyl trimethylammonium chloride) and its poly(oxyethylene) grafted analogue, Biomacromolecules 5 (2004) 1853–1861.
[49] A. Trewavas, A new method for counting labeled nucleic acids by liquid scintillation, Anal. Biochem. 21 (1967) 324–329.
[50] B. Pontius, P. Berg, Rapid renaturation of complementary-DNA strands mediated by cationic detergents—a role for high-probability binding domains in enhancing the kinetics of molecular assembly processes, Proc. Natl. Acad. Sci. U.S.A. 88 (1991) 8237–8241.
[51] D. Lasič, Liposomes in Gene Delivery, CRC Press, Boca Raton, FL, 1997.
[52] U. Henriksson, E.S. Blackmore, G.J.T. Tiddy, O. Söderman, Intermediate liquid crystalline phases in the binary system C_{16}TACl-H_2O: an NMR and low-angle X-ray diffraction study, J. Phys. Chem. 96 (1992) 3894–3902.
[53] H. Okuzaki, Y. Osada, Ordered-aggregate formation by surfactant-charged gel interaction, Macromolecules 28 (1995) 380–382.
[54] P. Ilekti, T. Martin, B. Cabane, L. Piculell, Effects of polyelectrolytes on the structures and interactions of surfactant aggregates, J. Phys. Chem. 103 (1999) 9831–9840.

[55] A.V. Mironov, S.G. Starodoubtsev, A.R. Khokhlov, A.T. Dembo, A.N. Yakunin, Ordered nonstoichiometric polymer gel-surfactant complexes in aqueous medium with high ionic strength, Macromolecules 31 (1998) 7698–7705.
[56] P. Scherrer, Bestimmung der grösse und der inneren struktur von kolloidteilchen mittels röntgenstrallen, Göttinger Nachrichten 2 (1918) 98.
[57] B.K. Vainshtein, Diffraction of X-Rays by Chain Molecules, Elsevier, New York, 1996.
[58] K. Kogej, E. Theunissen, H. Reynaers, Effect of polyion charge density on the morphology of nanostructures in polyelectrolyte-surfactant complexes, Langmuir 18 (2002) 8799–8805.
[59] K. Kogej, Study of the effect of polyion charge density on structural properties of complexes between poly(acrylic acid) and alkylpyridinium surfactants, J. Phys. Chem. B 107 (2003) 8003–8010.
[60] B. Magny, I. Iliopoulos, R. Zana, R. Audebert, Mixed micelles formed by cationic surfactants and anionic hydrophobically modified polyelectrolyte, Langmuir 10 (1994) 3180–3187.
[61] M. Benrraou, R. Zana, R. Varoqui, E. Pefferkorn, Study of the interaction between dodecyltrimethylammonium bromide and poly(maleic acid-co-alkyl vinyl ether) in aqueous solution by potentiometry and fluorescence probing, J. Phys. Chem. 96 (1992) 1468–1475.
[62] I. Iliopoulos, T.K. Wang, R. Audebert, Viscometric evidence of interactions between hydrophobically modified poly(sodium acrylate) and sodium dodecyl sulfate, Langmuir 7 (1991) 617–619.

CHAPTER EIGHT

Implications of Microvesicle and Cell Surface Protein Shedding for Biomarker Studies, Cancerogenesis, and Therapeutic Target Discovery in Ovarian Cancer

Katarina Černe*[1], Borut Kobal**

*Department of Pharmacology and Experimental Toxicology, Faculty of Medicine, University of Ljubljana, Ljubljana, Slovenia

**Department of Gynaecology, Division of Gynaecology and Obstetrics, University Medical Centre Ljubljana, Ljubljana, Slovenia

[1]Corresponding author: e-mail address: katarina.cerne@mf.uni-lj.si

Contents

1. Ovarian Cancer 240
   1.1 Theories of ovarian cancerogenesis 241
   1.2 Metastasis 243
   1.3 Therapy 246
   1.4 Serum biomarkers 246
2. Mechanisms of Soluble Protein Release 247
   2.1 Vesicle shedding 248
   2.2 Ectodomain shedding 249
   2.3 Alternative splicing 254
3. Role of Vesicle and Ectodomain and Shedding in Ovarian Cancer 254
   3.1 Vesicle shedding and ovarian cancer 254
   3.2 MMPs and ovarian cancer 260
   3.3 ADAMs and ovarian cancer 262
   3.4 Alternative splicing and ovarian cancer 263
4. Protein Secretion Rates and Blood Biomarkers' Level 264
5. MVs and Sheddases as Potential Therapeutic Targets 266
   5.1 MVs as therapeutic targets 266
   5.2 MMPs as therapeutic targets 267
   5.3 ADAMs as therapeutic targets 267
6. Conclusions 268
Acknowledgments 268
References 268

Advances in Planar Lipid Bilayers and Liposomes, Volume 16
ISSN 1554-4516
http://dx.doi.org/10.1016/B978-0-12-396534-9.00008-8

Abstract

Ovarian cancer is one of the most aggressive and lethal cancers in women. There is currently no accurate noninvasive diagnostic test for ovarian cancer; most patients are diagnosed at an advanced stage, presenting with peritoneal metastasis and ascites. Although ovarian cancer patients often respond initially to chemotherapy, recurrence is almost always accompanied by chemoresistance. The identification of proteins that are abundantly and predominantly expressed in ovarian cancer is therefore relevant to diagnosis, tumor imaging, and targeted therapies.

Proteins with high secretion rates or proteins that are extensively cleaved from the cell surface, specifically from tumor cells, are a potential source of circulating biomarkers for ovarian cancer. The process of surface protein shedding as observed in ascites-derived tumor cells from ovarian cancer patients is also relevant to tumor invasion and metastasis, as exemplified by the role of cadherin.

Additionally, proteins, as well as lipids, DNA, and RNA, can reach the blood in microvesicles that are shed from tumor cells. A roughly fivefold increase in their blood concentration is reported in ovarian cancer patients. Tumor-derived vesicles are fully equipped to facilitate the escape of tumor cells from immune surveillance. At the same time, they are involved in the establishment of an optimal environment for metastatic tumor cells. On the basis of the role of tumor microvesicles in tumor progression, another door has been opened to a new ovarian cancer therapy.

This review addresses the relevance of secretion and shedding of microvesicles and membrane surface protein from tumor cells for biomarker discovery, cancerogenesis, and new therapies in ovarian cancer.

1. OVARIAN CANCER

Despite advances in surgery and combination chemotherapy, ovarian cancer is third in terms of incidence of tumors of the female reproductive system and first in terms of death rates of gynecological malignancies, with a highly aggressive natural history, and it causes almost 125,000 deaths yearly. Its high mortality reflects the fact that less than 20% of all ovarian cancers are diagnosed at an early stage, due to subtle symptom development and the lack of robust and minimally invasive methods for early detection [1,2]. Although ovarian cancer patients often respond initially to chemotherapy, they usually develop chemoresistance [3]. Recurrence is almost always accompanied by the development of chemoresistance and carcinomatosis, which may not be amenable to surgery [4].

Ovarian tumors can be classified on the basis of the cells of origin into epithelial, stromal, and germ cell tumors (Fig. 8.1). Although approximately 40% of all ovarian tumors are nonepithelial in origin, such lesions rarely

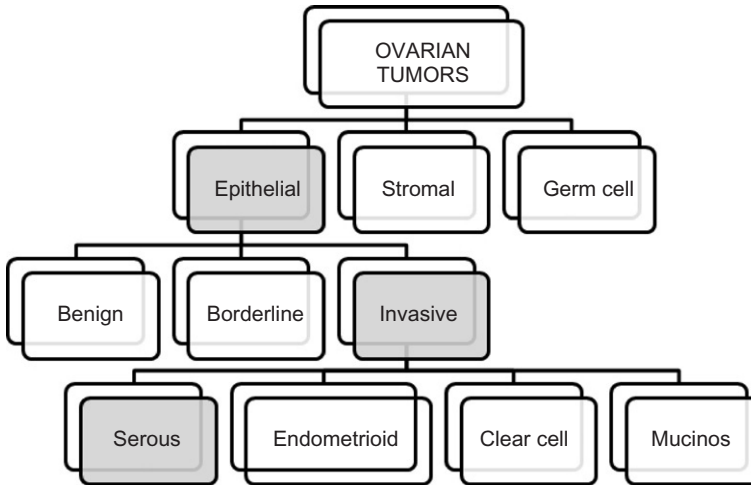

Figure 8.1 Histopathological classification of the main ovarian tumors. Majority of ovarian cancer is of the epithelial origin. The serous subtype is responsible for most ovarian deaths.

progress to a malignant state and account for only 10% of ovarian cancers [5]. Epithelial ovarian neoplasms display great histological heterogeneity and can be further subdivided into benign, intermediate or borderline, and invasive tumors. There are four major histological types of epithelial ovarian carcinoma: serous, endometrioid, clear cell, and mucinous, which differ in their clinical behavior and molecular characteristics. The serous subtype (Fig. 8.2) is the most commonly diagnosed and is responsible for most ovarian deaths [2].

In order optimally to manage a cancer, both the extent of the disease and knowledge of its biology are essential. The extent of the disease is generally expressed in terms of its stage. The most commonly utilized staging system is the FIGO (*International Federation of Gynecology and Obstetrics*) system. It is based on findings mainly through surgical exploration [6].

1.1. Theories of ovarian cancerogenesis

Several possible mechanisms have been suggested for ovarian cancerogenesis.

The incessant ovulation hypothesis assumes that the development of ovarian cancer is a consequence of repeated microtrauma to the ovarian surface epithelium during ovulation. It is hypothesized that repeated DNA damage during ovulation and dysfunction of its recognition and repair are crucial for ovarian cancerogenesis [7].

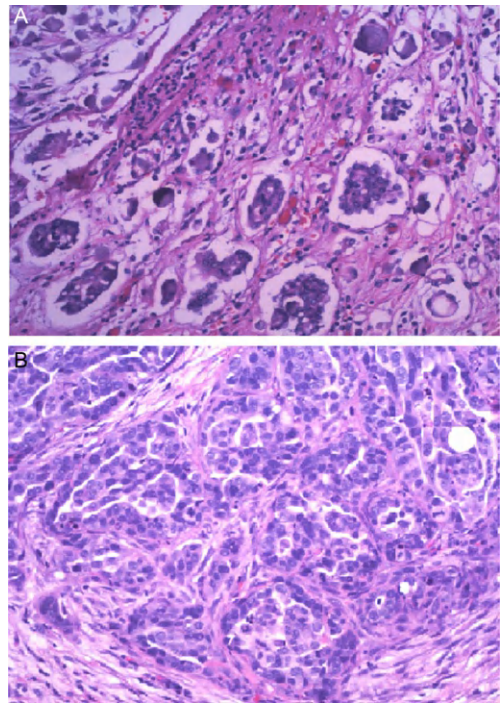

Figure 8.2 Serous ovarian carcinoma. (A) Low-grade tumor with psammoma bodies. (B) High-grade tumor without psammoma bodies. The presence of psammoma bodies is an indication of favorable serous ovarian carcinoma leading to better long-term survival.

The gonadotropin hypothesis states that malignant transformation can be caused by the exposure of the ovarian surface epithelium to excessive gonadotropin levels [8].

The hormonal hypothesis presumes a decisive role for ovarian hormones, progesterone in particular. In experimental studies, progesterone upregulated p53 tumor suppressor gene expression and inhibited proliferation of cultured sheep ovarian epithelial cells or induced apoptosis in normal and malignant human ovarian epithelial cell lines [9,10].

The secondary Müllerian system theory is, based on the possibility of developing epithelial cancer from one precursor cell, derived from the Müllerian duct. The Müllerian duct forms the fallopian tube, uterus, cervix, and upper vagina, and *HOX* genes play a significant role in such differentiation [11].

The cancer stem cell hypothesis, based on the similarities between normal and tumor stem cells, postulates that the former could themselves be targets of

stochastic transforming mutations or give rise to a hierarchy of progenitors and differentiated cells that make up the tumor mass. Continuing stochastic events of stem and progenitor cell transformation define the extremely aggressive disease associated with the lack of early symptoms [12,13].

None of these theories explain the epidemiology data in full. Moreover, there is an overlap in mechanisms involved in an individual hypothesis. Probably, several mechanisms contribute to ovarian cancerogenesis.

1.2. Metastasis

Ovarian carcinoma can spread by local extension, intraperitoneal implantation, lymphatic invasion, hematogenous dissemination, and/or transdiaphragmatic passage [14]. Unlike most other cancers, ovarian carcinoma rarely disseminates through the vasculature [15]. Many of the advanced stage cancers (stages III–IV) have pelvic lymph-node involvement with strong correlations between intraperitoneal and lymph-node spread [16]. Dissemination of tumor cells through the peritoneal cavity is most often described as a stepwise process (Fig. 8.3): (i) resistance to anoikis and cell detachment, (ii) dissemination of tumor cells via the natural flow of peritoneal fluid, (iii) evasion

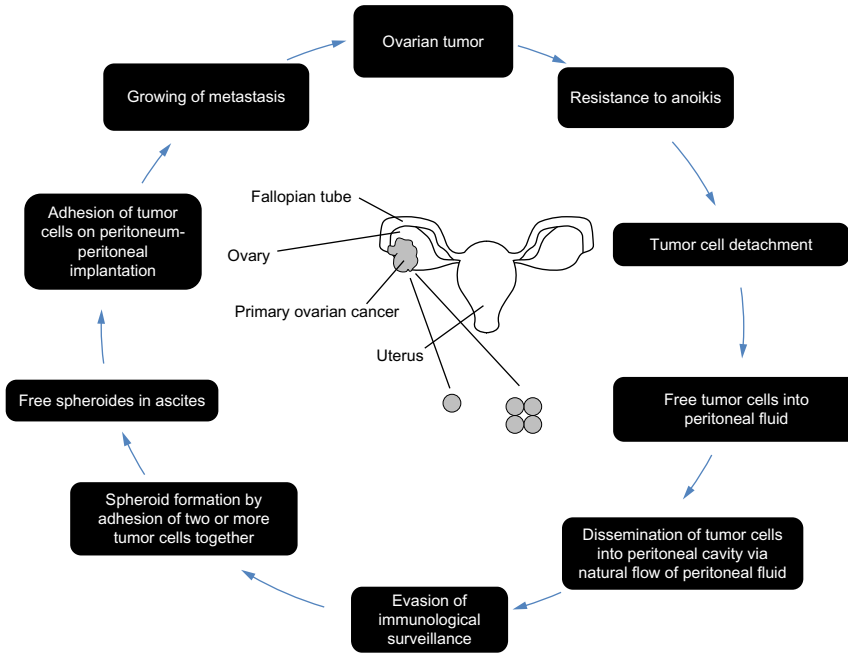

Figure 8.3 Schematic presentation of peritoneal spreading of ovarian cancer.

of immunological surveillance, (iv) spheroid formation, (v) ascites–a metastatic milieu, and (vi) peritoneal implantation [17].

Initially, ovarian carcinoma spreads by direct extension into the adjacent organs, especially the fallopian tubes, uterus, and contralateral adnexa. After direct extension, tumor cells become detached from the primary tumor and disseminate through the peritoneal cavity via the peritoneal fluid before seeding intraperitoneally [15,17]. Free fluid in the peritoneal cavity acts as a lubricant of the serosal surfaces and originates from the transduction of plasma through capillary membranes of the peritoneal serosa. Under physiological conditions, transudation is balanced by efflux of the peritoneal fluid via lymphatic vessels. The flow of intraperitoneal fluid is directed by gravity to its most dependent sites and then drawn in a cephalic direction along the paracolic gutter to the diaphragm by the generation of negative intra-abdominal pressure in the upper abdomen during respiration [17]. The natural flow of peritoneal fluid therefore provides a rout for the dissemination of detached tumor cells.

Extensive seeding of the peritoneal cavity by tumor cells is often associated with ascites, particularly in advanced, high-grade serous carcinomas [15]. In addition to hypoalbuminemia secondary to cachexia or dietary deficiency, at least three other pathological events can cause ascites: reduced lymphatic drainage from the peritoneal cavity, caused by obstruction of the lymphatic vessels by tumor cells, hyperpermeability of microvessels lining the peritoneal cavity, and tumor neoangiogenesis [18]. The cellular fraction of ascites mainly consists of ovarian cancer cells, lymphocytes, and mesothelial cells. The neoplastic cells in the ascites are present either as single cells or as aggregated ovarian neoplastic cells, also known as spheroids (Fig. 8.4). The acellular fraction of ascites contains the secretome of ovarian cancer cells, in addition to other soluble microenvironmental factors that have been associated with invasion and metastasis (e.g., cytokines, growth factors, adhesion molecules, matrix-degrading enzymes) [14,19]. The peritoneum and its extension, the intestinal serosa, pose no substantial barriers to inflammatory cytokines and chemokines and other molecules produced by the tumor, or its metastasis at least to a depth of approximately 1 mm [20].

After attachment, ovarian cancer spheroids have been shown to disaggregate on and invade the peritoneal mesothelium. Like the process of tumor cell detachment, the mechanism of peritoneal implantation is unclear but seems to involve the dynamic regulation of an ovarian cell's adhesiveness and its interaction with the underlying mesothelium. Histologically, the mesothelium is a single layer of mesothelial cells attached to a basement

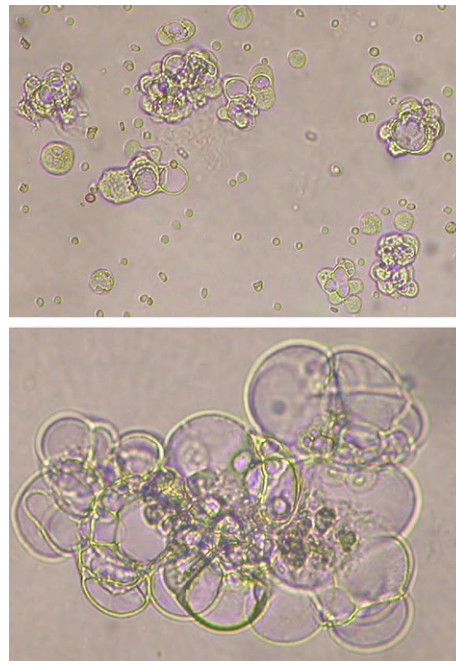

Figure 8.4 Cellular aggregates (also known as spheroids) from ascites of ovarian cancer patient.

membrane predominantly composed of collagen types I and IV, fibronectin, and laminin. The submesothelial stroma consists of a collagen-based matrix, blood vessels, lymphatics, nerve fibers, and rare hematogenous cells [15,21]. The attachment of ovarian carcinoma cells to the mesothelium is followed by pseudopodialike extensions of the tumor cells, disruption of the mesothelial intercellular junctions, and retraction of the mesothelial cells, with subsequent exposure of the underlying matrix where the tumor cells adhere and proliferate [19].

During these migratory processes, tumor cells reorganize their cytoskeleton and modulate the surrounding extracellular matrix (ECM). In addition, tumor cells continuously change their cell surface adhesion repertoire. These changes in adhesion not only allow migration directly, but they also modify intercellular communication of tumor cells with other cells and alter signaling from and to the surrounding ECM. Tumor cells may also use mechanisms that resemble transendothelial migration of leukocytes to sites of inflammation. Several adhesion molecules are involved in this process,

including E-, P-, and L-selectin; intercellular adhesion molecule 1 (ICAM-1); vascular cell adhesion molecule 1 (VCAM-1); platelet endothelial cell adhesion molecule 1 (PECAM-1); and integrins.

1.2.1 From peritoneum to circulation

The transcoelomic route provides direct access to the circulation. Ascites carrying ovarian cancer cells enter the subperitoneal lymphatic lacunae between the muscle fibers of the diaphragm. From the lacunae, fluid traverses the diaphragm via intrinsic lymphatics to reach collecting lymphatics beneath the diaphragmatic pleura. Intrinsic and collecting lymphatics contain valves that prevent backflow into the peritoneal cavity. The lymphatic fluid subsequently drains into retrosternal vessels and enters the thoracic duct before draining into the left subclavian vein. Interestingly, hematogenous metastases in ovarian cancer are rare, despite the presence of circulating tumor cells as early as initial diagnosis [22,23].

1.3. Therapy

Over the past decades, empirical optimization of cytotoxic chemotherapy combination and the surgical debulking procedure have improved outcomes and survival in epithelial ovarian cancer. Carboplatin and paclitaxel combination chemotherapy allows a disease response rate of 70–80%. Together with improved surgical staging and optimal debulking surgery, 5-year survival rose from 37% in the 1970s to 45% in the 1990s [24]. However, because of chemotherapy–chemoresistant cells, the majority of these patients relapse at a median of 15–20 months, ultimately resulting in fatal outcomes [25]. While some targeted agents have reached clinical testing (agents target, e.g., CD44, poly (ADP-ribose) polymerase, folate receptor α), the results are mixed. Epidermal growth factor receptor (EGFR) inhibitors have shown disappointing results, while the vascular endothelial growth factor (VEGF) inhibitor bevacizumab recently proved promising at phase III [26].

1.4. Serum biomarkers

Biomarkers can serve various purposes. They can detect early-stage disease, guide patient treatment, predict therapy outcome, and monitor recurrence. Currently, none of the promising potential single markers or combination of markers, which are more powerful and cancer specific than individual markers, have fulfilled the expectation of being able to predict ovarian cancer with a high enough sensitivity and specificity. Considering the low

prevalence of ovarian cancer (0.04% in postmenopausal women), a screening strategy must achieve a minimum specificity of 99.6% and a sensitivity of more than 75% for early-stage disease in order to avoid an unacceptable level of false-positive results and to achieve a positive predictive value of 10% [27,28]. Since the majority of adnexal masses are benign, it is also important to determine preoperatively whether a patient is at high risk for ovarian malignancy, in order to ensure proper management. Considering the heterogeneity of ovarian cancers from different patients and the different purposes of biomarkers, it is unlikely that any single marker will be sufficient.

While an annual pelvic examination is widely practiced, it lacks the sensitivity to be used as a screening strategy for ovarian cancer. Women at high risk for ovarian cancer may undergo screening with transvaginal ultrasound and serum cancer antigen or carbohydrate antigen 125 (CA-125). CA-125, however, remains a poor marker for early-stage disease. Additionally, it has been shown that even in a high-risk, screened population, incident cases are still more likely to be advanced stage [29]. The recent introduction of human epididymis protein 4 (HE4) might improve the detection of ovarian cancer, particularly in early-stage disease. A combination of CA-125 and HE4 predicts malignancy with a sensitivity of 76% and specificity of 95% [30].

In spite of intense work in the field of serum biomarkers to predict ovarian cancer, there is not a lot to show. It is important for the whole field to step back and look at what is wrong. The situation raises two questions: (1) do early-detection biomarkers exist in reality and (2) what are the limitations of serum biomarker research that has been done for decades? One approach for future research is systematically to characterize sets of proteins, the location of which makes them especially relevant for diagnosis and treatment, notably proteins at the cell surface or those released into the extracellular milieu. Proteins with high secretion rates or proteins that are extensively cleaved from the cell surface, specifically from tumor cells, are a potential source of circulating markers.

2. MECHANISMS OF SOLUBLE PROTEIN RELEASE

Several soluble proteins have been detected in patient body fluids and supernatant of tumor cell lines. The three most important mechanisms that result in the formation and/or release of soluble molecules are (i) vesicle release, (ii) ectodomain shedding, and (iii) alternative splicing of mRNA transcripts. Both ectodomain shedding and alternative splicing in general

lead to a truncated soluble ectodomain, in contrast to the full-length molecules liberated from cells by vesicle release.

2.1. Vesicle shedding

Membrane vesicles are membrane-covered cell fragments shedding from practically all cell types, constitutively and in response to an activation signal. The process of vesicle shedding is very active in proliferating cells, such as cancer cells. The nomenclature is still controversial: they are at present collectively called membrane vesicles. The term exosome comprises vesicles with a size from 30 to 100 nm, while larger ones are commonly referred to as microvesicles (MVs), ectosomes, microparticles, exovesicles, or apoptotic vesicles. In this review, the collective term microvesicle will be used for vesicles below 1000 nm. So-called apoptotic bodies differ from MV. They are released in the final stages of apoptosis, and their size is larger than 1000 nm. In contrast, apoptosis-induced MVs are formed at the beginning of apoptosis with a size smaller than 1000 nm and do not contain organelles [31].

The distinction between strictly called exosomes and vesicles with a size from 100 to 1000 nm is based on their formation. Small vesicles are formed via exocytosis, which explains the term exosome. They develop from endosomes. Instead of following the lysosomal pathway, these multivesicular bodies fuse with the plasma membrane and release their exosomes. Cytoplasmic protein can also enter future exosomes, which, together with the proteins of the invaginated cell membrane, represent the "donor cell." Vesicles shedding from tumor cells often fall into the exosome category. Since exosomes can be taken up by other cells, they may represent a novel intercellular signaling device. So-called reverse budding occurs for the release of most MVs between 100 and 1000 nm. Budding is coupled to the reorganization of the cytoskeleton, which is the result of multiple intracellular interactions. The elevation of intracellular Ca^{2+} ion concentrations plays a key role in the initiation of the disruption of actin cortex. Budding also occurs when an apoptotic signal reaches the cell and when the cell membrane becomes detached from the cytoskeleton. Since the budding vesicles contain cytoplasmic fragments and areas form the cell membrane, the origin of the cell type from which they derived can be identified [31].

Depending on the cellular origin, MVs recruit various cellular proteins, which can be different from the plasma membrane, including major histocompatibility complex (MHC) molecules, tetraspanins, metalloproteinases, single-stranded DNA, mRNA, miRNA, and siRNA [31–33].

2.2. Ectodomain shedding

Numerous integral plasma proteins also occur as a circulating, soluble form. These soluble forms are often derived from the membrane form; in this case, the secretory event involves their selective posttranslation hydrolysis from the cell surface. This secretion (often called "shedding" or "solubilization") involves either protease or phospholipase, depending on the type of membrane anchor on the protein. The group of enzymes involved in this process is referred to collectively as "secretases" or "sheddases." Individual secretases have revealed common features, particularly sensitivity to certain matalloprotease inhibitors and upregulation of activity by phorbol esters [34]. Proteins secreted in this fashion include cell adhesion molecules and leukocyte antigens, receptors and receptor ligands, ectoenzymes, and viral membrane proteins. Release of soluble growth factors and cytokines may change their biological activities, whereas shedding of transmembrane receptors may render cells unresponsive to particular ligands, and the resulting soluble molecules may act to modulate the activity of their ligands [34,35]. After transmembrane cleavage, the intracellular domain may gain entry to the nucleus, where it participates in transcriptional control of target genes (e.g., CD44, E-cadherin) [36,37].

Depending on the type of membrane anchor, proteins are divided into integral transmembrane proteins and lipid-anchored proteins. A distinction is made among integral transmembrane proteins on the basis of their orientation and the number of times the protein spans the lipid bilayer. Type I proteins (e.g., CA-125, VCAM-1, ICAM-3, L-selectin, human EGFR (HER-4), CD44, transforming growth factor α (TGF-α), IL-6 receptor, TGF-β receptor, Notch) with a cleaved N-terminal signal sequence face the extracellular space. They are retained in the membrane by a hydrophobic sequence of amino acids close to the C-terminus. Type II proteins (e.g., CD40, Fas, transferrin receptor) are similar to the type I class in that they span the membrane only once, but the membrane anchor is the uncleaved signal peptide, and the protein is oriented with a short, hydrophilic, cytoplasmic domain, including N-terminal, and with the bulk of the protein, including the C-terminus, facing the extracellular space. Type III proteins (e.g., cytochrome P450, CD20) have multiple transmembrane domains in a single polypeptide chain. Lipid-anchored proteins (e.g., carcinoembryonic antigen, neural cell adhesion molecule, CD14, alkaline phosphatase) use lipids to attach themselves to the plasma membrane. The most common attachment is the glycosylphosphatidylinositol (GPI) anchor (e.g., MT4- and MT6-MMP). The GPI anchor can be cleaved by the bacterial enzyme or phospholipase C or D [34,38].

The endogenous proteolytic release of integral proteins is limited to those of type I and type II structure, in which the cleavage site is generally located close to the membrane surface. In some cases, this is a process for rapidly downregulating the protein from the surface of the cell; in other cases, it may be to generate a soluble form of the protein that has properties either identical with or different from those of the membrane-bound form. Type III proteins cannot be released from the membrane by limited proteolysis, but specific proteolytic cleavage can, in some cases, modify their membrane activities. The cleavage could activate the receptor or terminate its action [34].

2.2.1 Proteases involved in ectodomain shedding

Ectodomain shedding can be mediated by both membrane-bound and soluble proteases. The vast majority of shedding events are mediated by the Zn^{2+}-dependent proteinase superfamily, also known as *metzincins*, including matrix metalloproteinases (MMPs), membrane-type MMPs (MT-MMPs), a disintegrin and metalloproteinases (ADAMs), and a disintegrin and metalloproteinases with thrombospondin motifs (ADAMTSs) (Fig. 8.5).

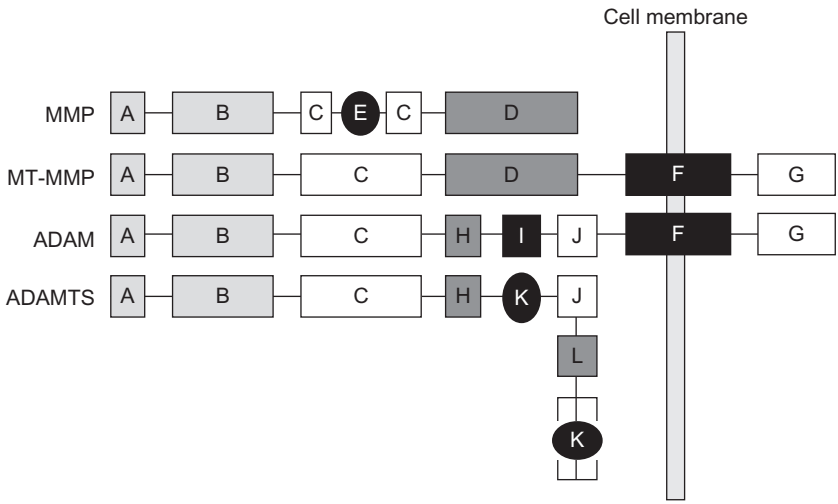

Figure 8.5 Schematic representation of the domain structure of metzincin proteases. (A) Signal peptide, (B) prodomain, (C) catalytic domain, (D) hemopexin-like domain, (E) fibronectin type II insert, (F) transmembrane domain, (G) cytoplasmatic tail, (H) disintegrin domain, (I) cysteine-rich domain, (J) EGF-like domain, (K) thrombospondin type I-like repeat, and (L) spacer region. The metalloproteinase (MMP) shown is of the gelatinase class. Other subclasses of MMPs lack hemopexin-like domain and/or fibronectin type II insert. MT-MMPs, membrane-type MMP; ADAM, a disintegrin and metalloproteinases; ADAMTS, a disintegrin and metalloproteinases with thrombospondin motifs.

In addition, other proteinases, such as serine proteinases (e.g., urokinase-type plasminogen activator (uPA), neutrophil elastase, proteinase-3), cysteine proteinases (e.g., cathepsin B, C, F, H, K, L, O, S, V, W, and X), and aspartate proteinases (cathepsin D, E, pepsin, renin), have also been implicated in the shedding of surface proteins [35,39].

2.2.1.1 Matrix metalloproteinases

Two groups are distinguished in the *matrixin* family of zinc proteinases: MMPs and MT-MMPs. Compared to MMPS, MT-MMPs possess an additional transmembrane domain and an intracellular domain.

In humans, there are 23 paralogs of MMPs (numbered 1–3, 7–17, 19–21, and 23–28 for historical reasons; there are two identical forms for MMP-23, encoded by two genes, *mmp-23a* and *mmp-23b*). Those MMPs bearing a membrane anchor give rise to the MT-MMP subfamily (MT1-MMP to MT6-MMP; in plain MMP nomenclature they are, respectively, MMP-14–17, MMP-24, and MMP-25). MMPs have the capacity to degrade virtually every component of the ECM. Based on their ECM substrate specificity, MMPs have been divided into distinct subclasses: (i) true collagenases, which cut triple-helical fibrillar collagen; (ii) gelatinases, which target denaturated collagens and gelatines; and (iii) stromelysins, which have broad specificity and may degrade proteoglycans [40]. MMPs substrates include also non-ECM molecules, ranging from growth factor precursors and cell surface adhesion molecules to angiogenic inhibitor precursors. MMPs have multiple functions in cancer progression. MMPs degrade components of the ECM, facilitating angiogenesis, tumor cell invasion, and metastasis. MMPs modulate interactions between tumor cells by cleaving E-cadherin (Fig. 8.6), and between tumor cells and ECM by processing integrins, which also enhances the invasiveness of tumor cells, MMPs also process and activate signaling molecules, including growth factors and cytokines, making these factors more accessible to target cells, either by liberating them from the ECM (e.g., VEGF, fibroblast growth factor) or by shedding them from the cell surface (e.g., heparin-binding epidermal growth factor) [41–43].

MMPs activity is regulated via modulation of gene expression, compartmentalization, and inhibition by protein inhibitors. Most MMPs are not constitutively transcribed but are expressed after external induction by cytokines and growth factors. In addition, some MMPs are stored in inflammatory cell granules, which restrict their range of action. Another regulatory mechanism is provided by zymogenicity (inactive enzyme precursor).

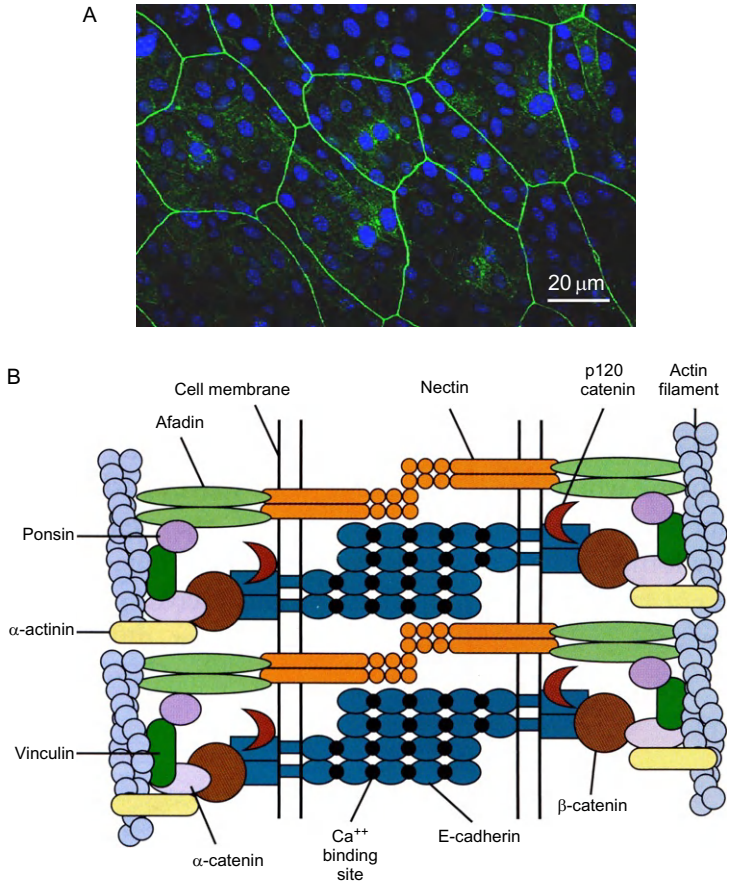

Figure 8.6 E-cadherin. (A) Three-dimensional reconstruction of optical sections of multilayer epithelium in cell culture. Green immunofluorescence shows E-cadherin. Nuclei are labeled with DAPI (blue fluorescence). (B) Schematic representation of an adherens junction. In adherens junctions, cadherin link to actin filaments. β-Catenin binds to cytosolic tails of the cadherins and to both actin filaments and vinculin. This forms a direct link between the transmembrane cadherins and the actin cytoskeleton.

All MMPs except MMP-23 are kept under control through prodomains, and activation proceeds through its removal. Once MMPs have been released into the extracellular space or anchored to the membrane and activated, they are kept in check by α_2-macroglobulin and by their endogenous tissue inhibitors, the cosecreted or ECM-anchored tissue inhibitors of metalloproteases (TIMPs). To date, four TIMPs have been identified:

TIMP-1, TIMP-2, TIMP-3, and TIMP-4. They inhibit active MMPs with relatively low selectivity. In addition to MMPs, TIMPs can inhibit ADAMs and ADAMTSs [40].

2.2.1.2 ADAMs and ADAMTSs

In the *adamalysin* family, three groups are distinguished: the membrane-anchored ADAMs, the secreted ADAMTSs, and class III snake venom metalloproteinases.

ADAMs are multidomain proteins composed of propeptide, metalloprotease, disintegrin-like, cysteine-rich, and epidermal growth factor-like domains. Twenty-five ADAMs are expressed in humans. However, only a subset of ADAMs have a Zn^{2+}-binding consensus sequence at their catalytic site and display proteolytic activity. Several ADAMs are expressed in multiple splice forms with no functional differences in these isoforms (e.g., ADAM-22, ADAM-29, ADAM-30), while in other cases, alternative splicing produces proteins with markedly different activities (e.g., ADAM-12) [44]. As with MMPs, a cysteine switch in the prodomain is believed to keep the protease in an inactive state. In order to be activated, the N-terminal prodomain needs to be cleaved from the rest of the protein by protein convertases in the trans-Golgi network [45]. Catalytic active ADAMs act as ectodomain sheddases that proteolitically cleave type I and type II transmembrane proteins within the juxtamembrane stalk region of the ectodomain to release soluble mature forms. ADAMs can modulate other cellular events by a process known as regulated intramembrane proteolysis, as described for Notch and HER-4, in which consecutive cleavage events of CD44 by an ADAM and a presenilin-dependent γ-secretase lead to the generation of intracellular domain fragments, which can influence signal transduction pathways, including acting as transcriptional coactivators/repressors [46,47].

ADAMTSs are characterized by the presence of additional thrombospondin type I motifs in their C-terminal part, while EGF-like transmembrane and cytoplasmic domains are missing. The complete human ADAMTS family comprises 19 *ADAMTSs* genes. Although ADAMTSs are soluble proteins, many of them appear to bind the ECM through their thrombospondin motifs or their spacer region [44]. Despite ADAMTSs being expressed in various cancers, no clear evidence of ectodomain shedding has been reported [45]. ADAMTS-1 and ADAMTS-8 have antiangiogenic properties. However, reported studies on correlation of the expression of ADAMTS-1 have shown contradictory results. As with MMPs, ADAMTSs

may have multiple, perhaps, opposing actions at particular stages during tumor progression [48,49].

TIMPs have demonstrated selectivity in their inhibition of ADAMs and ADAMTSs, which contrasts with their MMP-inhibitory features. For example, ADAM-17 is exclusively inhibited by TIMP-3, ADAM-10 is sensitive to TIMP-1 and TIMP-3 but not to TIMP-2 and TIMP-4. The activity of ADAM-8 and ADAM-9 is not controlled by any TIMP [50–52].

2.3. Alternative splicing

Alternative splicing of mRNA transcripts can result in the secretion of molecule variants or the truncation of membrane-bound molecules. Soluble adhesion molecules generated by alternative splicing contain signal peptides but lack the anchor of a transmembrane domain, resulting in a nearly complete secreted soluble extracellular variant, as seen for PECAM and P-selectin [53,54]. On the other hand, shorter forms of membrane-bound molecules containing only the membrane distal structures are found, as seen for the activated leukocyte cell adhesion molecule (ALCAM) in endothelial cells [45].

3. ROLE OF VESICLE AND ECTODOMAIN AND SHEDDING IN OVARIAN CANCER

Shedding of vesicles and ectodomain is a mechanism for fast changing the repertoire of cell surface proteins and alternative communication between cells. In combination with a mutagenic event, these processes might offer an additional explanation for the aggressive nature of ovarian cancer and for the development of chemoresistance in the case of recurrence.

3.1. Vesicle shedding and ovarian cancer

There is increasing evidence that MVs secreted from tumor cells participate in the development and spread of tumors (Fig. 8.7). The special role of MVs leading to malignancies lies in the method of their action. (i) MVs improve the biological distribution of molecules. They act in an autocrine or paracrine way on the immediate surroundings or travel further and finally appear in systemic circulation. (ii) They provide a more stable conformational condition for the protein content, since the protein milieu does not get altered, as it does when proteins are simply secreted into the ECM. The bioactivity of proteins in the exosome is thereby increased, since they stay in a transmembrane form. (iii) Finally, they represent a complex

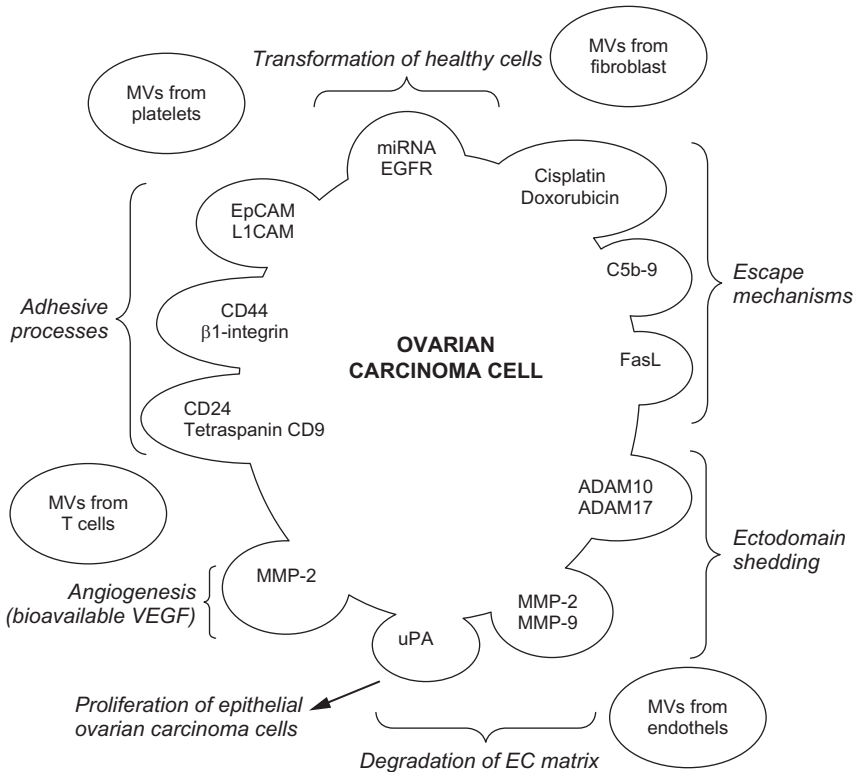

Figure 8.7 The role of microvesicles (MVs) secreted from ovarian carcinoma cell in cancerogenesis and chemoresistance. The tumor cell is surrounded by the MVs from other cell type, creating complex network between microvesicles for signalization and molecular transfer. ADAM, a disentigrin and metalloproteinase; MMP, matrix metalloproteinase; uPA, urokinase-type plasminogen activator; EpCAM, epithelial cell adhesion and activating molecule; L1CAM, cell adhesion molecule, member of the L1 protein family; EGFR, epidermal growth factor receptor; FasL, Fas ligand.

"packet" of molecules transmitted to the target cells, thus modifying their cellular physiology [31].

A roughly fivefold increase of MV blood concentration has been reported in ovarian cancer patients [55]. Exosomal secretion is initially confined to the abdomen. At later stages, ascites' formation and exchange with blood could lead to the systemic appearance of exosomes. Exosomes were simultaneously present in approximately 50% of samples. Other samples were only positive in the ascites but not in the serum. Phenotypically, paired serum/ascites' samples from the same ovarian carcinoma patients were similar [33].

Various combinations of adhesion proteins and receptors, proteases, inducers of vascularizations, cytosolic proteins and proteins involved in intracellular membrane fusion and transport, metabolic proteins, heat-shock proteins, proapoptotic proteins, proteins involved in antigen presentation, and miRNA have been found in MVs of human ovarian carcinoma cell lines and ovarian cancer patients' body fluids (Table 8.1) [32,33,55–62].

Table 8.1 Identified antigens associated with MVs isolated from body fluids of ovarian cancer patients or/and from cell-conditioned medium of human ovarian carcinoma cell lines

Indentified antigens associated with MVs	Detected in body fluid/cell medium	References
TCR-α, CD20, HLA-DR, B7-2, HER2/neu, CA125, histone H2A, FasL, TRAIL, MHC-I, HSP70, CD81	Ascites	[57]
HLA-A, FasL, B23/nucleophosmin, PLAP, TSG101	Ascites	[58]
MMP-2, MMP-9, MT1-MMP, uPA, uPAR, β1-integrin, EGFR	Ascites	[59]
EpCAM, CD24	Ascites	[60]
MMP-2, MMP-9, uPA, α-FR	Ascites, cell medium	[55]
ADAM-10, tetraspanin CD9, CD24	Ascites, cell medium, serum	[33]
EpCAM, L1CAM, annexin-1, β1-integrin	Ascites, cell medium	
EMMPRIN, proheparanase	Ascites	
MMP-2, MMP-9, FasL	Plasma	[61]
218 different miRNAs	Serum	[32]
Claudin-4	Serum	[62]
L1CAM, CD44, ADAM-10, ADAM-17, CD9, annexin I, moesin, Hsp70	Cell medium	[56]

TCR, T-cell receptor; HLA, human leukocyte antigen; HER, human epidermal growth factor receptor, also known as neu; CA, cancer antigen; FasL, Fas ligand; TRAIL, TNF-related apoptosis-inducing ligand; MHC, major histocompatability complex; HSP, heat-shock protein; PLAP, placental-type; alkaline phosphatase; TSG, tumor susceptibility gene; MMP, matrix metalloproteinase; MT1-MMP, membrane-type MMP; uPA, urokinase-type plasminogen activator; uPAR, urokinase-type plasminogen activator receptor; EGFR, epidermal growth factor receptor; EpCAM, epithelial cell adhesion and activating molecule; FL, folate receptor; ADAM, a disintegrin and metalloproteinase; L1CAM, cell adhesion molecule, member of the L1 protein family; EMMPRIN, extracellular matrix metalloproteinase inducer.

Taylor *et al.*, who analyzed serum from 62 women with FIGO stage III and stage IV ovarian cancer, 43 women with benign ovarian disease, and 50 female controls, found membrane fragments and specific proteins (MMP-2, MMP-9, and Fas ligand) associated with them in the circulation of women with ovarian cancer, although they were not present in control serum or serum with benign disease [61]. In another study, Taylor and Garcel-Taylor investigated miRNA from primary tumor cell cultures, established from six women with FIGO stage IIIC cystadenocarcinoma of the ovary, and their corresponding presurgery serum samples. Of the 218 positive miRNAs, the levels of 175 were not significantly different between the ovarian tumor cells and their corresponding circulating tumor exosomes. Furthermore, the levels of eight specific tumor-derived miRNA (miRNA-21, miRNA-141, miRNA-200a, miRNA-200c, miRNA-200b, miRNA-203, miRNA-205, and miRNA-214) exhibited a strong correlation with the level of serum-derived exosomal miRNA [32].

3.1.1 The effect of MVs in the establishment of an optimal environment for cancer development

MVs can facilitate the progression of a tumor through autocrine and paracrine signaling. They transfer growth factors and cognate receptors, DNA and RNA, and can thereby modify the phenotype of the cells, even in the absence of earlier mutagenic events. Several groups have described cocalled horizontal transfer by MVs between cells. MVs secreted by the human ovarian carcinoma SKOV3 cell line are internalized by the same cells. Internalization is energy dependent, and it occurs via various endocytic pathways. The internalization requires proteins from the cells and MVs [63].

Formation of metastasis greatly depends on their ability to anchor to the ECM, to degrade it, to migrate, and to become attached to a new surface. The process must be accompanied by the formation of vessels. Ovarian carcinoma ascites contain large amounts of exosomes that are derived from the carcinoma since they display tumor marker protein epithelial cell adhesion and activating molecule (EpCAM) and CD24, also called heat stable antigen [60]. Ongoing studies are investigating the role of EpCAM as a membrane-bound protease inhibitor, a function that may serve to protect tumor cells from their own secreted cathepsins during metastasis [64]. CD24 is involved in molecular adhesion and metastatic tumor spread and serves as a normal receptor for P-selectin. One of the most abundant protein families found in MVs is tetraspanin. Tetraspanin CD9 regulates cell motility and other adhesive processes in a variety of tissue types. It regulates β1-integrin activation

and enhances cell motility to fibronectin [65]. β1-Integrin, which can heterodimerize with many different α-integrin subunits, is key to the adhesion of ovarian carcinoma cells to mesothelial cells. Claudine detected in serum-derived MVs from ovarian cancer patients belongs to a family of transmembrane proteins crucial in the formation and function of tight junctions, the most apical contact between polarized cells [62]. MVs in ascites may serve as stores of active proteinases and, as such, may aid in metastatic processes. ECM-degrading proteinases, including uPA, MMP-2, and MMP-9, play a crucial role in metastasis by facilitating the invasion of epithelial ovarian cells [59]. MMPs degrade basement membrane collagen, whereas uPA catalyzes the conversion of plasminogen to plasmin, a broad spectrum serine protease that degrades numerous components of ECM, including fibrin, laminin, fibronectin, and vitronectin. Plasmin has also been implicated in the activation of some MMP zymogens, as well as in the conversion of pro-uPA to its two-chain active form. In addition to its proteolytic role, uPA stimulates the proliferation of epithelial ovarian carcinoma cells [66]. Taken together, MV shedding might be related to tumor progression and may be an important mechanism of cell–cell interaction and cell-ECM degradation.

3.1.2 The effect of MVs on the evasion of immunological surveillance

Tumor MVs may be important for the modulation of and escape from antitumor immune response [31,67]. The escape mechanisms of tumor cells include failure in tumor antigen presentation, expression of proapoptotic signals, and inhibitory cytokine secretion, possibly to induce immune tolerance and insensitivity to antitumor drugs [31].

The immunosuppressive effect of MVs from ovarian carcinoma cells was partially revealed by the group of Valenti [67]. When MVs from ascites of ovarian cancer were added to monocytes, they skewed the process of normal differentiation into defective dendritic cells. Their phenotype is characterized by the maintenance of CD14 surface expression, diminished expression of human leukocyte antigene (HLA) class II (HLA-DR negativity), and a lack of costimulatory molecule upregulation. Most importantly, these cells gain the ability spontaneously to secrete TGF-β. TGF-β inhibits not only the proliferation and effector function of T and B lymphocyte but also the induction of tumor cells apoptosis. One further form of escape from antitumor response established by tumor cells is the induction of apoptosis of T cells by proapoptotic molecules expressed on tumor cells. Ascites-derived epithelial ovarian cancer cells do not have membranal Fas ligand but constitutively secrete whole, intracellular Fas ligand via MV shedding [68]. MVs

expressing Fas ligand suppress T-cell signaling molecules (CD3 and Janus-activated kinase-3) and induce apoptosis [58]. Tumor cells not only induce cell death but also can escape themselves. Although the ovarian carcinoma cells in ascites are surrounded by a functional complement system, they are protected against complement activation [69]. They can avoid complement-induced immune destruction through vesicle shedding of the membrane attack complex that accumulates in the cell membrane [31].

MVs released by tumor cells may also represent a pathway for expelling toxic metabolites that could impair cell survival and growth. MVs may therefore play a role in the chemoresistance of tumor cells. Cisplatin and doxorubicin have been reported to accumulate in vesicles of ovarian carcinoma cells, which then shed from the cells, thus promoting an efficient drug efflux and the consequent evasion of any cytotoxic effect on tumor cells [70,71].

3.1.3 MVs and inflammation

MVs affect not only other tumor cells but also various cell types in the microenvironment of the developing tumor. Ascites MVs from ovarian carcinoma patients display phosphatidylserine in the outer phospholipid layer, which attract and stimulate macrophages [33], which can contribute to the induction of inflammation. The pelvic peritoneum exhibits a general pattern of chronic inflammation in epithelial ovarian cancer, represented primarily by differentiated monocytes/macrophages, distinct from that in benign conditions [21]. There is an increasing awareness of the role of inflammation in ovarian cancer. In The Lancet Oncology, Lin and colleagues report an association between pelvic inflammatory disease and ovarian cancer. Data were obtained from 67,936 women with pelvic inflammatory disease and 135,872 controls [72]. In the case of inflammation, macrophages are already in the immediate surroundings of tumor cells and help to create a beneficial microenvironment for tumor cells through their TGF-β1 secretion. Complementary to this, phagocytes and T lymphocytes were found to expose phosphatidylserine binding receptors, which help to capture MVs. Further macrophages from a longer distance can thus be recruited and activated [31]. In addition to immune cells, platelets, fibroblasts, and other cells release MVs in the hematopoietic environment of an inflammation. MVs secreted by activated platelets bind to endothelial cells, inducing the production of pro-inflammatory cytokines and products of the arachidonic acid pathway. In turn, pro-inflammatory cytokines (TNF-α, IL-1β) or the terminal complement complex C5b-9 can induce MV shedding of inflammatory cells [73]. These upregulate adhesion molecules in the endothelium and

leukocytes [74,75]. Taken together, the interplay between various cells and MVs of different origins modulates the cellular response in inflammation, which further influences the behavior of the tumor cells.

3.2. MMPs and ovarian cancer

The prognostic relevance of MMPs in ovarian cancer is still uncertain. Among the most studied MMPs as biomarkers for ovarian cancer are MMP-2, MMP-9, and MT1-MMP. MMP-2 and MMP-9 degrade type IV collagen, a major component of the basement membrane, and are associated with active neovascularization [76]. MT1-MMP cleaves pro-MMP-2 and is the key activator of MMP-2, and its colocalization has been well documented. MT1-MMP may also directly stimulate VEGF-A expression via the Src tyrosine kinase signaling pathway [77]. Importantly, the cellular source of MMPs must be considering when assessing their value as ovarian cancer biomarkers. MMPs can be produced by tumor cells, as well as the surrounding stromal cells, such as fibroblasts, infiltrating macrophage and endothelial cells [78]. As with other MMPs, MMP-2, MMP-9, and membrane-associated MT1-MMP cleave not only the components of the ECM, but also a number of nonmatrix substrates (Table 8.2) [79].

MMP-9 is induced through the clustering of collagen binding integrins ($\alpha_2\beta_1$- and $\alpha_3\beta_1$-integrin) on cancer cells, which cleaves the E-cadherin ectodomain, contributing to the loosening of cell–cell adhesion and allowing the transformed cells to shed as single cells or spheroids into ascites [80]. Davidson *et al.* reported that MMP-9 mRNA expression in tumor cells was an independent poor prognostic variable of survival in 45 patients with epithelial ovarian cancer ($p = 0.011$) [81]. Kamat *et al.*, who assessed tissue specimens from 90 epithelial ovarian cancers, reported that high epithelial and stromal expression of MMP-9 is significantly associated with shorter disease-specific survival ($p < 0.01$) on univariate analysis, and high stromal expression of MMP-9 ($p = 0.01$) was a poor predictor on multivariate analysis [78]. Sillanpaa *et al.*, who analyzed 292 tumor specimens from epithelial ovarian cancer patients, found that strong MMP-9 in cancer cells was related to a longer 10-year disease-related survival ($p = 0.05$), whereas high stromal expression was associated with a poor prognosis ($p = 0.01$) [82]. According to these data, MMP-9 might have a dual role in ovarian cancer, promoting tumor progression when expressed in the stroma and acting against tumor growth when expressed in the tumor epithelium.

MMP-2 is expressed by the majority of multicellular aggregates collected from ascites, which plays a major role in early metastasis. The spheroids

Table 8.2 Extracellular matrix (ECM) substrates, non-ECM substrates, and resultant effectors of matrix metalloproteinases (MMP-2, MMP-9) and membrane-type MMP (MT1-MMP)

Classification (trivial names)	ECM substrate	Non-ECM substrate	Resultant effector
MMP-2 (gelatinase A)	Gelatin	Decorin	Bioavailable TGFβ
	Elastin	Pro-TGF-β2	TGF-β2
	Fibronectin	Pro-IL-β	Active IL-β
	Collagen I/IV/V/ VII/X/XI	MCP-3	Inactive MCP-3
	Laminin	IGFBP-3/5	Bioavailable IGF
	Aggrecan	Pro-TNFα	TNFα
	Vitronectin	FGF-R1	Active FGF-R1
		Pro-MMP-1, 2, 13	MMP-1, 2, 13
MMP-9 (gelatinase B)	Gelatin	Unknown	Bioavailable VEGF
	Elastin	Pro-TGF-β2	TGF-β2
	Fibronectin	Pro-IL-β	Active IL-β
	Collagen I/IV/V/ VII/X/XI	Cell surface-bound IL-2RA	Release of IL-2RA
	Laminin	Plasminogen	Angiostatin
	Aggrecan	α1-Proteinase	Inactive serpin
	Vitronectin	Inhibitor	
		Pro-TNFα	TNFα
MMP-14 (MT1-MMP)	Gelatin	Pro-MMP-2, 13	MMP-2, 13
	Fibronectin	Cell surface-bound CD44	Release of CD44
	Vitronectin	Cell surface-bound tTG	Release of tTG
	Collagen I/II/III		
	Aggrecan		

TGF, transforming growth factor; IL, interleukin; MCP, monocyte chemoattractant protein; IGFBP, insulin-like growth factor-binding protein; FGF-R, fibroblast growth factor receptor; MMP, metalloproteinase; interleukin-2 receptor; tTG, tissue transglutaminase. Adapted from Ref. [79].

secrete more pro-MMP-2 than a monolayer culture made up of the same ovarian carcinoma cells. MMP-2 perhaps promotes the fast disaggregation of the spheroids on adhesion to the surface mesothelial cell layer. When an ovarian carcinoma attaches to mesothelial cells, the cancer cells upregulate MMP-2, which then cleaves the ECM proteins and vitronectin into smaller fragments. The cancer cells adhere much more strongly to these smaller fragments, using the fibronectin ($\alpha_5\beta_1$-integrin) and vitronectin ($\alpha_v\beta_3$-integrin) receptors [15]. Torng *et al.* found that stromal MMP-2 expression was a poor predictor of disease-specific survival for patients with endometrioid ovarian cancer but not for those with a serous histology [83]. Kamat *et al.*, who assessed tissue specimens from 90 epithelial ovarian cancers, reported that high epithelial and stromal expression of MMP-2 is significantly associated with shorter disease-specific survival ($p < 0.01$) on univariate analysis [78].

Active MT1-MMP on cancer cells cleaves α_3-integrin, contributing to the detachment of the spheroids from the primary tumor [15]. Patients with strong tumor epithelial MT1-MMP expression had the worst prognosis with the shortest disease-specific survival [78].

3.3. ADAMs and ovarian cancer

The ability of diverse extracellular signals (e.g., growth factors, cytokines, GPCRs, inflammatory stimuli, oxidative stress, etc.) to stimulate ADAMs proteolytic activity not only provides a mechanism for cells to sense their extracellular environment and to achieve the appropriate cellular response but also suggests that this mode of signal transduction may have a broader impact on the pathogenesis of inflammation and cancer. For example, ADAM-17 and ADAM-10 have been implicated in ectodomain processing and activation of several key signaling molecules associated with cancer development and tumor progression, including ErbB receptors and ligands, Notch and several cell adhesion molecules [84]. Deregulation of key chemokine/cytokine receptor signaling pathways, which are critical mediators of innate and adaptive immune responses, can lead to sustained exposure of pro-inflammatory stimuli. The fact that many cytokines and inflammatory stimuli (e.g., oxidative stress) associated with an immune response can also stimulate ADAM proteolytic activity suggests that inflammatory signals involved in chronic inflammation may promote ADAM-signaling events associated with an increased risk of carcinogenesis [84,85].

ADAM-17 or tumor necrosis factor-α-converting enzyme has been identified by its ability to cleave the transmembrane form of tumor necrosis

factor α (TNF-α) at its physiological processing site [86]. Results from animal studies show that TNF-α is involved in the initiation of ovarian cancer. ADAM-17 takes part in the shedding of ALCAM from epithelial ovarian cancer cells *in vitro* and *in vivo*, leading to the generation of a soluble ALCAM (sALCAM). sALCAM has been found in ascites and serum from epithelial ovarian carcinoma patients [87]. Cytoplasmic localization of ALCAM is a marker of a poorer outcome in ovarian carcinoma patients, as compared with its membrane expression [88]. ALCAM proteolysis may act in different ways to downregulate ALCAM-mediated intercellular adhesion, thus controlling the transition between cell clustering and cell movement. ALCAM shedding can be enhanced by stimuli, such as EGF or phorbol esters [87].

ADAM-15 is unique among ADAM proteins since it contains the integrin-binding motif Arg-Gly-Asp within its disintegrin region. An integrin-binding capacity for ADAM-15 has been observed, for example, for integrin αvβ3 and α9β1. Human ovarian carcinoma cell line OV-MZ-6 expresses both αvβ3 and ADAM-15. OV-MZ-6, in an αvβ3-dependent fashion, binds to ECM protein vitronectin, which is one of the most abundant adhesion substrates in a normal ovarian epithelium, as well as in differentiated ovarian tumors. In addition to the implication of αvβ3 in tumor angiogenesis, several lines of evidence point to its role during ovarian cancer invasion. In primary ovarian cancer, αvβ3 is detected at significantly higher levels than in ovarian tumors of low malignant potential. Cells (over)expressing ADAM-15-RGB exhibit a significantly reduced αvβ3-mediated adhesion to vitronectin, thereby loosening tumor cell adhesion to ECM and regulating mediating tumor cell migration and invasion [89].

ADAM-10, also called Kuzbanian, was the first disintegrin–metalloprotease to have a known proteolytic function [90]. ADAM-10 is the principal sheddase for several molecules associated with cancer proliferation, differentiation, adhesion, and migration, such as Notch, E-cadherin, CD44, L1CAM, and ErbB ligands, such as betacellulin in EGF [91]. ADAM-10 has been found in exosomes isolated from body fluids of ovarian cancer patients and from media of human ovarian carcinoma cell lines [33,56].

3.4. Alternative splicing and ovarian cancer

Up to 10 different CD isoforms have been documented for cell transmembrane glycoprotein CD44. CD44 is implicated in cell adhesion, motility, and metastases of ovarian cancer. Soluble forms of CD44 (sCD44) are generated via alternative splicing and have been found in ascites of ovarian cancer

patients. Gadducci *et al.*, who analyzed serum levels from 51 epithelial ovarian cancer patients, reported significantly lower sCD44-v5 and sCD44-v6 levels in advanced ovarian cancer (FIGO stages III–IV) than in stage I disease ($p < 0.001$ and $p = 0.001$), while standard CD44 isoforms (sCD44-st) were not related to the most common clinopathological variables of epithelial ovarian cancer [92]. Aberrant alternative splicing frequently occurs in cancers [93,94], but a direct link between alternative splicing and ovarian cancer progression has not been established.

4. PROTEIN SECRETION RATES AND BLOOD BIOMARKERS' LEVEL

Proteins secreted by cells are expected finally to reach the circulation. Secreted proteins, therefore, in contrast to intracellular proteins, may be more likely to be detectable in plasma. The distribution of proteins may vary because of differences in a number of factors, such as physicochemical characteristics of molecules (size/shape, lipid solubility/hydrophobicity, charge/polarity), access to systemic circulation, tissue vascularization and interindividual variation (e.g., ethnicity, age, genetic factors, hormones, disease). Stimuli that create stress in a patient may also influence protein distribution [95,96]. Additionally, the mechanism of secretion of a protein from the cell influences its stability. In this regard, proteins may be shed in a soluble form or in MVs, the former representing a more stable environment.

Important features of secreted or shed proteins that may serve as biomarkers include high secretion rates, specifically by tumor cells, and a low baseline concentration in normal plasma. A recent mathematical model has derived estimates of the balance between tumor biomarker secretion into and removal from the intravascular compartment, which takes into account protein secretion rates by tumor cells [97]. This model was primarily based on data available for the ovarian cancer biomarker CA-125. The study introduced a linear one-compartment mathematical model that allows the estimation of minimal detectable tumor size based on a blood tumor biomarker assay. The secretion rate of CA-125 secretion 130 U/10^5 cells/20 h/2 ml was used for the model. This value is based on *in vitro* data for the secretion rate of CA-125 into cell culture medium by selected human ovarian carcinoma cell lines (OVCAR-3, SK-OV-8, SK-OV-3, which secrete 2–13 U/10^5 cells/20 h/2 ml medium) [98]. In order to account for the potential enhancing influence of the tumor environment on actual tumor biomarker secretion *in vivo*, a higher secretion rate was used for the model.

Not all of the protein secreted by cells into the extracellular compartment will reach circulation. The model assumed that a range of 0.1–20% mean percentage of secreted biomarker reach the blood. In the plasma, the protein of interest has a distinct half-life, owing, for example, to degradation by proteases, hepatic metabolism or, in the case of a smaller protein, because of filtration by the kidney. More tumor biomarker must be secreted by tumor cells if the half-life is shorter. The half-life for CA-125 is 151 h [97]. Assuming biomarker secretion by tumor cells only, 10% of secreted tumor biomarker reaching the plasma and assay sensitivity of 1.45 U/ml (clinically realistic conditions), the calculated minimally detectable tumor size ranged between 0.11 and 3610.14 mm^3. If the tumor biomarker is secreted by tumor cells only, the test assay sensitivity basically defines the cutoff between healthy and diseased. When biomarker secretion by healthy cells and tumor cells was assumed, the calculated tumor size leading to positive test results ranged between 116.7 and 152×10^6 mm^3. If there is secretion by healthy cells, the cutoff value for distinction between healthy and diseased must be set at a point that offers a high specificity and beyond which few of the normal population will lie. In order to include less than 0.1% of the normal population in the range of positive test results assuming a Gaussian distribution of the CA-125 level, the cutoff value was therefore set at 3.09 times the standard deviation above the mean normal protein serum level in healthy women (34.11 U/ml). The calculated minimum detectable tumor size on the assumption of tumor marker secretion by healthy cells (it is known that healthy mesothelial cells secrete CA-125 [98]) is in qualitative agreement with the performance of CA-125 in clinical applications [97]. CA-125 tests are positive in up to 80% of patients with advanced stage disease (e.g., tumor volumes 10^6 mm^3 are reported for advanced ovarian cancer with peritoneal metastasis [99]) but are negative in up to 50% of patients with stage I disease, when the tumor burden is still limited [100].

Applying this model, it has been calculated that the secretion rates of TIMP-1, measured in human ovarian carcinoma cell lines CaOV3 and ES2, are in the order of nanograms of protein per million cells, per hour. This secretion rate suggests that a tumor approximately 2 cm in diameter would result in a detectable 50% increase in the serum level. The TIMP-1 level that occurs in normal serum is 87–524 ng/ml. Assumptions for the calculations were (i) a half-life in blood of 48 h; (ii) 50% of secreted protein reaching the blood [101].

A mathematical model developed by Lutz *et al.* may address the potential and limitations of tumor biomarkers, help prioritize biomarkers, and guide investments into early cancer detection research.

5. MVs AND SHEDDASES AS POTENTIAL THERAPEUTIC TARGETS

Given the important roles that MMPs, ADAMs, and MVs play in tumor growth, metastasis, and the deregulated angiogenesis that drives them, significant attention has been paid to the development of clinically useful agents that target MMPs, ADAMs, and MVs.

5.1. MVs as therapeutic targets

Considering that MVs are involved in tumorigenesis at multiple levels, and that drugs themselves can be excreted from tumor cells via MVs, interfering with the formation, release and propagation of these vesicles could be a novel approach in cancer treatment.

MVs' formation and release can be influenced by disturbing the exocytosis of exosomes and the budding of larger MVs. Paclitaxel and vinca alkaloids not only inhibit cell division but additionally decrease exosome release by inhibiting microtubule formation. Using proton pump inhibitors, exosome formation can be blocked in the absence of a gradually acidic milieu [102]. A large number of proteins participate in the complex cell biological process of vesicle trafficking. Of these, at least 21 have been implicated in tumorigenesis [103,104]. Normal vesicle physiology is a prerequisite for cell life, so the broad effects may have adverse effects in healthy cells, unless a tumor specific agent can be found. Independently of the rug mechanism for diminishing exosome release by tumor cells, the crucial point is to prove that this effect will improve the immunogenicity of cancer cells [102].

The idea of MV vaccination is based on the finding that exosomes efficiently transfer tumor antigens from tumor cells to other antigen-presenting cells, mostly to dendritic cells, allowing initiation and amplification of an antitumor response. Chaput and her group proposed an active "vaccination" method that involves the isolation of ascites-derived exosomes from patients with ovarian cancer, the addition of adjuvant, and the exosomes are then reinjected into the patient s.c. at different sites far from the existing tumor's immunosuppressive environment. "Adoptive transfer of tumor specific cytotoxic T-lymphocyte" also involves isolation of ascites-derived exosomes, which would first be added to dendritic cells isolated from the patient's blood, so that the exosome containing dendritic cells can then present the tumor antigen to specific T cells, which, after culturing, represent a specific cytotoxic T-cell clone against the tumor. The cytotoxic T cells would be

injected to the patient i.v./i.p. [105]. The effects of tumor-derived exosome vaccine alone are at least questionable, if not counterproductive, since the exosome might act as a vehicle for suppressive signals and have negative effects on antitumor immune response [102].

Ichim and his group proposed a physical approach in order to remove exosomes from the body fluids of patients. The method is an extracorporeal "dialysis" through a so-called Hemopurifier^{TM}. The immunosuppressive activity normally found in the ascites of patients with ovarian cancer was completely removed by the Hemopurifier^{TM} [106].

5.2. MMPs as therapeutic targets

The discovery of cell surface-localized MMPs started more than 20 years ago [107]. Today's challenge is to distinguish the action of MMPs that contribute to tumor progression from those that are crucial for host defense, as blocking the latter would worsen the clinical outcome. One of the major problems with targeting MMPs is that this enzyme family is highly similar, particularly in the vicinity of an active site. Importantly, the same MMP may play a contrasting role at different stages of cancer progression. TIMPs may actually be more effective when administrated at earlier stages of cancer progression, which may also provide the opportunity to use a lower drug dose, thereby perhaps limiting the toxicity that has so hampered clinical trials [43]. Novel mechanism-based TIMPs have also been reported. One possible mechanism is the participation of MMPs in the host defense against a tumor by modulating the activities of chemokine and cytokines [108]. Inhibitors that target MMP exosites have been developed and show enhanced selectivity for specific MMPs and MMP activities [109].

While intraperitoneal administration of TIMPs *in vivo* resulted in prolonged survival of mice carrying human ovarian xenografts, its application to the clinical setting using nonselective TIMPs (batimastat and marimastat) was limited by significant toxicity, probably due to a lack of specificity in targeting tumor-associated MMP [26].

5.3. ADAMs as therapeutic targets

Several small-molecule inhibitors targeted specifically at the ADAM family of enzymes have also been evaluated. Of these, inhibitors of ADAM-10 and ADAM-17 have reached the clinical stage of development [110], but not for ovarian cancer. Such inhibitors could prove to be particularly useful in targeting EGFR signaling, either as single agent or in a synergistic manner with currently approved tyrosine kinase inhibitors. Unlike the first-generation

TIMPs, they did not induce a muscoskeletal adverse effect in initial animal studies [111]. Several inhibitors of ADAM-17 have failed during clinical trials, especially because promising *in vitro* nanomolar range inhibitors do not always show efficacy *in vivo* [110].

6. CONCLUSIONS

Increasing efforts and financial resources are being invested in early ovarian cancer detection research. Blood assays detecting tumor biomarkers promise noninvasive and financially reasonable screening for early cancer, with a high potential positive impact on patient survival and quality of life. In spite of intense work in this field, there is not a lot to show. One approach for future research would be systematically to characterize sets of proteins whose location makes them especially relevant to diagnosis and treatment, notably proteins on the cell surface or those released into the extracellular milieu. Proteins with high secretion rates or proteins that are extensively cleaved from the cell surface, specifically from tumor cells, are a potential source of circulating markers. Proteins that are resistant to shedding and are detected exclusively on the cell surface have potential as imaging or therapeutic targets, including integrins and several other receptors and adhesion molecules. Sheddases (e.g., MMPs, ADAMs) involved in protein secretion may be a biomarker themselves or have potential as therapeutic targets. MVs that are extensively shed from tumor cells represent an additional release mechanism of a large number of proteins and lipids. Since their concentration in body fluids of ovarian patients increases with the progression of disease, they may serve as prognostic markers. Interfering with the formation, release or propaginations of MVs can be considered as a new approach in ovarian cancer therapy.

ACKNOWLEDGMENTS

This work was supported by research grants from the Ministry of Higher Education, Science and Technology (P3-067, L3-2371-0312), and the University Medical Centre Ljubljana (Project No. 20110224). The authors thank Assoc. Prof. M. Bracko (Division of Gynaecologic Pathology) for the photographs showing serous ovarian carcinoma and Prof. P. Veranic (Institute of Cell Biology) for the photograph showing E-cadherin.

REFERENCES

[1] P. Boyle, B. Levin, International Agency for Research on Cancer, and World Health Organization, World Cancer Report 2008, WHO Press, Geneva, 2008.
[2] A. Jemal, R. Siegel, E. Ward, Y. Hao, J. Xu, T. Murray, M.J. Thun, Cancer statistics, 2008, CA Cancer J. Clin. 58 (2008) 71–96.

[3] L. Hu, C. McArthur, R.B. Jaffe, Ovarian cancer stem-like side-population cells are tumourigenic and chemoresistant, Br. J. Cancer 102 (2010) 1276–1283.
[4] P.E. Schwartz, Current diagnosis and treatment modalities for ovarian cancer, Cancer Treat. Res. 107 (2002) 99–118.
[5] V.W. Chen, B. Ruiz, J.L. Killeen, T.R. Cote, X.C. Wu, C.N. Correa, Pathology and classification of ovarian tumors, Cancer 97 (2003) 2631–2642.
[6] J.L. Benedet, H. Bender, H. Jones 3rd, H.Y. Ngan, S. Pecorelli, FIGO staging classifications and clinical practice guidelines in the management of gynecologic cancers. FIGO Committee on Gynecologic Oncology, Int. J. Gynaecol. Obstet. 70 (2000) 209–262.
[7] M.F. Fathalla, Incessant ovulation—a factor in ovarian neoplasia? Lancet 2 (1971) 163.
[8] D.W. Cramer, W.R. Welch, Determinants of ovarian cancer risk. II. Inferences regarding pathogenesis, J. Natl. Cancer Inst. 71 (1983) 717–721.
[9] W.J. Murdoch, E.A. Van Kirk, Steroid hormonal regulation of proliferative, p53 tumor suppressor, and apoptotic responses of sheep ovarian surface epithelial cells, Mol. Cell. Endocrinol. 186 (2002) 61–67.
[10] V. Syed, S.M. Ho, Progesterone-induced apoptosis in immortalized normal and malignant human ovarian surface epithelial cells involves enhanced expression of FasL, Oncogene 22 (2003) 6883–6890.
[11] M. Shih Ie, R.J. Kurman, Ovarian tumorigenesis: a proposed model based on morphological and molecular genetic analysis, Am. J. Pathol. 164 (2004) 1511–1518.
[12] T. Reya, S.J. Morrison, M.F. Clarke, I.L. Weissman, Stem cells, cancer, and cancer stem cells, Nature 414 (2001) 105–111.
[13] S.A. Bapat, A.M. Mali, C.B. Koppikar, N.K. Kurrey, Stem and progenitor-like cells contribute to the aggressive behavior of human epithelial ovarian cancer, Cancer Res. 65 (2005) 3025–3029.
[14] M.L. Puiffe, C. Le Page, A. Filali-Mouhim, M. Zietarska, V. Ouellet, P.N. Tonin, M. Chevrette, D.M. Provencher, A.M. Mes-Masson, Characterization of ovarian cancer ascites on cell invasion, proliferation, spheroid formation, and gene expression in an in vitro model of epithelial ovarian cancer, Neoplasia 9 (2007) 820–829.
[15] E. Lengyel, Ovarian cancer development and metastasis, Am. J. Pathol. 177 (2010) 1053–1064.
[16] N. Tsuruchi, T. Kamura, N. Tsukamoto, K. Akazawa, T. Saito, T. Kaku, N. To, H. Nakano, Relationship between paraaortic lymph node involvement and intraperitoneal spread in patients with ovarian cancer—a multivariate analysis, Gynecol. Oncol. 49 (1993) 51–55.
[17] D.S. Tan, R. Agarwal, S.B. Kaye, Mechanisms of transcoelomic metastasis in ovarian cancer, Lancet Oncol. 7 (2006) 925–934.
[18] R.A. Adam, Y.G. Adam, Malignant ascites: past, present, and future, J. Am. Coll. Surg. 198 (2004) 999–1011.
[19] M. Rieppi, V. Vergani, C. Gatto, G. Zanetta, P. Allavena, G. Taraboletti, R. Giavazzi, Mesothelial cells induce the motility of human ovarian carcinoma cells, Int. J. Cancer 80 (1999) 303–307.
[20] R.L. Dedrick, M.F. Flessner, Pharmacokinetic problems in peritoneal drug administration: tissue penetration and surface exposure, J. Natl. Cancer Inst. 89 (1997) 480–487.
[21] X. Wang, M. Deavers, R. Patenia, R.L. Bassett Jr., P. Mueller, Q. Ma, E. Wang, R.S. Freedman, Monocyte/macrophage and T-cell infiltrates in peritoneum of patients with ovarian cancer or benign pelvic disease, J. Transl. Med. 4 (2006) 30.
[22] M.F. Abu-Hijleh, O.A. Habbal, S.T. Moqattash, The role of the diaphragm in lymphatic absorption from the peritoneal cavity, J. Anat. 186 (Pt 3) (1995) 453–467.

[23] P.L. Judson, M.A. Geller, R.L. Bliss, M.P. Boente, L.S. Downs Jr., P.A. Argenta, L.F. Carson, Preoperative detection of peripherally circulating cancer cells and its prognostic significance in ovarian cancer, Gynecol. Oncol. 91 (2003) 389–394.
[24] A. Jemal, R. Siegel, E. Ward, T. Murray, J. Xu, C. Smigal, M.J. Thun, Cancer statistics, 2006, CA Cancer J. Clin. 56 (2006) 106–130.
[25] A. Jemal, T. Murray, E. Ward, A. Samuels, R.C. Tiwari, A. Ghafoor, E.J. Feuer, M.J. Thun, Cancer statistics, 2005, CA Cancer J. Clin. 55 (2005) 10–30.
[26] R. Kalachand, B.T. Hennessy, M. Markman, Molecular targeted therapy in ovarian cancer: what is on the horizon? Drugs 71 (2011) 947–967.
[27] U. Menon, I.J. Jacobs, Ovarian cancer screening in the general population, Curr. Opin. Obstet. Gynecol. 13 (2001) 61–64.
[28] Z. Yurkovetsky, S. Skates, A. Lomakin, B. Nolen, T. Pulsipher, F. Modugno, J. Marks, A. Godwin, E. Gorelik, I. Jacobs, U. Menon, K. Lu, D. Badgwell, R.C. Bast Jr., A.E. Lokshin, Development of a multimarker assay for early detection of ovarian cancer, J. Clin. Oncol. 28 (2010) 2159–2166.
[29] L. Buchen, Cancer: missing the mark, Nature 471 (2011) 428–432.
[30] R.G. Moore, A.K. Brown, M.C. Miller, S. Skates, W.J. Allard, T. Verch, M. Steinhoff, G. Messerlian, P. DiSilvestro, C.O. Granai, R.C. Bast Jr., The use of multiple novel tumor biomarkers for the detection of ovarian carcinoma in patients with a pelvic mass, Gynecol. Oncol. 108 (2008) 402–408.
[31] E. Pap, The role of microvesicles in malignancies, Adv. Exp. Med. Biol. 714 (2011) 183–199.
[32] D.D. Taylor, C. Gercel-Taylor, MicroRNA signatures of tumor-derived exosomes as diagnostic biomarkers of ovarian cancer, Gynecol. Oncol. 110 (2008) 13–21.
[33] S. Keller, A.K. Konig, F. Marme, S. Runz, S. Wolterink, D. Koensgen, A. Mustea, J. Sehouli, P. Altevogt, Systemic presence and tumor-growth promoting effect of ovarian carcinoma released exosomes, Cancer Lett. 278 (2009) 73–81.
[34] N.M. Hooper, E.H. Karran, A.J. Turner, Membrane protein secretases, Biochem. J. 321 (Pt 2) (1997) 265–279.
[35] J. Arribas, A. Borroto, Protein ectodomain shedding, Chem. Rev. 102 (2002) 4627–4638.
[36] T. Itoh, M. Tanioka, H. Matsuda, H. Nishimoto, T. Yoshioka, R. Suzuki, M. Uehira, Experimental metastasis is suppressed in MMP-9-deficient mice, Clin. Exp. Metastasis 17 (1999) 177–181.
[37] G. Struhl, A. Adachi, Requirements for presenilin-dependent cleavage of notch and other transmembrane proteins, Mol. Cell 6 (2000) 625–636.
[38] M.G. Paulick, C.R. Bertozzi, The glycosylphosphatidylinositol anchor: a complex membrane-anchoring structure for proteins, Biochemistry 47 (2008) 6991–7000.
[39] S. Vozelj, N. Obermajer, J. Kos, Proteases and their inhibitors in body fluids as diagnostic and prognostic tumour markers, Farm. Vestn. 58 (2007) 133–138.
[40] C. Tallant, A. Marrero, F.X. Gomis-Ruth, Matrix metalloproteinases: fold and function of their catalytic domains, Biochim. Biophys. Acta 1803 (2010) 20–28.
[41] W. Cruz-Munoz, R. Khokha, The role of tissue inhibitors of metalloproteinases in tumorigenesis and metastasis, Crit. Rev. Clin. Lab. Sci. 45 (2008) 291–338.
[42] R. Roy, B. Zhang, M.A. Moses, Making the cut: protease-mediated regulation of angiogenesis, Exp. Cell Res. 312 (2006) 608–622.
[43] R. Roy, J. Yang, M.A. Moses, Matrix metalloproteinases as novel biomarkers and potential therapeutic targets in human cancer, J. Clin. Oncol. 27 (2009) 5287–5297.
[44] N. Rocks, G. Paulissen, M. El Hour, F. Quesada, C. Crahay, M. Gueders, J.M. Foidart, A. Noel, D. Cataldo, Emerging roles of ADAM and ADAMTS metalloproteinases in cancer, Biochimie 90 (2008) 369–379.

[45] J.W. van Kilsdonk, L.C. van Kempen, G.N. van Muijen, D.J. Ruiter, G.W. Swart, Soluble adhesion molecules in human cancers: sources and fates, Eur. J. Cell Biol. 89 (2010) 415–427.
[46] M.S. Wolfe, R. Kopan, Intramembrane proteolysis: theme and variations, Science 305 (2004) 1119–1123.
[47] H.C. Crawford, P.J. Dempsey, G. Brown, L. Adam, M.L. Moss, ADAM10 as a therapeutic target for cancer and inflammation, Curr. Pharm. Des. 15 (2009) 2288–2299.
[48] T. Masui, R. Hosotani, S. Tsuji, Y. Miyamoto, S. Yasuda, J. Ida, S. Nakajima, M. Kawaguchi, H. Kobayashi, M. Koizumi, E. Toyoda, S. Tulachan, S. Arii, R. Doi, M. Imamura, Expression of METH-1 and METH-2 in pancreatic cancer, Clin. Cancer Res. 7 (2001) 3437–3443.
[49] A. Luque, D.R. Carpizo, M.L. Iruela-Arispe, ADAMTS1/METH1 inhibits endothelial cell proliferation by direct binding and sequestration of VEGF165, J. Biol. Chem. 278 (2003) 23656–23665.
[50] A. Amour, C.G. Knight, A. Webster, P.M. Slocombe, P.E. Stephens, V. Knauper, A.J. Docherty, G. Murphy, The in vitro activity of ADAM-10 is inhibited by TIMP-1 and TIMP-3, FEBS Lett. 473 (2000) 275–279.
[51] A. Amour, C.G. Knight, W.R. English, A. Webster, P.M. Slocombe, V. Knauper, A.J. Docherty, J.D. Becherer, C.P. Blobel, G. Murphy, The enzymatic activity of ADAM8 and ADAM9 is not regulated by TIMPs, FEBS Lett. 524 (2002) 154–158.
[52] G. Murphy, V. Knauper, M.H. Lee, A. Amour, J.R. Worley, M. Hutton, S. Atkinson, M. Rapti, R. Williamson, Role of TIMPs (tissue inhibitors of metalloproteinases) in pericellular proteolysis: the specificity is in the detail, Biochem. Soc. Symp. (2003) 65–80.
[53] N. Ishiwata, K. Takio, M. Katayama, K. Watanabe, K. Titani, Y. Ikeda, M. Handa, Alternatively spliced isoform of P-selectin is present in vivo as a soluble molecule, J. Biol. Chem. 269 (1994) 23708–23715.
[54] A. Goldberger, K.A. Middleton, J.A. Oliver, C. Paddock, H.C. Yan, H.M. DeLisser, S.M. Albelda, P.J. Newman, Biosynthesis and processing of the cell adhesion molecule PECAM-1 includes production of a soluble form, J. Biol. Chem. 269 (1994) 17183–17191.
[55] V. Dolo, S. D'Ascenzo, S. Violini, L. Pompucci, C. Festuccia, A. Ginestra, M.L. Vittorelli, S. Canevari, A. Pavan, Matrix-degrading proteinases are shed in membrane vesicles by ovarian cancer cells in vivo and in vitro, Clin. Exp. Metastasis 17 (1999) 131–140.
[56] A. Stoeck, S. Keller, S. Riedle, M.P. Sanderson, S. Runz, F. Le Naour, P. Gutwein, A. Ludwig, E. Rubinstein, P. Altevogt, A role for exosomes in the constitutive and stimulus-induced ectodomain cleavage of L1 and CD44, Biochem. J. 393 (2006) 609–618.
[57] P. Peng, Y. Yan, S. Keng, Exosomes in the ascites of ovarian cancer patients: origin and effects on anti-tumor immunity, Oncol. Rep. 25 (2011) 749–762.
[58] D.D. Taylor, C. Gercel-Taylor, Tumour-derived exosomes and their role in cancer-associated T-cell signalling defects, Br. J. Cancer 92 (2005) 305–311.
[59] L.E. Graves, E.V. Ariztia, J.R. Navari, H.J. Matzel, M.S. Stack, D.A. Fishman, Proinvasive properties of ovarian cancer ascites-derived membrane vesicles, Cancer Res. 64 (2004) 7045–7049.
[60] S. Runz, S. Keller, C. Rupp, A. Stoeck, Y. Issa, D. Koensgen, A. Mustea, J. Sehouli, G. Kristiansen, P. Altevogt, Malignant ascites-derived exosomes of ovarian carcinoma patients contain CD24 and EpCAM, Gynecol. Oncol. 107 (2007) 563–571.
[61] D.D. Taylor, K.S. Lyons, C. Gercel-Taylor, Shed membrane fragment-associated markers for endometrial and ovarian cancers, Gynecol. Oncol. 84 (2002) 443–448.

[62] J. Li, C.A. Sherman-Baust, M. Tsai-Turton, R.E. Bristow, R.B. Roden, P.J. Morin, Claudin-containing exosomes in the peripheral circulation of women with ovarian cancer, BMC Cancer 9 (2009) 244.
[63] C. Escrevente, S. Keller, P. Altevogt, J. Costa, Interaction and uptake of exosomes by ovarian cancer cells, BMC Cancer 11 (2011) 108.
[64] P.A. Baeuerle, O. Gires, EpCAM (CD326) finding its role in cancer, Br. J. Cancer 96 (2007) 417–423.
[65] J. Kotha, C. Longhurst, W. Appling, L.K. Jennings, Tetraspanin CD9 regulates beta 1 integrin activation and enhances cell motility to fibronectin via a PI-3 kinase-dependent pathway, Exp. Cell Res. 314 (2008) 1811–1822.
[66] S.M. Ellerbroek, D.A. Fishman, A.S. Kearns, L.M. Bafetti, M.S. Stack, Ovarian carcinoma regulation of matrix metalloproteinase-2 and membrane type 1 matrix metalloproteinase through beta1 integrin, Cancer Res. 59 (1999) 1635–1641.
[67] R. Valenti, V. Huber, M. Iero, P. Filipazzi, G. Parmiani, L. Rivoltini, Tumor-released microvesicles as vehicles of immunosuppression, Cancer Res. 67 (2007) 2912–2915.
[68] V.M. Abrahams, S.L. Straszewski, M. Kamsteeg, B. Hanczaruk, P.E. Schwartz, T.J. Rutherford, G. Mor, Epithelial ovarian cancer cells secrete functional Fas ligand, Cancer Res. 63 (2003) 5573–5581.
[69] L. Bjorge, J. Hakulinen, O.K. Vintermyr, H. Jarva, T.S. Jensen, O.E. Iversen, S. Meri, Ascitic complement system in ovarian cancer, Br. J. Cancer 92 (2005) 895–905.
[70] K. Shedden, X.T. Xie, P. Chandaroy, Y.T. Chang, G.R. Rosania, Expulsion of small molecules in vesicles shed by cancer cells: association with gene expression and chemosensitivity profiles, Cancer Res. 63 (2003) 4331–4337.
[71] R. Safaei, K. Katano, B.J. Larson, G. Samimi, A.K. Holzer, W. Naerdemann, M. Tomioka, M. Goodman, S.B. Howell, Intracellular localization and trafficking of fluorescein-labeled cisplatin in human ovarian carcinoma cells, Clin. Cancer Res. 11 (2005) 756–767.
[72] H.W. Lin, Y.Y. Tu, S.Y. Lin, W.J. Su, W.L. Lin, W.Z. Lin, S.C. Wu, Y.L. Lai, Risk of ovarian cancer in women with pelvic inflammatory disease: a population-based study, Lancet Oncol. 12 (2011) 900–904.
[73] P.J. Sims, E.M. Faioni, T. Wiedmer, S.J. Shattil, Complement proteins C5b-9 cause release of membrane vesicles from the platelet surface that are enriched in the membrane receptor for coagulation factor Va and express prothrombinase activity, J. Biol. Chem. 263 (1988) 18205–18212.
[74] H.B. Wang, J.T. Wang, L. Zhang, Z.H. Geng, W.L. Xu, T. Xu, Y. Huo, X. Zhu, E.F. Plow, M. Chen, J.G. Geng, P-selectin primes leukocyte integrin activation during inflammation, Nat. Immunol. 8 (2007) 882–892.
[75] O.P. Barry, D. Pratico, R.C. Savani, G.A. FitzGerald, Modulation of monocyte-endothelial cell interactions by platelet microparticles, J. Clin. Invest. 102 (1998) 136–144.
[76] L.A. Liotta, P.S. Steeg, W.G. Stetler-Stevenson, Cancer metastasis and angiogenesis: an imbalance of positive and negative regulation, Cell 64 (1991) 327–336.
[77] N.E. Sounni, C. Roghi, V. Chabottaux, M. Janssen, C. Munaut, E. Maquoi, B.G. Galvez, C. Gilles, F. Frankenne, G. Murphy, J.M. Foidart, A. Noel, Up-regulation of vascular endothelial growth factor-A by active membrane-type 1 matrix metalloproteinase through activation of Src-tyrosine kinases, J. Biol. Chem. 279 (2004) 13564–13574.
[78] A.A. Kamat, M. Fletcher, L.M. Gruman, P. Mueller, A. Lopez, C.N. Landen Jr., L. Han, D.M. Gershenson, A.K. Sood, The clinical relevance of stromal matrix metalloproteinase expression in ovarian cancer, Clin. Cancer Res. 12 (2006) 1707–1714.
[79] L.J. McCawley, L.M. Matrisian, Matrix metalloproteinases: they're not just for matrix anymore!, Curr. Opin. Cell Biol. 13 (2001) 534–540.

[80] J. Symowicz, B.P. Adley, K.J. Gleason, J.J. Johnson, S. Ghosh, D.A. Fishman, L.G. Hudson, M.S. Stack, Engagement of collagen-binding integrins promotes matrix metalloproteinase-9-dependent E-cadherin ectodomain shedding in ovarian carcinoma cells, Cancer Res. 67 (2007) 2030–2039.
[81] B. Davidson, I. Goldberg, W.H. Gotlieb, J. Kopolovic, G. Ben-Baruch, J.M. Nesland, R. Reich, The prognostic value of metalloproteinases and angiogenic factors in ovarian carcinoma, Mol. Cell. Endocrinol. 187 (2002) 39–45.
[82] S. Sillanpaa, M. Anttila, K. Voutilainen, K. Ropponen, T. Turpeenniemi-Hujanen, U. Puistola, R. Tammi, M. Tammi, R. Sironen, S. Saarikoski, V.M. Kosma, Prognostic significance of matrix metalloproteinase-9 (MMP-9) in epithelial ovarian cancer, Gynecol. Oncol. 104 (2007) 296–303.
[83] P.L. Torng, T.L. Mao, W.Y. Chan, S.C. Huang, C.T. Lin, Prognostic significance of stromal metalloproteinase-2 in ovarian adenocarcinoma and its relation to carcinoma progression, Gynecol. Oncol. 92 (2004) 559–567.
[84] M.L. Moss, A. Stoeck, W. Yan, P.J. Dempsey, ADAM10 as a target for anti-cancer therapy, Curr. Pharm. Biotechnol. 9 (2008) 2–8.
[85] K.J. Garton, P.J. Gough, E.W. Raines, Emerging roles for ectodomain shedding in the regulation of inflammatory responses, J. Leukoc. Biol. 79 (2006) 1105–1116.
[86] R.A. Black, C.T. Rauch, C.J. Kozlosky, J.J. Peschon, J.L. Slack, M.F. Wolfson, B.J. Castner, K.L. Stocking, P. Reddy, S. Srinivasan, N. Nelson, N. Boiani, K.A. Schooley, M. Gerhart, R. Davis, J.N. Fitzner, R.S. Johnson, R.J. Paxton, C.J. March, D.P. Cerretti, A metalloproteinase disintegrin that releases tumour-necrosis factor-alpha from cells, Nature 385 (1997) 729–733.
[87] O. Rosso, T. Piazza, I. Bongarzone, A. Rossello, D. Mezzanzanica, S. Canevari, A.M. Orengo, A. Puppo, S. Ferrini, M. Fabbi, The ALCAM shedding by the metalloprotease ADAM17/TACE is involved in motility of ovarian carcinoma cells, Mol. Cancer Res. 5 (2007) 1246–1253.
[88] D. Mezzanzanica, M. Fabbi, M. Bagnoli, S. Staurengo, M. Losa, E. Balladore, P. Alberti, L. Lusa, A. Ditto, S. Ferrini, M.A. Pierotti, M. Barbareschi, S. Pilotti, S. Canevari, Subcellular localization of activated leukocyte cell adhesion molecule is a molecular predictor of survival in ovarian carcinoma patients, Clin. Cancer Res. 14 (2008) 1726–1733.
[89] V. Beck, H. Herold, A. Benge, B. Luber, P. Hutzler, H. Tschesche, H. Kessler, M. Schmitt, H.G. Geppert, U. Reuning, ADAM15 decreases integrin alphavbeta3/vitronectin-mediated ovarian cancer cell adhesion and motility in an RGD-dependent fashion, Int. J. Biochem. Cell Biol. 37 (2005) 590–603.
[90] L. Howard, P. Glynn, Membrane-associated metalloproteinase recognized by characteristic cleavage of myelin basic protein: assay and isolation, Methods Enzymol. 248 (1995) 388–395.
[91] X. Lu, D. Lu, M. Scully, V. Kakkar, ADAM proteins—therapeutic potential in cancer, Curr. Cancer Drug Targets 8 (2008) 720–732.
[92] A. Gadducci, M. Ferdeghini, A. Fanucchi, C. Annicchiarico, S. Cosio, C. Prontera, R. Bianchi, A.R. Genazzani, Serum assay of soluble CD44 standard (sCD44-st), CD44 splice variant v5 (sCD44-v5), and CD44 splice variant v6 (sCD44-v6) in patients with epithelial ovarian cancer, Anticancer Res. 17 (1997) 4463–4466.
[93] J.P. Venables, Unbalanced alternative splicing and its significance in cancer, Bioessays 28 (2006) 378–386.
[94] R.L. Brown, L.M. Reinke, M.S. Damerow, D. Perez, L.A. Chodosh, J. Yang, C. Cheng, CD44 splice isoform switching in human and mouse epithelium is essential for epithelial-mesenchymal transition and breast cancer progression, J. Clin. Invest. 121 (2011) 1064–1074.
[95] J.A. Timbrell, Principles of Biochemical Toxicology, third ed., Taylor & Francis, Padstow, UK, 2000.

[96] V.M. Faca, A.P. Ventura, M.P. Fitzgibbon, S.R. Pereira-Faca, S.J. Pitteri, A.E. Green, R.C. Ireton, Q. Zhang, H. Wang, K.C. O'Briant, C.W. Drescher, M. Schummer, M.W. McIntosh, B.S. Knudsen, S.M. Hanash, Proteomic analysis of ovarian cancer cells reveals dynamic processes of protein secretion and shedding of extra-cellular domains, PLoS One 3 (2008) e2425.
[97] A.M. Lutz, J.K. Willmann, F.V. Cochran, P. Ray, S.S. Gambhir, Cancer screening: a mathematical model relating secreted blood biomarker levels to tumor sizes, PLoS Med. 5 (2008) e170.
[98] A.G. Zeimet, C. Marth, F.A. Offner, P. Obrist, M. Uhl-Steidl, H. Feichtinger, S. Stadlmann, G. Daxenbichler, O. Dapunt, Human peritoneal mesothelial cells are more potent than ovarian cancer cells in producing tumor marker CA-125, Gynecol. Oncol. 62 (1996) 384–389.
[99] C.G. Mahlck, K. Grankvist, O. Kjellgren, T. Backstrom, Relationship between CA 125 and progesterone production in women with ovarian carcinoma, Cancer 65 (1990) 2058–2063.
[100] M.S. Schilthuis, J.G. Aalders, J. Bouma, H. Kooi, G.J. Fleuren, P.H. Willemse, H.W. De Bruijn, Serum CA 125 levels in epithelial ovarian cancer: relation with findings at second-look operations and their role in the detection of tumour recurrence, Br. J. Obstet. Gynaecol. 94 (1987) 202–207.
[101] V.M. Faca, S.M. Hanash, In-depth proteomics to define the cell surface and secretome of ovarian cancer cells and processes of protein shedding, Cancer Res. 69 (2009) 728–730.
[102] M. Iero, R. Valenti, V. Huber, P. Filipazzi, G. Parmiani, S. Fais, L. Rivoltini, Tumour-released exosomes and their implications in cancer immunity, Cell Death Differ. 15 (2008) 80–88.
[103] P.K. Wright, Targeting vesicle trafficking: an important approach to cancer chemotherapy, Recent Pat. Anticancer Drug Discov. 3 (2008) 137–147.
[104] M. Ostrowski, N.B. Carmo, S. Krumeich, I. Fanget, G. Raposo, A. Savina, C.F. Moita, K. Schauer, A.N. Hume, R.P. Freitas, B. Goud, P. Benaroch, N. Hacohen, M. Fukuda, C. Desnos, M.C. Seabra, F. Darchen, S. Amigorena, L.F. Moita, C. Thery, Rab27a and Rab27b control different steps of the exosome secretion pathway, Nat. Cell Biol. 12 (2010) 19–30 sup pp. 1–13.
[105] N. Chaput, J. Taieb, N.E. Schartz, F. Andre, E. Angevin, L. Zitvogel, Exosome-based immunotherapy, Cancer Immunol. Immunother. 53 (2004) 234–239.
[106] T.E. Ichim, Z. Zhong, S. Kaushal, X. Zheng, X. Ren, X. Hao, J.A. Joyce, H.H. Hanley, N.H. Riordan, J. Koropatnick, V. Bogin, B.R. Minev, W.P. Min, R.H. Tullis, Exosomes as a tumor immune escape mechanism: possible therapeutic implications, J. Transl. Med. 6 (2008) 37.
[107] S. Zucker, R.M. Lysik, J. Wieman, D.P. Wilkie, B. Lane, Diversity of human pancreatic cancer cell proteinases: role of cell membrane metalloproteinases in collagenolysis and cytolysis, Cancer Res. 45 (1985) 6168–6178.
[108] W.C. Parks, C.L. Wilson, Y.S. Lopez-Boado, Matrix metalloproteinases as modulators of inflammation and innate immunity, Nat. Rev. Immunol. 4 (2004) 617–629.
[109] J.L. Lauer-Fields, J.K. Whitehead, S. Li, R.P. Hammer, K. Brew, G.B. Fields, Selective modulation of matrix metalloproteinase 9 (MMP-9) functions via exosite inhibition, J. Biol. Chem. 283 (2008) 20087–20095.
[110] J. Arribas, C. Esselens, ADAM17 as a therapeutic target in multiple diseases, Curr. Pharm. Des. 15 (2009) 2319–2335.
[111] J.S. Fridman, E. Caulder, M. Hansbury, X. Liu, G. Yang, Q. Wang, Y. Lo, B.B. Zhou, M. Pan, S.M. Thomas, J.R. Grandis, J. Zhuo, W. Yao, R.C. Newton, S.M. Friedman, P.A. Scherle, K. Vaddi, Selective inhibition of ADAM metalloproteases as a novel approach for modulating ErbB pathways in cancer, Clin. Cancer Res. 13 (2007) 1892–1902.

CHAPTER NINE

A Comparison of the Hodgkin–Huxley Model and the Soliton Theory for the Action Potential in Nerves

Revathi Appali[*,†,1], **Ursula van Rienen**[*], **Thomas Heimburg**[†]
[*]Institute of General Electrical Engineering, University of Rostock, Rostock, Germany
[†]Membrane Biophysics Group, The Niels Bohr Institute, University of Copenhagen, Copenhagen, Denmark
[1]Corresponding author: e-mail address: revathi.appali@uni-rostock.de

Contents

1. Introduction 276
2. Lipids and Proteins in Neuronal Membranes 277
   2.1 The lipid membrane 278
   2.2 Membrane proteins 279
3. Electrical Circuits and the HH Model 279
4. Pulse Propagation Based on the Thermodynamics of the Biological Membrane: The Soliton Model 283
5. Comparison of HH and Soliton Models 289
   5.1 Numerical simulations of pulse collisions 291
   5.2 Can the two models be combined? 294
6. Conclusions 295
Acknowledgments 296
References 296

Abstract

We describe the origin and significance of electrical and mechanical observations on nerves. To this end, we compare two models for neural activity, which are the established Hodgkin–Huxley model and the more recent soliton theory, respectively. While the Hodgkin–Huxley model focuses particularly on the electrical aspects of the neural membranes, the soliton model is based on hydrodynamic and thermodynamic properties of the membrane, thus including changes in all thermodynamic variables.

Advances in Planar Lipid Bilayers and Liposomes, Volume 16
ISSN 1554-4516
http://dx.doi.org/10.1016/B978-0-12-396534-9.00009-X

1. INTRODUCTION

The action potential is a propagating voltage pulse traveling along the nerve axon. Since the first description of its electrical features by Luigi Galvani [1] and Volta [2] in the past decade of the eighteenth century, its nature has been in the focus of intense studies during the recent 200 years. Starting from a famous paper by Bernstein [3] in 1902, it has been assumed that the permeability of the neural membrane for ions is a necessary prerequisite for the propagation of the nervous impulse in excitable membranes. Bernstein based his considerations on the electrochemistry of semipermeable walls, leading to a voltage difference across a membrane upon uneven distribution of positive and negative ions (Nernst potentials). While Bernstein assumed that the permeability for ions breaks down in a nonspecific manner, the later Hodgkin–Huxley (HH) model [4] is based on the assumption that the membrane contains proteins that selectively conduct sodium and potassium ions in a time- and voltage-dependent manner. This model was at the basis of a rapid development in molecular biology, leading to numerous studies on ion channel proteins. Until today, permeation studies on ion channel proteins have been in the center of interest of molecular biology.

The HH model treats the nerve axon as an electrical circuit in which the proteins are resistors and the membrane is a capacitor. Ion currents flow through the membrane and along the nerve axon leading to a propagating pulse. The voltage dependence of the channel proteins results a characteristic spike (Fig. 9.1) described by a partial differential equation that exclusively contains electrical parameters. While the HH model describes various aspects of the action potential in a satisfactory manner (e.g., its velocity and the pulse amplitude), it fails to describe several other aspects of the nerve pulse that are

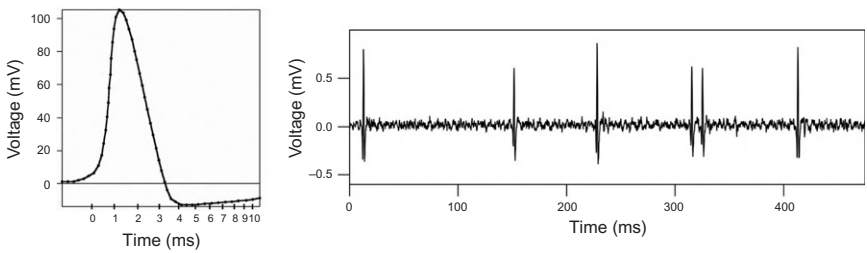

Figure 9.1 The action potential. Left: The action potential in a squid axon, *adapted from Ref. [5]*. Right: Extracellular recording of action potential from grasshopper nerves. Adapted from Ref. [6].

of nonelectrical nature. For instance, it is known that nerves display thickness and length variations under the influence of the action potential [7–13]. Interestingly, the action potential can be excited by a mechanical stimulus, indicating that the nerve pulse possesses a mechanical component. An even more important observation is the heat production of a nerve during the nerve pulse. During the first phase of the nerve pulse, heat is released from the membrane, while it is reabsorbed during the second phase [7,14–18]. The integrated exchange of heat is zero within experimental accuracy, indicating that the action potential is an adiabatic phenomenon. This later observation is in conflict with the HH model that is based on irreversible dissipative processes (currents through resistors) and should lead to dissipation of heat [19]. This, however, is not observed in nerves. In this context, it is interesting to note that a nerve pulse can also be stimulated by local cooling [20], indicating that heat changes take place during the action potential. Summarizing, it seems as if the mechanical and the heat signatures rather indicate that the nerve pulse is an adiabatic and reversible phenomenon such as the propagation of a mechanical wave.

To rationalize the above phenomena, it has been proposed that the propagating nerve pulse is an electromechanical soliton rather than a breakdown of membrane resistance [6,21–23]. The soliton theory is an alternative explanation of the nerve pulse based on the thermodynamics of the membrane and naturally includes all thermodynamic variables including volume, area, and enthalpy changes. In the context of this model, the pulse velocity is close to the velocity of sound in the membrane, and the experimentally observed reversible heat corresponds to the reversible heating of compressible media during the propagation of adiabatic waves.

In the present contribution, we review and compare the HH model and the soliton theory for neuronal signal propagation and discuss the implications of each model. A particular focus is on the collision of pulses.

2. LIPIDS AND PROTEINS IN NEURONAL MEMBRANES

The basic components of the nervous system are cells called neurons. Neurons transmit information by firing and propagating electrical impulses. These pulses (called *action potentials*) display typical amplitudes of 100 mV, velocities between 1 and 100 m/s, and display a characteristic timescale of about 1 ms.

The major units of a neuron are the soma (the cell body) including most organelles, the dendrites (receiving the signals), the axon (propagating

the signal), and synapses (chemical or electrical connections to other cells). Neurons possess a wide variety of shapes, sizes, and electrochemical properties [24]. They are similar to other eukaryotic cells which contain a nucleus and organelles surrounded by membranes [24]. These membranes are mainly composed of two classes of molecules: lipids and proteins.

2.1. The lipid membrane

The plasma membrane acts as the outer boundary of a neuron. It regulates the permeation of substances into and out of the cell. The membrane is composed of a lipid bilayer into which proteins are embedded [25] (Fig. 9.2C). Typical lipid/protein mass ratios of biomembranes are around one [27] (including the peripheral parts of the proteins).

The lipid bilayer consists of various small amphiphilic molecules ranging from phospholipids (Fig. 9.2A) and sphingolipids to cholesterol. The hydrophobic tails of these lipids are directed toward the membrane center and away from extra- and intracellular fluid. In contrast, head groups are zwitterionic, polar, or charged. Therefore, the head groups are exposed to the aqueous medium and are in contact with extra- and intracellular fluid. The lipid membrane displays order transitions as a function of temperature,

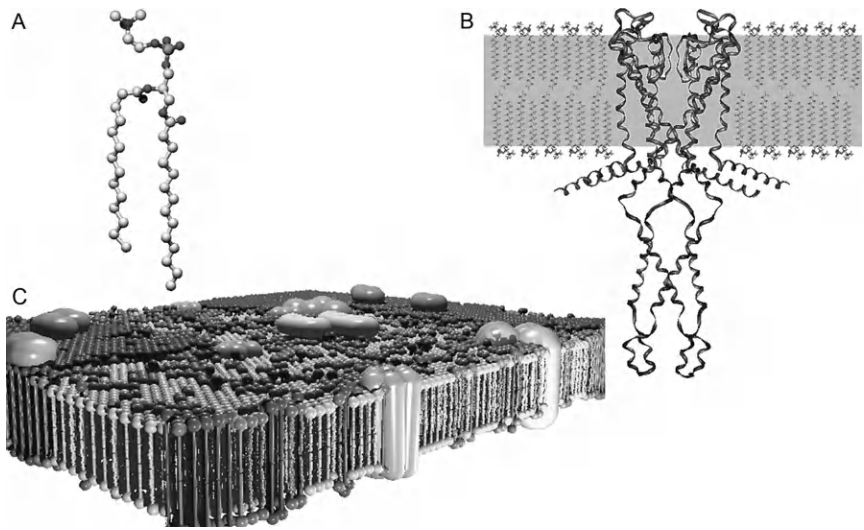

Figure 9.2 Schematic diagrams of a phospholipid (A) of the KscA potassium channel protein embedded in a lipid membrane (B) and the biomembrane in the presence of proteins and compositional separation of lipids into domains (C). *Reproduced with permission from Ref. [26].*

pressure, pH, or voltage. In these transitions, the number of configurations of individual lipid molecules increases dramatically. In the melting regime, one finds coexisting domains of ordered and disordered lipid. Figure 9.2C shows a membrane with coexisting domains of different physical states. Proteins are associated with the membrane.

2.2. Membrane proteins

While the lipid bilayer is often believed to mainly determine the basic structure of the plasma membrane, the embedded proteins are thought to be responsible for its function. They are involved in transport process into and out of the cell. A particular class of proteins abundant in neuronal membranes are the so-called channel proteins that are believed to form pores for particular ions. They contribute to the passive transport of ions. For instance, the Na^+-channel has been reported to display a specific conductance for sodium, while K^+-channel has been reported to show potassium conductance along concentration gradients between the inside and the outside of the cells. Figure 9.2B displays the crystal structure of the KscA potassium channel proteins embedded into a lipid membrane. Such ion channel proteins are considered to be responsible for the ion currents observed in conduction experiments on nerve membranes. The presently accepted model for nerve pulse generation and propagation proposed by Hodgkin and Huxley in 1952 [4] is based on voltage- and time-dependent properties of such ion channels. We will discuss the experimental results that lead to the theory as well as to the model in more detail in the next section.

However, it will be shown below that the lipid membrane itself plays a much more active role in biological processes than hitherto believed.

3. ELECTRICAL CIRCUITS AND THE HH MODEL

The present understanding of the nerve membrane is based on some important experimental works from the 1930s to the 1950s. The association of the action potential in nerves with a large increase in membrane conductance, first proposed by Ludwig Bernstein, was confirmed by Cole and Curtis [5] in 1939. These recordings demonstrated that the action potential is not just a reduction of the membrane potential due to an unspecific breakdown of membrane resistance during the action potential but involves a change in sign (overshoot), implying a more sophisticated mechanism. Hodgkin and Katz [28] explained the overshooting action potential as a result of an increase

in sodium permeability, thus supporting the suggestion of Overton [29]. Finally, Hodgkin, Huxley, and Katz developed the voltage-clamp circuit to facilitate quantitative measurement of ionic currents from squid axon. Hodgkin and Huxley proposed that the membrane can be selectively permeable for either sodium or potassium in a voltage- and time-dependent manner. This mechanism ultimately leads to the famous HH model [4].

Hodgkin and Huxley studied the conductance properties of nerve axons from squid in voltage-clamp experiments [30]. In such experiments, an electrode is inserted into a nerve axon such that the voltage difference between inside and outside is constant along the whole axon. Under such conditions no pulse can propagate. The voltage-clamp experiments by Hodgkin and Huxley showed that a stepwise depolarization (reduction of transmembrane voltage) of the membrane by electrodes first triggered an inward current (against the applied field) followed by an outward current (along the external field). With the aid of ionic substitution, they demonstrated that the net current could be separated into two distinct components: a fast inward current carried by Na^+ ions, and a more slowly activated outward current carried by K^+ ions. They concluded that these two currents result from independent permeation mechanisms for Na^+ and K^+ involving time- and voltage-dependent conductances of particular objects in the membrane. This new concept was named the "ionic hypothesis" [31]. The schematic diagram for the electrical circuit in the voltage-clamp experiment is shown in Fig. 9.3.

In the HH picture, three different ion currents contribute to the voltage signal of the neuron, that is, a sodium current, a potassium current, and a leak current that consists mainly of Cl^- ions. The flow of these ions through the cell membrane is controlled by their respective voltage-dependent ion

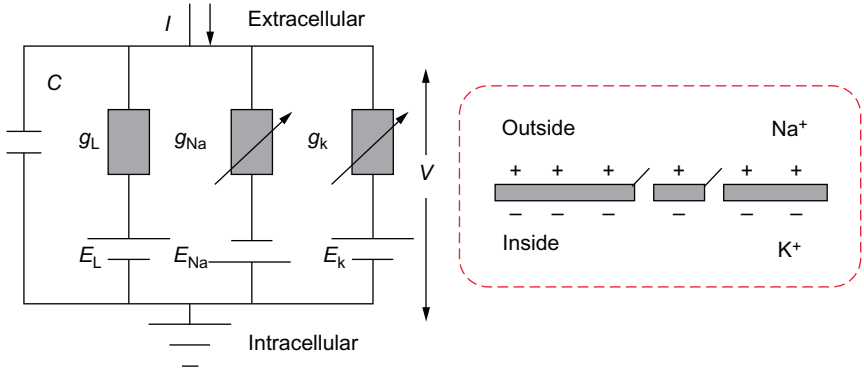

Figure 9.3 Schematic diagram of Hodgkin–Huxley circuit in a voltage-clamp experiment *adapted from Ref. [32].*

channels. The leak current also takes care of other channel types which are not described in particular. The most remarkable achievement of this theory was the self-consistent agreement of the experimental voltage-clamp data (in the absence of a pulse) with a quantitative model for the propagating nerve pulse [4], which made it the very first complete description of the excitability of a single neuron.

The semipermeable cell membrane separates the interior of the cell from the extracellular liquid. The lipid membrane is considered an insulator that acts as a capacitor with constant capacitance, C_m. The proteins are considered being resistors described by conductances g_i (i being the index for a particular channel and ion). Upon change of voltage, V_m, two currents can be observed—a capacitive current charging the capacitor and ohmic currents through the protein. The total current through the membrane, I_m, is the sum of these two currents. The equivalent circuit is shown in Fig. 9.3. The time-dependent membrane current I_m is given by the following equation:

$$I_{\mathrm{m}}(t) = C_{\mathrm{m}}\frac{\mathrm{d}V_{\mathrm{m}}}{\mathrm{d}t} + g_{\mathrm{Na}}(V_{\mathrm{m}} - E_{\mathrm{Na}}) + g_{\mathrm{K}}(V_{\mathrm{m}} - E_{\mathrm{K}}) + g_{\mathrm{L}}(V_{\mathrm{m}} - E_{\mathrm{L}}) \quad (9.1)$$

The last term in this equation accounts for small leak currents and will be omitted in the following. The quantities E_{Na}, E_{K} (and E_{L}) are the Nernst potentials of different ions. The concentrations of ions on the inner and outer side of the cell (c_{in} and c_{out}) are different (K^+ concentrations of the giant squid are 400 mM inside and 20 mM outside. Na^+ concentrations are 50 and 440 mM, respectively [33]). As a consequence, current flows even in the absence of an external voltage due to diffusion along the gradients. This is taken into account by the Nernst potentials in the above equation:

$$E_{\mathrm{i}} = \frac{RT}{zF}\ln\frac{c_{\mathrm{out}}}{c_{\mathrm{in}}} \quad (9.2)$$

If the external voltage is equal to the Nernst potential, no current flows. The Nernst potentials are different for different ions.

The functions g_{Na} and g_{K} are the conductances of the ion channel proteins for the respective ions. They are assumed to be functions of voltage and time. Hodgkin and Huxley parameterized these conductances by using their voltage-clamp data in the following manner:

$$\begin{aligned} g_{\mathrm{Na}} &= g_{\mathrm{Na},0}m^3h, \\ g_{\mathrm{K}} &= g_{\mathrm{K}_0}n^4 \end{aligned} \quad (9.3)$$

introducing the functions $m(V_m, t)$, $h(V_m, t)$, and $n(V_m, t)$ that depend on voltage and time. These functions range between 0 and 1 and are related to the likelihood that the channel is open. If $m^3h = 1$, the sodium channel is open and conducts with the characteristic conductance $g_{Na,0}$. If $n^4 = 1$, the potassium channel is open and conducts with its characteristic conductance $g_{K,0}$. The functions m, h, and n are called *gating variables*. Each of them follows a simple linear differential equation after changing voltage yielding an exponential relaxation in time:

$$\begin{aligned} \frac{dm}{dt} &= \alpha_m(V_m)(1-m) - \beta_m(V_m)m, \\ \frac{dn}{dt} &= \alpha_n(V_m)(1-n) - \beta_n(V_m)n, \\ \frac{dh}{dt} &= \alpha_h(V_m)(1-h) - \beta_h(V_m)h \end{aligned} \tag{9.4}$$

The newly introduced functions $\alpha_m(V_m)$, $\alpha_h(V_m)$, $\alpha_n(V_m)$ and $\beta_m(V_m)$, $\beta_h(V_m)$, $\beta_n(V_m)$ are voltage-dependent rate constants that cannot be derived by any theory. Instead, they are fitted to experimental data. Each of the rate constants requires several parameters to obtain an empirical fit. All together, one has more than 20 empirical fit parameters. This indicates that the HH model is not a theory based on first principles but rather a parameterization of the electrical features of the membrane.

The propagating action potential is now calculated by combining Eq. (9.1) with cable theory (Fig. 9.4). Using Kirchhoff's laws, cable theory describes the spreading of a voltage along a cylindrical membrane as a function of distance x, the specific resistance of the membrane (R_m) and the specific inner resistance of the intracellular medium along the cable (R_i). A central equation originating from cable theory is

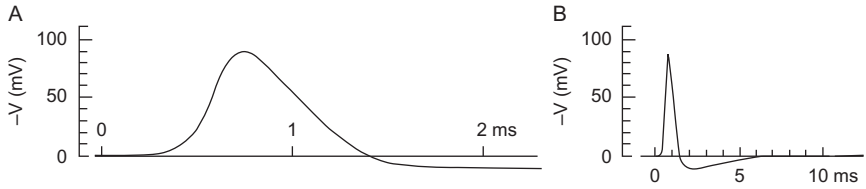

Figure 9.4 Action potential in squid axons simulated by Hodgkin and Huxley in 1952. The pulse is shown in two different time windows. *From Ref. [4].*

$$\frac{\partial^2 V_\mathrm{m}}{\partial x^2} = \frac{2R_i}{a} I_\mathrm{m} \tag{9.5}$$

for a cable with radius a, which together with Eq. (9.1) yields

$$\frac{\partial^2 V_\mathrm{m}}{\partial x^2} = \frac{2R_\mathrm{i}}{a}\left(C_\mathrm{m}\frac{\mathrm{d}V_\mathrm{m}}{\mathrm{d}t} + g_\mathrm{Na}(V_\mathrm{m} - E_\mathrm{Na}) + g_\mathrm{K}(V_\mathrm{m} - E_\mathrm{K})\right) \tag{9.6}$$

Finally, it is assumed that a pulse exists that propagates with constant speed θ independent of voltage. This implies that the wave equation

$$\frac{\partial^2 V_\mathrm{m}}{\partial t^2} = \theta^2 \frac{\partial^2 V_\mathrm{m}}{\partial x^2} \tag{9.7}$$

can be used. Combining Eq. (9.7) with Eq. (9.6) yields the final equation for the propagation of the electrical pulse:

$$\frac{a}{2R_\mathrm{i}\theta^2}\frac{\partial^2 V_\mathrm{m}}{\partial t^2} = C_\mathrm{m}\frac{\mathrm{d}V_\mathrm{m}}{\mathrm{d}t} + g_\mathrm{Na}(V_\mathrm{m} - E_\mathrm{Na}) + g_\mathrm{K}(V_\mathrm{m} - E_\mathrm{K}) \tag{9.8}$$

This partial differential equation has to be solved and yields the HH action potential.

The HH model can reproduce a wide range of data from squid axon, for instance the shape and propagation of the action potential (see Fig. 9.2), its sharp threshold, its refractory period, and the hyperpolarization. However, it has to be noted that the model contains a hidden complexity since the conductances are empirical functions of voltage and time that were parameterized from experiment (see above).

There have been various attempts to simplify the complexity of the equation, for instance by FitzHugh and Nagumo [34,35] (called the FitzHugh–Nagumo (FHN) model), Hindmarsh–Rose [36] and Rajagopal [37]. Such models are widely used in simulating the neural networks in order to rationalize experimental data.

4. PULSE PROPAGATION BASED ON THE THERMODYNAMICS OF THE BIOLOGICAL MEMBRANE: THE SOLITON MODEL

The HH model describes the electrical processes during signal generation and propagation in the nerves. However, the model fails to explain several nonelectrical properties observed during experiments. For instance, it has been observed that one finds a reversible release and reuptake of heat during the action potential [7,14–18]. The integral over the heat exchange

during the nerve pulse is zero within the experimental accuracy. While this is in conflict with a dissipative model based on electrical resistors, it is rather consistent with an adiabatic wave (e.g., a sound wave). In fact, mechanical changes during the action potential have been found in various experiments [7–13], indicating that the action potential is accompanied by a mechanical pulse. The thickness of the nerve increases, and a simultaneous shortening of the nerve can be observed. The HH model also fails to explain the effect of anesthetics on nerve pulse conduction.

In 2005, Heimburg and Jackson proposed a thermodynamic theory of nerve pulse propagation in which the action potential is a reversible electromechanical soliton [6,19,21,22,38]. It is based on the thermodynamics and in particular the phase behavior of the lipids which are the major components of the membrane. In the following, we will refer to this theory as the "soliton model." A central prerequisite of this theory is the chain-melting transition of the lipid membranes, which in biological cells can be found a few degrees below body temperature (see Fig. 9.5; Refs. [21,27]). At physiological temperatures, the state of the biological membranes is fluid. The melting transition is linked to changes in enthalpy, entropy, but also to changes in volume, area, and thickness. This implies that the state of the membrane can be influenced not only by temperature but also by hydrostatic pressure and lateral pressure in the membrane plane. Due to the fluctuation–dissipation theorem, the fluctuations in enthalpy, volume, and area in the transition are at a maximum. Therefore, the heat capacity and the volume compressibility all reach maxima. Simultaneously, the relaxation timescale reaches a

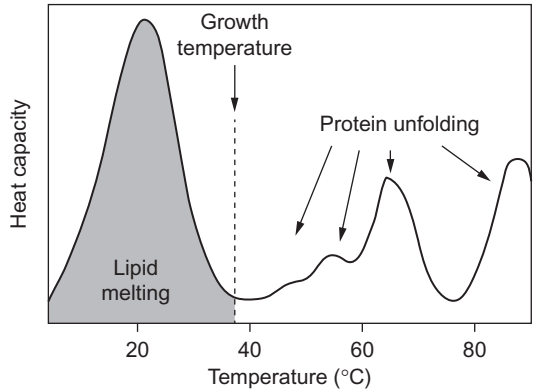

Figure 9.5 Heat capacity profile of native *Escherichia coli* membranes showing a lipid melting peak below physiological temperature. *Adapted from Ref. [26].*

maximum. This implies that the lateral compression of a fluid membrane leads to an increase in compressibility. This effect is known as a *nonlinearity*. From experiment, it is known that the compressibility is also frequency dependent, an effect that is known as *dispersion*. These two phenomena are necessary conditions for the propagation of solitons. It can be shown that the features of lipid membranes slightly above a transition are sufficient to allow the propagation of mechanical solitons along membrane cylinders [21]. The solitons consists of a reversible compression of the membrane that is linked to a reversible release of heat, mechanical changes in the membrane. Furthermore, the soliton model also implies a mechanism for anesthesia that lies in the well-understood influence that anesthetics have on the lipid phase transition [38].

The soliton model starts with the well-known wave equation for area density changes $\Delta\rho^A$

$$\frac{\partial^2}{\partial\tau^2}\Delta\rho^A = \frac{\partial}{\partial z}\left(c^2\frac{\partial}{\partial z}\Delta\rho^A\right) \tag{9.9}$$

that originates from the Euler equations of compressible media (e.g., [39,40]). Here, τ is the time, z is the position along the nerve axon, and c is the sound velocity. If $c = c_0$ is constant, one finds the relation for sound propagation $(\partial^2\rho/\partial\tau^2) = c_0^2(\partial^2\rho/\partial z^2)$.

However, it has been shown that close to melting transitions in membranes, the sound velocity is a sensitive function of density [41,42]. As shown in Fig. 9.5, such transitions are found in biomembranes. This is taken into account by expanding the sound velocity around its value in the fluid phase

$$c^2 = c_0^2 + p\Delta\rho^A + q(\Delta\rho^A)^2 + \cdots \tag{9.10}$$

up to terms of quadratic order. The parameters p and q describe the dependence of the sound velocity on density close to the melting transition and are fitted to experimental data [21].

It is further known that the speed of sound is frequency dependent. This effect is known as *dispersion*. In order to take dispersion into account, a second term is introduced into Eq. (9.9) that assumes the form:

$$-h\frac{\partial^4}{\partial z^4}\Delta\rho^A \tag{9.11}$$

where h is a constant. For low-amplitude sound, this term leads to the most simple dispersion relation $c^2 = c_0^2 + (h/c_0^2)\omega^2 = c_0^2 + \text{const}\cdot\omega^2$. Lacking

good data on the frequency dependence of sound in the kilohertz regime, the term given by Eq. (9.11) is most natural dispersion term.

Combining Eqs. (9.9)–(9.11) leads to the final time and position-dependent partial differential equation [21,23]:

$$\frac{\partial^2}{\partial\tau^2}\Delta\rho^A = \frac{\partial}{\partial z}\left[\left(c_0^2 + p\Delta\rho^A + q(\Delta\rho^A)^2 + \cdots\right)\frac{\partial}{\partial z}\Delta\rho^A\right] - h\frac{\partial^4}{\partial z^4}\Delta\rho^A \quad (9.12)$$

which describes the propagation of a longitudinal density pulse in a myelinated nerve. In this equation,

- $\Delta\rho^A$ is the change in lateral density of the membrane $\Delta\rho^A = \rho^A - \rho_0^A$;
- ρ^A is the lateral density of the membrane;
- ρ_0^A is the equilibrium lateral density of the membrane in the fluid phase;
- c_0 is the velocity of small-amplitude sound;
- p and q are the parameters determined from density dependence of the sound velocity. These two constants parameterize the experimental shape of the melting transition of the membrane and are given in Ref. [21];
- h is a parameter describing the frequency dependence of the speed of sound, that is, the dispersion.

All parameters except h are known from experiment. The empirical equilibrium value of ${\rho_0}^A$ is $4.035 \times 10^{-3}\,\mathrm{g/m^2}$, and the low-frequency sound velocity c_0 is 176.6 m/s. The coefficients p and q were fitted to measured values of the sound velocity as a function of density. The parameter h is not known experimentally due to difficulties to measure the velocity of sound in the kilohertz regime. However, Chapter 2 attempts to derive this parameter theoretically from relaxation measurements.

The nonlinearity and dispersive effects of the lipids can produce a self-sustaining and localized density pulse (soliton) in the fluid membrane (see Fig. 9.6). The pulse consists of a segment of the membrane that locally is found in a solid (gel) state. It preserves its amplitude, shape, and velocity while propagating along the nerve axon. Further, the pulse propagates over long distances without loss of energy.

In the following, we work with the dimensionless variables u (dimensionless density change), x, and t defined in Ref. [23] as

$$u = \frac{\Delta\rho^A}{\rho_0^A}, \quad x = \frac{c_0}{h}z, \quad t = \frac{c_0^2}{\sqrt{h}}\tau, \quad B_1 = \frac{\rho_0}{c_0^2}p, \quad B_2 = \frac{\rho_0^2}{c_0^2}q \quad (9.13)$$

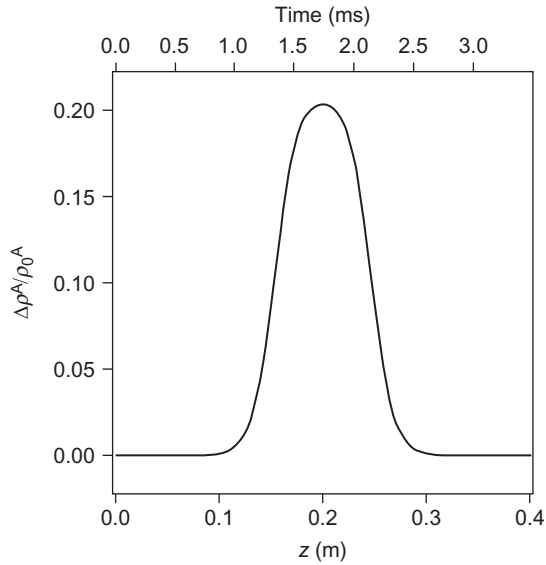

Figure 9.6 Calculated solitary density pulse as a function of lateral position calculated using experimental parameters for a synthetic membrane. The pulse travels with about 100 m/s. *From Ref. [43].*

Equation (9.12) now assumes the following form:

$$\frac{\partial^2 u}{\partial t^2} = \frac{\partial}{\partial x}(B(u))\frac{\partial u}{\partial x} - \frac{\partial^4 u}{\partial x^4} \tag{9.14}$$

with

$$B(u) = 1 + B_1 u + B_2 u^2 \tag{9.15}$$

$B_1 = -16.6$ and $B_2 = 79.5$ were determined experimentally for a synthetic lipid membrane in Ref. [21]. If we consider a density pulse u propagating with constant velocity, we can use the coordinate transformation $\xi = x - \beta t$ (where β is the dimensionless propagation velocity of the density pulse) and we yield the following form:

$$\beta^2 \frac{\partial^2 u}{\partial \xi^2} = \frac{\partial}{\partial \xi}\left(B(u)\frac{\partial u}{\partial \xi}\right) - \frac{\partial^4 u}{\partial \xi^4} \tag{9.16}$$

This is very much in the spirit of Eq. (9.7) used to obtain a propagating solution. Equation (9.15) displays exponentially localized *solitary* solutions which propagate without distortion for a finite range of subsonic velocities [21,23].

The above differential equation possesses analytical solutions given by

$$u(\xi) = \frac{2a_+a_-}{(a_+ + a_-) + (a_+ - a_-)\cosh(\xi\sqrt{1-\beta^2})} \tag{9.17}$$

where $u = a_\pm$ is given by

$$a_\pm = \frac{-B_1}{B_2}\left(1 \pm \sqrt{\frac{\beta^2 - \beta_0^2}{1-\beta_0^2}}\right) \tag{9.18}$$

for the velocity range $\beta_0 < |\beta| < 1$ (with 1 being the low-amplitude sound velocity). There exists a lower limit for the propagation velocity of the pulse given by $\beta_0 = 0.649851$ for a synthetic membrane. No solitons exist for slower velocities. The density change $u(\xi)$ describes the shape of the propagating soliton, which depends on the velocity β. A typical soliton generated by Eq. (9.16) is shown in Fig. 9.6. The minimum propagation velocity β is about 100 m/s, very similar to the measured propagation velocity of the action potential in myelinated nerves. Since the pulse describes a reversible mechanical pulse, it possesses a reversible heat production, a thickening and a simultaneous shortening of the nerve axon, in agreement with observation. Due to the electrostatic features of biomembranes, the pulse possesses a voltage component. Thus, the traveling soliton can be considered a piezoelectric pulse.

One feature of the soliton model not discussed here in detail is that it provides a mechanism for general anesthesia. It has been shown that general anesthetics lower the melting points of lipid membranes. At critical dose (where 50% of the individuals are anesthetized), the magnitude of this shift is independent of the chemical nature of the anesthetic drugs [38,44]. From this, one can deduce quantitatively how much free energy is required to trigger a soliton. In the presence of anesthetics, this free energy requirement is higher. As a result, nerve pulse stimulation is inhibited. In this respect, it is interesting to note that hydrostatic pressure reverses anesthesia. For instance, tadpoles anesthetized by ethanol wake up at pressures around 50 bars [45]. It is also known that hydrostatic pressure increases melting temperatures of lipid membranes due to the positive excess volume of the transition [46]. The effects of anesthetics and hydrostatic pressure are known quantitatively. Therefore, one can also quantitatively calculate at what pressure the effect of anesthetics is reversed. The resulting pressures are of the order of 25 bars at critical anesthetic dose, which is of same order than the observed pressure reversal of anesthesia [19,38].

Another important aspect discussed elsewhere is that melting of membranes results in quantized conduction events in lipid membranes due to thermal fluctuations. The conduction events are indistinguishable from protein ion channel traces [47–50]. Any change in a thermodynamics variable that is able to trigger a soliton in a nerve membrane is also able to generate lipid ion channel opening.

5. COMPARISON OF HH AND SOLITON MODELS

The HH model of nerve pulse propagation is a remarkable achievement in the field of physiology. It has shaped the thinking of a complete discipline for decades and is in line with the emergence of ion channel proteins and the influence of many drugs on the excitability of a nerve membrane. However, as already mentioned above, the HH model cannot explain several nonelectrical phenomena such as the finding of reversible heat changes [7,14–18], changes in nerve thickness, and nerve contraction described in mechanical and optical experiments [8,10,51–53]. The soliton model is an alternative model that can convincingly describe some of the unexplained observations found in the experiments. It also generates ion channel-like events and provides a mechanism for general anesthesia [38].

In the following, we list some of the major features of the two neural models:

HH model:

- The action potential is based on the electrical cable theory in which the pulse is the consequence of voltage- and time-dependent changes of the conductance for sodium and potassium.
- The nerve pulse consists of a segment of charged membrane capacitor that propagates driven by dissipative flows of ions.
- The model is consistent with quantized ion currents attributed to opening and closing of specific channel proteins.
- It is consistent with the channel-blocking effects of several poisons, such as tetrodotoxin.
- The underlying hypothesis is exclusively of electrical nature and does not refer to changes of any other thermodynamics variables other than charge and electrical potential.
- The HH model is based on ion currents through resistors (channel proteins) and is therefore of dissipative nature.

- Reversible changes in heat and mechanical changes are not explicitly addressed, but heat generation would be expected.
- The propagating pulse dissipates a significant amount of free energy [43].
- The HH model generates a refractory period (minimum distance between pulses) and hyperpolarization as a consequence of the complex time dependence of channel conduction.
- The theory does not provide an explanation of anesthesia.

Soliton model

- The nerve pulse is a solitary electromechanical soliton coupled to the lipid transition in the membrane.
- The solitary character is a consequence of the nonlinearity of the elastic constants close to the melting transition of the lipid membrane and of dispersion.
- The theory is based on macroscopic thermodynamics and implies a role for all thermodynamics variables.
- It does not contain an explicit role of poisons and protein ion channels.
- However, the theory is consistent with channel-like pore formation in lipid membranes that is indistinguishable from protein conductance traces [47–49].
- Additional to changes in the electrical potential and the charge of the membrane, the propagating pulse is associated with changes in all variables including temperature, lateral pressure, area, and length. As found in experiments, the nerve pulse is coupled to changes in thickness and length.
- In agreement with the experiment, the propagating pulse does not dissipate heat because it is based on adiabatic processes.
- The model generates a refractory period and a hyperpolarization that is a consequence of mass conservation [6].
- The soliton model implies a mechanism for general anesthesia [19,38].

Both the theories describe the existence of voltage pulse in nerve pulse propagation. In the HH model, the propagating potential change itself is the signal, while in the soliton model, it is only one inseparable aspect of a more generic adiabatic pulse that implies changes in all variables.

5.1. Numerical simulations of pulse collisions

One important difference between the two models is seemingly what they predict about colliding nerve pulses. Tasaki reported in 1949 that nerve pulses when colliding in an axon eliminate each other [54]. In the following, we discuss what the two models predict about pulse collisions. In particular, we present results of colliding nerve pulses with both models using numerical simulations.

5.1.1 Why performing a collision study?

It has been known since the 1940s that the nerve pulses are blocked upon collision [54]. In the HH model, the cause of the decay in signal amplitude upon collision is the refractory period. This is the minimum distance between two pulses that travel in the same direction. It is caused by the finite relaxation times of the protein conductances of the stimulation of a pulse. In the so-called refractory zone, a nerve fiber is unexcitable, and the existence of these zones prevents two colliding pulses from passing through each other. Simulations based on the HH equations support this view [55,56]. Our own simulations using the FHN model lead to the same results. Figure 9.7 shows that the pulses eliminate each other upon collision.

In contrast, the soliton model does not exhibit a complete annihilation. The pulses pass through each other almost undisturbed with the generation of some small-amplitude noise. Thus, soliton model contradicts the description of the cancelation of pulses suggested in the biology literature. The details of these findings are described in Ref. [23].

Figure 9.8 (left) shows two identical small-amplitude solitons traveling in opposite directions at a velocity of $\beta = 0.8$ (80% of the lateral speed of sound in fluid membranes) before and after a collision. Small-amplitude noise travels ahead of the postcollision pulses, indicating a small dissipation of energy of the order of $\ll 1\%$ compared to the soliton energy. The same was found for solitary pulses with different velocities and amplitudes. Surprisingly, upon the collision of solitons approaching the minimum velocity (maximum amplitude), the solitons fall apart in a sequence of lower amplitude solitons and some high-frequency noise (Fig. 9.8, right). This effect is more pronounced the closer the velocity is to the minimum velocity [23]. Only for the case of solitons approaching minimum velocity and maximum amplitude, the fraction of energy lost into smaller amplitude solitons and small-amplitude noise is significant (Fig. 9.9). Thus, we observed that most of the energy of the major soliton was conserved in collisions even if a maximum density was enforced.

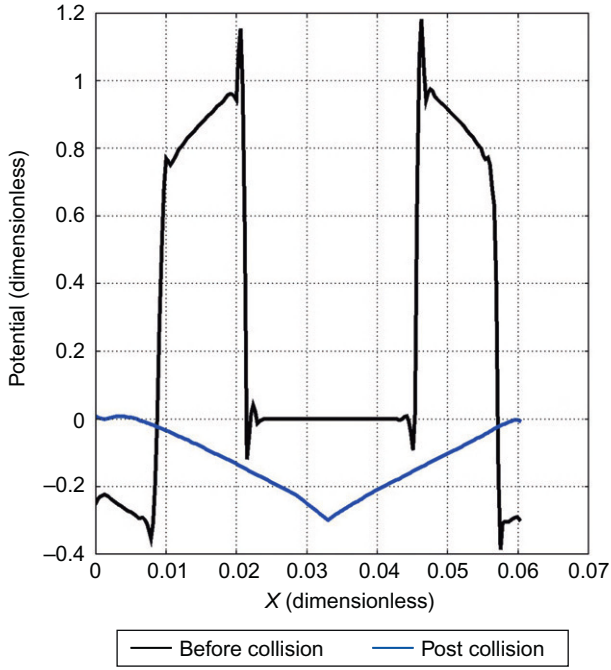

Figure 9.7 Collision of nerve pulses calculated with the FitzHugh–Nagumo equations. Two pulses traveling in opposite directions are shown before (black) and after the collision (blue). The pulses are annihilated after the collision.

Interestingly, soliton-like regimes can be also found in the HH model [55]. The term soliton is used here in a more mathematical sense meaning that one can generate pulses that reflect or penetrate each other when using certain parameters. Since the HH and the FHN models are based on dissipative processes, these are not solitons in a physical sense as in the soliton model.

Aslanidi and Mornev demonstrated that in excitable media under certain conditions, one can expect the emergence of a soliton-like regimes that corresponds to reflection (or loss-free penetration) of colliding waves. Figure 9.10 shows that $E_K = -12\,mV$ that colliding pulses annihilate. In contrast, a soliton-like regime was found for $-2.50\,mV < E_K < 2.46\,mV$ (Fig. 9.10). Furthermore, the pulses can also collide with the fiber boundaries and be reflected [55]. The authors of this study concluded that the soliton-like regime is described by spatially nonuniform time-periodic solutions of the HH equations. The mechanism of pulse reflection is explained as

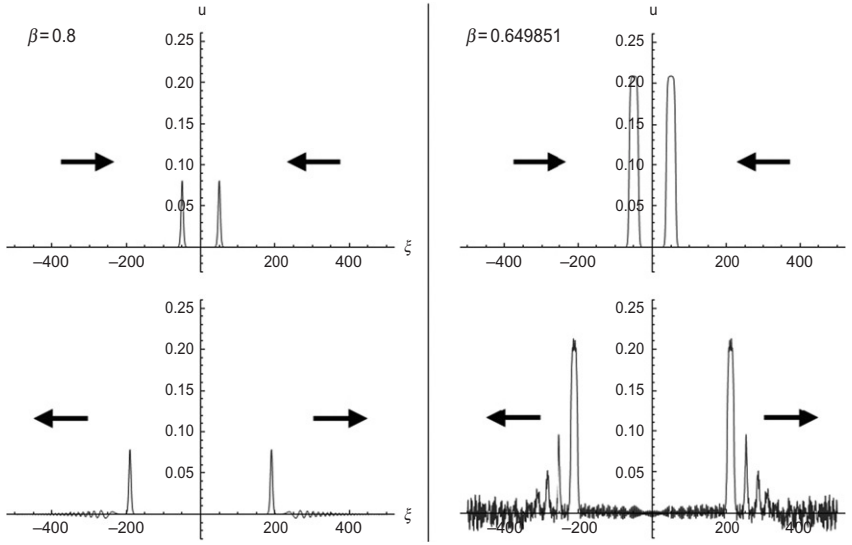

Figure 9.8 Collision of two solitons before (top panels) and after collision (bottom panels) for two different velocities (left and right panels). Left: soliton velocity of $\beta = 0.8$. Small-amplitude noise is traveling ahead of the postcollision pulses. This indicates some dissipation during the collision. Right: soliton velocity $\beta = 0.649850822$ (close to maximum amplitude). *Adapted from Ref. [23].*

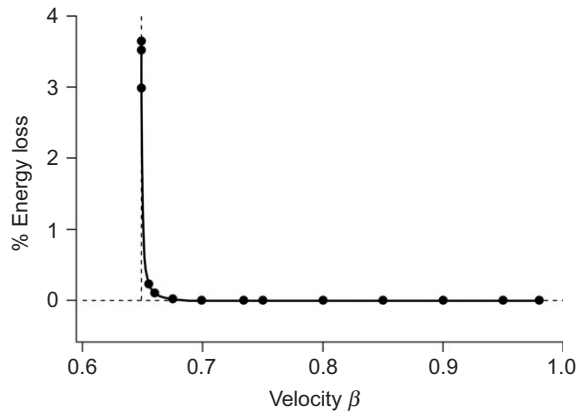

Figure 9.9 Energy loss of soliton after collision in %. The dissipation is significant only when the pulses reach their minimum velocity. *From Ref. [23].*

follows [55]: "In the soliton-like regime the traveling pulse presents a doublet consisting of a high-amplitude pulse-leader and a low-amplitude wave following this pulse. When doublets interact, the leaders are annihilated, and the collision of the low-amplitude waves after a short delay leads to their

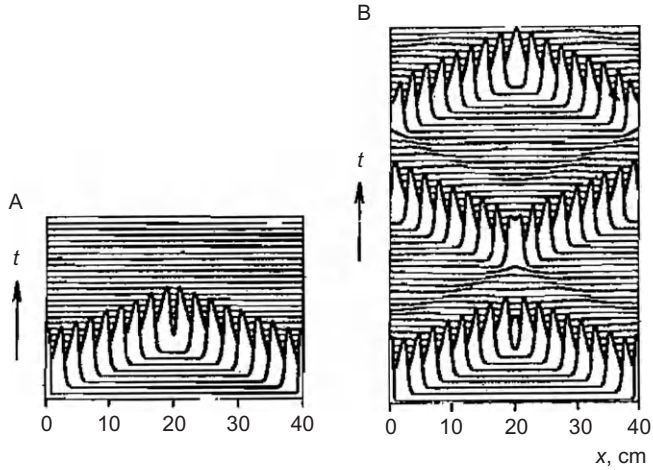

Figure 9.10 Collision of pulses in the HH model. Left: Annihilation of colliding nerve pulses at the standard value $E_K = -12.0\,mV$. Right: Reflection (or penetration) of pulses at $E_K = -2.5$ mV. *From Ref. [55] with permission.*

summation. As a result of the summation, the potential V at the site of the collisions reaches a super-threshold value, causing regeneration of the doublets, which thereafter move apart in opposite directions. The process of reflection of excitation pulses from impermeable fiber ends evolves according to the same scenario."

It was also noticed that low-amplitude waves can give rise to new extra pulses which also take part in interactions. When a doublet was initiated at the left end of a fiber, the amplitude of the following pulse rapidly increases while traveling. It reaches threshold value and initiates two "extra pulses." These pulses travel apart to the opposite ends of the axon and are reflected from them. This complex regime was observed for $-2.46\,mV < E_K < 2.40\,mV$.

Summarizing, the soliton model does not lead to annihilation of pulses, while the HH model allows for both annihilation and penetration depending on parameters.

5.2. Can the two models be combined?

It seems tempting to combine the two approaches such that the respective strengths of each model can be taken advantage of. Both models account for the occurrence of channel-like conduction events through membranes and the voltage pulse. The behavior upon collision of pulses is somewhat unclear in both models. But there are clear differences.

The protein-based picture of Hodgkin and Huxley provides a discrete target for poisons such as tetrodotoxin that eliminate the nerve pulse. Toxic substances are thought to block the ion channel proteins that are the primary players in this model. In contrast, the soliton model requires a more indirect role of poisons on the physics of membranes that has yet to be demonstrated experimentally. In the case of anesthetics, such an effect has been found in experiments and the effect is understood theoretically—but this is not the case for strong poisons. On the other hand, the soliton model provides a beautifully self-consistent explanation for mechanical and heat changes that occur under the influence of the nerve pulse. One would be inclined to keep this feature in a complete theory for the nerve pulse.

The main argument that lets it seem difficult to combine the models is the measured reversible heat production of the nerve pulse. The HH model is based on dissipative processes that should be related to heat dissipation at the site of the membrane. The soliton model, in contrast, is based on reversible processes and therefore consistent with the reversible heat production. The combination of a dissipative and a reversible model would still be of dissipative nature. The reversible heat observed during the nervous impulse is significantly larger than the capacitive energy of the membrane. This means that one has to assume that there exist relevant processes during the nerve pulse beyond the charging of a capacitor, which is the only process in the HH model associated with work and heat. The least one would have to conclude is that the mechanical (adiabatic) propagation phenomena are by far the dominating processes such that dissipative features are not readily visible in an experiment. Taking the reversible heat of the nerve pulse serious, one is inclined to state that the HH model in itself cannot be correct. The same argument would hold for a combination of both models. Thus, it seems necessary that any protein-based picture would still operate on the basis of reversible processes, for instance, by employing capacitive currents rather than ohmic currents, that is, by transporting charges forth and back in a reversible process. This implies that the HH picture cannot easily be combined with reversible physics and the soliton model without seriously changing its mechanism.

6. CONCLUSIONS

We have reviewed the well-known HH model and the emerging soliton theory of nerve pulse propagation and compared them in some detail. The two models are based on completely different assumptions. While the

HH model is based on microscopic consideration about the behavior of single proteins, the soliton model is a macroscopic thermodynamics theory. The HH model mostly considers the electrical aspects of nerve pulse and rationalizes them within the context of ion channel proteins that can be influenced by drugs. It is of dissipative nature due to fluxes of ions along gradients. The soliton theory is based on the assumption of an adiabatic density pulse in the nerve membrane. As typical for adiabatic phenomena, it goes along with variations in all thermodynamic quantities as thickness, length, lateral pressure, and temperature.

For both models, we show studies of colliding pulses that may help to discriminate between aspects of the models. The HH model can exhibit two regimes of annihilation and reflection (or penetration) depending on the parameters, whereas the soliton theory exhibits a single regime of reflection (or penetration). Mini solitons postcollision are observed in both models. It remains to be tested in experiments what precisely happens under different experimental conditions when two pulses collide.

Both models have advantages and disadvantages. Summarizing, however, it has to be concluded that the ionic hypothesis for explaining nerve pulse propagation (which is at the basis of the HH model) is in conflict with the experimental finding that the nerve pulse is an adiabatic phenomenon. In general, the soliton model has more predictive power due to the strict coupling of different thermodynamic variables. This also implies that it is easier to falsify.

ACKNOWLEDGMENTS

We thank DFG for funding within the Research Training Group "Welisa" under GRK 1505/1. We thank Andrew D. Jackson and Benny Lautrup from the NBI for helpful discussions.

REFERENCES

[1] L. Galvani, Abhandlung über die Kräfte der Electricität bei der Muskelbewegung, Series Ostwald's Klassiker der exakten Wissenschaften (1894), vol. 52, 1791.
[2] A. Volta, Untersuchungen über den Galvanismus, Ostwald's Klassiker der exakten Wissenschaften, vol. 118, 1900, pp. 1796–1800.
[3] J. Bernstein, Untersuchungen zur Thermodynamik der bioelektrischen Ströme Erster Theil, Pflügers Arch. 92 (1902) 521–562.
[4] A.L. Hodgkin, A.F. Huxley, A quantitative description of membrane current and its application to conduction and excitation in nerve, J. Physiol. 117 (1952) 500–544.
[5] K.S. Cole, H.J. Curtis, Electrical impedance of the squid giant axon during activity, J. Gen. Physiol. 220 (1939) 649–670.
[6] E. Villagran Vargas, A. Ludu, R. Hustert, P. Gumrich, A.D. Jackson, T. Heimburg, Periodic solutions and refractory periods in the soliton theory for nerves and the locust femoral nerve, Biophys. Chem. 153 (2011) 159–167.

[7] I. Tasaki, K. Kusano, M. Byrne, Rapid mechanical and thermal changes in the garfish olfactory nerve associated with a propagated impulse, Biophys. J. 55 (1989) 1033–1040.
[8] K. Iwasa, I. Tasaki, R.C. Gibbons, Swelling of nerve fibres associated with action potentials, Science 210 (1980) 338–339.
[9] E. Wilke, E. Atzler, Experimentelle Beiträge zum Problem der Reizleitung im Nerven, Pflügers Arch. 146 (1912) 430–446.
[10] K. Iwasa, I. Tasaki, Mechanical changes in squid giant-axons associated with production of action potentials, Biochem. Biophys. Res. Commun. 95 (1980) 1328–1331.
[11] I. Tasaki, K. Iwasa, R.C. Gibbons, Mechanical changes in crab nerve fibers during action potentials, Jpn. J. Physiol. 30 (1980) 897–905.
[12] I. Tasaki, K. Iwasa, Further studies of rapid mechanical changes in squid giant axon associated with action potential production, Jpn. J. Physiol. 32 (1982) 505–518.
[13] I. Tasaki, M. Byrne, Volume expansion of nonmyelinated nerve fibers during impulse conduction, Biophys. J. 57 (1990) 633–635.
[14] B.C. Abbott, A.V. Hill, J.V. Howarth, The positive and negative heat production associated with a nerve impulse, Proc. R. Soc. Lond. B 148 (1958) 149–187.
[15] J.V. Howarth, R. Keynes, J.M. Ritchie, The origin of the initial heat associated with a single impulse in mammalian non-myelinated nerve fibres, J. Physiol. 194 (1968) 745–793.
[16] J. Howarth, Heat production in non-myelinated nerves, Philos. Trans. R. Soc. Lond. 270 (1975) 425–432.
[17] J.M. Ritchie, R.D. Keynes, The production and absorption of heat associated with electrical activity in nerve and electric organ, Q. Rev. Biophys. 392 (1985) 451–476.
[18] I. Tasaki, P.M. Byrne, Heat production associated with a propagated impulse in bullfrog myelinated nerve fibers, Jpn. J. Physiol. 42 (1992) 805–813.
[19] T. Heimburg, A.D. Jackson, On the action potential as a propagating density pulse and the role of anesthetics, Biophys. Rev. Lett. 2 (2007) 57–78.
[20] Y. Kobatake, I. Tasaki, A. Watanabe, Phase transition in membrane with reference to nerve excitation, Adv. Biophys. 208 (1971) 1–31.
[21] T. Heimburg, A.D. Jackson, On soliton propagation in biomembranes and nerves, Proc. Natl. Acad. Sci. U.S.A. 102 (2005) 9790–9795.
[22] S.S.L. Andersen, A.D. Jackson, T. Heimburg, Towards a thermodynamic theory of nerve pulse propagation, Prog. Neurobiol. 88 (2009) 104–113.
[23] B. Lautrup, R. Appali, A.D. Jackson, T. Heimburg, The stability of solitons in biomembranes and nerves, Eur. Phys. J. E 34 (6) (2011) 1–9.
[24] K. Arms, P. Camp, Biology, fourth ed., Harcourt Brace College Publishers, New York, 1995.
[25] T. Heimburg, Physical properties of biological membranes, In: H.G. Bohr (Ed.), Encyclopedia of Applied Biophysics, Wiley VCH, Weinheim, 2009, pp. 593–616.
[26] T. Heimburg, Die Physik von Nerven, Phys. J. 8 (2009) 33–39. Note: English translation: "The physics of nerves". arXiv:1008.4279v1 [physics.bio-ph].
[27] T. Heimburg, Thermal Biophysics of Membranes, Wiley VCH, Berlin, Germany, 2007.
[28] A.L. Hodgkin, B. Katz, The effect of sodium ions on the electrical activity of the giant axon of the squid, J. Physiol. 108 (1949) 37–77.
[29] E. Overton, Beiträge zur allgemeinen Muskel- und Nervenphysiologie: II. Mittheilung. Ueber die Unentbehrlichkeit von Natrium- (oder Lithium-) lonen für den Contractionsact des Muskels, Pflügers Arch. 92 (1902) 346–386.
[30] A.L. Hodgkin, A.F. Huxley, Currents carried by sodium and potassium ions through the membrane of the giant axon of Loligo, J. Physiol. 116 (1952) 449–472.
[31] M. Haeusser, The Hodgkin-Huxley theory of the action potential, Nat. Neurosci. 3 (2000) 1165.

[32] R. Appali, S. Petersen, U. van Rienen, A comparison of Hodgkin-Huxley and soliton neural theories, Adv. Radio Sci. 8 (2010) 75–79.
[33] D. Johnston, S.M.S. Wu, Cellular Neurophysiology, MIT Press, Boston, 1995.
[34] R. FitzHugh, Impulses and physiological states in theoretical models of nerve membrane, Biophys. J. 1 (1961) 445–466.
[35] J. Nagumo, S. Arimoto, S. Yoshizawa, An active pulse transmission line simulating nerve axon, Proc. IRE 50 (1962) 2061–2070.
[36] J.L. Hindmarsh, R.M. Rose, A model of neuronal bursting using three coupled first order differential equations, Proc. R. Soc. Lond. B 221 (1984) 87–102.
[37] K. Rajagopal, A generalized-model for the nerve impulse propagation, Phys. Lett. A 99 (1983) 261–264.
[38] T. Heimburg, A.D. Jackson, The thermodynamics of general anesthesia, Biophys. J. 92 (2007) 3159–3165.
[39] L.D. Landau, E.M. Lifshitz, Fluid mechanics, In: Course of Theoretical Physics, vol. 6, Pergamon Press, Oxford, 1987.
[40] A. Sommerfeld, Mechanik der deformierbaren Medien, Vorlesungen über theoretische Physik, vol. 2, Harri Deutsch, Thun, 1992.
[41] S. Halstenberg, T. Heimburg, T. Hianik, U. Kaatze, R. Krivanek, Cholesterol-induced variations in the volume and enthalpy fluctuations of lipid bilayers, Biophys. J. 75 (1998) 264–271.
[42] W. Schrader, H. Ebel, P. Grabitz, E. Hanke, T. Heimburg, M. Hoeckel, M. Kahle, F. Wente, U. Kaatze, Compressibility of lipid mixtures studied by calorimetry and ultrasonic velocity measurements, J. Phys. Chem. B 106 (2002) 6581–6586.
[43] T. Heimburg, A.D. Jackson, Thermodynamics of the nervous impulse, In: K. Nag (Ed.), Structure and Dynamics of Membranous Interfaces, Wiley, Hoboken, NJ, 2008, pp. 317–339.
[44] D.P. Kharakoz, Phase-transition-driven synaptic exocytosis: a hypothesis and its physiological and evolutionary implications, Biosci. Rep. 210 (2001) 801–830.
[45] F.H. Johnson, E.A. Flagler, Hydrostatic pressure reversal of narcosis in tadpoles, Science 112 (1950) 91–92.
[46] H. Ebel, P. Grabitz, T. Heimburg, Enthalpy and volume changes in lipid membranes. I. the proportionality of heat and volume changes in the lipid melting transition and its implication for the elastic constants, J. Phys. Chem. B 105 (2001) 7353–7360.
[47] A. Blicher, K. Wodzinska, M. Fidorra, M. Winterhalter, T. Heimburg, The temperature dependence of lipid membrane permeability, its quantized nature, and the influence of anesthetics, Biophys. J. 96 (2009) 4581–4591.
[48] T. Heimburg, Lipid ion channels, Biophys. Chem. 150 (2010) 2–22.
[49] K.R. Laub, K. Witschas, A. Blicher, S.B. Madsen, A. Lückhoff, T. Heimburg, Comparing ion conductance recordings of synthetic lipid bilayers with cell membranes containing TRP channels, Biochim. Biophys. Acta 1818 (2012) 1–12.
[50] V.F. Antonov, V.V. Petrov, A.A. Molnar, D.A. Predvoditelev, A.S. Ivanov, The appearance of single-ion channels in unmodified lipid bilayer membranes at the phase transition temperature, Nature 283 (1980) 585–586.
[51] I. Tasaki, Physiology and Electrochemistry of Nerve Fibers, Academic Press, New York, 1982.
[52] I. Tasaki, Evidence for phase transition in nerve fibers, cells and synapses, Ferroelectrics 220 (1999) 305–316.
[53] I. Tasaki, A. Watanabe, R. Sandlin, L. Carnay, Changes in fluorescence, turbidity and birefringence associated with nerve excitation, Proc. Natl. Acad. Sci. U.S.A. 61 (1968) 883–888.
[54] I. Tasaki, Collision of two nerve impulses in the nerve fiber, Biochim. Biophys. Acta 3 (1949) 494–497.

[55] O.V. Aslanidi, O.A. Mornev, Can colliding nerve pulses be reflected?. JETP Lett. 65 (1997) 579–585.
[56] M. Argentina, P. Coullet, V. Krinsky, Head-on collisions of waves in an excitable FitzHugh-Nagumo system: a transition from wave annihilation to classical wave behavior, J. Theor. Biol. 205 (2000) 47–52.

CHAPTER TEN

Permeability of Phospholipid Membrane for Small Polar Molecules Determined from Osmotic Swelling of Giant Phospholipid Vesicles

Primož Peterlin*,[1], Vesna Arrigler[†], Haim Diamant[‡], Emir Haleva[‡]

*Institute of Oncology, Ljubljana, Slovenia
[†]Institute of Biophysics, Faculty of Medicine, University of Ljubljana, Ljubljana, Slovenia
[‡]Raymond and Beverly Sackler School of Chemistry, Tel Aviv University, Tel Aviv, Israel
[1]Corresponding author: e-mail address: ppeterlin@onko-i.si

Contents

1. Introduction 302
2. Experimental Section 305
   2.1 Materials and methods 305
   2.2 Experimental results 306
3. Theoretical Section 309
   3.1 Kedem–Katchalsky formalism 310
   3.2 Two-parameter model 313
   3.3 One-parameter model 316
   3.4 The influence of membrane elasticity 317
   3.5 Swelling–burst cycle 319
   3.6 Critical phenomena in osmotic swelling 324
4. Experimental Analysis 328
5. Discussion 331
References 332

Abstract

A method for determining permeability of phospholipid bilayer based on the osmotic swelling of micrometer-sized giant unilamellar vesicles (GUVs) is presented as an alternative to the two established techniques, dynamic light scattering on liposome suspension and electrical measurements on planar lipid bilayers. In the described technique, an individual GUV is transferred using a micropipette from a sucrose/glucose solution into an isomolar solution containing the solute under investigation. Throughout the experiment, vesicle cross-section is monitored and recorded using a digital camera mounted on a phase-contrast microscope. Using a least-squares procedure for circle fitting,

Advances in Planar Lipid Bilayers and Liposomes, Volume 16
ISSN 1554-4516
http://dx.doi.org/10.1016/B978-0-12-396534-9.00010-6

vesicle radius R is computed from the recorded images of vesicle cross-section. Two methods for determining membrane permeability from the obtained $R(t)$ dependence are described: the first one uses the slope of $R(t)$ for a spherical GUV, and the second one the $R(t)$ dependence around the transition point at which a flaccid vesicle transforms into a spherical one. We demonstrate that both methods give consistent estimates for membrane permeability.

1. INTRODUCTION

The cell membrane physically separates the cell interior from the environment. The membrane is selectively permeable: it permits the passage of some species of molecules or ions to and from the cell, while it blocks the transport for other species. Around 1900, while studying the working of general anesthesia, Meyer in Marburg [1] and Overton in Zürich [2] independently devised a simple rule to predict membrane permeability. They established that the more a molecule species is soluble in lipid, the greater the cell permeability for this molecule species is. While this rule cannot account for transport processes not known at that time, such as those mediated by membrane carriers, channels (e.g., aquaporins [3]), or pumps, nor does it acknowledge membrane inhomogeneities, such as rafts [4] present in the biological membrane, the Meyer–Overton rule seems to withstand the test of time [5,6]. At the same time, there is a continuing interest in both basic physics of general anesthesia [7] and passive membrane permeability [8].

While a significant corpus of publications on permeability properties of biological cells has been accumulated since Meyer and Overton, experimental access to an isolated lipid bilayer only became available in the early 1960s, when a technique for preparation of thin films separating two aqueous compartments has been devised, known as the black lipid membrane [9]. An arguably even more influential technique which was developed at roughly the same time allowed for producing artificial lipid vesicles or liposomes [10]. Vesicles are osmotically sensitive structures which swell and shrink in response to changed osmotic conditions. Even though the submicrometer liposomes which are the easiest to produce cannot be visualized directly, their size can be estimated via light scattering [11] (see Ref. [12] for a review on the optical methods in determining membrane permeability).

Both model lipid bilayer systems—planar lipid bilayers and liposomes—have proved extremely fruitful in the studies of membrane permeability [13]. Planar lipid bilayers are well suited to electrical characterization, as the two

chambers separated by the bilayer are both easily accessible, which allows simple placement of macroscopic electrodes. Finkelstein [14] measured the permeability of a planar lipid bilayer for water and seven other nonelectrolytes in an attempt to resolve the mechanism by which neutral molecules and ions permeate the membrane. One possibility is the solubility–diffusion mechanism, which assumes that the permeating species dissolves in the hydrophobic membrane, diffuses across, and leaves by redissolving into the other aqueous compartment. Another possibility is that permeation occurs through hydrated transient defects, which appear as a result of thermal fluctuations. That study concluded that both water and nonelectrolytes cross the membrane through the solubility–diffusion mechanism. A similar but more comprehensive study was repeated a few years later by Orbach and Finkelstein [15]. Walter and Gutknecht [16] examined the correlation between the membrane permeability for 22 solutes and their partition coefficient between water and any of the four examined organic solvents and found a very high correlation with hexadecane and olive oil, and a less pronounced correlation in the case of octanol and ether.

In an early work [17], Bangham and coworkers made use of the fact that the total volume of liposomes in the suspension is proportional to the reciprocal of the optical extinction, which allowed them to examine the permeability of membrane for water and various solutes via osmotic swelling and shrinking of liposomes. As early as 1933, Jacobs noticed [18] that the volume of a cell transferred into a solution of permeant solute transiently decreases, reaches some minimal value, and then starts increasing. Sha'afi and coworkers [19] employed this phenomenon and the Kedem–Katchalsky formalism [20] to compute the permeability of erythrocyte membrane for urea. de Gier and coworkers used the initial slope of the reciprocal of the optical extinction for determining membrane permeability of liposomes [21]. Hill and Cohen [22] brought the "minimal volume" technique to the experiment with liposomes as well. A comprehensive review of the use of liposomes in membrane permeability studies is given by de Gier [23]. Using established techniques, Paula *et al.* [24] did an extensive study in another attempt to resolve the standing debate between the solubility–diffusion mechanism and the hydrated transient defects as a primary pathway and concluded that except for ion permeability of lipid bilayers composed of phospholipids with short chain lengths, solubility–diffusion mechanism seems to be the dominant effect. Examining the known phenomenon that upon transfer into a hypotonic medium, vesicles swell, and, if the gradient is large enough, burst and expel part of their content, Shoemaker and Vanderlick

studied the influence of membrane composition on the extent of leakage [25] and found out a correlation between the membrane resistance to burst and its stretching modulus.

Both planar lipid bilayers and liposomes as model bilayer systems have their drawbacks, too. The original "brush" technique of producing planar lipid bilayers has been limited by pockets of residual solvent trapped between the two bilayer leaflets, which affects membrane properties. While an improved deposition method [26] virtually eliminated this problem, the limited lifetime of the membranes—most often less than 1 h—remains a persisting problem which limits the duration of the experiment. Liposomes, on the other hand—in particular large unilamellar vesicles (LUVs) with a diameter of 100–200 nm—have proved to be extremely stable. The interpretation of dynamic light scattering (DLS) experiments of osmotic shrinking of LUVs is not trivial, as it involves the transformation of shapes predicted by the area difference elasticity model [27] to the hydrodynamic radius, which is characterized by DLS [28,29]. Also, it has been argued that LUVs, which consist exclusively of high-curvature membrane regions, serve as a poor model of biological cell membranes. An attempt to resolve the possible dependence of permeability on the membrane curvature [30] was inconclusive, as the authors ascribe the observed differences in permeability to the problems they experienced with planar lipid membranes. Finally, an effect that occurs in both systems, but is more prominent with the planar lipid bilayer, is the unstirred layer effect [31]. In general, the concentration of solute adjacent to the membrane differs from its concentration in bulk. It is the concentration of solute immediately adjacent to the membrane which determines the permeation of solute across the membrane, while the concentration in bulk is the one that is usually known. In both the experiment design and the interpretation of the experimental findings, one needs to be aware of this discrepancy.

While both planar lipid bilayers and liposomes have been used as model membrane systems for studies of membrane permeability since 1960s, studies employing GUVs, which allow for a direct visualization of the process, appeared decades later [32], chiefly due to a lack of suitable techniques for preparation and manipulation of GUVs in those early days. In the paper by Boroske *et al.* [32], the authors describe the experiment in which GUVs were prepared in pure water and subsequently transferred into a solution of either glucose or NaCl (concentrations used ranged from 1.5 to 20 mM), while their size was monitored using phase-contrast microscopy. Upon transfer, vesicles shrank in size; the process of shrinking depended on the

vesicle size. Vesicles with radius $R \lesssim 10\,\mu m$ shrank with a linear time dependence: $R(t) = R_0 - \bar{V}_w P \Delta c t$, where $\bar{V}_w$ is the molar volume of water, P is the membrane permeability for water (water filtration coefficient), Δc the solute concentration difference, and t time. From measured data, the authors inferred the water filtration coefficient, $P = 41\,\mu m/s$. Larger vesicles ($r \gtrsim 10\,\mu m$) underwent a phase of "instability" in which the vesicle was flaccid, and after which a spherical shape was reestablished. The authors dismissed the idea of dissolving lipid molecules into the outer medium as a plausible explanation for the apparent decrease of vesicle surface area, in particular since they also noticed the formation of smaller satellite spherical vesicles, seemingly connected to the mother vesicle. Instead, they proposed a mechanism of concerted flipping of lipid molecules from the inner membrane leaflet into the outer membrane leaflet, induced by the flow of water. Recently, membrane permeability has also been studied of GUVs made of block copolymers [33,34].

The remaining of this chapter is structured as follows. First, the experimental section introduces the system and presents the immediate experimental results. A section on the theory of membrane permeability offers a review of the few selected phenomenological models for membrane permeability, with a special emphasis on the influence of membrane elasticity and the swelling–burst cycle. The section concludes with a theory of the continuous transition between the "ironing" and the stretching regimes of the osmotic swelling of a vesicle. Section 4 demonstrates the calculation of membrane permeability based on the swelling–burst cycle and compares its result with the calculation based on the analysis of the transition between the "ironing" and the stretching regimes. We conclude with a discussion of the merits and limitations of the presented method.

2. EXPERIMENTAL SECTION

2.1. Materials and methods

D-(+)-Glucose, D-(+)-sucrose, glycerol, urea, and ethylene glycol were purchased from Fluka (Buchs, Switzerland). Methanol and chloroform were purchased from Kemika (Zagreb, Croatia). 1-Palmitoyl-2-oleoyl-*sn*-glycero-3-phosphocholine (POPC) was purchased from Avanti Polar Lipids (Alabaster, USA). All the solutions were prepared in double-distilled sterile water.

A suspension of POPC GUVs in 0.1 or 0.2 mol/L 1:1 sucrose/glucose solution was prepared using an electroformation method, described in Ref. [35] with some modifications [36,37]. Lipids were dissolved in a

mixture of chloroform/methanol (2:1, v/v) to a concentration of 1 mg/mL. A volume of 25 μL of the lipid solution was spread onto a pair of Pt electrodes and dried under reduced pressure (water aspirator; ≈60 mmHg) for 2 h. The electrodes were then placed into an electroformation chamber, which was filled with 0.1 or 0.2 mol/L sucrose. AC current (8 V, 10 Hz) was applied, and the voltage and frequency were reduced in steps to the final values of 1 V and 1 Hz [37]. Subsequently, the chamber was first drained into a beaker and then flushed with an equal volume of isomolar glucose solution, thus resulting in a suspension of GUVs containing entrapped sucrose in a 1:1 sucrose/glucose solution, which increases the contrast in a phase-contrast setup and facilitates vesicle manipulation [38]. This procedure yields mostly spherical unilamellar vesicles, with diameters of up to 100 μm.

An inverted optical microscope (Nikon Diaphot 200, objective 20/0.40 Ph2 DL) with micro-manipulating equipment (Narishige MMN-1/MMO-202) and a cooled CCD camera (Hamamatsu ORCA-ER; C4742-95-12ERG), connected via an IEEE-1394 interface to a PC running Hamamatsu Wasabi software, was used to obtain phase-contrast micrographs. In the streaming mode, the camera provides 1344 × 1024 12-bit grayscale images at a rate of 8.9 images/s.

In the experiment, an individual spherical GUV is selected, fully aspirated into a glass micropipette whose inner diameter exceeds the vesicle's diameter, and transferred from a solution containing solutes of very low membrane permeability (1:1 glucose/sucrose) into an iso-osmolar solution of a more permeable solute (glycerol, urea, or ethylene glycol), where the content of the micropipette is released, and the micropipette is subsequently removed. Vesicle response is recorded using a CCD camera mounted on the microscope.

2.2. Experimental results

Upon transfer into a solution of permeating solute, vesicles start to swell until the membrane critical strain is reached. At that point, the membrane ruptures, and the vesicle ejects part of its internal solution (Fig. 10.1). After the burst, the membrane reseals, and another cycle of swelling starts. The observed sequences of swelling–burst cycles ranged from 3 to over 40 successive bursts, with an average in our sample being 15.4.

For a quantitative analysis, the radius of the vesicle cross-section in each recorded micrograph was determined with a GNU Octave script using a

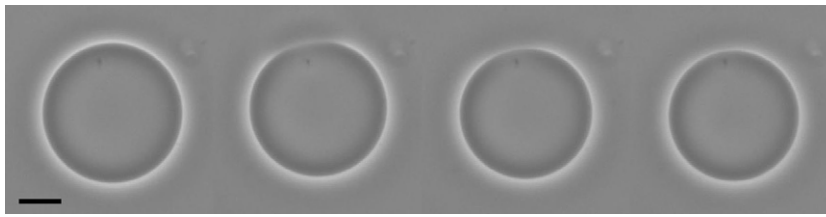

Figure 10.1 A sequence of micrographs showing an individual vesicle burst. Vesicle radius before the burst was 32.69 μm; immediately after the burst, it shrunk to 30.47 μm. The images were taken at 0.11 s intervals. The bar represents 20 μm.

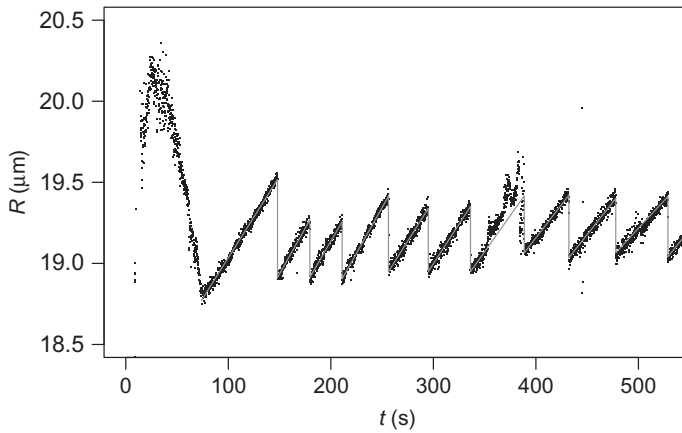

Figure 10.2 Time dependence of the radius of a vesicle cross-section upon transfer from a 0.1 mol/L 1:1 glucose/sucrose solution into a 0.1 mol/L solution of ethylene glycol. Clearly visible are the initial maximum, followed by a sawtooth pattern of repeated swelling–burst cycles.

least-squares procedure for circle fitting [39]. Figure 10.2 shows a typical time course of vesicle radius after transfer. In about 80% of all cases, we observed a transient maximum of radius shortly after the transfer. We attribute this phenomenon to a slight hypertonicity of the target solution. This causes the vesicle to deflate rapidly, the rate of volume change being determined by the vesicle size and the permeability of phospholipid membrane for water. A deflated vesicle changes its shape from spherical into a shape which can be approximated with an oblate spheroid. Small deviations from this shape, which originate from the effects of gravity [40], are neglected here. Due to gravity, the axis of rotational symmetry is aligned with the vertical, which, in our experimental setup, also coincides with the direction of the optical axis. Thus, the observed cross-section radius is the oblate spheroid longer

semiaxis, and consequently, it increases with the decreasing volume, while the membrane area remains unchanged.

Concurrently with the initial vesicle deflation due to the slight hypertonicity, diffusion of permeating solute into the vesicle interior, accompanied by the osmotic influx of water, also takes place. The rate of this latter process is, however, dominated by the permeability of the membrane for the given solute (in our case, glycerol, urea, or ethylene glycol) and is thus much slower than the initial rapid deflation due to the mismatch in tonicity. With time, however, the initial trend of vesicle deflation is overturned and the vesicle starts inflating again. Inflation can be qualitatively divided into two phases. In the first phase, the vesicle is still partially deflated, and the influx of solute and the accompanying osmotic influx of water increase the vesicle volume, all while the membrane area remains unchanged. This "ironing" phase is characterized by the decrease of the radius of vesicle cross-section. At some point, the vesicle reaches a spherical shape, which can be observed as a local minimum of the cross-section radius.

Further permeating of solute into the vesicle interior, accompanied by the osmotic influx of water, induces the transition into the second phase, in which the vesicle inflates while maintaining the spherical shape. In this phase, the increase of vesicle volume can be observed as an increase of vesicle cross-section. In order to accommodate the increased vesicle volume, the membrane needs to stretch. This stretching process continues until the critical strain for the membrane is reached. At this point, the membrane ruptures, and part of the vesicle interior is ejected outside. When the vesicle volume is thus reduced, the membrane reseals again. As the concentration difference for the permeating solute persists, which serves as a driving force for the diffusion of the permeating solute into the vesicle interior, this means that at the same moment, the vesicle volume starts increasing again, and another swelling cycle commences. Repeated swelling–burst cycles give yield to the characteristic sawtooth pattern, when the vesicle radius is plotted against the elapsed time (Fig. 10.2).

In total, 47 recordings of vesicle transfer from a 1:1 sucrose/glucose solution into an isomolar solution of glycerol, urea, or ethylene glycol were selected for further analysis. Of these, 15 transfers were into glycerol (5 at 0.1 M and 10 at 0.2 M), 15 transfers into urea (8 at 0.1 M and 7 at 0.2 M), and 17 transfers into ethylene glycol (12 at 0.1 M and 5 at 0.2 M). Figure 10.3 shows the critical strain $(A_{crit} - A_0)/A_0 = (R_{crit}/R_0)^2 - 1$, where R_0 is the radius of a relaxed spherical vesicle, and R_{crit} is the radius of a critically strained vesicle. The median critical strain obtained for a total

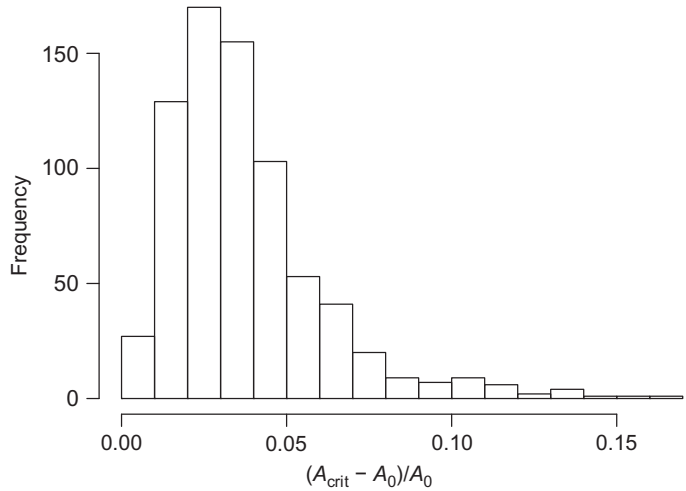

Figure 10.3 A histogram of experimentally determined critical strain, defined as $(R_{crit}/R_0)^2 - 1$, where R_0 is the initial and R_{crit} the final, or critical, radius for each of the swelling cycles.

of 738 recorded vesicle bursts is 0.033, and mean critical strain is 0.038 with standard deviation 0.024.

A published value for the critical strain is around 0.04 [41,42]. Our own estimate based on the first burst in the sequence alone is a little higher: 0.055 ± 0.02 [43]. This may indicate that the membrane might not always perfectly reseal, and that a local defect present in the membrane makes it more likely to rupture at a lower strain.

3. THEORETICAL SECTION

In this section, we briefly review a few theoretical models used for the description of solute permeation across cell membrane, starting from the most general Kedem–Katchalsky formalism, based on nonequilibrium thermodynamics [44], then showing how in the case of separate pathways for water and solute transport it can be simplified into a two-parameter model, and subsequently when a two-parameter model can be simplified into a one-parameter model in the case when the membrane permeability for water greatly exceeds its permeability for solute. We discuss the influence of finite membrane elasticity on the apparent membrane permeability, review the work on the repetitive swelling–burst cycles, and conclude with the theory of the continuous transition between the "ironing" and the stretching

regime of a vesicle which swells osmotically due to the permeation of a permeable solute.

3.1. Kedem–Katchalsky formalism

Starting from the principles of nonequilibrium thermodynamics, Kedem and Katchalsky arrived at a model with three parameters [20]. A simple qualitative argument can be offered why no less than three parameters are required for the description of the transport of solvent and solute across a membrane. In the simpler case of free diffusion of a single solute in a solvent, molecules of solute move relative to the molecules of solvent, and a single parameter—diffusion coefficient—is required to describe the friction between the solvent and the solute. In the case of membrane transport, two additional coefficients are required, one describing the friction between the molecules of solvent and the membrane, and another describing the friction between the molecules of solute and the membrane.

As their starting point, Kedem and Katchalsky [20] choose the rate of entropy production during the permeation of solute and water across the membrane separating the interior compartment from the exterior,

$$\frac{\mathrm{d}S}{\mathrm{d}t}=\frac{1}{T}\left(\mu_w^{\mathrm{e}}-\mu_w^{\mathrm{i}}\right)\frac{\mathrm{d}N_w^{\mathrm{i}}}{\mathrm{d}t}+\frac{1}{T}\left(\mu_s^{\mathrm{e}}-\mu_s^{\mathrm{i}}\right)\frac{\mathrm{d}N_s^{\mathrm{i}}}{\mathrm{d}t}. \tag{10.1}$$

Here, μ_s and μ_w denote the chemical potential of solute and solvent (water), respectively, and $\mathrm{d}N_s^{\mathrm{i}}/\mathrm{d}t$ and $\mathrm{d}N_w^{\mathrm{i}}/\mathrm{d}t$ denote the number of moles of solvent and water entering the interior compartment per unit time.

Formulating Eq. (10.1) in terms of a dissipation function per unit area, $\Phi=(T/A)\mathrm{d}S/\mathrm{d}t$, one obtains

$$\Phi=\left(\mu_w^{\mathrm{e}}-\mu_w^{\mathrm{i}}\right)\dot{n}_w+\left(\mu_s^{\mathrm{e}}-\mu_s^{\mathrm{i}}\right)\dot{n}_s. \tag{10.2}$$

Here, we have denoted $\dot{n}_w=(1/A)\mathrm{d}N_w^{\mathrm{i}}/\mathrm{d}t$ for water and accordingly for the solute. Equation (10.2) is a particular case of dissipation function, which in general assumes the form $\Phi=\sum_i J_i X_i$, where J_i represents flows and X_i represents the corresponding conjugate "forces." In Eq. (10.2), the differences in chemical potential act as conjugate forces. We shall now rewrite Eq. (10.2) in a way where the driving forces will be quantities easier to evaluate experimentally.

For an ideal solution, the difference in chemical potential can be expressed as

$$\mu^{\mathrm{e}}-\mu^{\mathrm{i}}=\bar{V}\Delta p+\alpha\Delta\ln x, \tag{10.3}$$

where $\bar{V}$ denotes the partial molar volume of the constituent, x its mole fraction, Δp the pressure difference between the external and the internal compartment, and $\alpha = RT$, with R being the molar gas constant and T the absolute temperature. Assuming a dilute solution, where the volume fraction φ of the solute is low, $\varphi = c_s \bar{V}_s \ll 1$, with $c_s = N_s / V_w$ being the molal concentration of solute, one can rewrite Eq. (10.3) for the solute:

$$\mu_s^{\mathrm{e}} - \mu_s^{\mathrm{i}} = \bar{V}_s \Delta p + \alpha \frac{\Delta c_s}{c_s}, \tag{10.4}$$

where $\Delta c_s = c_s^{\mathrm{e}} - c_s^{\mathrm{i}}$ is the difference, and $c_s = (c_s^{\mathrm{e}} + c_s^{\mathrm{i}})/2$ is the average of the concentration of solute in both compartments. An analogous relation can be written for the solvent,

$$\mu_w^{\mathrm{e}} - \mu_w^{\mathrm{i}} = \bar{V}_w \Delta p - \alpha \frac{\Delta c_s}{c_w}, \tag{10.5}$$

with $c_w = (1 - \varphi)/\bar{V}_w \approx 1/\bar{V}_w$. Introducing Eqs. (10.4) and (10.5) into Eq. (10.2) and rearranging, one arrives at another expression for the dissipation function:

$$\Phi = (\dot{n}_w \bar{V}_w + \dot{n}_s \bar{V}_s) \Delta p + \left(\frac{\dot{n}_s}{c_s} - \frac{\dot{n}_s}{c_s} \right) \alpha \Delta c_s. \tag{10.6}$$

In Eq. (10.6), Φ is expressed in terms of forces commonly used in the permeability studies: $X_v = \Delta p$ is the hydrostatic pressure, and $X_D = \alpha \Delta c_s$ is the osmotic pressure. The conjugate flows are $J_v = \dot{n}_w \bar{V}_w + \dot{n}_s \bar{V}_s$, the total volume flow per unit area, and $J_D = \dot{n}_s / c_s - \dot{n}_s / c_s$, the relative velocity of solute with respect to solvent, which serves as a measure of exchange flow.

It is assumed that each flow J present in the system in general depends on all the forces X acting in the system, and if the forces are sufficiently small, the relationship is linear:

$$J_1 = L_{11} X_1 + L_{12} X_2,$$
$$J_2 = L_{21} X_1 + L_{22} X_2.$$

Here, L_{ik} are phenomenological transport coefficients. The Onsager reciprocity relations [45,46] state that the matrix of transport coefficients is a diagonal one, $L_{ki} = L_{ik}$.

Applying this formalism to our case, we obtain

$$J_v = L_p \Delta p + L_{pD} \alpha \Delta c_s, \tag{10.7}$$

$$J_D = L_{pD}\Delta p + L_D \alpha \Delta c_s, \tag{10.8}$$

where we have already taken into account $L_{Dp} = L_{pD}$. The second law of thermodynamics requires that the diagonal terms are nonnegative, while the off-diagonal terms are only constrained by the relation $L_p L_D - L_{pD}^2 > 0$. It is the off-diagonal terms though which are responsible for a concentration difference producing a volume flow, or vice versa.

For easier comparison with the experimental results, it is convenient to transform $\{L_p, L_D, L_{pD}\}$ to another set of coefficients. One of them is the reflection coefficient σ, introduced with

$$L_{pD} = -\sigma L_p. \tag{10.9}$$

Two special cases which can be considered include a nonselective membrane ($\sigma = 0$) and an ideally selective membrane, permeable only for the solute ($\sigma = 1$). Another parameter commonly defined is the mobility of the solute ω:

$$\omega = \frac{L_p L_D - L_{pD}^2}{L_p} c_s = (L_D - L_p \sigma^2) c_s. \tag{10.10}$$

It can be shown that ω is chosen in such a way that for permeability measurement at constant volume ($J_v = 0$), one can write $\dot{n}_s = \omega RT \Delta c_s$.

Expressing the volume flow and the exchange flow in terms of $\{L_p, \omega, \sigma\}$, one obtains

$$J_v = L_p \Delta p - \sigma L_p RT \Delta c_s, \tag{10.11}$$

$$\dot{n}_s = (1-\sigma) L_p c_s \Delta p + \left[\omega - \sigma(1-\sigma) L_p c_s\right] RT \Delta c_s. \tag{10.12}$$

Equations (10.11) and (10.12) obtained above pertain to a two-component system, in which binary solutions of the same solvent and solute are separated by a membrane. In order to allow for a comparison with the experimental results, we need to consider a slightly more complicated system, comprising a membrane separating two ternary solutions of the same solvent and two different solutes. The membrane is permeable for the solvent and one of the solutes but impermeable for the other solute. As in the previous example, we treat the solution as ideal.

For a dilute solution, the difference in the chemical potential for the solvent (Eq. 10.5) can now be written as

$$\Delta \mu_w = -\alpha \frac{\Delta c_s}{c_w} - \alpha \frac{\Delta c_n}{c_w} + \bar{V}_w \Delta p, \tag{10.13}$$

where the index s pertains to the permeating solute, and the index n to the nonpermeating solute. While Eq. (10.4) remains valid, we have to consider the contribution of the nonpermeating solute to the difference in osmotic pressure,

$$\Delta\Pi_n = \alpha\Delta c_n. \tag{10.14}$$

Considering the same flows as before, one can write the expression for the dissipation function Eq. (10.2), and when substituting into it the expressions for the difference in the chemical potential for the solute, Eq. (10.4), and solvent, Eq. (10.13), one obtains the expressions for the forces conjugate to the flows:

$$X_v = \Delta p - \Delta\Pi_n, \tag{10.15}$$

$$X_D = \alpha\Delta c_s + \varphi\Delta\Pi_n. \tag{10.16}$$

Using the expressions (10.15) and (10.16), one can obtain expressions analogous to (10.11) and (10.12), obtained in the case of a binary solution:

$$J_v = L_p(\Delta p - \Delta\Pi_n) - \sigma L_p(\alpha\Delta c_s + \varphi\Delta\Pi_n), \tag{10.17}$$

$$\dot{n}_s = (1-\sigma)L_p c_s(\Delta p - \Delta\Pi_n) + \left[\omega - \sigma(1-\sigma)L_p c_s\right](\alpha\Delta c_s + \varphi\Delta\Pi_n). \tag{10.18}$$

A more condensed expression of Eq. (10.18) can be obtained if Eq. (10.17) is taken into account:

$$\dot{n}_s = (1-\sigma)c_s J_v + \omega(\alpha\Delta c_s + \varphi\Delta\Pi_n). \tag{10.19}$$

In dilute solutions, $\varphi\Delta\Pi_n$ is often negligible with respect to $\alpha\Delta c_s$. On the other hand, the contribution $\Delta\Pi_n$ is important. In many biologically relevant experiments, $\Delta p = 0$, while $\Delta\Pi_n \neq 0$.

3.2. Two-parameter model

Through the reflection coefficient σ, the Kedem–Katchalsky formalism resolves the competition between solvent and solute being transported through a shared pathway, for example, a cotransporting channel permeable to both the solute and the solvent. The formalism itself, however, applies to any simple transport problem, regardless of whether a cotransporting channel is present or not [47]. In the latter case, not all three parameters $\{L_p, \omega, \sigma\}$ are independent. It can be shown [20] that in this case, σ can be written as

$$\sigma = 1 - \frac{\omega\bar{V}_s}{L_p}. \tag{10.20}$$

Introducing Eq. (10.20) into Eqs. (10.17) and (10.19), one obtains the transport equations for the case where the solute and the solvent do not compete for the same cotransporting channel, for example, in the case where they both diffuse through the phospholipid bilayer. Along the way, we will use the following simplifications: $\alpha\Delta c_s \gg \varphi\Delta\Pi_n \approx 0$, $\Delta p = 0$, and introduce the notation more appropriate for describing the experimental setup: $J_v = (1/A)\mathrm{d}V/\mathrm{d}t$, $\dot{n}_s = (1/A)\mathrm{d}N_s/\mathrm{d}t$, $P_s = \omega\alpha$. Here, V is the total volume of the internal compartment, A is the area of the membrane, N_s is the number of moles of permeating solute inside the internal compartment, and P_s is the permeability of the membrane for the permeating solute. Using the described simplifications, the transport equations (10.17) and (10.18) can be written as

$$\frac{\mathrm{d}V}{\mathrm{d}t} = -L_p\alpha A\left[\left(c_n^{\mathrm{e}} + c_s^{\mathrm{e}}\right) - \left(c_n^{\mathrm{i}} + c_s^{\mathrm{i}}\right)\right] + P_s\bar{V}_s A\left(c_s^{\mathrm{e}} - c_s^{\mathrm{i}}\right), \tag{10.21}$$

$$\frac{\mathrm{d}N_s}{\mathrm{d}t} = -P_s\bar{V}_s c_s A\left(c_n^{\mathrm{e}} - c_n^{\mathrm{i}}\right) + P_s A\left(c_s^{\mathrm{e}} - c_s^{\mathrm{i}}\right). \tag{10.22}$$

Two terms contribute to the volume change in Eq. (10.21): the first one corresponds to the transport of solvent due to the osmotic pressure gradient, and the second one to the transport of solute. For dilute solutions, the second term is much smaller. Similarly, in Eq. (10.22), the first term is proportional to $\bar{V}_s c_s$, which makes this term negligible for dilute solutions.

As an example, we will apply the two-parameter model to the case which corresponds to the experimental setup: a single vesicle filled with a non-permeating solute is transferred to a reservoir filled with an isotonic solution of a permeating solute. Even though the solutions are isotonic, permeating solute diffuses into the vesicle, thus causing an osmotic pressure, which is in turn balanced by the inflow of water. Two cases can be distinguished: a flaccid vesicle changes its shape and becomes ever more spherical, while a spherical vesicle has already reached its limiting shape and can only grow by stretching the membrane. In this case, $c_n^e = 0$, $c_s^e = \text{const.}$, and initially, $c_s^i = 0$, $c_n^i = c_{n0}^i$; which is equal to c_s^e.

In the case of a flaccid vesicle, membrane area A is constant, and the system can be characterized with the vesicle volume V and the amount of permeating solute in the vesicle interior, N_s. Using the simplifications $V_w \approx V$, which is appropriate for dilute solutions, Eqs. (10.21) and (10.22) transform into

$$\frac{\mathrm{d}V}{\mathrm{d}t} = -L_p \alpha A \left(c_s^e - \frac{N_s}{V} - c_{n0}^i \frac{V_{\mathrm{ini}}}{V} \right), \tag{10.23}$$

$$\frac{\mathrm{d}N_s}{\mathrm{d}t} = P_s A \left(c_s^e - \frac{N_s}{V} \right). \tag{10.24}$$

Here, V_{ini} denotes the initial volume of the vesicle, and c_{n0}^{i} denotes the initial partial concentration of the nonpermeating solute inside the vesicle. Often, the permeability of membrane for water is expressed as water filtration coefficient P_f instead of hydraulic conductivity L_p, the two quantities being bound by the relation $P_f = \alpha L_p / \bar{V}_w$. Alternatively, one can use the reduced volume $v = V/V_0$, instead of V, with $V_0 = A^{3/2}/(6\sqrt{\pi})$ being the volume of a sphere with an area equal to A:

$$\frac{\mathrm{d}v}{\mathrm{d}t} = -\frac{P_f \bar{V}_w A}{V_0} \left(c_s^e - \frac{N_s}{v V_0} - c_{n0}^i \frac{v_0}{v} \right), \tag{10.25}$$

$$\frac{\mathrm{d}N_s}{\mathrm{d}t} = P_s A \left(c_s^e - \frac{N_s}{v V_0} \right). \tag{10.26}$$

Here, $v_0 = V_{\mathrm{ini}}/V_0$ is the initial reduced volume of the vesicle.

The other case is a spherical vesicle. In this case, neither its area A nor its volume V is constant; both can be, however, expressed in terms of the vesicle radius R, which is a convenient parameter in this case. Substituting $A = 4\pi R^2$ and $V = 4\pi R^3/3$ into Eqs. (10.23) and (10.24), one obtains

$$\frac{\mathrm{d}R}{\mathrm{d}t} = -P_f \bar{V}_w \left[c_s^e - c_s^i - c_{n0}^i \left(\frac{R_0}{R} \right)^3 \right], \tag{10.27}$$

$$\frac{\mathrm{d}c_s^{\mathrm{i}}}{\mathrm{d}t} = \frac{3P_s}{R} \left(c_s^e - c_s^i \right). \tag{10.28}$$

Here, R_0 is the initial vesicle radius; $V_0 = 4\pi R_0^3/3$.

As Fig. 10.2 shows, both flaccid and spherical regimes can appear in the course of a single vesicle transfer. The two-parameter model allows us to mimic the same behavior. Figure 10.4 shows a time course of the radius of a vesicle cross-section upon transfer into a slightly hypertonic solution of a solute which can permeate the vesicle membrane. A spherical vesicle with $R_0 = 10\,\mu\mathrm{m}$ is initially filled with a 0.1 mol/L solution of a solute which cannot permeate the membrane then transferred into a 0.105 mol/L solution of a solute which can permeate the membrane ($P_s = 2 \times 10^{-8}$ m/s). Other parameters used were $\bar{V}_w = 1.806 \times 10^{-2}$ L/mol and $P_f = 2.23 \times 10^{-4}$ m/s. Upon

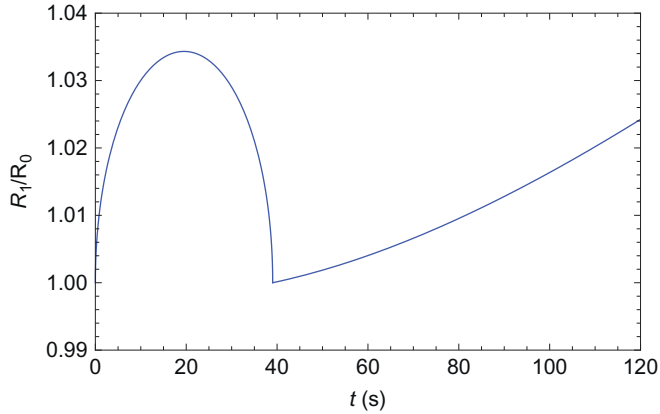

Figure 10.4 The radius of a vesicle cross-section upon transfer into a hypertonic solution of a solute which can permeate through the vesicle membrane, as calculated by the two-parameter model. Calculation parameters are given in the text.

transfer into a hypertonic solution, two processes are competing: the efflux of water, driven by the osmotic pressure mismatch, is the quicker of the two, while the influx of the solute, accompanied by the concomitant influx of water, is the slower one. Therefore, we first have to solve the system defined by Eqs. (10.23) and (10.24), with $V(0) = V_0$ and $N_s(0) = 0$ as initial conditions.

A deflated vesicle deforms into an approximate oblate spheroid; since in the experimental setup, the optical axis is usually aligned with the symmetry axis of the spheroid, the cross-section radius increases with the decreasing volume. Introducing $v = V/V_0$ and $x = R_1/R_0$, R_1 being the spheroid visible semiaxis, one obtains the following relationship between v and x:

$$2x^2 + \frac{v^2}{x^4\sqrt{1 - v^2/x^6}} \ln\left(\frac{1 + \sqrt{1 - v^2/x^6}}{1 - \sqrt{1 - v^2/x^6}}\right) = 4. \tag{10.29}$$

After a certain time, the vesicle becomes spherical again. From this point onward, it starts to grow while maintaining a spherical shape, and its behavior is governed by Eqs. (10.27) and (10.28), with initial conditions $R(0) = R_0$ and $c_s^i(0)$ equal to the concentration of the permeable solute, which diffused into the vesicle during the previous step.

3.3. One-parameter model

Vesicle swelling is a two-step process: in the first step, permeating solute diffuses into vesicle interior and thus causes osmotic nonequilibrium, and in the second step (which constitutes the bulk of swelling), it is followed by the water influx,

which balances the osmotic nonequilibrium. Equations (10.23) and (10.24) can be regarded as a kinetic system. In the systems treated here, however, the influx of water is a much faster process than the solute diffusion, and thus Eq. (10.24) represents the rate-limiting step. In the case where solute diffusion is a much slower process than the influx of water, a simpler description can be obtained.

In this simpler description, Eq. (10.24) is retained, while Eq. (10.23) is replaced by an instantaneous osmotic equilibrium:

$$c_s^e = \frac{N_s + N_n}{V}. \tag{10.30}$$

With c_s^e and N_n being constant, this leads to $\mathrm{d}N_s/\mathrm{d}t = c_s^e \mathrm{d}V/\mathrm{d}t$. Taking this into account and inserting Eq. (10.30) into Eq. (10.24), one obtains

$$\frac{\mathrm{d}V}{\mathrm{d}t} = \frac{P_s A}{c_s^e} \frac{N_n}{V}. \tag{10.31}$$

Equation (10.31) is general in the case that both A and V may vary with time. Again, two special cases can be considered: flaccid vesicles, where $A = \text{const.}$, and spherical vesicles, where both A and V can be expressed in terms of the vesicle radius R. In the latter case, a further simplification is possible by assuming that initially, the vesicle was spherical and osmotic equilibrium, that is, $c_s^e = N_n/(4\pi R_0^3/3)$. In this case, Eq. (10.31) can be rewritten into

$$\frac{\mathrm{d}R}{\mathrm{d}t} = P_s \left(\frac{R_0}{R}\right)^3, \tag{10.32}$$

which can be readily integrated:

$$R(t) = R_0 \left(1 + \frac{4P_s t}{R_0}\right)^{1/4}. \tag{10.33}$$

As long as deformations are small, R exhibits linear growth, $R(t) \approx R_0 + P_s t$. In this model, which assumes that the membrane permeability for water exceeds the permeability for solute by such a large margin that water transport can be considered instantaneous, the only parameter governing the vesicle volume change is P_s. Despite its simplifications, the one-parameter model has proved to be useful in certain situations [48,49].

3.4. The influence of membrane elasticity

The treatment of osmotic swelling of spherical vesicles presented so far assumes that the membrane is infinitely "soft" and does not oppose its stretching as the vesicle swells. In reality, the stretching modulus of a

phospholipid membrane is finite. This means that the apparent value of membrane permeability derived from the experiments with osmotic swelling of spherical vesicles is slightly underestimated: because the vesicle membrane opposes its stretching, the radius increases slightly less in a given interval of time than it would if the limiting factor was the membrane permeability alone.

It is common to assume that the membrane area has a certain relaxed area A_0, and expand the free energy of membrane stretching around this value:

$$W = \frac{K}{2A_0}(A - A_0)^2. \tag{10.34}$$

Here, K is the membrane stretching modulus, and $A_0 = 4\pi R_0^2$. We consider now the work $p\,\mathrm{d}V$, needed to increase the radius of a spherical vesicle by a small amount $\mathrm{d}R$. The corresponding change in the free energy is

$$\mathrm{d}W = K\frac{A - A_0}{A_0}\mathrm{d}A.$$

Substituting $\mathrm{d}V = 4\pi R^2 \mathrm{d}R$, $\mathrm{d}A = 8\pi R\,\mathrm{d}R$, and equating $p\,\mathrm{d}V$ with the change in the free energy, one obtains

$$p = \frac{2K}{R}\frac{R^2 - R_0^2}{R_0^2}. \tag{10.35}$$

In the case of osmotic equilibrium, this pressure is balancing the difference in the osmotic pressure: $p = \Delta\Pi$.

When the pressure exerted by the membrane is taken into account, Eq. (10.23) transforms into

$$\frac{\mathrm{d}V}{\mathrm{d}t} = -L_p A(\Delta\Pi - \Delta p). \tag{10.36}$$

Here, $\Delta\Pi = \alpha(c^e - c^i)$ and $\Delta p = p^e - p^i = 0 - p$, where $c^e = c_s^e$, $c^i = c_n^i + c_s^i$, and p is defined by Eq. (10.35). In the system defined by Eqs. (10.27) and (10.28), the vesicle membrane would in theory grow indefinitely because the osmotic pressure is never entirely balanced. A membrane which opposes vesicle-swelling limits the extent of swelling by the condition $\Delta\Pi = \Delta p$.

Rewriting Eq. (10.36) for a spherical vesicle, one obtains an equation analogous to Eq. (10.28):

$$\frac{\mathrm{d}R}{\mathrm{d}t} = -L_p\left[\alpha\left(c_s^e - c_s^i - c_{n0}^i\left(\frac{R_0}{R}\right)^3\right) + \frac{2K}{r}\left(\left(\frac{R}{R_0}\right)^2 - 1\right)\right]. \tag{10.37}$$

For realistic parameter values, membrane stretching only adds a minor correction to the vesicle-swelling rate. Figure 10.5 shows the swelling of a spherical vesicle upon transfer into an isotonic medium of permeating solute ($P_s = 2 \times 10^{-8}$ m/s), obtained by the numerical solution of the two-parameter system defined by Eqs. (10.37) and (10.28), with $R(0) = R_0$ and $c_s^i(0) = 0$ as initial conditions. The upper curve disregards the membrane stretching energy ($K = 0$), while the lower uses the value $K = 0.23\ \mathrm{Nm}^{-1}$. Other parameters used in calculation are $c_s^e = c_{n0}^i = 0.1$ mol/L, $R_0 = 20\,\mu$m, $L_p = 1.645 \times 10^{-13}$ m/(s Pa), and $\alpha = RT = 2477$ J/mol at $T = 298$ K.

3.5. Swelling–burst cycle

In reality, vesicles approximately follow the swelling course shown in Fig. 10.5 only until the critical strain of the membrane is reached. Once the critical strain is reached, the membrane ruptures, and the vesicle bursts. Subsequently, the membrane is resealed and another cycle of swelling commences. Experimentally, long trains of ~50 vesicle bursts have been observed.

The phenomenon has been predicted and thoroughly worked out from the theoretical point of view by Kozlov and Markin [50]; apparently unaware of their work, other authors attempted the same decades later [51]. Experimentally, the effect has been observed on erythrocytes when their suspending medium has been exchanged with a hypotonic one [52], on giant

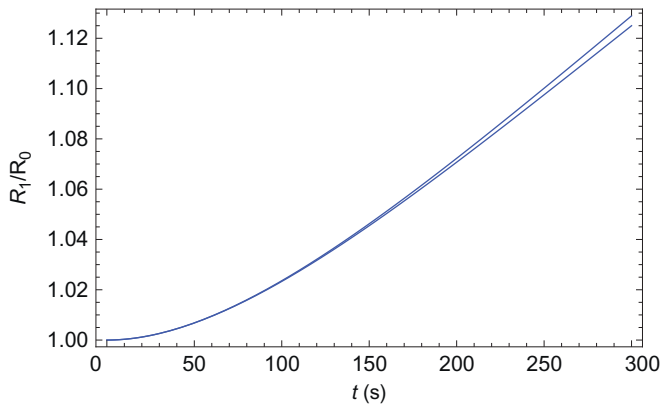

Figure 10.5 The radius of a vesicle cross-section upon transfer into a isotonic solution of a solute which can permeate vesicle membrane, as calculated by the two-parameter model. The lower curve shows the rate of vesicle growth when the finite membrane stretching modulus K is taken into account, while the upper curve shows the dependency for $K = 0$. Calculation parameters are given in the text.

adhering vesicles [53], on giant vesicles with equinatoxin-II-induced pores [54], on giant vesicles with photoinduced pores [55], on giant vesicles with melittin-induced pores [56], and on giant vesicles upon transfer from a solution of a nonpermeating solute to a solution of a permeating solute [37].

Kozlov and Markin [50] consider a vesicle filled with an osmotically active solute (i.e., nonpermeating) and write an expression for the osmotic influx J_{inf} of water:

$$J_{\text{inf}} = -L_p A(\Delta\Pi - \Delta p), \tag{10.38}$$

where L_p is the permeability of membrane for water (hydraulic conductivity), A is the membrane area, $\Delta\Pi = \Pi^e - \Pi^i$ is the difference in osmotic pressure, and $\Delta p = p^e - p^i$ is the difference in the hydraulic pressure. Equation (10.38) is identical to Eq. (10.36).

The vesicle is treated as spherical, its radius denoted by R. Due to osmotic swelling, $R > R_0$, where R_0 denotes the value of a nonexpanded vesicle. Denoting $R = R_0 + \Delta R$, the corresponding changes in the vesicle volume and membrane area are $\Delta A/A_0 \approx 2\Delta R/R_0$ and $\Delta V/V_0 \approx 3\Delta R/R_0$, respectively. A stretched membrane creates a pressure inside the vesicle—cf., Eq. (10.35), which opposes the swelling,

$$\Delta p = \frac{2K}{R}\frac{\Delta A}{A_0},$$

with K being the membrane stretching modulus. The elastic free energy associated with membrane stretching is given according to Eq. (10.34):

$$W_a = \frac{K}{2}\frac{(\Delta A)^2}{A_0}.$$

A pore present in the membrane lowers ΔA and thus reduces this energy term. However, on the other hand, creating a tension pore increases the total energy by the edge energy, equal to the product of the length of the pore edge, $2\pi r$, and the linear tension γ:

$$W_p = 2\pi\gamma r. \tag{10.39}$$

Here, r refers to the radius of a circular tension pore. Equation (10.39) is an approximate expression, valid for large pores. A consequence of a pore having a nonzero energy is that the intravesicular pressure does not drop to zero after the membrane ruptures. Instead, a residual intravesicular pressure remains:

$$\Delta p_r = \frac{2\gamma}{R_0 r}. \tag{10.40}$$

This residual intravesicular pressure causes the efflux of the intravesicular solution once the vesicle ruptures. The efflux J_{eff} is approximately equal to

$$J_{\text{eff}} = \frac{r^3 \Delta p_r}{\eta}. \tag{10.41}$$

Here η denotes the viscosity.

Substituting Eq. (10.40) into Eq. (10.36) and integrating it, one obtains the time course of vesicle volume upon transfer into a hypotonic medium:

$$\Delta V(t) = \frac{\pi R_0^4 \alpha \Delta c_n}{K}\left[1 - \exp\left(-\frac{4KL_p}{R_0^2}t\right)\right]. \tag{10.42}$$

Here, $\alpha = RT$. The elastic energy of a vesicle with a pore is the sum of the membrane stretching energy and the linear energy of the pore:

$$W = \frac{K}{2}\frac{(\Delta A - A_p)^2}{A_0} + 2\sqrt{\pi}\gamma\sqrt{A}. \tag{10.43}$$

At a given ΔA, the area of the tension pore A_p adapts in such a way as to minimize the total energy given by Eq. (10.43). If W is plotted against pore radius r for realistic values of K and γ and for different values of $\Delta V/V_0$, one can prove that for low values of $\Delta V/V_0$, W is a monotonously increasing function of pore radius r (Fig. 10.6). If $\Delta V/V_0$ is increased, we reach a critical value $\Delta \widetilde{V}/V_0$ at which $W(r)$ has an inflection point. By increasing $\Delta V/V_0$ even further, a local minimum becomes a global one, meaning that at some nonzero pore radius, the energy of the vesicle is lower than at $r = 0$, and by overcoming the energy barrier, the vesicle can jump from a poreless state into a state with a pore.

Kozlov and Markin show that based on the difference between the influx and the efflux, given by Eqs. (10.38) and (10.41), three different scenarios are possible:

$J_{\text{inf}} > J_{\text{eff}}$ instant efflux of the whole vesicle interior,
$J_{\text{inf}} = J_{\text{eff}}$ steadily open pore,
$J_{\text{inf}} < J_{\text{eff}}$ pulse − wise regime.

Kozlov and Markin conclude that for realistic parameter values, the pulse-wise regime is the most probable one, which is consistent with our own observations.

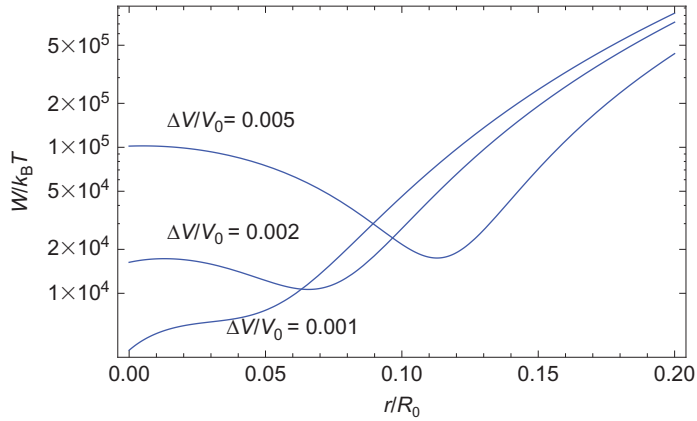

Figure 10.6 The elastic energy of a vesicle with a pore plotted against reduced pore radius r/R_0 for several different values of $\Delta V/V_0$. Vesicle elastic energy is given by Eq. (10.43), with $R_0 = 5\,\mu$m, $K = 240$ mN/m, $\gamma = 20$ pN.

In the pulse-wise regime, it is possible to infer some relationships between relevant quantities during successive bursts by employing two assumptions:

1. During the swelling phase, the amount of the nonpermeating solute inside the vesicle remains constant.
2. At burst, partial concentrations of both the permeating and the nonpermeating solute remain constant.

The first assumption is valid if the characteristic time for solute exchange is long compared with the time course of the experiment; the second assumption assumes that the interior of the vesicle is well mixed.

While the validity of the above assumptions is more general, some simple formulas can be obtained for the linearized one-parameter case. Let us consider a vesicle in the pulse-wise regime (Fig. 10.7). Due to osmotic swelling, the vesicle radius R increases from its relaxed value R_0 until a critical value R_c is reached, at which the critical strain for the membrane is reached, upon which membrane ruptures, ejects a part of the internal volume, and reseals in a relaxed state. As the $(A_c - A_0)/A_0$ amounts to a few percent, Eq. (10.33) can be linearized.

Equation (10.33) is valid only up to the first burst. Deriving it, we assumed $c_s^e = N_n/V_0$. We can derive the concentration of nonpermeating solute in subsequent swelling cycles using the assumptions above. Denoting the amount of nonpermeating solute inside the vesicle after n bursts by $N_n^{(n)}$,

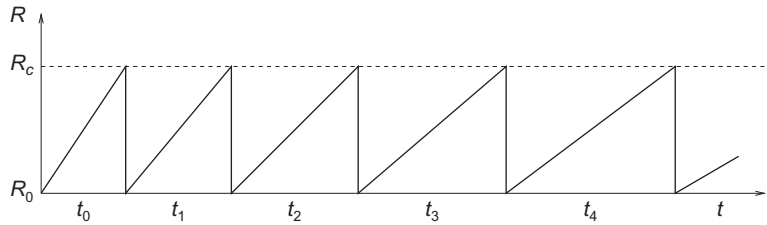

Figure 10.7 In the pulse-wise regime, vesicle radius R increases due to osmotic swelling from its relaxed value R_0 until it reaches its critical value R_c, at which the critical strain for the membrane is reached. At that point, membrane ruptures, vesicle ejects part of its interior, upon which the membrane reseals and the radius returns to its relaxed value.

the concentration of nonpermeating solute inside the vesicle after n bursts by $c_n^{(n)}$, $V_0 = 4\pi R_0^3/3$, and $V_c = 4\pi R_c^3/3$, one can write

$$N_n^{(0)} = c_n^{(0)} V_0 = c_n^{(1)} V_c,$$
$$N_n^{(1)} = c_n^{(1)} V_0 = c_n^{(2)} V_c,$$
$$\dots$$

A general expression for $c_n^{(n)}$ is then

$$c_n^{(n)} = c_n^{(0)} \left(\frac{V_0}{V_c}\right)^n. \tag{10.44}$$

In our experimental setup, $c_n^{(0)} = c_s^e$ holds. Substituting c_n^i with $c_n^{(n)}$ in the derivation of Eq. (10.33), one obtains the temporal dependence of vesicle radius after n bursts:

$$R^{(n)}(t) = R_0 \left[1 + \left(\frac{V_0}{V_c}\right)^n \frac{4P_s t}{R_0}\right]^{1/4}. \tag{10.45}$$

Or, linearized, $R^{(n)}(t) = R_0 + (V_0/V_c)^n P_s t$. The time between two successive bursts is then

$$t_n = \left(\frac{V_0}{V_c}\right)^n \frac{R_c - R_0}{P_s}.$$

Denoting $\alpha_c = (A_c - A_0)/A_0$ and expressing $V_c/V_0 \approx 1 + (3/2)\alpha_c$, $R_c/R_0 \approx 1 + (1/2)\alpha_c$, one obtains after linearization for the time elapsed between the nth and the $n+1$th burst:

$$t_n \approx \frac{R_0}{P_s}\left(1 + \frac{\alpha_c}{2} + \frac{3\alpha_c}{2} n\right). \tag{10.46}$$

In this linear model, the time elapsed between subsequent bursts increases linearly with n.

As the formation of a tension pore is a stochastic event, R_c is not a constant but can vary from one burst to another. To account for this, Eq. (10.44) can be written as

$$c_n^{(n)} = c_n^{(0)} \prod_{j=0}^{n-1} \frac{V_0}{V_c^{(j)}}, \tag{10.47}$$

where the index j denotes each of the n bursts. We have introduced $V_c^{(j)} = 4\pi R_c^{(j)}/3$, the volume of vesicle at which the critical strain for the membrane is reached in the jth burst.

3.6. Critical phenomena in osmotic swelling

Upon transfer of vesicles from a solution of a nonpermeating solute into a solution of a permeating solute, vesicles often exhibit a transient increase of cross-section radius (Fig. 10.2). We attribute this behavior to a slight hypertonicity of the target solution, which causes the vesicles to slightly deflate and change their shapes from an initially spherical shape into an oblate spheroid. The concentration gradient, however, drives the permeating solute into the vesicle interior, and the ensuing osmotic pressure difference serves as a driving force for water, which causes the vesicle to reinflate. The inflation process has two stages: initially, the vesicle is flaccid and approaching the spherical shape, while in the second stage, the vesicle is spherical, its membrane being increasingly stretched.

It has been shown that an inflating vesicle reaches the end of the first stage critically, through a continuous transition. This was initially demonstrated for unstretchable membrane [57], and later the theory has been extended in order to account for membrane stretching [43]. We shall provide a brief outline of the underlying theory, which employs a thermodynamic framework [58].

Let us consider a vesicle with Q entrapped molecules of a nonpermeating solute. We assume that the vesicle is brought into a thermal equilibrium with the surroundings, characterized by temperature T and pressure p_0. Both the vesicle volume V and the surface area A are treated as free, independent thermodynamic variables. The Gibbs free energy of the system contains volume and surface contributions:

$$G = G_{3D} + F_{2D}. \tag{10.48}$$

Considering the enclosed solution as ideal and dilute, one can write

$$G_{3D} = k_B T Q \left(\ln \frac{Q \bar{V}_w}{V} - 1 \right) + p_0 V. \tag{10.49}$$

The surface terms comprise the stretching and the bending parts,

$$F_{2D} = F_s + F_b. \tag{10.50}$$

The stretching part is assumed to have a minimum at some value A_0; a quadratic expansion is used:

$$F_s = \frac{K}{2} \frac{(A - A_0)^2}{A_0}.$$

In regarding the bending free energy, only the contribution from undulation entropy is included, which describes the suppression of bending fluctuations as the vesicle shape approaches a sphere. Assuming small fluctuations around a spherical shape, it is given by [57]

$$F_b = -\frac{N}{2} k_B T \ln(1 - v). \tag{10.51}$$

Here, N is the total number of independent bending modes contributing to the membrane thermodynamics, and v is the vesicle reduced volume. It is important to note that through the reduced volume (which depends on both volume and surface area), F_b provides the coupling between the volume part G_{3D} and the surface part F_{2D}. The number of modes N is not known in advance and is a parameter extracted from the experiment.

Using Eqs. (10.48)–(10.51), the Gibbs free energy of a vesicle is defined via (T, p_0, Q, N), as well as via A and V. By minimizing G with respect to A and V, the equilibrium free energy can be obtained. Introducing an intensive area $a = A/N$ and its relaxed value $a_0 = A_0/N$ along the way, one obtains a set of equations from which a and v can be calculated as

$$\frac{1}{2} \delta_N \frac{v}{1 - v} + \left(\frac{a}{a_0} \right)^{3/2} v = \frac{Q}{Q_c}, \tag{10.52}$$

$$\frac{2}{3} \frac{\delta_N}{\delta_K} \frac{a(a - a_0)}{a_0^2} + \left(\frac{a}{a_0} \right)^{3/2} v = \frac{Q}{Q_c}. \tag{10.53}$$

In Eqs. (10.52) and (10.53), we have defined

$$Q_c = \frac{p_0 V_0}{k_B T}, \quad \text{where } V_0 = \frac{A_0^{3/2}}{6\sqrt{\pi}}, \tag{10.54}$$

and parameters δ_N and δ_K, the first one related to the finite vesicle size, and the second one to the finite membrane stretchability:

$$\delta_N = \frac{N}{Q_c} \propto N^{-1/2}, \tag{10.55}$$

$$\delta_K = \frac{k_B T}{K a_0} \propto K^{-1}. \tag{10.56}$$

Two limiting cases of the described system can be considered. Setting $N \to \infty$, $\delta_N \to 0$ while keeping the stretching modulus finite brings us to the usual thermodynamic limit of an infinite system. In this limit, Eqs. (10.52) and (10.53) are degenerate and yield the expected equilibration of the internal and the external pressure: $Qk_BT/V = p_0$. The second limiting case corresponds to an unstretchable membrane: $K \to \infty$, $\delta_K \to 0$. In this case, Eq. (10.53) requires $a = a_0$, while Eq. (10.52) yields the behavior studied in Ref. [57], with v exhibiting a critical behavior as $N \to \infty$.

Away from either limit, Eqs. (10.52) and (10.53) yield

$$\delta_K \frac{v}{1-v} = \frac{4}{3} \frac{a(a-a_0)}{a_0^2}. \tag{10.57}$$

We can see from Eq. (10.57) that attaining a perfectly spherical shape ($v = 1$) would require infinite strain $a \to \infty$, which is not realistic. The deviation of the area from its relaxed state, $a - a_0$, is inversely proportional to the deviation of the vesicle shape from a sphere, $1 - v$. As $\delta_K \ll 1$, it takes a highly swollen vesicle, $1 - v \sim \delta_K$, to produce a significant membrane strain $(a - a_0)/a_0$.

In order to provide an adequate description of the transition, we define the control parameter $q = Q/Q_c - 1$, proportional to the number of enclosed molecules, and order parameter $M = 1 - v$, which serves as a measure of the deviation of vesicle shape from a sphere. Solving Eqs. (10.52) and (10.53) for M in the vicinity of the transition, one obtains

$$M(q) = \frac{\Delta}{2} \left(\sqrt{1 + \left(\frac{q}{\Delta}\right)^2} - \frac{q}{\Delta} \right), \quad \Delta = \sqrt{2\delta_N + \frac{9}{2}\delta_K}. \tag{10.58}$$

For $q < 0$, $M(q) \simeq |q|$, which is appreciable, while for $q > 0$, $M(q) \sim \Delta/(4q)$, which is very small. The transition occurs over a region, determined by Δ. Thus, both the finite vesicle size and the membrane stretchability contribute to widening of the transition. In the limit $\Delta \to 0$, that is, for an

infinitely large vesicle enclosed by a nonstretchable membrane, $\mathrm{d}M/\mathrm{d}q$ has a discontinuity at $(q=0, M=0)$. Setting $\delta_K=0$ while keeping δ_N finite yields back the results obtained in Ref. [57]. Which of the two factors entering Δ is dominant, δ_N or δ_K, depends on their ratio

$$\frac{\delta_N}{\delta_K} \sim \frac{K/R_0}{p_0}.$$

Using the values from our experiments—$R_0 \sim 20$–$50\ \mu\mathrm{m}$, $c_0 \sim 0.1$–$0.2\ \mathrm{mol/L}$—as well as $K = 240\ \mathrm{mN/m}$ [59], we obtain $\delta_N/\delta_K \sim 0.01$–$0.1$. Therefore, in our conditions, the transition width is governed by the finite stretching modulus and can be approximated by

$$\Delta \approx \left(\frac{9}{2}\delta_K\right)^{1/2} = \left(\frac{9k_\mathrm{B}T}{2Ka_0}\right)^{1/2}. \tag{10.59}$$

While Eq. (10.58) fully describes the law of corresponding states for osmotic swelling of nearly spherical vesicles, we would like to transform it into a form which would allow us to compare it with the experiment, that is, with the function $R(t)$.

The simpler part is the transformation of the time axis. As the concentration of the permeating solute inside the vesicle is approximately two orders of magnitude lower than its concentration in the surrounding medium, the former can be neglected, yielding $\mathrm{d}Q/\mathrm{d}t \approx PA_0c_0$, which further leads to

$$q = (3P/R_0)t + \mathrm{const.} \tag{10.60}$$

Equation (10.60) gives a simple linear relationship between the time t and the control parameter q.

The transformation for the radius is less straightforward. Here, we only reproduce the result, which is worked out in detail in Ref. [43]. Denoting $g_\mathrm{exp} = (R_1(t)/R_0)^3 - 1$, where $R_1(t)$ is the radius of vesicle projected cross-section, one arrives at the following scale and shift transformation:

$$f(\xi) = \sqrt{\frac{8}{15\Delta}}\left[g_\mathrm{exp}\left(\xi - \frac{1}{4}\left(\frac{15}{\Delta}\right)^{1/3}\right) - \xi\Delta + \frac{3}{4}\left(15\Delta^2\right)^{1/3}\right], \tag{10.61}$$

where $\xi = q/\Delta$ and $q = (3P/R_0)t$. Using the permeability P and the transition width Δ as two fitting parameters, one can verify that the experimental data for all recorded vesicle transfers collapse onto a single universal function,

$$f(\xi) = \left(\sqrt{1+\xi^2} - \xi\right)^{1/2}. \tag{10.62}$$

Fitting Eq. (10.62) to the recorded data $R_1(t)$ of vesicle transfer into an isotonic solution of urea yields the permeability of membrane for urea, $P_s = 0.013 \pm 0.001\,\mu m/s$. The obtained permeabilities for glycerol and ethylene glycol, on the other hand, exhibit concentration dependence. The values obtained for glycerol range from 0.0053 at $c_0 = 0.1\,M$ to $0.019 \pm 0.006\,\mu m/s$ at 0.2 M, and those for ethylene glycol range from $0.046 \pm 0.006\,\mu m/s$ at 0.1 M to $0.085 \pm 0.01\,\mu m/s$ at 0.2 M.

4. EXPERIMENTAL ANALYSIS

In this section, we present a method for determining membrane permeability for a given solute from the analysis of swelling–burst cycles [39] and demonstrate that its results are consistent with the analysis of the osmotic swelling of flaccid vesicles [43].

In Section 3, Eq. (10.45) has been obtained, which, when linearized, shows that before the first burst, the slope of $R(t)$ equals to the permeability P_s, and after n bursts, the slope becomes $(V_0/V_c)^n P_s$ if all bursts are equal, and $P_s \prod_{j=0}^{n-1} \left(V_0/V_c^{(j)}\right)$ if they are not. The underlying assumptions are that the vesicle is spherical at the onset of the first swelling cycle, and the concentration of the nonpermeating solute in its interior is equal to the concentration of the permeating solute outside.

These assumptions are not always met. In 37 of 47 recorded vesicle transfers in our experiments, the dependence of the vesicle cross-section radius as a function of time exhibits an initial transient maximum or "bulge" like the one seen in Fig. 10.2. In those cases, the vesicle is filled with a mixture of a nonpermeating and permeating solute already at the onset of the first swelling cycle, and Eq. (10.45) needs a small correction to take that into account.

An estimate of the mole fraction of the nonpermeating and the permeating solute at the onset of the first swelling cycle can be obtained from the initial transient maximum. If we approximate the shape of a partially deflated vesicle with an oblate spheroid and denote $x = R_1/R_0$, where R_1 is the radius of the vesicle cross-section at the crest of the "bulge" and R_0 is its value in the "valley," that is, at the onset of the first swelling cycle, we can compute the reduced volume of the vesicle (v) using Eq. (10.29).

We can show that the reduced volume of the vesicle is equal to the mole fraction of the osmotically active solute at the onset of the first swelling cycle. At the crest of the bulge, the vesicle is flaccid with a volume $V = vV_0 < V_0$, and containing N_n moles of nonpermeating solute. At the onset of the first swelling cycle, the vesicle is spherical with a radius R_0, and containing N_n

moles of nonpermeating solute and N_s moles of permeating solute. As the rapid osmotic exchange of water ensures that the total concentration is equal in both cases, $N_n/V=(N_n+N_s)/V_0$, it follows

$$v=\frac{N_n}{N_n+N_s}=x_n.$$

We can amend Eq. (10.45) with this correction, yielding

$$R^{(n)}(t)=R_0\left[1+\left(\frac{V_0}{V_c}\right)^n\frac{4x_nP_st}{R_0}\right]^{1/4}. \tag{10.63}$$

We need to note that taking the value of x_n at the onset of a swelling cycle is an approximation, as x_n actually changes during the course of a swelling cycle.

Treating the vesicle swelling–burst cycles as piecewise linear, the slope of the kth cycle can be expressed as

$$\frac{\Delta R^{(k)}}{\Delta t^{(k)}}=x_nP_s^{(k)}\prod_{j=0}^{k-1}\frac{V_0}{V_c^{(j)}}. \tag{10.64}$$

While membrane permeability for the permeating solute can be in principle computed from an individual vesicle-swelling phase between two bursts, a more reliable estimate is obtained by averaging it over all n bursts in the cycle:

$$\bar{P}_s=\frac{1}{n}\sum_{k=1}^{n}\frac{1}{x_n}\frac{\Delta R^{(k)}}{\Delta t^{(k)}}\prod_{j=0}^{k-1}\frac{V_0}{V_c^{(j)}}. \tag{10.65}$$

Equation (10.65) gives the estimate for the membrane permeability based on a single recording of a vesicle transfer. Averaging over several recordings of vesicle transfer is needed to obtain a more reliable estimate of membrane permeability.

Table 10.1 summarizes the permeability data for glycerol, urea, and ethylene glycol, obtained by using two different analyses. The term "burst train" refers to the analysis presented here, while the term "critical swelling" refers to the alternative analysis presented in the preceding section [43], where vesicle transition from a flaccid to a spherical state before the first burst is observed.

One can see that in the case of urea, the estimate for membrane permeability is independent of solute concentration, which is consistent with our finding in Ref. [43]. On the other hand, both polyols exhibit a

Table 10.1 Permeability estimates for glycerol, urea, and ethylene glycol, determined from series of micrographs of giant unilamellar vesicles upon transfer from a sucrose/glucose solution into an isomolar solution of a given solute.

Solute	Permeability P_s (μm/s)			
	"Burst train"		"Critical swelling"	
	0.1 M	0.2 M	0.1 M	0.2 M
Glycerol	0.0077 ± 0.0009	0.016 ± 0.003	0.0053	0.019 ± 0.06
Urea	0.014 ± 0.001	0.013 ± 0.001	0.013 ± 0.001	
Ethylene glycol	0.054 ± 0.005	0.10 ± 0.01	0.0460 ± 0.006	0.085 ± 0.01

"Burst train" refers to the analysis presented here, and "critical swelling" to an alternative analysis [43] on the same data set.

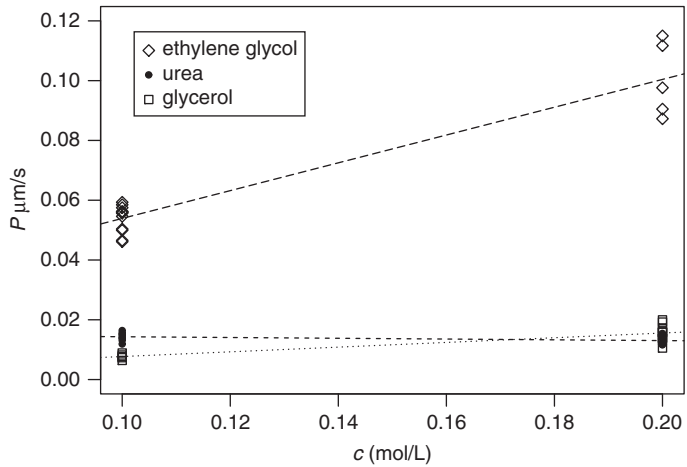

Figure 10.8 The apparent permeability of POPC membrane for glycerol, urea, and ethylene glycol, obtained by the "burst train" analysis. Figure 6 in Ref. [43] shows analogous results obtained by the "critical swelling" analysis.

concentration dependence of the (apparent) membrane permeability, which is again in agreement with our own recent findings [43]. The trend is even more apparent in Fig. 10.8. A possible explanation for the concentration dependence of the apparent membrane permeability is strong evidence for the affinity of polyols to phospholipid headgroups [60,61], which results in the solute concentration adjacent to the membrane being larger than in the bulk solution, which consequently leads to an apparent permeability coefficient which is larger than the actual one. This affinity of polyols to phospholipid

headgroups may also account for a large scatter of published data on membrane permeabilities for polyols.

5. DISCUSSION

The existence of reproducible techniques for producing giant unilamellar vesicles (GUVs) [35,62] and the availability of phase-contrast microscopy and high-resolution digital cameras, along with the efficient procedures for automated extraction of vesicle contour from the images and determination of the radius of vesicle cross-section [39], render the determination of membrane permeability of GUVs a viable alternative to the established techniques employing either DLS on submicrometer vesicles or planar lipid membranes.

GUVs were used before in studies of membrane permeability [32]. The study by Boroske *et al.*, however, was designed to observe osmotic shrinking of GUVs, while in our study, vesicles swell osmotically (with the exception of the initial phase, where a transient osmotic shrinking may be observed). Osmotic swelling of vesicles in a controlled manner guarantees a simpler spherical geometry, through which both the vesicle area and its volume are experimentally accessible variables. By contrast, in the experiment of Boroske *et al.*, vesicle volume was the only experimentally observable variable, and the authors had to come up with a plausible explanation for the apparently "missing" membrane area.

On a very superficial level, the continuous transition between the "ironing" and the stretching regime of a vesicle which swells osmotically due to the permeation of a permeable solute might seem similar to the "minimal volume" technique employed by Sha'afi *et al.* (cf., fig. 3 in Ref. [19] and fig. 1 in Ref. [43]). However, one needs to be aware of the fact that fig. 3 in Ref. [19] shows vesicle volume as a function of time, while fig. 1 in Ref. [43] shows the radius of a nonspherical vesicle cross-section, and throughout the course shown in the diagram, vesicle volume is monotonously increasing. In our experiment, minimal vesicle volume appears at the top of the initial bulge (visible around 40 s on the graph in Fig. 10.2). We have not attempted an analysis analogous to the one performed by Sha'afi *et al.* [19] or Hill and Cohen [22] because the initial moment in which the vesicles are brought in contact with the target solution is not defined as well as in the stopped flow experiments. The authors of earlier studies, on the other hand, seem to be unaware of the critical transition between the "ironing" and the stretching regime in the course of osmotic swelling of a vesicle.

While offering a direct visualization of osmotic swelling, the method described here has its limitations. The three solutes tested here—glycerol, urea, and ethylene glycol—induce significant changes in vesicle size on the timescale of minutes. With solutes which are much more or much less permeable, the rate of changes may be either too fast for video camera or so slow that other effects start to dominate the experiment (e.g., convection in the measuring chamber). Another limitation is imposed by the refractive index of the solution. The refractive index of the target solution in general differs from that of the vesicle interior, and the difference between the two refractive indices increases with the increasing concentration of solutions. At high enough concentration, the halo around the vesicle becomes blurred, and the algorithm used to determine vesicle contour [39] fails. With our present equipment, we estimate that concentrations significantly higher than 0.2 mol/L are outside our reach.

Finally, we want to compare the results of two techniques dubbed "burst train" and "critical swelling" in Table 10.1. As can be seen, they produce consistent results which are within the experimental error of each other. The experimental error estimates for both methods are also approximately the same. The "burst train" technique is more forgiving toward minor glitches, such as vesicle temporarily drifting slightly out of focus, which results in an overestimate of vesicle radius (seen around 370 s in Fig. 10.2). However, one needs to keep in mind that the "burst train" technique requires approximately five times as much data as the "critical swelling," and consequently, minor glitches are more likely to occur during a longer period. We therefore lean toward recommending the "critical swelling" technique, which is less resource greedy while giving the results with the same precision. Our recommended procedure is therefore to keep recording the vesicle transfer up to the first burst (which is easy to notice during the experiment) and carry out the analysis described in Ref. [43].

REFERENCES

[1] H. Meyer, Welche Eigenschaft der Anästhetica bedingt ihre narkotische Wirkung? Arch. Exp. Pathol. Pharmakol. 42 (1899) 109–118.
[2] C.E. Overton, Studien über die Narkose: Zugleich ein Beitrag zur all-gemeinen Pharmakologie, Gustav Fischer, Jena, 1901.
[3] G.M. Preston, T. Piazza Caroll, W.B. Guggino, P. Agre, Appearance of water channels in *xenopus* oocytes expressing red cell CHIP28 protein, Science 256 (1992) 385–387.
[4] L.J. Pike, Rafts defined: a report on the Keystone symposium on lipid rafts and cell function, J. Lipid Res. 47 (2006) 1597–1598.
[5] Q. Al-Awqati, One hundred years of membrane permeability: does Overton still rule? Nat. Cell Biol. 1 (1999) E201–E202.

[6] A. Missner, P. Pohl, 110 years of the Meyer-Overton rule: predicting membrane permeability of gases and other small compounds, ChemPhysChem 10 (2009) 1405–1414.
[7] T. Heimburg, A.D. Jackson, The thermodynamics of general anesthesia, Biophys. J. 92 (2007) 3159–3165.
[8] J.F. Nagle, J.C. Mathai, M.L. Zeidel, S. Tristram-Nagle, Theory of passive permeability through lipid bilayers, J. Gen. Physiol. 131 (2008) 77–85.
[9] P. Mueller, D.O. Rudin, H.T. Tien, W.C. Wescott, Reconstitution of cell membrane structure in vitro and its transformation into an excitable system, Nature 194 (1962) 979–980.
[10] A.D. Bangham, Membrane models with phospholipids, Prog. Biophys. Mol. Biol. 18 (1968) 27–95.
[11] B.E. Cohen, A.D. Bangham, Diffusion of small non-electrolytes across liposome membranes, Nature 236 (1972) 173–174.
[12] A.S. Verkman, Optical methods to measure membrane transport processes, J. Membr. Biol. 148 (1995) 99–110.
[13] H.T. Tien, Bilayer Lipid Membranes (BLM), Theory and Practice, Marcel Dekker, New York, 1974.
[14] A. Finkelstein, Water and nonelectrolyte permeability of lipid bilayer membranes, J. Gen. Physiol. 68 (1976) 127–135.
[15] E. Orbach, A. Finkelstein, The nonelectrolyte permeability of planar lipid bilayer, J. Gen. Physiol. 75 (1980) 427–436.
[16] A. Walter, J. Gutknecht, Permeability of small nonelectrolyte molecules through lipid bilayer-membranes, J. Membr. Biol. 90 (1986) 207–217.
[17] A. Bangham, J. de Gier, G.D. Greville, Osmotic properties and water permeability of phospholipid liquid crystals, Chem. Phys. Lipids 1 (1967) 225–246.
[18] M.H. Jacobs, The simultaneous measurement of cell permeability to water and to dissolved substances, J. Cell. Comp. Physiol. 2 (1933) 427–444.
[19] R.I. Sha'afi, G.T. Rich, D.C. Mikulecky, A.K. Solomon, Determination of urea permeability in red cells by minimum method. A test of the phenomenological equations, J. Gen. Physiol. 55 (1970) 427–450.
[20] O. Kedem, A. Katchalsky, Thermodynamic analysis of the permeability of biological membranes to non-electrolytes, Biochim. Biophys. Acta 27 (1958) 229–246.
[21] J. de Gier, J.G. Mandersloot, J.V. Hupkes, R.N. McElhaney, W.P. van Beek, Mechanism of non-electrolyte permeation through lipid bilayers and through biomembranes, Biochim. Biophys. Acta 233 (1971) 610–618.
[22] M.W. Hill, B.E. Cohen, A simple method of determining relative permeabilities of liposomes to non-electrolytes, Biochim. Biophys. Acta 290 (1972) 403–407.
[23] J. de Gier, Osmotic behaviour and permeability properties of liposomes, Chem. Phys. Lipids 64 (1993) 187–196.
[24] S. Paula, A.G. Volkov, A.N. Van Hoek, T.H. Haines, D.W. Deamer, Permeation of protons, potassium ions, and small polar molecules through phospholipid bilayers as a function of membrane thickness, Biophys. J. 70 (1996) 339–348.
[25] S.D. Shoemaker, T.K. Vanderlick, Stress-induced leakage from phospholipid vesicles: effect of membrane composition, Ind. Eng. Chem. Res. 41 (2002) 324–329.
[26] M. Montal, P. Mueller, Formation of bimolecular membranes from lipid monolayers and a study of their electrical properties, Proc. Natl. Acad. Sci. U.S.A. 69 (1972) 3561–3566.
[27] U. Seifert, Configurations of fluid membranes and vesicles, Adv. Phys. 46 (1997) 13–137.
[28] J. Pencer, G.F. White, F.R. Hallett, Osmotically induced shape changes of large unilamellar vesicles measured by dynamic light scattering, Biophys. J. 81 (2001) 2716–2728.

[29] J. Pencer, F.R. Hallett, Effects of vesicle size and shape on static and dynamic light scattering measurements, Langmuir 19 (2003) 7488–7497.
[30] J. Brunner, D.E. Graham, H. Hauser, G. Semenza, Ion and sugar permeabilities of lecithin bilayers: comparison of curved and planar bilayers, J. Membr. Biol. 57 (1980) 133–141.
[31] P.H. Barry, J.M. Diamond, Effects of unstirred layers on membrane phenomena, Physiol. Rev. 64 (1984) 763–872.
[32] E. Boroske, M. Elwenspoek, W. Helfrich, Osmotic shrinkage of giant egg-lecithin vesicles, Biophys. J. 34 (1981) 95–109.
[33] J.-Y. Wang, J. Chin, J.D. Marks, K.Y.C. Lee, Effects of PEO-PPO-PEO triblock copolymers on phospholipid membrane integrity under osmotic stress, Langmuir 26 (2010) 12953–12961.
[34] A. Carlsen, N. Glaser, J.-F. Le Meins, S. Lecommandoux, Block copolymer vesicle permeability measured by osmotic swelling and shrinking, Langmuir 27 (2011) 4884–4890.
[35] M.I. Angelova, D.S. Dimitrov, Liposome electroformation, Faraday Discuss. Chem. Soc. 81 (1986) 303–311.
[36] V. Heinrich, R.E. Waugh, A piconewton force transducer and its application to measurement of the bending stiffness of phospholipid membranes, Ann. Biomed. Eng. 24 (1996) 595–605.
[37] P. Peterlin, V. Arrigler, Electroformation in a flow chamber with solution exchange as a means of preparation of flaccid giant vesicles, Colloids. Surf. B 64 (2008) 77–87.
[38] R. Dimova, S. Aranda, N. Bezlyepkina, V. Nikolov, K.A. Riske, R. Lipowsky, A practical guide to giant vesicles. Probing the membrane nanoregime via optical microscopy, J. Phys. Condens. Matter 18 (2006) S1151–S1176.
[39] P. Peterlin, G. Jaklič, T. Pisanski, Determining membrane permeability of giant phospholipid vesicles from a series of videomicroscopy images, Meas. Sci. Technol. 20 (2009) 055801.
[40] H.-G. Döbereiner, E. Evans, M. Kraus, U. Seifert, M. Wortis, Mapping vesicle shapes into the phase diagram: a comparison of experiment and theory, Phys. Rev. E 55 (1997) 4458–4474.
[41] E. Evans, W. Rawicz, Entropy-driven tension and bending elasticity in condensed-fluid membranes, Phys. Rev. Lett. 64 (1990) 2094–2097.
[42] M. Bloom, E. Evans, O.G. Mouritsen, Physical properties of the fluid lipid-bilayer component of cell-membranes—a perspective, Q. Rev. Biophys. 24 (1991) 293–397.
[43] P. Peterlin, V. Arrigler, E. Haleva, H. Diamant, Law of corresponding states for osmotic swelling of vesicles, Soft Matter 8 (2012) 2185–2193.
[44] A. Katchalsky, P.F. Curran, Nonequilibrium Thermodynamics in Biophysics, Harvard University Press, Cambridge, MA, 1965.
[45] L. Onsager, Reciprocal relations in irreversible processes. I, Phys. Rev. 37 (1931) 405–426.
[46] L. Onsager, Reciprocal relations in irreversible processes. II, Phys. Rev. 37 (1931) 2265–2279.
[47] F.W. Kleinhans, Membrane permeability modeling: Kedem-Katchalsky vs a two-parameter formalism, Cryobiology 37 (1998) 271–289.
[48] P. Mazur, S.P. Leibo, R.H. Miller, Permeability of the bovine red cell to glycerol in hyperosmotic solutions at various temperatures, J. Membr. Biol. 15 (1974) 107–136.
[49] P. Mazur, R.H. Miller, Permeability of human erythrocyte to glycerol in 1 and 2 M solutions at 0 or 20 °C, Cryobiology 13 (1976) 507–522.
[50] M.M. Koslov, V.S. Markin, A theory of osmotic lysis of lipid vesicles, J. Theor. Biol. 109 (1984) 17–39.
[51] D. Popescu, A.G. Popescu, The working of a pulsatory liposome, J. Theor. Biol. 254 (2008) 515–519.

[52] A.M.M. Zade-Oppen, Repetitive cell 'jumps' during hypotonic lysis of erythrocytes observed with a simple flow chamber, J. Microsc. 192 (1998) 54–62.
[53] O. Sandre, L. Moreaux, F. Brochard-Wyart, Dynamics of transient pores in stretched vesicles, Proc. Natl. Acad. Sci. U.S.A. 96 (1999) 10591–10596.
[54] M. Mally, J. Majhenc, S. Svetina, B. Žekš, Mechanisms of equinatoxin II-induced transport through the membrane of a giant phospholipid vesicle, Biophys. J. 83 (2002) 944–953.
[55] E. Karatekin, O. Sandre, H. Guitouni, N. Borghi, P.-H. Puech, F. Brochard-Wyart, Cascades of transient pores in giant vesicles: line tension and transport, Biophys. J. 84 (2003) 1734–1749.
[56] M. Mally, J. Majhenc, S. Svetina, B. Žekš, The response of giant phospholipid vesicles to pore-forming peptide melittin, Biochim. Biophys. Acta 1768 (2007) 1179–1189.
[57] E. Haleva, H. Diamant, Critical swelling of particle-encapsulating vesicles, Phys. Rev. Lett. 101 (2008) 078104 4 pages.
[58] H. Diamant, Model-free thermodynamics of fluid vesicles, Phys. Rev. E 84 (2011) 061123.
[59] W. Rawicz, K.C. Olbrich, T. McIntosh, D. Needham, E. Evans, Effect of chain length and unsaturation on elasticity of lipid bilayers, Biophys. J. 79 (2000) 328–339.
[60] N. Krasteva, D. Vollhardt, G. Brezesinski, H. Möhwald, Effect of sugars and dimethyl sulfoxide on the structure and phase behaviour of DPPC monolayers, Langmuir 17 (2001) 1209–1214.
[61] L. Pocivavsek, K. Gavrilov, K.D. Cao, E.Y. Chi, D. Li, B. Lin, M. Meron, J. Majewski, K.Y.C. Lee, Glycerol-induced membrane stiffening: the role of viscous fluid adlayers, Biophys. J. 101 (2011) 118–127.
[62] J.I. Pavlič, J. Genova, G. Popkirov, V. Kralj-Iglič, A. Iglič, M.D. Mitov, Mechanoformation of neutral giant phospholipid vesicles in high ionic strength solution, Chem. Phys. Lipids 164 (2011) 727–731.

SUBJECT INDEX

Note: Page numbers followed by "*f*" indicate figures, and "*t*" indicate tables.

A

Action potential. *See* Nerve action potential
Activated leukocyte cell adhesion molecule (ALCAM), 254, 262–263
Adhesion rafts, 186
Adiabatic lateral compressibility
  chain-melting transition, 63–64
  definition, 62
  DPPC, 62, 69–70
  dynamic heat capacity, 62–63, 64
  heat reservoir, 64
  Pippard–Buckingham–Fairbank relations, 62–63
  temperature wave, 63
Adiabatic pressure perturbations
  change in entropy, 58, 59
  Clausius–Clapeyron relation, 58–59
  Fourier transformation, 60
  frequency-dependent transfer function, 60
  heat capacity, 59–60
  Maxwell relation, 58
  nonequilibrium process, 59
  relaxation function, 61
  response function, 61–62
A disintegrin and metalloproteinases (ADAMs), 250–251. *See also* Ovarian cancer
A disintegrin and metalloproteinases with thrombospondin motifs (ADAMTSs), 250–251
ALCAM. *See* Activated leukocyte cell adhesion molecule (ALCAM)
Alternative splicing mechanism, 263–264
Aspiration pressure, 5–6

B

Bilayer bending rigidity, 5
Biopolymer chitosan. *See* Chitosan
Bipolar lipids, 94
Black lipid membrane, 302
Bolalipids, 94–98, 101, 104, 105, 107, 108, 113–123

C

CA-125 biomarker, 264–265
CAC. *See* Critical association concentration (CAC)
Cahn–Hilliard regime, 157–158
Caveolae, 174, 186
Chain structure-dependent self assembly
  C32 alkyl chain, 104, 104*f*
  C34 alkyl chain, 104–106, 105*f*
  DSC curves, 104, 105*f*
  PC-C32diAc-PC
    suspensions, 104–106, 106*f*
    TEM image, 107, 107*f*
  PC-C32SS-PC, 104, 105*f*
Charged membranes
  EDTA, 30–31
  PC:PG vesicles, 30–31
  phosphatidylglycerol/phosphatidylserine, 29
  plasma membranes, 31
Chitosan
  absorption enhancer
    Caco-2 cells, 81
    permeability enhancement, 82
    tissue permeability and bioadhesive properties, 77
    urinary bladder (*see* Urinary bladder)
  cytolytic effect
    chitosan layer, 82, 82*f*
    urinary bladder epithelial cells, 83–85, 84*f*, 85*f*
    urothelium, 85–86, 86*f*
  cytotoxic effect, 77
  definition, 76
  electrostatic and hydrophobic interactions, 76
  tissue engineering
    basolateral membrane, 87–88

Chitosan (*Continued*)
glutaraldehyde, 87
regenerative medicine, 86–87
Cholesterol, 169–170, 171
bilayer stacks, properties, 9
DOPC membrane, 9
membrane bending rigidity, 8–9, 10*f*, 10*t*
saturated/mono-unsaturated lipids, 12
Clausius–Clapeyron relation, 58–59
Convolution theorem
Debye relaxation term, 72
Fourier transform, 71, 72
relaxation function, 70
Critical association concentration (CAC)
binding isotherms
C atoms number and, 211, 212*f*
CMC values and, 210, 210*t*
C_nPC surfactants, 212–213
DPC and CPC, 209–210, 209*f*
free energy change, 211
CMC, 207–208
Critical micelle concentration (CMC), 206
Critical packing parameter (CPP), 206–207
Critical strain, 308–309
optical microscope, 2–3, 4*f*, 305–307
osmotic swelling, 301–332

D

Debye relaxation term, 72
Detergent-resistant membranes (DRMs), 167–168, 173, 174–175. *See also* Lipid microdomains
Dioleoylphosphatidyl-ethanolamine (DOPE) membrane, 34–35
Dioleoyphosphatidylcholine (DOPC) membrane, 9, 130–132
Dispersion, 284–285
Dissipative particle dynamics (DPD), 147–148
DRMs. *See* Detergent-resistant membranes (DRMs)
Dynamic light scattering (DLS), 99–100, 101*f*, 219

E

E-cadherin, 251, 252*f*
ECM. *See* Extracellular matrix (ECM)
Ectodomain shedding
proteases
ADAMs and ADAMTSs, 253–254
matrix metalloproteinases, 251–253
metzincins, 250–251, 250*f*
proteins classification, 249, 250
Edge tension, 7
EDTA. *See* Ethylenediaminetetraacetic acid (EDTA)
Effective diffusion coefficient
analytical expression, 142
correlation length, 140–142, 141*f*
critical exponents, 142–143
wave number, 139–140, 139*f*, 140*f*
Electric double layer, 203–204
Electrodeformation
edge tension, 26–27
ellipsoidal vesicle, 24–26, 25*f*
relaxation dynamics, 24–26
Entropic tension, 5–6
Epithelial cell adhesion and activating molecule (EpCAM), 257–258
Ethylenediaminetetraacetic acid (EDTA), 30–31
Evans and Sackmann (ES) hydrodynamic screening length, 136
External electric fields
AC fields
lipid flow trigger, 22–24, 23*f*
vesicle deformation, 19–22, 21*f*
DC pulses
charged membranes, 29–31, 30*f*
electrodeformation and electroporation, 24–27, 25*f*
electrohydrodynamic instability, 32–33
flexoelectric properties, 32–33
fluid-phase vesicles, 35
fusion dynamics (*see* Vesicle electrofusion)
gel-phase membranes, 27–29, 28*f*
giant vesicle fusion (*see* Vesicle electrofusion)
membrane edge tension measurement, 33–35, 34*f*
membrane electrofusion, 35, 36*f*
spherocylindrical deformation, 31, 32*f*

in vivo and *in situ* applications, 17
Maxwell–Wagner timescale, 17, 18
transmembrane potential and conditions, vesicle electroporation, 18–19
vesicle membrane, capacitor, 17–18
Extracellular matrix (ECM), 245–246, 260, 261*t*

F

FIGO. *See* International Federation of Gynecology and Obstetrics (FIGO)
FitzHugh–Nagumo (FHN) model, 283, 291, 292*f*
Fluctuation spectroscopy method, 5
Fluid membrane heterogeneity dynamics
concentration fluctuations
2D microemulsions, 143–145
effective diffusion coefficient (*see* Effective diffusion coefficient)
theoretical works, 145–146
time-dependent Ginzburg–Landau model, 136–138
hydrodynamics
3D viscosity, 134
ES hydrodynamic screening length, 136
mobility tensor, 134–135
planar liquid membrane, 133–134, 133*f*
lipid rafts, 130
multicomponent membranes, 131–132, 132*f*
phase separation
block copolymer systems, 158–159
correlated diffusion, 151–154
domain coarsening, 146–147
domain growth, 148–151
DPD study, 155–157
model and simulation technique, 147–148
numerical simulations, 157
ternary giant vesicles, 154–155, 154*f*
time evolution, 157–158, 158*f*
ternary vesicle phase behavior, 130–131, 131*f*
viscoelasticity and microrheology technique, 160
Fourier transform, 71, 72
Fusion dynamics
electrophysiological methods, 35–37
ligand-mediated fusion, 37–38
membrane tension, 38–39
rescaled fusion neck diameter, 37, 38*f*, 39
stages, 37

G

Ganglioside, 170–171
Gel-phase membranes, 27–29, 28*f*
Giant phospholipid vesicles. *See* Phospholipid membrane permeability
Giant unilamellar vesicles (GUVs), 171–172, 184, 304–305
anchored molecules
avidin, 12–14
DNA molecules, 12–14, 13*f*
glycocalix, 12
polymer/membrane architecture, 12–14
surface concentration control, 14
bottom-up approach, 42–43
bounding membrane, 2
cholesterol
bilayer stacks, properties, 9
DOPC membrane, 9
membrane bending rigidity, 8–9, 10*f*, 10*t*
saturated/mono-unsaturated lipids, 12
classification, vesicles, 2–3
external electric fields (*see* External electric fields)
membrane material properties
bilayer bending rigidity, 5
edge tension, 7
entropic tension, 5–6
flaccid vesicle, shape fluctuations, 6–7
gel phase, 5
lipid membrane values, 7, 8*t*
lysis tension, 7
permeability, 301–331
phospholipid membranes, 5
physical properties, 3
shear surface viscosity, 5

Giant unilamellar vesicles (GUVs) (*Continued*)
stretching elasticity modulus, 6
model membranes, 2
optical microscope, 2–3, 4*f*
transmembrane peptides
DOPC bilayers, 15–17
elasticity constant, 15–17
HIV FP FP23, 14–15, 16*f*
interleaflet interaction parameter, 15–17
Ginzburg–Landau model, 136–138
Glycerophospholipids (GPLs), 168
GUVs. *See* Giant unilamellar vesicles (GUVs)

H

Headgroup structure-dependent self-assembly
chain length-dependent behavior, 113–114
fiber–micelle transition, 115–116
intermolecular hydrogen bonds, 107–108
Me_2PE-C32-Me_2PE
amplitude and frequency sweep, 108, 109*f*
cryo-TEM image, 115, 117*f*
DSC curves, 108–110, 110*f*, 111–112, 112*f*
phase diagram, 113–114
rheological measurements, 110, 111*f*
Me_2PE-C34-Me_2PE
gel cake formation, 114, 115*f*
molecular arrangement, 114–115, 116*f*
TEM image, Me_2PE-C36-Me_2PE, 114
worm-like micelles, 108
Helical nanofibers and micellar aggregation
hydrogel character, 98–99
Monte Carlo simulation, 98
PC-C32-PC
CH_2 -stretching vibrational band, 98–99, 100*f*
DLS experiments and electron microscopy, 99–100, 101*f*
DSC curves, 98–99, 100*f*
SANS, 100–101, 101*f*
viscoelastic behavior, 98, 99*f*
PC-C34-PC, 97–98, 97*f*
Hemopurifier™, 267
Heterogeneity dynamics. *See* Fluid membrane heterogeneity dynamics
Hodgkin–Huxley (HH) model, 52–53. *See also* Nerve action potential
collision study, 291–294
combination of, 294–295
features, 289–290
Hydrophobically associating polymers (HAPs), 201

I

Immunological synapses, 185
International Federation of Gynecology and Obstetrics (FIGO), 241

K

Kedem–Katchalsky model, 310–313

L

Large unilamellar vesicles (LUVs), 304
Lidocaine hydrochloride, 179
Lipid microdomains
biological importance
disease pathogenesis, 187–188
signaling and sorting platforms, 184–186
definition, 174
detergent insolubility
curvature factor and DRMs' structure, 176–178
vs. DRMs, 174–176
isolation method, 167–168
lateral organization, 168–171
outer and inner membrane leaflets, 171–172
PM fluid mosaic model, 166
proteins, 172–173
universal marker, 178–179
visualization
GM1 cross-linking, 181, 182*f*, 183
microscopic techniques, 180–181
model systems, 184
working hypothesis, 167
Lipid rafts, 130
Liposomes, 303–304

Low-frequency sound propagation
action potential, 52–53
adiabatic lateral compressibility
chain-melting transition, 63–64
definition, 62
DPPC, 62, 69–70
dynamic heat capacity, 62–63, 64
heat reservoir, 64
Pippard–Buckingham–Fairbank relations, 62–63
temperature wave, 63
adiabatic pressure perturbations
change in entropy, 58, 59
Clausius–Clapeyron relation, 58–59
Fourier transformation, 60
frequency-dependent transfer function, 60
heat capacity, 59–60
Maxwell relation, 58
nonequilibrium process, 59
relaxation function, 61
response function, 61–62
convolution theorem (*see* Convolution theorem)
definition, 56
dispersion relation, 66–68, 67*f*
effective speed, 56–57, 64–65
elastic constants, 52–53
frequency dependence, 65–66
Hodgkin–Huxley model, 52–53
lateral speed, 64–65, 66*f*
low-amplitude wave equation, 56
nerve membrane, soliton propagation
mechanical pulse, 55–56
nonlinear function, 55
Taylor expansion, 54–55
unilamellar DPPC vesicles, 55, 56*f*
wave equation, 54–55
phase transition, 52
polyatomic molecules, internal vibrational mode, 57
relaxation rate, 57–58
second-order transition, 57
thermodynamics and linear response theory, 68
two-dimensional lipid layers, 52
Lysis tension, 7

M

Matrix metalloproteinases (MMPs), 250–251. *See also* Ovarian cancer
Maxwell relation, 58
Maxwell stress tensor, 18–19
Maxwell–Wagner timescale, 17, 18
Membrane edge tension
DOPC membrane, 34–35
membrane resealing mechanisms, 33
egg PC vesicle, 33–34, 34*f*
pore closure process, 33–34
Membrane spontaneous curvature, 6–7
Membrane-type matrix metalloproteinases (MT-MMPs), 250–251
Metastasis, 243–246
Methyl-β-cyclodextrin (MβCD), 178–179
Metzincins, 250–251, 250*f*
Meyer–Overton rule, 302
Microrheology technique, 160
Microvesicles (MVs), 248. *See also* Ovarian cancer
Monosialoganglioside M1 (GM1), 179, 181, 182*f*, 183
Monte Carlo simulation, 98
Müllerian system theory, 242

N

Nerve action potential
electrical circuits and HH model, 279–280
conductance parameterization, 281–282
vs. soliton model (*see* Soliton model)
squid axons simulation, 282–283, 282*f*
time-dependent membrane current, 281
voltage-clamp experiment, 280–281, 280*f*
lipid membrane, 278–279
membrane proteins, 279
molecules classification, 277–278
pulse propagation (*see* Soliton model)
squid axon, 276–277, 276*f*
Nonlinearity, 284–285
N-palmitoyl-d-sphingomyelin (PSM), 130–131

O

Ovarian cancer
ADAMs, 262–263
alternative splicing mechanism, 263–264
cancerogenesis theories, 241–243
chemotherapy–chemoresistant cells, 246
histopathological classification, 240–241, 241*f*, 242*f*
incidence and chemoresistance, 240
metastasis, 243–246
MMPs, 260–262
protein secretion rates and blood biomarkers level, 264–265
serum biomarkers, 246–247
soluble protein release mechanism
alternative splicing, 254
ectodomain shedding (*see* Ectodomain shedding)
vesicle shedding, 248
therapeutic targets
ADAMs, 267–268
MMPs, 267
MVs, 266–267
vesicle shedding and MVs
antigen identification, 256, 256*t*
immunological surveillance, 258–259
inflammation and, 259–260
optimal environment establishment, 257–258
role, 254–255, 255*f*
serum and miRNA analysis, 257
Overton rule. *See* Meyer-Overton rule

P

PELs. *See* Polyelectrolytes (PELs)
Phase separation dynamics. *See* Fluid membrane heterogeneity dynamics
Phosphatidylcholine, 168–169
Phosphatidylethanolamine, 168–169
Phosphodimethylethanolamines
Me_2PE-C32-Me_2PE
amplitude and frequency sweep, 108, 109*f*
cryo-TEM image, 115, 117*f*
DSC curves, 108–110, 110*f*, 111–112, 112*f*
phase diagram, 113–114
rheological measurements, 110, 111*f*
Me_2PE-C34-Me_2PE
gel cake formation, 114, 115*f*
molecular arrangement, 114–115, 116*f*
Phospholipid membrane permeability
critical phenomena in osmotic swelling, 324–328
critical strain vesicle, 308–309, 309*f*
dynamic light scattering, 302–304
ethylene glycol, 308, 329–331
experimental analysis, 328–331
glycerol, 308, 329–331
GUVs
osmotic shrinking, 304–305
osmotic swelling, 305–309
individual vesicle burst, 306, 307*f*
Kedem–Katchalsky model, 310–313
least-squares procedure, 306–308, 307*f*
liposomes, 303–304
LUVs, 304
materials and methods, 305–306
membrane elasticity influences, 317–319
membrane stretching modulus, 317–319
Meyer-Overton rule, 302
one-parameter model, 316–317
osmotic swelling critical phenomena, 324–328
planar lipid bilayer, 302–303
swelling-burst cycle, 319–324
two-parameter model, 313–316
urea, 308, 329–331
vesicle deflation, 308
Pippard–Buckingham–Fairbank relations, 62–63
Plasma membrane (PM), 166
Plasmodium falciparum, 188
Poly(styrenesulfonate) (PSS), 201
Polyelectrolytes (PELs)
counterion distribution, 203–204, 205*f*
HAPs and, 232–233
mixed PEL-surfactant solutions (*see* Polyelectrolytes-surfactant complexes (PSCs))
NaCl effects, 203, 204*f*
polyions, 202–203, 203*f*
properties and functions, 200
PSS, 201

surfactants and (*see* Surfactants)
Polyelectrolytes-surfactant complexes (PSCs), 200
binding isotherms and CAC
C atoms number and, 211, 212*f*
CMC values and, 210, 210*t*
C_nPC surfactants, 212–213
DPC and CPC, 209–210, 209*f*
free energy change, 211
bound surfactant effects, 229–232
interactions, 208
polyion-induced micelles, 207–208
size
CPC and NaCl effects, 221–222
DNA, 222
hydrodynamic radii, 219–220, 220*f*
interpolyelectrolyte complexes, 221
redissolved complexes, 222–223
solubility
associative phase separation, 213–214
CPPSS, 215–216, 215*f*
CTAPSS, 213–214, 216, 217*f*
PEL-rich regime, 218
schematic representation, 214, 214*f*
simple salt addition, 218–219
structure
CTAPSS and CPPSS, 228, 229*f*
formation, 223–224
hexagonal closed-packed arrangement, 228
methods, 224
parameters, 226–227, 227*t*
SAXS, 224–226, 225*f*
scattering domains size, 226
Polymethylene-1-ω-bis-phosphocholines
chain length, 101–104, 102*f*, 103*f*
PC-C32-PC
CH_2 -stretching vibrational band, 98–99, 100*f*
DLS experiments and electron microscopy, 99–100, 101*f*
DSC curves, 98–99, 100*f*
SANS, 100–101, 101*f*
viscoelastic behavior, 98, 99*f*
Prion diseases, 187
Proteases
ADAMs and ADAMTSs, 253–254
matrix metalloproteinases, 251–253
metzincins, 250–251, 250*f*
PSCs. *See* Polyelectrolytes-surfactant complexes (PSCs)
PSM. *See* N-palmitoyl-d-sphingomyelin (PSM)

S

Saffman and Delbrück (SD) hydrodynamic screening length, 135
SANS data. *See* Small angle neutron scattering (SANS) data
SAXS. *See* Synchrotron small-angle X-ray scattering (SAXS)
Scaffolding rafts, 186
Secretases, 249
Serous ovarian carcinoma, 240–241, 242*f*
Shear surface viscosity, 5
Simian SV40 virus (SV40), 188
Single-chain bolaphospholipids
archaeal liposomes, 94
bipolar tetraether lipids, 94
hydrophobic effect, 94
PC-C32-PC/DPPC
calorimetric measurements, 122–123
chemical structure, 120
cryo-TEM image, 121, 122*f*
DSC curves, 121
transmembrane conformation, 123
polar phosphocholine/phosphodimethylethanolamine, 95–96
synthetic bolalipids, 94–95
temperature-dependent self-assembly
chain length, 101–104, 102*f*, 103*f*
chain structure (*see* Chain structure-dependent self assembly)
chemical structure, 96, 96*f*
fiber–micelle transition, 117–118
headgroup structure (*see* Headgroup structure-dependent self-assembly)
helical nanofibers and micellar aggregates (*see* Helical nanofibers and micellar aggregation)
hydrogel-forming systems, 119–120
lamellar lyotropic phases, 116–117
Me_2PE-C28/32-ME_2PE, 117–118, 118*f*

Single-chain bolaphospholipids (*Continued*)
PC-C32-PC/Me_2Pe-C32-Me_2PE, 119, 119*f*
physicochemical characteristics, 97
Small angle neutron scattering (SANS) data, 100–101, 101*f*
Soliton model
anesthesia and, 288
dispersion, 285–286
heat capacity profile, 284–285, 284*f*
vs. HH model
collision study, 291–294
combination of, 294–295
features, 289–290
longitudinal density pulse, 286, 287*f*
nonelectrical properties, 283–284
sound velocity, 285
Soliton propagation
mechanical pulse, 55–56
nonlinear function, 55
Taylor expansion, 54–55
unilamellar DPPC vesicles, 55, 56*f*
wave equation, 54–55
Spheroids, 244, 245*f*
Sphingomyelinase (SMase), 179
Stretching elasticity modulus, 6
influencing membrane permeability, 317–319
Surfactants
CMC, 206
composition, 205
CPP, 206–207
mixed PEL-surfactant solutions (*see* Polyelectrolytes (PELs))
types, 202
Swelling-burst cycle. *See* Phospholipid membrane permeability
Synchrotron small-angle X-ray scattering (SAXS), 224–226, 225*f*

T

Taylor expansion, 54–55
Tetraspanin, 257–258
Time-dependent Ginzburg–Landau model, 136–138
Tissue engineering
basolateral membrane, 87–88
glutaraldehyde, 87
regenerative medicine, 86–87
Tissue inhibitors of metalloproteases (TIMPs), 251–253
Transmembrane peptides
DOPC bilayers, 15–17
elasticity constant, 15–17
HIV FP FP23, 14–15, 16*f*
interleaflet interaction parameter, 15–17
Transporter rafts, 186
Triton X-100 (TX-100), 167–168, 174–175

U

Urinary bladder
calcium ions, 79–80
epithelial cells
fluorescein-isothiocyanate, 84–85, 85*f*
necrotic superficial cells, 83–84, 84*f*
urothelial desquamation, 83
urothelial plaques, 84
heparin, 81
moxifloxacin, 77–78, 78*f*
polysaccharide dispersion, 77–78
urothelium, permeability barrier, 78–79, 79*f*, 80*f*

V

Vesicle deformation
AC fields
Maxwell stress, 20
membrane tension and hydrodynamic force, 22
prolate-to-oblate transition, 19
gel-phase membranes, 27–29, 28*f*
Vesicle electrofusion, 35, 36*f*
fluid-phase vesicles, 35
fusion dynamics
ligand-mediated fusion, 37–38
membrane tension, 38–39
rescaled fusion neck diameter, 37, 38*f*, 39
stages, 37
gaint vesicle fusion
content-mixing reactions, 40

multidomain vesicle creation, 39–40, 40*f*
nanoparticle synthesis, 40, 41–42, 41*f*
quantum-dot-like CdS nanoparticles, 40–41
Vesicle electroporation
electrodeformation, fluid phase
edge tension, 26–27
ellipsoidal vesicle, 24–26, 25*f*
relaxation dynamics, 24–26
surface dilatational viscosity, 26
membrane edge tension measurement
DOPC membrane, 34–35
membrane resealing mechanisms, 33
egg PC vesicle, 33–34, 34*f*
pore closure process, 33–34
transmembrane potential and conditions, 18–19
Vesicle shedding
microvesicles
antigen identification, 256, 256*t*
immunological surveillance, 258–259
inflammation and, 259–260
optimal environment establishment, 257–258
role, 254–255, 255*f*
serum and miRNA analysis, 257
ovarian cancer (*see* Ovarian cancer)
Vibrio cholerae, 187